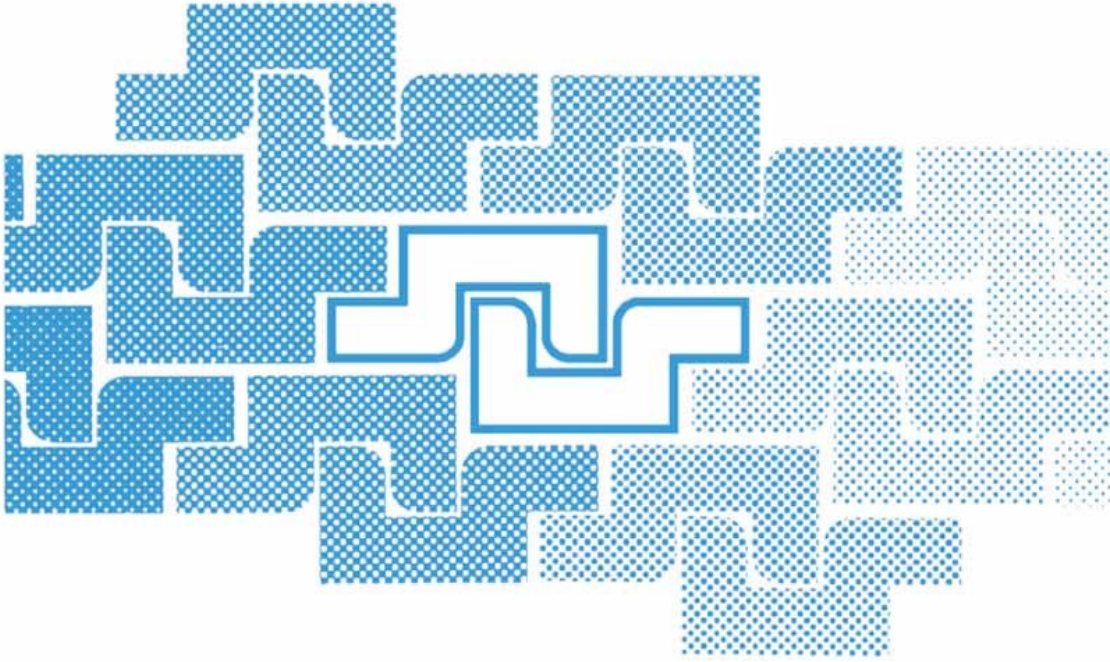

Spectroscopy of Emerging Materials

Edited by

Eric C. Faulques, Dale L. Perry and Andrei V. Yeremenko

NATO Science Series

II. Mathematics, Physics and Chemistry – Vol. 165

Spectroscopy of Emerging Materials

NATO Science Series

A Series presenting the results of scientific meetings supported under the NATO Science Programme.

The Series is published by IOS Press, Amsterdam, and Kluwer Academic Publishers in conjunction with the NATO Scientific Affairs Division

Sub-Series

I. Life and Behavioural Sciences	IOS Press
II. Mathematics, Physics and Chemistry	Kluwer Academic Publishers
III. Computer and Systems Science	IOS Press
IV. Earth and Environmental Sciences	Kluwer Academic Publishers
V. Science and Technology Policy	IOS Press

The NATO Science Series continues the series of books published formerly as the NATO ASI Series.

The NATO Science Programme offers support for collaboration in civil science between scientists of countries of the Euro-Atlantic Partnership Council. The types of scientific meeting generally supported are "Advanced Study Institutes" and "Advanced Research Workshops", although other types of meeting are supported from time to time. The NATO Science Series collects together the results of these meetings. The meetings are co-organized bij scientists from NATO countries and scientists from NATO's Partner countries – countries of the CIS and Central and Eastern Europe.

Advanced Study Institutes are high-level tutorial courses offering in-depth study of latest advances in a field.
Advanced Research Workshops are expert meetings aimed at critical assessment of a field, and identification of directions for future action.

As a consequence of the restructuring of the NATO Science Programme in 1999, the NATO Science Series has been re-organised and there are currently Five Sub-series as noted above. Please consult the following web sites for information on previous volumes published in the Series, as well as details of earlier Sub-series.

http://www.nato.int/science
http://www.wkap.nl
http://www.iospress.nl
http://www.wtv-books.de/nato-pco.htm

Series II: Mathematics, Physics and Chemistry – Vol. 165

Spectroscopy of Emerging Materials

edited by

Eric C. Faulques

Institut des Matériaux Jean Rouxel,
Nantes, France

Dale L. Perry

Lawrence Berkeley National Laboratory,
University of California,
Berkeley, CA, U.S.A.

and

Andrei V. Yeremenko

Verkin Institute for Low Temperature Physics & Engineering,
Kharkov, Ukraine

KLUWER ACADEMIC PUBLISHERS
NEW YORK, BOSTON, DORDRECHT, LONDON, MOSCOW

eBook ISBN: 1-4020-2396-0
Print ISBN: 1-4020-2394-4

Created in the United States of America

Visit Springer's eBookstore at: http://ebooks.kluweronline.com
and the Springer Global Website Online at: http://www.springeronline.com

CONTENTS


6

Preface

This book contains contributions from the NATO Advanced Research Workshop (ARW), "Frontiers in Spectroscopy of Emergent Materials: Recent Advances toward New Technologies," held 14-18 September, 2003, in the pleasant resort town of Sudak, Crimea, Ukraine.

The two main themes of the volume are spectroscopy and emerging materials, which by themselves encompass an enormous field of material science. Therefore, selection of highly relevant topics has been made, most of them having in common the investigations of emergent materials relevant to devices and applicative purposes. It should be noted that two specific talks of general interest were given, the first concerning the Science and Technology Center in Ukraine (STCU, Kyiv), presented by the STCU Executive Director, Dr.Y. Carmel. A second overview talk on advanced spectroscopic archaeometry was given by Dr. T. Calligaro of the Centre for Research and Restoration of the Museums of France (Louvre).

From the point of view of spectroscopy, it has seemed essential to us to include reviews of work using synchrotron and particle accelerator facilities. The spectroscopies exemplified in this volume are optical, electronic and magnetic: UV-visible absorption, Rayleigh scattering, photoluminescence, vibrational spectroscopy (Raman, infrared), magnetic resonance investigations (NMR, EPR), electron energy loss, extended X-ray absorption fine structure and X-ray absorption near edge strructure (EXAFS, XANES), optical tomography, time-resolved spectroscopy, and point-contact spectroscopy.

Materials studies presented during this meeting were also highly topical and focused on carbon and silicon nanomaterials including nanotubes, fullerenes, nanoclusters, metallic-superconducting phases, molecular materials, magnetic and charge-stripe oxides, biomaterials. Almost all currently emerging materials investigated worldwide were thus represented at this workshop.

In addition to the experimental aspects of the different types of materials, theoretical treatments also were discussed. These included the presentation of studies related to molecular vibrational dynamics, the problem of vibration-induced decay of electronic excited states, nanoscale spin-orbit coupling in two-dimensional silicon-based structures, and the growth of semiconductor clusters by combining both theoretical approaches with actual experimental data.

The aim of the workshop was indeed to bring together scientists from different areas of spectroscopy having various interests in emergent material studies so that they could discuss their research methods and techniques and

better learn the tools used by their colleagues. To that end, a quick poll showed that participants have benefited greatly from those discussions and exchanges. To the best of our knowledge, such conferences of general interest are rare and have not been organized before at previous NATO-sponsored workshops. The present event provided the opportunity for scientists to become more familiar with famous research institutions and their up-to-date research interests.

The year 2003 coincided with the 75th year of the Raman effect discovery. Thus, eight contributions dealing with this technique were presented at the workshop under various aspects: micro-Raman and surface enhanced Raman scattering, combined XAS-Raman studies, investigation of phonon and magnon scattering in oxides and carbon nanotubes. Raman spectroscopy has an intrinsic nano-specificity, since it probes the ionic-covalent bonds of materials and can be used to understand and predict physical properties of nanostructured objects. Also, its complementary technique, infrared spectroscopy, was not forgotten, among several papers, high resolution FTIR. The Verkin Institute for Low Temperature Physics and Engineering contributed papers to a very relevant technique, point-contact spectroscopy, which was discovered there.

A number of review papers are included in this volume on light scattering, light absorption, light emission, synchrotron spectroscopy, electron energy loss spectroscopy, nuclear magnetic resonance, and time-resolved spectroscopy, all of them featuring original research.

The key role of modern spectroscopic investigations in interdisciplinary materials science and engineering was discussed comprehensively within the scope of this workshop. This important field is shared by chemical, physical, geo- and bio- researchers and engineers, *et al*. Emerging materials topics were classified as (a) absolutely novel, recently synthesized compounds and new forms (ultrathin, nanostructured, etc.) of known materials, and (b) well-known materials with recently discovered exciting properties. With the development of user-friendly instrumentation, spectroscopy techniques, being an exciting subject for fundamental investigations, find increasing use for comprehensive research of emerging materials and further high-tech applications in various forms of controlled devices. Various spectroscopic instrumentation and measurements are indispensable for the continual advances in contemporary materials science as well as for progress in opto-, magneto-, and molecular electronics, magneto-optics and photonics. This includes, for example, the last generation synchrotron based techniques, ultrafast and high-resolution spectroscopy, etc. The organization of the NATO ARW meeting made it possible to bring together the experts working in adjacent scientific areas, emphasizing the multidisciplinary and international status of this meeting, cultivating an effective exchange among researchers from the various scientific and technological areas, resulting in

consequent benefits to the fields, and serving to forge new links between basic and applied research.

The workshop presentations and the informal, friendly atmosphere of Sudak enabled the participants to be active contributors in the numerous discussions. The ARW ended with a panel discussion in which the main issues of the talks and possible future developments in the field were discussed. The success of an ARW is very dependent upon the venue. In this respect Sudak, located in the beautiful Crimean peninsula of Ukraine, was an excellent choice as a location for holding the workshop. The organizers are convinced that as many personal contacts were established in the dining room and during the many informal meetings which occurred in the evenings as during the formal sessions.

Finally, the editors would like to thank the members of the organizing committee, Dr. D. Lockwood, and Prof. I. Yanson, as well as all the participants of the workshop for their production of excellent papers and talks and for their conscientious attendance through the entire workshop. The editors, as well as all of the participants in the ARW, extend their warm thanks to the gracious staff of the Sudak tourist-health complex for their help in making an event so pleasant. The editors also wish to thank Louise Perry for her editorial assistance with respect to the final preparation of the manuscripts.

Finally, this NATO ARW could not have taken place without financial support provided by the Scientific and Environmental Affairs Division of NATO. The support of Dr.F. Pedrazzini, Physical and Engineering Science and Technology Programme, is gratefully appreciated. The STCU, Ministry of Education and Science of Ukraine and Verkin Institute for Low Temperature Physics and Engineering are acknowledged for providing support to observer participants.

E. C. Faulques
D. L. Perry
A. V. Yeremenko

February, 2004

PROBING WORKS OF ART WITH PHOTONS AND CHARGED PARTICLES

Thomas Calligaro
Centre de Recherche et de Restauration des Musées de France, CNRS UMR-171, Palais du Louvre, 75041 Paris cedex 01, France. e-mail thomas.calligaro@culture.gouv.fr

Abstract: The Centre for research and restoration of the museums of France (C2RMF), located in the Louvre palace in Paris routinely uses advanced scientific methods for the study of objects of cultural heritage. Among these techniques, those based on photons or ion beams meet the harmless character required for the study of these invaluable artefacts. The first step of the investigation, namely the examination is advantageously achieved with X-ray, ultraviolet and infrared imaging. Secondly, chemical and structural characterization of materials constituting the objects are performed using a large panel of analytical methods. The chemical composition is delivered either by X-ray fluorescence or by ion beam methods such as particle induced X-ray emission (PIXE) and particle induced γ-ray emission (PIGE) with the 3-MeV proton beam produced by the AGLAE[1] electrostatic accelerator facility of the Centre. As far as the structure is concerned, it is obtained by X-ray diffraction or by μ-Raman spectrometry. These non destructive, non-invasive, rapid and sensitive analytical methods enable to answer three major issues in the field of Art and Archaeology: 1) identification of the material, 2) determination of the provenance and 3) study of surface modification (ageing, alteration). Selected case studies performed at the Centre illustrate the benefits of these methods. For instance, underlying compositions and artists' signatures are revealed by X-rays in painted masterpieces, while the gemstones mounted on Medieval jewels are characterized by PIXE and μ-Raman spectrometry. The provenance of the pyraldine garnets ($X_3Al_2Si_3O_{12}$, X=Fe, Mg, Mn) determined by the composition and by identification of microscopic inclusions yields an historical implication to the evolution of gems routes during the Dark ages. As a conclusion, new trends in the use of non-destructive techniques in Art and Archaeology are presented.

[1] AGLAE : Accélérateur Grand Louvre pour l'Analyse Elémentaire

Keywords: ion beam analysis, Raman spectrometry, archaeometry, PIXE, RBS, NRA, garnets

E. C. Faulques et al. (eds.), Spectroscopy of Emerging Materials, 1–13.

1. INTRODUCTION

Since 1932, the laboratory of the Centre for research and restoration of the museums of France has been studying works of cultural heritage [1]. A large set of modern techniques is currently applied to get a better insight on art objects as well as to contribute to their conservation and restoration. However these techniques have to meet drastic constraints due to the precious and sometime unique character of works of art. Consequently, non-destructive techniques and even those requiring no (or only minute) sampling, are preferred. Other features should be taken into account, such as the complex shapes and structures, the great variety of constituent materials quite often mixed, their possible alteration state susceptible to modify the chemical composition of the outer parts. These features generally require the development of a specific experimental approach, combining several techniques of examination and chemical analysis. In this context, methods based on the use of photons and charged particles to probe art objects and archaeological artefacts constitute one of the best choices, since they combine quite good analytical performances and non-destructiveness.

2. EXAMINATION TECHNIQUES

The main examination methods available at the Centre are photography under different wavelengths (direct and grazing light, ultraviolet and infrared radiations), radiography, electron emission radiography, β-radiography and infrared reflectography. Radiography provides several informations : concerning easel paintings, it permits to identify the nature of the supports, their assembling and any later modifications, and shows the successive phases of the creation (composition, *pentimenti*, restorations). For instance, as can be seen in Fig. 1, the radiography of the painting “L’homme blessé” by Gustave Courbet reveals two previous compositions : first, the profile of a lady wearing a dark headband, secondly, a man resting against a tree with the head of a woman over his shoulder.

Figure 1. The radiography of "L'homme blessé" by Gustave Courbet , 1844 – 1854, 815 x 975 mm, Musée d'Orsay, Paris reveals two previous compositions. Left figure: visible image, right figure : radiography.© C2RMF.

As to objects like stone or bronze statues, furniture, jewellery, pottery, ceramics or musical instruments, the radiography obtained with a high energy X-ray generator (420 kV) shows their internal structure. Electron emission radiography is used to obtain images when the target is too thick to be X-rayed or to increase the contrast of the X-ray image obtained from high Z targets, whereas β-radiography (using a ^{14}C extended radiosource) is widely used to image watermarks and fabrics. Infrared reflectography (λ = 1.8 to 2.0 μm) is mostly applied to investigate carbon-based underdrawings in easel paintings [2]. For example, the infrared reflectography image from "Saint Jérôme lisant" by Georges de La Tour in Fig. 2 reveals the hidden signature of the artist.

Figure 2. Infrared reflectography – detail of the inferior left corner of the painting "Saint Jérôme lisant" by Georges de La Tour, 1650, 952 x 725 mm, Musée historique lorrain, Nancy.- showing the hidden signature of the artist. © C2RMF.

3. ANALYTICAL TECHNIQUES FOR CULTURAL HERITAGE

Concerning art history, the main objective of applying methods originating from the physical sciences is to complement conventional typological approach and contribute to a better understanding of the technique of the artist through the identification of the raw materials used, the way they have been mixed, the treatments applied [3]. The data obtained constitute solid grounds for the authentication of a work or its attribution to an artist, a workshop, etc.

In the field of conservation-restoration, the knowledge of the chemical composition and particularly the elemental depth distribution, is essential for checking the state of conservation of the work and in some cases inferring the ageing mechanism by comparison with materials of similar composition submitted to accelerated ageing tests. Furthermore this kind of investigation can yield useful guidelines for choosing the proper restoration procedure.

In archaeology, the main purpose of analysis of artefacts is to contribute to a better understanding of the technical development in the remote past and to identify the sources of raw materials and the trade routes. It can also serve as an indirect dating by compositional similitude with well-dated objects.

3.1 Elemental analysis

Besides the classical tools for elemental analysis available at the centre such as SEM-EDX or ICP-AES, some analytical methods have been developed or adapted to meet the harmlessness requirements for the study of materials of cultural heritage: no sampling, no damage, no sample preparation nor dismounting. Among these techniques, it is worth mentioning two developments. First, a portable XRF system for *on the field* analysis (e.g. in museums or in archaeological excavations) was designed on the basis of a silicon-drift electrically cooled X-ray detector (5 mm^2, 142eV at 5.9keV, Röntec GmbH) and a lightweight X-ray generator (50 kV, 1 mA, Mo anode, Dr Warrikhoff GmbH) [4]. The combination of a tight geometry and a helium atmosphere surrounding the analysed area enables the measurement of all elements down to magnesium. X-ray spectra are acquired with a compact MCA and processed with a laptop computer (fundamental parameter method, X-spec32 program). A second and major development is the implantation in the Centre of an accelerator-based facility called AGLAE (Accélérateur Grand Louvre pour l'Analyse Élémentaire). Being until now the only one entirely dedicated to the study of cultural heritage [5], this

system permits the apply the vast panel of ion beam analytical techniques (IBA) to works of art and archaeological artifacts.

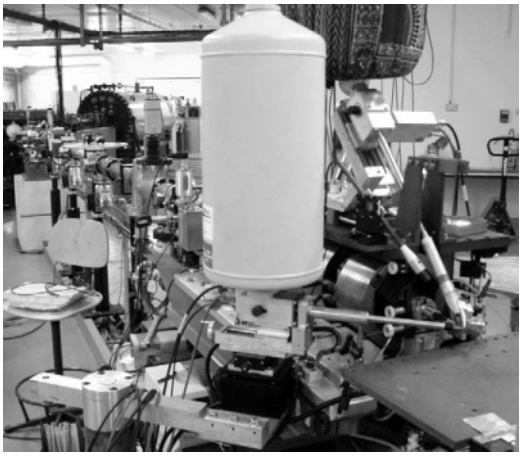

Figure 3 : View of the external nuclear microprobe beam line of the“AGLAE” accelerator. © C2RMF.

The IBA techniques are based on the interaction of light ions having and energy of a few MeV produced by a small particle accelerator with the materials of the sample. The characterization relies upon the measurement of the energy of various emitted products (X-rays, γ-rays or charged particles) resulting from this ion bombardment. The main IBA techniques and their features are the following [6]:

· *Particle-induced X-ray emission (PIXE)*. This method, which has a similar principle to X-ray fluorescence, is well suited to the determination of the bulk composition of the sample. PIXE allows the simultaneous measurement of all elements above sodium. Due to the low background produced by the PIXE process, the sensitivity can reach the µg/g level. Ideally, incident particles are 3-MeV protons [7].

· *Particle-induced γ-ray emission (PIGE)* is based on the emission of *γ-rays* resulting from nuclear reactions between in the incident ion and the nucleus of target atoms. As this process only happen on light target nuclei, the PIGE method usefully extends the PIXE bulk characterization to elements lighter that sodium, such as Be, B, or F. The incident particle are the same than for PIXE, i.e. 3-MeV protons.

· *Rutherford backscattering spectrometry (RBS)*, relies on the detection of ions of the beam elastically backscattered by target nuclei. Since the energy of the outgoing ion depends on its path inside the sample, all methods based on the detection of charged particle, including RBS, have intrinsic profiling capabilities. RBS is ideally suited for determination of layers of heavy elements on top of a substrate composed of lighter elements (case of guiding, glazes, etc.). The incident beam is usually He ions [8].

· *Nuclear reaction analysis (NRA)*. Based on the detection of charged particles emitted during nuclear reaction, NRA can be considered as an inelastic counterpart of RBS. NRA is useful in the reverse case as for RBS, namely the depth profiling light elements in a sample composed of heavy elements. (e.g. corroded layers on metallic samples containing O, C, and N). Incident ions are protons (^{1}H) or deuterons (^{2}H).

· *Elastic recoil detection analysis (ERDA)* is specifically used for the determination of hydrogen profile in samples. The incident beam is composed of He ions [9].

IBA techniques have most of the qualities required for the study of materials of cultural heritage, which can be summarized below. These techniques are:

1. non-destructive for most materials with the possible exception of some inorganic materials (paper, parchment) which could be sensitive to heating or radiation damage
2. quantitative with an accuracy generally better than 5%
3. multi-elemental including light elements down to hydrogen
4. very sensitive for at least one of them, PIXE which is well adapted to trace element determination; this high sensitivity permits to limit the irradiation dose necessary for getting a significant signal and thus to reduce the risk of damaging the objects by irradiation
5. complementary and can to be carried out simultaneously
6. able to yield information on the spatial distribution of elements (depth profile and mapping with a resolution down to the micrometer range)

One should however keep in mind the following limitations:

1. the analysis is limited to the outer layers of the material (up to several tens of micrometers) and thus can be irrelevant to the bulk

composition in case of surface alteration (corroded metals, hydrated glasses, for example)
2. no information is provided on the chemical state of elements

The features mentioned above show that IBA techniques and particularly PIXE, because of its high sensitivity, constitute an extremely useful tool for the knowledge and the preservation of cultural heritage. A decisive improvement has been achieved in developing an experimental set-up permitting the direct analysis of objects without sampling. This is carried out by means of a 20-µm diameter micro-beam extracted in air through an ultra-thin exit window, as shown in fig. 3 [10].

3.2 Structural analysis

Most of the routine work in structural analysis is performed with D5000 Siemens diffractometer equipped with a Gobel mirror and an energy-dispersive detector. Raman micro-spectrometry has been recently introduced with a Labram infinity spectrometer with two laser sources, fitted with a horizontal output adapted to the investigation of vertical items like paintings or statues. For the most fine structural investigations, experiments are conducted with EXAFS, XANES or diffraction lines from various synchrotron facilities (ESRF at Grenoble, BESSY at Berlin, LURE at Paris).

3.3 Dating

Two methods are available for the direct dating of items of art and archeology. First, thermo-luminescence dating is applied to objects that has been fired like ceramics. This method is based on the detection photons released during heating of a 100 mg sample taken from the item. This light emission results from the release of energy produced by natural radioactivity and stored during time in traps of the materials. Although hardly quantitative this method is routinely applied for the authentication of earthenware. The second method concerns the dating of organic samples by means of the measurement of ^{14}C content, a radioactive isotope of carbon decaying with life-time of 5700 years. When performed by accelerator-based mass spectrometry (AMS), the weight of the sample is very small, as it may vary from 5mg to 2g according to the conservation state of the object. The Center participates is involved in the installation and operation of a new AMS facility installed close to Paris.

4. EXAMPLE OF APPLICATION : THE ORIGIN OF ANCIENT GEMSTONES OF THE DARK AGES

The following example is a illustration of how photon and charged particles techniques like the micro-PIXE and micro-Raman spectrometry can be combined to solve an important archaeological issue, namely to unveil the intriguing provenance of the red gemstones mounted on barbarian jewels from the early Middle-Ages [11].

The Germanic peoples who settled in Western Europe at the fall of the Roman Empire and have established the geopolitical grounds of modern Europe have also introduced a very specific type of jewels named *"Cloisonné"*. The main gemstones used in these jewels are red garnets cut in thin slices (<1mm) which were inserted in a honeycomb metallic structure, as shown in fig. 4. The determination of the provenance of these garnets is an important issue, particularly if we consider the huge quantity of gems necessary to make these artefacts, which were not re-used but buried in tombs according to the Barbarian custom.

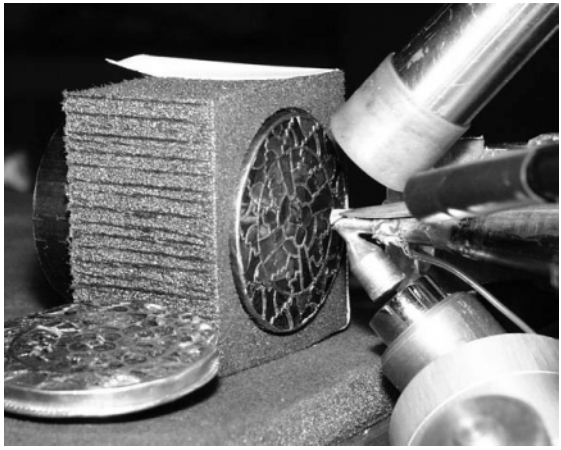

Figure 4. Brooch of the Frankish queen *Aregonde* with garnets set in "cloisonné" style placed in the external beam of the AGLAE accelerator

Approximately 1000 garnets set on jewels excavated in the necropolis of the Saint-Denis basilica, near Paris, have been investigated. The artefacts span the entire Merovingian period (5^{th}-7^{th} c. AD.) and comprise the famous jewels of the Frankish queen *Aregonde* exhibited in the Louvre museum [12]. From a mineralogical point of view, natural garnets usually have a complex composition. The most common type of garnet is the pyraldine

family of chemical formula $X_3Al_2(SiO_4)_3$, where X can be a divalent ion like Fe (almandine), Mg (pyrope) or Mn (spessartite), each combination being called an *end-member*. The situation is actually more complex as natural garnets are a solid solution of end-members in variable proportion. Because garnets are relatively widespread and their composition is highly variable, it was necessary to cross many criteria to determine their origin. The first criterion is the composition; which was determined by external beam PIXE for major constituents (Mg, Al, Si, Ca, Mn, Fe) and trace elements (Ti, V, Cr, Y). As shown in fig. 5, three groups of garnets were identified. Most garnets belong to the first group (almandine, Fe-rich). The second group (one jewel) consists of intermediate almandine-pyrope garnets sometimes called "rhodolite". The third group comprises pyrope garnets (Mg-rich).

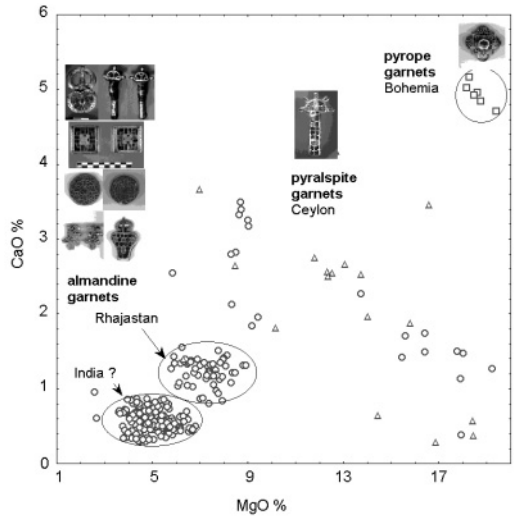

Figure 5. The CaO vs MgO plot for garnets from various jewels shows 4 provenances: *pyropes* from Bohemia, *rhodolites* from Ceylon and two sources of *almandine* in India

The trace elements content and slight differences in major composition permit to split these three groups in five different sources: two sources of pyrope garnets (with and without chromium) and two sources for almandine garnets (distinctive calcium, magnesium and yttrium contents).

Comparison with the composition of natural garnets published in the literature suggests that almandine garnets observed on archaeological jewels have been mined from India while "rhodolite" garnets may have been imported from Ceylon (Sri Lanka). The sources of pyrope garnets likely correspond to the Bohemian deposits (Czech republic).

The second provenance criterion is based on the identification of inclusions in gemstones. Micro-Raman spectrometry was used for this task in almandine garnets. Various inclusions were observed like apatite, zircon, monazite, calcite, and quartz and two of them, curved needles of sillimanite (Al_2SiO_5) and 10-µm metamict radioactive crystals, were specifically found in archaeological garnets. Fig. 6 shows the Raman spectra of a sillimanite needle, which is a mineral formed under a high temperature and high pressure metamorphism.

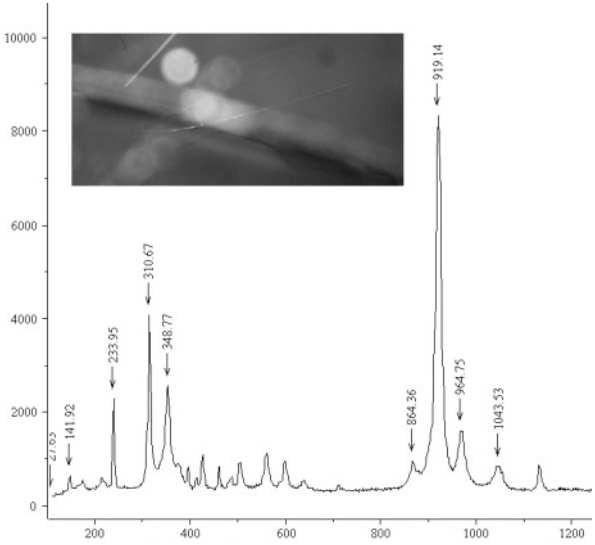

Figure 6. Raman spectrum of a *sillimanite* elongated and curved inclusion indicating a high Pressure-Temperature metamorphism of the crystal

The radioactive crystal was analyzed by PIXE with an external micro-beam of 20 µm diameter. As can be seen in Fig. 7, uranium and lead were found as the major constituents of this inclusion. As the Pb content is attributed to the radioactive decay of ^{235}U and ^{238}U (0.7 and 4.46 billion-year half live, respectively), this inclusion can be used as a geochronometer. The Pb/U ratio gives a crystal formation age ranging between 1 to 1.5 billion years. To sum it up, the almandine composition of the garnets, the presence of sillimanite and the very ancient age of the crystal converge towards highly metamorphised rocks of the Precambrian period. One of the only parts of earth's crust remaining from that period exhibiting these specific mineralogical features is a metamorphic belt located in India, a region presenting garnets deposits of gem quality. This confirms the Indian origin

of most of the garnets used in Barbarian jewellery, a witness of a gem route between Asia and Western Europe during the Dark Ages.

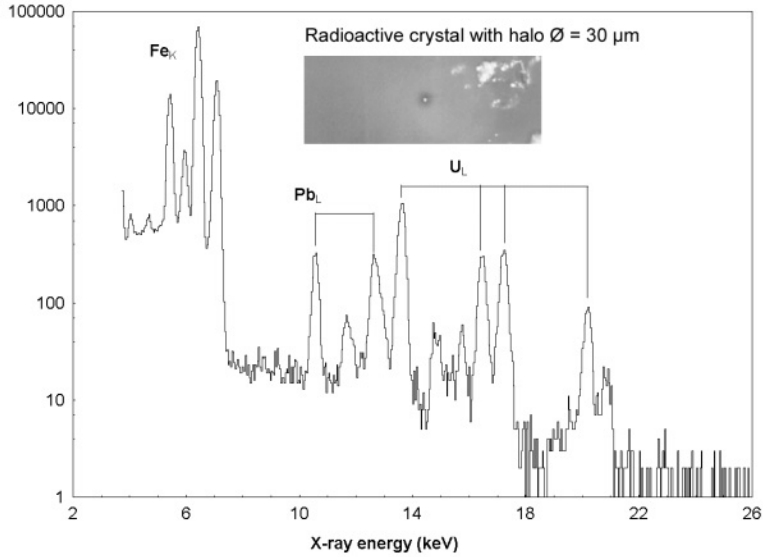

Figure 7. PIXE spectrum of a *radioactive* inclusion. The relative uranium and lead contents yields an approximate crystal age of 1.5 Ga.

The presence of pyrope garnets from Bohemia might also have a historical significance. Pyrope garnets only appear in jewels dated after the end of the 7th century; this indicates that starting from that period Merovingians had to use European garnets instead of Indian ones. This major change in gem supply is likely a consequence of the closing of the garnet route to India, due to the invasion of the Arabic peninsula by the Sassanids at the end of the 6th century, a troubled period announcing the rise of Islam.

5. CONCLUSIONS AND PERSPECTIVES

Thanks to their outstanding analytical capability and their non-destructive character, analytical techniques based on the use of photons and ions have proved their usefulness for the study of works of art and archaeology.

Photon-based imaging techniques provide invaluable information for the examination of works of cultural heritage. Concerning the determination of the composition, methods like X-ray fluorescence or ion beam methods

provided by small accelerators, thanks to the development of external beam set-ups, permits a direct in-air analysis, thus avoiding taking off even minute samples from precious items or even putting them inside a vacuum chamber, a potentially detrimental operation. Among the numerous IBA methods, the PIXE technique, often combined with PIGE, is the most widely spread technique in this field, due to its high sensitivity and ease of implementation in air. It can be used either for the quick identification of materials via the detection of major elements, or for provenance determination using the trace element content. However, as PIXE hardly provides depth information, much effort has been made to associate it charged particle spectrometry such as RBS and/or NRA, two methods which can yield elemental depth profiles particularly useful for inferring the conservation state of artefacts and alteration mechanisms. In addition, the use of ultra-thin exit windows, permits to extract micro-beams with a size as low as 10 μm and to obtain elemental micro-maps with lateral resolution of about the same value, but with the possibility to scan large areas up to 100x100 mm [13]. In spite of these qualities, IBA techniques are not a panacea, especially because they do not provide any information on either the structure of materials or the chemical state of constituent elements. It is frequently needed to rely on complementary techniques such as X-ray diffraction or Raman spectrometry. The latter is gaining a growing popularity in the field of cultural heritage, due to the development of portable instruments and the wealth of information it yields. Moreover IBA techniques necessitate the access to medium scale facilities ordinarily not situated close to museums. In the mean time, XRF portable systems have been developed which to some extent can be a satisfactory alternative to IBA. On the other hand, analytical methods based on large scale facilities like synchrotron rings, are increasingly applied, specially to gain structural information by X-ray absorption spectrometry such as EXAFS or XANES.

ACKNOWLEDGEMENTS

We wish to thank the members of the AGLAE group of the C2RMF: J. Salomon, L. Pichon, B. Moignard. The author is deeply indebted to Dr J.-C. Dran for many suggestions and highlighting comments. We acknowledge the support of organizing committee of the NATO Advanced Research Workshop in Ukraine, specially Dr Yeremeko and Dr Faulques.

REFERENCES

[1] Didier Dubrana, Histoire secrète des chefs-d'œuvre, éditions SPE- Barthelemy, 2001.
See also http://www.c2rmf.fr
[2] Technè 2, "Autoportrait d'un laboratoire, le Laboratoire de recherche des musées de France", 1995, Réunion des Musées Nationaux eds, Paris.
[3] Technè 13/14 : "Découvrir Transmettre", 2001, Réunion des Musées Nationaux eds, Paris.
[4] T. Calligaro, J.-C. Dran, M. Klein, Nucl. Instr. and Meth. A504 (2003) 213
[5] M. Menu, Nucl. Instr. and Meth. B45 (1990) 597.
[6] J.R. Bird, R.A Brown, D.D. Cohen and J.S. Williams, "Ion Beams for Material Analysis", eds J.R. Bird and J.S. Williams, Academic Press, Sidney, 1989
[7] J.C. Dran, T. Calligaro, J. Salomon, "Particle induced X-ray emission" In "Modern Analytical Methods in Art and Archaeology",. E. Ciliberto and G. Spoto eds, John Wiley and Sons, New York 2000.
[8] W.-K. Chu, J.W. Mayer, M.A. Nicolet, "Backscattering Spectrometry", Academic Press, Boston, 1978.
[9] T. Calligaro, J. Castaing, J.-C. Dran, B. Moignard, J.-C. Pivin, G.V.R. Prasad, J. Salomon, P. Walter, Nucl. Instr. and Meth. B181 (2001) 180
[10] T. Calligaro, J.-C. Dran, E. Ioannidou, B. Moignard, L. Pichon, J. Salomon, Nucl. Instr. and Meth. B161 (2000) 180
[11] T. Calligaro, S. Colinart, J.-P. Poirot, C. Sudres, Nucl. Instr. and Meth. B189 (2002) 320.
[12] Fleury, M., France-Lanord, A, 1998. "Les trésors mérovingiens de la basilique de Saint-Denis", Gérard Klopp eds, Woippy, France, 1998
[13] T. Calligaro, J.-C. Dran, B. Moignard, L. Pichon, J. Salomon, P. Walter, Nucl. Instr. and Meth. B188 (2002) 135

APPLICATIONS OF X-RAY ABSORPTION SPECTROSCOPY IN MATERIALS SCIENCE

V. Briois (1), Ch. Giorgetti (1), F. Baudelet (1), A. M. Flank (1), M. S. Tokumoto (2), S. H. Pulcinelli (2) and C. V. Santilli (2)
(1) LURE, Centre Universitaire Paris-Sud, BP 34, 91898 Orsay, France and (2) UNESP, Instituto de Quimica, CP 355, 14800-900 Araraquara-SP, Brazil

Abstract: Short-range order information around a given atom obtained by the EXAFS (Extended X-ray Absorption Fine Structure) technique, concerning nanocrystalline materials, is reviewed. The potentialities of the technique to characterise bulk materials, thin films, and structural evolution during the preparation of nanoparticles using *in situ* set-ups are presented.

Key words: Synchrotron Radiation, X-ray absorption spectroscopy, EXAFS, nanocrystalline materials

1. INTRODUCTION

A non exhaustive description of the history of X-ray Absorption Spectroscopy (XAS) can be found in Ref. 1. The modern EXAFS (Extended X-ray Absorption Fine Structure) technique began in the early seventies of the last century. It corresponds to the concomitance of both theoretical and experimental developments. Between 1969 and 1975, Stern, Sayers and Lytle succeeded in interpreting theoretically the X-ray Absorption Structures observed above an absorption edge [2], while during the same period, the advent of synchrotron radiation (SR) sources reduced drastically the acquisition time of a spectrum if compared to data obtained with conventional X-ray tubes. XAS provides essential information about the local atomic geometry and the electronic and chemical state of a specific atom, for almost any element of the periodic table ($Z \geq 5$). This prime tool for

E. C. Faulques et al. (eds.), Spectroscopy of Emerging Materials, 15–30.

materials science has benefited from almost all the exceptional properties of SR, such as the continuous range of energy, high degree of photon polarizations, and high brilliance (which corresponds to the number of photons emitted per unit source area per second per unit solid angle).

In the first section will be presented XAS from the physical principles to data analysis and measurements. Then section 2 will be devoted to a discussion of a few examples to illustrate the power and limitations of XAS for gaining structural information. Examples are focused on EXAFS studies on nanocrystalline materials. Detailed reviews for applications on other fields of materials science or for presenting the complementary information available by the study of the X-ray Absorption Near Edge Structure (XANES) part of the X-ray absorption spectrum can be found in a number of books [3-5]. A brief overview of the recent development of the technique regarding the use of X-ray microbeams available on the third generation light sources will be finally presented in the last section.

1.1 Basic Principles of XAS

XAS refers to the measurement of the variation of the linear absorption coefficient, μ, as a function of the energy E of the incident photons. In a transmission experiment, the absorption coefficient of a sample of thickness x is related to the intensities of the incident (I_0) and transmitted (I) beams through the Beer-Lambert's law: $I = I_0 \exp(-\mu x)$. The X-ray absorption spectrum is typically plotted as μx *vs* E as shown in Figure 1.

The physical process underlying XAS is the excitation of a core electron, called photoelectron, towards empty states when X-ray photons are absorbed by the matter. When the photon energy E is equal to the binding energy E_0 of a core electron of a given species, an abrupt increase in the absorption coefficient, called the absorption edge, is observed corresponding to the ejection of the photoelectron (1s for a K edge, 2p for $L_{2,3}$ edges...). This absorption follows the dipolar electric selection rules. For $E>E_0$, the photoelectron is ejected towards the continuum states with a kinetic energy $E_c = E - E_0$. Due to the particle-wave dualism, this photoelectron may be viewed as an outgoing wave originating from the absorbing atom with a wavevector given by

$$\hbar k = (2m_e E_c)^{1/2} \qquad (1)$$

where m_e is the electron mass.

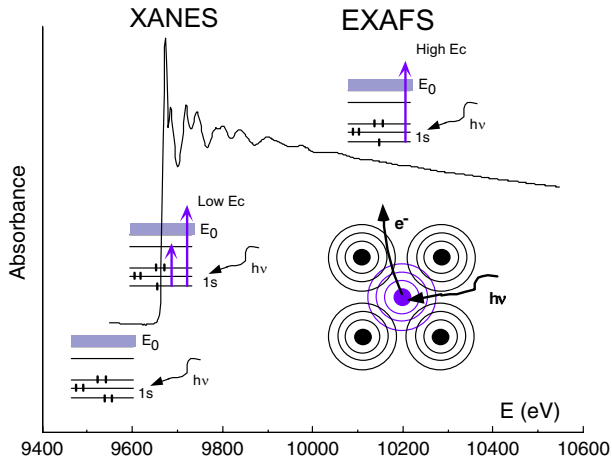

Figure 1. Typical X-ray absorption spectrum, μx = Ln(I_0/I) *vs* E (in electron Volt) recorded for a crystalline ZnO reference at the Zn K edge (E_0 ≈ 9659 eV). A two dimensional model of the XAS process is presented.

The photoelectron can be involved in scattering processes with the surrounding atoms. Two scattering regimes are distinguished according to the E_c value. At high kinetic energy, the mean free path of the photoelectron is of about 10 Å. Therefore the photoelectron will be mainly involved in single scattering processes with the first or second nearest neighbours. Here the modulation in the absorption coefficient is substantially due to constructive or destructive interferences of the outgoing photoelectron wave issued from the absorbing atom with the backscattered wave from each surrounding atom. The single scattering regime determines the EXAFS spectrum ranging from 50 to 1000 eV above the edge. On the contrary, at low kinetic energy, the photoelectron mean free path is longer. This photoelectron will be scattered by atoms located at longer distances or scattered many times by the close neighbours. The part of the spectrum, ranging from some eV below the edge to about 50 eV above the edge, consisting of the preedge, edge regions, and multiple scattering regime is called XANES spectrum. It can be used to extract electronic (e.g. spin and oxidation states) and stereochemical information about the selected absorbing atom.

1.2 EXAFS data processing

There are two primary tasks in data analysis: first, to extract the EXAFS function, χ(k), from the μx *vs* E data, second to determine the structural

parameters of interest from this function. The first point will not be discussed herein but can be found in specialized books [3, 6].

In the classical framework of single scattering (SS), the EXAFS signal, $\chi(k)$, is related to the sum of sinusoidal oscillations for each shell of neighbours around the absorbing atom :

$$\chi(k)=\sum_j S_0^2 N_j A_j(\pi,k)/(kR_{ij}^2).\exp(-2\sigma_j^2 k^2).\exp(-2R_{ij}/\lambda(k)) \\ .p_j(\varepsilon).\sin(2kR_{ij}+\Phi_{ij}(k)) \quad (2)$$

where N_j is the number of atoms in the j^{th} scattering shell at distance R_{ij} from the absorbing atom i, σ_j is the Debye-Waller factor which takes into account thermal and static disorders inside the j^{th} shell, $\lambda(k)$ is the photoelectron mean free path, S_0^2 is an amplitude reduction factor reflecting multi-electron effects, $A_j(\pi,k)$ is the backscattering amplitude function relative to the j^{th} shell and Φ_{ij} (k) is the phase shift relative to the absorbing i and neighbour j pair. Finally $p_j(\varepsilon)$ accounts for the possible polarization of the incident radiation. The phase shift correction is not large and is predominantly linear in k. Therefore a Fourier transform (FT) of the weighted $k^n.\chi(k)$ EXAFS spectrum (where n is an integer from 1 to 3) will provide a pseudo-radial distribution function, in which the different peaks correspond to the contributions of atoms located at each scattering distance, R_{ij} - α. The factor α is due to the phase shift term not included in the Fourier transform. The EXAFS spectrum of the crystalline ZnO reference and its corresponding FT are shown in Figure 2.

A back Fourier transform on individual peak can be then applied to isolate individual contributions. The so-obtained filtered EXAFS signal is analyzed in order to determine the related structural parameters N, R and σ. A common method consists to build a theoretical model from the relation (2) using known electronic parameters for $\lambda(k)$, S_0^2, $A_j(\pi,k)$ and Φ_{ij} (k), and, by treating N, R, and σ as free parameters, to minimize the difference between the theoretical and experimental curves. The electronic parameters can be evaluated from EXAFS signals recorded for references of known structures or from theoretical calculations using the efficient *ab initio* FeFF codes [7, 8].

It is noteworthy that the theoretical developments incorporated into the FeFF codes have led to go beyond the single scattering approximation supposed by the expression (2). High order multiple scattering (MS) events, generally neglected in the past making results beyond the first coordination shell often unreliable, can be now efficiently and accurately treated to calculate EXAFS spectra as illustrated in Figure 2 for an isotropic ZnO crystalline reference.

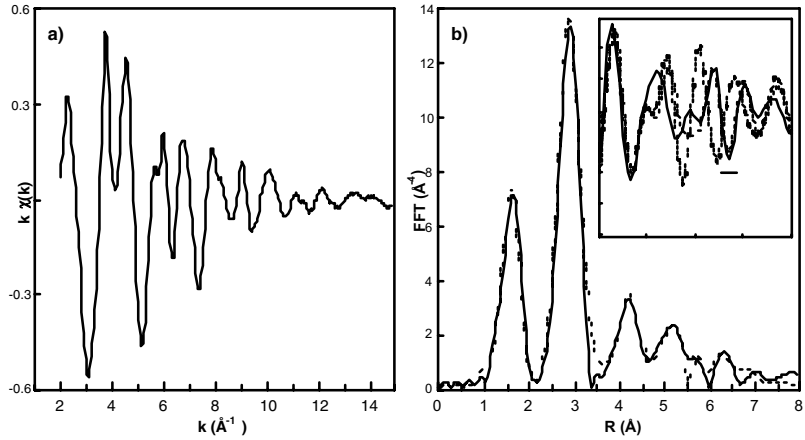

Figure 2. a) kχ(k) EXAFS spectrum and b) corresponding FT (solid line) of the weighted $k^3\chi(k)$ EXAFS spectrum for isotropic crystalline ZnO. The dashed line is a multiple scattering calculation using the FeFF6 code. The structural input for this calculation is the crystalline structure of ZnO, no parameters were adjusted, except the Debye-Waller factors. In the insert of b) is reported a comparison between the imaginary parts of the FT for the experiment and for SS and MS calculations in the region in which the SS calculation fails in reproducing the experimental results.

The accuracy of structural parameters extracted from EXAFS depends on many factors such as the disorder, the extension of the experimental spectra and quality of these data. Typical accuracies for the determination of parameters are 1% for interatomic distances, 15% for the coordination numbers and 20% for Debye-Waller factors [6]. But, in a situation more complex where several shells must be fitted simultaneously, one must be satisfied with much less accurate results.

1.3 EXAFS measurements

In concentrated systems obtained in a thin uniform shape, the simplest way to record X-ray absorption data is the transmission mode in which the incident and transmitted photons are directly measured by means of ionisation chambers. However, in dilute systems or for surface characterisations, data are usually recorded using secondary effects resulting from the creation of the core hole during the absorption process and from its subsequent relaxation by radiative or non-radiative decays. These processes are the X-ray fluorescence emission and the total electron yield (TEY) emission, respectively. In these detection modes, the linear absorption coefficient is proportional to the ratio of the fluorescence or TEY intensity to

incident radiation intensity. The EXAFS data presented in Section 2 were recorded at LURE, the French synchrotron radiation laboratory, using the DCI storage ring (1.85 GeV and 300 mA) at the D44 set-up or at the energy-dispersive D11 [9] station.

2. SPECIFICITIES OF XAS AND APPLICATIONS

2.1 XAS is an element-specific technique

Since the binding energy of a given core electron depends on the atomic number of the absorbing atom, XAS is an element-selective technique. By recording EXAFS spectra at one edge of each atomic species in a material, one can obtain complementary and often unique information on the local arrangement around each element. The atomic species under study can be at concentration ranging from a few ppm to the pure element. Thus EXAFS technique can be applied to systems like dopant in matrixes by studying both the main component of the matrix and the dopant [10-14]. The atomic specificity is illustrated herein with the study of the cationic order of [Zn-Cr-Cl] and [Cu-Cr-Cl] Layered Double Hydroxyde (LDH) compounds [15].

LDHs, which belong to the clay family, present several and various applications in different fields, such as catalysis or medicine. The general formula for these compounds is $[M_{1-x}^{II}M_x^{III}(OH)_2]^+.A_x^-.nH_2O$ (labelled $[M^{II}$-M^{III}-A]) where the Ms are divalent and trivalent cations and A is an anion. LDH is composed of infinite sheets of positively charged brucite-type $Mg(OH)_2$, where trivalent cations have replaced a fraction x of divalent cations in octahedral coordination. The interlamellar space is occupied by anions, keeping the electroneutrality of the structure, and completed by water molecules.

Cationic order in most LDHs is proposed by several authors [16, 17] but not demonstrated. LDHs are generally prepared by coprecipitation method by mixing solutions of trivalent and divalent salts at controlled pH. Among all LDHs, the [Zn-Cr-Cl] compound is a good candidate for cationic ordering due to its particularity to be synthesized only with the ratio Zn/Cr=2, whatever the proportion of di- and trivalent cations in the starting solutions. In this case the cationic order within sheets of the LDH is based on six divalent cations around trivalent metals, and three divalent and three trivalent cations around divalent metals [17]. Unfortunately X-Ray Diffraction (XRD) does not evidence superstructure reflections and the low electronic contrast between Zn (Z=30) and Cr (Z=24) backscattering atoms does not allow EXAFS to discriminate between models with cationic ordering and the other

without ordering. As an evidence, you can note in Figure 3 that the FT recorded at the Cr and Zn K edges for [Zn-Cr-Cl] present a very similar shape. Note that the difficulty in EXAFS to distinguish backscattering atoms with close atomic number is an intrinsic limitation of the technique.

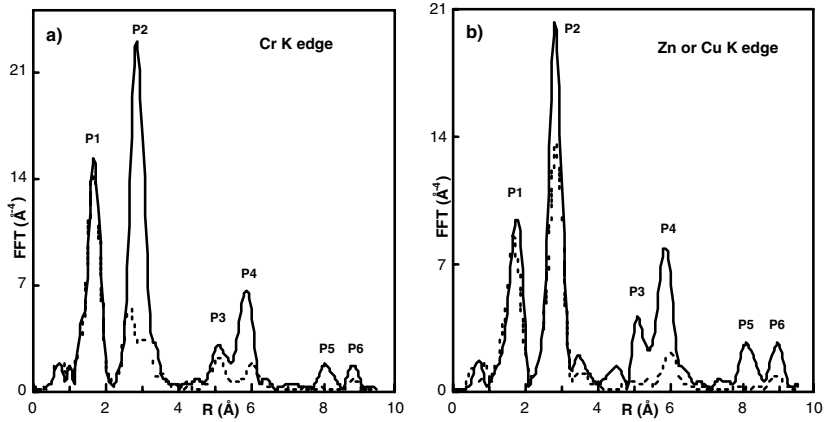

Figure 3. FT of the EXAFS $k^3\chi(k)$ spectra for [Zn-Cr-Cl] (solid lines) and [Cu-Cr-Cl] (dashed lines) a) at the Cr K edge and b) at the Zn or Cu K edges.

Interestingly, and although the electronic constrast between Cu and Cr is of the same order of magnitude than those for Zn and Cr, the peaks of the FT of [Cu-Cr-Cl] prepared also with the ratio Cu/Cr=2 display strong differences in shape and intensity above the first coordination shell (peak P1). This is due to the Jahn-Teller distorsion suffered by Cu, which induces a significant structural "contrast" between both cations. Indeed, quantitative simulations based on least square fitting procedure show that [Cu-Cr-Cl] is based on regular CrO_6 (d(Cr-O) = 1.98 Å) and distorted CuO_6 (d(Cu-O) = 1.97 and 2.31 Å) octahedra. On the other hand, the distribution of cations as second neighbours (Peak P2) at the Cu K edge presenting the best reliability factor in the fitting procedure is fully in agreement with the ordered model of cations within the sheets.

Local description of the arrangement around cations concludes unambiguously for [Cu-Cr-Cl] in a cationic ordering. The evidence of similar ordering for [Zn-Cr-Cl] was only obtained by a combined EXAFS and UV-Vis study of the formation of this LDH in solution [18]. The structural pathway so-reported involves the heterocondensation between hexa-aquo zinc(II) complexes and deprotonated chromium monomers.

2.2 Polarization Dependent XAS study on thin films

Synchrotron radiation produced by a bending magnet is linearly polarized in the orbit plane of electrons (or positrons) and actually the term $p_j(\varepsilon)$ of polarization dependence in formula (2) is equal to $3<\cos^2\theta>$ for K edges where

$$<\cos^2\theta> = 1/N_j \sum_h \cos^2\theta_h \quad (3).$$

The angle θ_h is the angle between the X-ray polarization direction, **ε**, and the direction to the atom h in the j shell. For isotropic materials, like powders, the sum becomes $N_j/3$. For thin films like heteroepitaxial metallic films [19], there is often an intrinsic asymmetry leading to different in-plane and out-of-plane bonds. Otherwise, the polarization dependence of EXAFS can be also an important tool for studying texturized films providing an alternative probe to the long range order technique such as diffraction when XRD diffraction is dominated by that from the substrate.

Such polarized EXAFS measurements were carried out to study the structure of undoped and indium doped ZnO thin films prepared by the pyrosol process [11, 20]. Such films are promising materials as gas sensors, ultrasonic oscillators, piezoelectric transducers, and transparent electrodes in solar cells.

In Figure 4 a) is presented the polarized Zn K edge EXAFS measurements for undoped and 5 at. % In-doped ZnO films. The orientation of films with respect to the X-ray beam is also schematically displayed in Fig. 4 a). Normal incidence data were obtained with the X-ray polarization nearly perpendicular (10° of deviation) to the surface whereas the grazing incidence data were recorded with the X-ray polarization lying in the surface plane. On one hand, strong polarization dependence affects the peaks located in the FT above the first three peaks (R > 4.5 Å), suggesting an anisotropic growth of ZnO. On the other hand, the 5 at. % In-doped ZnO films is clearly more anisotropic than the undoped ZnO films. Such anisotropy was simulated using *ab initio* FeFF6 calculations in which the linear polarization of the X-rays has been taken into account, as shown in Figure 4 b). A satisfactorily reproduction of the polarization-dependent measurements is obtained by considering for normal incidence **ε** parallel to the [101] ZnO direction and for grazing incidence **ε** parallel to the [010] ZnO direction. Then this indicates that the normal to the film surface lies in the (xz) plane where vectors **x**, **y** and **z** defined the orthorombic referential such as **x**.**a** = cos30°, **y**=**b** and **z**=**c**. In other words, a preferential orientation along the *c*-axis, slightly tilted with respect to the film surface, is responsible for the polarization dependence of the EXAFS measurements.

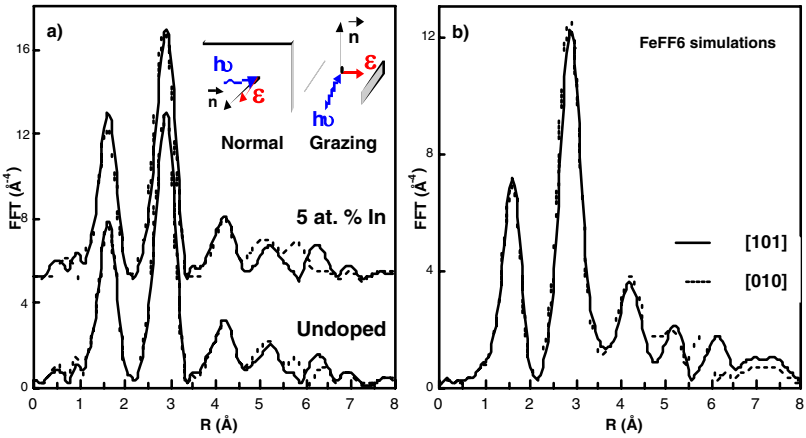

Figure 4. a) FT of the polarized Zn K-edge EXAFS $k^3\chi(k)$ spectra for undoped and indium doped ZnO films at normal (full line) and grazing (dashed line) incident angles. b) Polarized FeFF6 simulations with the X-ray polarization vector parallel to the [101] direction (full line) and to the [010] direction (dashed line).

The motivation of this study was to establish a relationship between the structure of the films and their electrical and optical characteristics, which strongly depend on the indium concentration [11, 20]. The conclusion of this study is clearly beyond the scope of this review. But the polarized EXAFS study has clearly evidenced that the indium doping affects the grain growth process by increasing the surface anisotropy of films. Finally this example shows that we have powerful experimental but also theoretical tools to study surfaces or oriented systems.

2.3 Time-Resolved XAS study of the formation of ZnO nanoparticles

The high intensity of photons delivered by synchrotron sources was essential for reducing data time collection and so providing time-resolved studies of dynamic processes, like phase transitions [21] or catalysis reactions [22]. Indeed XAS, unlike XRD, does not rely on long-range crystalline order and can be used to study local structure in gaseous states, liquids and amorphous or crystalline solids. An example of time-resolved study is given in this section with the investigation of the formation of ZnO nanoparticles from solutions.

The control of the size of nanoparticles is of prime importance on the optimisation of the properties of the final materials. For chemical preparation

routes involving hydrolysis-condensation processes, this task can be achieved by XAS investigation of the structure of the different building blocks during the solid-state growth, as reported for Ce [23], Cr and Zn [18], Ga [24] or Ni [25] cations. An emergent perspective for time-resolved studies is the possibilities of combining several experimental techniques simultaneously so that vibrational, electronic or themodynamic information can be obtained with the structural features provided by XAS. This has been recently illustrated with the combination of XAS with Raman spectroscopy, UV-Vis spectroscopy or Differential Scanning Calorimetry [26]. Such approach presents clearly several advantages compared to separate experiments: firstly it permits to totally eliminate artefacts due to sample history and environment, second it is the unique way to accurately determine the order of occurrence of physical and chemical events in time-resolved experiments.

Since a quantum confinement phenomenon by excitons for particles smaller than 7 nm exists, ZnO nanoparticles are promising materials in many technologies, such as solar energy conversion or optoelectronic devices. Such exciton levels around 300-360 nm can be well evidenced by UV-Vis spectroscopy, allowing an easy determination of particle sizes [27]. Kinetics of formation of ZnO nanoparticles were recently investigated by combining UV-Vis spectroscopy with energy-dispersive EXAFS measurements at the Zn K edge. Energy-dispersive XAS set-up allows the fast and simultaneous full spectral collection of EXAFS data over about 1000 eV above the absorption edge. For the experiments presented herein, the time framing is of 140 ms. 100 frames must be added in order to improve the signal to noise ratio, leading finally to a data collection of 1 min per spectrum. Concomitantly a scanning rate of 600 nm/min was chosen for recording the UV-Vis spectra from 220 to 820 nm using a Varian Cary 50 apparatus equipped with a fiber optic coupler.

Nanosized ZnO particles are prepared by hydrolysis-condensation at moderate temperature (from 20 to 70°C) [27-29] of zinc-acetate precursors [30] in ethanolic medium. Besides the determination of local order around Zn and of the particle sizes during the nanosized ZnO preparation, the motivation of the combined investigation was also to clarify the occurrence of a Zn-based hydroxy double salt phase, $Zn_5(OH)_8(OCOCH_3)_2.2H_2O$ (labeled hereafter Zn-HDS) observed as final solid mixed with ZnO and zinc acetate phases [29]. In particular, we were interested in determining whether the formation of the Zn-HDS phase was concomitant to the ZnO formation or arose from the reaction of ZnO with zinc acetate precursors during ageing of the colloidal suspension before extraction of solids.

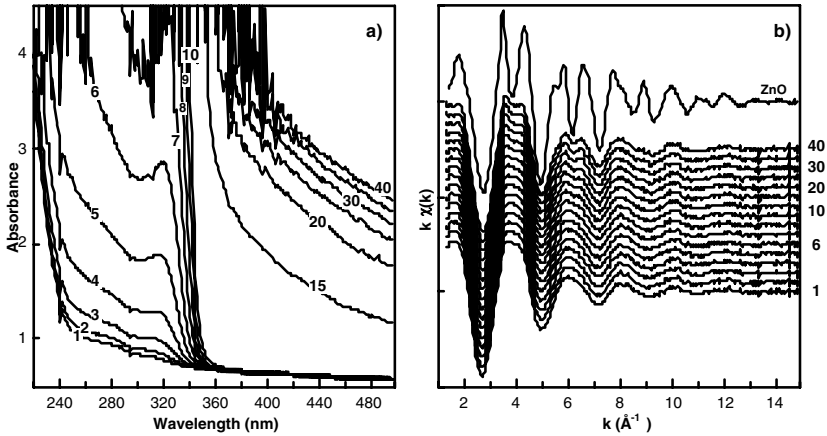

Figure 5. Selected time-resolved a) UV-Vis spectra and b) Zn K-edge EXAFS $k^3\chi(k)$ spectra recorded during the formation of ZnO quantum dot nanoparticles by heating of a precursor solution at 70°C in presence of LiOH. The ageing time ranges from 1 to 40 minutes. At the top of b) is reported for comparison purpose the EXAFS spectrum of a crystalline ZnO reference.

Figure 5a) displays the optical UV-Vis absorption spectra recorded during heating of a precursor solution at 70°C, whereas Figure 5 b) shows the corresponding Zn-K edge EXAFS spectra. From the relationship between the volume-weigthed size D and the onset of the ZnO band gap absorption established in [27], the calculated size of ZnO particles formed at the early stage of the kinetic ($t \leq 6$ min), is almost constant and equal to $\approx$ 2.5 nm. Despite an increasing number of nanosized ZnO particles in solution evidenced by the increase of the intensity of the HOMO-LUMO transition centred at $\approx$ 320 nm, the associated EXAFS spectra do not evidence significant changes compared to the initial solution for $t \leq 6$ min. For time larger than 15 min, the EXAFS technique becomes sensitive to the formation of ZnO colloidal particles in solution. In turn, the UV-Vis spectroscopy becomes less efficient for characterizing the particle growth since the UV-Vis absorbance is over the photometric range of 3.3. Nevertheless a shift of the absorption onset to longer wavelength is clearly evidenced at prolonged ageing at 70°C indicating that ZnO nanoparticles continue to grow. At the end of the process (at 40 min), the EXAFS spectrum presents features in phase with the characteristic oscillations measured on ZnO bulk crystals but with damped intensities. This is an illustration of the use of EXAFS to establish a relationship between oligomeric species and final solid phases. The time-resolved study clearly evidences that the formation of Zn-HDS is not concomitant to the formation of ZnO particles under the investigated

conditions. EXAFS is the only praticable method for obtaining the structural information directly. Indeed, it deals with very small oligomeric species in solution, what makes difficult the use of diffraction technique. This study shows also the benefit that XAS can get when combined with complementary techniques.

Finally it is noteworthy herein that the damping of EXAFS oscillations is not only due to the nanocrystalline size of ZnO particles but also to the fact that the solution is a mixture of different species, here ZnO and Zn precursors. The access by XAS to an average picture of the environment of the target atoms in various phases or in different crystallographic sites in a solid is sometimes a limitation of the technique. However, the identification and isolation of the different components of the mixture can allow access to its composition. This approach is for example illustrated in Ref. 29. Furthermore, with the advent of microbeams allowing spatial resolution information combined to spectrocopic ones, this drawback should be overcome in the next years for heterogeneous solid systems at the micron scale, as discussed in the last section.

3. X-RAY SPECTROMICROSCOPY

The above results are typical applications of EXAFS to nanocrystalline materials obtained by using a first-generation light source. Recently, the third-generation light sources for which the production of SR from insertion devices like undulators is a figure of merit have become available. The photon density at the sample position with these new sources is higher by several orders of magnitude than the one at the first-generation one. The combination of imaging at the micron level and XAS is now possible. Such combination should have a major scientific impact in years to come.

3.1 LUCIA: a future SOLEIL's beamline for X-ray Spectromicroscopy

The soft x-ray micro-XAS beamline (μ-XAS) named LUCIA (Line for Ultimate Characterisation by Imagery and Absorption) is a joint effort by the swiss and french user community. It is going to be installed at the X07M straight section of the SLS (Switzerland) with a commissioning expected by the end of 2003, prior to its installation on SOLEIL (France) at the beginning of 2008. The experimental set-up is schematized in Fig. 6.

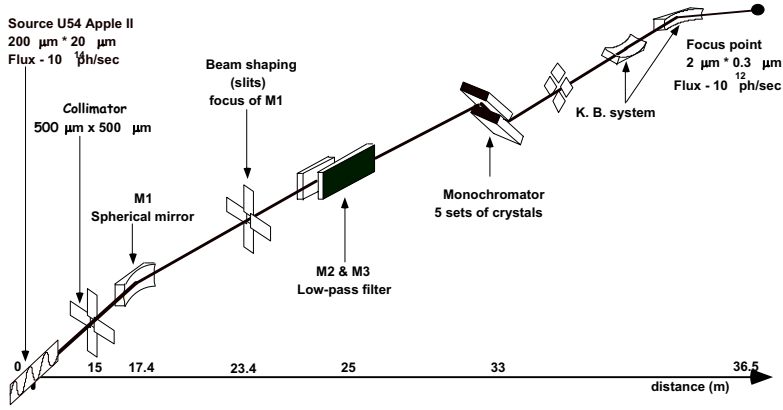

Figure 6. Schematic experimental set-up of the LUCIA beamline for µ-XAS.

The goal of this beamline is to achieve a spot size on the sample of the order of 2x1 μm^2, with a photon flux of the order of 10^{12}ph/sec, keeping the possibility to widely scan in energy. So the beam characteristics have to fulfill all the necessities required for optimized XAS measurements such as spatial stability, high photon flux, high energy resolution, and minimized contamination by energy radiation (harmonics). The beamline will be installed on the 7 m straight section of the SLS machine, equipped with an Apple-II type ondulator, which emits linearly polarized light with variable direction as well as circular polarisation. The beam is prefocused by a spherical mirror followed downstream by a double fixed-exit flat mirrors, which acts as a low-pass filter. The double crystal monochromator (DCM) based on a double Bragg reflection is equipped with a double cam, which provides a fixed exit geometry. The use of five different crystals with different d-spacings, namely beryl, YB66, KTP, InSb, and Si(111) allows us to cover an energy range from 0.8 keV to about 7 keV which corresponds to the cut-off of nickel coated mirrors. This energy domain cover the K edges of elements from Ne to Fe, L edges of the 3d and 4d transition metals and of the first rare earths, M edges of rare earths, actinides and 5d elements.

Finally in order to insure the best focusing and the achromaticity (with a focal distance which does not change with energy) a Kirkpatrick-Baez (KB) optic will be installed, next to the experimental chamber where the sample is placed on a motorized (x,y,z,Φ) stage, allowing its precise positionning and mapping.

An energy dispersive fluorescence Si drift detector associated to a multichannel analyzer will allow to do elemental 2D cartography with spatial resolution at the photon spot scale.

The micro-XAS spectra will be measured either by collecting the drain

current (TEY), the fluorescence yield or by measuring the transmitted beam.

3.2 An example of spatially Resolved XAS Study

Primary basaltic glass inclusions trapped in olivines and representative of magmas from active volcanoes have been studied by X-ray spectromicroscopy, in order to understand the excess degassing of sulfur dioxide (SO_2) [31]. The µ-XANES experiments at the sulfur K edge were carried out on the x-ray microspectroscopy beamline ID21 (ESRF, France) with a spot size range from 0.5x0.5 μm^2.

The energy separation of the thresholds allows a clear distinction between sulfide S^{II-} (2470eV), sulfite S^{IV} (2478eV) and sulfate S^{VI} (2482eV). It is then possible to image profiles (Fig. 7b) of the different sulfur species across the inclusion (Fig. 7 a), even for very low sulfur concentrations.

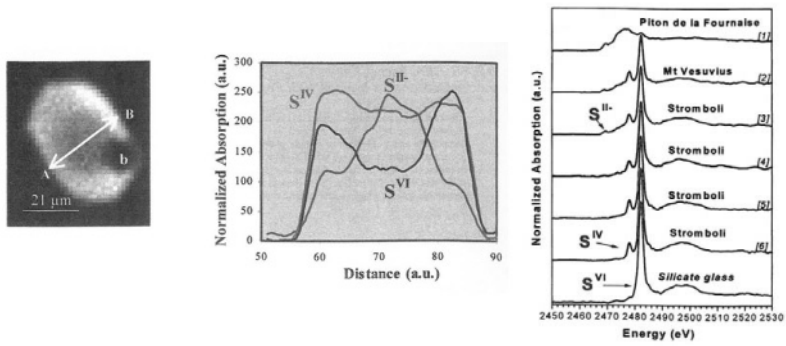

(a) **(b)** **(c)**

Figure 7. a) Mapping of one glass inclusion at 2482.1 eV showing the presence of sulfate (S^{VI}). b) Profiles along the direction AB across the inclusion for 3 energies (2469 eV, (S^{II-}), 2478 eV (S^{IV}) and 2482.1 eV (S^{VI}). c) µ-XANES spectra of glass inclusions trapped in olivines and of one oxidized silicate glass containing sulfur in sulfate form. (Figures reproduced from Reference 31 with permission from EDP Sciences).

Depending on the provenance of the olivine, the relative proportion of the sulfur species is different (Fig. 7 c). But the presence of sulfite S^{IV} in addition to sulfate is demonstrated in oxidized and water rich basaltic magmas. The sulfite S^{IV} may act as an intermediate metastable species, which results in partitionning of sulfur into the volcanic gaz emissions.

4. CONCLUSION

The above examples have demonstrated that the XAS technique is a powerful and versatile tool for gaining local order information of any specific element, but also for following structural changes occurring during the synthesis of materials, like nanomaterials prepared by sol-gel methods. In some cases, XAS is even the only suitable method to provide data on the local environment of a given atom. Experimental approach for studying materials processing based on the simultaneous combination of XAS with techniques routinely applied in materials science, such as UV-Vis spectroscopy, but also DSC or Raman techniques offers also new potentials to the materials science community. It allows for example a better understanding of the mechanisms involved in soft chemistry methods or of the phase transformation suffered by samples under consolidation, sintering... The access to set-ups with fast data acquistion allows real time studies of rapid physical and chemical processes. Finally with the advent of microfocus beamlines, the spatial distribution of different elements in a material, or even of the same element in different sites, can be determined with a micrometer resolution. The drawback of average technique associated to conventional XAS then disappears with this spatially resolved XAS technique. The field of applications of the spectromicroscopy is very large from environmental science to materials science.

REFERENCES

1. R. Stumm von Bordwehr, *Ann. Phys. Fr.* **14**, 377, (1989).
2. See references [8-99] to [8-102] of Reference 1.
3. D. C. Koningsberger and R. Pins (Eds), *X-ray Absorption Principles, Applications, Techniques of EXAFS, SEXAFS and XANES* (John Wiley, New York, 1988).
4. T. K. Sham (Ed), *Chemical Applications of Synchrotron Radiation, Part II:X-ray Applications*, Advanced Series in Physical Chemistry – Vol. 12B (World Scientific, New Jersey, 2002);
5. J. Stöhr, *NEXAFS Spectroscopy* (Springer, Berlin, 1992).
6. B. K. Teo, *EXAFS: Basic Principles and Data Analysis* (Springer, Berlin, 1986).
7. S. I. Zabinsky, J. J. Rehr, A. Ankudinov, R. C. Albers and M. J. Eller, *Phys. Rev*. **B52**, 2995, (1995).
8. A. Ankudinov, B. Ravel, J. J. Rehr and S. Conradson, *Phys. Rev*. **B58**, 7565, (1998).
9. F. Baudelet *et al. Phys. Rev.* **B 43**, 5857, (1991).
10. C. V. Santilli, S. H. Pulcinelli, G. E. S. Brito and V. Briois, *J. Phys. Chem.* **B 103**, 2660, (1999).
11. M. S. Tokumoto, A. Smith, C. V. Santilli, S. H. Pulcinelli, E. Elkaim and V. Briois, *J. Non Cryst. Sol.* **273**, 302, (2000).
12. V. Briois, S. H. Pulcinelli and C. V. Santilli, *J. Mat. Sc. Lett.* **20**, 555, (2001).

13. V. R. Mastelaro, V. Briois, D. P. F. de Souza and C. L. Silva, *J. Eur. Ceram. Soc.* **23**, 273, (2003).
14. A. P. Rizzato, C. V. Santilli, S. H. Pulcinelli, D. Stuerga, D. Chaumont and V. Briois, in press in Physica Scripta A.
15. H. Roussel, V. Briois, E. Elkaim, A. de Roy and J.-P. Besse, *J. Phys. Chem.* **B 104**, 5915, (2000).
16. M. Bellotto, B. Rebours, O. Clause, J. Lynch, D. Bazin and E. Elkaim, *J. Phys. Chem.* **100**, 8527, (1996).
17. W. Hofmeister and H. V. Platen, *Crystallogr. Rev.* **3**, 3, (1992).
18. H. Roussel, V. Briois, E. Elkaim, A. de Roy, J. P. Besse and J. P. Jolivet, *Chem. Mater.* **13**, 329, (2001).
19. P. Le Fevre, H. Magnan, O. Heckmann, V. Briois and D. Chandesris, *Phys. Rev.* **B52**, 11462, (1995).
20. M. S. Tokumoto, A. Smith, C. V. Santilli, S. H. Pulcinelli, A. F. Craievich, E. Elkaim, A. Traverse and V. Briois, *Thin Solid Films* **416**, 284, (2002).
21. A. M. Beale and G. Sankar, *J. Mater. Chem.* **12**, 3064, (2002).
22. J-D Grunwaldt, D. Lützenkirchen-Hecht, M. Richwin, S. Grundmann, B. S. Clausen and R. Frahm, *J. Phys. Chem.* **B105**, 5161, (2001).
23. V. Briois, C. E. Williams, H. Dexpert, F. Villain, B. Cabane, F. Deneuve and C. Magnier, *J. Mater. Sci.* **28**, 5019, (1993).
24. L. J. Michot, A. Montargès-Pelletier, B. S. Lartiges, J. B. d'Espinose de la Caillerie, and V. Briois*, J. Am. Chem. Soc.* **122**, 6048, (2000).
25. G. Defontaine et al. In press in Langmuir.
26. V. Briois *et al.* in press in Physica Scripta A.
27. E. Meulenkamp *J. Phys. Chem.* **B102**, 5566, (1998).
28. L. Spanhel and M. A. Anderson*, J. Am. Chem. Soc.* **113**, 2826, (1991).
29. M. S. Tokumoto, S. H. Pulcinelli, C. V. Santilli and V. Briois, *J. Phys. Chem.* **B107**, 568, (2003).
30. M. S. Tokumoto, V. Briois, C. V. Santilli and S. H. Pulcinelli, *J. Sol-Gel Sc. & Techno.* **26**, 547, (2003).
31. N. Métrich, J. Susini, L. Galoisy, G. Calas, M. Bonnin-Mosbah and B. Ménez, J. Phys. IV France, **104**, 393, (2003).

STRUCTURAL STUDIES OF BIO- AND RELATED MATERIALS USING SYNCHROTRON RADIATION:

*The Structure of Tetra(imidazole)chlorocopper(II) Chloride***.**

DALE L. PERRY[1], A. BOWMAN[2], S.J. TEAT[3], MARIO ORTEGA[4] AND A.C. THOMPSON[1]

[1] *Lawrence Berkeley National Laboratory, Berkeley CA 94720 dlperry@lbl.gov*

[2] *Fisk University, Nashville, TN 37208,*

[3] *CCLRC Daresbury Laboratory, Daresbury Cheshire, UK WA4 4AD,*

[4] *University of California, Davis, Davis, CA 95616*

Abstract: The complex tetra(imidazole)chlorocopper(II) chloride, [Cu(imidazole)$_4$Cl]Cl, has been synthesized, and the structure has been determined at the Small Crystal X-ray Crystallography Beamline (11.3.1) of the Advanced Light Source (ALS) at Lawrence Berkeley National Laboratory (LBNL), USA. Structural parameters of the parent complex are compared to similar materials previously reported in the literature. The particles in the present study can be used to prepare nanoparticle materials, or, by controlled growth, can be formed as nanoparticles initially. The structural data are important for making detailed calculations, models, and deriving reaction mechanisms involving metal ion-based biochemical systems.

Keywords: imidazole, copper(II), nanochemistry, nanoparticles, tetra(imidazole)chlorocopper(II) chloride, synchrotron, x-ray crystallography, biomaterials, [Cu(imidazole)$_4$Cl]Cl.

1. INTRODUCTION

In the biochemical world, there are thousands of bioinorganic compounds that have been identified, but many of them have not been significantly analyzed for their important relevant properties and biological roles and uses.

E. C. Faulques et al. (eds.), Spectroscopy of Emerging Materials, 31–43.

Imidazole ($C_3H_4N_2$) (IUPAC name 1,3-diazole) is a fundamental building block of many biological proteins and other biological systems. Imidazole and related compounds constitute the backbone of histidine and many peptides involved in human biological processes. Imidazole acts as a ligand, or electron donor, which will bond readily when introduced to a metal ion via metal ion salts in aqueous systems. The imidazole molecule is the core component of histamine, whose structures with transition metal ions have been studied as model quasi-enzyme compounds [1], along with other structural reports [2]. Imidazole-copper metal complexes with thiol systems also have been studied with respect to their biologically-related importance [3], as have vanadyl-imidazole complexes [4]. Other similar class copper(II) organic aromatic heterocyclic compounds have been reported because of their structural interests [5] and their chemical applications such as catalysis [6].

In the present study, the complex, tetra(imidazole)chlorocopper(II) chloride, $[Cu(imidazole)_4Cl]Cl$, has been synthesized, and the structure has been determined at the Small Crystal X-ray Crystallography Beamline (11.3.1) of the Advanced Light Source (ALS) at Lawrence Berkeley National Laboratory (LBNL)(Fig.1)[7]. Structural parameters are compared to similar compounds previously reported in the literature. The particles in the present study can be used to prepare nanoparticle materials, or the crystals can be grown under conditions to form nanoparticles or nanoparticle clusters. The molecular structure of the complex here can be used as a model to correlate with its magnetic and electronic properties. Structural parameters for the present complex of copper(II) are compared to similar compounds previously reported in the literature. With the data accumulated here, some previously unexplained bioinorganic chemistry and related phenomena may be explained in the context of the compounds' molecular and electronic properties.

2. EXPERIMENTAL DETAILS

2.1 Reagents

All chemicals used in the work were reagent grade, including imidazole (Aldrich Chemical), absolute ethanol (Aldrich), and copper(II) chloride dihydrate (Alfa Aesar), and they were used without further purification.

2.2 Preparation of [Cu(imidazole)$_4$Cl]Cl

The parent imidazole complex was produced by means of a wet synthesis using millimolar amounts in a slightly greater ratio of 4:1 ratio of the imidazole ligand and the parent copper(II) chloride. All syntheses were conducted in standard Pyrex glassware. The reaction solution of $CuCl_2$ $(H_2O)_2$ and imidazole was combined slowly into a heated beaker using the copper(II) salt first. Immediately following the mixture of the reagents, 0.1 *M* NaOH was added drop wise until the solution changed color and a solid purple product precipitated. Several cycles of heating and cooling were instituted during and after the reaction, to help stimulate crystal growth. The crystals were then washed with ice-cold 100 % methanol on a Buchner funnel and allowed to air-dry. After collection, the crystals were stored in a dark, dry environment and transferred to Beamline 11.3.1 at the ALS for structural study.

2.3 Beamline 11.3.1.

Beamline 11.3.1, the Small Crystal X-Ray Crystallography Beamline at the Advanced Light Source (ALS) at Lawrence Berkeley National Laboratory (LBNL), has been described previously [7].Small crystals about 180μm x 60μm x 10μm were studied at 14 keV with an exposure time of 5 sec/frame. With 900 frames of data, a resolution of 0.8

Angstroms was achieved. Experimental details regarding the X-ray crystallography used in determining the structure are in Table 1.

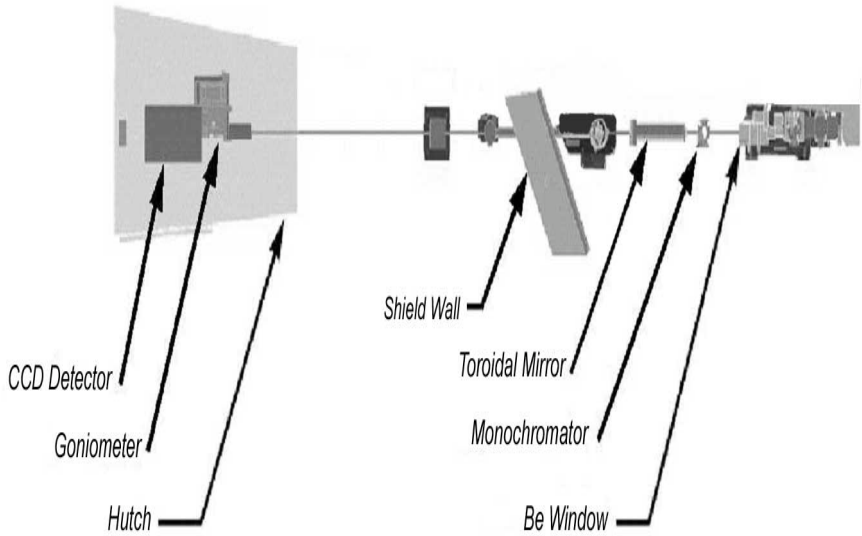

Figure 1. Schematic of Beamline 11.3.1 at the Advanced Light Source used for structural determination of small crystals.

3. RESULTS AND DISCUSSION

The complex, tetra(imidazole)chlorocopper(II) chloride, $[Cu(imidazole)_4Cl]Cl$, exhibits a square pyramidal structure (Fig. 2) with respect to the actual bonds formed between the copper(II), the imidazole, and the chloride ions. The four copper-nitrogen bonds are 1.99, 2.00, 2.00, and 2.00 Angstroms, in very good agreement with copper(II)-nitrogen bond

lengths of copper-nitrogen complex structural data reported in the literature for very similar copper(II)-imidazole systems [8].

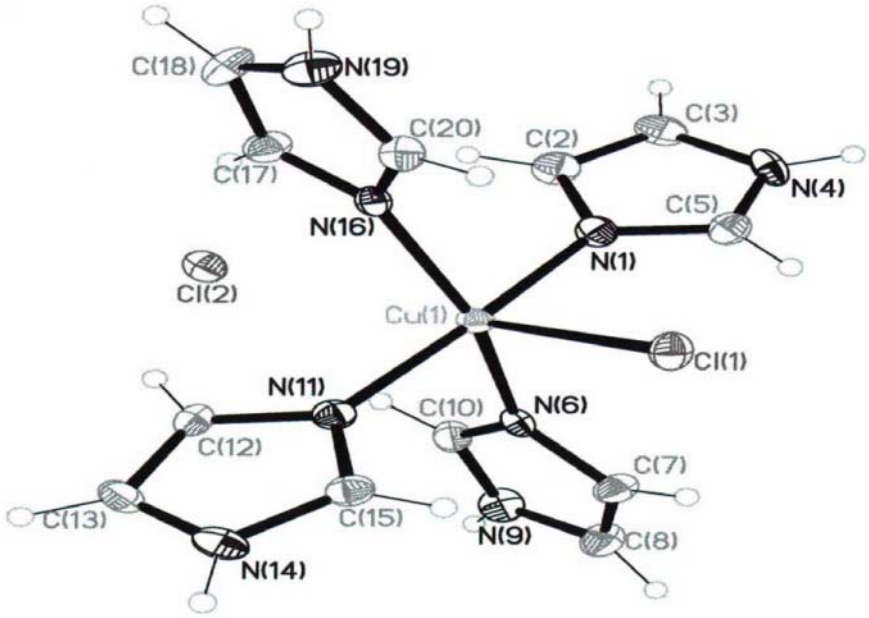

Figure 2. Structure of [Cu(imidazole)$_4$Cl]Cl

The two copper-chloride linkages, however, represent two differences in bond lengths. One of the chloride ions is actually bonded to the copper(II) central ion (Cu-Cl bond distance of 2.6 Angstroms), while the second chloride is at a 4.12 Angstrom distance from the copper(II) ion and thus a non-bonding chloride lattice ion. This non-bonding chloride ion is in a pseudo-*trans* position to the bonded chloride ion through the plane generated by the copper(II) ion-imidazole coordination core. The 2.6 Angstrom Cu-Cl

distance is in excellent agreement with analogous bonding in copper(II) coordination schemes for histidine in the copper blue protein azurin and other biologically-related compounds [9]. Structural data concerning hydrogen bonding in the parent material are in Table 5.

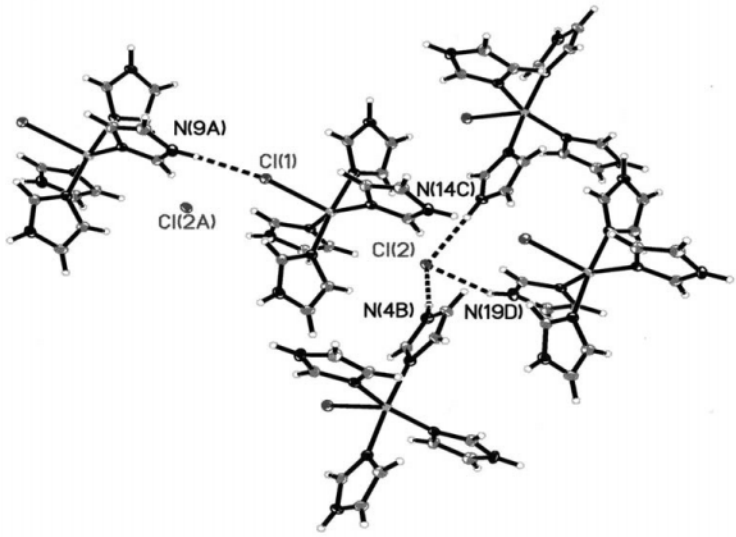

Figure 3. Hydrogen bonding schemes for [Cu(imidazole)$_4$Cl]Cl.

The structure of the parent material in this study---due to its uniqueness with respect to its inequivalent chloride ions both as coordinated and lattice chlorides---represents yet still another example of a solid state copper imidazole material. Others include copper(II) perchlorate salts complexed with amines [10] and copper(I) imidazole complexes based on a cavitand ligand design [11]. Copper(I) imidazole complexes have been

used as subjects for luminescence spectral studies [12], the luminescence being dependent on the structure of the material. Structural characteristics of a copper(II) saccharin material have been used to compare both the structure and infrared spectra to a cadmium(II) analog [13]. Yet still other copper-imidazole materials have been used to model intermediate and metabolic reaction species involved in human biochemistry [14].

In summary, x-ray crystallographic investigations of metal-aromatic hydrocarbon materials such as the parent material studied here will continue to be of extreme importance with respect to the correlation of molecular structure with spectroscopic properties, along with their importance as models for materials reaction chemistry intermediates and mechanisms. A large part of this field of study will undoubtedly depend on the use of x-ray synchrotron approaches for the structural elucidation of samples that heretofore were too small to be structurally studied using traditional x-ray crystallographic approaches.

ACKNOWLEDGMENTS

This work was performed under the Center for Science and Engineering Education (CSEE) at the Lawrence Berkeley National Laboratory with support from the Director, Office of Energy Research, Office of Basic Energy Sciences, Materials Science Division, and the Division of University and Science Education Programs, U. S. Department of Energy, under Contract Number DE-AC03-76SF00098.

REFERENCES

1. P. Kita, *J. Polish Chem.,* ***56,*** 913(1982).
2. N. Sakagami, E. Kita, P. Kita, J. Wisniewska, and S. Kaizaki, *Polyhedron,* ***18,*** 2001(1999).
3. C. Gielens, N. Degeest, X-Q. Xin, B. Devreese, J. van Beeumen, and G. Preux, *Eur. J. Biochem.,* ***248,*** 869(1997).
4. T.S. Smith, II, C.A. Root, J. Kampf, and P.G. Rasmussen, V.L.

Pecoraro, *J. Am. Chem. Soc.,* ***122***, 767(2000).
5. K. J. Catalan, S. Jackson, J. D. Zubkowski, D. L. Perry, E. J. Valente, L. A. Feliu, and A. Polanco, *Polyhedron,* ***14***, 2165(1995).
6. H. N. Choksi, A. Zippert, P. Berdahl, J. A. Bertrand, D. L. Perry, M. B. Mitchell, and M. G. White, *J. Molec. Catal. A: Chemical*, ***97***, 85(1995).
7. For information concerning more details of Beamline 11.3.1 at the Advanced Light Source at Lawrence Berkeley National Laboratory, see the Website at http://www-als.lbl.gov/als/techspecs/bl11.3.1.html
8 S. D. Longal, I. Asconc, A. Bianconi, A. Bonfigli, A. C. Castellano, O. Zariviv, and M. Miranda, *J. Biol. Chem*., **271**, 21025(1996).
9. L. Jeuken, Thesis, Univ. of Leiden, 2001.
10. K. Miki, S. Kaida, M. Saeda, K. Yamatoya, N. Kasai, M. Sato and J.-I. Nakaya, *Acta Cryst.,* **C42,** 1004(1986).
11. Janis K. Voo, K. C. Lam, Arnold L. Rheingold and Charles G. Riordan, *J. Chem. Soc., Dalton Trans.,* 1803(2001).
12. T. N. Sorrell, A. S. Borovik, *J. Am. Chem. Soc.*, **108**, 2479(1986).
13. P. Naumov and G. Jovanovski, *Acta Chim. Slov*., **46**, 389(1999).
14. S. Karlin, Z.-Y. Zhu, and K. D. Karlin, *Proc. Natl. Acad. Sci. USA,* **94**, 14225(1997).

Table 1. Crystal data and structure refinement for [Cu(imidazole)$_4$Cl]Cl

Molecule	[Cu(imidazole)$_4$Cl]Cl
Chemical formula	$C_{12}H_{16}Cl_2CuN_8$
Formula weight	406.77
Temperature	173 (2) K
Radiation, wavelength	Synchrotron, 0.8850 Angstroms
Crystal system, space group	Monoclinic, $P2_1/n$
Unit cell parameters	a = 8.8186(5) Angstroms $\alpha = 90°$ b = 13.1916(10) A $\beta = 90.018(4)°$ c = 13.8354(8) Angstroms $\gamma = 90°$
Cell volume	1609.49(18) Angstroms^3
Z	4
Calculated density	1.679 g/cm^3
Absorption coefficient μ	1.700 mm^{-1}
F(000)	828
Crystal color and size	Dark blue, 0.18 x 0.06 x 0.03 mm^3
Reflections for cell refinement	8018 (θ range 2.62 to 30.22°)
Data collection method diffractometer	Bruker SMART PROTEUM 300 CC
θ range for data collection	1.83 to 30.22°
Index ranges	h-9 to 10, k-15 to 15, l-15 to 15
Completeness to $\theta = 30.22°$	99.9 %
Reflections collected	17426
Independent reflections	2468 (R_{int} = 0.0490)
Reflections with $F^2 > 2\sigma$	2299
Absorption correction	Semi-empirical from equivalents
Min. and max. transmission	0.72 and 0.97
Structure solution	Direct methods
Refinement method	Full-matrix least-squares on F^2
Weighting parameters a,b	0.0338, 1.5176
Data/restraints/parameters	2468 / 0 / 209
Final R indices [$F^2 > 2\sigma$]	R1 = 0.0315, wR2 = 0.0710
R indices (all data)	R1 = 0.0347, wR2 = 0.0720
Goodness-of-fit on F^2	1.114
Largest and mean shift/su	0.001 and 0.000
Largest diff. peak and hole	0.293 and - 0.302 e

Table 2 Atomic coordinates and equivalent isotropic displacement parameters (Angstroms^2) 1 for [Cu(imidazole)$_4$Cl]Cl, U_{eq} is defined as one third of the trace of the orthogonalized U^{ij} tensor.

Cu(l)	0.18942(4)	0.21442(3)	0.87752(3)	0.01448(13)
Cl(1)	- 0.05277(9)	0.10122(6)	0.87920(6)	0.01990(19)
Cl(2)	0.55482(9)	0.40901(6)	0.87492(6)	0.0223(2)
N(1)	0.1982(3)	0.22234(19)	1.02122(18)	0.0178(6)
C(2)	0.2712(4)	0.2949(3)	1.0759(2)	0.0223(8)
C(3)	0.2584(4)	0.2711(3)	1.1701(2)	0.0238(8)
N(4)	0.1770(3)	0.1830(2)	1.17368(19)	0.0227(7)
C(5)	0.1432(4)	0.1565(3)	1.0833(2)	0.0201(8)
N(6)	0.3601(3)	0.11389(19)	0.87995(19)	0.0162(6)
C(7)	0.3500(4)	0.0111(2)	0.8834(2)	0.0204(7)
C(8)	0.4907(4)	-0.0296(3)	0.8796(3)	0.0255(8)
N(9)	0.5879(3)	0.00498(2)	0.8742(2)	0.0229(6)
C(10)	0.5055(4)	0.1346(3)	0.8747(3)	0.0215(7)
N(11)	0.1987(3)	0.2135(2)	0.73387(10)	0.0167(6)
C(12)	0.2856(4)	0.2779(2)	0.6790(2)	0.0206(8)
C(13)	0.2676(4)	0.2555(3)	0.5849(2)	0.0225(8)
N(14)	0.1700(3)	0.1757(2)	0.58183(19)	0.0212(6)
C(15)	0.1312(4)	0.1524(2)	0.6720(2)	0.0179(7)
N(16)	0.0866(3)	0.34991(18)	0.87428(19)	0.0159(6)
C(17)	0.1482(4)	0.4456(2)	0.8758(3)	0.0200(7)
C(18)	0.0363(4)	0.5144(2)	0.8736(2)	0.0246(8)
N(19)	-0.0963(3)	0.4616(2)	0.9705(2)	0.0230(6)
C(20)	-0.0614(4)	0.3633(2)	0.8715(2)	0.0186(7)

Table 3. **Bond lengths [Angstroms] and angles [Degrees] for [Cu(imidazole)$_4$Cl]Cl**

Cu(1)–Cl(1)	2.6062(8)	Cu(1)– Cl(2)	4.1200(9)
Cu(1)–N(1)	1.992(3)	Cu(1)-N(6)	2.006(3)
Cu(1)-N(11)	1.989(3)	Cu(1)–N(16)	2.005(2)
N(1)-C(2)	1.379(4)	N(1)–C(5)	1.315(4)
C(2)-C(3)	1.345(5)	C(3)–N(4)	1.366(5)
N(4)-C(5)	1.332(4)	N(6)–C(7)	1.359 (4)
N(6)-C(10)	1.313(4)	C(7)–C(8)	1.353(5)
C(8)-N(9)	1.356(4)	N(9)–C(10)	1.333(4)
N(11)-C(12)	1.373(4)	N(11)–C(15)	1.318(4)
C(12)-C(13)	1.345(5)	C(13)–N(14)	1.361(5)
N(14)-C(15)	1.330(4)	N(16)–C(17)	1.374(4)
N(16)-C(20)	1.317(4)	C(17)–C(18)	1.341(5)
C(18)-N(19)	1.362(4)	N(19)–C(20)	l1.332(4)
Cl(1)-Cu(1)-Cl(2)	176.42(2)	Cl(1)-Cu(1)–N(1)	93.03(8)
Cl(1)-Cu(1)-N(6)	103.64(7)	Cl(1)–Cu(1)–N(11)	92.25(8)
Cl(1)-Cu(1)-N(16)	98.07(7)	Cl(2)–Cu(1)–N(1)	86.89(8)
Cl(2)-Cu(1)-N(6)	79.94(7)	Cl(2)–Cu(1)-N(11)	87.86(8)
Cl(2)-Cu(1)-N(16)	78.35(7)	N(1)–Cu(10)–N(6)	89.36(11)
N(1)-Cu(1)-N(11)	174.70(11)	N(1)–Cu(1)-N(6)	89.60(11)
N(6)-Cu(1)-N(11)	88.96(11)	N(6)-Cu(1)–N(16)	158.29(10)
N(11)-Cu(1)-N(16)	90.09(11)	Cu(1)–N(1)–C(2)	127.0(2)
Cu(1)-N(1)-C(5)	127.1(2)	C(2)–N(1)–C(5)	105.8(3)
N(1)-C(2)-C(3)	109.2(3)	C(2)–C(3)–N(4)	106.2(3)
C(3)-N(4)-C(5)	107.9(3)	N(1)–C(5)–N(4)	110.9(3)
Cu(1)-N(6)-C(7)	127.7(2)	Cu(10)–N(6)–C(10)	126.5(2)
C(7)-N(6)-C(10)	105.8(3)	N(6)–C(7)–C(8)	109.6(3)
C(7)-C(8)-N(9)	105.9(3)	C(8)–N(9)–C(10)	107.7(3)
N(6)-C(10)-N(9)	111.0(3)	Cu(1)-N(11)–C(12)	124.8(2)
Cu(1)-N(11)-C(15)	129.4(2)	C(12)–N(11)–C(15)	105.8(3)
N(11)-C(12)-C(13)	109.5(3)	C(12)–C(13)–N(14)	105.9(3)
C(13)-N(14)-C(15)	108.2(3)	N(11)–C(15)–N(14)	110.6(3)
Cu(1)-N(16)-C(17)	129.7(2)	Cu(1)–N(16)–C(20)	124.6(2)
C(17)-N(16)-C(20)	105.6(2)	N(16)–C(17)–C18)	109.3(3)
C(17)-C(18)-N(19)	106.7(3)	C(18)–N(19)–C(20)	107.4(3)
N(16)-C(20)-N(19)	111.1(3)		

Table 4. Anistropic displacement parameters (Angstroms^2) for [Cu(imidazole)$_4$Cl]Cl. The anistropic displacement factor exponent takes the form: $-2\pi^2[h^2a^{*2}U^{11} + ... + 2hka^*b^*U^{12}]$

	U^{11}	U^{22}	U^{33}	U^{23}	U^{13}	U^{12}
Cu(l)	0.0166(2)	0.0149(2)	0.0119(2)	-0.00003(17)	-0.00115(16)	0.00274(16)
Cl(1)	0.0187(4)	0.0205(4)	0.0205(4)	0.0020(4)	-0.0014(4)	-0.0040(3)
Cl(2)	0.0197(4)	0.0287(4)	0.0185(4)	0.0018(4)	-0.0016(4)	0.0054(3)
N(I)	0.0195(14)	0.0187(14)	0.0152(14)	0.0015(12)	-0.0008(12)	0.0019(12)
C(2)	0.0236(19)	0.0228(18)	0.0205(18)	-0.0043(15)	-0.0035(15)	-0.0020(15)
C(3)	0.0235(19)	0.030(2)	0.0178(19)	-0.0066(15)	-0.0037(15)	-0.0011(16)
N(4)	0.0214(16)	0.0333(17)	0.0134(15)	0.0071(13)	0.0020(12)	0.0011(14)
C(5)	0.0203(18)	0.0181(18)	0.0218(18)	0.0014(14)	-0.0036(14)	0.0007(14)
N(6)	00175(15)	0.0198(14)	0.0114(13)	0.0010(12)	-0.0009(12)	-0.0004(11)
C(7)	0.0202(18)	0.0150(17)	0.0261(18)	-0.0012(15)	-0.0012(15)	0.0001(13)
C(8)	0.032(2)	0.0176(17)	0.027(2)	0.0006(16)	-0.0005(16)	0.0021(15)
N(9)	0.0129(14)	0.0295(16)	0.0263(15)	0.0026(14)	-0.0014(13)	0.0057(12)
C(IO)	0.0217(19)	0.0224(18)	0.0204(18)	0.0015(16)	0.0001(15)	-0.0032(14)
N(II)	0.0164(14)	0.0165(13)	0.0172(14)	0.0006(12)	0.0002(12)	0.0025(12)
C(12)	0.0247(19)	0.0153(17)	0.0218(19)	-0.0001(14)	0.0002(15)	-0.0011(15)
C(13)	0.025(2)	0.0263(19)	0.0161(17)	0.0022(14)	0.0038(15)	0.0021(15)
N(14)	0.0224(16)	0.0265(15)	0.0147(14)	-0.0056(12)	-0.0032(12)	0.0009(13)
C(15)	0.0158(17)	0.0174(17)	0.0205(18)	-0.0007(14)	-0.0006(14)	0.0021(14)
N(16)	0.0188(15)	0.0174(14)	0.0114(13)	0.0017(12)	-0.0011(12)	0.0014(11)
C(17)	0.0158(17)	0.0161(16)	0.0281(18)	-0.0024(16)	0.0009(16)	-0.0015(13)
C(18)	0.0267(19)	0.0146(16)	0.033(2)	-0.0015(16)	-0.0033(17)	-0.0013(14)
N(19)	0.0186(15)	0.0228 (15)	0.0277(16)	-0.0019(14)	-0.0048(13)	0.0070(12)
C(20)	0.0196(18)	0.0174(17)	0.0189(17)	0.0008(14)	-0.0032(15)	0.0003(14)

Table 5. Hydrogen bonds for [Cu(imidazole)$_4$Cl]Cl. [Angstroms and Degrees]

D-H…A	d(D-H)	d(H…A)	d(D…A)	<<DHA)
N(4)-H(4A)...Cl(2A)	0.88	2.36	3.223(3)	168.3
N(9)-H(9A)...Cl(IB)	0.88	2.41	3.241(3)	158.5
N(14)-H(14A)...Cl(2C)	0.88	2.37	3.236(3)	169.7
N(19)-H(19A)...Cl(2D)	0.88	2.49	3.155(3)	132.3

Symmetry operations for equivalent atoms

A x-1/2,-y+1/2,z+1/2 B x+1,y,z C x-1/2,-y+1/2,z-1/2 D x-l,y,z

ADVANCES IN SPECTROSCOPY OF SUBTHRESHOLD INELASTIC RADIATION-INDUCED PROCESSES IN CRYOCRYSTALS

A.N.Ogurtsov
Institute of Low Temperature Physics & Engineering of NASU, Kharkov 61103, Ukraine; National Technical University "KhPI", Kharkov 61002, Ukraine

Abstract: A review is given on the recent spectroscopic studies of the electronic excitation induced processes of large-scale atomic displacements in atomic cryocrystals, including defect formation, atomic and molecular desorption.

Key words: Rare-gas solids, Cryocrystals, Electronic excitations, Self-trapping, Frenkel pairs, Desorption

1. INTRODUCTION

Fundamental excitation of non-metallic solids by photons and beams of particles with a kinetic energy below the threshold of knock-on of atoms from the lattice sites – the subthreshold excitation – is a powerful tool for material modification by selective removal of material, controlled changes in selected regions, altering the balance between the process steps, quantum control, etc. [1]. The scission of the bonds, which stabilize the ground-state configuration, by transferring the electronic excitation energy to the lattice requires trapping or self-trapping of electronic excitations [2]. However, the range of materials which exhibit the inelastic subthreshold processes induced by electronic excitation is limited to specific classes of materials, such as alkali halides, alkali earth fluorides and fused quartz [1].

Rare-gas solids (RGS), or atomic cryocrystals, are the model systems in physics and chemistry of solids, and enormous amount of information about electronic excitations in RGS has been documented in several books [2–5]

E. C. Faulques et al. (eds.), Spectroscopy of Emerging Materials, 45–56.

and reviews [6–9]. As a consequence of the closed electronic shells, solid Xe, Kr, Ar, and Ne are the simplest known solids of the smallest binding energy between atoms in the lattice. On the other hand, solid Ar and Ne have band-gap energies, E_g, exceeding that of LiF and may be cited as the widest band-gap insulators. Therefore, RGS are very promising systems for study the mechanisms of subthreshold radiation-induced processes.

The present paper reviews the updated understandings of the subthreshold inelastic processes induced by electronic excitations in RGS.

2. EXPERIMENTAL

Rare-gas samples exist only at cryogenic temperatures and most of the optical spectroscopy of electronic processes should be done in the vacuum ultraviolet. Making experiments requires an indispensable combination of liquid-helium equipment with windowless VUV-spectroscopic devices and synchrotron radiation as a photon source. To study the electronic excitation energy pathways and a variety of subthreshold inelastic processes, we used the complimentary advantages of cathodoluminescence (possibility to vary the excitation depth beneath the sample surface), photoluminescence (selective-state excitation by synchrotron radiation at high-flux SUPERLUMI-station at HASYLAB, DESY, Hamburg) and thermoactivation spectroscopy (sequential release of electrons from traps of different depth ended in thermoluminescence and thermostimulated exoelectron emission). The experimental setups and methods of sample preparation from vapor phase were described in detail elsewhere [10].

3. ELECTRONIC EXCITATIONS AND LUMINESCENCE OF ATOMIC CRYOCRYSTALS

The electronic properties of RGS have been under investigation since seventies [3–7] and now the overall picture of creation and trapping of electronic excitations is basically complete. Because of strong interaction with phonons the excitons and holes in RGS are self-trapped, and a wide range of electronic excitations are created in samples: free excitons (FE), atomic-like (A-STE) and molecular-like self-trapped excitons (M-STE), molecular-like self-trapped holes (STH) and electrons trapped at lattice imperfections. The coexistence of free and trapped excitations and, as a result, the presence of a wide range of luminescence bands in the emission spectra enable one to reveal the energy relaxation channels and to detect the elementary steps in lattice rearrangement.

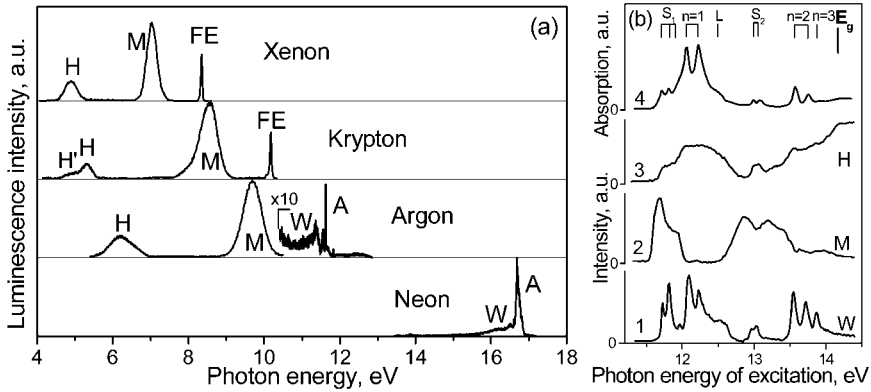

Figure 1. (a) – Photoluminescence spectra of atomic cryocrystals at T=5 K under excitation energy $h\nu=E_g$. (b) – (1-3) Excitation spectra of molecular luminescence bands of solid Ar; (4) – absorption spectrum of solid Ar (from Ref.7).

The most prominent feature in luminescence of Xe, Kr and Ar – the so-called *M*-band (Fig.1a) – is formed by $^{1,3}\Sigma_u^+ \rightarrow {}^1\Sigma_g^+$ transitions in (R_2^*) excimer M-STE (R=rare gas atom). The negative electron affinity (Table 1) is a moving force of the cavity ("bubble") formation around A-STE in the bulk of crystal, and the desorption of atoms and excimers from the surface of solid Ne and Ar [11]. Radiative "hot" transitions in desorbed excimers of Ar and Ne result in a *W*-band. *A*-bands are emitted by A-STE (R*).

Recent study of charged centers in RGS [12-14] reveal the nature of *H*-bands. These bands correspond to the third continua in rare gas emission [15], which are formed by transitions $(R_2^+)^* \rightarrow (R_2^+)$ in molecular ions [16]. A tiny amount of impurity Xe atoms in solid Kr results in the formation of heteronuclear excited ions $(KrXe^+)^*$ and a corresponding *H'*-band (Fig.1a).

Radiative decay of free excitons from the bottom of the lowest Γ(3/2), n=1 excitonic band produces strong lines *FE* (Fig.1a) in spectra of solid Xe,

Table 1. Some parameters of energetic structure and luminescence of RGS [2,7]

	Xe	Kr	Ar	Ne
Band-gap energy at the Γ-point, E_g (eV)	9.298	11.59	14.14	21.58
Binding energy per atom, ε_b (eV)	0.172	0.123	0.088	0.026
Electron affinity, χ (eV)	0.5	0.3	–0.4	–1.3
Bottom of the lowest excitonic band Γ(3/2), *FE* (eV)	8.37	10.14	12.06	17.36
Barrier height against M-STE formation, H^M_{max} (meV)	20	10	2	0.3
Barrier height against A-STE formation, H^A_{max} (meV)		30	10	1
Energy release at M-STE formation, E_M* (eV) [17]	0.45	0.75	1.25	
Energy release at A-STE formation, E_A* (eV) [17]			0.2	0.58
Threshold energy for M_1 subband, E_1 (eV) [18]	8.18	9.87	11.61	
Threshold energy for M_2 subband, E_2 (eV) [18]	8.28	10.03	11.81	

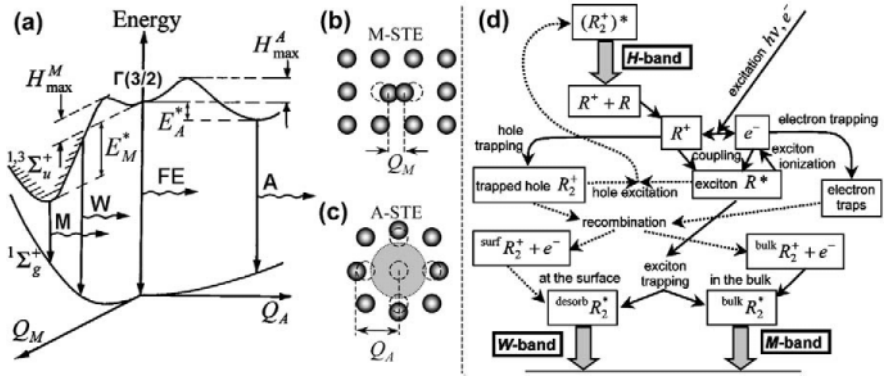

Figure 2. (a) – Potential curves of M-STE and A-STE. (b,c) – Simplified geometrical structure of M-STE and A-STE. (c) – Scheme of the population of molecular neutral and charged trapped centers in atomic cryocrystals.

Kr and Ar [19].

The schematic representation of A-STE and M-STE and luminescence transitions in neutral centers is shown in Fig.2a. In M-STE the configuration co-ordinate, Q_M, is an internuclear distance of the molecule (Fig.2b). In A-STE (Fig.2c), the configuration co-ordinate, Q_A, is a radius of microcavity (nearest-neighbor distance) [7].

The commonly used scheme of energy relaxation in RGS includes some stages (Fig.2d, solid arrows). Primary excitation by VUV photons or low energy electrons creates electron-hole pairs. Secondary electrons are scattered inelastically and create free excitons, which are self-trapped into atomic or molecular type centers due to strong exciton-phonon interaction.

Complementary studies of neutral [20] and charged [16] intrinsic trapped centers, comparison of cathodoluminescence [21] and thermoluminescence data [12] with results of analysis of photoelectron scattering [13] and pump-probe experiments [14] allow us to extend the energy relaxation scheme (Fig.2d, dotted arrows) including electron-hole recombination channels. The formation of *H*-band emitting centers $(R_2^+)^*$ occurs through the excitation of STH by an exciton. The bulk recombination of trapped holes with electrons populates the (R_2^*) states with subsequent *M*-band emission [22]. After surface recombination of STH with electrons the excited dimers escape from the surface of the crystal with subsequent *W*-band emission.

The general behavior of the excitation spectra of *H*- and *W*-bands (Fig.1b) reproduces all surface (*S*) and bulk (transverse n=1,2,3 and longitudinal *L*) features of photoabsorption. The opposite behavior of the *M*-band underlines the branching of competing channels of population neutral and charged trapped centers [16].

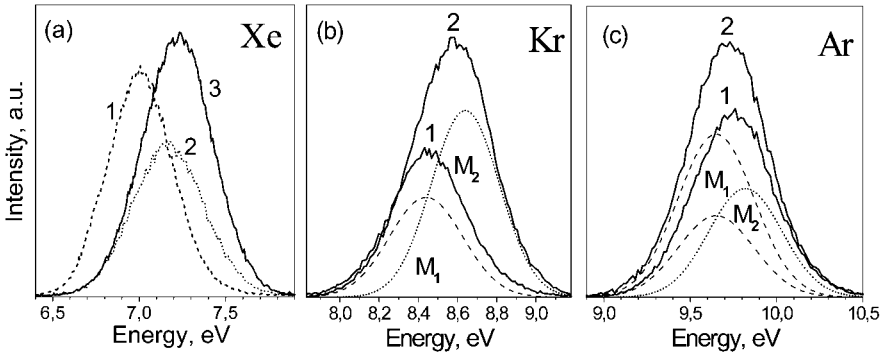

Figure 3. M-bands of RGS at *T*=5 K under photoexcitation with energies listed below. (a) Xe – (1) 8.25 eV, and (2,3) 8.89 eV before (2) and after (3) annealing at 60 K. (b) Kr – (1) 10.02 eV, and (2) 10.6 eV. (c) Ar – 12.06 eV before (1) and after (2) 15 min of wide-band synchrotron-beam irradiation with energies centered at $h\nu$=20 eV with FWHM=13 eV.

4. FRENKEL PAIRS FORMATION BY ELECTRONIC EXCITATIONS

The interatomic bond scission in the crystal lattice may be simulated either by elastic encounters between atoms composing solids and incoming particles or by creation of electronic excitations which transfer the energy to a specified crystal cell. The energy stored by electronic excitations in RGS is much higher than the binding energy ε_b (Table 1), and various trapping processes concentrate the energy within a volume of about a unit cell. The extremely high quantum yield of luminescence [23] allows one to neglect non-radiative transitions, and the population of antibonding $^1\Sigma_g^+$ ground molecular state is usually considered as a main source of kinetic energy for a large-scale movement of atoms finishing in the Frenkel defects or desorption of atoms in the ground state – ground-state (GS) mechanism.

On the other hand, the processes of formation of A-STE and M-STE centers themselves are accompanied by a considerable energy release (E_A* and E_M*) to the crystal lattice (see Fig.2a. and Table 1) which also exceeds the binding energy ε_b. Such an excited-state (ES) mechanism of the large-scale atomic movement was the subject of our recent investigations.

The analysis of the luminescence spectra of solid Xe, Kr, and Ar (Fig.3) under different excitation conditions, excitation energies and crystal-growth conditions made it possible to elucidate the internal structure of *M*-bands. Each of the *M*-bands can be well approximated by two Gaussians: low

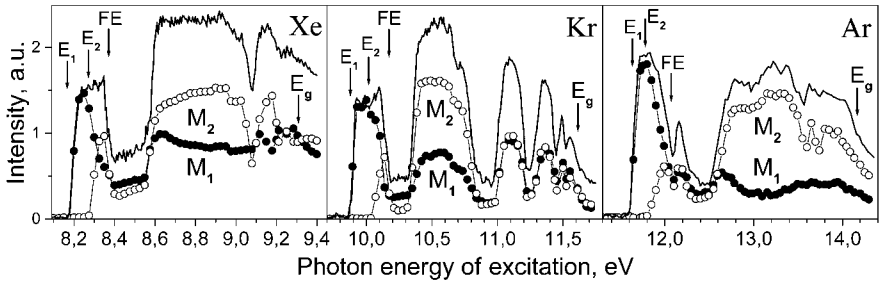

Figure 4. Excitation spectra of *M*-bands and subbands M_1 (●) and M_2 (○) of RGS.

energy subband M_1 and high energy one M_2. The subband M_2 is dominant in the luminescence of more perfect samples. The spectra of samples with a great number of initial defects are mainly determined by the component M_1.

This suggests that the subband M_2 is emitted by the excitons which are self-trapped in the regular lattice (M_2-centers) while the component M_1 is emitted by the centers (M_1-centers) which are populated during trapping that occurs with the lattice imperfections involved.

Because of the strong overlapping of molecular subbands there is no way of recording the excitation spectra of the M_1 and M_2 subbands separately and we restored these spectra by decomposing the sequence of the luminescence spectra measured at different excitation energies (Fig.4) [18]. Using the restored excitation spectra one can determine their threshold energies E_1 and E_2 for the M_1 and M_2 subbands to appear (Table 1). In all cases the excitation spectra of the M_1-subbands exhibit preferential excitation at energies below the n=1 exciton and in the range $E_1<E<E_2$ the direct photoabsorption by defect-related centers produces the only M_1 component in the spectra [24]. The transformation of the *M*-band due to the sample annealing (Fig.3a) or irradiation, resulting in the lattice degradation (Fig.3c), in all cases may be described by the intensity redistribution between two subbands.

The *A*-bands of solid Ar and Ne have a similar two-component internal structure [6,19]. Each band of the bulk emission associated with the transitions $^3P_1 \rightarrow {}^1S_0$ and $^1P_1 \rightarrow {}^1S_0$ consists of a high-energy component stemmed from A-STE in a regular lattice and a low-energy one which appears to be associated with structural defects.

The time (or dose) dependences of the subbands turned out to be a very precise and sensitive tool to study the defect formation, and STE can be used to both trigger and probe the dynamics of lattice rearrangement in RGS. Figures 5 and 6 show examples of evolution of luminescence spectra of RGS under irradiation by electrons (Fig.5) and photons (Fig.6). In all cases a pronounced increase in the intensity of the defect component during

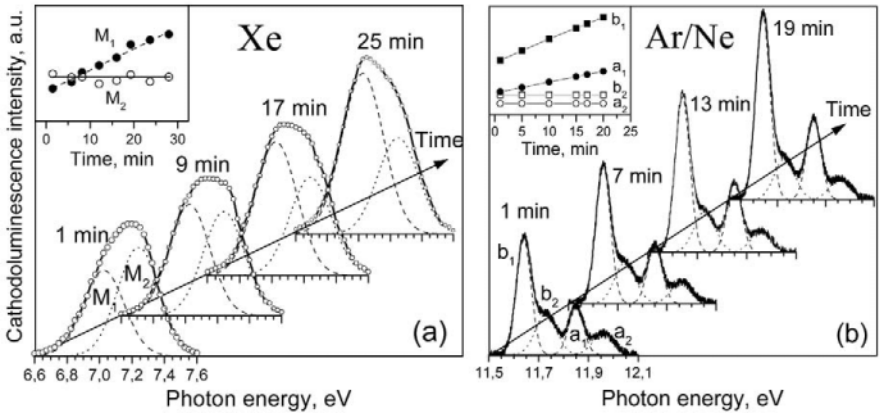

Figure 5. Evolution with exposure time (dose) of cathodoluminescence of solid Xe (a) and Ar atoms in Ne matrix (b). The insets show the dose dependences of the subbands.

irradiation has been observed for A-STE (Fig.6a–c), M-STE (Fig.5a) and for impurity atomic emissions (Fig.5b) in solid Xe [10,18,19], Kr [18,20], Ar [18,22,25] and Ne [6,25,26], evidencing the accumulation of stable long-lived defects in the lattice. Since the energy of STE is transferred into kinetic energy of atomic motion over a unit cell, the formation of three-, two-, or one-dimensional defects is ruled out. In this case, only the point defects, Frenkel-pairs, may emerge in the bulk of the crystal.

M-STE is the main channel of exciton self-trapping in solid Xe, Kr, and Ar. In addition to the GS-mechanism, we proposed an ES-mechanism of M-STE to Frankel-pair conversion [20] which consists of three stages (Fig.7). The process is supposed to occur by (stage 1) self-trapping of an exciton (Fig.7a→b) with a subsequent displacement (stage 2) of M-STE from the centrosymmetric position in the <110> direction (Fig.7b→c) followed by (stage 3) reorientation to the <100> direction (Fig.7d) to

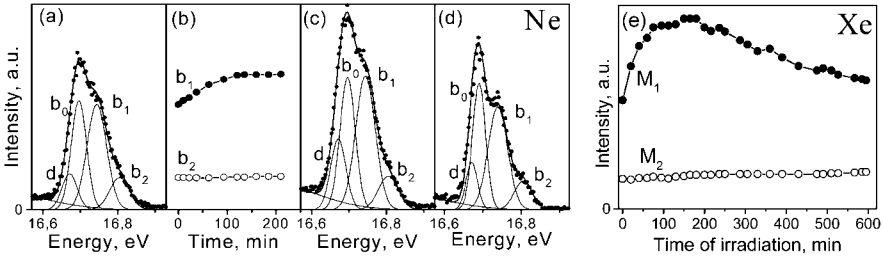

Figure 6. (a)–(d) Evolution of *A*-band of solid Ne at T=5 K: (a–c) – under irradiation by 20 eV photons, (d) – after annealing at T=11.5 K. (e) – Dose dependence of M_1 and M_2 subbands of solid Xe excited by photons with $h\nu$=9.15 eV at T=21 K.

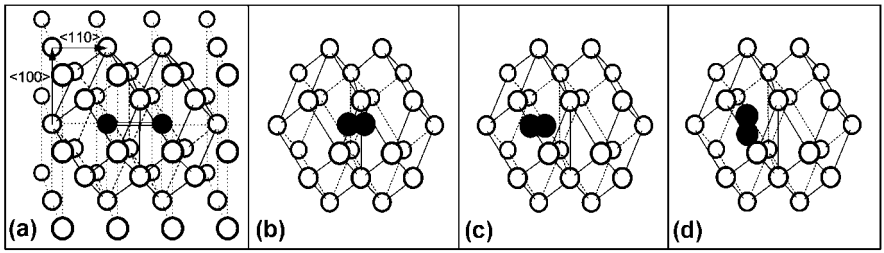

Figure 7. Scheme of ES-mechanism of Frenkel-pair formation induced by exciton self-trapping into quasi-molecular state.

stabilize the defect. The radiative decay of the stabilized excimer (Fig.7d) results in the creation of a stable point defect, Frenkel-pair, in the lattice, whereas the radiative decay of M-STE in the off-center position (Fig.7c) returns the lattice into the initial (Fig.7a) state without permanent defect. Thus, the state Fig.7c may be considered as a metastable short-lived lattice defect, which, together with stable defects, emits the M_1-subband, but is not accumulated in the crystal lattice. The M_2-subband is emitted by radiative decay of M-STE in the on-center position Fig.7b.

Increase of the stable Frenkel-pair concentration under irradiation of the samples is saturated (Fig.6) when the trapping of excitons at defects exceeds the exciton self-trapping in the perfect lattice. Further long-time irradiation of the samples results in an aggregation of vacancies and interstitials, which results in decrease of intensity of defect subbands (Fig.6e).

The Frenkel-pair formation induced by excitation of Rydberg states of atomic-like centers was studied both for the intrinsic process of lattice degradation (exciton self-trapping in solid Ne [26]) and for the extrinsic process of lattice degradation induced by excitation of impurity atoms (trapping of exciton at Ar impurity in Ne matrix [25] (Fig.5b) and selective photoexcitation of Xe impurity in Ar matrix [27]). The strong repulsion of the Rydberg electron with a closed shell of surrounding atoms induces a substantial local lattice rearrangement. In solid Ar and Ne this rearrangement leads to a "bubble" formation, i.e., the surrounding atoms are pushed outwards and a cavity is formed around the excited atom (Fig.2c and Fig.8a).

The ES-mechanism of Frenkel-pair formation as a result of excitation of Rydberg atomic states was confirmed by recent molecular dynamics calculations [28,29]. After the bubble formation the surrounding ground state atoms appear to have moved to the second shell. It was found that the second-nearest neighboring vacancy-interstitial pairs could create the permanent defects, which remain in the lattice after exciton annihilation (Fig.8b) [29].

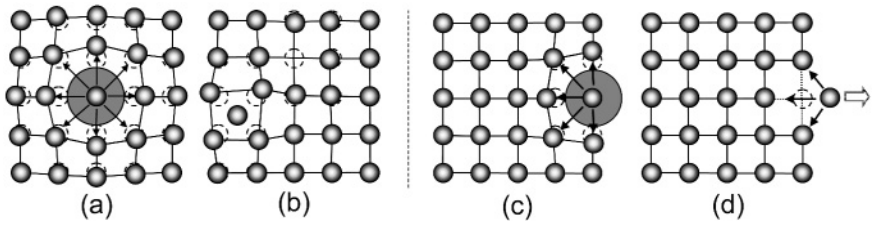

Figure 8. Scheme of inelastic processes induced by A-STE in atomic cryocrystals: (a→b) – Frenkel-pair formation; (c→d) – desorption of excited atoms.

In all RGS selective excitation of excitons by photons of energies below the band-gap energy E_g results in accumulation of Frenkel-pairs, which is a direct proof of the excitonic nature of the ES-mechanism of defect formation.

5. DESORPTION INDUCED BY ELECTRONIC EXCITATIONS

The ejection of atoms or molecules from the surface of solid in response to primary electronic excitation is referred to as electronically stimulated desorption (ESD) or desorption induced by electronic transitions (DIET). Localization of electronic excitations at the surface of RGS induces DIET of atoms both in excited and in ground states, excimers and ions. Most authors (see e.g. Refs. [8,11,23,30] and references therein) discuss their results on DIET from RGS in terms of three different desorption mechanisms namely (i) M-STE-induced desorption of ground-state atoms; (ii) "cavity-ejection" (CE) mechanism of desorption of excited atoms and excimers induced by exciton self-trapping at surface; and (iii) "dissociative recombination" (DR) mechanism of desorption of excimers induced by dissociative recombination of trapped holes with electrons.

(i) After the radiative decay of M-STE (Fig.2a) the strongly repulsive $^1\Sigma_g^+$ ground molecular state is populated. The nonradiative transfer of electronic energy to the kinetic energy of two involved atoms induces the Frenkel-pair formation (GS-mechanism) in the bulk of the sample or ESD of the ground-state atom, if such a process occurs at the surface. Desorption occurs either directly by the escape of one of these "fast" atoms or through secondary processes like collision cascades initiated by the fast particles.

(ii) The "cavity-ejection" mechanism (Fig.8c,d) is a consequence of repulsive force between the excited atom (A-STE) and its neighbors due to the overlap of their electron wave functions. For solid Ne and Ar which have

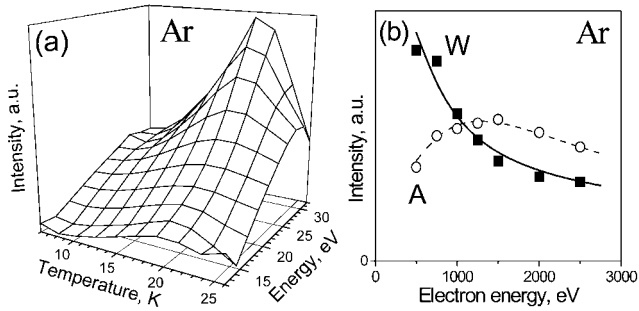

Figure 9. (a) – The dependence of integral intensity of *W*-band of solid Ar on temperature and photoexcitation energy. (b) – The dependence of integral intensity of *W* and *A* bands on energy of electrons in cathodoluminescence of solid Ar.

a negative electron affinity (Table 1) the free exciton self-trapping in the bulk results in a cavity ("bubble") formation around A-STE (Fig.8a). At the surface the short-range repulsion is no longer spherically symmetric like in the bulk but effectively directed outside the surface, leading to the ejection of the excited atom (Fig.8d) or excimer [11]. DIET by the CE-mechanism has unambiguously been verified by the detection of luminescence light originated from electronically excited species in the bloom of gas in front of the surface under irradiation [11,30], and by the detection of metastable particles in ESD [31]. In luminescence spectra the desorption of excited atoms manifests itself as narrow resolution-limited atomic lines [10,19] (e.g. line b_0 of solid Ne in Fig.6a-d).

(iii) The DR-mechanism was proposed to explain the desorption of excimers from the surface of solid Ar. In luminescence spectra the DIET of vibrationally excited dimers of Ar manifests itself as a *W*-band (Fig.1a). The recombination of self-trapped hole Ar_2^+ with an electron at the surface of the sample results in the separation of the Ar and Ar* atoms along the repulsive $3\Pi_u$ potential of Ar_2*. The dimerization of the moving energetic Ar* with a neighboring Ar results in the desorption of Ar_2* [11].

Direct verification of DR-mechanism of DIET was provided [21] by combining the state-selective photoexcitation of the sample and the controlled thermally induced release of electrons from electron traps (Fig.9a). In RGS, after electron-hole pair creation at selective excitation by photons with energies $E>E_g$, the hole may survive and be self-trapped if the electron is captured by any kind of traps [32]. In solid Ar at $T>21$ K the main part of electron traps is not active [12], the electron-hole recombination occurs before self-trapping the holes, and, therefore, the concentration of *W*-band emitting centers decreases (Fig.9a). On the contrary, the heating

above T=21 K at selective excitation of solid Ar in the excitonic energy range $E<E_g$ produces no decrease in the intensity of the *W*-band.

Cathodoluminescence provides an additional evidence of non-excitonic nature of the mechanism of excimer desorption. The dependences of integral intensity of luminescence bands on electron beam energy (Fig.9b) for *A*-band (excitonic CE-mechanism) and *W*-band (non-excitonic DR-mechanism) are quite different. Changing the electron energy varies the excitation depth beneath the sample surface. The electronic excitations propagate through the bulk as free excitons or mobile holes and are localized at the surface, causing desorption distant from the site of primary excitation [8]. The mobility of holes is much smaller than that of free excitons [33], and just the energy transfer to the surface by excitons or holes governs the efficiency of DIET of excited atoms (*A*-band) or excimers (*W*-band).

6. CONCLUSIONS

Atomic cryocrystals which are widely used as inert matrices in the matrix isolated spectroscopy become non-inert after excitation of an electronic subsystem. Local elastic and inelastic lattice deformation around trapped electronic excitations, population of antibonding electronic states during relaxation of the molecular-like centers, and excitation of the Rydberg states of guest species are the moving force of Frenkel-pairs formation in the bulk and desorption of atoms and molecules from the surface of the condensed rare gases. Even a tiny probability of exciton or electron-hole pair creation in the multiphoton processes under, e.g., laser irradiation has to be taken into account as it may considerably alter the energy relaxation pathways.

ACKNOWLEDGEMENTS

I have the pleasure of expressing my thanks to Prof. G. Zimmerer and Dr. E. Savchenko for fruitful discussions. The support of DFG grant 436 UKR 113/55/0 is gratefully acknowledged.

REFERENCES

[1] N. Itoh, A.M. Stoneham, Materials Modification by Electronic Excitation, Cambridge University Press, Cambridge, 2001.
[2] K.S. Song, R.T. Williams, Self-Trapped Excitons, Springer-Verlag, Berlin, 1996.
[3] Rare Gas Solids, eds. M.L. Klein and J.A. Venables, Academic Press, New York, 1977.

[4] Cryocrystals, eds. B. Verkin and A. Prichot'ko, Naukova Dumka, Kiev, 1983.
[5] N. Schwentner, E.-E. Koch, J. Jortner, Electronic Excitations in Condensed Rare Gases, Springer-Verlag, Berlin, 1985.
[6] I.Ya. Fugol, Adv. Phys. 37, 1 (1988).
[7] G. Zimmerer, in: Excited-State Spectroscopy in Solids, eds. U.M. Grassano and N. Terzi, North-Holland, Amsterdam, 1987, p.37.
[8] P. Feulner, D. Menzel, in: Laser Spectroscopy and Photochemistry on Metal Surfaces, eds. H.-L. Dai, W. Ho, World Scientific, Singapore, 1995, p.627.
[9] V.A. Apkarian, N. Schwentner, Chem. Rev. 99, 1481 (1999).
[10] A.N. Ogurtsov, E.V. Savchenko, E. Sombrowski, S. Vielhauer, G. Zimmerer, Fizika Nizkikh Temperatur 29, 1125 (2003).
[11] C.T. Reimann, W.L. Brown, D.E. Grosjean, M.J. Nowakowski, W.T. Buller, S.T. Cui, R.E. Johnson, Nucl. Instrum. Meth. Phys. Res. B 58, 404 (1991).
[12] A.N. Ogurtsov, E.V. Savchenko, O.N. Grigorashchenko, S.A. Gubin, I.Ya. Fugol, Low Temp. Phys. 22, 922 (1996).
[13] A.N. Ogurtsov, E.V. Savchenko, J. Becker, M. Runne, G. Zimmerer, Chem. Phys. Lett. 281, 281 (1997).
[14] A.N. Ogurtsov, E.V. Savchenko, J. Becker, M. Runne, G. Zimmerer, J. Luminesc. 76&77, 478 (1998).
[15] A.M. Boichenko, V.F. Tarasenko, S.I. Yakovlenko, Laser Physics 9, 1004 (1999).
[16] A.N. Ogurtsov, E.V. Savchenko, M. Kirm, B. Steeg, G. Zimmerer, J. Electron Spectrosc. Relat. Phenom.101-103, 479 (1999).
[17] O.N. Grigorashchenko, A.N. Ogurtsov, E.V. Savchenko, I.Ya. Fugol, in: Proc. Int. Conf. on Radiation Materials Science (Alushta 1990) v.10, p.53.
[18] A.N. Ogurtsov, E.V. Savchenko, J. Low Temp. Phys. 122, 233 (2001).
[19] I.Ya. Fugol, E.V. Savchenko, Yu.I. Rybalko, A.N. Ogurtsov, Sov. J. Low Temp. Phys. 12, 439 (1986).
[20] E.V. Savchenko, A.N. Ogurtsov, O.N. Grigorashchenko, S.A. Gubin, Chem. Phys. 189, 415 (1994).
[21] O.N. Grigorashchenko, A.N. Ogurtsov, E.V. Savchenko, J. Becker, M. Runne, G. Zimmerer, Surf. Sci. 390, 277 (1997).
[22] E.V. Savchenko, A.N. Ogurtsov, O.N. Grigorashchenko, S.A. Gubin, Low Temp. Phys. 22, 926 (1996).
[23] D.E. Grosjean, R.A. Vidal, R.A. Baragiola, W.L. Brown, Phys. Rev. B 56, 6975 (1997).
[24] A.N. Ogurtsov, E.V. Savchenko, E. Gminder, S. Vielhauer, G. Zimmerer, Surf. Rev. Lett. 9, 45 (2002).
[25] E.V. Savchenko, A.N. Ogurtsov, O.N. Grigorashchenko, Solid State Phys. 40, 903 (1998).
[26] E.V. Savchenko, A.N. Ogurtsov, G. Zimmerer, Low Temp. Phys. 29, 270 (2003).
[27] A.N. Ogurtsov, E. Gminder, M. Kirm, V. Kisand, B. Steeg, S. Vielhauer, G. Zimmerer, HASYLAB Annual Report 1999, Hamburg, 2000, p.249.
[28] G. Rojas-Lorenzo, J. Rubayo-Soneira, F. Vigliotti, M. Chergui, Phys. Rev. B 67, 115119 (2003).
[29] C. Fu, K.S. Song, J. Phys. Condens. Matter 9, 9785 (1997).
[30] T. Kloiber, G. Zimmerer, Radiat. Eff. Def. Solids 109, 219 (1989).
[31] G. Leclerc, A.D. Bass, A. Mann, L. Sanche, Phys. Rev. B 46, 4865 (1992).
[32] A.N. Ogurtsov, A.M. Ratner, E.V. Savchenko, V. Kisand, S. Vielhauer, J. Phys.: Condens. Matter 12, 2769 (2000).
[33] A.M. Ratner, Low Temp. Phys. 29, 174 (2003).

PROGRESS ON ELECTRON ENERGY LOSS SPECTROSCOPY OF NANOMATERIALS

P. MOREAU
Institut des Matériaux Jean Rouxel, UMR6502 CNRS - Université de Nantes, Laboratoire de Chimie des Solides, 2 rue de la Houssinière, BP 32229, 44322 Nantes Cedex3, FRANCE

Abstract: Electron Energy Loss Spectroscopy in a Transmission Electron Microscope now has a very high energy resolution (0.1 eV) associated with a sub-nanometer probe. All elements of the periodic table can be detected, which makes it an essential technique for nanomaterial studies. After presenting the basis of the technique, a review of the most recent results is presented with a focus on: interfaces (Si-SiO_2 and derivatives), nano-objects (nanotubes, onions…), nanomaterials (composites, quantum wells…). Special consideration is given to the simulation of EELS spectra, showing the crucial explanatory aspect provided by theory. Finally, a more prospective part envisages possible near future developments in EELS which may help us solve forth-coming challenges in nanometer-scale analysis.

Key words: EELS, LELS, Electron-Energy-Loss Spectroscopy, Nanomaterials, interfaces

1. INTRODUCTION

In the past ten years the tremendous development of the manufactured nano-world has generated an ever greater interest for analytical tools with high spatial resolution. Up to now, Electron Energy Loss Spectroscopy (EELS) in a Transmission Electron Microscope (TEM) is the only method meeting the criteria for nanometer or sub-nanometer analysis, in the bulk and for any element of the periodic table. As will be shown in the following, the limits of the technique seem to have disappeared and it is now possible to attain the ultimate sub-atomic resolution. Before illustrating these advances however, which were clearly present in the SALSA meeting in Guadeloupe

E. C. Faulques et al. (eds.), Spectroscopy of Emerging Materials, 57–68.

[1], let us remind ourselves of some of the basic principles of EELS (for an exhaustive review, see the reference book by Egerton [2]).

High energy electrons (typically 100 - 400 keV) are focused onto a sample which they are transmitted through. These electrons interact with the sample, thereby losing a certain amount of energy, which is determined via a spectrometer. Considering the inelastic mean free path for these high energy electrons, the typical thickness of the studied sample ranges from 100 to 500 nm. Special techniques can fashion samples of this thickness, although in the present context, nanometer-size samples are obviously often small enough. A spectrum characteristic of the sample is thus produced. The inelastic interaction of the fast electron with the material induces electronic transitions from occupied to empty levels above the Fermi level (Figure 1a).

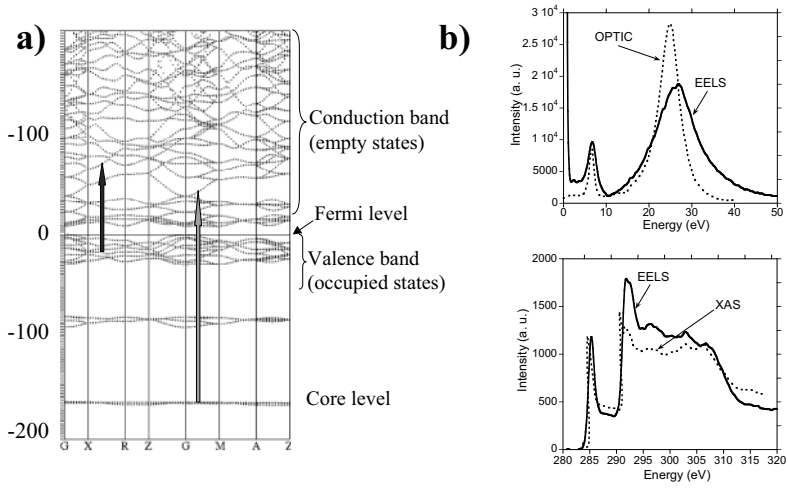

Figure 1. a) Schematic band structure illustrating transitions from the valence band to the conduction band (black arrow) and from core levels to the empty states above Fermi level (grey arrow).b) comparison, for graphite, (top) of LELS with optic measurements (optic data from [3]) and (bottom) of Core Losses with XAS (XAS data from [4])

Owing to the different dispersion degrees of the starting levels, Low Energy Losses (LELS) are, by convention, separated from Core Losses (say, below and above 100 eV). Dielectric medium theory shows that the energy loss spectrum is proportional to $\mathrm{Im}(-1/\varepsilon(E,q))$ with $\varepsilon(E,q)$ the energy and momentum dependent dielectric function of the medium. Low loss spectra can readily be compared to optic measurements even though the q-dependency differs in the two spectroscopies (Figure 1b). It can be shown that core loss spectra are proportional to ε_2 and, providing q is small enough, the matrix elements formula is very similar to that obtained for X-ray Absorption Spectroscopy (XAS) :

$$\varepsilon_2(q \to 0, E) \propto \sum_{\substack{\text{empty,} \\ \text{occupied,k}}} \left| \left\langle \psi_k^{\text{occupied}} \middle| q.r \middle| \psi_k^{\text{empty}} \right\rangle \right|^2$$

Here, the diffusion vector **q** plays the same role as the electric field in XAS (Figure 1b). Hence, the spectra are element, *l* (azimutal quantum number) and *m* (magnetic quantum number) dependent. XAS and EELS can be seen as complementary since, due to the fast decay of the EELS signal as a function of the energy loss, EELS is best suited for light element studies (via their K edges). Very useful information can also be obtained from heavier elements via their $L_{2,3}$ edges (→ Yttrium) or $M_{4,5}$ edges (→ Platinum). But what makes EELS the ideal tool for nanomaterial analysis is its ability to add a spatial dependency to the recorded spectrum. Indeed, the routine probe size available in recent TEMs is around 1 nm. This resolution would not be of any use if it were not associated with images with a comparable resolution : around 2Å in phase contrast or Annular Dark Field (in a Scanning-TEM, STEM). Other standard tools for TEM users, like diffraction or Energy Dispersive X-Rays spectrometers, are essential complements to an exhaustive analysis. Consequently, even if the vacuum in the microscope, the possible high energy beam damages or the sometimes delicate specimen preparation might harden the sample study, EELS must be considered in the course of nanomaterials research.

The small size of a nanomaterial implies the existence of interfaces between its components, or between itself and vacuum. These interfaces are often responsible for the special properties observed. That is why the first part of this paper deals with some remarkable and illustrative examples of technologically important interfaces. The second part focuses on nano-objects, potentially nanomaterials because of their small size but whose application is not yet effective. The third part is dedicated to well-established nanomaterials, the knowledge of which has been vastly improved thanks to EELS in a (S)TEM. Finally, a more prospective part presents the very next challenges to be faced in a near future. In all these parts, both Core Loss and LELS examples are given to demonstrate the complementarity of the two energy domains.

2. INTERFACES

The Si-SiO_2 interface is one of the most studied interfaces in the semi-conductor industry. The technological limit of ultrathin gate oxides based on SiO_2 is about to be reached and it is essential to fully understand the Si-SiO_2 interface to move on to next generation gates. The first atomic resolution

EELS study of this interface was carried out by Batson [5]. It revealed the presence of Si^{2+} (SiO like layer) and possible defect states at the boundary (Figure 2a). LELS can also give information about the interface. We showed that the use of relativistic formula was essential to explain the shift of the interface plasmon peak (IPP) as the probe was moved away from the interface (Figure 2b). The agreement with the experiment allowed us to conclude that a 1 nm thick SiO layer had to be introduced between Si and SiO_2 to fit the IPP position precisely [6].

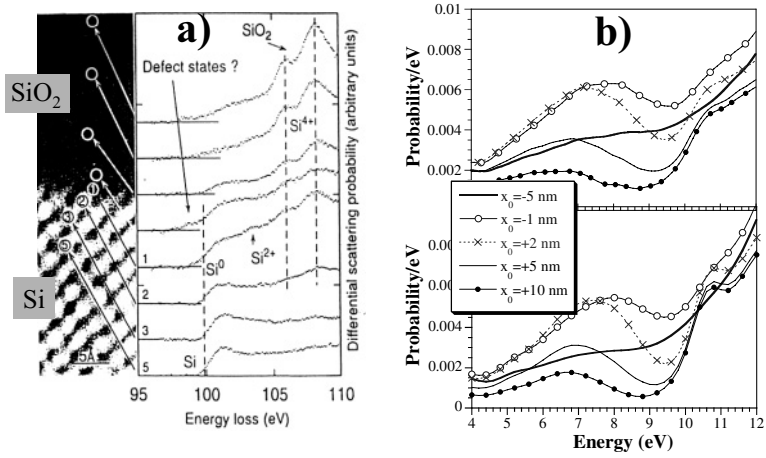

Figure 2. a) EELS silicon $L_{2,3}$ edges on a Si-SiO_2 interface. Left: annular dark field image of the interface ; right: corresponding EELS spectra for different probe positions, reprinted from [5] Copyright (1993) with permission from Nature Publishing Group. b) Top : experimental interface plasmon peak as a function of the probe position (x_0=0 : on the interface). Bottom : corresponding calculated relativistic spectra.

The next step on was to study double interfaces present in thin gate oxides. In order to get a better picture of the interfaces, Muller *et al.* [7] recorded the oxygen K-edge through the Si-SiO_2-Si gate, with an atomic resolution. Noticing the step like spectrum obtained for interfacial oxygen compared to the white line one for bulk SiO_2, they managed to fit each spectrum of the line scan with a linear combination of these two spectra. In doing so, they showed that before annealing, two well-separated areas of interfacial states existed (Figure 3a top). For thin gates, these two areas merged after annealing leading to a leakage current of 10 Acm^{-2} (Figure 3a middle). For thicker gates (typically 1.8 nm, Figure 3a bottom), even after annealing, a sizable amount of bulk-like SiO_2 persisted, which lead to a reduced leakage current (10^{-5} Acm^{-2}). Similar recent studies have been completed on other candidates for future gates, for example Gd_2O_3 [8] or ZrO_2 [9]. Chemical analysis is not the only information that can be retrieved

from these high resolution spectra: associated with *ab initio* calculations, they also allow researchers to pinpoint the reasons for non abrupt interfaces, for example. In particular, it was shown that the second oxygen nearest neighbor was crucial to the local density of states at the interface [10].

IPPs are modified by the presence of a second interface, even tens of nanometers apart. The position of the Double Interface Plasmon Peak depends essentially on the distance between the two interfaces and is not shifted as the probe position is changed (Figure 3b), contrary to the single interface case. The 0.5 eV difference between experiment and theory in the peak position for abrupt interfaces is compatible with the existence of a SiO thin layer on each interface. More details will be given elsewhere [11]. Other studies have also been performed recently on grain boundaries [12, 13] and dislocations [14], helping to choose between various possible structures.

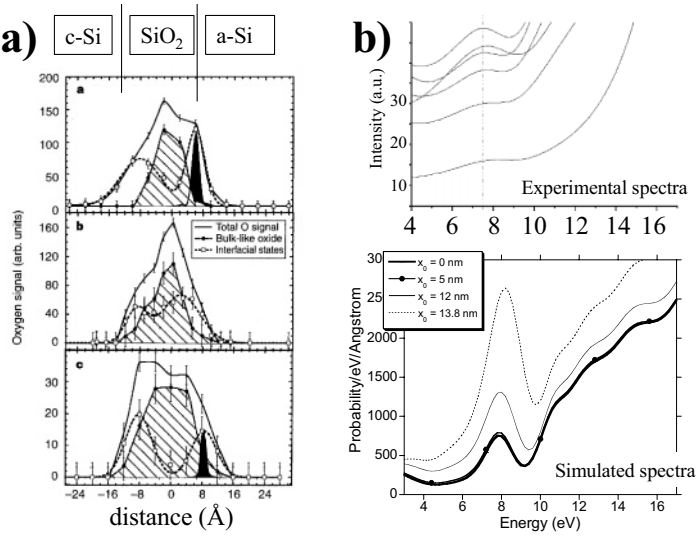

*Figure 3.*a) Interfacial and bulk oxygen signals, as a function of the probe position, in three different double interfaces, reprinted from [7] Copyright (1997) with permission from Nature Publishing Group. b) experimental and calculated LELS spectra for a 28 nm thick gate.

Providing the existence of extra lenses in the spectrometer, element selective images can be obtained. A few eV-wide slit selects electrons that have lost an energy characteristic of the desired element. Bright spots on the CCD camera are consequently representative of a locally large quantity of the imaged element. Chang *et al.* [15] used this technique to reveal an increased carbon amount at the SiC-SiO_2 interface which they attributed to the thermal growth process creating CO molecules at the interface (Fig. 4).

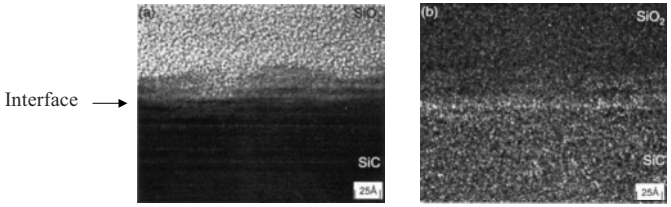

Figure 4 . Left : High resolution TEM image of a SiC-SiO_2 interface. Right : corresponding EELS carbon map. (from Chang K. C., Nuhfer N. T., Porter L. M. and Wahab Q., Appl. Phys. Lett. 77 (2000) 2186 with permission from American Institute of Physics)

3. NANO-OBJECTS

Nanotubes represent the typical nano-objects and this presentation would not be representative without at least one example. The high resolution image on the left-hand side of Figure 5 represents a nanotube, the detailed composition of which cannot be deduced from the image or any technique other than EELS. By performing line scans, it was possible to quantify all the detected elements (B, C, N) as a function of the probe position. From the atomic ratios and the shape of the atomic distribution, Suenaga *et al*. [16] demonstrated that this particular nanotube was made of a succession of 3 carbon layers, 6 boron nitride layers and finally 5 carbon layers.

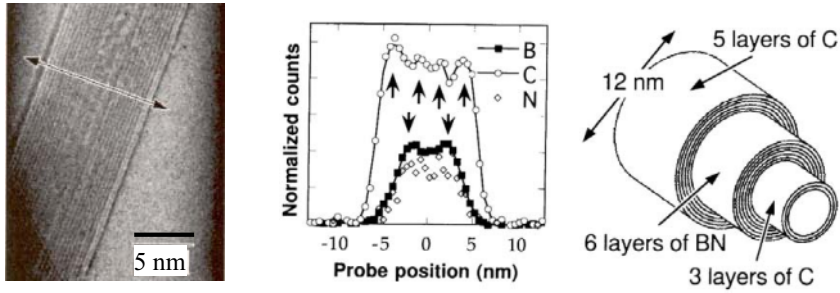

Figure 5. EELS analysis of a multiwall nanotube. Left: TEM image; middle: element analysis as a function of probe position; right: schematic view of the different layers constituting the tube. (from Suenaga K. *et al*, Science 278 (1997) 653 with permission from Science)

More recently, a chemical map of gadolinium atoms in metallofullerene molecules (Gd@C_{82}), themselves inside a single-wall carbon nanotube was obtained. Individual Gd atoms could be detected [17]. Nanotubes [18, 19] and spheres [20, 21] were also studied, introducing anisotropy and relativistic effects in the simulation of LELS. The agreement is particularly

remarkable for the simulation of BN nanofilaments where *ab initio* calculations of the boron nitride dielectric function and anisotropic and relativistic formulae were used [22]. The 10-15 eV region was shown to be very sensitive to possible atomic defects in the walls.

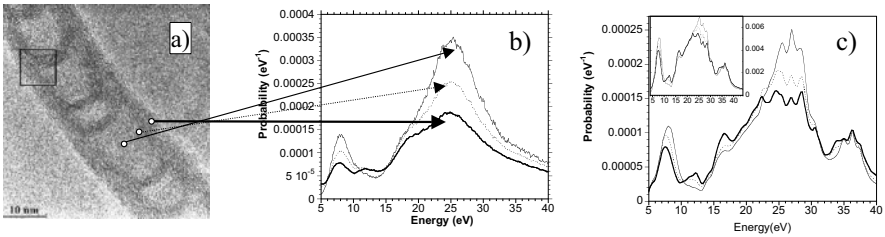

Figure 6. LELS on a BN nanofilaments. a) TEM image; b) experimental spectra for 3 probe positions; c) simulated relativistic spectra (inset: non-relativistic spectra)

Quantum confinement could be evidenced on small silicon nanowires [23]. Focusing the probe on different diameter nanowires, a blue shift of the silicon L_{23} edges which was not detected in a spatially average technique such as XAS. Similar LELS spectra could be conclusively interpreted using the boundary charge method [24].

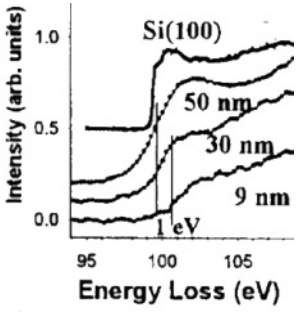

Figure 7. EELS L_{23} silicon edges spectra on various silicon nanowires. (Sun *et al*., J. Appl. Phys. 90 (2001) 6379 with permission from American Institute of Physics)

4. NANOMATERIALS

As materials are getting smaller, how large they have to be to still present bulk properties becomes a very relevant issue. To obtain experimental evidence on that subject and more generally on charge screening in complex

oxides, Ohtomo *et al*. [25] performed line scans on perovskite titanate superlattices. $LaTi^{III}O_3/SrTi^{IV}O_3$ superlattices were grown with different numbers of layers of each compound. The Ti^{3+} and Ti^{4+} distribution was found by fitting the EELS spectra recorded across 1, 2 … layers of $LaTiO_3$ in $SrTiO_3$. The authors showed that the Ti^{3+} signal could be detected up to 2 nm away from a $LaTiO_3$ monolayer. By increasing the number of $LaTiO_3$ layers, they also showed that at least 5 layers were necessary to recover the characteristic bulk Ti^{3+} signal.

$In_xGa_{1-x}N$ quantum wells (QW) separated by GaN barriers were analyzed and experimental spectra compared to *ab initio* calculations (Figure 8). The observed differences with respect to the GaN matrix depend on the degree of indium substitution and also reflect the strain over the QW induced by the barrier lattice. Indeed, by fixing the a and b parameters of the QW to the GaN values, very good agreement EELS/calculation was obtained, as opposed to relaxed $In_xGa_{1-x}N$ parameters [26].

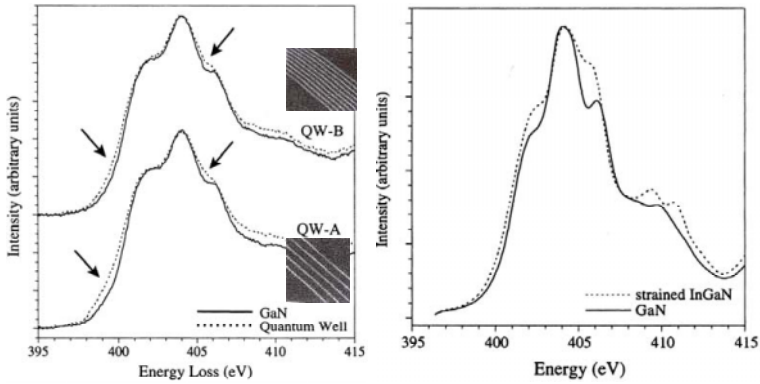

Figure 8. Left : experimental spectra obtained on 2.5 nm (QW-A) and 1.5 nm (QW-B) thick quantum wells. Both spectra are compared with the GaN matrix spectrum. Right : *ab initio* calculations of the strained $In_xGa_{1-x}N$ and of the GaN. (From *J. Microscopy*, Keast V.J., Kappers M.J. and Humphreys C.J., 210 (2003) 89, with permission from Blackwell Publishing)

Nanoporous materials are of great interest for example for their photoluminescent properties (silicon) or possible use as templates (alumina). The types of synthesis of these materials are numerous and the etching/ anodization influences the results [27 - 29]. A detailed studied of Cherenkov radiation in nanoporous alumina membranes has been done which explains the existence of low energy peaks around 7-8 eV [30] (Figure 9 left). Whereas for a cylindrical hole in alumina the simulation does not show a peak, a cylindrical shell of alumina does. The Cherenkov radiation is confined in the shell, as in a wave guide, and a peak appears. If an effective

medium dielectric function is used for the outerspace, the position of the peak can be tuned to the experimental value. Maxwell-Garnett-like functions have long been proven to be useful approximations in the case of dispersed nano-objects in a matrix [31].

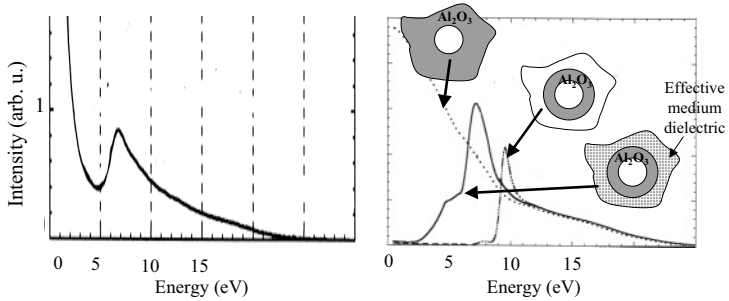

Figure 9. Left: experimental spectrum obtained in the center of a hole in porous alumina. Right: three LELS relativistic simulations. (Reprinted from *Surface Science* 532-535 Zabala N, Rivacoba, Garcia de Abajo F.J. and Pattantyus A., Cherenkov radiation effects in EELS for nanoporous alumina membranes, 461-467 Copyright (2003) with permission from Elsevier)

Typical but precise element analysis was also used to characterize cobalt-carbon nanocluster magnets [32], ferric iron in geologically important minerals [33] or cerium ions in Ce-doped α-sialon [34]. The imaging properties of the new spectrometers were exploited to reveal the magnitude of Young's modulus in carbon-carbon composites [35] as well as to obtain phase specific images of AlN precipitates usually found in steel (Figure 10). At the Al $L_{2,3}$ edge, spectra corresponding to cubic phase particles and hexagonal phase particles differ in their Near Edge Structures (ELNES). By choosing appropriate energy windows, AlN particle phases could be identified [36].

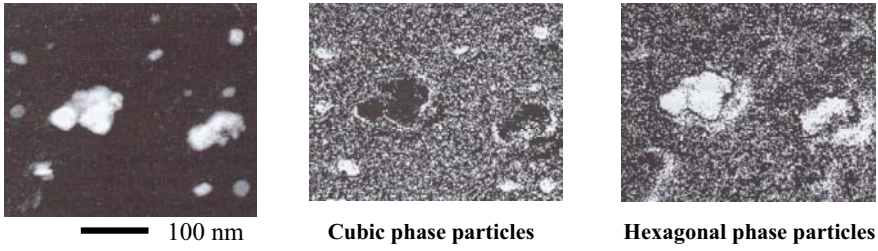

Figure 10. AlN precipitates with different structures. EFTEM images reveal the cubic phase and the hexagonal phase particles (middle and right). (From *J. Microscopy*, Bayle-Guillemaud P, Radtke G. and Sennour M., 210 (2003) 66, .with permission from Blackwell Publishing)

5. FUTURE DEVELOPMENTS

As material science progresses, the size and complexity of the created structures increase. The pursuit of analytical solutions for LELS of these objects becomes very cumbersome and the future could well be in numerical solutions. The Boundary Element Method (BEM) has recently [37] been proven successful in calculating relativistic spectra of any-shape objects. Although anisotropic dielectric functions are not yet implemented, the LELS region, thanks to these new computing tools, should grow in use in a very near future. Indeed, the spectra are material-shape dependent which should be seen, not as a drawback, but as a very valuable piece of additional information.

As suggested by Howie [38], the strong convergence between LELS and Scanning Near-field Optical Microscopes (SNOM) should motivate collaborations. As an example, the LELS spectrum obtained on a gold sphere (D = 100 nm) embedded in a TiO_2 anatase matrix was simulated and compared to recent SNOM results (Figure 11) [39]. A peak around 2 eV is clearly seen in both techniques due to the similar processes involved in the creation of interface plasmon peaks. In connection with the BEM presented above, optimal shapes and configurations could be tested experimentally and theoretically in LELS with a much higher resolution.

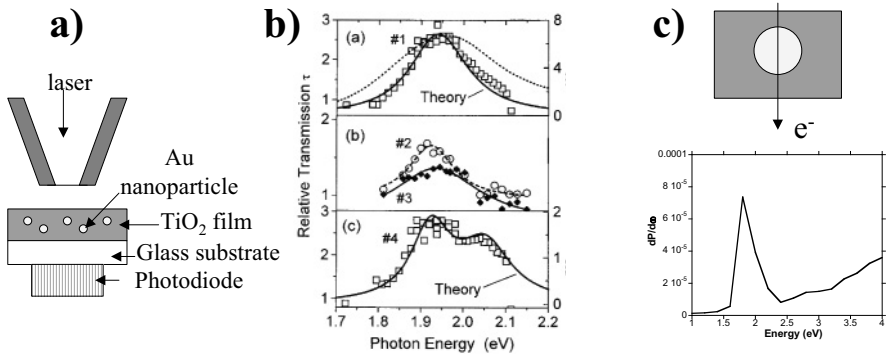

Figure 11. SNOM and LELS. a) schematic SNOM experiment; b) spectra following transmission enhancement via surface plasmon excitations, from [39] Copyright 1998 by the American Physical Society; c) LELS simulation of a similar experiment for a fast (100 kV) electron.

In the core loss region, major advances in the last couple of years allow us to envisage a very bright future for EELS. New generations of high resolution spectrometers (sub-50 meV) associated with improved detection capabilities lead to spectrum quality (Figure 12) only limited by life time broadening [40, 41]. With this energy resolution, magnetic circular

dichroism experiments could be performed in the same way as the XAS community [42] but more generally this will allow a better knowledge of the nanomaterial's electronic structures.

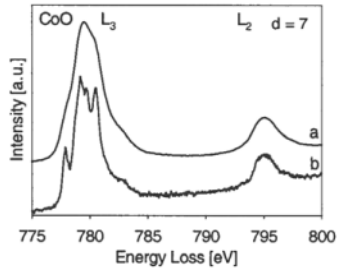

Figure 12. Comparison of old generation TEM-spectrometer typical spectrum (top) with new generation TEM-spectrometer spectrum (bottom). (Reprinted from *Ultramicroscopy* 96, Mitterbauer C., Kothleitner G., Grogger W., Zandbergen H., Freitag B., Tiemeijer P and Hofer F., Electron energy-loss near-edge structures of 3d transition metal oxides recorded at high-energy resolution, 469-480, Copyright (2003) with permission from Elsevier)

Progress on spectrometers was concomitant with TEM improvements. Sub-0.5Å resolution is on the way thanks to aberration correctors [43, 44]. Although these advances are mainly targeted for high resolution images, they also improve the electron density in the probe which increases the signal to noise ratio in EELS spectra. This raises a lot of theoretical questions about nanobeam propagation: for example, as a function of the depth in the sample, the beam can be delocalized on an adjacent atomic column to the one of interest [45, 46]. Once again, this should not necessarily be viewed as a strong issue but a further tool towards, for example, 3D-EELS. Indeed, tomography experiments can now be performed with energy-filtered images showing the precise location, within a nanometer-size particle, of any selected element (Cr, Fe, O…) [47, 48].

As sub-angstrom resolution is now achieved, another dimension is being added to EELS. Another frontier for this amazing technique, till the next one (beyond first Born approximation ? [49]).

REFERENCES

1. Proceedings published in Ultramicrosc. 96 (2003) n°3-4 and J. Microsc. 210 (2003) n°1
2. Egerton R.F., *Electron Energy Loss Spectroscopy in the Electron Microscope* (Plenum Press, New York, 1996), 2nd edition.
3. Taft E.A. and Philipp H.R., Phys. Rev. 138 (1965) 197)
4. Skytt P. *et al*. Phys. Rev. B 50 (1994) 10457

5. Batson P. E., Nature 366 (1993) 727.
6. Moreau P. *et al*., Phys. Rev. B 56 (1997) 6774.
7. Muller D. A. *et al*., Nature 399 (1997) 758
8. Botton G. A. *et al*., J. Appl. Phys. 91 (2002) 2921
9. Muller D. A. and Wilk G. D., Appl. Phys. Lett. 79 (2001) 4195.
10. Neaton J. B., Muller D. A. and Ashcroft N. W., Phys. Rev. Lett. 85 (2000) 1298.
11. Gautier E. and Moreau P., to be published.
12. Kim M. *et al*., Phys. Rev. Lett. 86 (2001) 4056.
13. Nufer S. *et al*. Phys. Rev. Lett. 86 (2001) 5066.
14. Batson P. E., Phys. Rev. B 61 (2000) 16633.
15. Chang K. C., Nuhfer N. T., Porter L. M. and Wahab Q., Appl. Phys. Lett. 77 (2000) 2186.
16. Suenaga K. *et al*, Science 278 (1997) 653
17. Suenaga K *et al*, Science 290 (2000) 2280
18. Taverna D. *et al*. J. Elect. Spect. Rel. Phen. 129 (2003) 293
19. Kociak M. *et al*. Phys. Rev. Lett. 87 (2001) 075501
20. Stöckli T *et al*, Phys. Rev. B 61 (2000) 5751
21. Garcia de Abajo F. J. Phys. Rev. B 59 (1999) 3095
22. Moreau P and Cheynet M-C, Ultramicroscopy 94 (2003) 293
23. Sun *et al*., J. Appl. Phys. 90 (2001) 6379
24. Zabala N., Ogando E., Rivacoba A. and Garcia de Abajo F.J., Phys. Rev. B 64 (2001) 205410
25. Ohtomo A, Muller D. A., Grazul J. L and Hwang H. Y., Nature 419 (2002) 378.
26. Keast V.J., Kappers M.J. and Humphreys C.J., J. Microscopy 210 (2003) 89.
27. Williams P. *et al*., J. Porous Mat. 7 (2000) 159.
28. Massami Sassaki R., Galemback F and Teschke O., Appl. Phys. Lett. 69 (1996) 206
29. Song M., Fukuda Y. and Furuya K., Micron 31 (2000) 429
30. Zabala N, Rivacoba, Garcia de Abajo F.J. and Pattantyus A., Surf. Sci. 532-535 (2003) 461.
31. Howie A. and Walsh C.A. Microsc. Microanal. Microstruct. 2 (1991) 171.
32. Nishi N. *et al*. Chem. Phys. Lett. 369 (2003) 198.
33. Garvie L.A.J. and Busek P.R., Nature 396 (1998) 667.
34. Xu F.F. and Bando Y., J. Appl. Phys. 89 (2001) 5469.
35. Daniels H.R., Brydson R., Brown A. and Rand B, Ultramicroscopy 96 (2003) 547.
36. Bayle-Guillemaud P, Radtke G. and Sennour M., J. Microsc. 210 (2003) 66.
37. Garcia de Abajo F.J and Howie A., Phys. Rev. B 65 (2002) 115418.
38. Howie A., Micron 34 (2003) 121.
39. Klar T. *et al*., Phys. Rev. Lett. 80 (1998) 4249.
40. Mitterbauer C. *et al*. Ultramicroscopy 96 (2003) 469
41. Brink H.A., Barfels M.M.G, Burgner R.P. and Edwards B.N., Ultramicroscopy 96 (2003) 367
42. Hébert C. and Schattschneider P., Ultramicroscopy 96 (2003) 463.
43. Batson P.E., Delby N. and Krivanek O.L., Nature 418 (2002) 617
44. Krivanek O.L. *et al*., Ultramicroscopy 96 (2003) 229
45. Möbus G. and Nufer S., Ultramicroscopy 96 (2003) 285
46. Dwyer C. and Etheridge, Ultramicroscopy 96 (2003) 343
47. Migley P.A. and Weyland M., Ultramicroscopy 96 (2003) 413
48. Möbus G, Doole R.C. and Inkson B.J., Ultramicroscopy 96 (2003) 433
49. Howie A., private communication.

PHOTOELECTRONS SPECTROSCOPY OF ORGANIZED ORGANIC THIN FILMS

Ron Naaman
Department of Chemical Physics, Weizmann Institute, Rehovot 76100, Israel

Abstract: Low energy electron photoemission spectroscopy (LEPS) allows the study of the electronic properties of organized organic thin films (OOTF) adsorbed on conducting surfaces by monitoring the energy and angular distribution of electrons emitted from the substrate and transmitted through the film. This technique provides unique information on the electronic properties of the adsorbed layer.

The electron transmission properties are explained by electronic band structure in the organic film. This band is an example of an electron resonance that is delocalized in the layer. It results from the two dimensional nature of the layer. Other resonances in the transmission spectra are also discussed, as well as their experimental manifestation.

Despite the fact that the molecules in the OOTF are weakly interacting, when not charged, the electron transmission through the film is governed by cooperative effects. These effects must be taken into account when considering electronic properties of adsorbed layers.

Key words: monolayer, electron transmission, supra-molecular

E. C. Faulques et al. (eds.), Spectroscopy of Emerging Materials, 69–82.

1. INTRODUCTION

Close-packed, organized organic layers have been the focus of substantial studies in recent years, due to their abilities to modify electronic properties of substrates[1,2], metals or semiconductors[3,4,5], and applications as elements electronic devices,[6,7,8,9] light emitting diodes[10], sensors,[11] etc. It is usually assumed that the electronic properties of the molecules, assembled in a close packed layer, are similar to that of the isolated molecule or of the molecule embedded in an isotropic medium. The weak coupling between the neutral, ground state molecules in a monolayer seems to support this notion and is taken as a justification for using molecular based calculations to predict the properties of the monolayer.[12,13] However, some simple electrostatic arguments indicate that the pseudo-two-dimensional structure of the organized organic thin films (OOTF) may introduce cooperative properties that can not be inferred from those of the isolated molecule.[14]

Here we discuss the application of low energy photoelectron transmission spectroscopy (LEPS) as a means for investigating the electronic properties of OOTF. In a typical experiment photoelectrons are ejected from the conductive substrate and after being transmitted through the adsorbed layer, the energy (and or angle) dependent electrons flux is measured as a function of incident photon energy, molecular film thickness, adsorbate and substrate types and temperature.

Electron transmission through organic thin films condensed on metal substrates has been investigated in the past mainly by low-energy electron-transmission (LEET) spectroscopy, in which single energy electrons are injected into the layer from the vacuum side and are collected on the conductive substrate.[15,16] It was suggested that for films of saturated hydrocarbon chains of various lengths, the low-energy electron transmission is governed mainly by the film's electronic band structure.[17,18,19,20] Also in the case of ordered rare gas and other simple molecular layers, the transmission,[21,22] as well as the reflection[23] were found to correlate strongly with the band structure of the corresponding crystals. Recently, the electronic properties of adsorbed organic molecules have been investigated by two photon photoemission (TPPE) spectroscopy. Experiments have been performed both with sub-picosecond[24,25] and nanosecond laser pulses[26]. In these studies, the first photon excites electrons in the substrate, which can electron transfer to either a surface state or to a negative ion state on the adsorbate. A second photon detaches the electron from the metastable state and its kinetic energy and angular distribution is measured. The TPPE technique has been used to study the electronic structure of the adsorbed layer,[27] the nature of the electronic states,[28] and the effect of the thickness of the adsorbed layer.[26]

When electrons are ejected from a conductive substrate their energy distribution, $P_0(E)$, depends on the photon energy, the density of states in the substrate, the barrier for electrons to escape from the substrate (work function), and the electron-affinity of the detector. Special attention should be given to the low and high energy cut-offs (LECO and HECO respectively) in the energy distribution. The LECO depends on the work function of the substrate and the difference between it and that of the detector. The HECO is a function only of the photon energy and the electron affinity of the detector. When OOTF is adsorbed on the surface, it may change its work function by exchanging charge with the substrate or by applying force on the ejected electrons, due to the intrinsic dipole moment of the molecules on the layer. Now, the LECO depends on the new work function of the metal-OOTF system. In addition, there is an energy dependent probability, T(E), for electrons to be transmitted through the layer. Hence the final energy distribution of the electrons P(E) is given by:

$$P(E) = P_0'(E) \cdot T(E) \qquad (1)$$

when P_0'(E) is the **modified energy distribution** of the photoelectron ejected from the substrate, due to the chemical bonding of the OOTF. From equation (1) it is clear that in the LEPS studies T(E) cannot be obtained simply by measuring P(E) and the pure substrate - $P_0(E)$, since $P_0 \neq P_0$'. Still, as will be shown, LEPS provides direct information on the electronic properties of the adsorbed film.

In what follows we will discuss the mechanism that controls the electron transmission through OOTFs, the resonances expected in the energy resolved transmission and how the dependence of the transmission on the initial direction of the electrons affects the temperature dependence of the transmission.

2. EXPERIMENTAL

2.1 Film Preparation and Characterization

Several type of OOTFs have been prepared, usually on 100 nm thick gold or silver films that are deposited on glass slides or silicon (100) wafers. OOTFs were deposited using either Langmuir-Blodgett (LB) or Self-Assembly (SA) techniques. The LB films were made from cadmium salts of arachidic [Cdar;$(CH_3(CH_2)_{18}COO^-)_2Cd^{2+}$], brassidic [Cdbr;$CH_3(CH_2)_7CH{=}CH(CH_2)_{11}COO^-)_2Cd^{+2}$] or stearic [Cdst;

$(CH_3(CH_2)_{16}COO^-)_2Cd^{2+}$] acids. Self-assembled films were made from octadecylmercaptane [OM; $CH_3(CH_2)_{17}SH$] and from the molecules shown in Figure 1.

The quality of the layers was determined by the transfer ratio from the trough in the case of LB films, by ellipsometric studies that probe the thickness of the layers and by IR spectroscopy. For successfully deposited films, the contact angle with water was typically 111-113°, except for the molecules shown in Fig. 1 where lower angles were observed. The ellipsometric data for Cdst and Cdbr show that the thickness of each single layer is about 2.40±0.05 nm, independent of the film composition. This number indicates that the Cdbr layers, despite being slightly longer than CdSt, are tilted relative to the surface normal and therefore the thickness of the layers of the two types of film are almost identical. Atomic force microscopy studies confirmed the results obtained from ellipsometry. Layers in which a 1:1 mixture of the Cdbr and Cdst were also produced and probed by the same methods, and their quality was found to be the same as that of the other layers.[29] From other studies[30] it is known that the 1:1 mixed layer is homogenous and no domains are formed.

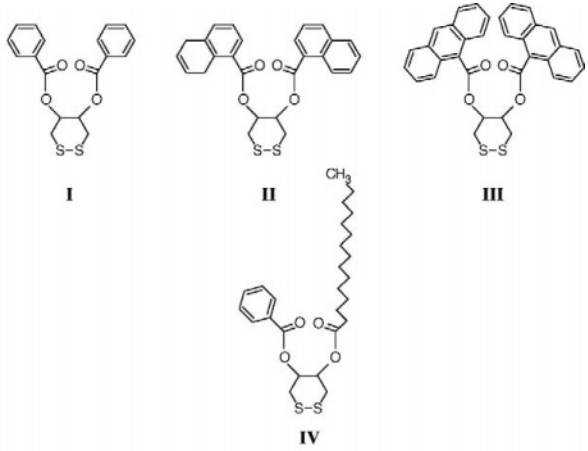

Figure 1: The structure of the molecules adsorbed on the gold surface.

2.2 Photoelectron Energy Distribution Measurements

The slides coated with the OOTF were attached to a temperature controlled holder and inserted into a UHV chamber pumped to below 10^{-8} mbar.[31,32] Various lasers were used to eject photoelectrons from the conducting substrate. The lasers' wavelengths were chosen so that the photon energy will be above the substrate work function, below the

ionization potential of the molecules and will not be absorbed by the adsorbed film. The lasers have 10-20 nsec long pulses and the pulse energy was kept below about 0.1μJ to avoid non-linear effects.

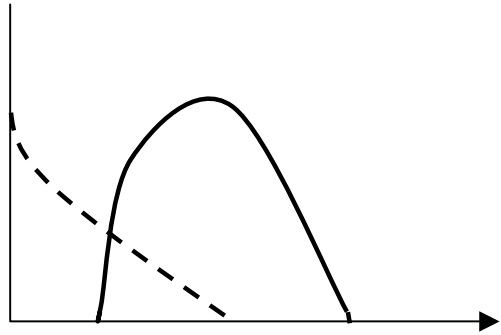

Figure 2: The expected electron energy distribution assuming a "classical" scattering process (dashed line). The initial photoelectron spectrum is shown as solid line.

The laser beam is introduced into the chamber and after reflecting from the sample it exits through quartz windows. The photoelectron kinetic energy distribution was measured either via the retarding field method or by a time of flight electron energy analyzer. In the first method, a grid made of nickel was placed 3 mm in front of and parallel to the OOTF coated slide. The grid could be biased with a negative or positive voltage relative to the metal surface which was kept at ground potential. The close proximity of the grid and the sample ensures high collection efficiency and unperturbed collection of low energy electrons. Although the method is inherently of low resolution, it has the advantage of being sensitive to the low energy electrons. The details of the time of flight energy analyzer are given in ref. 33. In this setup the resolution is of better than 30 meV. The electron energy distributions obtained by both methods were consistent.

3. THE TRANSMISSION MECHANISM- ELECTRONIC BAND STRUCTURE

If one thinks of the electron transmission process as a random scattering process in which electrons change their momentum due to the collision with the atoms, it is expected that any initial energy distribution will become broader and some of the transmitted electrons will have lower energy than

their initial energy. In the case of thick enough layers, this "relaxed" energy distribution may look as shown in Figure 2. Figure 3 presents the actual electron energy distribution of photoelectrons from gold coated with one (A), three (B), five (C) and 13 (D) monolayers of Cdst. From the spectra shown in Figs. 3A-3C it is evident the electrons energy distribution is not "relaxed". Rather it shows a high transmission probability for energies above ca. 0.8 eV and low transmission probability for electrons with lower energies. The energy distribution actually becomes narrower with increasing thickness of the layer. Only when the film becomes relatively thick (about 25 nm), does a somewhat relaxed distribution evolve (Figure 3D). The importance of film order in the electron transmission process is demonstrated in Figure 4, which presents the current density as a function of electron energy for photoelectrons transmitted through 13 layers of Cdar, before (circles) and after (squares) they were heated to 378 K and cooled back again to room temperature. Thus, before heating, electrons with energies near ca. 1eV are transmitted through the band very efficiently with little energy loss. Following the heating, the electron energy distribution indicates that extensive random scattering processes occur.

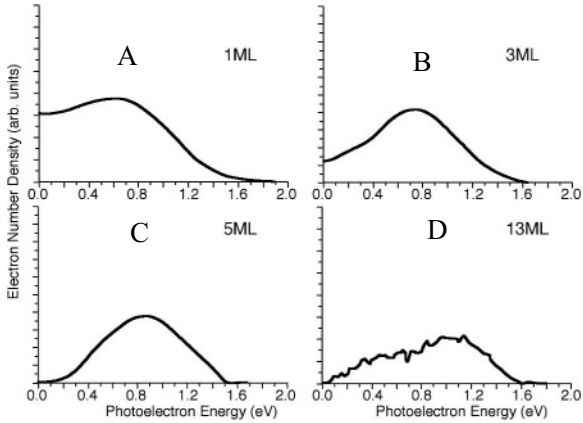

Figure 3: The electron energy distribution of photoelectrons from gold coated with one (A), three (B), five (C) and thirteen (D) monolayers of cadmium stearate.

The results presented above indicate a "non-classical" scattering process which can in principle result from two different effects. One is related simply to the fact that thin layers exist with their thickness comparable to the electrons' wavelength, hence interferences in the transmission result in what is known as "shape resonances". These resonances are very sensitive to the thickness of the layer, but only weakly depend on the electronic properties of

the molecules. Another origin for the structure in the transmission spectrum may arise from the negative ion states of the adsorbed molecules. Since the radius of the electron's orbital in these states is large, it causes coupling with nearby molecules in the layer and electronic bands are formed. In both cases the layer must be well organized.

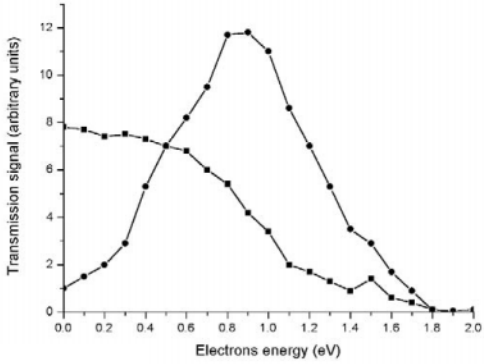

Figure 4: The electron energy distribution as measured by the retarding field method for photoelectrons transmitted through 13 organized (circles) and unorganized (squares) layers of Cdar.

The positions of the maxima of the distributions in Fig. 3 are almost independent of the thickness of the films (1,3 or 5 layers). This is inconsistent with shape resonances and indicates that the second type of resonances is controlling the electron transmission. The transmission indeed depends on the film being well organized, organization which is lost upon warming the layer. The same conclusion has been reached based on LEET studies, where it was suggested that for films of saturated hydrocarbon chains of various lengths, the LEET is governed mainly by the film electronic band structure[17,18]. Other LEET studies have established that the conduction band in many alkane layers is at about 0.2-0.8 eV above the vacuum level.[20]

In the OOTF, periodicity in the potential exists both in the direction perpendicular to the layer's plane (z-axis) and in the directions parallel to the layer (x,y). In the z direction, the periodicity is a result of almost all the chemical functionalities being identical, CH_2 groups. The situation in the xy plane is different, here the periodicity results from having the molecules adsorbed in an organized layer. However, the interaction between the molecules is weak and therefore no band structure can be observed without an additional electron.

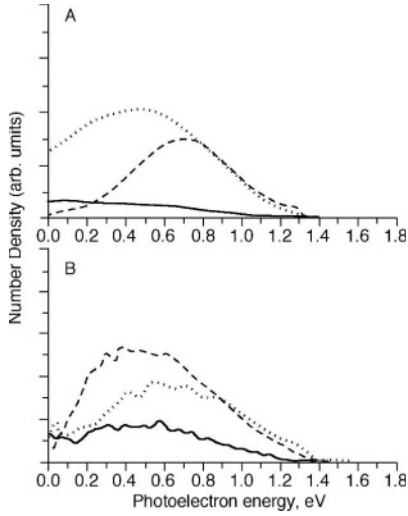

Figure 5: The photoelectron energy distribution is shown for electrons transmitted through layers of Cdar (dashed), Cdbr (dotted) and of mixed monolayers (solid) for three (A) and nine (b) layers.

While in a bulk solid, addition of an electron does not affect the interaction between sub-units, in the OOTFs the additional electron makes all the difference. This can be understood as follows. In bulk solids, the total Hamiltonian describing the system is given by $H = \sum h_n + \sum V_{nm}$ when h_n is the Hamiltonian of each subunit in the solid and V_{nm} is the interaction between the sub-units. The bandwidth is characterized by V_{nm}, which in typical, non-molecular, solids is large. When an additional electron is added to the system, it induces new interaction between the subunits, V'_{nm}, and the Hamiltonian is now given by

$$H = \sum_n h_n + \sum_{n \neq m} V_{nm} + \sum_{n \neq m} V'_{nm} \qquad (2)$$

Since in a typical solid $V_{nm} > V'_{nm}$, the addition of an electron does not change significantly the interaction between the sub-units and therefore does not affect the band structure. In OOTFs, the interaction between the subunits is weak and therefore no band structure can be observed in the spectroscopy of the neutral system. However, when an electron is added to the system, $V'_{nm} >> V_{nm}$. Hence the addition of the electron significantly increases the coupling between the sub-units. This "electron induced coupling" results from the size of the system and its molecular properties, which forces the electron to be localized, at least in one

dimension. Therefore, significant "band structure" exists **only** in the presence of an additional electron.

The importance of the two dimensional periodicity on the transmission properties is demonstrated in Figure 5, which presents the transmission probability of electrons as a function of the photoelectron energy for layers of Cdar (dashed), Cdbr (dotted) and of mixed layers (solid) for three (Fig. 5A) and nine (Fig. 5B) layers. As is clearly evident, the electron transmission through the mixed layers is significantly less efficient than that through the Cdar or Cdbr layers themselves. Moreover, the spectrum for the mixed layers is much closer to the relaxed type (Fig. 2).

Some word of caution is needed at this point. The notion of electronic bands is of course related to the electronic structure of ordered bulk solids, and applying it to thin films is in principle questionable. Indeed, it is sufficient to associate high transmission probabilities with states of the excess electron in the film which are extended on the scale of the film thickness. In fact, numerical results[34] suggest that the correspondence with the band structure of the bulk material is substantial even for very thin films.

The results presented above indicate that 'band conduction', or transmission through electronic states which are extended, is the cause of the efficient electron transmission through amphiphiles. It also rationalizes the observation that electrons are better conducted through all-trans amphiphilic chains than through chains containing some gauche bonds:[35] When the chains are in an "all-trans" configuration, the layer is ordered and the electronic wavefunctions in the band are delocalized. The formation of the gauche bonds amounts to introducing disorder which increases scattering and reflection and, when pronounced enough, localizes the electronic wave function.

4. RESONANCES IN ELECTRON TRANSMISSION THROUGH OOTF

The formation of transient anion states, or electron resonances, plays an important role in low-energy electron-molecule scattering in the gas phase[36]. When electrons are transmitted through thin molecular films, the transmission probability is energy dependent and therefore the energy spectrum is structured.[37,38] The structure may have several origins. The broader peaks are related to the electronic band structure, as discussed above. Namely, they relate to an excess electron being delocalized in the film and the formation of "global" states, electronic states that are delocalized over many molecules (See Fig. 6A). Such resonances are expected for layers made from identical molecules containing repetitive functional groups, like the CH_2 groups in the alkyl chains.

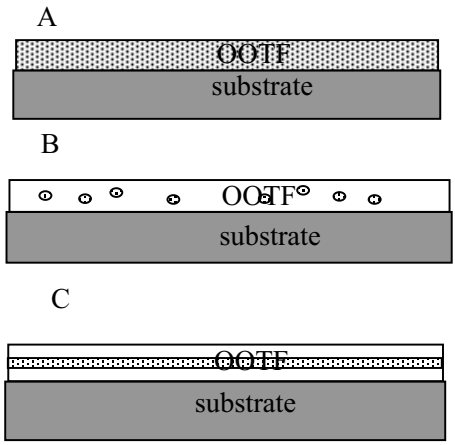

Figure 6: A scheme of the three possible resonances in OOTF. i) Global resonance (A). Very weak electron-vibration interaction is expected ii) Localized resonances or traps (B).Usually the LEPS experiments are not detecting electrons trapped in these resonances and they appear as a reduction in the transmission probability. iii) Quantum well structure (C). Here the electron is localized in one dimension, while it is delocalized in the other two dimensions. There is a significant electron-vibration coupling.

Another type of structure may result from localized resonance states formed by either traps or impurities in the film[39] (see Fig. 6B). In this case, the electrons are localized at the "trap" and due to the high charge concentration strong electron-vibration interactions exist that result in inelastic processes in the film. While these traps are observed clearly in LEET,[39] in the LEPS experiments they are manifest by reduction in the transmission probability and sometimes by charging effects, but cannot be observed as modulation on the amplitude of the spectra.

A third type of resonance may result from the two dimensional structure of the organized organic films. In this case the electron is delocalized in two dimensions but localized in the third one (see Fig. 6C).[40] Hence, the structure in the transmission probability is not a result of complete delocalization of the electron (as in the case of band structure) nor to complete localization of the electron on a single molecule (as in a typical "trap"). As expected, also in this process strong electron-vibration coupling occurs and evidence for inelastic scattering is observed.

This type of resonance is apparent for OOTFs that were formed by self-assembling the molecules shown in Fig. 1 on a 100-nm polycrystalline Au film. The films were well characterized in past studies[41]. Figures 7A present the electron energy distributions obtained for electrons transmitted through films made of molecules I,II and III (see Fig. 1), while Figure 7B shows the

distribution obtained for a monolayer made of molecule IV. The spectra in Fig. 7A consist of two broad bands peaking at about 0.7 and 1.3 eV for all three molecules. On top of these bands fine structure is shown, which is better resolved on the low energy band. In the case of benzene substituted molecule (molecule I) a progression in the fine structure is observed with energy separation of 0.12±0.01 eV. In the case of naphthalene substituted molecules, the progression is composed from two energy intervals 0.80±0.10 and 0.16±0.02 eV. These results are in surprising good agreement with the vibrational resonances reported for benzene and naphthalene in the gas phase, where the resonances are at 0.123 eV for benzene and at 0.78 and 0.170 eV for naphthalene[42]. In the case of anthracene substituted molecule (molecule III), a long and strong anharmonic progression is observed with energy gaps of ΔE=0.18, 0.15, 0.11, 0.09, 0.08 eV. The structure in the spectrum is more pronounced when the aromatic system becomes larger, indicating longer resonance delay for larger systems. When the aromatic rings in molecules I,II and III were substituted by CN, NO_2 or CF_3 the sharp vibronic resonances vanish. This effect is similar to that obtained in the gas phase where it was found that substituted aromatic do not show vibrational structure, due to breaking of the symmetry and shortening of the resonance life-time[42].

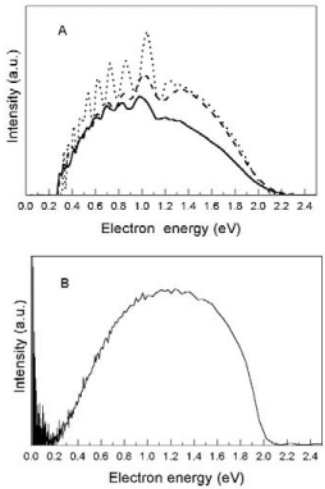

Figure 7: A) The electron energy distribution obtained for electrons transmitted through an organized monolayer made of molecule I (solid line) II (dashed line) and III (dotted line). The molecules are shown in Figure 1. B) The electron energy distribution obtained for electrons transmitted through organized monolayer made of molecule IV (Fig. 1).

The observation that the fine structure in the spectra relate to the vibrational states of the anions of the aromatic parts of the molecule, indicates that the extra electron is delayed near the aromatic groups and therefore electron-vibrational coupling occurs.

Figure 7A displays interference between fine structure due to vibrational coupling and a broad structure which is almost identical for the three types of monolayers. The question that arises is why such vastly different size molecules show similar broad transmission of electrons. Studies of electron scattering from these molecules in the gas phase indicated that the two first electronic resonances for benzene and naphthalene are at 1.12, 4.8 eV and 0.19, 0.9 eV respectively. For anthracene the two first electronic resonances (above the vacuum level) are observed at about 0.6 and 1.13 eV[42]. Hence, we must conclude that despite the fact that the vibrational structure relates to the negative aromatic ions, the electronic structure, observed here, has a different origin.

A model that explains all these observations assumes that the electrons are localized on the aromatic rings, but are delocalized between the molecules, namely the extra electron has a state which is delocalized in the XY plane parallel to the substrate, but is localized on the Z axis (normal to the substrate) so that the extra electron wavefunction has high probability on the aromatic rings. Hence the energy of the electronic states is determined by the size of the "box" in the Z direction and by the polarizability of the aromatic rings.

For calculating the electronic states the following assumptions were made-

1. We assumed boxes with a length that corresponds to the length of the aromatic rings, taking into account their tilt angle vs. surface normal.

2. The energy levels of each box were down shifted by the polarization energy.

Based on these assumptions the observed electronic resonances could be obtained, based on the polarizability of the aromatic components and their length.[43]

5. SUMMARY

Transmission of electrons through organized organic thin films depends on the film's global properties, like order and alignment relative to the

substrate, as well as the properties of the molecules themselves. These findings are of importance when considering the charging/conductive properties of thin organic layers and deviate from the "classical" point of view in which a simple scattering process was assumed to operate. The LEPS technique, as applied, is a relatively simple method that extracts information on electronic properties of adsorbed films. In general, it is complementary to the more established LEET technique. In LEPS one measures the momentum distribution of the electrons after the transmission, while in LEET the momentum is defined before the transmission, but cannot be measured following the transmission process. However, by varying the light-surface incident angle and the photon energy, methods were developed for controlling, to some extent, the momentum distribution of photoelectrons also in the LEPS process. This ability allowed us to obtain information on the momentum dependent electron transmission through OOTFs.

ACKNOWLEDGEMENTS

This work was partially supported by the Israel Science Foundation and by the US-Israel Binational Science Foundation.

REFERENCES

1. Ishii, H.; Sugiyama, K.; Ito, E.; Seki, K. *Adv. Mater.* **1999**, *11*, 605-625.
2. Yaliraki, S.N.; Roitberg, A.E.; Gonzalez, C.; Mujica V.; Ratner, M.A. *J. Chem. Phys.* **1999**, *111*,6997-7002.
3. Vilan, A.; Shanzer, A; Cahen, D. *Nature,* **2000**, *404***,** 166-168.
4. I.H. Campbell, J.D. Kress, R.L. Martin, D.L. Smith, N.N. Barashkov, J.P. Ferraris, *Appl. Phys. Lett.* 1997, **71***,*3528-3530.
5. Hill, I.G.; Milliron, D.; Schwartz, J.; Kahn, A.; *Appl. Surf. Sci.* **2000**, *166*,354-362.
6. C.P. Collier, E.W. Wong, M. Belohradsky, F.M. Raymo, J.F. Stoddart, P.J. Kuekes, R. S. Williams, J.R. Heath, *Science*, 1999, **285**,391-394.
7. Chen, J.; Reed, M.A.; Rawlett, A.M.; Tour, J.M.; *Science*, **1999**, *286*,1550-1552.
8. Vuillaume, D; Chen B.; Metzger, R.M. *Langmuir,* **1999**, *15*,4011-4017.
9. E. Punkka and R.F. Rubner, *J. Elect. Mat.* **1992**, *21*,1057-1063.
10. See for example: Yamamori, A.; Hayashi, S.; Koyama, T.; ; Taniguchi, Y. *App. Phys. Lett.* **2001,***78,* 3343-3345; Crone, B. K.; Davids, P. S.; Campbell, I. H.; Smith, D. L. *J. Appl. Phys.* **2000**, *87*, 1974-1982.
11. Wu, D. G.; Cahen, D.; Graf, P.; Naaman, R.; Nitzan, A.; Shvarts, D.; *Chem. Eur. J.* **2001**, *7*,1743-1749.
12. Nitzan A.; Benjamin, I. Acc. Chem. Res., **1999**, *32*, 854-861.
13. Hutchison, G.R.; Ratner, M.A.; Marks, T.J.; Naaman, R. *J. Phys. Chem. B.* **2001**, *105*,2881-2885.

14. Vager, Z.; Naaman, R., *Chem. Phys.* **2002**, *281*, 305-309.
15. Sanche, L. in *Excess Electrons in Dielectric Media,* edited by Ferradini, C.; and Jay-Gerin, J.-P., (CRC Press, Boca Raton, **1991**), Chap. 1, p. 1.
16. Sanche, L. *Scanning Microscopy*, **1995**, *9*, 619-656.
17. Perluzzo, G.; Bader, G.; Caron L.G.; and Sanche, L. *Phys. Rev. Lett.* **1985**, *55*, 545-548.
18. Caron, L.G.; Perluzzo, G.; Bader, G.; and Sanche, L. *Phys. Rev. B* **1986**, *33*, 3027.
19. G. Dutton, X.-Y. Zhu, *J. Phys. Chem. B*, **2001**, *105*, 10912-10917.
20. a. Maeda, T.; Miyano, K.; Sugita, K.; Ueno, N., *Thin Solid Films* **1989**, *179*, 327-334. b. Ueno, N.; Nakahara, H.; Sugita, K.; and Fukuda, K.; ibid **1989**,*179*, 161-170. c. Ueno, N.; and Sugita, K.; *Phys. Rev. B* **1990**,*42*, 1659-1662.
21. Bader, G.; Perluzzo, G.; Caron, L.G.; Sanche, L. *Phys. Rev. B* **1984**, *30*, 78.
22. Yamane, H.; Setoyama, H.; Kera, S.; Okudaira, K. K.; Ueno, N. *Phys. Rev. B*. **2001**, *64*, 113407.
23. (a) Michaud, M.; Sanche, L.; Gaubert, C.; Baudoing, R. *Surf. Sci.* **1988**, *205*, 447-464. (b) Goulet, T.; Jung, J.-M.; Michaud, M.; Jay-Gerin, J.-P.; and Sanche, L. *Phys. Rev. B* **1994**, *50* 5101-5109.
24. Ge, N-H; Wong, C.M.; Harris, C.B.; *Acc. Chem. Res.* **2000** *33*,111-118; Harris, C.B.; Ge, N.-H.; Lingle, Jr. R.L.; McNeil, J.D.; Wong, C.M. *Annu, Rev. Phys. Chem.* **1997**, *48*, 711-744.
25. Wong, C.M.; McNeill, J.D.; Gaffney, K.J.; Ge, N.-H.; Miller, A.D.; Liu, S.H.; Harris, C.B.; *J. Phys. Chem. B* **1999,** *103*,282-292.
26. Wang, H.; Dutton, G.; Zhu, X.-Y. *J. Phys. Chem. B*, **2000,** 104,10332-10338; Zhu, X.-Y. *Annu. Rev. Phys. Chem.* **2002**, *53*, 221-247.
27.Vondrak, T.; Cramer, C.J.; Zhu, X.-Y.; *J. Phys Chem. B* **1999,** *103*,8915-8919.
28. Lingle, Jr. R.L.;. Padowitz, D.F; Jordan, R.E.; McNeill, J.D.; Harris, C.B.; *Phys. Rev. Lett.* **1994,** *72*,2243-2246.
29. Kadyshevitch A.; Ananthavel S.P.; Naaman R.; *J. Chem. Phys.* **1997,***107*,1288-1290.
30. Popovitz-Biro, R.; Wang, J.L.; Majewski, J.; Shavit, E.; Leiserovitch, L.; Lahav, M., *J. Am. Chem. Soc.* **1994,** *116*,1179-1191.
31. Kadyshevitch A.; and Naaman R. *Phys. Rev. Lett.* **1995**, 74,3443-3446.
32. Kadyshevitch A.; and Naaman R. *Thin Solid Films*, **1996,** *288*,139-146.
33. Naaman, R.; Haran, A.; Nitzan, A.; Evans, D.; Galperin, M.; *J. Phys. Chem. B,* **1998,** *102*,3658-3668.
34. Haran, A.; Kadyshevitch, A.; Cohen H.; Naaman, R.; Evans, D.; Seidman, T.; Nitzan, A.; *Chem. Phys. Lett.* **1997**, *268*,475-480.
35. Haran, A.; Waldeck, D.H.; Naaman, R.; Moons E.; and Cahen, D. *Science* **1994**, *263*,948-950.
36. Jordan, K.D.; Burrow, P.D., *Chem. Rev*. **1987**, *87*,557-588 and references cited therein.
37. Palmer R.E.; Rous, P.J. *Rev. Mod. Phys.* **1992,***64*,383-440.
38. Sanche, L. *J. Phys. B* **1990,** *23*,1597-1624.
39. For example see: M. Michaud, M. Lepage, and L. Sanche, *Phys. Rev. Lett.* **1998,** *81*,2807-2810 and references cited therein.
40. McNeill, J.D.; Lingle, Jr., R.L.;. Jordan, R.E; Padowitz, D.F.; Harris, C.B. *J. Chem. Phys.* **1996,***105*,3883-3891.
41. Bruening, M.; Cohen, R.; Guillemoles, J.F.; Moav, T.; Libman, J.; Shanzer, A.; Cahen D., *J. Amer. Chem. Soc*. **1997,***119*,5720-5728.
42. Burrow, P.D.; Michejda J.A.; Jordan, K.D.; *J. Chem. Phys.* **1987,** *86,*9-24.
43. Ray, K.; Shanzer, A.; Waldeck, D.H.; Naaman, R. *Phys. Rev. B* **1999**, *60*, 13347-13350.

GROWTH OF SILICON NANOCLUSTERS

Elucidation by gas-phase experiments and DFT calculations

Alexandre A. Shvartsburg, Mihai Horoi, and Koblar A. Jackson

Pacific Northwest National Laboratory, MS K8-98, 3335 Q Avenue, Richland, WA 99352, USA; Department of Physics, Central Michigan University, Mt. Pleasant, MI 48859, USA

Abstract: Semiconductor nanostructures are of great interest from both fundamental and applied perspectives. They are intriguing scientifically because their bonding and properties deviate strongly from those of their bulk solids and relevant industrially since nanodevices now approach the scale of large clusters. Understanding the behavior of any molecular system starts from ascertaining its structure. So a colossal effort was expended over the last two decades on characterizing semiconductor cluster geometries. As silicon is the most critical semiconductor, that effort largely focused on Si clusters. Structures of small Si clusters were elucidated early on by *ab initio* calculations, vibrationally resolved spectroscopy, and optical spectroscopies of matrix-isolated species. Progress for larger systems was enabled in late 1990s by an integrated suite of new tools. It includes ion mobility spectrometry, photoelectron spectroscopy, collisional dissociation, and threshold ionization on the side of experiment, and novel molecular optimization algorithms based on evolution paradigm and fast, but accurate semiempirical protocols for energy evaluation on the theory side. Coherent application of these methods has characterized Si clusters up to the region of radical transition from prolate to spherical growth at ~ 25 atoms.

Key words: clusters, ion mobility spectrometry, photoelectron spectroscopy, collision-induced dissociation, molecular structure optimization

1. SMALL SI CLUSTERS (LESS THAN 10 ATOMS)

Since the mid-1980s, semiconductor and particularly silicon nanosystems have fascinated theorists and experimentalists alike. Both *ab initio*[1] and density functional theory[2] calculations for Si clusters with under 10 atoms produced geometries completely unrelated to the tetrahedral diamond packing of bulk silicon (Fig. 1a). Instead, driven by a huge energy gain from

E. C. Faulques et al. (eds.), Spectroscopy of Emerging Materials, 83–96.

tying up dangling bonds on surface atoms, Si_n with $n \geq 5$ assume compact highly coordinated structures. These are the Si_5 D_{3h}, Si_6 D_{4h}, and Si_7 D_{5h} bipyramids, the Si_8 octahedron, and the Si_9 distorted capped cube (Fig. 1 b-d, Fig. 2 a,c). The morphologies of Si_{10} and Si_{11} are built on the exceptionally stable tricapped trigonal prism (TTP) nine-atom unit (Fig. 1 e,f).[1-3]

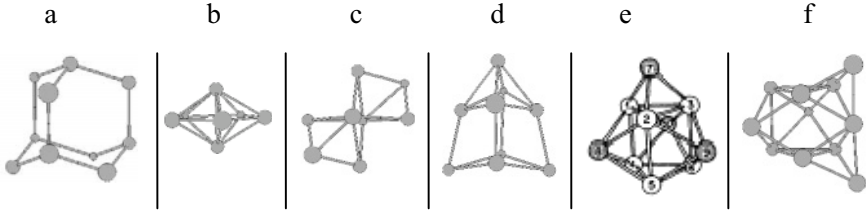

Figure 1. The "adamantane" unit of Si tetrahedral bulk packing (a) vs. small clusters: Si_7 D_{5h} bipyramid (b), Si_8 C_{2h} bicapped octahedron (c), Si_9 C_{2v} Bernal's structure (d), Si_{10} C_{3v} tetracapped trigonal prism (e), and Si_{11} C_{2v} (I) (f). The trigonal prism unit in (e) is highlighted.

The structures for small Si clusters were verified in several experiments. Small clusters can be soft-landed on an inert gas matrix, permitting Raman[4] or IR[5] spectroscopy. This confirmed the Si_n geometries for $n \leq 7$. Further proof came from vibrationally resolved photoelectron spectroscopy (PES),[6] which exposed some normal modes of anions as overtones on the photoelectron spectra. The electronic transitions also contain structural information about anions.[7] PES established a major difference between Si_6 and Si_6^-, revealing the charge-dependence of Si cluster geometries (Fig. 2).[7]

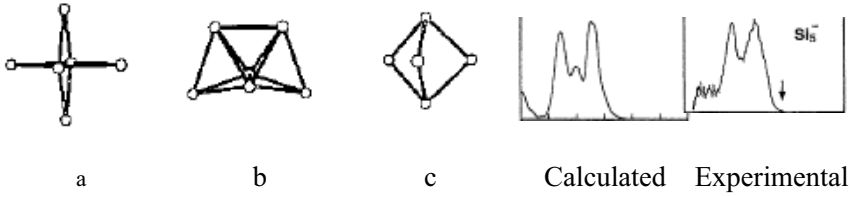

Figure 2. Geometries of Si_6 neutral (D_{4h}, a) and anion (C_{2v} (II), b) are grossly dissimilar. The panel on the right illustrates a typical agreement between simulated (left) and measured (right) photoelectron spectra (Ref. [7]), here for the Si_5^- C_{2v} (II) trigonal bipyramid (c).

2. TOOLS FOR LARGER GAS-PHASE CLUSTERS

Vibrationally resolved PES and matrix-isolation spectroscopy are classic tools for systems of a few atoms but fail for larger sizes, the former because of spectral congestion and the latter for inadequate signal intensity.

A decade ago, several novel experimental methods began furnishing rich information on gas-phase semiconductor clusters (both neutrals and ions) in

the size range of > 10 atoms. The seminal role belonged to ion mobility spectrometry (IMS), followed by collisional dissociation, photoelectron spectroscopy, and threshold ionization measurements. Still, characterization of Si_n beyond $n = 10$ stalled, as the properties for any conceivable geometry did not match the measurements. Here we review how those data were obtained, and how they were explained by new structures found from calculations based on advanced evolutionary search algorithms.

IMS made the decisive contribution to our knowledge about larger semiconductor clusters.[8] In IMS/MS, ions selected by mass spectrometry are injected into a tube filled with an inert buffer gas, through which they drift pulled by a weak uniform electric field. The drift velocity of an ion is set by its mobility, which depends on the ion geometry. Rigorously, the mobility is related to the first-order orientationally-averaged collision integral (cross section) between the ion and the buffer gas atoms. Densely packed, compact, near-spherical objects have high mobilities, while loosely packed or extended ones with high aspect ratios have low mobilities. Since 1991, IMS has been the tool of choice to characterize sizable gaseous ions.[9]

The first IMS study of Si_n cations discovered a structural transition over the $n \cong 24$-30 size range between two growth sequences, assigned as prolate "sausages" and compact "spheres" (Fig. 3).[10] The resolving power of IMS instruments was then limited to ~ 15. With the advent of high-resolution IMS/MS,[11] multiple isomers were found for nearly all clusters with $n \geq 17$, in both "prolate" and "compact" families.[12] For some sizes in the transition region (e.g. Si_{27}^+ in Fig. 3), at least six geometries co-exist. A similar transformation occurs[12] in Si_n^-, though the geometries of most cations and anions differ in detail. An issue in such experiments is whether the source-generated isomer distribution reflects the thermodynamics rather than kinetics of cluster growth. This can be assessed via "annealing", where ions injected at a high energy into a pressurized gas in IMS tube convert to lowest-energy geometries in a heating-cooling cycle. Such annealing of Si_n^+ has proven[10] that the structural transition at $n \sim 27$ is of true thermodynamic origin.

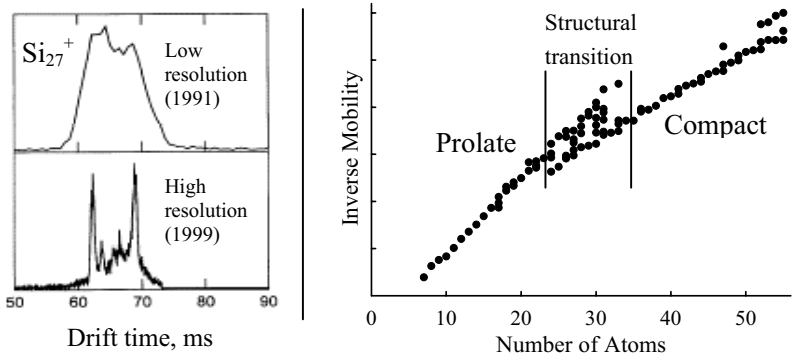

Figure 3. IMS findings (Ref. [8]) for Si_n cations: examples of raw spectra (left) and summary plot exhibiting a transition to compact structures once clusters grow beyond $n = 24$ (right).

The attainment of an IMS resolving power[11] of > 100 brought the challenge of data interpretation forward. Features observed in IMS are assigned by matching measured mobilities vs. those evaluated for plausible candidate geometries. Previously, rough estimates such as the approximation of collision cross section by projection[9] had usually sufficed: while the computational error margin was ~ 10 %, measurements had a similarly poor resolution. A drastic tightening of IMS resolution and accuracy to < 1 % raised the requirements for accuracy of mobility calculations by an order of magnitude. Novel computational methods based on detailed molecular dynamics modeling of ion-buffer gas scattering in a realistic pair potential (including the attractive interactions) were a crucial advance.[13-15] Further improvements arose from the new paradigm of scattering on electronic density isosurfaces[16] (SEDI) that represents ions as electron clouds and not by nuclear coordinates. This proved critical for precise calculation of mobilities for anions that often have extended electronic orbitals.[16] However, SEDI ignores the attractive molecular potential accounted for in classical trajectory calculations.[14,15] This is remedied in the hybrid SEDI-TC method that combines the scattering on atomic nuclei and electron orbitals.[17]

The second most important role in unraveling the growth of semiconductor nanosystems belonged to collision-induced dissociation (CID). In CID, mass-selected ions are fragmented by collisions with inert gas molecules at a defined energy and the products are monitored. This not only reveals the preferred dissociation channels, but also quantifies their activation barriers.[18] Experiments are normally carried out in triple-quadrupole instruments, where a parent ion is selected in the 1st quad and dissociated in a cell within the 2nd, with fragments identified in the 3rd. While usually CID is performed under single-collision conditions, Si clusters were probed in the multicollisional regime.[19,20] This is commonly perceived to yield less reliable data, but those for Si_n^+ proved surprisingly accurate.

Dissociation energies of clusters normally increase with increasing size and asymptotically approach the bulk vaporization enthalpy, save for small local oscillations due to even/odd alternation or completion of electronic or geometric shells. In contrast, the dissociation energies of Si_n^+ drop from 5 eV for Si_6^+ to 2 eV for Si_{21}^+, and start rising only then[20] (§ 4). The coincidence of size ranges for this trend inversion and the onset of structural transition in IMS data suggest that these phenomena are related. Further, typical clusters dissociate by loss of a monomer or, rarely, a dimer. Si_n cations with $n \geq 9$ exhibit a remarkable fission, eliminating chunks of 6, 7, or 10 atoms.[19,20]

Dissociation energies play a singular role in characterizing gas-phase clusters, since they uniquely determine whether the global minimum has been found. Indeed, agreement between calculations and measurements for any other quantity (e.g. mobility, photoelectron spectrum, or ionization

energy) shows only that the geometry is consistent with experiment. It cannot rule out the possibility of an equally good agreement for an unknown lower-energy isomer. A systematic set of measured sequential binding energies creates a robust "depth gauge" for the potential energy surface that tells if calculations reached the global minimum.[21] Thus, in principle, while other methods check if a structure may be the right one, CID confirms it.

In its many forms, spectroscopy is the main structural tool of chemistry. While standard optical spectroscopies are powerful for studying gaseous neutrals, they fail for ions because of low target density. However, photodissociation and especially photoelectron[22,23] "half-spectroscopies" prove useful. In PES, electrons detached from mass-selected anions by a laser are dispersed by kinetic energy, which uncovers the electronic structure of the neutral at the anion geometry. Structural interpretation of PES data (without vibrational resolution) requires modeling of electronic transitions that accounts for the thermal motion of the precursor by sampling instantaneous geometries.[7] Unlike IMS or CID that work for ions of either charge state, PES is restricted to anions. Another limitation is that PES obtains a weighted average over the spectra of all isomers present, with weights given (on top of abundances) by unknown photoabsorption efficiencies. This severely degrades the utility of PES for isomeric mixtures, such[12] as all Si_n^- for $n >$ 20. This problem may be solved by isomer-resolved spectroscopy, where isomers are separated by IMS prior to PES.[24] However, a major sensitivity gain is needed to make IMS/PES a routine technique.

All three methods listed above (IMS, CID, and PES) explore ions only, whether positive or negative. Information on neutrals is often more relevant to materials research and easier to compare with theory. The single probe accessing neutrals is threshold ionization, where a tunable laser (or several lasers with different wavelengths) ionize a neutral beam and the resulting cations are identified by MS. This technique determines vertical ionization energies (IE) that can be matched with values predicted for trial geometries. Experiments for Si_n revealed[25] an abrupt fall of IE at $n = 22$. The coincidence of this size with the onset of the structural transition in IMS and the inversion of the dissociation energy trend in CID suggests that the IE drop is also associated with conversion to compact geometries.

Other reported measurements include Si_n polarizabilities[26] and chemical reactivities of Si_n^+ and Si_n^- vs. several simple gases, such as O_2, H_2O, NH_3, and ethylene.[27-32] The polarizability data could not be explained in terms of cluster structure,[33] and reactivity studies largely remain controversial.

In summary, new experimental tools had measured diverse properties of Si_n, Si_n^+, and Si_n^- for $n > 10$, and procedures accurately relating those to cluster structure had been developed. It remained to create potent, unbiased search protocols for finding low-energy geometries of large Si clusters.

3. OPTIMIZATION OF SI CLUSTER GEOMETRIES

The morphologies for small Si clusters (§ 1) were first obtained by comparing the few reasonable isomers constructed by hand.[1] Those findings were confirmed in an unbiased simulated annealing optimization coupled with density functional theory (DFT) in the local density approximation (LDA).[2] In this approach, a heated cluster explores diverse minima on its potential energy surface. As the system cools gradually, the accessible phase space shrinks and the structure is forced into a potential energy well. This procedure located[2] the lowest-energy Si_n for n = 7-10, but the properties of geometries[34,35] generated for Si_{12} and Si_{13} already deviated from the experimental findings (§ 4). Candidate geometries for still larger clusters were manually constructed following hypothetical bonding patterns: (1) hexagon stacking,[36] (2) triangle stacking,[37] (3) icosahedral packing,[38] or (4) "stuffed fullerenes".[32] These motifs were guided by certain experimental observations, such as frequent Si_6 loss[19,20] in CID (1) or low reactivity of Si_{13}^+ (closed atomic shell for icosahedra) vs. some common gases[27,29] (3). However, none of the geometries fit the majority of experimental data. Thus the progress in unraveling the growth of semiconductor clusters had stopped at n = 11 until the advent of novel structural optimization methods.

The breakthrough in this problem was achieved by two developments. One was the genetic algorithm (GA)[39] inspired by biological evolution via mating. In nature, parent genes mix in the offspring, creating organisms with unprecedented genes in each generation. New gene lines include both those fitter and less fit than the parents, but the former are chosen by natural selection and preferentially pass their genes to the next generation. The GA mimics this process to optimize molecular structures. Namely, in each generation, a population of four parent clusters combines to produce 16 offspring that are relaxed to the nearest local minima.[40] A structure replaces a member of the parent population if its energy is below that of the parents, else discarded. This engenders diverse offspring while preserving beneficial parental features. The diversity is augmented by occasional "mutations". The procedure is repeated for ~ 1000 generations and (to ensure convergence) for multiple "ecologies" (colonies drawn from different original ancestors).

The other key component of optimization is the evaluation of cluster energies. The major early pitfall was an adoption of empirical potentials (for example, Stillinger-Weber) fit to bulk Si properties.[38] The outcome was inevitably disastrous, since bonding in Si_n of relevant sizes has nothing in common with the bulk. For instance, these potentials typically predict Si_{13} to be icosahedral, a structure that is enormously high in energy and not even a stationary point.[35] At the other extreme, first-principles methods such as LDA and particularly gradient-corrected DFT functionals (PWB 88 or PBE) deliver superb Si_n energies.[41] DFT is practical in simulated annealing,[2,35] but

its computational cost remains prohibitive for genetic algorithms that process ~ 10^4 offspring per ecology considered. What is needed are much faster (even though less accurate) methods that are still vastly superior to empirical potentials. The density-functional tight-binding (DFTB) approach[42,43] fits this niche well. While DFTB is aimed to track DFT as closely as possible, it necessarily is less exact. Thus a two-step protocol was designed. First, an extensive database of Si_n geometries with energies under a certain cutoff was built for each *n* by the DFTB/genetic algorithm, then ranked by energy using DFT itself. The global minima found for Si_n ($n \leq 18$) are presented in Fig. 4.

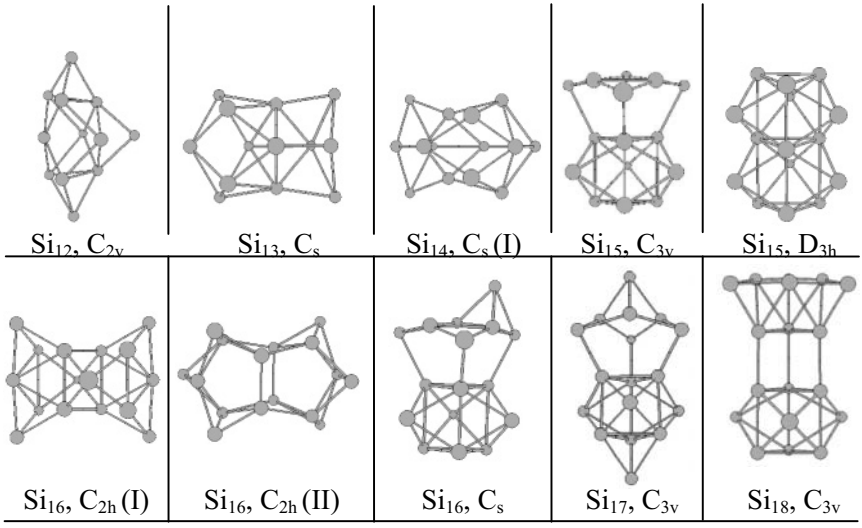

Figure 4. Lowest-energy Si_n neutrals (n = 12-18) found by genetic algorithm coupled with DFT (Ref. [40]). Geometries within 5 meV/atom above global minima are also shown.

These geometries were much lower in energy than any known before, e.g. by 0.6 eV, 1.2 eV, and 2.7 eV for n = 12, 14, and 17. In fact, for Si_{17} and Si_{18}, they were first structures that do not break into pieces[40] spontaneously! Most species in Fig. 4 are clearly based on one or two TTP units. For Si_{19} and Si_{20}, GA produced differing, compact morphologies, with elongated geometries like those in Fig. 4 lying slightly higher in energy.[40] This appears connected to the structural transition (Fig. 3), but that sets on later at n = 24. This indicated that the true global minima for $n \geq 19$ had not been found.

Continuing the biological analogy, simple life forms procreate asexually, each offspring having a single parent. This seems to limit evolutionary diversity, but must benefit small organisms somehow. We translated this concept into a single-parent evolution algorithm for molecular optimization. A cluster is cut by two random parallel planes such that the outer sections

contain equal number of atoms.[44] Then we execute a "rotation" (an outer piece turned by a random angle about an axis normal to said planes) or a "reflection" (an outer piece is replaced by the other reflected through a third parallel plane including the cluster center of mass), Fig. 5. Upon either procedure, the geometry is relaxed to the nearest local minimum. Offspring substitute for their parents with a probability depending on the energy, unless in a rare mutation when they are accepted regardless. The search continues for hundreds of generations, alternating rotations and reflections.

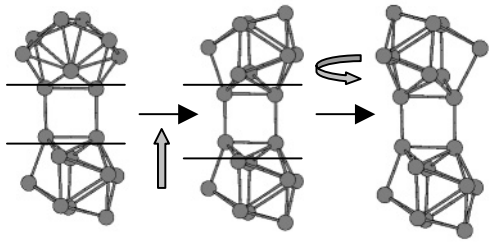

Figure 5. Operations involved in the single-parent evolution algorithm (Ref. [44]): "reflection" (left) and "rotation" (right). The rotation is by a random angle, 180^0 in this case.

The method was validated for Lennard-Jones systems and applied[44] to Si_n and Si_n^+. This discovered lower-energy isomers for $n \geq 19$. All structures for n = 19-23 are prolate (Fig. 6). "Compact" geometries first become competitive in energy at n = 24 - 25, exactly as observed in IMS. Our ongoing studies for $n \geq 24$ will be presented in future publications.

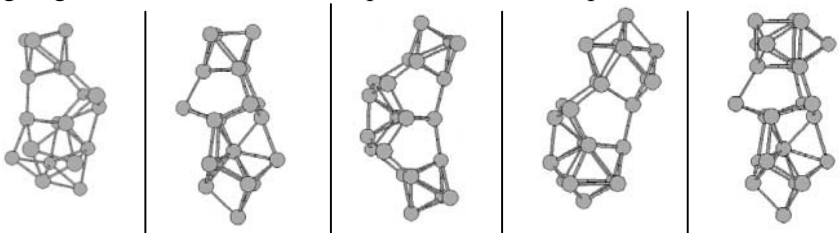

Figure 6. Global Si_n minima (n = 19-23) found by the single-parent evolution algorithm/DFT.

Most experimental data on clusters are for cations or anions (§ 2), so ionic geometries are needed. Ions are treatable in simulated annealing using DFT, but not readily in GA as most DFTB methods exist for neutrals only. The ionic structures may be obtained by relaxing the database of low-energy neutrals, as long as (i) the ionic global minimum is at least a local minimum for the neutral, and (ii) the change in isomer energies between neutrals and ions is limited to the database "depth". If both conditions hold, the ground state ion geometry must be in the database. Using this approach, lists of favorable Si_n^+ and Si_n^- geometries were created.[16,44,45] However, some Si_n^+

and Si_n^- have no neutral analogs: the geometry is not a stationary point for the neutral and thus is not in the database.[16] To find those structures, a search was run with DFTB amended for an ionic charge state.[44] Global minima for Si_n^+ and Si_n^- often differ from each other and from Si_n: all three are almost never identical. Rearrangements may be dramatic, e.g. Si_9^- is the TTP (Fig. 7) while Si_9 and Si_9^+ assume the Bernal's structure (Fig. 1d). Some cation and anion geometries that differ from the neutrals are shown in Fig. 7.

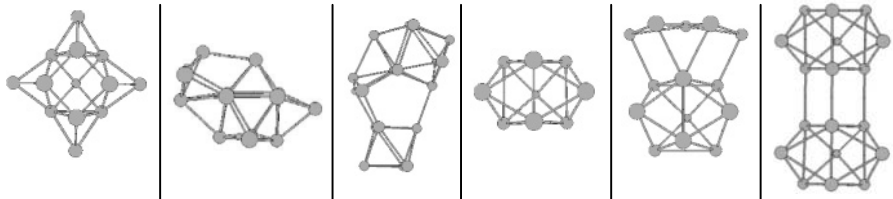

Figure 7. Geometries for selected Si_n^+ and Si_n^- (Ref. [16,37]) that differ from the neutrals.

4. VALIDATING STRUCTURES BY EXPERIMENTS

The structures of Si clusters derived from various optimizations (§ 3) were vetted by comparisons with experiments (§ 2). Table 1 presents calculated and measured mobilities for lowest-energy Si_n cations and anions.

Table 1. Computed cohesive energies (PWB 88) and mobilities of low-energy isomers for Si_n ($n \le 20$) neutrals, cations, and anions vs. measured mobilities (in He at 298 K, Ref. [16,44]), and calculated binding energies for Si_n^+ vs. CID data (Ref. [20]). Global minima are in bold. Multiple features observed for Si_n cations ($n \ge 17$) are ranked by decreasing abundance.

n	Point Group	Cohesive energy, eV			Inverse mobility, Vs/m^2				Cation binding energy, eV	
					Cations		Anions			
		Cation	Neutral	Anion	Calc.	Exp.	Calc.	Exp.	Calc.	Exp.
3	C_{2v}	**–0.165**	**2.537**	**3.267**			**915**	920	3.86	
4	D_{2h}	**1.106**	**3.042**	**3.565**	**930**	915	**1040**	1040	4.92	4.95
5	D_{3h}	1.642	**3.266**	**3.733**	1020	1005	**1115**	1115	3.92	3.90
	C_{2v} (II)	**1.669**	none	none	**1020**		n/a			
6	D_{4h}	2.145	**3.439**	3.778	1105	1105	1210	1215	4.78	5.00
	C_{2v} (I)	**2.187**	**3.438**	none	**1110**		n/a			
	C_{2v} (II)	none	none	**3.789**	n/a		**1210**			
7	D_{5h}	2.410	**3.555**	**3.828**	1190	1195	**1295**	1295	4.04	4.00
	C_{2v} (II)	**2.452**	none	none	**1195**		n/a			
8	C_{2h}	**2.596**	**3.491**	3.752	**1300**	1315	1390	1400	3.60	3.90
	C_1/C_s	**2.596**	3.422	3.736	**1290**		1385			
	C_{2v}	2.517	3.445	**3.791**	1310		**1395**			
9	C_{2v} (I)	**2.753**	**3.580**	3.772	**1375**	1380	1465	1440	4.01	3.75

	C_s (II)	2.727	3.527	**3.819**	n/a		**1440**			
10	C_{3v}	2.900	**3.682**	**3.897**	1425	1415	**1510**	1520	3.95	3.80
	C_s	**2.924**	none	none	**1415**		n/a			
11	C_{2v} (I)	2.985	**3.618**	3.777	1520	1505	1620	1615	3.87	3.85
	C_s (I)	**3.029**	**3.620**	3.803	**1515**		1610			
	C_{2v} (II)	2.986	3.577	**3.821**	1505		**1595**			
12	C_{2v}	3.034	**3.648**	**3.826**	1615	1600	**1695**	1700	2.72	2.80
	C_s	**3.040**	3.593	3.821	**1595**		1700			
13	C_s	3.093	**3.634**	**3.860**	1670	1680	**1760**	1775	2.71	2.70
	C_{2v} (II)	**3.132**	3.629	3.855	**1675**					
14	C_s (I)	3.181	**3.677**	3.830	1745	1755	1845	1850	2.58	2.70
	C_s (II)	3.114	3.621	**3.860**	1770		**1855**			
	C_s (III)	**3.188**	3.668	3.836	**1755**					
15	C_{3v}	**3.225**	**3.701**	3.837	**1845**	1840	1945	1915	2.72	2.75
	C_s (III)	none	none	**3.862**	n/a		**1945**			
	C_{2v}	3.221	3.659	**3.860**	1795		**1895**			
16	C_{2h} (II)	**3.265**	**3.672**	3.837	**1950**	1930	2055	2010	2.30	2.30
	C_s	3.240	3.661	**3.865**	1925		**2035**			
17	C_{3v}	3.298	**3.703**	3.850	2010	1985	2130	2105	2.01	2.10
	C_s (I)	3.287	3.681	**3.869**	2015	2050	**2120**			
	C_{2v}	**3.302**	3.693	3.837	**1990**	1935				
	C_{3v} (II)	**3.301**	3.689	3.826	**1995**					
18	C_{3v}	3.340	**3.720**	3.830	2170	2115	2270	2155	2.01	2.15
	D_{3h}	3.329	3.704	**3.881**	2095	2155	**2185**			
	C_s	**3.345**	3.711	3.863	**2105**					
19	C_1	**3.380**	**3.719**	3.853	**2185**	2200		2265	2.62	2.70
	C_1 (II)	3.362	3.712	**3.871**	2185	2165	**2260**			
20	C_1	**3.393**	3.721	3.852	**2255**	2245		2330	1.80	2.15
	C_{3v}	**3.393**	**3.736**		2295					
	C_2	3.381	3.712	**3.866**	2295		**2395**			
21	C_{2v} (I)	**3.423**	**3.746**		**2425**	2415			1.74	2.05
	C_s (I)	3.420	3.727		2340	2325				
	C_s (II)	3.419	3.733		2340					
	C_s (III)	3.411	3.722		2340					
	C_{2v} (II)	3.411	3.719		2340					
22	C_s (I)	**3.453**	3.747		**2400**	2360			2.67	2.65
	C_s (II)	3.452	**3.748**		2400	2380				
	C_1	3.446	3.745		2380	2425				
	C_s (III)	3.446	3.745		2455					
23	C_1 (I)	**3.475**	3.741		**2480**	2460			2.39	2.75
	C_1 (II)	3.474	3.744		2475					
	C_1 (III)	3.472	3.743		2475					
	C_1 (IV)	3.471	3.742		2475					
	C_1 (V)	3.470	3.745		2480					
	C_1 (VI)	3.469	3.745		2475					

The combined error of calculation and experiment is 1.0 - 1.5 %, and the predictions for global minima match the measurements within this margin.

For $n \leq 13$, many plausible isomers are compact and have similar mobilities. Still, IMS excludes[40] all bulklike, tetrahedral, octahedral, and icosahedral species discussed in the literature. The differentiating ability of IMS increases for larger clusters, where it rules out most higher energy isomers, including the putative icosahedra and triangle/hexagon stack families (§ 3).

IMS is especially powerful for multi-isomer systems, as abundances can be correlated with the energies of candidate geometries. For example,[44] the 1st and 3rd lowest-energy Si_{18}^+ isomers with computed inverse mobilities of respectively 2105 and 2095 Vs/m^2 match the major peak observed at 2115 Vs/m^2, while the 2nd lowest isomer with mobility of 2170 Vs/m^2 fits the minor peak at 2155 Vs/m^2. Likewise for Si_{22}^+, the inverse mobilities computed for the four lowest-energy isomers are 2400 (two), 2380, and 2455 Vs/m^2, matching the observed peaks at respectively 2380 Vs/m^2 (major), 2360 Vs/m^2 (major), and 2425 Vs/m^2 (minor). For some sizes, a single feature is observed. While the energy density of isomers in smallest clusters may be so low that only the global minimum is produced, this is implausible for species as large as Si_{23}^+. Indeed, the calculations reveal that at least six lowest-energy isomers have identical mobilities matching the experiment.

Given the assumptions inherent in the data analysis, CID[20] measures the relative dissociation energies much more reliably than absolute ones. Adjusting for that, the values computed for Si_n^+ are in a near-perfect agreement with experiment (Table 1). This proves that the geometry optimization reached (at least very close to) the global minima. Further, fragmentation pathways for almost every Si_n^+ are sensitive to the relative energies of many competing potential products, both neutrals and cations.[21] Thus reproducing the fragmentation pattern of all Si_n^+ at once requires satisfying a greatly overdefined system of equations, and so is an extremely stringent test for the accuracy of cluster energies.[46] As shown in Table 2, primary fragmentation channels predicted for Si_n^+ always match the CID data, and there is a substantial agreement even for the secondary channels.

Table 2. Calculated (c) and experimental (e) Si_m fragments of Si_n^+ ($n \leq 29$). Primary *m* (I) and secondary *m* (II) channels are shown. Pathways computed to lie within 0.12 eV are bunched.

n		3	4	5	6	7	8	9	10	11	12	13	14	15	16
m (I)	c	1	1	1	1	1	1	1,3,5	4	4,5	6	7	7	7	6,10
	e	1	1	1	1	1	1	3	4	4	6	7	7	7	6
m (II)	c	2	3	4	2,5	6	2,4,7		6		5	6	6	4,5	
	e	2	2	2	2	2,3	4	1	6	5	5	6	6	6	10

n		17	18	19	20	21	22	23	24	25	26	27	28	29
m (I)	c	7	7	10	10	10	7,10	10	10	7,10	7,10	10	10	10
	e	7	7	10	10	10	10	10	10	10	10	10	10	10
m (II)	c	6,10	10	9	7,9	7		7	7			7	7	7
	e	6	no	7	no	no	7	7	13,17	7	7	7	7	7

The final proof for TTP structures of mid-sized Si clusters came from PES (Fig. 8). The match of modeled and measured spectra is striking, except for Si_{12}^- and (perhaps) Si_{20}^-. For some n where several Si_n^- geometries are near-degenerate, PES elucidates the structure. For example, in DFT three Si_{11}^- isomers closely compete for the ground state (Fig. 8). The one observed in PES is C_s (II), the 3rd-lowest by DFT calculations.[22] This assignment could not be made using IMS or CID, since the mobilities calculated for all three species are within 1 % and total cohesive energies are within 0.06 eV.

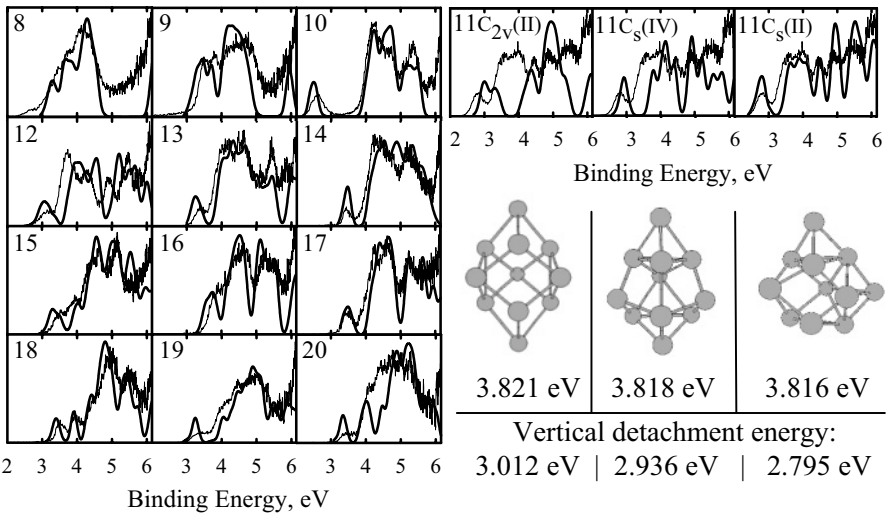

Figure 8. Photoelectron spectra for Si_n^- (n = 8-20), experiment (bold) and LDA simulations for the global minima (Ref. [22]). For Si_{11}^-, we show modeling for three low-energy isomers.

This agreement is unique to lowest-energy Si_n^-: it is absent even for other favorable isomers,[22] e.g. those best for Si_n or Si_n^+. This is clear simply from the inspection of vertical detachment energies (VDE)[22] presented in Fig. 9:

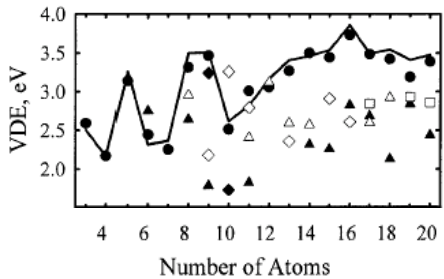

Figure 9. VDE of Si_n anions. The line indicates measurements. Symbols mark calculated values (LDA) for various geometries: global minima for Si_n^- (circles), Si_n (filled triangles), Si_n^+ (empty triangles), and some other low-energy geometries (diamonds and squares).

For the neutrals, DFT ionization energies of global minima are in excellent agreement[45] with the threshold ionization data (Fig. 10). This is not the case for many alternative structures proposed in the literature.[45]

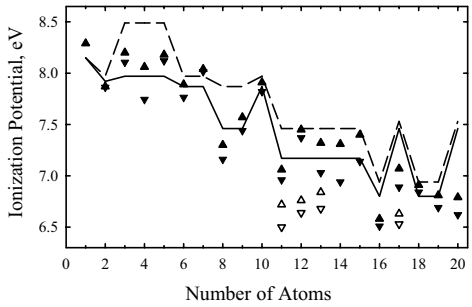

Figure 10. Ionization potentials of Si clusters. Solid and dashed lines are the boundaries obtained in experiment. Triangles are the vertical and adiabatic IPs computed using PWB: filled for the global minima and empty for some other low-energy neutrals (Ref. [45]).

In summary, a synergistic blend of experimental and theoretical tools has revealed the Si nanostructure growth in fine detail. This success provides a robust blueprint for the full characterization of virtually any nanosystem.

ACKNOWLEDGEMENTS

We are grateful to all colleagues who have contributed to our understanding of semiconductor nanosystems. Their huge number testifying to the vitality of this field, we can mention just a few: Kai-Ming Ho and Bei Liu who made the breakthrough in optimization of Si clusters by using the genetic algorithm, Thomas Frauenheim whose density-functional tight-binding proved critical in searches for large cluster geometries, and James Chelikowsky and Gerd Gantefor who fashioned the photoelectron spectroscopy of semiconductor clusters into a powerful structural tool. We thank Richard D. Smith for broadly supporting IMS-related work at PNNL.

REFERENCES

1. K. Raghavachari, C.M. Rohlfing, J. Chem. Phys. 89, 2219 (1988).
2. P. Ballone, W. Andreoni, R. Car, M. Parrinello, Phys. Rev. Lett. 60, 271 (1988).
3. C.M. Rohlfing, K. Raghavachari, Chem. Phys. Lett. 167, 559 (1990).
4. E.C. Honea, A. Ogura, C.A. Murray, et al., Nature 366, 42 (1993).
5. S. Li, R.J. Van Zee, W. Weltner Jr., K. Raghavachari, Chem. Phys. Lett. 243, 275 (1995).
6. C.C. Arnold, D.M. Neumark, J. Chem. Phys. 99, 3353 (1993).
7. N. Binggeli, J.R. Chelikowsky, Phys. Rev. Lett. 75, 493 (1995).
8. A.A. Shvartsburg, R.R. Hudgins, Ph. Dugourd, M.F. Jarrold, Chem. Soc. Rev. 30, 26 (2001).

9. G. von Helden, M.T. Hsu, N.G. Gotts, M.T. Bowers, J. Phys. Chem. 97, 8182 (1993).
10. M.F. Jarrold, V.A. Constant, Phys. Rev. Lett. 67, 2994 (1991).
11. Ph. Dugourd, R.R. Hudgins, D.E. Clemmer, et al, Rev. Sci. Instrum. 68, 1122 (1997).
12. R.R. Hudgins, M. Imai, M.F. Jarrold, Ph. Dugourd, J. Chem. Phys. 111, 7865 (1999).
13. A.A. Shvartsburg, M.F. Jarrold, Chem. Phys. Lett. 261, 86 (1996).
14. M.F. Mesleh, J.M. Hunter, A.A. Shvartsburg, G.C. Schatz, M.F. Jarrold, J. Phys. Chem. 100, 16082 (1996).
15. A.A. Shvartsburg, G.C. Schatz, M.F. Jarrold, J. Chem. Phys. 108, 2416 (1998).
16. A.A. Shvartsburg, B. Liu, M.F. Jarrold, K.M. Ho, J. Chem. Phys. 112, 4517 (2000).
17. A.A. Shvartsburg, B. Liu, K.W.M. Siu, K.M. Ho, J. Phys. Chem. A 104, 6152 (2000).
18. N.F. Dalleska, K. Honma, P.B. Armentrout, J. Am. Chem. Soc. 115, 12125 (1993).
19. M.F. Jarrold, J.E. Bower, J. Phys. Chem. 92, 5702 (1988).
20. M.F. Jarrold, E.C. Honea, J. Phys. Chem. 95, 9181 (1991).
21. A.A. Shvartsburg, M.F. Jarrold, B. Liu, Z.Y. Lu, C.Z. Wang, K.M. Ho, Phys. Rev. Lett. 81, 4616 (1998).
22. J. Muller, B. Liu, A.A. Shvartsburg, S. Ogut, J.R. Chelikowsky, K.W.M. Siu, K.M. Ho, G. Gantefor, Phys. Rev. Lett. 85, 1666 (2000).
23. M.A. Hoffman, G. Wrigge, B. von Issendorff, J. Muller, G. Gantefor, H. Haberland, Eur. Phys. J. D 16, 9 (2001).
24. R. Fromherz, G. Gantefor, A.A. Shvartsburg, Phys. Rev. Lett. 89, # 083001 (2002).
25. K. Fuke, K. Tsukamoto, F. Misaizu, M. Sanekata, J. Chem. Phys. 99, 7807 (1993).
26. R. Schafer, S. Schlecht, J. Woenckhaus, J.A. Becker, Phys. Rev. Lett. 76, 471 (1996).
27. M.F. Jarrold, J.E. Bower, K.M. Creegan, J. Chem. Phys. 90, 3615 (1989).
28. U. Ray, M.F. Jarrold, J. Chem. Phys. 93, 5709 (1990).
29. U. Ray, M.F. Jarrold, J. Chem. Phys. 94, 2631 (1991).
30. M.F. Jarrold, Y. Ijiri, U. Ray, J. Chem. Phys. 94, 3607 (1991).
31. L.R. Anderson, S. Maruyama, R.E. Smalley, Chem. Phys. Lett. 176, 348 (1991).
32. J.M. Alford, R.T. Laaksonen, R.E. Smalley, J. Chem. Phys. 94, 2618 (1991).
33. K. Jackson, M. Pederson, C.Z. Wang, K.M. Ho, Phys. Rev. A 59, 3685 (1999).
34. M.V. Ramakrishna, A. Bahel, J. Chem. Phys. 104, 9833 (1996).
35. U. Rothlisberger, W. Andreoni, P. Giannozzi, J. Chem. Phys. 96, 1248 (1992).
36. E. Kaxiras, K.A. Jackson, Phys. Rev. Lett. 71, 727 (1993).
37. J.C. Grossman, L. Mitas, Phys. Rev. Lett. 74, 1323 (1995).
38. J.C. Phillips, Phys. Rev. B 47, 14132 (1993).
39. D.M. Deaven, K.M. Ho, Phys. Rev. Lett. 75, 288 (1995).
40. K.M. Ho, A.A. Shvartsburg, B. Pan, et al., Nature 392, 582 (1998).
41. J.P. Perdew, K. Burke, M. Ernzerhof, Phys. Rev. Lett. 77, 3865 (1996).
42. C.Z. Wang, B.C. Pan, K.M. Ho, J. Phys.: Condens. Matter. 11, 2043 (1999).
43. D. Porezag, T. Frauenheim, T. Köhler, G. Seifert, R. Kaschner, Phys. Rev. B 51, 12947 (1995).
44. I. Rata, A.A. Shvartsburg, M. Horoi, T. Frauenheim, K.W.M. Siu, K.A. Jackson, Phys. Rev. Lett. 85, 546 (2000).
45. B. Liu, Z.Y. Lu, B. Pan, C.Z. Wang, K.M. Ho, A.A. Shvartsburg, M.F. Jarrold, J. Chem. Phys. 109, 9401 (1998).
46. A.A. Shvartsburg, B. Liu, et al, Phys. Rev. Lett. 83, 2167 (1999).

PROGRESS IN LIGHT EMISSION FROM SILICON NANOSTRUCTURES

DAVID J. LOCKWOOD
Institute for Microstructural Sciences, National Research Council, Ottawa K1A 0R6, Canada

Abstract: The many and diverse approaches to materials science problems have greatly enhanced our ability in recent times to engineer the physical properties of semiconductors. Silicon, of all semiconductors, underpins nearly all microelectronics today and will continue to do so for some time to come. However, in optoelectronics, the severe disadvantage of an indirect band gap has limited the application of elemental silicon. Here we review a number of diverse approaches to engineering efficient light emission in silicon nanostructures. These different approaches are placed in context and their prospects for application in silicon-based optoelectronics are assessed.

Key words: Silicon, germanium, carbon, alloys, nanostructures, optoelectronics, light emission, photoluminescence, electroluminescence, quantum well, quantum wire, quantum dot, superlattices, quantum confinement.

1. INTRODUCTION

The ubiquitous silicon microelectronics "chip" is taken for granted in modern society. There has been much research involved in producing these high technology marvels and such research continues unabated at a faster and faster pace. Despite the often stated announcement that "the age of GaAs has arrived", it never quite has, and continued developments in Si and, more recently, $Si_{1-x}Ge_x$ alloy technology[1-3] continue to advance the frontiers of microminiaturization, complexity, and speed. This continued advance has been driven by application requirements in switching technology (*e.g.,* computers) and high-speed electronics (*e.g.,* wireless telecommunications). Gallium arsenide and other compound semiconductors have, however, maintained a significant role in the construction of optoelectronic and

E. C. Faulques et al. (eds.), Spectroscopy of Emerging Materials, 97–114.

purely photonic devices where the medium of switching and communication is light itself.[4]

The merging of Si-based electronics with photonics has largely required the pursuit of hybrid technologies for light emitters and modulators (see, for example, Ref. 5), which are often both expensive and complicated to produce. The most satisfactory solution and still mostly a dream as far as light sources are concerned would be optoelectronic devices created entirely from Si-based materials, where the extensive experience in Si fabrication and processing could be put to best use. Already, a wide range of optoelectronic integrated circuits (OEICs) incorporating Si or $Si_{1-x}Ge_x$ as a detector or waveguide have been elaborated.[1,5-8] Despite these advances, the major deficiency in Si-based optoelectronic devices remains the lack of suitable light emitters and especially lasers.

The general requirements in Si-based light sources are efficient light emitting diodes (LEDs), lasers, and optical amplifiers for use in optical communications technologies such as fiber optics and displays. Operating wavelengths in the range 0.45–1.6 μm are needed to cover both full-color displays and the fiber-optic operating wavelengths of 1.3 and 1.55 μm. Specific applications for such sources include fiber-optic transmitters, optical interconnects within and between computer chips, optical controllers for phased-array microwave antennas, information display screens, printing elements in xerography, and writing and readout of optical compact disc information.

Many quite different approaches to alleviating the miserable light emission in bulk Si (~10^{-4} quantum efficiency at 300 K) have been proposed and are actively being explored.[9-14] Some, such as $Si_{1-x}Ge_x$ quantum well or Si/Ge superlattice structures, rely on band structure engineering, while others rely on quantum confinement effects in low dimensional structures, as typified by quantum dots or porous Si (π-Si[15]). Still another approach is impurity-mediated luminescence from, for example, isoelectronic substitution or by the addition of rare earth ions. An overview of results obtained with some of these methods is given below. However, in order to understand more fully the reasons why such different approaches are necessary, it is appropriate to review first what creates the optical emission problem in crystalline Si (c-Si).

2. OPTICAL EMISSION IN SILICON

Silicon crystallizes in the diamond structure,[16] which consists of two interpenetrating face-centered cubic lattices displaced from each other by one quarter of the body diagonal. In zinc blende semiconductors such as GaAs, the Ga and As atoms lie on separate sublattices, and thus the inversion symmetry of Si is lost in III–V binary compounds. This difference in their crystal structures underlies the disparate electronic properties of Si and GaAs. The energy band structure in

semiconductors is derived from the relationship between the energy and momentum of a carrier, which depends not only on the crystal structure but also on the bonding between atoms, the respective bond lengths, and the chemical species. The band structure is often quite complex and can only be calculated empirically.[17]

The valence band structure is much the same for many semiconductors and exhibits a maximum at the Brillouin zone center or Γ point (i.e., at wave vector $\boldsymbol{k} = 0$). The notable difference between Si and GaAs is that the degeneracy in the $\Gamma_{25'}$ band maximum at $\boldsymbol{k} = 0$ is removed in the case of GaAs, because of the spin-orbit interaction, into Γ_8 and Γ_7 subbands. In general, $E(\boldsymbol{k})$ has maxima or minima at zone center and zone boundary symmetry points, but additional extrema may occur at other points in the Brillouin zone. In the case of Si, the lowest point in the conduction band occurs away from high symmetry points near the X point at the Brillouin zone boundary (along <001>), whereas in GaAs it occurs at the Γ point. The energy gap in a semiconductor is defined as the separation between this conduction band minimum and the valence band maximum at the Γ point. For GaAs, the energy gap is classified as direct, because a transition can occur directly at $\boldsymbol{k} = 0$ between initial and final states having the same wave vector. Correspondingly, Si is termed an indirect gap semiconductor, because the initial and final states have different wave vectors.

In direct gap GaAs, an excited electron at the bottom of the conduction band can relax spontaneously back into a hole in the valence band by emitting a photon at the band gap energy. This electron-hole radiative recombination process can only occur in Si if momentum is conserved, i.e., the excited electron wave vector must be reduced to zero. This, in pure Si, occurs via the transfer of momentum to a phonon that is created with equal and opposite wave vector to that of the initial state in the conduction band. Such a three-body process is quite inefficient compared with direct gap recombination.[12,18] This is why Si is such a poor light emitter.

The indirect band gap of Si is 1.12 eV at room temperature. The weak band-to-band emission at this energy in the near infrared was first observed by Haynes and Briggs[19] using visible light excitation or by forward-biasing Si diodes. A review of the early work on intrinsic and extrinsic radiative recombination in Si has been given by Dean.[20] Intriguingly, broad-band white light emission can also be seen by reverse biasing the Si diode to avalanche breakdown conditions.[21] After decades of speculation, the most probable explanation of this phenomenon is a recombination model[22] in which hot carriers are produced by impact ionization and subsequently recombine via a direct conduction-band to valence-band transition.[23]

Electron-hole pairs may bind to each other to form excitons, which can be either free or tied to impurities or defects.[12,18] The decay of such excitons can lead to light emission that may be tunable by, for example, quantum confinement. Such excitonic emission is thus under active investigation in quantum well, wire, and dot

structures[24] corresponding to carrier confinement in 1, 2, and 3 dimensions, respectively.

3. OVERCOMING THE INDIRECT BAND GAP

Materials engineering, a relatively new phenomenon in materials science, is now being actively applied to Si in an attempt to overcome the indirect band gap limitations in light emission from Si.[1] In these various attempts, the aim is (1) to increase the efficiency of the luminescence by increasing the overlap of the electron and hole wavefunctions via, for example, confinement and band structure engineering, (2) to tune the wavelength of the emission by forming alloys, molecules, and clusters, or (3) to induce recombination at impurity centers.[8] Such attempts can often involve several of these factors. Alternatively, hybrid methods are being explored where, for example, direct gap GaAs is joined with Si. Reviews of each of these methods have been given earlier.[1,11] Here we consider just Si structures of nanometer dimensions.

Research on the quantum confinement of carriers in silicon-based nanostructures including π-Si, nanoclusters, and quantum wells, wires, and dots forms a large part of the work on light emission in silicon. Much of this work was stimulated by the discovery of bright visible light emission at room temperature in π-Si reported in 1990.[25] The number of papers published per year on π-Si alone has been approximately 500 for the last several years.[26] The interest in nanostructures of Si stems from the effects of confinement on carrier wave functions when the crystallite diameter is less than the size of the free exciton Bohr radius of 4.3 nm[24] in bulk c-Si. The quantum confinement increases the electron-hole wave function overlap, resulting in increased light emission efficiency, and shifts the emission peak to higher energy.[12,27]

3.1 Porous silicon

Porous silicon was discovered over 35 years ago by Uhlir.[28] The porous material is created by electrochemical dissolution in HF-based electrolytes. Hydrofluoric acid, on its own, etches single-crystal Si extremely slowly, at a rate of only nanometers per hour. However, passing an electric current between the acid electrolyte and the Si sample speeds up the process considerably, leaving an array of deep narrow pores that generally run perpendicular to the Si surface. Pores measuring only nanometers across, but micrometers deep, have been achieved under specific etching conditions.

In July 1989, Canham conceived the idea of fabricating Si quantum wires in π-Si by reverting to the much slower chemical HF etch after electrochemically etching c-Si. In this way Canham proposed to join up the pores leaving behind an irregular

array of undulating freestanding pillars of c-Si only nanometers wide. In 1990, Canham[25] observed intense visible PL at room temperature from π-Si that had been etched under carefully controlled conditions. Visible luminescence ranging from green to red in color was soon reported by Canham *et al.* for other π-Si samples and ascribed to quantum size effects in wires of width ~3 nm.[25,29] Independently, Lehmann and Gösele[30] reported on the optical absorption properties of π-Si. They observed a shift in the bulk Si absorption edge to values as high as 1.76 eV that they also attributed to quantum wire formation. Visible PL in π-Si at room temperature was soon also reported by Bsiesy *et al.*[31] Koshida and Koyama,[32] and Gardelis *et al.*[33] while visible electroluminescence was observed by Halimaoui *et al.*[34] during the anodic oxidation of π-Si and, later, by Richter *et al.*[35] and Koshida and Koyama[36] with a diode cell.

Tremendous activity on research into the physical and associated chemical characteristics of π-Si has ensued from these early reports with, unfortunately, considerable duplication of effort. It is impossible to mention all of this work here and interested readers are directed to recent reviews and books[15,26,37-47] for further aspects of this work.

A strong PL signal has been observed from π-Si at wavelengths from the near infrared through the visible to the blue depending on the sample porosity and the surface chemical treatment. It has even been possible using specialized preparation techniques to produce "white" light emitting π-Si.[37] For discussion purposes, it is convenient to divide these wavelength regions into three: near infrared, red-yellow, and blue.

The most widely studied PL is in the far-red to orange-yellow region, which we shall denote simply as the "red" PL. This PL shifts to shorter wavelength with increasing chemical dissolution time. It was soon found that much smaller immersion times were required to produce noticeable blue shifts when the chemical dissolution was carried out in the presence of light. The spectra also show a blue shift with increasing anodization current density. The porosity of π-Si increases with increasing anodization current density. Therefore, the behavior of the red PL spectra qualitatively reflects the differences in sample porosity and hence in the dimensions of Si nanocrystallites within π-Si. The blue shift of the PL and optical absorption with increasing porosity provided the first important evidence that quantum confinement plays a significant role in π-Si, which has since been confirmed by the observation of the splitting of the luminescent states, the polarization of the PL, and the phonon replicas seen in the PL under resonant excitation.[47] Nevertheless, after much research, the controversy over the origin(s) of the red PL in π-Si has persisted. This is because the PL peak wavelength and intensity are sensitive to the surface chemistry of π-Si, particularly with regard to the relative amounts of hydrogen and oxygen on the surface. Thus, besides the quantum confinement mechanism, various surface state and defect models have been invoked to explain the various results.[15,47]

Although direct evidence of quantum confinement effects in π-Si has been obtained via optical absorption measurements,[48,49] the problems in explaining the PL of some samples in such a way are amply demonstrated by a study of oxidized π-Si samples.[50] In this case the samples had a sphere-like morphology (spherites) and the optical gap was seen to be in good agreement with theoretical predictions for quantum dots, but there was a substantial energy difference between the absorption and emission data at small spherite diameters. Very recently, this energy difference has been described as being due to an oxygen passivation effect.[51] For H-passivated Si, recombination is via free exciton states for all crystallite sizes and follows the expected quantum confinement behavior. For oxygen-passivated nanocrystals, a stabilized electronic surface state is postulated to form on a Si=O covalent bond and three different recombination mechanisms can be invoked depending on the crystallite size. For larger sizes, recombination occurs via free excitons since the band gap is not wide enough to stabilize the Si=O surface state; for intermediate sizes, recombination involves a trapped electron localized on the Si atom of the Si=O bond and a free hole; and for smaller sizes, recombination is via electrons trapped on the Si=O bond. Thus the respective roles of quantum confinement and surface passivation in red light emission from π-Si are now understood and the controversy has been resolved.

Oxidation of the π-Si surface has been shown to produce blue PL.[15] The blue PL is quite weak in as-prepared π-Si and becomes intense only after strong oxidation. The blue PL has a much faster decay than the red PL and its origin is of some debate at present. Models currently under consideration include band-to-band recombination in Si nanocrystals, emission from oxide, and emission due to surface states. Blue PL has been observed also in oxide-free π-Si simply by decreasing the size of the Si crystallites in accordance with the quantum confinement mechanism.[51,52] In fact, the PL can be tuned from the c-Si band gap of 1.1 eV all the way up to ~3 eV by a judicious choice of the porosity in unoxidized π-Si.[51-53]

The near-infrared PL[15] at ~0.8 eV (below the bulk Si band gap) exhibits complex nonexponential dynamics, with a wide distribution of decay times, and has been assigned to deep level transitions associated with dangling bonds on the surface of the Si nanocrystallites.[54]

From these considerations it is apparent that PL in π-Si is very sensitive to the chemistry of π-Si production and treatment. Crystalline-Si wires, c-Si spherites, and amorphous Si (a-Si) material, or any combination of them, may be formed in a given sample. The π-Si layers thus formed may be far from uniform, which adds to the difficulties in analyzing their optical properties. Other light emitting species may also be formed on the surfaces of the anodized and otherwise chemically treated Si.

Despite all these disadvantages, the ease of production of π-Si and the facts that the room temperature PL is very efficient (1–10% external quantum efficiency)[26,46] and that it is tunable through blue to near infrared wavelengths have led to impressive efforts to produce practical room-temperature devices. The latest red

LEDs have exhibited external quantum efficiencies greater than 0.1% and lifetimes of the order of months.[44,46,55] Most recently, π-Si LEDs have been integrated into Si microelectronic circuits to provide an addressable LED display[56] and a focused-ion-beam (FIB) patterning technology has been developed[57] that permits a π-Si display technology with pixel sizes down to 100 nm. However, improvements in efficiency and power dissipation are necessary for display applications, while an increased modulation frequency (presently ~1 MHz[58] is required for optical interconnects. One way to improve the EL efficiency, to narrow the band width, to improve the directionality, and to increase the long-term stability is to insert the LED into a π-Si resonant cavity.[59] Even so, the long switching times observed in present π-Si LEDs may yet prove to be an Achilles' heel in optoelectronic applications.

The nonlinear optical properties of π-Si may also prove useful for devices. Second harmonic generation has been observed from π-Si with a magnitude two orders greater than that from c-Si owing to the large surface-to-volume ratio of π-Si.[60] A large optically induced absorption change has been observed in π-Si.[61] This phenomenon has been used to form all-optical logic gates in π-Si and raises the possibility of fabricating all-optical integrated circuits on Si.[41,61,62]

3.2 Silicon nanocrystals

Rather than produce nanometer-size Si crystals by etching, as in π-Si, there have been numerous attempts at growing them either directly from a gas phase or indirectly by recrystallization within a matrix.[12,24,63-65] In fact, the observation of a nanoparticle-size dependence of the PL energy in very small Si crystals passivated with hydrogen[66] predates the similar finding in π-Si.[25] Takagi *et al.*[66] found that the PL peak energy varied as $1/d^2$ ($3 < d < 5$ nm), where d is the Si nanocrystal diameter, in accordance with quantum confinement effects predicted by a simple effective mass model. As for π-Si, however, the emitted light energy generally falls below that expected from calculations of the energy gap for Si spheres.[15] Also, the confinement effect is seen[66-68] or not seen[69] in emission depending on sample preparation. Interpretation of the nanocrystal PL spectra suffers from the same ambiguities as π-Si, *i.e.,* nanocrystal size distribution effects and surface chemistry effects.[65] In addition, the nanocrystal structure may deviate from the cubic diamond structure for very small Si nanoclusters.[12] Calculations[70,71] have shown that luminescence in Si nanocrystals can be due to excitons trapped at the surface, which is passivated by hydrogen or silicon oxide, while the optical absorption is characteristic of quantum confinement effects. In definitive experiments,[72] the indirect nature of the Si band gap has been seen from phonon-assisted PL and absorption spectra for small (1–2 nm in diameter) surface-oxidized nanocrystals. The red PL quantum efficiency and lifetime is similar to that found for π-Si, [72] indicating a similar light emission mechanism involving quantum-confined

nanocrystal states. The observation of phonon assisted optical transitions in oxidized Si nanocrystals has also been reported by Kovalev *et al.*[73] and they found that for confinement energies above 0.7 eV the radiative transitions are governed by no-phonon quasidirect processes. Direct measurements of the conduction and valence band edges of Si nanocrystals with diameters from 1 to 5 nm using x-ray absorption and photoemission spectra have confirmed the quantum size effect in the band structure.[74] However, the increase of the band gap with decreasing nanocrystal size is lower overall than that predicted by theory. Thus, the vagaries and complexities of the nanocrystal-interface-surface system are still proving difficult to unravel.

Interesting new results have come from a PL study of individual oxidized Si nanocrystals imaged in the far field using a laser scanning confocal microscope.[75] Mason *et al.* observed a distribution of emission wavelengths, vibronic structure, and, notably, luminescence intermittency and irreversible photobleaching. The blinking nature of the PL from individual nanocrystals indicates a strong coupling between excitons and the surface of the quantum-dot-like nanocrystal. The phonon-assisted PL structure exhibits a much larger splitting than that found in c-Si and is ascribed to Si-O-Si vibrational stretching modes associated with the oxide passivating layer on the nanocrystal. Thus in this system the PL is mediated by the surface of the Si nanocrystal: Excitons are confined near the surface and emission from these excitons is strongly coupled to vibrations in the surface passivating layer. The results imply that controlled modification of the surface by species other than oxygen should produce large differences in the PL yield. An unexpected verification of this idea has come from a totally unrelated development: The observation of intense blue PL at room temperature from Si nanocrystals formed within an a-Si matrix.[76] The PL energy exhibits a size dependence and has a short lifetime (~500 ps), which is attributed to a novel quantum size effect resulting from the generation of resonant electronic states[77] in the Si nanocrystals.

Nanocrystals of Si trapped in some matrix form an attractive system for device fabrication when compared with π-Si, because of the increased surface stability and material rigidity. Visible EL has been observed, for example, from Si nanocrystals embedded in films of a-Si:H[78] and from an electrochemically-formed nanocrystalline Si thin film deposited on SnO_2.[79] In the latter case the p-i-n LED at room temperature emitted orange-red light (1.8 eV) that was readily visible to the eye. The light emission is ascribed variously to near surface states[78] and the quantum size effect.[79] Also, infrared emission near 1.1 eV has been obtained from a room-temperature EL device comprised of Si nanocrystals embedded within a Si-rich SiO_{2-x} matrix.[80] The PL from this structure has an external quantum efficiency of 10^{-3}. Substantial progress in the development of such nanocrystalline-Si EL structures can be expected over the next few years.

3.3 Quantum wells, wires, and dots

One of the major problems involved in π-Si and Si-nanocluster research and development work is the inhomogeneity of the material. Such inhomogenous broadening effects in the PL and EL can be minimized by preparing *uniform* Si structures in the form of quantum wells, wires, or dots. Such structures can readily be produced directly by modern epitaxial growth techniques such as planar epitaxy, quantum wire formation along wafer steps, and dot self assembly, or indirectly by etching appropriate planar structures in the case of wires and dots. The predicted Si transition energies[81,82] due to the different degrees of quantum confinement show that appreciable confinement effects are seen only for diameters less than 3 nm. Etched structures of this size have been difficult to produce in Si until very recently.

The simplest approach is to grow thin quantum wells of Si separated by wide band gap barriers. Suitable barrier candidates are SiO_2, CaF_2, and Al_2O_3,[83] and SiO_2 has the additional advantage of being an excellent passivator of Si.[84] Although a number of Si/barrier superlattices have been produced in the past[85] none has produced convincing evidence for quantum confinement induced emission until recently. In 1995, Lu *et al.*[86] reported visible light emission at room temperature from ultrathin-layer Si/SiO_2 superlattices grown by molecular beam epitaxy (MBE) that exhibited a clear quantum confinement shift with Si layer thickness. According to effective mass theory and assuming infinite potential barriers, which is a reasonable approximation since wide-gap (9 eV) 1-nm-thick SiO_2 barriers are used, the energy gap E for one-dimensionally confined Si should vary as

$$E = E_g + \frac{\pi^2}{2d^2}\left(\frac{1}{m_e^*} + \frac{1}{m_h^*}\right) \tag{1}$$

where E_g is the bulk material band gap and m_e^* and m_h^* are the electron and hole effective masses.[87] This simple model is a reasonable first approximation to compare with experiment for quantum wells.[82] The shift in PL peak energy with Si well thickness d is well represented by Eq. (1), with $E(eV) = 1.60 + 0.72d^{-2}$. The very thin layers of Si ($1 < d < 3$ nm) have a disordered, but nearly crystalline, structure owing to the growth conditions and the huge strain at the $Si–SiO_2$ interfaces.[88] (By reducing considerably the SiO_2 thickness, epitaxial growth of the Si layers can be achieved.[89]) The fitted E_g of 1.60 eV is larger than that expected for c-Si (1.12 eV at 295 K), but is in excellent agreement with that of bulk a-Si (1.5–1.6 eV at 295 K). The indications of direct band-to-band recombination were confirmed by measurements via x-ray techniques of the conduction and valence band shifts with layer thickness.[86,90] The fitted confinement parameter of 0.72 eV/nm^2 indicates $m_e^* \approx m_h^* \approx 1$, comparable to the effective masses of c-Si at room temperature.[87] The integrated intensity at first rises sharply with decreasing Si

thickness until $d \approx 1.5$ nm and then decreases again, which is consistent with quantum well exciton emission.[91,92] The PL intensity is enhanced by factors of up to 100 on annealing and is also selectively enhanced and band-width narrowed by incorporation into an optical microcavity.[93] In a higher quality cavity, a very sharp (17 meV full width at half maximum) PL peak has been observed.[94]

Room temperature PL at visible wavelengths has also been observed from MBE-grown nanocrystalline Si/CaF_2 superlattices,[85] but in this case the luminescence is related to localized states located well below the Si layer optical absorption edge.[95] Nevertheless, these states do exhibit some sensitivity to confinement effects. Likewise, the visible PL observed in Si/SiN_x superlattices grown by MBE in association with an electron-cyclotron-resonance plasma surface treatment[96] exhibited only a weak dependence on quantum well confinement compared with Si/SiO_2. Further evidence of confinement-induced PL in plasma-enhanced chemical vapor deposition (PECVD)-grown Si/SiN_x single quantum well structures has been obtained by Steigmeier *et al.*[97]

Theoretical calculations of the optical properties of Si/SiO_2 superlattices based on an empirical pseudopotential homojunction model[98] revealed that for Si layers in the (100) direction the energy gap is pseudodirect, *i.e.,* the optical transition matrix element is smaller than that of a direct transition as in bulk GaAs. Nevertheless, the energy increases with decreasing Si quantum-well thickness and the transition matrix element increases steeply up to ~2 nm thickness and then decreases again in general agreement with the experimental results. Tight binding bandstructure calculations for $Si_m/(SiO_2)_n$ crystalline superlattices with the number of unit cells $m,n \leq 5$[99] show a striking new feature. Besides the expected increase in the band gap due to quantum confinement, the confined bands along the Γ–Z symmetry direction are essentially dispersionless and exhibit a strongly-nested direct band gap character at the minimum energy gap of the system. Thus, these superlattices produce a high radiative efficiency for a 1–3 nm (m=2–5) Si layer thickness,[99] as found experimentally. The self-consistent electronic structures of Si/CaF_2 superlattices have been calculated by means of the linear muffin-tin orbital method in the atomic-sphere approximation.[100] These calculations could not explain the experimental difference between absorption and PL in such superlattices (see Ref. 95 and references therein), but they did emphasize that both quantum confinement and adequate passivation of the Si layers are necessary in order to observe visible wavelength PL.

The bright PL obtained from as-grown and annealed Si/SiO_2 superlattices offers interesting prospects for the fabrication of a Si-based light emitter that can be tuned from 500 to beyond 800 nm by varying the Si layer thickness and/or the annealing conditions, all using available vacuum deposition technology and standard Si wafer processing techniques. The next important step is to develop LEDs based on such superlattices. Several prototype devices have been constructed in Si/SiO_2[101-104] and Si/CaF_2[105] and all report visible EL, although as yet there is no strong evidence that

the emission originates from confined states in the Si quantum wells. The EL from the Si/SiO_2 superlattices is notably stable.[101,102]

Quantum wires obtained by etching $Si/Si_{1-x}Ge_x$ heterostructures have been investigated by several groups (see, for example, Refs. 106 and 107). In PL measurements, wires defined by electron beam lithography and reactive ion etching have shown small blue shifts of up to 30 meV in the $Si_{1-x}Ge_x$ alloy peak at ~1.1 eV due to a combination of strain and confinement.[106,107] Alternatively, $Si_{1-x}Ge_x$ wires have been grown on V-groove patterned Si substrates[108]: The infrared emission (PL and EL) in this case exhibits a large optical anisotropy.[109] No significant intensity enhancements compared with PL from quantum well transitions have been realized in these wire structures.

Until recently, it has not been possible to produce thin enough freestanding wires of c-Si by etching techniques to observe quantum confinement effects, although room temperature PL at wavelengths from 400–850 nm is found for pillars with diameters ~10 nm (see, for example, Refs. 110-112 and references therein). Recently, an EL device based on such Si nanopillars has been produced: The device emitted red light that was visible to the naked eye.[113] New etching techniques have now been developed for fabricating Si quantum wires with dimensions in the sub-10-nm region that after thermal oxidation should allow investigation of the optical properties of sub-2-nm wires in conventional wire[114] and free-standing pillar[115] form.

Theoretical calculations of the electronic structure and optical properties of H-passivated Si quantum wires have been reported by a number of research groups (see, for example, Ref. 116 and references therein). First principles calculations show the same band nesting phenomenon and near-flat dispersion along the Γ–Z symmetry (wire) direction, as described above for Si quantum wells, and the occurrence of direct gaps.[116,117]

Attention has now turned mainly to the production of $Si_{1-x}Ge_x$ quantum dots, as these produce the strongest confinement effects for a given diameter or can achieve desired confinements with smaller diameters than for wires. A number of first principles calculations have been performed for H-passivated Si quantum dots (see Ref. 118 and references therein) and they all show a steep increase in the optical gap energy with decreasing dot size below 3–5 nm. Quantum dots fabricated by etching $Si/Si_{1-x}Ge_x$ superlattices have produced 4 K PL at 0.97 eV that is 200 times brighter in 60 nm dots compared with the unetched superlattice PL.[119] Similar studies of $Si_{1-x}Ge_x$ dots fabricated by self-assembling island growth on Si have shown an increased luminescence efficiency due to the localization of excitons in the dots.[120] In the latter case, the dots were buried in Si, which has the advantage of minimizing surface defect recombination. In both cases, EL has been observed from diode structures at low temperatures[120,121] and at room temperature.[121] The infrared EL at 4.2 K in the dot is two orders of magnitude higher in intensity than in the as-grown superlattice.

At room temperature, the dot EL at 1.3 μm is only 50% less efficient, with a threshold injection current of ~0.1 pA/dot and an electrical-input to optical-output power conversion efficiency of 0.14%.[121]

In subsequent work on Si quantum dots ~10 nm in size formed in a-Si/SiO_2 superlattices by controlled crystallization, Tsybeskov *et al.*[122] have shown that the PL emitted near 1.1 eV is remarkably efficient (~0.2% external quantum efficiency at 300 K) compared with c-Si. The observation of sharp structure in the superlattice PL spectrum proves that the Si dots are extremely pure, primarily as a result of self-purification during thermal crystallization.[122] The high room temperature quantum efficiency indicates that strong luminescence in indirect gap semiconductor dots does not necessarily require strong quantum confinement, but can arise simply from spatial confinement in well passivated nanocrystals. Finally, a shift of the PL peak toward higher energies was found with smaller-size (<10-nm) Si dots. The PL in such dots can be tuned up in energy by confinement and down in energy by alloying of Ge with Si. The latter case has been investigated in MBE-grown $Si_{0.5}Ge_{0.5}$ dots in a coherent wave superlattice structure. Here, strong no-phonon PL was obtained at ~0.8 eV (1.55 μm) that could easily be varied in wavelength by changing the Ge content.[1]

It is conceivable that this diverse work on Si quantum dots could soon lead to a new generation of $Si/Si_{1-x}Ge_x$ optoelectronic devices at the optical fiber communication wavelengths of 1.3 and 1.55 μm.

4. PROSPECTS FOR SILICON-BASED OPTOELECTRONIC DEVICES

Although a considerable number of optical detectors and waveguide structures have been created from Si-based materials[5,8,123.124] there is still a paucity of LEDs constructed from Si and, most importantly for many all-Si optoelectronic applications, no lasers. The requirements for an acceptable semiconductor laser for optical fiber applications are rather stringent: 5–10 mW of laser facet power at 1.3 μm, maximum laser threshold less than 70 mA, spectral width less than 10 nm, operation over the temperature range -40°C to +85°C, average lifetime of 10^6 hr, and low cost.[123]

Of the materials systems reviewed here, LEDs made from Si:Er show the most immediate promise for device applications at 1.54 μm. An optoelectronic device has been constructed[1] comprising an edge emitting Si:Er LED integrated with a Si waveguide on a SOI substrate. The EL linewidth of such LEDs at room temperature is approximately 10 nm.[125] This narrow linewidth and the fixed emission wavelength augers well for optical fiber communication systems with high bandwidth capacity. Optical gain at 1.54 μm has already been obtained in suitable Si waveguide

structures[126] and laser emission could soon follow if the room temperature quantum efficiency can be improved sufficiently.

Porous Si LEDs emitting at orange-red wavelengths are no longer just a curiosity with the announcement of LEDs having reasonable external quantum efficiencies (0.1%), lifetimes of the order of months, and low driving voltages (2–5 V) in forward bias[127] and also of devices with integrated Si transistor drivers.[56] Apart from display applications,[56] however, the long lifetime and broad linewidth of the optical emission will limit optical communications applications of π-Si LEDs, and it is not clear whether current injection lasers will ever be made from π-Si. The need to be compatible with existing large-scale Si processing also leads to difficulties with electrochemically created π-Si. It is likely that oxidized Si nanoparticles will eventually prove to be superior to π-Si in this regard and also in device stability, but the long lifetime and wide band width of the emitted light are still going to limit device performance. Nevertheless, π-Si is a versatile material and offers extremely diverse optoelectronic functionality to Si in the areas of infrared and visible waveguiding, photodetection, and photomodulation.[128]

Light emission from quantum well and dot structures may yet hold the most promise for producing lasers at wavelengths across the visible into the infrared. The Si/SiO_2 multiple quantum well structures[85] are well suited for visible wavelength lasers at room temperature. Their optical absorption characteristics are ideal for optical pumping in a planar microcavity, but it is not yet certain if their electrical characteristics are amenable to injection laser design. Quantum dot LEDs made from $Si/Si_{1-x}Ge_x$[121] show considerable potential for laser applications at 1.3 and possibly 1.55 μm. However, much more research and development work on these structures is required before this potential can be realized.

In conclusion, considerable progress has been made over the last decade on obtaining efficient light emission from a wide variety of Si-based materials. This work has led to the development of light emitting devices that are just now reaching useful performance levels. The intensity of research and development on light emission in Si is increasing as a result of these stimulating advances in materials engineering and technology. It is likely that a Si-based laser will emerge from this research in the very near future, although the actual active laser material could be none of those discussed here, because of the burgeoning diversification[7,129-143] in Si-based materials.

REFERENCES

1. D.J. Lockwood, in *Silicon-Based Materials and Devices*, edited by H.S. Nalwa (Academic Press, San Diego, 2001), p. 225.
2. E. Kasper and F. Schäffler, in *Strained-Layer Superlattices: Materials Science and Technology,* edited by T.P. Pearsall (Academic Press, Boston, 1991), p. 223.

3. G. Abstreiter, *Physics World* **5** (3), 36 (1992).
4. B.A. Saleh and M.C. Teich, *Fundamentals of Photonics* (Wiley, New York, 1991).
5. R.A. Soref, *Proc. IEEE* **81**, 1687 (1993).
6. E. Kasper and H. Presting, *SPIE Proc.* **1361**, 302 (1990).
7. R.A. Soref, *J. Vac. Sci. Technol. A* **14**, 913 (1996).
8. R. Soref, *MRS Bulletin* **23** (4), 20 (1998).
9. S.S. Iyer and Y.-H. Xie, *Science* **260**, 40 (1993).
10. L.T. Canham, *MRS Bulletin* **18** (7), 22 (1993).
11. D.J. Lockwood, *Light Emission in Silicon: From Physics to Devices* (Academic Press, San Diego, 1997).
12. L.C. Kimerling, K.D. Kolenbrander, J. Michel, and J. Palm, *Solid State Phys.* **50**, 333 (1997).
13. R.W. Collins, P.M. Fauchet, I. Shimizu, J.-C. Vial, T. Shimada, and A.P. Alivisatos, *Advances in Microcrystalline and Nanocrystalline Semiconductors—1996* (Materials Research Society, Pittsburgh, 1997).
14. L.T. Canham, M.J. Sailor, K. Tanaka, and C.-C. Tsai, *Microcrystalline and Nanocrystalline Semiconductors—1998* (Materials Research Society, Pittsburgh, 1999).
15. D.J. Lockwood, *Solid State Commun.* **92**, 101 (1994).
16. *Properties of Silicon* (INSPEC, London, 1988).
17. J.R. Chelikowsky and M.L. Cohen, *Phys. Rev. B* **14**, 556 (1976).
18. J.I. Pankove, *Optical Processes in Semiconductors* (Dover, New York, 1971).
19. J.R. Haynes and H.B. Briggs, *Phys. Rev.* **86**, 647 (1952).
20. P.J. Dean, *Luminescence of Inorganic Solids* (Academic Press, New York, 1966), Chapter 3.
21. R. Newan, *Phys. Rev.* **100**, 700 (1955).
22. P.A. Wolf, *J. Phys. Chem. Solids* **16**, 184 (1960).
23. A.T. Obeidat, Z. Kalayjian, A.G. Andreou, and J.B. Khurgin, *Appl. Phys. Lett.* **70**, 470 (1997).
24. A.D Yoffe, *Advan. Phys.* **42**, 173 (1993).
25. L.T. Canham, *Appl. Phys. Lett.* **57**, 1046 (1990).
26. A.G. Cullis, L.T. Canham, and P.D.J. Calcott, *J. Appl. Phys.* **82**, 909 (1997).
27. L. Brus, *Appl. Phys. A* **53**, 465 (1991).
28. A. Uhlir, Jr., *Bell Syst. Tech. J.* **35**, 333 (1956).
29. A.G. Cullis, and L.T. Canham, *Nature* **353**, 335 (1991).
30. V. Lehmann and U. Gösele, *Appl. Phys. Lett.* **58**, 856 (1991).
31. A. Bsiesy, J.C. Vial, F. Gaspard, R. Herino, M. Ligeon, F. Muller, R. Romestain, A. Wasiela, A. Halmaoui, and G. Bomchil, *Surf. Sci.* **254**, 195 (1991).
32. N. Koshida and H. Koyama, *Jpn. J. Appl. Phys.* **30**, L1221 (1991).
33. S. Gardelis, J.S. Rimmer, P. Dawson, B. Hamilton, R.A. Kubiak, T.E. Whall, and E.H.C. Parker, *Appl. Phys. Lett.* 59, 2118 (1991).
34. A. Halimaoui, C. Oules, G. Bomchil, A. Bsiesy, F. Gaspard, R. Herino, M. Ligeon, and F. Muller, *Appl. Phys. Lett.* **59**, 304 (1991).
35. A. Richter, P. Steiner, F. Kozlowski, and W. Lang, *IEEE Electron Device Lett.* **12**, 691 (1991).
36. N. Koshida and H. Koyama, *Appl. Phys. Lett.* **60**, 347 (1992).
37. D.C. Bensahel, L.T. Canham, and S. Osscicini, *Optical Properties of Low Dimensional Structures* (Kluwer, Dordrecht, 1993).
38. P.M. Fauchet, C.C. Tsai, L.T. Canham, I. Shimizu, and Y. Aoyagi, *Microcrystalline Semiconductors: Materials Science and Devices* (Materials Research Society, Pittsburgh, 1993).

39. Z.C. Feng and R. Tsu, *Porous Silicon* (World Scientific, Singapore, 1994).
40. A. Hamilton, *Semicond. Sci. Technol.* **10**, 1187 (1995).
41. Y. Kanemitsu, *Phys. Reports* **263**, 1 (1995).
42. J.C. Vial and J. Derrien, *Porous Silicon Science and Technology* (Springer-Verlag, Berlin, 1995).
43. R. Hérino and W. Lang, *Porous Silicon and Related Materials* (Elsevier, Amsterdam, 1995).
44. D.J. Lockwood, P.M. Fauchet, N. Koshida, and S.R.J. Brueck*, Advanced Luminescent Materials* (The Electrochemical Society, Pennington, NJ, 1996).
45. P.M. Fauchet, *J. Lumin.* **70**, 294 (1996).
46. P.M. Fauchet, in *Light Emission in Silicon,* edited by D.J. Lockwood (Academic Press, San Diego, 1997), Chapter 6.
47. P.D.J. Calcott, *Mat. Sci. Eng. B* **51**, 132 (1998).
48. I. Sagnes, A. Halimaoui, G. Vincent, and P.A. Badoz, *Appl. Phys. Lett.* **62**, 1155 (1993).
49. D.J. Lockwood, A. Wang, and B. Bryskiewicz, *Solid State Commun.* **89**, 587 (1994).
50. D.J. Lockwood, and A.G. Wang, in *Photoluminescence in Porous Silicon Due to Quantum Confinement,* edited by D.J. Lockwood, P.M. Fauchet, N. Koshida, and S.R.J. Brueck (The Electrochemical Society, Pennington, NJ, 1996), p. 166.
51. M.V. Wolkin, J. Jorne, P.M. Fauchet, G. Allan, and C. Delarue, *Phys. Rev. Lett.* **82**, 197 (1999).
52. H. Mizuno, H. Koyama, and N. Koshida, *Appl. Phys. Lett.* **69**, 3779 (1996).
53. G. Polisski, H. Heckler, D. Kovalev, M. Schwartzkoff, and F. Koch, *Appl. Phys. Lett.* **73**, 1107 (1998).
54. F. Koch, *Mater. Res. Soc. Symp. Proc.* **298**, 319 (1993).
55. B. Gelloz, T. Nakagawa, and N. Koshida, *Appl. Phys. Lett.* **73**, 2021 (1998).
56. K.D. Hirschman, L. Tsybeskov, S.P. Duttagupta, and P.M. Fauchet, *Nature* **384**, 338 (1996).
57. P. Schmuki, L.E. Erickson, and D.J. Lockwood, *Phys. Rev. Lett.* 80, 4060 (1998).
58. L. Tsybeskov, S.P. Duttagupta, K.D. Hirschman, and P.M. Fauchet, *Appl. Phys. Lett.* **68**, 2058 (1996).
59. L. Pavesi, R. Guardini, and C. Mazzoleni, *Solid State Commun.* **97**, 1051 (1996).
60. K.-Y. Lo and J.T. Lue, *IEEE Photon. Technol. Lett.* **5**, 651 (1993).
61. T. Matsumoto, N. Hasegawa, T. Tamaki, K. Ueda, T. Futagi, H. Mimura, and Y. Kanemitsu, *Jpn. J. Appl. Phys.* **33**, L35 (1994).
62. T. Matsumoto, M. Daimon, H. Mimura, Y. Kanemitsu, and N. Koshida, *J. Electrochem. Soc.* **142**, 3528 (1995).
63. H. Kamimura, *Light Emission from Novel Silicon Materials,* Supplement B to J. Phys. Soc. Japan, Vol. 63 (Physical Society of Japan, Tokyo, 1994).
64. T. Ogawa and Y. Kanemitsu, *Optical Properties of Low-Dimensional Materials* (World Scientific, Singapore, 1995).
65. Y. Kanemitsu, in *Light Emission in Silicon,* edited by D.J. Lockwood (Academic Press, San Diego, 1997), Chapter 5.
66. H. Takagi, H. Ogawa, Y. Yamazaki, A. Ishizaki, and T. Nakagiri, *Appl. Phys. Lett.* 56, 2379 (1990).
67. S. Schuppler, S.L. Friedman, M.A. Marcus, D.L. Adler, Y.-H. Xie, F.M. Ross, T.D. Harris, W.L. Brown, Y.J. Chabal, L.E. Brus, and P.H. Citrin, *Phys. Rev. Lett.* **72**, 2648 (1994).
68. Y. Kanzawa, T. Kageyama, S. Takeoka, M. Fujii, S. Hayashi, and K. Yamamoto, *Solid State Commun.* **102**, 533 (1997).

69. Y. Kanemitsu, T. Ogawa, K. Shiraishi, and K. Takeda, *Phys. Rev. B* **48**, 4883 (1993).
70. G. Allan, C. Delerue, and M. Lannoo, *Phys. Rev. Lett.* **76**, 2961 (1996).
71. B. Delerue, G. Allan, and M. Lannoo, in *Light Emission in Silicon,* edited by D.J. Lockwood (Academic Press, San Diego, 1997), Chapter 7.
72. L.E. Brus, P.F. Szajowski, W.L. Wilson, T.D. Harris, S. Schuppler, and P.H. Citrin, *J. Amer. Chem. Soc.* **117**, 2915 (1995).
73. B. Kovalev, H. Heckler, M. Ben-Chorin, G. Polisski, M. Schwartzkopff, and F. Koch, *Phys. Rev. Lett.* **81**, 2803 (1998).
74. T. van Buuren, L.N. Dinh, L.L. Chase, W.J. Siekhaus, and L.J. Terminello, *Phys. Rev. Lett.* **80**, 3803 (1998).
75. M.D. Mason, G.M. Credo, K.D. Weston, and S.K. Buratto, *Phys. Rev. Lett.* **80**, 5405 (1998).
76. X. Zhao, S. Komuro, S. Fujita, H. Isshiki, Y. Aoyagi, and T. Sugano, *Mat. Sci. Eng. B* **51**, 154 (1998).
77. S. Nomura, T. Iitaka, X. Zhao, T. Sugano, and Y. Aoyagi, *Mat. Sci. Eng. B* 51, 146 (1998).
78. S. Tong, X.-N. Liu, L.-C. Wang, F. Yan, and X.-M. Bao, *Appl. Phys. Lett.* **69**, 596 (1996).
79. T. Toyama, T. Matsui, Y. Kurokawa, H. Okamoto, and Y. Hamakawa, *Appl. Phys. Lett.* **69**, 1261 (1996).
80. L. Tsybeskov, K.L. Moore, D.G. Hall, and P.M. Fauchet, *Phys. Rev. B* **54**, R8361 (1996).
81. D.J. Lockwood, G.C. Aers, L.B. Allard, B. Bryskiewicz, S. Charbonneau, D.C. Houghton, J.P. McCaffrey, and A. Wang, *Can. J. Phys.* **70**, 1184 (1992).
82. A. Zunger and L.-W. Wang, *Appl. Surf. Sci.* **102**, 350 (1996).
83. R. Tsu, *Nature* **364**, 19 (1993).
84. C.J. Frosch and L. Derick, *J. Electrochem. Soc.* **104**, 547 (1957).
85. D.J. Lockwood, *Phase Transitions* 68**,** 151 (1999).
86. Z.H. Lu, D.J. Lockwood, and J.-M. Baribeau, *Nature* **378**, 258 (1995).
87. D.J. Lockwood, Z.H. Lu, and J.-M. Baribeau, *Phys. Rev. Lett.* **76**, 539 (1996).
88. Z.H. Lu, D.J. Lockwood, and J.-M. Baribeau, *Solid-State Electron.* **40**, 197 (1996).
89. R. Tsu, A. Filios, C. Lofgren, K. Dovidenko, and C.G. Waugh, *Electrochem. Solid-State Lett.* **1**, 80 (1998).
90. D.J. Lockwood, J.-M. Baribeau, and Z.H. Lu, in *Advanced Luminescent Materials,* edited by D.J. Lockwood, P.M. Fauchet, N. Koshida, and S.R.J. Brueck (The Electrochemical Society, Pennington, NJ, 1996), p. 339.
91. J.A. Brum and G. Bastard, *J. Phys. C. Solid State Phys.* **18**, L789 (1985).
92. Z.H. Lu, J.-M. Baribeau, D.J. Lockwood, M. Buchanan, N. Tit, C. Dharma-wardana, and G.C. Aers, *SPIE Proc.* **3491**, 457 (1998).
93. B.T. Sullivan, D.J. Lockwood, H.J. Labbé, and Z.-H. Lu, *Appl. Phys. Lett.* **69**, 3149 (1996).
94. D.J. Lockwood, B.T. Sullivan, and H.J. Labbé, *J. Lumin.* **80**, 75 (1999).
95. B. Basani, S. Ménard, and F. Arnaud d'Avitaya, *Phys. Stat. Sol. (a)* **165**, 49 (1998).
96. J.-M. Baribeau, D.J. Lockwood, Z.H. Lu, H.J. Labbé, S.J. Rolfe, and G.I. Sproule, *J. Lumin.* **80**, 417 (1999).
97. E.F. Steigmeier, R. Morf, D. Grützmacher, H. Auderset, B. Delley, and R. Wessicken, *Appl. Phys. Lett.* **69**, 4165 (1996).
98. J.-B. Xia and K.W. Cheah, *Phys. Rev. B* **56**, 14925 (1997).
99. N. Tit and M.W.C. Dharma-wardana, *Solid State Commun.* **106**, 121 (1998).
100. E. Degoli and S. Ossicini, *Phys. Rev. B* **57**, 14776 (1998).

101. R. Tsu, Q. Zhang, and A. Filios, *SPIE Proc.* **3290**, 246 (1997).
102. A.G. Nassiopoulou, V. Ioannou-Sougleridis, P. Photopoulos, A. Travlos, V. Tsakiri, and D. Papadimitriou, *Phys. Stat. Sol. (a)* **165**, 79 (1998).
103. G.G. Qin, S.Y. Ma, Z.C. Ma, W.H. Zong, and L.P. You, *Solid State Commun.* **106**, 329 (1998).
104. L. Heikkilä, T. Kuusela, H.-P. Hedman, and H. Ihantola, *Appl. Surf. Sci.* **133**, 84 (1998).
105. V. Ioannou-Sougleridis, V. Tsakiri, A.G. Nassiopoulou, P. Photopoulos, F. Bassani, and F. Arnaud d'Avitaya, *Phys. Stat. Sol. (a)* **165**, 97 (1998).
106. Y.S. Tang, C.D.W. Wilkinson, C.M. Sotomayor Torres, D.W. Smith, T.E. Whall, and E.H.C. Parker, *Solid State Commun.* **85**, 199 (1993).
107. J. Lee, S.H. Li, J. Singh, and P.K. Bhattacharaya, *J. Electron. Mat.* **23**, 831 (1994).
108. N. Usami, T. Mine, S. Fukatsu, and Y. Shiraki, *Appl. Phys. Lett.* **63**, 2789 (1993).
109. N. Usami, T. Mine, S. Fukatsu, and Y. Shiraki, *Appl. Phys. Lett.* **64**, 1126 (1994).
110. H.I. Liu, N.I. Maluf, R.F.W. Pease, D.K. Biegelsen, N.M. Johnson, and F.A. Ponce, *J. Vac. Sci. Technol. B* **10**, 2846 (1992).
111. A.G. Nassiopoulos, S. Grigoropoulos, and D. Papadimitriou, in *Advanced Luminescent Materials,* edited by D.J. Lockwood, P.M. Fauchet, N. Koshida, and S.R.J. Brueck (The Electrochemical Society, Pennington, NJ, 1996), p. 296.
112. S.H. Zaidi, A.-S. Chu, and S.R.J. Brueck, in *Advanced Luminescent Materials,* edited by D.J. Lockwood, P.M. Fauchet, N. Koshida, and S.R.J. Brueck (The Electrochemical Society, Pennington, NJ, 1996), p. 307.
113. A.G. Nassiopoulos, S. Grigoropoulos, and D. Papadimitriou, *Appl. Phys. Lett.* **69**, 2267 (1996).
114. B. Namatsu, K. Kurihara, M. Nagase, and T. Makino, *Appl. Phys. Lett.* **70**, 619 (1997).
115. H.I. Liu, D.K. Biegelsen, F.A. Ponce, N.M. Johnson, and R.F.W. Pease, *Appl. Phys. Lett.* **64**, 1363 (1994).
116. F. Buda and J. Kohanoff, *Prog. Quant. Electr.* **18**, 201 (1994).
117. S. Ossicini, C.M. Bertoni, M. Biagini, A. Lugli, G. Roma, and O. Bisi, *Thin Solid Films* **297**, 154 (1997).
118. F.A. Reboredo, A. Franceschetti, and A. Zunger, *Phys. Rev. B* **61**, 13073 (2000).
119. Y.S. Tang, C.M. Sotomayor Torres, R.A. Kubiak, D.A. Smith, T.E. Whall, E.H.C. Parker, H. Presting, and H. Kibbel, in *The Physics of Semiconductors, Vol. 2,* edited by D.J. Lockwood (World Scientific, Singapore, 1995), p. 1735.
120. R. Apetz, L. Vescan, A. Hartmann, C. Dieker, and H. Lüth, *Appl. Phys. Lett.* **66**, 445 (1995).
121. Y.S. Tang, W.-X. Ni, C.M. Sotomayor Torres, and G.V. Hansson, *Electron. Lett.* **31**, 1385 (1995).
122. L. Tsybeskov, K.D. Hirschman, S.P. Duttagupta, M. Zacharias, P.M. Fauchet, J.P. McCaffrey, and D.J. Lockwood, *Appl. Phys. Lett.* **72**, 43 (1998).
123. D.G. Hall, *Mat. Res. Soc. Symp. Proc.* **298**, 367 (1993).
124. R. Bozeat and A. Loni, *Laser Focus World* **31** (4), 97 (1995).
125. B. Zheng, J. Michel, F.Y.G. Ren, L.C. Kimerling, D.C. Jacobson, and J.M. Poate, *Appl. Phys. Lett.* **64**, 2842 (1994).
126. X. Zhao, S. Komuro, H. Isshiki, Y. Aoyagi, and T. Sugano, *Appl. Phys. Lett.* **74**, 120 (1999).
127. R.T. Collins, P.M. Fauchet, and M.A. Tischler, *Physics Today* **50** (1), 24 (1997).
128. L.T. Canham, T.I. Cox, A. Loni, and A.J. Simons, *Appl. Surf. Sci.* **102**, 436 (1996).
129. G.F. Grom, D.J. Lockwood, J.P. McCaffrey, H.J. Labbé, P.M. Fauchet, B. White Jr., J. Diener, D. Kovalev, F. Koch, and L. Tsybeskov, *Nature* **407**, 358 (2000).

130. L. Pavesi, L. Dal Negro, C. Mazzoleni, G. Franzo, and F. Priolo, *Nature* **408**, 440 (2000).
131. B. Dehlinger, L. Diehl, U. Gennser, H. Sigg, J. Faist, K. Ensslin, D. Grützmacher, Science **290,** 2277 (2000).
132. L. Tsybeskov, G.F. Grom, R. Krishnan, L. Montes, P.M. Fauchet, D. Kovalev, J. Diener, V. Timoshenko, F. Koch, J.P. McCaffrey, J.-M. Baribeau, G.I.Sproule, D.J. Lockwood,. Y.M. Niquet, C. Delerue, and G. Allan, *Europhys. Lett* **55**, 552 (2001).
133. W.L. Ng, M.A. Lourenço, R.M. Gwilliam, S. Ledain, G. Shao, and K.P. Homewood, *Nature* **410**, 192 (2001).
134. M. A. Green, J. Zhao, A. Wang, P. J. Reece and M. Gal, *Nature* **412**, 805 (2001).
135. R. Boukherroub, D.D.M. Wayner, G.I. Sproule, D.J. Lockwood and L.T. Canham, *Nano Lett.* **1**, 713 (2001).
136. Z.H. Lu, and D. Grozea, *Appl. Phys. Lett.* **80**, 255 (2002).
137. N. Shastin, R. Kh. Zhukavin, and E. E. Orlova, S. G. Pavlov, M. H. Rummeli, H.-W Hubers, J. N. Hovenier, T. O. Klaassen, H. Riemann, I. V. Bradley, and A. F. G. van der Meer, *Appl. Phys. Lett*. **80,** 3512 (2002).
138. R. Boukherroub, D.D.M. Wayner and D.J. Lockwood, *Appl. Phys. Lett.* **81**, 601 (2002).
139. L. Diehl, S. Mentese, H. Sigg, E. Müller, D. Grützmacher, U. Gennser, I. Sagnes, T. Fromherz, J. Stangl, T. Roch, G. Bauer, Y. Campidelli, O. Kermarrec, D. Bensahel, and J. Faist, *Appl. Phys. Lett*. **81**, 4700 (2002).
140. D.J. Lockwood, Z.H. Lu, and D. Grozea, *SPIE Proc.* **4808**, 40 (2002).
141. Y. Nakajima, A. Kojima, and N. Koshida, *Appl. Phys. Lett.* **81**, 2472 (2002).
142. T. Trupke, J. Zhao, A. Wang, R. Corkish, and M.A. Green, *Appl. Phys. Lett*. **82**, 2996 (2003).
143. B. Gelloz, H. Sano, R. Boukherroub, D. D. M. Wayner, D. J. Lockwood, and N. Koshida, *Appl. Phys. Lett*. **83**, in press (2003).

NANOSCALE RANDOM SPIN-ORBIT COUPLING IN LOW-DIMENSIONAL STRUCTURES

E.Ya. Sherman [1,2], S. Sharma [2], and C. Ambrosch-Draxl [2]
[1] *Institute for Theoretical Physics, RWTH-Aachen, 52056 Aachen, Germany*
[2] *Institute for Theoretical Physics, Karl-Franzens-University, Graz, A-8010, Graz, Austria*
eugene.sherman@kfunigraz.ac.at

Abstract Spin-orbit coupling is a crucial parameter controlling the spin relaxation rate in solids. Here we review recent theoretical results on the randomness of spin-orbit coupling in two-dimensional structures and show that it exists in a form of random nanodomains. The spin relaxation rate arising due the randomness is analyzed. The random spin-orbit coupling leads to a measurable intensity of electric dipole spin resonance, that is to spin-flip transitions caused by the electric field of an electromagnetic wave.

Keywords: Spin-orbit coupling, spin relaxation, spin resonance, Monte Carlo simulations

1. Introduction: Spin-orbit coupling and spin relaxation

Spintronics, a prospective technology which should allow to use spins of single electrons for storage and transportation of information, is based on a possibility to manipulate the spins, and if necessary to preserve them in definite controlled states as long as necessary to avoid loss of the information. In solids, electrons interact with impurities, surfaces, phonons, and each other. These interactions lead to momentum and energy relaxation of carriers. If the orbital and spin degrees of freedom were completely uncoupled, the spin states would persist for an infinite time and spin relaxation would never occur. Therefore, understanding and controlling of the spin-orbit (SO) coupling and, in turn, the spin relaxation are important for the design of intended spintronics devices [1–5].

As the prospective systems for spintronics, two-dimensional semiconducting electron structures where electrons are localized in the z-direction and free in the lateral ones, are assumed. High mobilities of electrons ($\mu > 10^5$ $\mathrm{cm}^2/(\mathrm{Vs})$) achievable there make the electron transport easy. In order to discuss the possible effects of SO coupling we will consider three types of structures shown in Fig.1. In these structures, the electron states are extended along

E. C. Faulques et al. (eds.), Spectroscopy of Emerging Materials, 115–126.

the z-axis on the scale of the order of 10 nm. These are arranged according to the strength of their artificial growth-induced macroscopic asymmetry. The first structure (Fig.1(a)) is the heterojunction of two different materials (e.g. GaAs/$Al_xGa_{1-x}As$) with the strongest asymmetry. The electrons are localized due to the mismatch of the conduction bands of these two materials and the electric field of the dopant ions attracting them to the interfaces. The next structure (Fig.1(b)) is an asymmetrically doped quantum well (QW) where the electrons localized in the GaAs layer due to the GaAs/$Al_xGa_{1-x}As$ edges are influenced by a strong electric field of the ionized dopants. In these two structures their structural inversion asymmetry (SIA) leads to SO coupling which can be qualitatively understood as follows. For an electron moving with velocity $\vec{v}$ in an electric field $\vec{E}$, the spatial symmetry of the electron envorinment is lifted. If $\vec{v} \perp \vec{E}$ the magnetic field $H = (v/c)E$ arising in its eigenframe acts on the electron spin, thus coupling it to the electron momentum. From this symmetry point of view the SO coupling in these systems described by the Rashba Hamiltonian [6] can be understood:

$$\hat{H}^R_{\rm SO} = \alpha[\hat{\vec{\sigma}} \times \vec{k}_\parallel]\vec{\nu}, \tag{1}$$

where α is the coupling constant, $\hat{\sigma}$ are the Pauli matrices, $\vec{k}_\parallel = -i\hbar\nabla_\parallel - (e/c)\vec{A}_\parallel$ is the in-plane momentum of a carrier, $\vec{A}$ is vector-potential of external field, and $\vec{\nu}$ is the unit vector in the growth direction shown in Fig.1. $\hat{H}_{\rm SO}$ describes a $\vec{k}_\parallel$ -dependent "magnetic" field $\vec{h}_R \perp \vec{k}_\parallel$ acting on the spin of a carrier. The field leads to a spin splitting $2\alpha k_F$ of the electron states in the vicinity of the Fermi momentum k_F, a renormalization of the electron g-factor, a splitting of the cyclotron resonance, and the electron spin dipole (combined) resonance, where an external periodic electric field causes spin-flip transitions. In GaAs/$Al_xGa_{1-x}As$ heterojunctions [7] and Si-based transistors [8] where the structure asymmetry is strong [9], the value of α is of the order of 10^{-10} eV·cm leading to $2\alpha k_F \sim$1 meV for $k_F \sim 10^6$ cm^{-1} corresponding to a two-dimensional (2D) concentration of carriers $n_{2D} \sim 10^{11}$ cm^{-2} [10]. By changing the asymmetry of the doping on the well sides, it is possible to manipulate the magnitude and the sign of α [11].

Let us turn now to Fig. 1(c) where the structure seems to be symmetric. If it was produced of crystals with the unit cell (bulk) inversion asymmetry (BIA) like GaAs, the bulk SO (Dresselhaus) term inherited by the 2D system $\hat{H}_D = \alpha_c(\vec{\sigma}\vec{\kappa})$, with $\kappa_x = k_x(k_y^2 - k_z^2)$, $\kappa_y = k_y(k_z^2 - k_x^2)$, and $\kappa_z = k_z(k_x^2 - k_y^2)$, leads to the 2D Hamiltonian:

$$\hat{H}^D_{\rm SO} = \alpha_D\left(-\hat{\sigma}_x k_x + \hat{\sigma}_y k_y\right), \tag{2}$$

which is different from Eq.(1), but has similar physical consequences. The coupling constant $\alpha_D = \alpha_c(\pi/a)^2$, where a is the well thickness [12, 13],

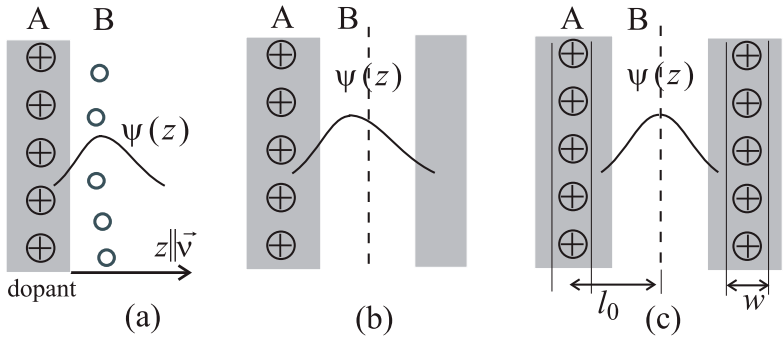

Figure 1. The two-dimensional systems with different types of SO coupling. Possible realizations for A/B are, for example, $Al_xGa_{1-x}As/GaAs$ or $Ge_{1-x}Si_x/Si$, respectively. (a) Heterojunction with the strongest asymmetry arising due to the interfaces. (b) One-side doped QW with the asymmetry arising due to the doping. (c) Symmetrically doped QW with a random local asymmetry.

and α_c is the Dresselhaus SO coupling constant. For holes, the $k_\parallel$-dependence of the SO coupling is rather complicated [13–15] and the resulting spin splitting can be non-monotonic [13]. In the asymmetric zincblend structures, the $H_{\rm SO}^D$ and the $H_{\rm SO}^R$-originated effects which are typically of the same order of magnitude can be distinguished at certain conditions [16].

Another mechanism of a $k_\parallel$-dependent spin splitting in zincblend-based QWs, a native interface asymmetry (NIA), arises due to changes in the interionic bonds at the interfaces [17]. In asymmetric $Si/Si_{1-x}Ge_x$ QWs, where neither a BIA nor a NIA term contributes, the value of α is much smaller being 0.55×10^{-12} eV·cm as measured by electron spin resonance (ESR) [18]. Also, holes in these systems show a weak SO coupling [19].

Spin-orbit coupling leads to spin precession, however, it doesn't cause an irreversible spin relaxation itself since for this purpose a randomness in the spin precession is needed. It is usually accepted that for the SO coupling discussed above the Dyakonov-Perel' [20] mechanism is responsible for the spin relaxation in semiconductors with one type of carriers [21]. This mechanism can be described as follows. Due to scattering by impurities, phonons and other electrons, the momentum of the electron randomly changes in time. Therefore, also, the direction of the precession axis changes randomly in time. If the SO coupling is relatively weak, the precession angle between the collisions with impurities is small, and the spin direction randomly goes back and forth with a small random angle. The resulting spin movement is a diffusion in the spin space and the relaxation rate is $\Gamma_{\rm DP} \sim (\alpha k_\parallel/\hbar)^2\tau$, where τ is the momentum relaxation time. For a typical example of GaAs at electron concentration of 5×10^{11} cm^{-2}, α of 5×10^{-10} eV·cm, and a mobility μ of 10^5 cm^2/(Vs) one

obtains an estimate for the relaxation time of the order of 0.1 ps. We point out that the spin and momentum relaxation rates are are *inversely* proportional to each other, and, therefore, in high-mobility systems spin relaxes fast. For Si the relaxation time can be from five to six orders of magnitude larger, making it a promising material for the spintronics applications.

Due to the effects of the SO coupling, it is important to understand the possibilities to manipulate its strength. For example, in QWs the asymmetry can be removed by an equivalent doping on the sides or effectively by applying an external bias which also can lead to a compensation of the $H_{\rm SO}^D$ and $H_{\rm SO}^R$ terms [22] for some electron momenta. By changing the bias one can manipulate the spin dynamics. In order to understand the limits of spin manipulation, it is necessary to find the lowest limit of the SO coupling when all asymmetries seem to disappear. We will show that an SO coupling is present even in "perfectly" symmetric systems and leads to a spin relaxation and an electric spin dipole resonance. This kind of coupling can be regarded as minimal SO coupling achiavable in 2D electron systems.

2. Random spin-orbit coupling: a model

Most of theories of spin dynamics in semiconductors, as discussed above, consider the SO coupling as uniform, that is electron-coordinate independent. The reality is, however, different: the coupling produced by randomly distributed charged impurities is spatially random as well.

The idea of a random SO coupling stems from a work of Mel'nikov and Rashba [23] on bulk Si and Ge with charged impurities. It seems that in Si localized large-radius dopant states should not demonstrate SO coupling. However, on each site the random electric field is nonzero due to fluctuations of the concentration of randomly distributed surrounding dopants. This field leads to a local SO coupling, which randomly changes from site to site. Below, we review the dopant fluctuation-induced random Rashba field in two-dimensional structures and show that this SO coupling exists in a form of random domains on a spatial scale of the order of 10 nm.

As an example we consider an symmetric structure consisting of a 2D conducting channel and two dopant layers at $-l - w/2 < z < -l + w/2$ and $l - w/2 < z < l + w/2$ (Fig. 1c). With the mean concentration of dopant ions per side $\overline{n}$, the 2D concentration of carriers in the well is $n_{2D} = 2\overline{n}w$. As the factor that determines the strength of the SO coupling we consider the $z-$component of electric field of the dopant ions $E_z(\vec{\rho})$ in a point with the 2D coordinate $\vec{\rho}$ at the well symmetry plane ($z = 0$), where the charge density $|\psi^2(z)|$ for the first subband of the size quantization is close to the maximum. A nonzero $E_z(\vec{\rho})$ arises randomly due to unavoidable fluctuations in the dopant concentration. Therefore, the asymmetry always exists locally. We assume

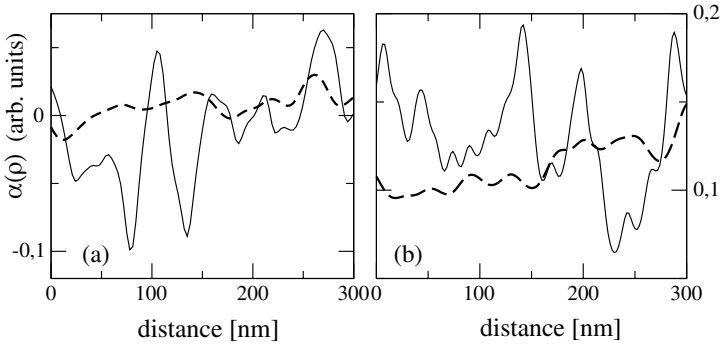

Figure 2. A typical realization of a random SO coupling in a quantum well. (a) symmetrically doped, (b) asymmetrically doped well. The parameters are chosen as follows. The concentration of electrons is 5×10^{11} cm^{-2} as achieved by the one-side doping in Fig.2(b) and symmetric doping in Fig.2(a). The mean SO coupling in Fig.2(b) is $\langle\alpha\rangle_a = 8.5 \times 10^{-10}$ eV·cm, the distance between the dopant layer and the well symmetry plane l_0 is 10 nm (solid lines) and 20 nm (dashed lines), respectively.

also that the SO coupling is a linear function of the electric field, and, therefore $\alpha(\vec{\rho}) = \zeta E_z(\vec{\rho})$, where ζ is a system-dependent parameter. For example, in Si-based structures $\zeta \approx 0.2|e|\text{A}^2$ [18]. The z-component of the Coulomb field of the dopants with concentration $n(\vec{r})$ is given by

$$E_z(\vec{\rho}) = -\frac{|e|}{\epsilon}\int n(\vec{r}) f(\vec{\rho},\vec{r}) d^3r, \quad f(\vec{\rho},\vec{r}) = \frac{z}{[(\vec{\rho}-\vec{r}_\parallel)^2 + z^2]^{3/2}}, \qquad (3)$$

where $\vec{r} = (\vec{r}_\parallel, z)$, and ϵ is the dielectric constant. The integration is performed over the two dopant layers. We assume that the correlation function of the dopant concentration $n(\vec{r})$ is the "white noise":

$$\langle (n(\vec{r}_1) - \overline{n})(n(\vec{r}_2) - \overline{n})\rangle = \overline{n}\delta(\vec{r}_1 - \vec{r}_2), \qquad (4)$$

where $\langle ...\rangle$ stands for averages and define the correlation function of the Rashba parameter $F_{\rm corr}(\rho)$ as:

$$\langle \alpha(0)\alpha(\vec{\rho})\rangle = \langle\alpha^2\rangle F_{\rm corr}(\rho). \qquad (5)$$

$\langle\alpha^2\rangle$ and $F_{\rm corr}(\rho)$ in Eq.(5) can be obtained using the technique of Ref. [24]:

$$\langle\alpha^2\rangle = 4\pi\frac{\zeta^2 e^2}{\epsilon^2}\frac{n_{2D}}{4l_0^2 - w^2}, \quad F_{\rm corr}(\rho) = \frac{\int f(\vec{0},\vec{r'}) f(\vec{\rho},\vec{r'}) d^2\rho' dz}{\int f^2(\vec{0},\vec{r'}) d^2\rho' dz}, \qquad (6)$$

where $\vec{r'} = (\vec{\rho}, z)$. For a very thin dopant layer with $w \ll l_0$ $\alpha_{\rm rnd} \equiv \sqrt{\langle\alpha^2\rangle} = \zeta\,|e|\,\sqrt{\pi n_{2D}}/\epsilon l_0$. For comparison, in a one-side doped QW (maximal asym-

metry), α_a is a sum of a regular average $\langle\alpha\rangle_a$ and a random term with the mean ρ-independent contribution

$$\langle\alpha\rangle_a = 2\pi\zeta\left(\frac{e}{\epsilon}\right)n_{2D}. \tag{7}$$

By comparing Eqs.(6) and Eq.(7) one concludes that at $n_{2D}l_0^2 \sim 0.1$, a typical parameter for QWs [18], $\alpha_{\rm rnd}$ can vary between $\sim 0.1\langle\alpha\rangle_a$ and $\sim \langle\alpha\rangle_a$. At $\rho \sim l_0$, $F_{\rm corr}(\rho)$ decays as $(l_0/\rho)^3$ and therefore, establishes a common spatial nanoscale in the lateral and the $z-$axis directions. A typical realization of a random $\alpha(\vec{\rho})$ in shown in Fig.2.

Above we did not consider the screening of the $E_z(\vec{\rho})$ field for the following reason. The lateral charge redistribution in the field of the dopant ions [25] causing the lateral screening, doesn't change $E_z(\vec{\rho})$. Therefore, the screening corrections to $E_z(\vec{\rho})$ arise due to the polarization of the wavefunctions along the $z-$axis. This linear in $E_z(\vec{\rho})$ correction leads to a small renormalization of the constant ζ.

We also assume that $k_\parallel l_0 \gg 1$, and, therefore, the Rashba Hamiltonian can be treated locally as uniform field that describes the random SO coupling in the semiclassical approximation as:

$$\hat{H}_{\rm SO}(\vec{\rho}) = \vec{h}_R(\vec{\rho})\hat{\vec{\sigma}} \quad \vec{h}_R(\vec{\rho}) = \alpha(\vec{\rho})(k_{\parallel,y}, -k_{\parallel,x}), \tag{8}$$

with the mean value $\langle\vec{h}_R(\vec{\rho})\rangle = 0$. This random term in III-V quantum wells is added to the $\hat{H}^D_{\rm SO}$ Hamiltonian. In the symmetric Si-based wells it gives the only contribution. Therefore, the symmetrically-doped Si/$\rm Si_xGe_{1-x}$ wells demonstrate the minimal nonzero SO coupling arising due to random doping on their sides.

3. Random spin-orbit coupling: experimental consequences

Having established the mechanism, the spatial scale, and the strength of the random SO coupling, we will discuss the possibility of its experimental manifestations below.

Spin relaxation rate

For the Dyakonov-Perel' mechanism the randomness enters the spin precession due to the random time dependence of the momentum. However, as we have seen above, the randomness is an intrinsic property of the SO coupling. Therefore, it should lead to a spin relaxation even if the momentum of the electron remains constant. Below, we discuss this mechanism both for asymmetrically and symmetrically doped structures. Even in the latter case where

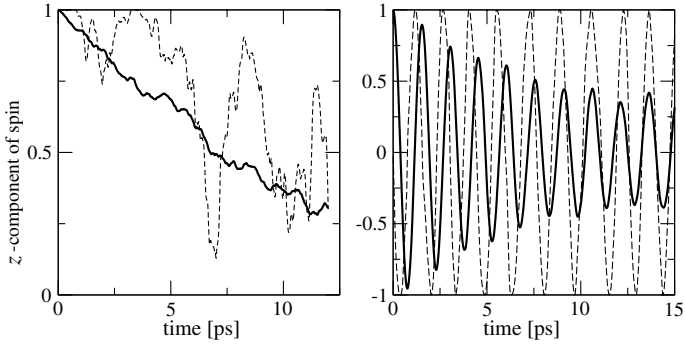

Figure 3. Spin relaxation obtained by the Monte Carlo simulation with $N = 64$ electrons in the system. (a) Symmetrically doped, (b) asymmetrically doped well. Solid lines: the total spin polarization, dashed lines: one selected spin.

the mean SO coupling is zero, the spin relaxation occurs, as can be seen from the following qualitative arguments.

The spin precession rate and direction at a point $\vec{\rho}$ are determined by $|\alpha\,(\vec{\rho})\,|$, and its sign, respectively. Therefore, for a moving electron it is a random function of time without any scattering by impurities or phonons. The change of the precession angle $\delta\phi_d$ during the motion through a domain of a lateral size of the order of l_0 is $\delta\phi_d \sim k_\parallel \langle\alpha^2\rangle^{1/2}\tau_d$, where $\tau_d = l_0/v$ is the time necessary to pass through one domain. In the next domain of the same lateral size the sign of $\alpha\,(\vec{\rho})$ is most probably opposite leading to the spin precession in the other direction. Thus, the spin precession is stochastic even for a carrier moving in a straight line.

Let us consider the spin relaxation of an ensemble of $j = 1, N$ electrons moving with the velocities $\vec{v}_j$, $|\vec{v}_j| = v$ for all electrons assuming that the free path $\ell = v\tau \gg l_0$. We select one representative of the ensemble which starts at a point $\vec{\rho}_i$ in the fully polarized state with $\langle s_z\rangle_j = 1/2$. Its path is then $l = vt'$ and the coordinate $\vec{\rho}(t') = \vec{\rho}_i + \vec{v}_j t'$. Each electron in the ensemble interacts with the random Rashba field corresponding to its path. The spin precesses randomly and when an electron arrives at time t at the point $\vec{\rho}_f$, its z-component and the mean z-polarization of the ensemble $S_z(t)$ are given by:

$$\langle 2s_z(t)\rangle_j = \cos\left(\frac{2}{\hbar}\int\limits_{\vec{\rho}_i}^{\vec{\rho}_f}\alpha(\vec{\rho})k_\parallel\frac{dl}{v}\right), \quad \langle S_z(t)\rangle = \frac{2}{N}\sum_{j=1}^{N}\langle s_z(t)\rangle_j, \qquad (9)$$

where the integral is taken along the path of the particle. The spin polarization $\langle S_z(t)\rangle$ is the sum of random variables, which tends to zero at $t \to \infty$ since the summands cancel each other. Two approaches can be applied to cal-

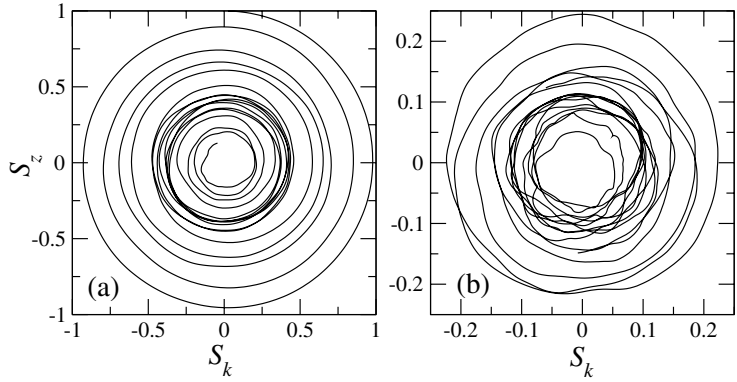

Figure 4. The trajectory in the $S_k S_z$ space for two different time scales: (a) $t < 25$ ps, (b) 25 ps$< t < 50$ ps. The figure shows the random character of the spin relaxation.

culate $\langle S_z(t)\rangle$. One is analytical, the other one is the Monte Carlo simulation which was successfully used in calculations of the spin relaxation for regular SO coupling [26].

The analytical solution found in Ref. [27] gives the rexation time $\tau_{\rm sp} \approx 2\pi\langle\alpha^2\rangle k_\parallel^2 \tau_d$, which can be understood as follows. If $t \gg \tau_d$, the precession angle is estimated from the diffusion picture as $\left\langle (\Delta\phi)^2 \right\rangle \sim (\delta\phi_d)^2\, t/\tau_d$. At $t \sim \tau_{\rm sp}$, $(\Delta\phi)^2 \sim 1$ that leads to this result.

Below we concentrate on the Monte Carlo approach which allows to investigate the movement of each electron. Figs. 3(a) and 3(b) present the results of a simulation for a selected particle and the total spin of the system for a symmetrically and asymmetrically doped well, respectively. As demonstrated in this Figure, the relaxation times are similar in both cases. The randomness of the spin movement is clearly seen in the figure. The relaxation of the in-plane components of the spin is determined by the same random mechanism, and, therefore, occurs at the same time scale.

In Fig.4 we present the trajectory of the system in the (S_k, S_z)-spin space where S_k is the mean value of the spin projection on the momentum axis: $S_k(t) = (2/N)\sum_j \langle \hat{\vec{s}}\vec{k}/k\rangle$. The $(0,0)$ point in this space is the attractor, where the system path finally comes in as a result of a stochastic movement.

Now we can estimate the relaxation rates for spins arising due to impurities within the Dyakonov-Perel mechanism and due to the randomness under the ballistic movement. From the formula for $\Gamma_{\rm DP}$ we obtain an estimate: $\Gamma_{\rm r}/\Gamma_{\rm DP} \sim \tau_d/\tau$, which gives for the mobility $\mu > 10^5$ cm^2/(Vs), $l_0 = 10$ nm, and $v = 3 \times 10^7$ cm/s the ratio of the order of 100. Therefore, for the

ballistically moving carriers in symmetrically doped systems with a high mobility, the total spin relaxes by two orders of magnitude more slowly than in the asymmetrically doped systems due to the Dyakonov-Perel' mechanism. With the decrease of the mobility this ratio decreases, and, therefore, the relaxation rates in the symmetrically and asymmetrically doped systems can be of the same order of magnitude.

Electric dipole spin resonance

An interesting manifestation of the SO coupling is the electric dipole spin resonance, where spin-flip transitions are caused by the *electric* field of an electromagnetic wave [28]. Let us consider a response of a 2D electron gas in a magnetic field $\vec{H} \parallel z$ to a relatively weak external electromagnetic (EM) wave propagating along the $z-$axis with magnetic and electric fields $\widetilde{\vec{H}} = \vec{H}_0 e^{-i\omega t} \parallel x$ and $\widetilde{\vec{E}} \perp \widetilde{\vec{H}}$, respectively. The ratio of the fields amplitudes is given by $E_0/H_0 = 1/\sqrt{\epsilon}$. The interaction of the electron charge with the wave of the vector-potential $\widetilde{\vec{A}}$ and amplitude $A_0 = (c/\omega)\, E_0$ can be treated as a perturbation given by: $\hat{V}_A = -(e/c)\hat{\vec{v}}\widetilde{\vec{A}}$. Here $\hat{\vec{v}} = \nabla_{\vec{k}}\hat{H}$ is the velocity operator. For the Hamiltonian $\hat{H} = \hbar^2\hat{k}^2/2m^* + \hat{H}_{\rm SO}$, the velocity acquires also a spin-dependent term $\nabla_{\vec{k}}\hat{H}_{\rm SO}$ [28, 29]:

$$\hat{v}_x = \frac{\hbar k_{\parallel,x}}{m^*} - \frac{\alpha(\vec{\rho})}{\hbar}\hat{\sigma}_y, \qquad \hat{v}_y = \frac{\hbar k_{\parallel,y}}{m^*} + \frac{\alpha(\vec{\rho})}{\hbar}\hat{\sigma}_x, \tag{10}$$

where m^* is the lateral effective mass. The terms in $\hat{v}_x$ and $\hat{v}_y$ containing the Pauli matrices cause the spin-flip transitions in electric field. The matrix elements of $\hat{v}_y$ between the states $\psi_i(\vec{\rho})\,|\uparrow\rangle$ and $\psi_f(\rho)\,|\downarrow\rangle$ are:

$$v_{fi} = \frac{1}{\hbar}\int \psi_f^*(\vec{\rho})\alpha(\vec{\rho})\psi_i(\vec{\rho})d^2\rho, \tag{11}$$

with the average $\langle v_{fi}\,\rangle = 0$ due to $\langle\alpha(\vec{\rho})\rangle = 0$. However, the parameter which determines the measured intensity of spin-flip transitions, $\left\langle |v_{fi}\,|^2 \right\rangle$ is nonzero and given in Ref. [30] as:

$$\left\langle |v_{fi}\,|^2 \right\rangle = \frac{\alpha_{\rm rnd}^2}{\hbar^2}\int \psi_i^*(\vec{\rho}_1)\psi_f^*(\vec{\rho}_1)F_{\rm corr}(\vec{\rho}_{12})\psi_i(\vec{\rho}_2)\psi_f(\vec{\rho}_2)d^2\rho_1 d^2\rho_2. \tag{12}$$

where $\vec{\rho}_{12} = |\vec{\rho}_1 - \vec{\rho}_2|$. We consider the quantum limit of the problem, with maximal four ocupied Landau levels (quantum numbers $n = 0, 1$, two spin-up and two spin-down). For a carrier concentration of n_{2D} =2×10^{11} cm^{-2}, this occurs at $H > 2.3$ T. The wave function in the magnetic field

$$\psi_{nm}(\vec{\rho}) = \frac{1}{\sqrt{2\pi}l_H}\exp(-\rho^2/4l_H^2)L_{nm}(\rho/l_H)e^{im\varphi} \tag{13}$$

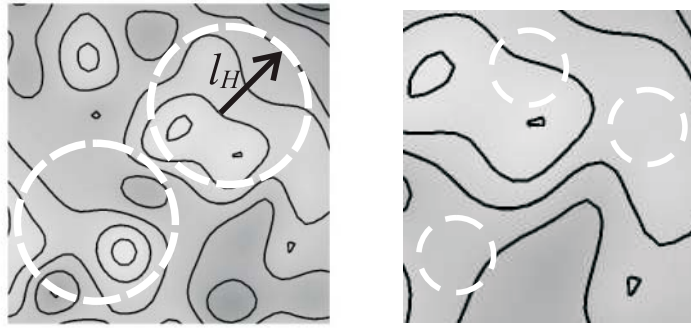

Figure 5. A schematic plot of the the spatial scale of the electron wavefunction in the case of a weak (a) and a strong (b) magnetic field on a two-dimensional scan of random SO coupling obtained by a Monte Carlo simulation.

where m is the orbital momentum, φ is the azimuthal angle, the magnetic length $l_H \equiv \sqrt{\hbar c/|e|\,H}$, and $L_{nm}(\rho/l_H)$ is a polynomial. We consider the zero orbital momentum ground state ($L_{00} = 1$) and the first excited state ($L_{10}(z) = 1 - z^2/2$) in the static magnetic field with the gauge $\vec{A} = [\vec{H}, \vec{r}]/2$. The spin-flip-transitions as $\psi_i(\rho)\,|\uparrow\rangle \rightarrow \psi_i(\vec{\rho})\,|\downarrow\rangle$ without change of the Landau level occur at the frequency $g\mu_B/\hbar$. The transitions between Landau levels accompanied by a spin flip occur at frequencies $\omega_c \pm g\mu_B/\hbar$ forming satellites of the synchrotron resonance peak at $\omega_c = |e|\,H/m^*c$. Here we neglected the influence of the random potential on the wave function of electrons since under typical experimental conditions ($\mu > 10^5$ cm^2/(Vs), $H > 1$ T) $\omega_c\tau \gg 1$. We also assumed that the magnetic field is sufficiently strong and so the influence of the SO term on the spin states can be neglected. The role of the randomness strongly depends on the ratio of the spatial scales of the electron wave function and the SO coupling. Fig.5 shows their relative spatial scales in the case of a weak ($l_H \gg l_0$) and a strong ($l_H \ll l_0$) magnetic field. For $l_H \gg l_0$, all transition matrix elements are small (proportional to l_0^2/l_H^2) because of oscillations in the sign of the SO coupling on the spatial scale of the order of l_H (Fig. 5(a)) with neighboring domains contributing with opposite signs. This is analogous to the mechanism of the spin relaxation discussed above. For "pure" spin-flip transitions in a strong field $\left\langle |v_{fi}\,|^2 \right\rangle \rightarrow \alpha_{\rm rnd}^2/\hbar^2$. For a $\psi_{00}(\vec{\rho})\,|\downarrow\rangle \longrightarrow \psi_{10}(\vec{\rho})\,|\uparrow\rangle$ transition, $\left\langle |v_{fi}\,|^2 \right\rangle$ vanishes both in a weak (as l_0^2/l_H^2) as well as in a strong (as l_H^4/l_0^4) field.

Now we can estimate the static magnetic field, where the electric field - induced spin-flips have a larger probability than the transitions due to the magnetic field of the EM wave. With the Hamiltonian of interaction of the spin with the magnetic field $\hat{V}_H = (g\mu_B/2)(\widetilde{\vec{H}}\vec{\sigma})$, we obtain for the "pure" spin-flip transitions:

$$\frac{\langle\downarrow\left|\hat{V}_H\right|\uparrow\rangle}{\langle\downarrow\left|\hat{V}_A\right|\uparrow\rangle} \sim \frac{\alpha_{\rm rnd}|e|}{\mu_B^2 H}\frac{1}{\sqrt{\epsilon}}\frac{l_0}{\max(l_0, l_H)}. \tag{14}$$

It can be seen in Eq.(14) that the dipole spin transitions dominate up to fields of

$$H < H_{\rm cr} \sim \frac{\alpha_{\rm rnd}\,|e|}{\mu_B^2\sqrt{\epsilon}}\frac{l_0^2}{\max(l_0^2, l_\alpha^2)}, \tag{15}$$

where $l_\alpha = (\mu_B/\,|e|)\,\sqrt{\hbar c/\alpha_{\rm rnd}}\epsilon^{1/4}$. For example, with an experimental value of $\langle\alpha\rangle_a$ in Si QWs [18] and the minimal estimate $\alpha_{\rm rnd}/\langle\alpha\rangle_a \sim 0.1$ one obtains $\alpha_{\rm rnd} \sim 5\times10^{-14}$ eV·cm. This leads to $\alpha_{\rm rnd}\,|e|\,/\mu_B^2\sqrt{\epsilon} \sim 10$ T, with $l_\alpha \sim 10$ nm. Therefore, at $H < 10$ T the spin-flip transitions caused by electric field are still more probable than the transitions due to the magnetic field.

4. Summary

We demonstrated that SO coupling in 2D structures exists in a form of random nanodomains and is present even in 'perfectly' symmetric systems. This 'minimal' coupling which can be close in magnitude to the coupling induced by the asymmetric doping, imposes restrictions on the possibilities to manipulate artificially the SO coupling. The effect of the minimal SO coupling manifests itself even when the regular contribution is suppressed by applying an external bias. Experimentally, it can have the following indications:

- It causes a random precession of the electron spin and, in turn, a finite spin relaxation rate thus imposing restrictions on the possibilities of spin manipulation.
- It leads to an intense electric dipole spin resonance even if the mean value of the coupling vanishes. It can be measured with the electron spin resonance technique even in Si-based quantum wells, where the SO coupling is very weak.

Acknowledgments

We are grateful to J.K. Dewhurst, J. Fabian, G. Guntherodt, W. Jantsch, P. Lemmens, E.I. Rashba, M. Valin-Rodriguez, and Z. Wilamowski for valuable interesting remarks and suggestions. Financial support by the Austrian Science Fund projects P15520 and P16227 is acknowledged.

References

[1] S. Datta and B. Das, Appl. Phys. Lett. **56**, 665 (1990)

[2] G. Burkard, D. Loss, and D.P. DiVincenzo, Phys. Rev. **B 59**, 2070 (1999)

[3] A. V. Khaetskii and Y. V. Nazarov, Phys. Rev. **B 61**, 12639 (2000)

[4] F. Mireles and G. Kirczenow, Europhys. Lett. **59**,107 (2002)

[5] I. Zutic, J. Fabian, and S. Das Sarma, Phys. Rev. Lett. **88**, 066603 (2002)

[6] Yu. A. Bychkov and E. I. Rashba, JETP Lett. **39**, 79 (1984), E.I. Rashba, Sov. Phys. - Solid State **2**, 1874, (1964)

[7] D. Stein, K. v. Klitzing, and G. Wiemann, Phys. Rev. Lett. **51**, 130 (1983)

[8] A. D. Wieck *et al.*, Phys. Rev. Lett. **53**, 493 (1984)

[9] P. Pfeffer and W. Zawadzki, Phys. Rev. **B 59**, R5312 (1999)

[10] B. Jusserand *et al.*, Phys. Rev. **B 51**, 4707 (1995)

[11] T. Koga *et al.*, Phys. Rev. Lett. **89**, 046801 (2002)

[12] M.I. Dyakonov and Y.Yu. Kachorovskii, Sov. Phys. Semicond. **20**, 110 (1986)

[13] E.I. Rashba and E.Ya. Sherman, Phys. Lett. **A 129**, 175 (1988)

[14] R. Winkler *et al.*, Phys. Rev. Lett., **85**, 4574 (2000)

[15] O. Mauritz and U. Ekenberg, Phys. Rev. **B 60**, R8505 (1999)

[16] W. Knap *et al.*, Phys. Rev. **B 53**, 3912 (1996)

[17] O. Krebs and P. Voisin, Phys. Rev. Lett. **77**, 1829 (1996), J.T. Olesberg *et al.*, Phys. Rev. B **64**, R201301 (2001), U. Røssler and J. Kainz, Solid State Commun, **121**, 313 (2002)

[18] Z. Wilamowski *et al.*, Physica **E 16**, 111 (2003), and Phys. Phys. Rev. **B 66**, 195315 (2002)

[19] S.D. Ganichev *et al.*, Phys. Rev. **B 66**, 075328 (2002)

[20] M.I. Dyakonov and V.I. Perel', Sov. Phys. -Solid State **13**, 3023 (1972)

[21] For a review, see : J. Fabian and S. Das Sarma, J. Vac. Sci. Technol. **B 17**, 1708 (1999)

[22] J. Schliemann, J.C. Egues, and D. Loss, preprint cond-mat/0211603

[23] V.I. Mel'nikov and E.I. Rashba, Sov. Phys. JETP **34**, 1353 (1972)

[24] A.L. Efros and B.I. Shklovskii, *Electronic Properties of Doped Semiconductors*, Springer, Heidelberg (1989)

[25] T. Ando, A.B. Fauler, and F. Stern, Rev. Mod. Phys. **54**, 437 (1982)

[26] H.X. Tang *et al.*, in *'Semiconductor Spintronics and Quantum Computation'*, (D.D. Awschalom, D. Loss, and N. Samarth, Eds.), Springer, 2002, p. 31, M. Shen, S. Saikin, M.-C. Cheng, V. Privman, preprint cond-mat/0309118

[27] E.Ya. Sherman, Appl. Phys. Lett. **82**, 209 (2003)

[28] E.I. Rashba, Sov. Phys. - Solid State **2**, 1109 (1960)

[29] E.I. Rashba and V.I. Sheka, Sov. Phys. - Solid State **3**, 1718 (1962)

[30] E.Ya. Sherman, Phys. Rev. **B 67**, R 161303 (2003)

RAMAN AND SERS STUDIES OF CARBON NANOTUBES

S. LEFRANT[a], J.P. BUISSON[a], J. SCHREIBER[a], J. WERY[a], E. FAULQUES[a], O. CHAUVET[a], M. BAIBARAC[a,b] and I. BALTOG[b]

a) Laboratoire de Physique Cristalline, Institut des Matériaux Jean Rouxel, BP 32229, 44322 Nantes Cedex 03, France; b) National Institute of Materials Physics, Lab.160, Bucharest, PO Box MG-7, Romania*

Abstract: We present a survey of Raman and Surface Enhanced Raman Scattering (SERS) studies carried out on carbon nanotubes systems, including single walled nanotubes (SWNTs), multi-walled nanotubes (MWNTs) and nanotubes/polymers composites. We first recall the main features of Raman spectra taken at different excitation wavelengths and we particularly focus on the interactions that take place between tubes when they are in bundles. We predict an upshift of the radial breathing mode (RBM) and we demonstrate this effect experimentally. In the case of tubes deposited on a rough gold or silver layer, i.e. in SERS conditions, we show that interactions take place also with the metallic surface giving rise at some degradation of the tubes. Then, we present results on MWNTs and interpret the low frequency Raman modes, as originating from the RBM of isolated tubes whose interaction between the concentric shells lead again to an up-shift of the frequency of these modes. Finally, we have undertaken a careful study of composites prepared with nanotubes and either saturated or non-saturated polymers. For example, with Poly-(phenylene-vinylene)/nanotubes composites, it is shown that the luminescence properties of such compounds are strongly affected by the presence of the nanotubes.

Key words: Raman Scattering, Surface Enhanced Raman Scattering, Carbon Nanotubes, Composites.

E. C. Faulques et al. (eds.), Spectroscopy of Emerging Materials, 127–138.

1. INTRODUCTION

Carbon nanotubes have been studied extensively since their first observation in 1991 by Ijima [1]. Several techniques of preparation have been developed such as laser ablation [2], arc electric procedure [3] or decomposition of hydrocarbides [4]. The tremendous interest of scientists towards this new class of carbon materials is due to several reasons. First, the electronic properties are of primary importance on a fundamental point of view, but more importantly, potential applications are proposed every day [5], far beyond the use of nanotubes as electron emitters in flat screen as reported some time ago.

Let us recall that nanotubes can be considered as graphene sheets rolled up in different ways. If we consider the so-called chiral vectors $\mathbf{c} = n\mathbf{a}_1 + n\mathbf{a}_2$, in which $\mathbf{a}_1$ and $\mathbf{a}_2$ are the basis vectors of a 2D graphite lattice, depending on the value of the integers n and m, one can define three families of tubes : "armchair" tubes (n = m), "zig-zag" tubes (n or m = 0), and chiral tubes ($n \neq m \neq 0$). Band structure calculations have demonstrated that tubes are either metallic compounds, or zero-gap semiconductors, or semiconductors [6,7]. More commonly, they are divided into metallic tubes (when n-m is a multiple of 3) or semiconducting ones.

2. GENERAL PROPERTIES AND RAMAN SCATTERING

From the early days of investigation of carbon nanotubes, two spectroscopic techniques emerged as needed tools, namely high resolution transmission electron microscopy (HRTEM), and Raman scattering [3]. On one hand, HRTEM permits a direct observation of single-walled nanotubes (SWNTs) either isolated or in bundles providing then an estimation of the average diameter of the tubes. In the case of multiwalled nanotubes (MWNTs) HRTEM allows a determination of the size of the inner and outer diameters, as well as the averaged number of shells. As it will be seen later, these parameters turn out to be important for the simulation of Raman spectra for example. On the other hand, Raman scattering, via the vibrations, provides additional information, especially when performed at different wavelength excitations (Fig.1). Three domains of frequencies can be distinguished: i) the 1400-1700 cm^{-1} range where the so-called "G" modes around1600 cm^{-1} are seen, originating from a graphite vibration which is splitted as a consequence of the curvature of the tubes, ii) the frequency domain ranging from 1100 to 1400 cm^{-1} in which the "D" band is observed,

as a signature of defects, iii) the low frequency range in which appear the radial breathing modes of the tubes.

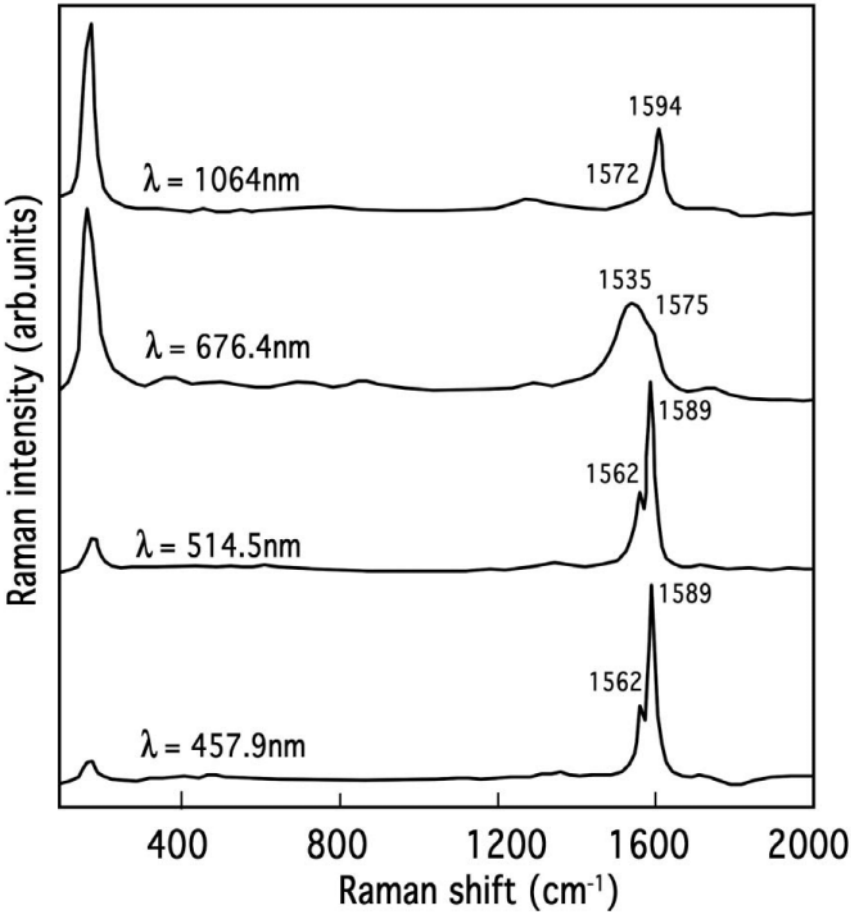

Figure 1. Raman spectra of single-walled carbon nanotubes recorded at room temperature for different excitation wavelengths: 457.9 nm; 514.5 nm; 676.4 nm and 1064 nm, as indicated on the curves.

The theoretical prediction of these vibrations was made by several authors (see for example refs. 8,9). Two main characteristics in the Raman spectra of SWNTs can be raised. First, the radial breathing mode, hereafter referred to RBM, is strongly dependant upon the diameter of the tubes.

Performing Raman scattering in high resolution in this domain reveals several components and several models have been built [10,11,12] to establish a direct relationship between the frequency of this mode and the tube diameter. In our group, we use the expression $\nu(cm^{-1}) = 2238/d(Å)$ as published by J.P. Buisson et al [13]. As a consequence, one can determine some kind of diameter distribution of tubes in a sample, if one keeps the laser excitation unchanged, since resonance effects are not taken into account. Secondly, a peculiar result is observed in the behavior of the "G" band when one uses a red light excitation. This Raman band exhibits a Breit-Wigner-Fano component on the low frequency side, modifying the band profile. This is due to a resonance effect since the energy of the laser excitation matches the electronic transition of metallic tubes, as demonstrated by Brown et al. [14]. The energy window for exciting metallic tube goes from 1.7 to 2.2 eV, while for other excitations, the Raman spectrum reveals mostly semiconducting tubes.

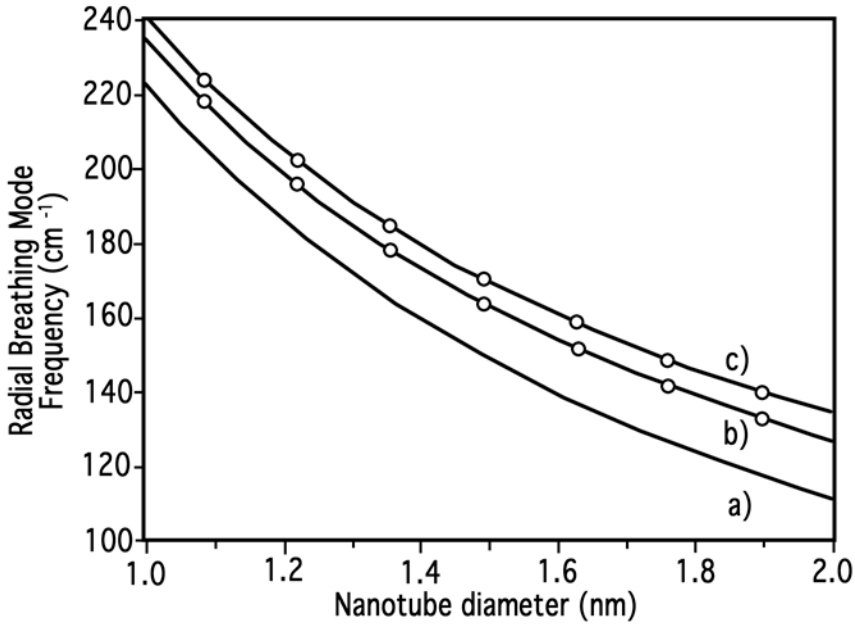

Figure 2. Calculations of the radial breathing mode frequency of (10,10) armchair single-walled nanotubes: a) isolated tubes; b) bundle of 7 tubes and c) bundle with an infinity of tubes.

Carbon nanotubes therefore exhibit different electronic properties and their incorporation in electronic devices is rather promising. Nevertheless, it is of crucial importance to synthesize tubes in reproducible ways and to be

able to characterize them precisely. In this respect, and as far as Raman scattering is concerned, single-walled nanotubes are produced most of the time in bundles, and determining their diameter in a reliable manner is a difficult task. As a matter of fact, one has to take into account the Van der Waals interactions between tubes. Different models have been proposed, and in our case, we have described the carbon-carbon interaction by a Lennard Jones potential and we derived the tube-tube force constant from Cg, the adjacent inter-plane force constant of graphite. In these conditions, the diagonalization of the dynamical matrix leads to modifications of the radial breathing mode (RBM) frequencies, and the most intense one can be written as follows: $\omega^2_1 = \omega^2_0 + \eta\ C/m_c$, in which ω_0 is the frequency of an isolated tube, m_c the mass of a carbon atom and η a parameter which depends on the number of tubes constituting the bundle. Detailed calculations [13] have been published elsewhere and results can be viewed on Fig.2. We just recall here that for a bundle made of an infinite number of (10,10) armchair tubes, the upshift that is calculated is 16.2 cm^{-1}. Even if such theoretical prediction is difficult to be proved experimentally, we have observed in isolated tubes prepared via a fluorination–defluorination procedure [15] that two RBM bands are observed at 177 and 194 cm^{-1}, and the lowest in frequency (177 cm^{-1}) is attributed to isolated tubes. The frequency shift $\Delta\omega$ = 23 cm^{-1} is rather close to our predictions. This result is corroborated by temperature effect measurements showing that these two components have a different behavior when the temperature is increased up to 600K [16].

3. SERS EXPERIMENTS

SERS stands for Surface-Enhanced Raman Scattering. Introduced three decades ago [17] for studying monolayers, the SERS technique is used to provide a drastic amplification of the Raman signal. Most commonly, it is based on the use of a rough metallic surface that leads to such an amplification by resonantly exciting surface plasmons, the enhancement of the signal depending on the dielectric constant of the metal. Silver and gold turn out to be the most appropriate metals. It is known that the observed enhancement has a two-fold origin, one through an electromagnetic mechanism and the other having a chemical nature, i.e. being due to an increased polarisibility of the molecule adsorbed on the metal as a result of charge transfer processes. Depending on the method used for coupling to the surface plasmons, one can obtain amplification factors as high as 10^{12}-10^{14} [18] although rough surfaces lead more commonly to 10^6-10^8.

In our studies, we have used the SERS technique to amplify the Raman signal in an ultimate attempt to record Raman spectra on individual

nanotubes and prove experimentally the bundle effect, as explained above. In the case of SWNTs deposited on films of 100-150 nm in thickness, no significant differences are observed in comparison with Raman spectra of powders, if one excepts the amplification of the signal. On the contrary, when thinner films of nanotubes (below 100 nm) are used, SERS experiments have demonstrated the occurrence of interfacial reactions between nanotubes and the metallic support. The experiments have been carried out at different excitation wavelengths and the film thickness has been decreased from 150 nm down to 10 nm. Films were deposited on a

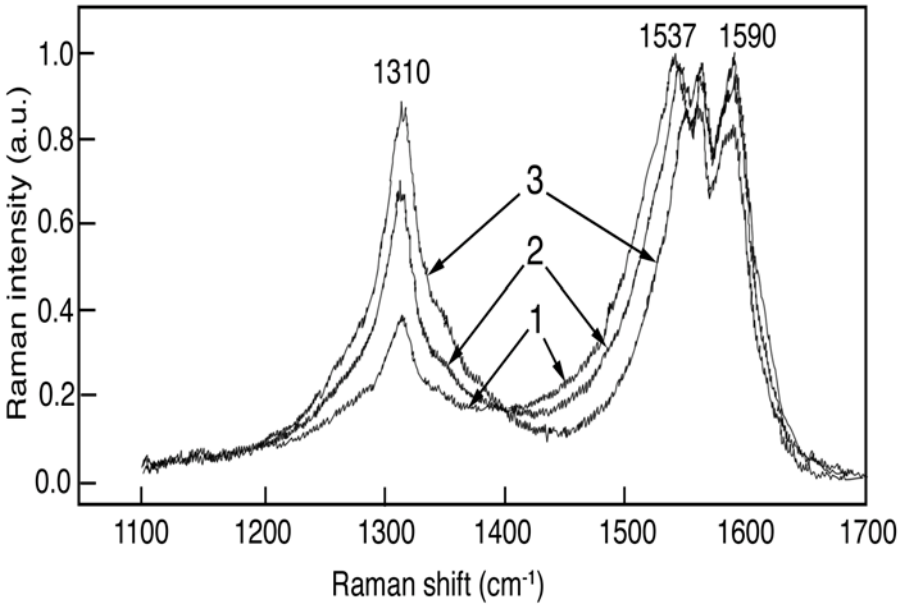

Figure 3. SERS spectra recorded at room temperature with $\lambda_{exc.}$=676.4 nm of SWNTs deposited onto a rough gold substrate as a function of the film thickness: Curves 1, 2 and 3 are for 150nm, 60 nm and 30 nm, respectively.

gold or a silver substrate. In SERS spectra, the relative variations in intensity of some Raman lines, peak shifts and line shape changes resulting from the gradual decrease of the film thickness were studied [19], considered as originating from interactions between the substrate and the nanotube film. For laser wavelengths for which semiconducting tubes are predominantly excited (i.e. 514.5 or 1064 nm), the “D” band exhibits a relative increase of

intensity and the "G" band is not particularly affected neither in shape nor in frequency. This result can be interpreted by an increased disorder and/or formation on defects on nanotubes.

Contrarily, using an excitation energy of 676.4 nm, for which the Raman response of metallic tubes is resonantly enhanced, a striking result is observed in the behaviour of the "D" and "G" bands, especially when Au is used as support. A gradual increase of the "D" band is recorded suggesting as before an enhanced degree of disorder, with a concomitant modification of the "G" band profile, consisting in a gradual narrowing of its low energy side (Fig.3).

This modification can be interpreted again by a partial degradation of carbon nanotubes, leading to the formation to graphite-like or carbon particles. This result is further put in evidence if the film thickness decreases until 10 nm. We observe in the Raman spectrum the features attributed to amorphous carbon together with new bands characteristics of C_{60}-like molecules. One may then consider the breaking of the nanotubes into species such as amorphous carbon, tubular fragments and closed-shell fullerenes. Such reactions are of chemical nature occurring at the nanotube-metal substrate interface. These results may appear as surprising. Nevertheless, previous studies reported in the literature show that SWNTs submitted to ball milling may be transformed into spherical carbon particles that are precursors of closed-shell fullerenes [20]. It has also been shown that electrochemical transformation of nanotubes can lead to the formation of C_{60} molecules [21].

These modification are indicative of a chemical mechanism in the SERS process in particular in very thin films for which chemical reactions are optimised. These experiments show in addition that metallic tubes are mainly involved, evidenced by the decrease of the Breit-Wigner-Fano component, as due to a possible direct interaction between nanotubes and C_{60} leading to the formation of $SWNTs^{+}C_{60}^{-}$ complexes [19].

4. MULTI-WALLED CARBON NANOTUBES

Multi-walled nanotubes are made of concentric tubes whose number can be as high as 50. Prepared also by the electric arc technique, they can be purified in air at ≅ 600°C. High Resolution transmission Electron Microscopy images reveals clear images and in our case, we could for example statistically determine an average number of 18 tubes with inner diameters between 1 and 1.5 nm and outer diameters between 5 and 15 nm.

Such MWNTs exhibit Raman features (Fig. 4) that consist of the "G" band, the "D" band, but also low frequency modes whose origin is not straightforward.

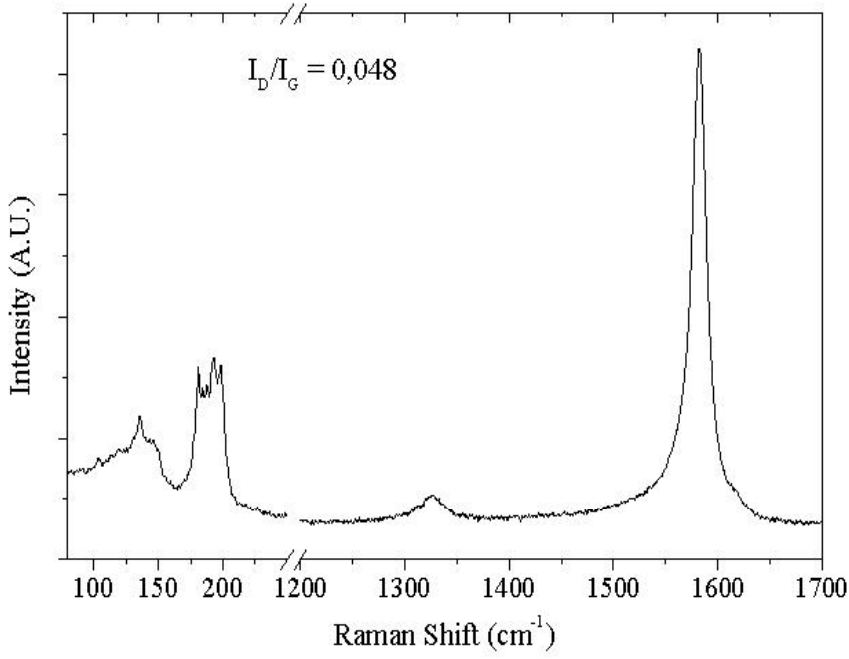

Figure 4. Raman spectrum of multi-walled carbon nanotubes after purification recorded for $\lambda_{exc.}$ = 676.4 nm [22]. The low frequency modes have been calculated as explained in the text.

In order to interpret these Raman characteristics, we have carried out calculations [23] by again introducing Van der Waals interaction between concentric tubes, on the basis on a Lennard-Jones potential as described in the case of bundles. It is obtained that modes that are seen in the low frequency domain originate from the RBM of individual tubes, the frequency of which being upshifted. In addition, we were able to evaluate the intensity of such modes by using a bond polarization theory [24]. We were able to reproduce Raman spectra taken at 647.1 and 514.5 nm by introducing different types of MWNTs. It is to be noticed that the main experimental parameters that have to be taken into account are the number of shells constituting the MWNTs and then the inner diameters. Such parameters have been extracted from HRTEM images. Our simulated Raman spectra [23] are

close to experimental ones, although a more sophisticated treatment would be needed to take into account the resonance effects that have been seen by different groups [25,26] when Raman spectra are recorded at different excitation wavelengths.

5. POLYMER/NANOTUBES COMPOSITES

Polymer nanotubes composites are now extensively studied. Indeed, one may associate the properties of the polymer with those of nanotubes. This is the case of the mechanical reinforcement of standard polymer for example, but also one can take advantage of the specific electronic properties of the nanotubes. Therefore, we prepared composites with either saturated polymers like polymethylmethacrylate and MWNTs [27]. The electrical conductivity of these compounds as a function of the nanotube content exhibits for example a very low percolation threshold, (a few % in mass) and therefore they can be used as conducting and transparent layers in electronic devices such as Light Emitting Diodes (LEDs). Another type of composite that we have studied is based on the use of a conjugated polymer, polyphenylene-vinylene (PPV) known for its photoluminescence properties and SWNTs. We prepared this composite by mixing SWNTs to the precursor polymer of PPV. The conversion into PPV was subsequently performed by a thermal treatment at 300°C under dynamical vacuum [28].

We studied these materials by means of several optical spectroscopies including optical absorption, photoluminescence and Raman scattering in order to follow their properties as a function of the SWNT content. We observed drastic changes, as due to strong electronic interactions between SWNTs and the PPV precursor polymer. As an example, the photoluminescence spectra obtained at room temperature after excitation at 2.48 eV (500 nm) and 2.81 eV (440 nm) when the weight percentage of nanotubes x is varied from 0.5 to 64% are shown in Fig.5.

When x is higher than 12, significant changes are observed, namely an increase of an emission peak at 2.43 eV, and the appearance of a new feature at 2.57 eV (482 nm) for x = 64 %. All the results have been interpreted by a model presented elsewhere [28] which takes into account the effective conjugation length distribution in the sample with the help of Raman spectra. Also, a blue-shift of the absorption band of the polymer in the composite is recorded. In brief, one can explain all these data by the formation of short conjugated segments whose relative weight dominate over longer segments, as due to the addition of SWNTs in the precursor polymer solution. In terms of applications, one can then monitor the maximum emission of the

compound by an appropriate amount of nanotubes. This technique is easier to achieve than modifying chemically the PPV polymer into a derivative whose emission properties are changed not as gradually as in the case of composites.

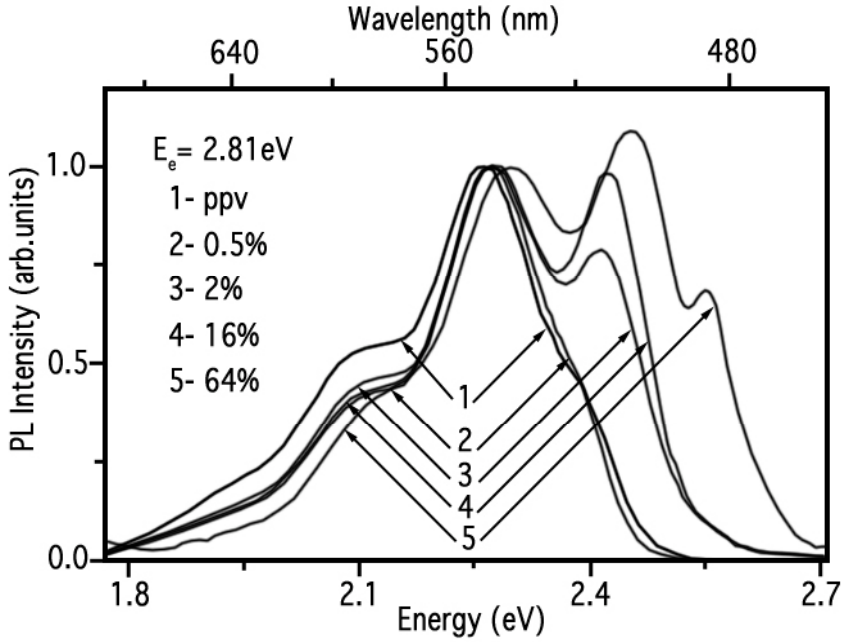

Figure 5. Luminescence spectra of poly-phenylene-vinylene/SWNTs composites as a function of the nanotube content expressed in mass percentage (x) from 0 to 64 %.

6. CONCLUSION

In this paper, we have shown the importance of Raman Scattering and Surface Enhanced Raman scattering to study carbon nanotubes together with High Resolution Transmission Electron Microscopy. This technique is a powerful tool to characterize different systems. In the case of SWNTs, one can deduce the diameter distribution in a specific sample by measuring the radial breathing mode frequency, and the nature of the tubes by changing the excitation wavelength. Using SERS, one can in addition test the model that uses Van der Waals interactions by allowing to record Raman spectra of individual tubes. Also, we could put in evidence interfacial reactions that

take place at the interface nanotube/metallic substrate, as a signature of a chemical component in the SERS mechanism. Raman scattering permits also to characterize multi-walled nanotubes and again, the introduction of Van de Waals interactions between the shells leads to a clear interpretation of the low frequency Raman modes.

Finally, the study of different types of composites has been briefly discussed, as an example to exploit the properties of the carbon nanotubes to modify those of conducting polymers, and monitor their emission features as needed in devices like light emitting diodes.

Acknowledgments: Samples of SWNTs used in our experiments were provided by Dr P. Bernier, University of Montpellier II. A large part of this work has been carried out in the frame of the European program COMELCAN (HRPN-CT-2000-00128) and a scientific collaboration between the Institut des Matériaux Jean Rouxel and the Laboratory of Optics and Spectroscopy of the National Institute of Bucharest.

* The Institut des Matériaux Jean Rouxel is “Unité Mixte de Recherche” CNRS-Université de Nantes n° 6502 and is part of the “Ecole Polytechnique” of the University of Nantes.

REFERENCES

1. Iijima S. , Nature (London), 354, 56 (1991).
2. Thess A. et al Science, 273, 483 (1996).
3. Journet C. et al., Nature, 388, 756 (1997).
4. See for example, Kong J., Cassell A.M. and Dai H., Chem.Phys.Lett. 292, 567 (1998).
5. See for instance "Physical properties of carbon nanotubes", ed. Saito R., Dresselhaus G., Dresselhaus M., Imperial College Press, London (1998).
6. Dresselhaus M.S., Jishi R.A., Dresselhaus G., Inomata D., Nakao K. and Saito R., Molecular Materials 4, 27 (1994).
7. Jishi R.A., Inomata D., Nakao K., Dresselhaus M.S. and dresselhaus G., J. Phys. Soc. Jpn 63, 2252 (1994).
8. Eklund P.C., Holden J.M. and Jishi A., Carbon 33, 959 (1995).
9. Rao A.M. , et al. Science, 275, 187 (1987).
10. Henrard L. et al., Phys. Rev. B 60, R8514 (1999).
11. Kahn et al., Phys. Rev. B 60, 6535 (1999).
12. Lefrant S., Buisson J.P., Chauvet O. and Benoit J.M., Proceedings of the MRS Fall meeting 2001, 706, Z 7.2
(2002).
13. Buisson J.P., Chauvet O ., Lefrant S., Stephan C. and Benoit J.M., Proceedings of the MRS Fall meeting 2000,
633, A.14.12.1 (2001).

14. Brown S.D.M., Corio P., Marucci A., Dresselhaus M.A., Pimenta M.A. and Kneipp K., Phys.Rev. 61, R5137 (2000).
15. Marcoux P., Schreiber J., Batail P., Lefrant S., Renouard J., Jacob G., Albertini D. and Mevellec J.Y., Phys. Chem. Chem. Phys. 4, 2278 (2002).
16. Schreiber J., Ph.D. thesis, University of Nantes, unpublished (2002).
17. Fleischmann M., Hendra P. and McQuillan A.J., Chem. Phys. Lett. 26, 163 (1974).
18. Kneipp K. et al., Phys. Rev. Lett. 84, 3470 (2000).
19. Lefrant S., Baltog I., Baibarac M., Schreiber J. and Chauvet O., Phys. Rev. B 65, 235401 (2002).
20. Dravid V.P., Lin X. ,Yang Y., WangX.K. ,Yee A. ,Ketterson J.B. and Chang R.P.H., Science,259, 1601,(1993).
21. Lefrant S. et al., to be published in Synth. Metals (2003).
22. Benoit J.M., Ph.D. thesis, University of Nantes, unpublished (2001).
23. Benoit J.M., Buisson J.P., Chauvet O., Godon C. and Lefrant S., Phys. Rev. B 66, 073417 (2003).
24. Guha S., Menendez J., Page J.B. and Adams G.B., Phys. Rev. B 53, 13106 (1996).
25. Jantoljak H., Salvetat J.P., Forro L. and Thomsen C., Appl. Phys. A: Mater. Sci. process 67, 113 (1998).
26. Kataura H., Achiba Y., Zhao X. and Ando Y., in Amorphous and Nanostructured Carbon, ed. By Robertson J. et al., Mater. Res. Soc. Symp. Proc. 593, 113 (2000).
27. Stephan C., Nguyen T.P., Lahr B., Blau W., Lefrant S. and Chauvet O., J. Mat. Res. 17, 396 (2002).
28. Wéry J., Aarab H., Lefrant S., Faulques E., Mulazzi E. and Pérego R., Phys. Rev. B 67, 115202 (2003).

NONCOVALENT FUNCTIONALIZATION OF SINGLE-WALLED CARBON NANOTUBES FOR BIOLOGICAL APPLICATION: RAMAN AND NIR ABSORPTION SPECTROSCOPY

V.A. Karachevtsev, A.Yu. Glamazda, U. Dettlaff-Weglikowska, V.S. Leontiev, A.V. Peschanskii, A.M. Plokhotnichenko, S.G Stepanian and S. Roth

Institute for Low Temperature Physics and Engineering, NAS of Ukraine, 47 Lenin Ave., 61103, Kharkov, Ukraine;Max-Planck Institute for Solid State Research, Heisenberg Str.1,, 70569 Stuttgart, Germany

Abstract: Raman spectra of film HiPCO carbon single-walled nanotubes (SWNTs) with organic molecules (pyrene, naphthalene) and nanotubes aqueous solutions with different type surfactants are studied. In the spectra of these complex systems the spectral shift of the line position and intensity redistribution among the lines, compared with the spectra of pristine SWNT in KBr pellet or film, is observed that indicates interaction between nanotubes and molecules. Influence of different type surfactants on visible-near-infra-red absorption spectra of SWNTs in water solutions is investigated. The most essential spectral changes are observed for nanotube with the surfactant containing a charge group. Effect of noncovalent interaction of SWNTs with organic molecules and surfactants of different types on optical spectra is discussed.

Key words: Single-wall carbon nanotube, noncovalent nanotube functionalization, Raman spectroscopy, near-infra-red absorption, surfactant, phonon.

1. INTRODUCTION

Single-walled carbon nanotubes are novel molecular scale wires exhibiting unusual useful properties for various potential applications

E. C. Faulques et al. (eds.), Spectroscopy of Emerging Materials, 139–150.

including creation of miniature biological devices. The central direction in creating such devices is surface functionalization [1-8] of nanomaterial and elucidating interactions between nanotubes and biomolecules. The modification of nanotubes can be performed by two ways: a) covalent functionalization [1-4] as a result of the direct attachment of functional groups to the graphitic surface or functionalization reactions with defects; b) noncovalent functionalization [5-9]**.** It is suggested that weak van der Waals interaction, charge transfer or π-π interaction between NT and organic molecules/polymers will provide convenient and quick functionalization of NT without essential changes of nanotube physical properties. Recently, π-π interaction between NT and pyrene derivative was used for immobilization of protein on the nanotube surface [7].

In many cases the potential application of single-walled carbon nanotubes is associated with solubility of this nanomaterial in different solvents. Unfortunately, nanotubes are poorly soluble in the most of organic solvents and are insoluble in water, and this fact especially hinders biological using SWNT. Weak solubility of SWNT is a result of substantial van der Waals attractions between nanotubes aggregated in bundles. To solve nanotubes in water without any covalent functionalization, a surfactant would be added into aqueous solution, and then this mixture is suspended by sonication. It is supposed that the sound wave splits bundles in aqueous solution. A surfactant in suspension adsorbed onto the nanotube surfaces precludes aggregation of nanotubes in bundles.

At high volume fraction of suspensions a self-assembly is formed in this complex fluids. If the surfactant concentration exceeded some critical point, micelles appeared in solution. The input surfactant concentration for nanotube research exceeded usually critical micelle concentrations. The ratio of nanotube to surfactant is varied from 1:5 to 1:10 by weight. Sodium dodecyl sulfate, SDS, Triton X-100 and Tween are the most widely used surfactants [2-12]. The length of alkyl chains, presence of a charge group and benzene ring moiety influence the nanotube solubility in water. SDS and TX100 have alkyl chains and SDS contains a negative charged group. TX-100 has no charged group but is of benzene ring moiety. In spite of wide usage of surfactants as material favored for nanotube water solubility, the SWNT behavior in surfactant micelle surrounding has not been yet investigated properly.

In this report we represent the results of Raman and NIR absorption spectroscopy of SWNT with organic molecules (pyrene and naphthalene) in a film and with various surfactants (cationic, anionic and nonionic) in aqueous solution.

2. EXPERIMENTAL.

SWNTs were prepared by high-pressure CO decomposition over the Fe catalyst (HiPco method [13]) at Carbon Nanotechnologies Inc. Houston, Texas, USA. The raw sample was purified by controlled thermal oxidation in air followed by sonication in HCl. The purity estimated by elemental analysis, TGA, XRD and TEM gave in result 99% content of SWNT in the samples studied [4].

The nanotubes suspension in toluene (0.1 mg/mL) after short sonication was deposited onto a quartz substrate to form a thin film for Raman measurements. SWNTs in KBr pellets obtained after pressing were used for NIR absorption study.

Pyrene and naphthalene were purified by zone refinement for more than 130 passes (Bridgmen method). After such purification the central part of the glass ampoule was extracted and used in the sample preparation. Drop coating of the pyrene (naphthalene) with SWNT suspension in toluene on a quartz substrate was used to form a thin film for Raman measurements. The film was deposited onto the quartz substrate from nanotube suspension in toluene (0.1 mg/mL) and from suspension of nanotube with pyrene (or naphthalene) after short sonication (20 minutes 44 kHz). The weight ratio was 1:1 and 1:4 for mixture with pyrene (samples P1 and P2, respectively) and 1:1 with naphthalene (sample N).

Aqueous solution of SWNTs was suspended with different types of surfactants: a) anionic (SDS) ($CH_3(CH_2)_{11}(SO_4)^-$ Na^+), b) cationic (hexadecyltrimethylammonium bromide (CTAB) ($CH_3(CH_2)_{15}N^+(CH_3)_3Br^-$) and c) and non-ionic (Tween-80) $H(Et\text{-}O)_nO(C_4H_6O_2CHOHCH_2O\ CO(C_{18}H_{23})$. Surfactants SDS and CTAB were purchased from “Serva”, Tween-80 from “Shuchard” (Germany). 0.05 mg/mL nanotube dispersion with surfactant was mixed and then the suspension was sonicated for 40 minutes. A concentration of surfactants in water solution was 1%. Water was prepared by distillation and then passed through Multi-Q system. The deionized water has resistance 18 MΩ.

The Raman experiments were performed using the backscattering configuration. The He-Ne laser at λ_{exc}=632.8 nm (1.96 eV) was used for excitation. The laser light was focused on a spot of about 50 μm in the diameter. The laser power density was not higher than 300 W/cm^2. The spectra were recorded using a Raman double monochromator with the reverse dispersion of 3 Å/mm. NIR absorption spectra were observed with the help of NIR spectrometer equipped with a liquid nitrogen-cooled NIR sensor (PbS). Water solution of SWNTs was investigated in narrow cells

with small light way (0.5 mm in both registration and comparison channels) to escape influence of water absorption.

3. RESULTS AND DISCUSSION.

3.1 Raman spectroscopy of SWNT with pyrene and naphthalene.

The Raman spectrum of HiPco SWNT obtained at the He-Ne laser excitation of 1.96 eV has three characteristic regions: four bands in the low frequency region at 100-300 cm^{-1} (radial breathing mode (RBM)), two intensive bands at 1500-1600 cm^{-1} (tangential mode (G-mode)) of the spectrum and D mode (near 1300 cm^{-1}) [14-18]. At He-Ne laser excitation 4 intensive bands (RBM) are observed in Raman spectra of HiPCO nanotubes, corresponding to SWNTs of different diameters and chirality.

Noncovalent coupling between nanotubes and pyrene or naphthalene gives rise to the change in the Raman spectra, which is quite weak. So, in the spectral region corresponding to RBM for three complex samples a small spectral shift of lines is observed that does not exceed 0.7-0.9 cm^{-1} and intensity redistribution among the lines is within 10 %. (Fig.1). But it is not the case for the G mode in the Raman spectra presented in Fig. 2. The most intensive high-frequency component of the G mode (G^+) of SWNT with pyrene and naphthalene becomes narrower and the maximum of the band is shifted to the low frequency region by 1, 1.5 and 2.5 cm^{-1} (for samples of SWNT with P1, N and P2, respectively), comparing with the SWNT spectrum. The width of the G^+ band for these samples is by 2, 1.5 and 3 cm^{-1} narrower (Table 1) than in pristine nanotubes. In each spectrum the additional control of the spectral line position is achieved by determination of plasma line (at ν=1648.8 cm^{-1}) of He-Ne laser.

The most significant change of the SWNT Raman spectrum due to the interaction with pyrene or naphthalene was observed in the intensity of the low-frequency component of the G mode (G^-), which decreased by about 16, 15 and % 30 for SWNT with P1, N and P2, respectively. To estimate the intensity of all the bands in the spectra, the bands were normalized to the most intensive G^+ band in each spectrum. All these changes are the spectral manifestations of the complex formation between the nanotubes and the pyrene/naphthalene molecules. However, all the observed changes of the SWNT Raman spectrum are not strong. This was not unexpected because

intermolecular stacking interaction causes usually small changes of the vibrational frequency [19].

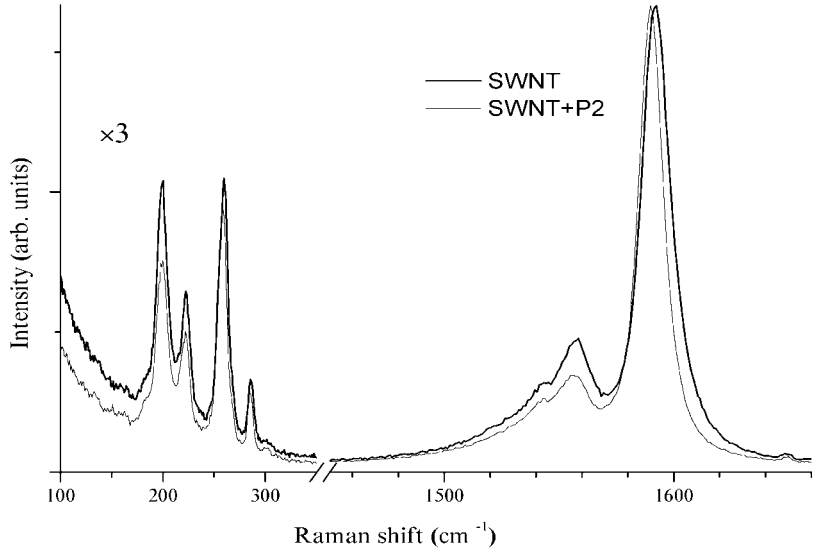

Figure 1. Raman spectra of SWNT film (bold line) and SWNT+P2 film (thin line)

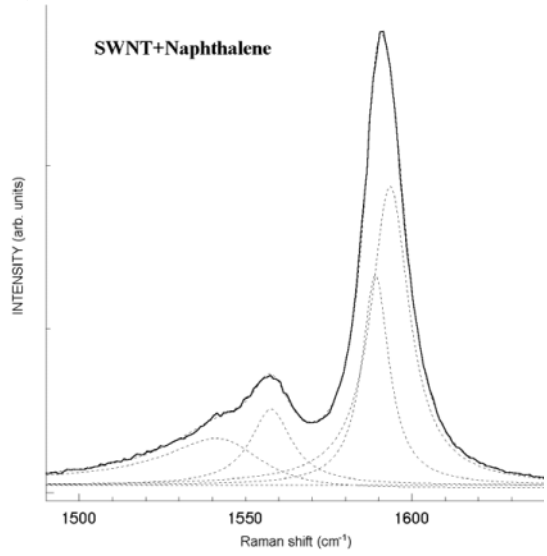

Figure 2. Raman spectra of SWNT+Naphthalene in the G mode region. Broken lines are Lorentzian curves and BWF line fitted to Raman spectra with parameters listed in Table 1 and 2.

Table 1. Spectral position (ω) of peak, full-width (ΔΓ) at half-maximum (FWHM) intensity of G^+ band, normalized intensity ratio of SWNT with pyrene/naphthalene to SWNT $(I_G^-/I_G^+)^*/(I_G^+/I_G^-)$ and parameter of BWF curve (1/q) obtained with laser excitation at λ_{exc}=632.8 nm.

	SWNT	SWNT+P1	SWNT+P2	SWNT+N
ω, cm^{-1}	1592,5	1591,5	1590	1591
ΔΓ, cm^{-1}	16,4	14,4	13,4	15,1
$(I_G^-/I_G^+)^*/$ (I_G^+/I_G^-), %/	85	84	70	100
1/q	-0.15	-0.16	-0.12	-0.17

Structures and interaction energies of complexes of pyrene and nanotubes of various sizes (from 0.49 to 1.58 nm) were determined using the quantum-chemical calculations (see in detail [20]). The interaction energy in the complex is -30.8 kJ mol^{-1}. Increasing the nanotube diameter leads to enhancement of the interaction energy till -37.2 kJ mol^{-1} in the case of the planar carbon surface. It is shown that for the zigzag (n,0) SWNT with n > 10 the interaction pyrene-nanotube is more preferable than a interaction pyrene-pyrene, and for nanotubes with n < 10 the interaction energies with pyrene are lower than interaction energies in pyrene dimers.

Table 2. Frequencies (ω) and full-width (ΔΓ) at half-maximum (FWHM) intensity of Lorentzian and BWF curves used to fit bands associated with G^+ of SWNT and SWNT with pyrene/naphthalene at 295 K obtained with laser excitation at λ_{exc}=632.8 nm.

SWNT+N		SWNT+P1		SWNT+P2		SWNT	
ω, cm^{-1}	ΔΓ, cm^{-1}	ω, cm^{-1}	ΔΓ, cm^{-1}	ω, cm^{-1}	ΔΓ, cm^{-1}	ω, cm^{-1}	ΔΓ, cm^{-1}
1592,8	14,1	1592,6	12,9	1591,4	11,8	1594,7	15,6
1588,4	9,8	1588,2	7,4	1587,2	8,7	1590	10,6
1556,9	14,7	1556,9	12,5	1557,1	13,4	1557,6	14,7
1543,5	38,8	1549,9	53,5	1546,2	42,8	1543,9	38,6

The G^+ band of the SWNT and SWNT complex (Fig.2) can be well fitted with 2 Lorentzian curves with parameters listed in Table 2. The G^- band is wide with an asymmetric form, which is strongly broadened in the region of

lower frequencies. The lower-frequency front of the band can be connected with metallic nanotubes. The shape of such a band is well described by Breit-Wigner-Fano (BWF) function [15,16,21] ($I(\omega)=I0\{1+(\omega-\omega0)/q\Gamma\}2/\{1+[(\omega-\omega0)/\Gamma]2\}$, where I0, ω0, Γ and q are intensity, the BWF peak frequency, broadening parameter, and the asymmetry parameter, respectively). The G-bands of pristine nanotubes and ones with pyrene/naphthalene were fitted with Lorentzian and BWF curves (see Table 2). The parameter 1/q for different samples is shown in Table 1.

3.2 Aqueous solution of SWNTs with various surfactants.

Fig. 3 presents NIR absorption spectra of SWNT in aqueous solutions with different surfactants: SDS, Tween and CTAB. For comparison, the absorption spectrum of SWNTs in KBr pellet is shown in this Figure. Light absorption of SWNT in NIR region is caused by electronic transitions between pairs of van Hove singularities in the density of states. So, light absorption in the region 0.6-1.2 eV can be assigned to electronic transitions E_{11}^{S} in the semiconducting nanotube (band gap transition), absorption at the energy 1.2-2.2 eV results from the E_{22}^{S} transitions of these types of SWNTs and absorption at 2.2-3.2 eV is assigned to the E_{11}^{m} transition in the metallic SWNTs [10]. Several bands are observed in the absorption spectrum of HiPco nanotubes for every electronic transition, corresponding to the tubes with different diameters and chilarity, predominant in the sample. As seen from Fig. 3, the bands in the region of the E_{11}^{S} transition are shifted to the high energy in absorption spectra of aqueous solutions SWNTs with various surfactants from each other as well as from the absorption spectrum of SWNT in KBr. Note that spectral shifts for bands in the region of the E_{22}^{S} and E_{11}^{m} transitions are very small. As compared with the spectrum of SWNT in KBr, bands corresponding to the E_{11}^{S} transition in nanotubes with CTAB are shifted by about (16-32 meV) to the higher energy.

Small shifts of the same bands are observed for nanotubes solutions with Tween but these shifts are smaller (by about 5-7 meV). The greatest shift of bands (up to 70 meV) can be seen for absorption spectra of nanotubes with SDS. So, the interaction between SWNT and surfactant in aqueous solution leads to the increase of the semiconducting nanotubes band gap, especially for a surfactant with a charge group.

SWNT interactions with different surfactants in aqueous solution result in changes in Raman spectra, as compared with spectra of a nanotube in films (Fig. 4). In this Figure two spectral intervals with bands corresponding to RBM and G mode are shown. Each Raman spectrum is normalized to the most intense band corresponding to the G-mode. The interaction with different surfactants leads to the intensity decrease and shift of lines attributed to the RBM. The essential changes in spectra are observed for this mode of SWNT in aqueous solutions with SDS. The intensity of the low-

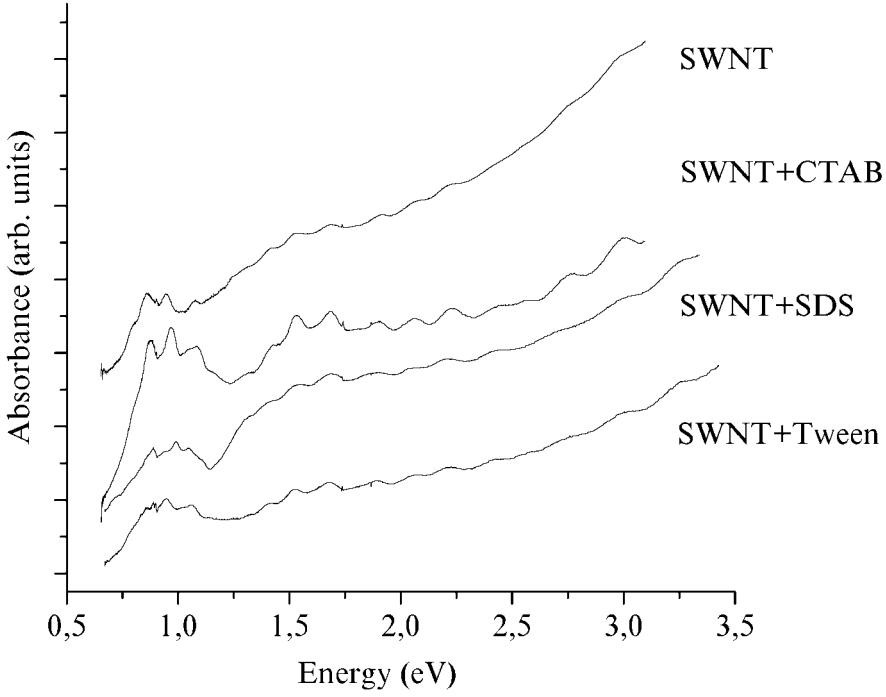

Figure 3. Absorption spectra of SWNT in KBr and nanotubes in aqueous solution with different surfactants: SDS, CTAB and Tween.

frequency band decreases significantly as compared with the intensity of other bands and shifts into the high-frequency region by 5 cm^{-1}. Some redistribution of band intensities is observed in spectra of the nanotubes in other solutions too. The intensity of the G^- mode is decreasing also, in comparison with the high-frequency (1580-1600 cm^{-1}) component of this band. It should be noted that the greatest changes are observed for nanotubes suspension with SDS and small ones are revealed for suspension with Tween.

A surfactant interaction with SWNT in aqueous solutions is determined by the surfactant micelle formation around the nanotube. Two types of micelles can be discussed: 1) surfactant molecules surround tubes so that the alkyl chain and charged group of some surfactant molecules lie flat on the graphite SWNT surface along the tube axis and other molecules with the hydrophilic part of the surfactant are oriented toward the aqueous phase and hydrophobic part of the SDS/CTAB in the direction of the nanotube surface (forming half-cylinders (belt) similarly on the graphite surface [22]), 2) surfactant molecules are distributed uniformly around the tubes with hydrophobic chains close to the tube surface. For micelle of the second type the surfactant molecules interact with nanotube by ends of the alkyl chain, and generally this interaction will be similar for all the surfactants. As coupling between the surfactant with a charge group and the nanotube leads to more essential transformation of Raman spectra and shift of bands corresponding to E11S transition (NIR absorption spectra) in comparison with nonionic surfactant and pristine SWNT, a conclusion can be made that the role of the charge in forming spectra is very decisive and, consequently, the first model of the micelle formation is preferable. The line shape and intensity of the band described by the BWF curve are very sensitive to an interaction among nanotubes in bundles or between nanotubes and surrounding molecules. BWF band was assigned [14,16,21,23] to coupling phonon (A_{1g} component of the G mode) with continuum electronic π plasmon excitation in metallic nanotubes. The intensity of BWF bands is enhanced in thick bundles and decreased in thin ones [23,24]. It is supposed that the nanotube-nanotube van der Waals interaction increases the plasmon-phonon coupling [25] and, as a result, it leads to enhancement of the intensity of BWF band. A similar picture is observed in our Raman spectra of nanotubes with pyrene or naphthalene in film and aqueous SWNT solution. The intensity of the G^- band is lower in solution, which contains mainly a single nanotube and thin bundles. In SWNT:pyrene/naphthalene films the intensity of the G^- band is also decreased.

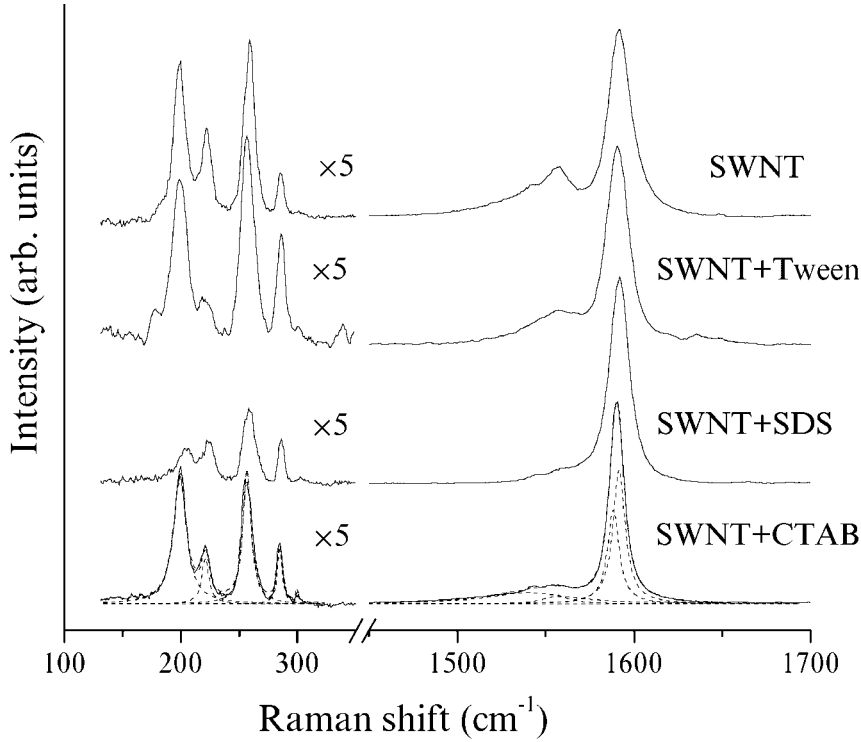

Figure 4. Raman spectra of nanotube film and SWNT in aqueous solution with various surfactants in range of RBM and G mode obtained at λ_{exc}=632.8 nm laser excitation.

During sonication of nanotubes with these organic molecules in toluene the bundles became thinner. In solution, as a result of an interaction of nanotubes with the pyrene/naphthalene molecules, these molecules lie flat on the surface of the nanotube and hinder formation of thick bundles after sonication stopping and during film growing. At least, the organic molecules are arranged among nanotubes, and a nanotube-nanotube van der Waals interaction is decreased. Essential changes of the G profile were observed upon doping by alkali metals. In the first steps of doping, the BWF line shape of the G^- is suppressed [14,26,27].

It is possible that the decrease of intensity of the BWF band is a result of not only lowering interaction between nanotubes but coupling with organic molecules too.

4. CONCLUSION.

Noncovalent interaction of SWNTs with organic molecules (pyrene and naphthalene) and surfactants of different types in aqueous solutions leads to the spectral shift of lines and its intensity redistribution in spectra in comparison with the spectra of pristine SWNT.

In Raman spectra the most essential changes are observed for the G mode. For SWNT with pyrene or naphthalene the high-frequency component of the G mode becomes narrower and the maximum of the band is shifted to the low frequency, the intensity of the low-frequency component of the G mode is decreased.

In NIR absorption spectra of aqueous solutions of SWNTs with various surfactants, the bands in the region of the first electronic transition (E_{11}^{S}) in the semiconducting nanotube are shifted to the high energy, as compared with a spectrum of SWNT in KBr. In Raman spectra of aqueous solution of SWNT with different surfactants the intensity of the low-frequency component of the G mode decreases in comparison with spectra of the nanotube in films. In the spectrum of SWNT with SDS the intensity of this component is very weak.

So, in both Raman and NIR absorption spectra the most essential spectral changes are observed for nanotube aqueous solution with the surfactant containing a charged group.

The model of the micelle formation in which some surfactant molecules lie flat on the graphene SWNT surface along the tube axis is preferable than the model with surfactant molecules distributed uniformly around the tube with hydrophobic chains close to the SWNT surface.

Decreasing the BWF component of the G-mode in nanotube water solution and in a film with organic molecules supports the assumption that coupling between plasmon modes and the G-mode is weaker in individual nanotubes and thin bundles than in thick bundles.

ACKNOWLEDGMENTS

This work was supported in part by STCU projects No 1934 and No 2155.

REFERENCES

1. V. Georgakilas, K. Kordatos, M. Prato, D.M. Guldi, M. Holzinger, A. Hirsch, J. Am. Chem. Soc. 124, 760 (2002).
2. W.J. Huang, S. Taylor, K.F. Fu, Y. Lin, D.H. Zhang, T.W. Hanks, A.M. Rao, Y.P. Sun, Nano Lett. 2, 311 (2002).
3. S.E. Baker, W. Cai, T.L. Lasseter, K.P. Weidkamp, R.J. Hamers, Nano Letters 2, 1413 (2002)
4. U. Dettlaff-Weglikowska, J.-M. Benoit, P.-W. Chiu, R. Graupner, S. Lebedkin, S. Roth, Current Applied Physics 2, 497 (2002).
5. M. Shim, N. Kam, R.J. Chen, Y. Li, H. Dai, Nano Letters 2, 285 (2002).
6. K. Otobe, H. Nakao, H. Hayashi, F. Nihey, M. Yudasaka, S. Iijima, Nano Lett. 2, 1157 (2002).
7. R.J. Chen, Y.G. Zhan, D.W. Wang, H.J. Dai, J. Am. Chem. Soc. 123, 3838 (2001).
8. F. Balavoine, P. Schultz, C. Richard, V. Mallouh, T.W. Ebbesen, C. Mioskowski, Angew. Chem., Int. Ed. 38, 1912 (1999).
9. M. Shim, A. Javey, N.W.S. Kam, H.J. Dai, J. Am. Chem. Soc. 123,11512 (2001).
10. M.J. O'Connell, P. Boul, L.M. Ericson, C. Huffman, Y.H. Wang, E. Haroz, C. Kuper, J. Tour, K.D. Ausman, R.E. Smalley, Chem. Phys. Letters 342, 265 (2001).
11. M.J. O'Connell, S.M. Bachilo, C.B. Huffman, V.C. Moore, M.S. Strano, E.H. Haroz, K.L. Rialon, P.J. Boul, W.H. Noon, C. Kittrell, et al., 279, 593 (2002).
12. M.F. Islam, E. Rojas, D.M. Bergey, A.T. Johnson, A.G. Yodh, Nano Letters 3**,** 269 (2003).
13. P. Nikolaev, M.J. Bronikowski, R.K. Bradley, F. Rohmund, D.T. Colbert, K.A. Smith, R.E. Smalley, Chem. Phys. Lett 313(1–2), 91 (1999)
14. M.S. Dresselhaus, P.C. Eklund, Adv Phys 49, 705 (2000)
15. A.M. Rao, P.C. Eklund, S. Bandow, A. Thess, R.E. Smalley, Nature 388 (6639), 257 (1997).
16. S.D.M. Brown, A. Jorio, P. Corio, M.S. Dresselhaus, G. Dresselhaus, R. Saito, K. Kneipp, G.R. Harrison, Phys Rev B 63, 155414 (2001).
17. H. Kuzmany, W. Plank, M. Hulman, C. Kramberger, A. Gruneis, T Pichler, T. Pichler, H. Peterlik, H. Kataura, Y. Achiba, Eur. Phys. J. B 22, 307 (2001).
18. V.A. Karachevtsev, A.Yu. Glamazda, U. Dettlaff-Weglikowska, V.S. Kurnosov, E.D. Obraztsova, A.V. Peschanskii, V.V. Eremenko, S. Roth, Carbon 41, 1567 (2003).
19. A.M. Plokhotnichenko, E.D. Radchenko, S.G. Stepanian, L. Adamowicz, J. Phys. Chem. A 103, 11052 (1999).
20. S.G. Stepanian, V.A. Karachevtsev, A.Yu Glamazda, U. Dettlaff-Weglikowska, L. Adamowicz, Molecular Physics 101, 2609 (2003).
21. H. Kataura, Y. Kumazawa, Y. Maniwa, I. Umezu, S. Suzuki, Y. Ohtsuka, Y. Achiba, Synth. Metals 103, 2555 (1999).
22. E.J. Wanless, W.A. Ducker, J. Phys. Chem. 100, 3207 (1996).
23. C. Jiang, K. Kempa, J. Zhao, U. Kolb, U. Schlech, T. Basche, M. Burghard, A. Mews, Phys. Rev. B, 66, 161404 (2002).
24. N. Bendiab, R. Almairac, M. Paillet, J.-L. Sauvajol,, Chem. Phys. Letters 372, 210 (2003).
25. K. Kempa, Phys. Rev. B 66, 195406 (2002).
26. M.E. Itkis, S. Niyogi, M.E. Meng, M.A. Hamon, H. Hu, R.C. Haddon, Nano Letters 2, 155 (2002).
27. N. Bendiab, E. Anglaret, J.-L. Bantignies, A. Zahab, J.-L. Sauvajol, P. Petit, C. Mathis, S. Lefrant, Phys. Rev. B 64, 245424 (2001).

PECULIARITIES FOR LUMINESCENCE IN SYSTEMS WITH FULLERENE C60-WATER INTERFACE

Peculiarities for C_{60} Luminescence

G.V. Andrievsky[a], A.A. Avdeenko[b], L.I. Derevyanchenko[a], V.I. Fomin[b], V.K. Klochkov[a], V.S. Kurnosov[b], A.V. Peschanskii[b]

[a] *Institute for Therapy of Ukrainian Academy of Medical Sciences*

[b] *B.Verkin Institute of Low Temperature Physics and Engineering of Ukrainian Academy of Sciences*

Abstract: The "additional" wide photoluminescence band is observed first in highly stable and finely dispersed colloidal solutions of fullerenes C_{60} in water. Unusual dependence on exciting light wavelength for this band is found. The position of the band maximum exhibits long-wavelength shift following the excited light wavelength, when last one becomes longer then 440 nm. A very simple "additional" luminescence band is found in the interface of water and fullerite C_{60} thin films also.

Key words: Luminescence, fullerene C_{60}, colloidal solution.

1. INTRODUCTION

Fullerenes are widely investigated with the respect to their interesting physical properties for the one hand and their biological activity for the other hand. It is clear that for medical and biological applications the fullerenes must be solved in water in any way. It is well known that fullerenes are not soluble in water per se [1]. That is why most attention is presently paid to investigation of water-soluble C_{60} derivatives, which, in turn, can be able to form colloidal solutions. Mono-functional fullerene C_{60} derivatives have the

E. C. Faulques et al. (eds.), Spectroscopy of Emerging Materials, 151–160.

tendency to form more or less large particles in concentrated solutions; such colloidal particles may have size up to 1-10 μm [2].

That fact that the diameter of C60 molecule equals to 10 Å makes one possible to considerate this molecule as a colloidal particle itself. This originates from the traditional point of view that 10-Å boundary corresponds to low boundary of colloidal range of dispersity, and the range of true solution is under this limit [3]. Thus, it is clear that aqueous solutions of any fullerenes must have properties of colloidal systems, which contain associates of solvated fullerenes of different size.

A technology, which has allowed producing of fullerene molecular-colloidal water solutions (FWS), has made new step for the biological applications of fullerenes. Such technology is now available [4], and C_{60}FWS produced by means of it is highly stable (8-24 months and longer) and finely dispersed without any stabilizers. The fact that this colloid consists of individual molecules of C_{60} and the water only has been proved earlier by means of different experimental methods.

In spite of this, the structure of colloidal particles of FWS remains yet hypothesized only. Current model, which is not at variance with known experimental data, intends that FWS contains both single fullerene molecules and their fractal clusters in hydrated state [5].

Spectroscopic investigations were directed for the first time measurements of C_{60}FWS in order to elucidate a structure of hydrated particles in the colloid and a structure of interface layer of water molecules surrounded them. The results obtained in these experiments proved to be enough unexpected and unusual, and served as a spur to present investigations and present paper.

2. EXPERIMENTAL PROCEDURE AND SAMPLES

Experimental technique used during these investigations is usual for Raman scattering and photoluminescence spectroscopy. For luminescence excitation He-Cd, He-Ne, and Ar^+ ion lasers were used. The exciting light power not exceeds 25 mW in all experiments.

In experiments with liquid solutions laser beam was focused inside the parallelepiped or cylindrical quvettes. The beam had the minimal cross section diameter not lower then 0.2 mm. In experiments with solid samples the beam was stretched in one direction by means of cylindrical lens, so the ellipse projected on a surface had dimensions of about 2×0.2 mm^2. In such conditions the density of exciting light power did not excite 65 W/cm^2 for the experiments with liquids and was at least 10 times smaller for the

experiments with solid samples. All the experiments have been performed at room temperature.

In addition to light sources the experimental setup contains Jobin Yvon U-1000 double monochromator, a cooled photomultiplier, and a photon counting system as well. The signal-to-noise ratio was improved by the spectrum acquisition method with a multiple scanning of the frequency range studied. Because of investigated spectral ranges were enough wide (from 11700 to 22600 cm^{-1}) all recorded spectra were corrected on spectral response of the setup, so the resulted ones are presented in the kind of quantum yield.

Samples that were used for investigations are the following:

- benzene solution of fullerene C_{60};
- molecular-colloidal aqueous solutions of fullerene C_{60};
- thin solid porous films of C_{60} deposited in vacuum on mica substrate;
- solid films of C_{60} deposited in vacuum on crystalline silicon substrate;
- C_{60} fullerite single crystal.

All pure solvents and substrates used for the sample preparation were characterized also by means of Raman and photoluminescence spectroscopy.

Procedures of the sample preparation are enough trivial now with the exception of producing of C_{60}FWS. This was produced without using of any solubilizers and chemical modification [4]. The method is based on transferring of fullerene from organic solution into the aqueous phase with the help of ultrasonic treatment [6]. The highest concentration of the solution used in present experiments was 400 μM/l.

3. RESULTS AND DISCUSSION

It is well known that in the red and near IR wavelength range fullerene C_{60} shows wide structural luminescent band which may easy be excited by light with a wavelength shorter then 700 nm. According to [7] this luminescence resulted from parity forbidden electronic transition between t_{1u} and h_u energy levels of C_{60}. Fine distinctions in the shape of this, called "usual", luminescent band strongly depend on an environment of fullerene C_{60} molecules, such as different solvents, ions or molecules in single crystals, and so on. Some of the distinctions one can see in the figures below.

The most interesting and unexpected feature of C_{60}FWS photoluminescence spectrum was the presence of a very wide, nonstructural, and enough intensive band in it, which has maximum at a wavelength of about 530 nm (correspondent wavenumber is about 19000 cm^{-1}). We have called this band as an "additional" or an "unusual" because we were not able

to find something similar in known to us papers devoted to investigations of fullerenes. The typical spectrum of C_{60}FWS excited by Ar^+ ion laser is shown in Fig. 1. It consists of overlapped Raman spectrum of water and luminescent spectrum of fullerene including the "unusual" band (upper solid curve). The most of characteristic Raman lines of fullerene C_{60} are presented in spectra also, but they are very narrow and weak in comparison to water and luminescent spectra and are not visible in the figures presented.

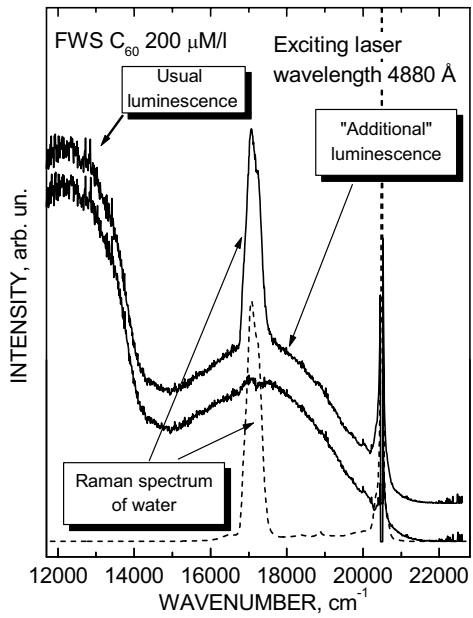

Figure 1. Typical spectrum of C_{60}FWS excited by 488 nm line of Ar^+ ion laser. Spectral resolution over all spectral range is 6÷11 cm^{-1}. Upper solid curve represents an original spectrum. Lower solid curve is a result of subtraction of the Raman spectrum of pure water (dashed curve).

It is well known that luminescence bands have absolute spectral position in contrast to Raman spectra whose absolute frequency position follows on exciting light frequency. There is a tradition to check what part of a spectrum in Raman experiment belongs to scattering, and what part is a luminescence. The easiest way is to do several records of the same spectrum using different wavelengths of exciting light. Such checking in a case of FWS led us to conclusion that the so-called "additional" luminescence is "unusual" really, because the spectral position of their band maximum depends on exciting light frequency. In spite of this fact, we continue to believe that this spectral feature belongs to luminescent process. The

dependence on exiting light wavelength does not reveal a strong character required for Raman scattering process (Fig. 2). Last experiments land support to the validity of our conclusion; the shift of the "additional" band maximum comes to stop when an exciting wavelength becomes shorter then 440 nm.

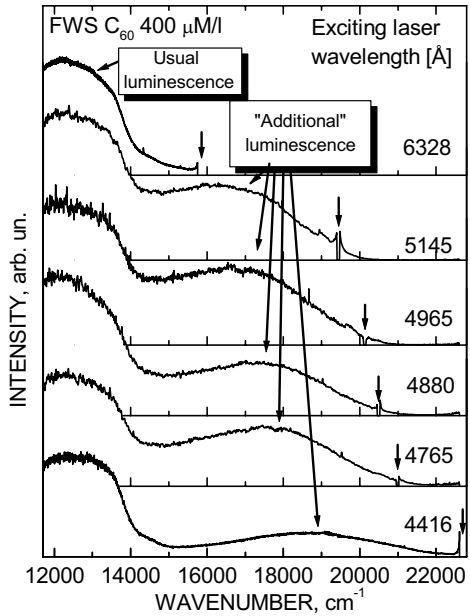

Figure 2. Luminescence spectra of C_{60}FWS excited by different laser wavelengths. Raman spectrum of water is subtracted.

The different ratio of usual and "additional" luminescent bands integral intensities for different exciting laser wavelengths may partially be caused by influence of large reabsorption of light inside of a sample (see Fig. 3). Another cause, which may be responsible for this effect, is different excitation spectra for the luminescence of two types. Moreover, if energy relaxation pathways, which lead to occupation of excited electronic luminescent levels of two types, are not independent, this may cause the observed effect also.

Reabsorption plays a great role in the experiments with FWS. Fig. 3 shows clearly its influence on obtained experimental data. Two spectra in Fig. 3 was recorded for a C_{60}FWS sample placed in a rectangular quartz quvette and excited by focused He-Cd laser beam passed along the side surface of the quvette. In the first case the beam was located at a distance of 0.1 mm from the cuvette surface, in the second — at 1.0 mm. The whole investigated spectral range is overlapped by two luminescent bands, so the

illuminated volume of the solution in the cuvette may be considered as "white" light source inside the absorbing media. It made us possible to calculate extinction coefficient of the C_{60}FWS. In the contrast to standard method of extinction measurement using spectrophotometer, this result has no errors connected with the reflection on the surfaces of cuvettes.

The molar extinction coefficient α is calculated with the following formula:

$$\alpha = \ln(I_1/I_2)/(x_2 - x_1)c\,,$$

where I_i is intensity of spectrum number i, x_i is distance of the exciting laser beam from the quvette surface for this spectrum, c is molar concentration of fullerene in FWS.

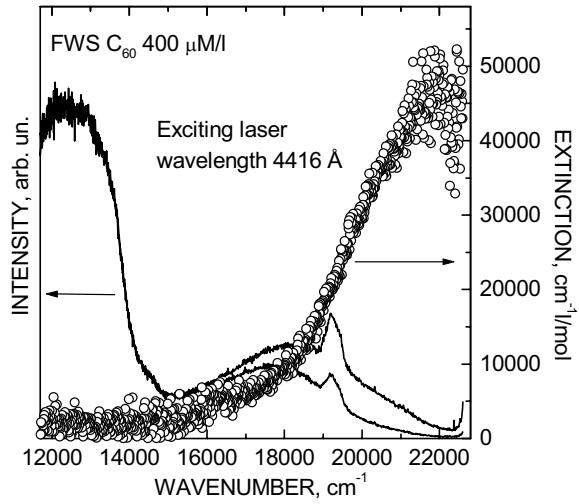

Figure 3. Spectrum of the extinction coefficient (open circles) calculated from the experimental spectra (solid curves) of C_{60}FWS at concentration 400μM/l recorded at right angle for different distance of the excited laser beam from the side surface of a quartz cuvette.

To investigate conditions in which "unusual" luminescence appears, we did comparison with spectra obtained on C_{60} benzene solution, C_{60} single crystal, two kinds of crystalline thin films on mica and silicon substrates (Fig. 4). They clearly showed, that the "unusual" luminescence presents only in FWS.

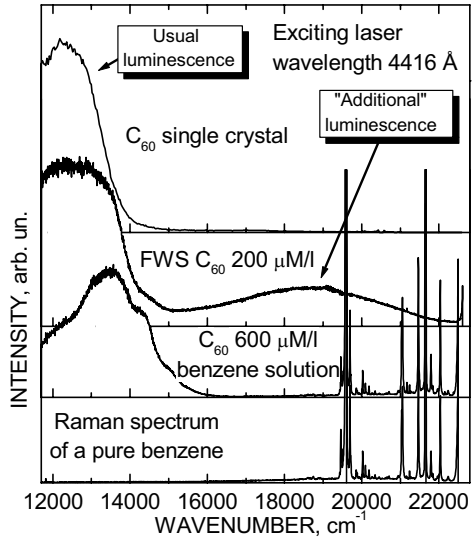

Figure 4. Comparison of photoluminescence spectra obtained on C_{60} single crystal, C_{60}FWS, and C_{60} benzene solution. Raman spectrum of pure benzene is presented also.

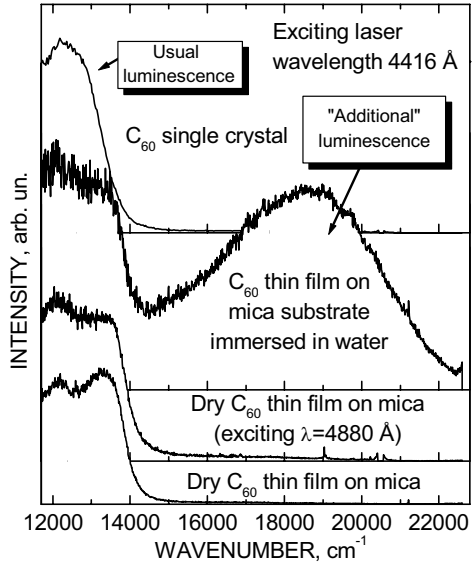

Figure 5. Photoluminescence of C_{60} film on mica substrate in the immersed in water state and initially dry. Upper spectrum of photoluminescence in single crystal is given for comparison.

The further step was an investigation of interface between water and fullerene C_{60} in solid state. A result of these experiments had validated the

occurred conjecture that "additional" luminescence is a result of some interaction between water and fullerene C_{60} at least. Fig. 5 shows comparison of photoluminescence spectra of C_{60} single crystal and C_{60} thin solid film deposited in vacuum on mica substrate in initially dry and immersed in water states. Unfortunately the experiments with C_{60} films on mica were irreversible. After film was immersed in water and then was subsequently dried, even at vacuum and heating up to 170 °C during several hours, its initial state was not restored. The dried film showed presence of "additional" luminescent band like in moisturized state.

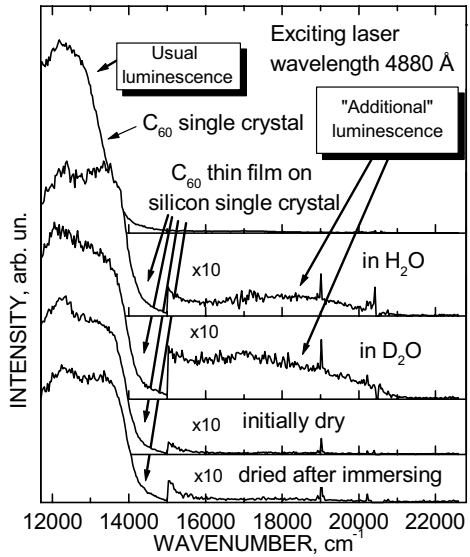

Figure 6. Photoluminescence of C_{60} film on silicon substrate in the immersed in water, initially dry, and dried after immersion on water states.

Another solid state fullerene samples were prepared by deposition in vacuum on silicon single crystal substrate. The films were thicker, then in the case with mica, and had optically perfect surface. Their immersing in water and subsequent drying had reproducible character, as one can see in Fig. 6. That fact that intensity of "additional" luminescence in last experiments is essentially lower then usual one, whereas in previous case with films on mica they are about equal, one can explain easily taking into account a big difference of films thickness. The film on mica is practically transparent, so its thickness may be estimated as 20÷30 nm. The film on silicon, on the other hand, is enough thick to absorb light at the range of 500÷440 nm fully. This gives essential difference in the ratio of

photoexcited molecules numbers belonged to surface and bulk, and lends support of validity of an assignment once more that the "additional" luminescence is originated from water-fullerene interface. Moreover, thin film on mica probably more porous then film on silicon, that is why it demonstrate irreducible property in relation to water moisturizing.

During the experimental work we treated our results from the following point of view: how do they relay to main hypothesis about the structure of fullerene colloidal particles in C_{60}FWS [5]? The basis of this structure is hydrated C_{60} fullerene molecules, the molecules with a shell consisted of oriented water molecules. The diameter of the shell is about 1.6-1.7 nm. Icosahedral clusters can be constructed from 13 hydrated C_{60} molecules, and have diameter of about 3.4 nm. Lager clusters are built from $13C_{60}$ hydrated clusters and individual hydrated fullerene molecules. The experimental fact, that "additional" luminescence presents not only in FWS but also in the other water-fullerene interface systems, argues that the nature of the luminescence not connected with specific formation of a water shell around C_{60} molecules. It is well known that FWS not exists in heavy water, so hypothetical shells are not formed here. The "additional" luminescence, nevertheless, appears in fullerene-heavy water interface also (Fig. 6.). In addition, it is useful to note that a pure carbon system as crystalline graphite, which also was examined in our experiments, exhibits no luminescence in spectral range of visible light. Thus, this phenomenon may be specific for fullerenes only due to peculiar structure of their π orbitals.

The nature of the "additional" luminescence in systems with C_{60} fullerene-water interface remains unknown yet, but we can just advocate that the role of water (or maybe oxygen ion) is essential to formation of this luminescence mechanism. It reflects an existence of high interaction between water and C_{60} fullerene molecules.

4. CONCLUSIONS

Unusual band was revealed in photoluminescence spectra of different systems that included C_{60} fullerene contacted with water. This phenomenon was investigated experimentally for the first time. It was found that the maximum of the unusual luminescence band depends on the exciting light wavelength if it is longer than 440 nm. Probably, the nature of this luminescence lies in charge transfer processes between molecules of water and C_{60} fullerene, which leads to redistribution of fullerene surface density of charge and formation of new energy levels for this bounded system.

ACKNOWLEDGEMENTS

The research described in this publication was made possible in part by Award No. UC2-2440-KH-02 of the U.S. Civilian Research & Development Foundation for the Independent States of the Former Soviet Union (CRDF).

REFERENCES

[1]. M.T. Beck, G. Mándi, Fullerene Sci. Technol. 5, 291 (1997)
[2]. M.E. Vol'pin, E.M. Belavtseva, V.S. Romanova, A.I. Lapshin, L.I. Aref'eva, Z.N. Parnes, Mendeleev Commun. 4, 129 (1995)
[3]. H.R. Kruyt (Ed.), Colloid Science, vol. 1, Izdatinlit, Moscow, 1955, 538 p. (Russ. Transl.)
[4]. G.V. Andrievsky, M.V. Kosevich, O.M. Vovk, V.S. Shelkovsky, L.A. Vashenko, J. Chem. Soc., Chem. Commun. 12, 1282 (1995)
[5]. G.V. Andrievsky, V.K. Klochkov, E.L. Karyakina, N.O. Mchedlov-Petrossyan, Chem. Phys. Lett. 300, 392 (1999)
[6]. G.V. Andrievsky, M.V. Kosevich, O.M. Vovk, V.S. Shelkovsky, L.A. Vashchenko, in: Chemistry and Physics of Fullerenes and Related Materials (R.S.Ruoff and K.M.Kadish, Edt.) in the Electrochem. Soc. Proc. Series, Pennington, NJ. PV 95-10, 1591 (1995)
[7]. S. Saito and A. Oshiyama, Phys. Rev. Lett. 66, 2637 (1991)

PHOTOLUMINESCENCE AND STRUCTURE OF FULLERITE C_{60} INTERCALATED WITH HELIUM

A.A.Avdeenko, V.V.Eremenko, I.V.Legchenkova, A.I.Prokhvatilov, N.B.Silaeva, Yu. E. Stetsenko, M. A. Strzhemechny, K. A. Yagotintsev, P. V. Zinoviev, and V. N. Zoryansky

B. Verkin Institute for Low Temperature Physics and Engineering, 47 Lenin Ave., Kharkov 61103, Ukraine

Abstract: Powder x-ray diffractometry was employed to study infusion of He into C_{60} fullerite. It has been shown that the intercalation at a pressure of 0.1 MPa is a two-stage process, the first stage being the saturation of the octahedral voids, virtually complete after 55 hr. Photoluminescence spectra have been measured at 5 K on C_{60} with virtually completely saturated octahedral voids. Helium in the lattice voids is shown to reduce that part of the luminescent emission which is due to 0-0 transitions around 1.69 eV from the so-called deep traps, or according to existing notions, covalently bound pairs of C_{60} molecules. The effect of intercalation with helium on dimer formation in fullerite C_{60} is ascribed to a combined action of the following factors: intercalation-related changes of the pentagon to hexagon configuration ratio, formation of a bonded state of He in the C_{60} lattice, and moderation by helium of the orientational phase transition near 260 K, the last factor resulting in a reduced number of dislocations (which also promotes dimer formation).

Key words: fullerite C_{60}, powder x-ray diffractometry, He infusion, low temperature photoluminescence spectroscopy, dislocation, dimer

1. INTRODUCTION

Currently, intercalation of C_{60} with the rare gases into octahedral and tetrahedral interstitial voids of the fullerite C_{60} crystal is broadly studied (see

E. C. Faulques et al. (eds.), Spectroscopy of Emerging Materials, 161–166.

review [1] and references therein). First of all, this is connected with certain perspectives of solid-state gas storage. On the other hand, such examinations of rare gas intercalates allow to reveal physical and chemical properties of novel fullerene materials both in the molecular form and in the solid state.
In the present paper, we report on the dynamics of He filling the fullerite C_{60} fcc lattice octahedral and tetrahedral interstitial voids with the respective sizes of 4.12 and 2.26 Å [2], both larger than the helium Van der Waals diameter of 2.14 Å [3]. We also present results of study of influence of He intercalation on of photoluminescence spectra of C_{60} single crystal in the low temperature phase. The measurement technique as well as the experimental setup for structural [4-6] and luminescent [5, 6] studies have been reported elsewhere.

2. RESULTS AND DISCUSSION

In the first stage of this work we studied the kinetics of saturation of fullerite C_{60} with He at room temperature and at pressures close to 10^5 Pa., The temperature dependences of the lattice parameter of C_{60} being saturated with helium was investigated within the temperatures interval of 30-300 K under warm-up and cool-down conditions.

The room-temperature cubic lattice parameter ***a*** as a function of the exposure time of the uninterrupted intercalation process is plotted on Figure 1.

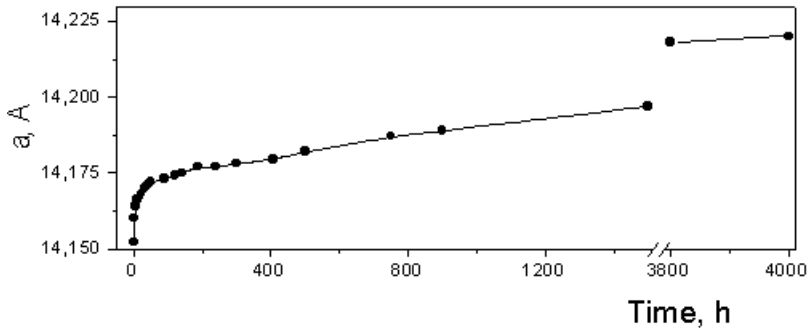

Figure 1. Lattice parameter versus the duration of intercalation; pressure near 0.1 MPa; room temperature. The error of the fullerite lattice parameter determined by powder x-ray diffractometry was 0,02 %.

Noteworthy is the rather fast increase of ***a*** during the initial 25–30 h of intercalation, which then converted to a much slower gradual increase with

distinct indications of a tendency to saturate only after 4000 h of exposure to helium atmosphere. The half-widths of all reflections versus time have a maximum approximately in the same region where the saturation regime changeover was documented for the $\boldsymbol{a}(t)$ dependence. This temporal behavior of the structure characteristics allows us to tentatively reconstruct the scenario of helium penetration into the sample. During the first stage, octahedral cavities are filled, which are larger in size and have much wider passes in between, as compared to tetrahedral cavities. A characteristic feature of the beginning of stage 1 is an inhomogeneous distribution of helium over the sample (helium diffuses from the sample surface inward), which manifests itself through a substantial broadening of the reflections. As the He concentration in octahedral voids gets more homogeneous, the half-width is restored to a value that differs little from that in pure starting fullerite. After that, a much slower filling of tetrahedral vacancies begins. Estimates of the typical energies of helium in the respective environments of both vacancy types l as ell as the relevant diffusion problem can be found elsewhere [7]. It should be noted here that, unlike octahedral vacancies, the system of tetrahedral vacancies is filled virtually homogeneously over the whole sample. The He content can be roughly (to within 5–10%) evaluated from the exponential dependence characteristic of the second saturation stage [7].

Figure 2 shows the lattice parameter $\boldsymbol{a}$ dependence on temperature for a fullerite C_{60} sample, saturated with helium to a high content.

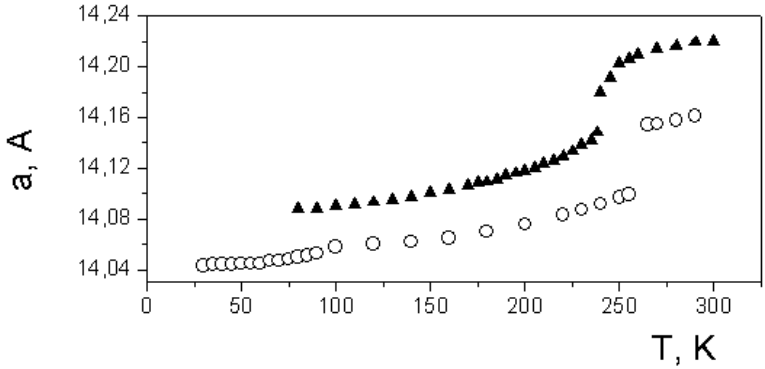

Figure 2. Temperature dependences of pure fullerite C60 cubic lattice parameter (o) [8] and fullerite C_{60} intercalated with helium (▲).The error of the pure and intercalated fullerite lattice parameter determination was 0,02 %.

One can see that the filling of octahedral and tetrahedral voids of the C_{60} cubic lattice with helium results in an appreciable increase of the lattice parameter (on the average, by about 0.3 %) over the entire explored

temperature interval, in a shift of the orientational phase transition to lower temperatures by nearly 10 K, and to a barely discernable lattice parameter jump. The anomaly at the orientational glassification temperature (90 K) is much less pronounced, which suggests that hexagon configurations are fewer.

In the next stage of this work we studied effects of intercalation on low-temperature photoluminescence spectra of fullerite C_{60} single crystal. Figure 3 shows photoluminescence spectra, normalized to integrated intensity, for pure fullerite and fullerite with helium impurities taken at 5 K, as well as a difference between the two.

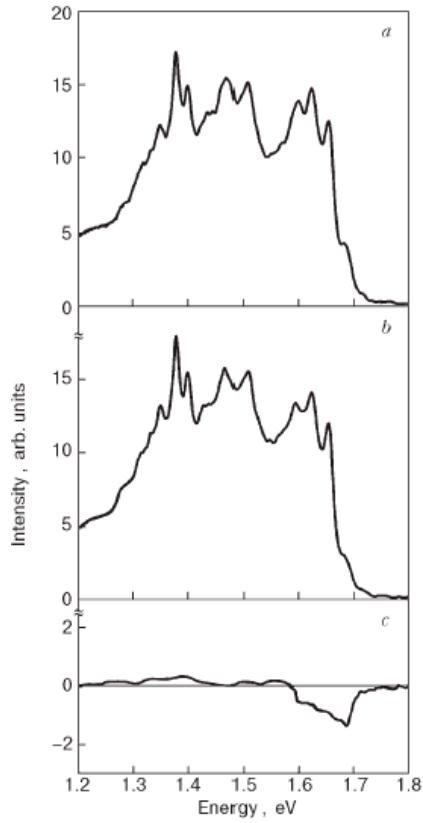

Figure 3. Normalized to their integral intensities photoluminescence spectra of C_{60} single crystal at 5 K under excitation of light with energy of 2.84 eV: a) pure fullerite C_{60}; (b) helium-intercalated fullerite C_{60}; (c) differed spectrum. The (a) and (b) PL spectra were corrected for instrumental response. The recording spectrometer slit width was 2.6 nm.

This difference spectrum is consistent with the luminescence spectrum of «type *A*» [9], which originates at the so-called deep traps (the 0–0 transition energy being equal to 1.69 eV), formed by a pair or a chain of C_{60} molecules [9,10]. Thus, we can infer that the helium impurity, which can form a weak chemical bond with C_{60} [11] and increase the crystal lattice parameter, hinders the formation of radiation centers that could be responsible for type-*A* luminescence. A possible mechanism of this phenomenon might be as follows. As shown by Davydov et al. [12], polymerization of C_{60} in its low-temperature phase is affected by the number ratio of hexagon and pentagon pair-wise configurations, the hexagon configuration being the one that favors polymerization.

The helium impurity is expected to promote a depletion of hexagon configurations due to larger lattice parameters in doped crystals and, thereby, inhibit polymerization, which is often initiated by stresses around dislocations [10]. The anomaly at the orientational glassification temperature (90 K) is less pronounced (Figure 2), which again suggests that hexagon configurations are fewer.

From Figure 2 one can see that the lattice parameter jump in doped fullerite C_{60} at the orientational phase transition is barely discernable. Most likely, it is connected with a lesser number of dislocations at the orientational phase transition. The less is the number of dislocations, the lower is the probability of dimer formation [10]. The only known mechanism of producing covalent bonding in the low-temperature phase of C_{60} is polymerization in distorted areas around dislocations [10]. Generally speaking, since dimerization is hardly possible even in a purely hexagonal state of C_{60}, orientational disorder, irrespective of its origin, is the necessary condition for the formation of covalent dimers [12]. The presence of orientational disorder in the C_{60} low-temperature phase is confirmed by the inhomogeneous broadening of the photoluminescence bands, which is removed using site selective excitation [9]. Thus, the hypothesis that the type-*A* luminescence spectrum in the low-temperature phase of fullerite C_{60} is due to covalent bonded molecules is confirmed by our measurements on C_{60} intercalated with helium.

3. CONCLUSIONS

1. Infusion of helium into fullerite C_{60} occurs in two stages. Intercalation of helium entails an increase of the lattice parameter.

2. The orientational transition temperature goes down by about 12 K. The lattice parameter jump is less pronounced. The anomaly near the orientational glass transition (around 90 K) is smoothed out.

3. Luminescence spectra give evidence that the concentration of dimers in C_{60} with He in octahedral cavities is notably lower than in pristine material. This inference is corroborated by our structure findings.

4. Two possible reasons for this reduction are: (i) helium doping decreases the number of hexagon configurations; (2) helium moderates the 260 K phase transition, thereby decreasing the number of dislocations (which also promote dimer formation).

ACKNOWLEDGEMENTS

A.I.P., Yu.E.S., and M.A.S. acknowledge support of the Science and Technology Center of Ukraine (grant 2669). A.A.A and P.V.Z. thank the CRDF (grant UC2-2240-KH-02) for financial support.

REFERENCES

1. B. Sundqvist, Low Temp. Phys. 29, 440 (2003)
2. R.A. Assink, J.E. Schirber, D.A. Loy, B. Morosin, G.A. Carlson, J. Mater. Res. 7, 2136 (1992).
3. J.K. Badenhoop and F. Weinhold, J. Chem. Phys. 107, 5422 (1997)
4. Yu.E. Stetsenko, I.V. Legchenkova, K.A. Yagotintsev, A.I. Prokhvatilov, and M.A. Strzhemechnyi, Low Temp. Phys. 29, 445 (2003).
5. I.V. Legchenkova, A.I. Prokhvatilov, Yu.E. Stetsenko, M.A. Strzhemechny, K.A. Yagotintsev, A.A. Avdeenko, V.V. Eremenko, P.V. Zinoviev, V.N. Zoryansky, N.B. Silaeva, and R.S. Ruoff, Low Temp. Phys. 28, 942 (2002).
6. A.A. Avdeenko, N.I. Gorbenko, V.V. Eremenko, P.V. Zinoviev, A.T. Pugachev, N.B. Silaeva, Yu.A. Tiunov, and N.P. Churakova, Low Temp. Phys. **25**, 37 (1999).
7. K.A.Yagotintsev, I.V.Legchenkova, Yu.E.Stetsenko, A.I.Prokhvatilov, and M.A.Strzhemechny, (in preparation).
8. S.V. Lubenets, V.D. Natsik, L.S. Fomenko, A.P. Isakina, A.I. Prokhvatilov, M.A. Strzhemechny, N.A. Aksenova, and R.S. Ruoff, Low. Temp. Phys. 23, 251 (1997).
9. I. Akimoto and K. Kan'no, J. Phys. Soc. Japan. 71, 630 (2002).
10. D.V. Dyachenko-Dekov, Yu.V. Iunin, A.N. Izotov, V.V. Kveder, R.K. Nikolaev, V.I. Orlov, Yu.A. Ossipyan, N.S. Sidorov, and E.A. Steinman, Phys. Stat. Sol. (b), 222, 111 (2000).
11. K. Ichimura, K. Imaeda and H. Inokuchi, Chem. Lett. 196 (2000).
12. V.A. Davydov, L.S. Kashevarova, A.V. Rakhmanina, V.M. Senyavin, O.P. Pronina, N.N. Oleynikov, V. Agafonov, R. Ceolin, H. Allouchi, and H. Szwarc, Chem. Phys. Lett. 333, 224 (2001).

INFLUENCE OF STATIC AND MICROWAVE MAGNETIC FIELDS ON PHOTOGENERATION OF FREE CHARGE CARRIERS IN DONOR-ACCEPTOR COMPLEX TBPDA·$(C_{60})_2$

D.V. Lopatin[1], V.V. Rodaev[1], A.V. Umrikhin[1], D.V. Konarev[2], A.L. Litvinov[2], R.N. Lyubovskaya[2]

1. Tambov State University, Tambov, 392622 Russia

2. Institute of Problems of Chemical Physics RAS, Chernogolovka, 142432 Russia

Key words: photoconductivity, magnetic field, fullerene C_{60}, donor-acceptor complex

Abstract: The effect of a weak magnetic field with B_0<1 T on photoconductivity of the donor-acceptor complex TBPDA·$(C_{60})_2$ has been found. The RYDMR spectrum is evidence of a spin nature of the mechanism of free charge carrier generation in magnetic fields. A model of triplet-triplet annihilation of charge transfer excitons has been suggested. The model interprets the effect of a weak magnetic field on photoconductivity in TBPDA·$(C_{60})_2$.

Fullerene C_{60} is a new π–acceptor, which essentially differs from other planar π-acceptors by large size, spherical shape, high symmetry and polarizability [1]. These features provide the design of materials possessing unusual magnetic and conductive properties [2]. Fullerenes also have unique photoacceptor properties. Different fullerene based composites, dyads and triads show efficient electron transfer from chromophores to fullerenes and the formation of charge separated states with lifetimes up to tens ms [3]. This makes fullerene compounds promising materials for photovoltaic devices. Thus, it seems interesting to study electron-optical properties of C_{60} compounds, particularly, donor-acceptor complexes with amines.

The goal of this work was to find and study the effect of weak static and microwave magnetic fields on electron-optical properties, particularly, photoconductivity of C_{60} complex with N,N,N',N'–tetrabenzyl-*p*-phenylenediamine: TBPDA·$(C_{60})_2$ [4].

E. C. Faulques et al. (eds.), Spectroscopy of Emerging Materials, 167–172.

Synthesis of single crystals of TBPDA·$(C_{60})_2$ was described elsewhere [4]. Photoconductivity was excited by white light of a 150 W halogen tube. Photoconductivity was characterized by current "I" running through indium contacts attached to one of the faces of the samples with silver paste. The contacts were under direct voltage of 10-50 V. Current values were measured with a charge amplifier connected with PC. The cell filled with the sample was put in a resonator of a standard Radiopan SE/X 2547 spectrometer.

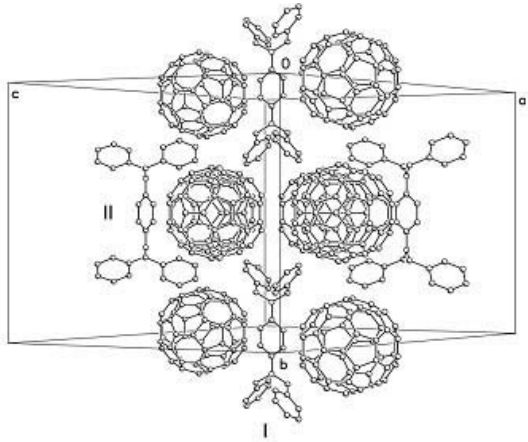

Figure -1. The projection of crystal structure of TMPDA·$(C_{60})_2$ along the c-axis.

TBPDA·$(C_{60})_2$ has a layered structure [4]. Fullerenes form distorted puckered layers arranged along a diagonal to the *ac* plane (Fig. 1). Each C_{60} molecule has 5 neighboring C_{60} ones in the layer with center-to-center distances of 9.77-10.67 Å, several of them being shorter than the van der Waals diameter of the C_{60} molecule (10.18 Å). Due to strong puckering of the C_{60} layers, each C_{60} molecule also has two neighboring C_{60} ones from the adjacent layer with a center-to-center distance of 10.25 Å. TBPDA molecules occupy cavities between the C_{60} layers (Fig. 1) and form van der Waals contacts with the C_{60} molecules by phenyl substituents (molecule ***I***, the C…C distances in the 3.42 – 3.55 Å range) and the central phenylene groups (molecule ***II***, the C…C distances in the 3.33 – 3.52 Å range).

The UV-vis-NIR spectrum of TBPDA·$(C_{60})_2$ is a superposition of the spectra of TBPDA and C_{60}. A broad band in the 700-1100 nm range and the maximum at 896 mn can be attributed to charge transfer (CT) from TBPDA to C_{60} at the absorption of light quantum. However, the IR and EPR spectra of TBPDA·$(C_{60})_2$ indicate the absence of any charge transfer from TBPDA to C_{60} in the ground state. Thus, TBPDA·$(C_{60})_2$ is a neutral CT complex.

Different mechanisms of photoinduced electron transfer are possible under excitation of C_{60} complexes with amines by white light (Fig. 2) [4].

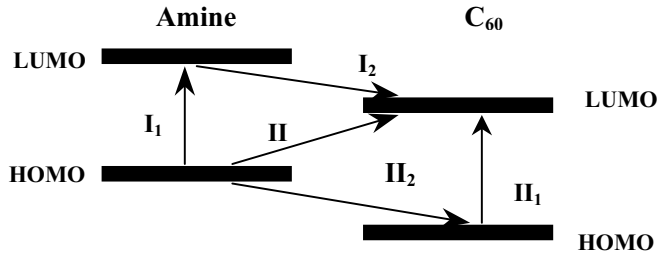

Figure -2. The diagram of possible mechanisms of photoinduced electron transfer in the C_{60} complexes with amines.

Photoexcitation of the donor component (Fig. 2, I_1) is followed by electron transfer to the C_{60} molecule (Fig. 2, I_2). However, photoexcitation of amines is possible only in the UV-range.

Since the C_{60} molecule is a stronger acceptor in the excited than in the ground state, photoexcitation of C_{60} (Fig. 2, II_1) can also result in electron transfer from the donor to the excited C_{60} molecule (Fig. 2, II_2). Due to that the direct HOMO-LUMO transitions are symmetry forbidden in the C_{60}, photoexcitation is realized mainly at energies higher than 2 eV.

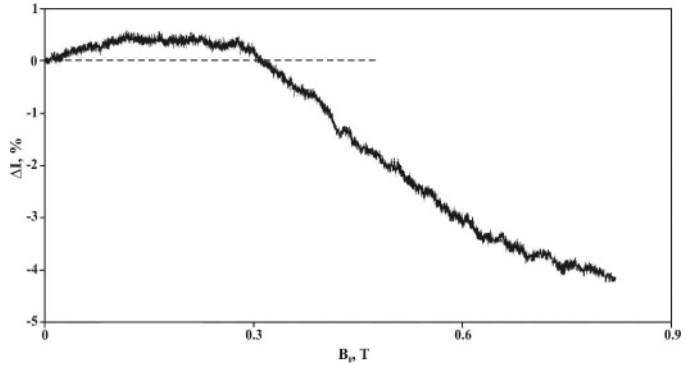

Figure -3. The dependency of relative changes of photocurrent ΔI in TBPDA·$(C_{60})_2$ on magnetic field induction B_0.

Direct intermolecular charge transfer from the donor to the C_{60} molecule (Fig. 2, III) is also possible at the excitation by white light. As it was mentioned above, the CT band in the TBPDA·$(C_{60})_2$ is observed at 1-2 eV.

It was found that in the TBPDA·$(C_{60})_2$ single crystals in neutral ground state show low conductivity, $\sigma \sim 10^{-12}$ $(\Omega * cm)^{-1}$. Upon illuminating the sample with white light one observes the 10^3 increase of photocurrent, which remains unchanged for 10^4 s. It was found that photoconductivity of TBPDA·$(C_{60})_2$ is sensitive to magnetic field (MF) with $B_0 < 1$ T. The dependency of photocurrent on B_0 is characterized by sign inversion at 0.3 T (Fig. 3) and conceivably attains saturation at 1 T. The sign inversion field dependency is characteristic of processes associated with the effect of MF on concentration of triplet charge transfer excitons in molecular crystals [5].

Photoexcitation of the complex is accompanied by charge transfer from the donor TBPDA molecule to the acceptor C_{60} one and CT-exciton is formed. Depending on mutual orientation of spins of components (electrons and holes), CT-exciton can be either a singlet or a triplet one. Free charge carriers are formed in molecular crystals mainly due to thermal or impurity dissociation of triplet CT-excitons [6].

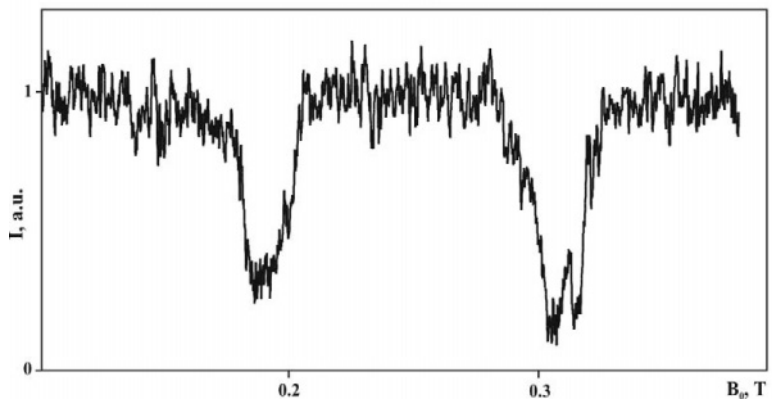

Figure -4. The RYDMR spectrum for TBPDA·$(C_{60})_2$. Microwave magnetic field frequency ν=8.96 GHz.

A spin nature of the effect of MF on photogeneration of free charge carriers was verified under experimental conditions of the registration of an EPR spectrum detected by photoconductivity measurements (RYDMR-Reaction Yield Detected Magnetic Resonance) of TBPDA·$(C_{60})_2$. The spectrum (Fig. 4) contains two resonance peaks of negative polarity at 0.189 and 0.312 T, the peak halfwidth is 0.009 T. The second peak has a fine structure.

The effect of magnetic field on a spin - dependent reactions in solids is valid, provided that [7]: the time τ_{pair} of particles staying in the paired state must be longer than the time needed for mixing the spin states τ_{ev}, but shorter than the relaxation time τ_{rel} with the value typical for molecular crystals $10^{-6} - 10^{-8}$ s: $\tau_{ev} < \tau_{pair} < \tau_{rel}$.

The time τ_{ev} depends on the mechanism of spin evolution. For the dipole-dipole mechanism $\tau_{ev} = \hbar / g\mu D$, where D is the dipole-dipole energy of interaction, μ is the Bohr magneton. The values $\tau_{ev}=2.7\cdot10^{-11}$ s, and $\tau_{pair}=3.1\cdot10^{-9}$ s were calculated for TBPDA·$(C_{60})_2$.

The RYDMR spectrum of the TBPDA·$(C_{60})_2$ crystals is interpreted by a model, which considers external-field modulation of a triplet-triplet exciton annihilation rate constant [6]. The kinetic model of triplet-triplet exciton annihilation can be presented as follows:

$$T + T \underset{K_{-1}}{\overset{\frac{1}{9}K_1}{\rightleftarrows}} {}^{1,3,5}(T...T)_i \xrightarrow{K_S|S_i|^2} S_1 + S_0, \qquad (1)$$

where $(T\ldots T)_i$ - intermediate pair state formed in one of nine possible, *i*th, a spin state; K_1, K_{-1} - rate constants of collision and back scattering; $K_S \left| S_i \right|^2$ - the rate constant of annihilation for the *i*th spin state, S_i-amplitude of singlet components in this state.

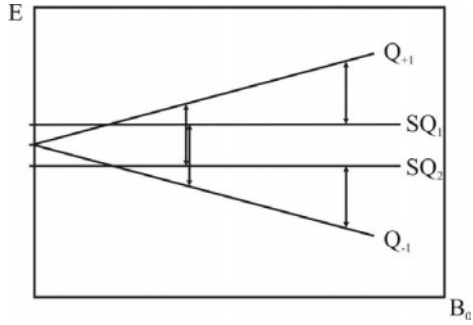

Figure -5. The scheme of resonance transitions in the (T…T) complex.

In magnetic fields with B_0>0.1 T only two levels, SQ_1 and SQ_2 generally contain a singlet component S, which defines the transition of a pair to a final singlet state. These transitions cause partial emptying of the SQ_1 and SQ_2 levels. Microwave magnetic field stimulates mainly transitions from the quintiplet levels Q_{+1} and Q_{-1} to the SQ_1 and SQ_2 ones (Fig. 5), whose occupancy increases. Since the total rate constant (1) defined as

$$\gamma = \frac{1}{9} K_1 \sum_i^9 \frac{K_S |S_i|^2}{K_{-1} + K_S |S_i|^2},$$

is a function of stationary occupancies of the levels of the (T…T) complex, the above mentioned resonance transitions result in the increase of γ.

The increased yield of the reaction products of (1) results in lower concentration of triplet excitons and, consequently, a lower number of free charge carriers formed in molecular crystals that is justified by two resonance peaks of negative polarity in the RYDMR spectrum of TBPDA·$(C_{60})_2$.

The effect of weak magnetic field with B_0 <1 T on photoconductivity of the donor-acceptor layered complex TBPDA · $(C_{60})_2$ has been found. The RYDMR spectrum is evidence of a spin nature of the mechanism of free charge carrier generation in magnetic fields. The information on structure, energy and time performances of short-lived intermediate charge transfer states can be obtained from the analysis of the RYDMR spectrum. A model of triplet-triplet annihilation of charge transfer excitons has been suggested. The model interprets the effect of weak magnetic field on photoconductivity in TBPDA·$(C_{60})_2$.

ACKNOWLEDGEMENTS

The work was supported by RFBR (grant No 02-02-17571, No 03-02-06181 and No 03-03-32699a).

REFERENCES

1. Dresselhaus M. S., Dresselhaus G., Eklund P.C. Science of Fullerenes and Carbon Nanotubes, Academic Press, San Diego, 1996.
2. Konarev D.V., Lyubovskaya R.N., *Russ. Chem. Reviews,* 1999, **68** (1), 19-38.
3. Sariciftci N.S., Heeger A.J. Handbook of organic conductive molecules and polymers», ed. H.S. Nalwa, John Wiley and Sons, 1997, **1**, p. 414.
4. Konarev D.V., Kovalevsky A.Yu., Litvinov A.L., Drichko N.V., Tarasov B.P., Coppens P., Lyubovskaya R.N., *J. Solid State Chem.*, 2002, **168** (2), 474-485.
5. Johnson R.C., Merrifield R.E., Avakian P., Flippen R.B., *Phys. Rev. Lett.* 1967. **19** (6), 285-287.
6. Pope M., Swenberg C. Electronic processes in organic crystals, Clarendon Press, Oxford, 1982.
7. Buchachenko A.L., Frankevich E.L., Chemical generation and reception of radio and microwaves, VCH Publishers, New York, 1994.

LIGHT SCATTERING OF MAGNETS IN THE PROXIMITY TO QUANTUM CRITICALITY

Peter Lemmens
Max Planck Institute for Solid State Research, MPI FKF
70569 Stuttgart, Germany
P.Lemmens@fkf.mpg.de, www.peter-lemmens.de

Abstract In the investigation of quantum critical spin systems light scattering experiments prove to be especially useful due to their high sensitivity and spectral resolution that perfectly match the relevant energy scales. The observed low energy collective excitations or bound states with singlet character play an important role characterizing fluctuations of the system. Furthermore, often spin or orbital related phonon anomalies are observed that include important symmetry information. The use of this experimental technique will be demonstrated on three model systems, the frustrated spin dimer system $SrCu(BO_3)_2$, the spin tetrahedra system $Cu_2Te_2O_5Br_2$ and the layered pseudo gap system TiOCl.

Keywords: magnetic light scattering, singlet bound states, quantum criticality, spin frustration, spin gap, electronic correlation, transition metal oxides

Introduction

The use of light scattering experiments to investigate transition metal oxides with small spin moments and strong magnetic fluctuations has evolved from investigations of high temperature superconductors (HTSC) [1]. These materials, with their two dimensional (2D) layered structure and spin moments based on the $3d^9$ configuration of Cu^{2+}, represent up to today the most interesting class of quantum spin systems. Here, long range magnetic ordering due to strong antiferromagnetic (AF) superexchange is suppressed by doping charge carriers and a spin liquid state evolves [2]. Many interesting aspects of electron correlation, such as renormalized two-magnon scattering, pseudo gap formation and phase separation, have been revived and intensified in the much broader class of transition metal oxides studied in the following [3]. The richness of these compounds is mainly based on two aspects, the use of a larger group of transition metal ions, such as Ti^{3+}, V^{+4}, Co^{4+}, and the overwhelm-

E. C. Faulques et al. (eds.), Spectroscopy of Emerging Materials, 173–184.

ingly large number of different spin topologies that are realized in these systems [4].

In the following we will discuss three systems that on one hand can be regarded as model systems, however, on the other hand have extraordinary and unusual magnetic properties that distinguish them from other more classical materials. This exotic behavior is the basis for the fascination they raised in the community devoted to quantum magnetism.

An antiferromagnetically coupled spin dimer of two s=1/2 has a spin singlet as its lowest energy state. The first excited state is a spin triplet and the energy between these two states is denoted as the spin gap Δ. If such dimers are coupled in one dimension a dimerized spin chain is formed. Such spin chains exist in several spin systems, e.g. in $CuGeO_3$ [5]. Properties of this and related compounds are further discussed in Ref. [3].

1. The frustrated spin dimer system $SrCu(BO_3)_2$

Spin dimers can be coupled in 2D and form a planar arrangement where each spin has one next neighbor and four next nearest neighbors. The couplings with these neighbors are shown in Fig. 1a) by dashed and full lines, respectively. For small coupling J within a dimer such a lattice is equivalent to a square lattice. For strong coupling J the antiferromagnetic interaction between three spins, two on one dimer and one on an adjacent dimer, cannot be satisfied simultaneously. The system is frustrated due the competing interactions J'. A classical system consisting of spin triangles would form a long range ordered state with a compromise of significantly low energy [6]. In a quantum spin system such an ordering is usually suppressed as sufficient low energy states and fluctuations exist to destabilize it. In contrast, local short range correlations develop that evade competing interactions, a singlet ground state is formed. The competition and interplay between short range and long range states at the T=0K critical point governed by quantum fluctuations is in the center of our interest [7]. Such a quantum critical point (QCP) has also important implications for the excitation spectrum and thermodynamic properties of these systems at finite temperature [8].

The compound $SrCu(BO_3)_2$ realizes such a system [9]. Its exchange topology can be compared to an earlier theoretical model [10] although also evidence for additional Dzyaloshinskii-Moriya and spin-phonon interactions exist [11, 12]. In neutron scattering experiments on $SrCu(BO_3)_2$ a flat and dispersionless triplet branch has been detected as shown in Fig. 1b) [13]. In addition to this elementary triplet further s=1 pair states exist that have considerable spectral weight only at certain points of $\mathbf{q}$ space. These composite or pair states show strong level repulsion that depresses the dispersion [15]. In Raman scattering investigations a larger number of nearly equidistant s=0 singlet states

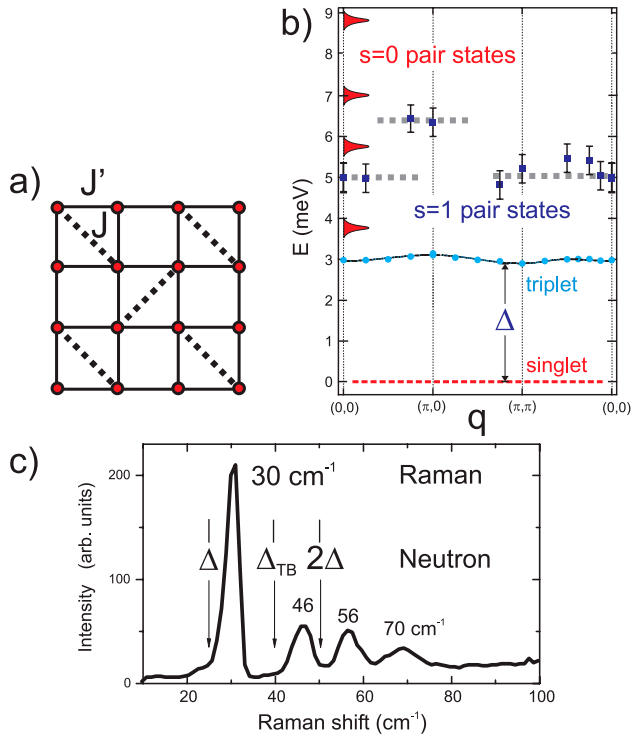

Figure 1. a) Spin topology of $SrCu(BO_3)_2$ with intradimer J and interdimer J' couplings. b) Dispersion of the triplet and triplet pair states from neutron scattering [13] and energies of the Raman scattering s=0 pair states at q=0. Triplet pair states of related branches are connected by thick dashed lines. c) Raman scattering intensity in (a'b') polarization showing four singlet bound states at 30, 46, 56, 70 cm^{-1} and the onset of a broader mode at about 100 cm^{-1} [14]. Arrows denote the elementary triplet (spin gap Δ), a bound triplet pair state Δ_{TB} and the doubled spin gap from neutron scattering.

are observed. The composite states with singlet and triplet nature alternate in energy and form a dense spectrum of low energy modes.

This behavior matches quite well to the scenario that has recently been developed for 2D spin systems in the proximity to a quantum critical point [16] and is a direct fingerprint of the tendency to form local correlations. It has to be mentioned, however, that the lowest energy excitation still has triplet character. For compounds with closer proximity to quantum criticality, such as the 1/6 depleted triangular lattice (Kagome) [6] and the 1/5 depleted square lattice, also exists a dense singlet spectrum within the singlet triplet gap [17–20]. Unfortunately no Raman scattering data for the related compounds are available up to now.

In applying a large magnetic field of 0 - 70 Tesla $SrCu(BO_3)_2$ crosses over into new quantum phases observable as distinct plateaus in the magnetization [21–23]. These plateaus correspond to 1/8, 1/4 and 1/3 of the saturation magnetization of the spin system [24–26] and are understood as field induced triplet states that are divided in a commensurate way on the dimer lattice. Recent NMR experiments on the 1/8 plateau at 28 Tesla and at very low temperatures (35 mK) show a transition-like crystallization of triplets within a larger supercell and Friedel-like oscillations of the field induced spin polarization [27].

2. The spin tetrahedra system $Cu_2Te_2O_5Br_2$

The above mentioned experimental results show unquestionably the rich physics of quantum spin systems in the singlet phase. It is, however, of similar interest how correlations develop for compounds where “some" long range ordering of the spin moments is achieved. There are different techniques to induce a crossover from a short range correlated state to a long range ordered state and all have specific advantages and disadvantages. Applying large magnetic fields or large hydrostatic pressures can be used for this purpose. However, also chemical means are used as substituting magnetic or nonmagnetic sites in the compound. In this case the effect of static disorder of the coupling constants leads to universal scaling relations of thermodynamic properties [28–31].

A different but successful approach starts with chemical building blocks that allow open frameworks and weak coupling of subgroups [4, 35]. These techniques are also important for other functional compounds, as ion conductors, catalysts or thermoelectric materials. In a thermoelectric oxide with large Peltier effect based on mixed Co^{3+}/Co^{4+} on a layered triangular lattice superconductivity has been found with a T_c=4.6 K [36–38]. Also lone pair cations, e.g. Te^{4+}, Se^{4+} or As^{3+}, can be used to introduce an electronic charge distribution that is not involved in a chemical bond [4]. In this way, a structural/chemical basis for interesting magnetic properties has been developed.

The most spectacular example of such a directed chemical approach toward quantum magnetism is $Cu_2Te_2O_5Br_2$, a system with weakly connected Cu^{2+} tetrahedra, as sketched in Fig. 2a) [39]. The magnetic susceptibility data given in Fig. 2b) show a broad maximum at T_{max}=30 K and a decrease at low temperatures, a behavior that is consistent with weakly coupled tetrahedra of AF coupled spins. A fit to this temperature dependence gives a typical energy scale for the intra-tetrahedra coupling of J=40 K for this compound. A kink at T_c=14.4 K in the susceptibility marks a transition [32].

Recent muon spin rotation (μ-SR) experiments evidence the existence of internal fields. Hence, a weak Neel ordering is assumed [40]. The substitution of Br by Cl reduces the unit cell volume by 7% and increases the transition

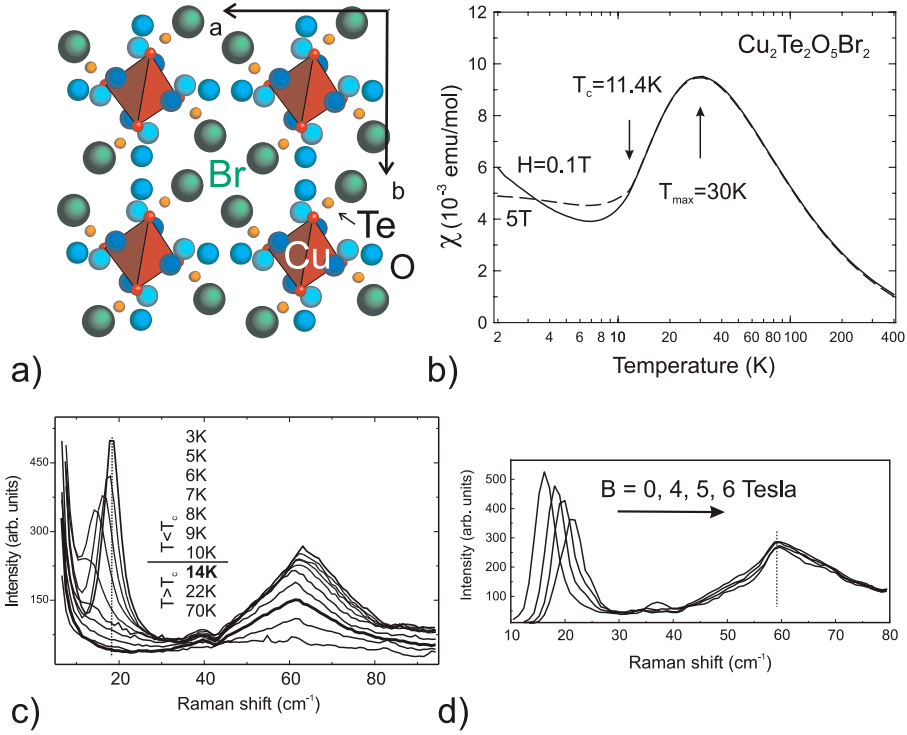

Figure 2. a) Projection on the ab plane of the crystal structure of $Cu_2Te_2O_5Br_2$. The "magnetic" Cu tetrahedra are surrounded by Te and O ions. The unit cell volume and the inter-tetrahedra coupling are strongly affected by the bromide ions. b) Magnetic susceptibility at 0.1 and 5 Tesla [32]. c) Raman spectra in (cc) polarization in the 3 - 70 K temperature range. The data for T=14 K are shown with a thicker line for clarity. A low energy mode at 18 cm^{-1} with a soft mode behavior and a continuum centered at about 60 cm^{-1} are observed. d) Magnetic field dependence of the Raman modes for fields in the 0 - 6 Tesla range [33, 34].

temperature of $Cu_2Te_2O_5Cl_2$ to T_c=18.2 K. An analysis of the entropy change at the transition shows in the chloride ΔS_m=0.36 · Rln2. In the bromide it is only ΔS_m=0.16 · Rln2 [32]. These and other experimental data can be taken as evidence for a proximity of the system to a QCP [33, 34].

Raman scattering spectra show a symmetric continuum of scattering centered at about 60 cm^{-1} in the temperature range where the susceptibility has a maximum (see Fig. 2c) [32]). This corresponds to two-magnon scattering with a typical energy scale of 2J=84 K, in good agreement with fits to the magnetic susceptibility data mentioned above. The lineshape and scattering selection rules of this scattering intensity have been described within a chain model of tetrahedra [41–43].

The low energy excitation is observed at finite frequencies only for $T < T_c$. In moderate magnetic fields its frequency is increasing as shown in Fig. 2d). Such a shift of the low temperature mode and the order parameter-like dependence on temperature has been taken as evidence that the mode cannot be related to a singlet state and must be identified as a longitudinal magnon [33, 34].

Longitudinal fluctuations of a Neel-ordered state are usually strongly damped and not included in a spin-wave approximation of its excitation spectrum. Until now similar modes have been only observed in neutron scattering on spin chain systems as broadened maxima [44–46]. The present narrow linewidth is probably related to the small scattering vector involved in light scattering experiments.

3. Orbital-related fluctuations in the layered system TiOCl

The examples presented above demonstrate the high sensitivity of light scattering techniques to magnetic excitations. This progress is among other things based on experimental improvements, such as the broader availability of CCD detectors with quantum efficiencies close to or above 90% and the use of triple spectrometer with strong quasi-elastic light rejection and high resolution at low energies. On the other hand, the detection of light scattering by phonons with this technique is well established in the characterization of semiconductors and other insulating systems. It is therefore not surprising that phonon studies also gained importance in the investigation of quantum criticality in transition metal oxides.

Phonons may couple to spin systems in various ways. A modulation of the exchange coupling or the spin gap is possible [1, 47]. In systems with charge fluctuations similar effect exist [48]. Due to the low symmetry of the local exchange paths in many systems, the phonon modulation of the coupling constants do not compensate each other and the resulting spin-phonon coupling is large [3]. An interesting effect in this context is that, in depleted spin topologies with nonequal bonds, some phonon modes stabilize local singlet correlations and phases [49] and shift the corresponding critical lines.

An aspect that will be discussed in the following is the effect of orbital degrees of freedom and orbital fluctuations. As the occupation and possible degeneracy of orbital states strongly depend on the local geometries, this problem is also related to spin-phonon coupling and, in some cases, similar conclusions can be drawn. Recent theoretical models using spin and orbital degrees of freedom on equal footing [SU(4) symmetry] [50, 51] found nontrivial extensions of this problem, such as the destabilization of long range ordering and/or unconventional spin gap formation [52] with spin-orbit coupled excitations [53]. The extension of such models from 1D spin-orbital chains to 2D triangular sys-

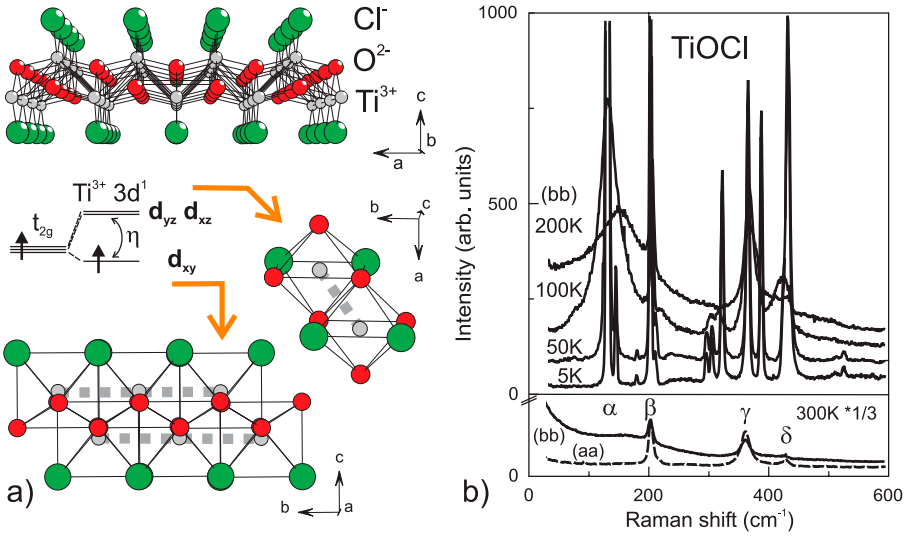

Figure 3. a) Projections on the crystallographic structure of TiOCl and the CEF level scheme of Ti^{3+} with $3d^1$ in a t_{2g} orbital. The in-plane d_{xy} orbitals that form chains along the b axis direction and the interplane d_{yz} and d_{xz} orbitals are given by dashed lines within TiO_4Cl_2 octahedra. b) Raman scattering intensity in (bb) polarization as a function of temperature [55]. In the lower panel the scattering intensity parallel and perpendicular to the b-axis are compared at T=300 K. The three symmetry allowed phonon modes are denoted by β, γ and δ. A low temperature excitation which shows extreme fluctuation effects in the pseudo gap phase is denoted by α. It steams from the folded phonon branch corresponding to the *beta* mode.

tems shows the wider applicability of such concepts. The compounds $LiNiO_2$ and $BaVS_3$ have been discussed in this context [54].

The break down of usual concepts of spin gap formation can be studied very well in the recently established Ti^{3+} systems $MgTi_2O_4$ [56], TiOCl [57] or $NaTiSi_2O_6$ [58]. In all these compounds a crystallographic distortion is accompanied with the formation of an unusually large spin gap and strong fluctuations exist, pointing to electronic energy scales involved.

A broad fluctuation regime and a pseudo spin gap have been observed in the 2D system TiOCl that motivated a comparison with HTSC [57, 59]. The relevance of the orbital sector is evident here due to pronounced phonon anomalies [55, 60]. The crystal structure of this material is sketched in Fig. 3. It consists of double layers of edge-sharing and strongly distorted TiO_4Cl_2 octahedra. Such a distortion leads to lifting of the t_{2g} orbital degeneracy, as shown in the crystalline electric field (CEF) level scheme given in Fig. 3a). The character of the lowest energy level, either an in-layer d_{xy} orbitals that form chains along

the b-axis direction or interlayer d_{yx} and d_{xz} orbitals, is less clear, as it depends on the detailed balance of local fields, covalency, and correlations effects.

The magnetic susceptibility of TiOCl is very flat and structureless in the temperature regime T>T*=135 K, which might be indicative of slowly evolving magnetic correlations typically observed in spin chains or planar geometries [57]. NMR/NQR experiments, on the other hand, show evidence for strong lattice fluctuations for T<200 K and the opening of a spin gap with a characteristic temperature T*=135 K [61]. In the magnetic susceptibility, however, transition-like phenomena are observed only at T_{c2}=94 K and T_{c1} = 66 K as a kink and a sharp drop, respectively [57, 61]. The low temperature transition also leads to a doubling of the unit cell in the b-axis direction, while for $T>T_{c1}$ incommensurate superlattice peaks are observed [62]. Therefore and as the behavior of the nuclear spin-lattice relaxation rate $(1/T_1T)$ resembles to HTSC, this phenomenon is denoted as a pseudo gap formation. The relaxation rate can be used to estimate the pseudo-gap $\Delta_{fluct}\approx$430 K (Ref. [61]). This is extraordinarily large when compared to the transition temperatures, leading to $2\Delta_{fluct}/k_BT_c$=9.1 and 13 for T_{c2} and T_{c1}, respectively. These ratios are not consistent with a mean field theory or spin-Peierls mechanism for this gap formation [63].

Raman scattering spectra of TiOCl with in-plane polarization show three phonon modes in (aa) polarization, denoted by β, γ and δ in the lower inset of Fig. 3. Following a shell model calculation, these modes are the three A_{1g} out-of-plane vibrations of the structure that are Raman allowed. In the (bb) scattering geometry, with the same symmetry selection rules but with incident and scattered light parallel to the chains of the d_{xy} orbitals, an extremely broad mode is observed, denoted by α in the figure. In the upper panel of Fig. 3b) the temperature dependence of the phonon spectra is shown for this polarization. The α mode shows a “giant" softening (by 20%) with decreasing temperatures for $T>T_{c2}$ that is accompanied by a reduction of the quasielastic background and the linewidth of this mode. Finally, for $T\leq T_{c1}$ only well-defined modes with sharp sidebands exist.

The origin of this strongly fluctuating mode is proposed to be the zone folded branch of the β mode. Zone folding occurs due to the above mentioned structural distortion [55]. The β mode is a good candidate for the respective Γ-point phonon, as this Tl-Cl in-phase vibration modulates the interlayer Ti-Ti distance and should therefore effectively modulate the energy of the interlayer with respect to the chain orbitals.

There are several arguments that support a causality between the phonon anomalies and the pseudo gap formation in the spin fluctuation spectrum. The connecting element is a coupling of the lattice displacement of the α phonon to the occupancy and admixture of interlayer d_{yz} and d_{xz} orbitals. The energy of this mode softens from 155 to 130 cm^{-1} in the temperature range from 200 to

100 K. As the energy of this mode is similar to the temperature scale, a drastic change of the phonon population is induced for T≈T*=135 K. Furthermore, in two-magnon scattering observed at higher energies (600-1500 cm^{-1}) an intensity modulation with a periodicity of 65 cm^{-1} is observed. This difference corresponds to the separation of the α and the β mode. Hence, the pronounced phonon anomalies of the β mode in the pseudo gap phase of TiOCl are related to the peculiar electronic configuration of the $\mathrm{t}_{2\mathrm{g}}$ states on $\mathrm{TiO_4Cl_2}$ double layers [55]. The compound TiOCl therefore gives an impressive example of orbital-related phonon anomalies that are present in such systems.

Acknowledgments

Important support by DFG SPP1073, NATO Grant PST.ARW.979393, PST.CLG.9777766 and INTAS 01-278 is acknowledged.

References

[1] E. Ya. Sherman, O. V. Misochko, and P. Lemmens, in *Spectroscopy of High Temperature Superconductors*, Ed. N.M. Plakida (Taylor & Francis Inc., London and New York, 2003), Chap. What can one learn from Raman Spectra of High Temperature Superconductors?, pp. 97–157, and references within.

[2] F. Mila, Eur. J. Phys. **21**, 499 (2000), and references within.

[3] P. Lemmens, G. Guntherodt, and C. Gros, Physics Reports **375**, 1 (2003), and references within.

[4] P. Lemmens and P. Millet, in *Quantum Magnetism: Microscopic Techniques for Novel States of Matter* (Springer, Heidelberg, 2004), Chap. Spin - Orbit - Topology, a triptych, and references within.

[5] M. Hase, I. Terasaki, and K. Uchinokura, Phys. Rev. Lett. **70**, 3651 (1993).

[6] J. E. Greedan, J. Mater. Chem. **11**, 37 (2001).

[7] S. Sachdev, Science **288**, 475 (2000).

[8] A.J. Millis, Phys. Rev. B **48**, 7183 (1993).

[9] S. Miyahara and K. Ueda, Journ. Phys.: Cond. Mat. **15**, R327 (2003).

[10] B. S. Shastry and B. Sutherland, Phys. Rev. Lett. **47**, 964 (1981).

[11] B. Wolf, S. Zherlitsyn, S. Schmidt, B. Luthi, H. Kageyama, and Y. Ueda, Phys. Rev. Lett. **86**, 4847 (2001).

[12] K.-Y. Choi, Yu. G. Pashkevich, K. V. Lamonova, H. Kageyama, Y. Ueda, and P. Lemmens, Phys. Rev. B **68**, 104418 (2003).

[13] H. Kageyama, M. Nishi, N. Aso, K. Onizuka, T. Yoshihama, K. Nukui, K. Kodama, K. Kakurai, and Y. Ueda, Phys. Rev. Lett. **84**, 5876 (2000).

[14] P. Lemmens, M. Grove, M. Fischer, G. Guntherodt, V. N. Kotov, H. Kageyama, K. Onizuka, and Y. Ueda, Phys. Rev. Lett. **85**, 2605 (2000).

[15] Ch. Knetter and G. S. Uhrig, cond-mat/0309408 (2003).

[16] V. N. Kotov, M. E. Zhitomirsky, and O. P. Sushkov, Phys. Rev. B **63**, 64412 (2001).

[17] Ch. Waldtmann, H.-U. Everts, B. Bernu, C. Lhuillier, P. Sindzingre, P. Lecheminant, and L. Pierre, Eur. Phys. J. B **2**, 501 (1998).

[18] M. Mambrini and F. Mila, Eur. Phys. J. B **17**, 651 (2000).

[19] A. P. Ramirez, B. Hessen, and M. Winklemann, Phys. Rev. Lett. **84**, 2957 (2000).

[20] R. Moessner, Canad. Jour. of Physics **79**, 1283 (2001).

[21] S. Miyahara and K. Ueda, Phys. Rev. Lett. **82**, 3701 (1999).

[22] E. Muller-Hartmann, R. R. P. Singh, Ch. Knetter, and G. S. Uhrig, Phys. Rev. Lett. **84**, 1808 (2000).

[23] T. Momoi and K. Totsuka, Phys. Rev. B **62**, 15067 (2000).

[24] H. Kageyama, K. Yoshimura, R. Stern, N. V. Mushnikov, K. Onizuka, M. Kato, K. Kosuge, C. P. Slichter, T. Goto, and Y. Ueda, Phys. Rev. Lett. **82**, 3168 (1999).

[25] K. Onizuka, H. Kageyama, Y. Narumi, K. Kindo, Y. Ueda, and T. Goto, J. Phys. Soc. Jpn. **69**, 1016 (2000).

[26] S. Zherlitsyn, S. Schmidt, B. Wolf, H. Schwenk, B. Luthi, H. Kageyama, K. Onizuka, Y. Ueda, and K. Ueda, Phys. Rev. B **62**, R6097 (2000).

[27] K. Kodama, M. Takigawa, M. Horvati, C. Berthier, H. Kageyama, Y. Ueda, S. Miyahara, F. Becca, and F. Mila, Science **298**, 395 (2003).

[28] R. N. Bhatt and P. A. Lee, Phys. Rev. Lett. **48**, 344 (1982).

[29] E. Westerberg, A. Furisaki, M. Sigrist, and P. A. Lee, Phys. Rev. Lett. **75**, 4302 (1995).

[30] N. Nagaosa, A. Furusaki, M. Sigrist, and H. Fukuyama, J. Phys. Soc. Jpn. **65**, 3724 (1996).

[31] A. Osterloh, L. Amico, G. Falci, and R. Facio, Nature **416**, 608 (2002).

[32] P. Lemmens, K.-Y. Choi, E. E. Kaul, C. Geibel, K. Becker, W. Brenig, R. Valent‟, C. Gros, M. Johnsson, P. Millet, and F. Mila, Phys. Rev. Lett. **87**, 227201 (2001).

[33] C. Gros, P. Lemmens, M. Vojta, R. Valenti, K. Y. Choi, H. Kageyama, Z. Hiroi, N.V. Mushnikov, T. Goto, M. Johnsson, and P. Millet, Phys. Rev. B **67**, 174405 (2003).

[34] J. Jensen, P. Lemmens, and C. Gros, Europhys. Lett. in print (2003).

[35] P. Y. Zavalij and M. S. Wittingham, Acta Cryst. B **55**, 627 (1999).

[36] I. Terasaki, Y. Sasago, and K. Uchinokura, Phys. Rev. B **56**, R12685 (1997).

[37] K. Takada, H. Sakurai, E. Takayama-Muromachi, F. Izumi, R. A. Dilanian, and T. Sasaki, Nature **422**, 53 (2003).

[38] P. Lemmens, V. Gnezdilov, N. N. Kovaleva, K. Y. Choi, H. Sakurai, E. Takayama-Muromachi, K. Takada, T. Sasaki, F. C. Chou, D. Chen, C. T. Lin, and B. Keimer, cond-mat/0309186 (2004), to be published in J. Phys.: Cond. Mat. (2004).

[39] M. Johnsson, K. W. Tørnroos, F. Mila, and P. Millet, Chem. Mater. **12**, 2853 (2000).

[40] H. H. Klauss, A. Amato, M. Johnsson, and P. Lemmens, unpublished (2003).

[41] W. Brenig, Phys. Rev. B **56**, 2551 (1997).

[42] W. Brenig and K. W. Becker, Phys. Rev. B **64**, 214413 (2001).

[43] W. Brenig, K. W. Becker, and P. Lemmens, Physica **B 312**, 594 (2002).

[44] B. Lake, D. A. Tennant, and S. E. Nagler, Phys. Rev. B **85**, 832 (2000).

[45] M. Enderle, Z. Tun, W. J. L. Buyers, and M. Steiner, Phys. Rev. **B 59**, 4235 (1999).

[46] A. Zheludev, M. Kenzelmann, S. Raymond, T. Masuda, K. Uchinokura, and S.-H. Lee, Phys. Rev. B **65**, 014402 (2002).

[47] E. Ya. Sherman, P. Lemmens, B. Busse, A. Oosawa, and H. Tanaka, Phys. Rev. Lett. **91**, 057201 (2003).

[48] E. Ya. Sherman, M. Fischer, P. Lemmens, P. H. M. van Loosdrecht, and G. Gʉntherodt, Europhys. Lett. **48**, 648 (1999).

[49] O. A. Starykh, M. E. Zhitomirsky, D. I. Khomskii, R. R. P. Singh, and K. Ueda, Phys. Rev. Lett. **77**, 2558 (1996).

[50] Y. Q. Li, M. Ma, D. N. Shi, and F. C. Zhang, Phys. Rev. Lett. **81**, 3527 (1998).

[51] Y. Yamashita, N. Shibata, and K. Ueda, J. Phys. Soc. Jpn. **69**, 242 (2000).

[52] S. K. Pati and D. I. Khomskii R. R. P. Singh, Phys. Rev. Lett. **81**, 5406 (1998).

[53] A K. Koleshuk, H.-J. Mikeska, and U. Schollwœck, Phys. Rev. B **63**, 064418 (2001).

[54] K. Penc, M. Mambrini, P. Fazekas, and F. Mila, Phys. Rev. **B 68**, 012408 (2003).

[55] P. Lemmens, K.-Y. Choi, G. Caimi, L. Degiorgi, N. N. Kovaleva, A. Seidel, and F. C. Chou, cond-mat/0307502 (2003).

[56] M. Isobe and Yu. Ueda, Journ. Phys. Soc. Jpn. **71**, 1848 (2002).

[57] A. Seidel, C. A. Marianetti, F. C. Chou, G. Ceder, and P. A. Lee, Phys. Rev. B **67**, 020405 (2003).

[58] M. Isobe, E. Ninomiya, A. V. Vasil'ev, and Yu. Ueda, Jour. Phys. Soc. Jpn. **71**, 1423 (2002).

[59] R. J. Beynon and J. A. Wilson, J. Phys. Cond. Mat. **5**, 1983 (1993).

[60] G. Caimi, L. Degiorgi, N. N. Kovaleva, P. Lemmens, and F. C. Chou, cond-mat/0308273 (2003).

[61] T. Imai and F. C. Chou, cond-mat/0301425 (2003).

[62] Y. S. Lee, E. Abel, and F. C. Chou, private communication (2003).

[63] J. W. Bray, L. V. Iterrante, I. S. Jacobs, and J. C. Bonner, in *Extended Linear Chain Compounds*, edited by J. S. Miller (Plenum Press, New York, 1983), Chap. 7, pp. 353–415.

GIANT PHONON SOFTENING IN FERROMAGNETIC $LAMNO_{3+\delta}$

Yu.G. Pashkevich
A.A.Galkin Donetsk Phystech NASU, 83114 Donetsk, Ukraine

V.P. Gnezdilov
B.I. Verkin Inst. for Low Temp. Physics NASU, 61103 Kharkov, Ukraine

P. Lemmens
Max-Planck-Institut für Festkörperforschung, 70569 Stuttgart, Germany

K.-Y. Choi and G. Güntherodt
2. Physikalisches Institut, RWTH Aachen, 52056 Aachen, Germany

A.V. Yeremenko
B.I. Verkin Inst. for Low Temp. Physics NASU, 61103 Kharkov, Ukraine

S.N. Barilo, S.V. Shiryaev and A.G. Soldatov
Institute of Physics of Solids & Semiconductors, Academy of Sciences, 220072 Minsk, Belarus

Abstract High quality single crystals of $LaMnO_{3+\delta}$ with δ =0.071, 0.085, 0.092, 0.097, 0.125 that extend from antiferromagnetic insulating (δ = 0.071, T_N=128 K) to ferromagnetic metallic state (δ =0.125, T_C=248 K) have been investigated by polarized Raman light scattering. A giant softening up to 30 cm^{-1} of the 490- and 620-cm^{-1} phonon modes has been observed below the Curie temperature. We interpret this phenomenon as a manifestation of an orbital fluctuating state which exists in a wide temperature range in ferromagnetic $LaMnO_{3+\delta}$.

Keywords: manganites, Raman light scattering, orbital degrees of freedom

E. C. Faulques et al. (eds.), Spectroscopy of Emerging Materials, 185–194.

Introduction

Some well known materials become emergent due to a manifestation of an unusual degrees of freedom. Two regime of conductivity presented in manganese oxides drastically changed the state of orbital subsystem from orbital liquid state in metallic phase to orbital ordered state in insulating phase. The role and state of orbitals at an intermediate regime of doping remains unclear. Raman light scattering (RLS) could be a powerful spectroscopic tool for investigation of orbital subsystem via its interconnection with lattice, electronic and magnetic degrees of freedom.

The low doped manganese oxide compounds $La_{1-x}Sr_xMnO_3$ ($0.11 \leq x \leq 0.17$) and $LaMnO_{3+\delta}$ ($0.075 \leq \delta \leq 0.15$) unambiguously belong to emergent materials as natural model systems which show a metal-insulator phase transition from the ferromagnetic metallic (FM) to the ferromagnetic insulating (FI) states under temperature decrease [1–5]. The resistivity of these compounds tends to drop or at least to be flatness just below the Curie temperature T_C with a following sharp upturn at lower temperatures [2]. Such a behavior points to the emergence of some kind of charge order (CO) that stabilizes a ferromagnetic but insulating state.

The evolution of the orbital subsystem in these compounds as function of temperature is of similar interest [6]. It was found that in $La_{0.88}Sr_{0.12}MnO_3$ orbital degrees of freedom play a decisive role in FM/FI transition enforcing ferromagnetic superexchange (SE) interaction below orbital ordering (OO) through spin-orbital coupling [1, 7]. One can expect that the orbital subsystem changes from orbital disordered state in the paramagnetic phase just above T_C to the orbital ordered state in FI phase. In the intermediate FM phase orbitals are strongly fluctuating and this dynamic orbital disordered state appears exactly below T_C [8]. The relatively high absolute values of resistivity in FM state of low doped $La_{1-x}Sr_xMnO_3$ [2] could be interpreted as a manifestation of diffuse scattering of charges on orbital fluctuations [6, 8, 9]. However, there are no reasons for a coincidence of charge - T_{CO} and orbital-T_{OO} order temperatures at low doping. Thus, in spite of charge (hole) order, orbital subsystem may remain in a fluctuating state and orbital order may occur at lower temperatures far below T_{CO}.

We obtained evidence for orbital fluctuations in the ferromagnetic insulate phase in the oxygen doped manganites $LaMnO_{3+\delta}$ with help of Raman light scattering technique. We argue that a giant softening of high frequency (HF) phonons below T_C, which is smooth and does not show saturation behavior under temperature decrease, is inspired by orbital fluctuations.

Table 1. O ($c \leq b/\sqrt{2} < a$) and O' ($b/\sqrt{2} < c < a$) orthorhombic phases have both Pnma space group symmetry. R is the rhombohedral phase with R$\bar{3}$c space group symmetry.

Sample	Magnetic order	Critical temperature	$V_{f.u.}$(Å^3) T =300 K	$3+\delta$	Crystal structure
M1	AFM	T_N= 128 *K*	59.73	3.071	O'
M2	FM	T_C= 148 *K*	59.54	3.085	O'
M3	FM	T_C= 178 *K*	59.45	3.092	O
M4	FM	T_C= 186 *K*	59.41	3.096	O or R
M5	FM	T_C= 248 *K*	59.06	3.125	R

1. Experimental

$LaMnO_{3+\delta}$ single crystals were grown by electrolysis of a melt obtained from a mixtures of Cs_2MoO_4 and MoO_3 of the molar ratio 2.2/1 to which MnO and La_2O_3 were added. This is some modification of the growing method given by McCarrol *et al.* [10]. The subsequent crystal growth was performed with an average current density of 5-10 mA/cm^2 during 80-100 hours in the temperature range 830-1170 °C. The true crystallographic formula of the studied series is $La_{1-x}Mn_{1-y}O_3$. The lowering of the melt temperature leads to an increase of the level of cation vacancies $3/2(x+y) \approx \delta$. The crystals have a cubic-like habit with a size up to 2-3 mm and do not contain twins. The latter property allows to observe anisotropic magnetic properties in FM/FI states along three different crystallographic axes [11].

Samples were characterized by X-ray diffraction, magnetic susceptibility and chemical analysis with some results summarized in Table 1. The electrical resistivity measurements were made down to 80 K using a four-probe method. Raman scattering experiments used the excitation line $\lambda = 514.5$ nm of an Ar^+ laser in a quasi-backscattering geometry. The laser power of 5 mW was focused to a 0.1 mm diameter spot on the (010) surface. The averaged laser power density amounts to $\sim 6 \cdot 10^5$ W/m^2 which is much less compared to earlier Raman studies in manganites [12–15].

2. Results and Discussion

Fig. 1 displays the temperature- and doping-dependence of the resistivity of samples M1 - M5. The resistivity of the antiferromagnetic (AF) sample (M1) exhibits an insulating behavior with a kink near the Néel temperature T_N. Our ferromagnetic (FM) single crystals samples show clear resemblance in resistivity behavior with $La_{1-x}Sr_xMnO_3$ ones in the range $0.10 \leq x \leq 0.14$ [2]. Upon cooling their resistivity increases up

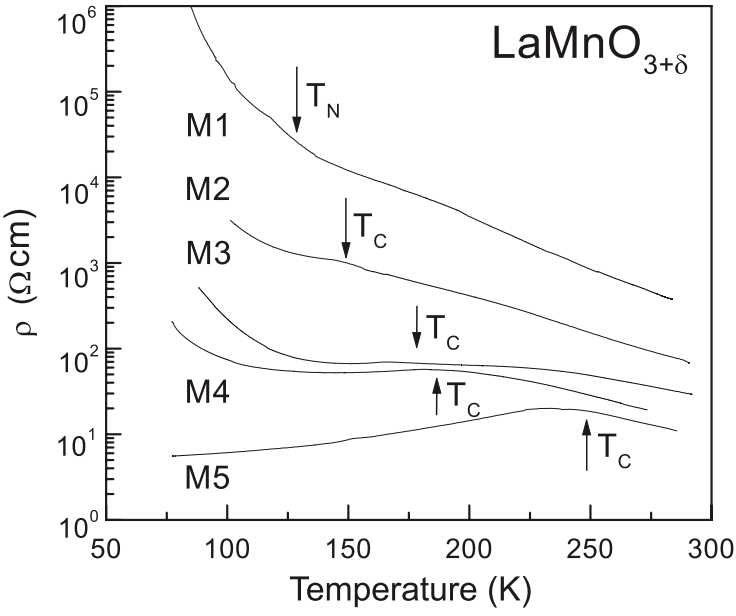

Figure 1. Resistivity of $LaMnO_{3+\delta}$ as a function of temperature and doping.

to the Curie temperature T_c, then becomes flat and finally exhibits a strong upturn when further lowering the temperature. Such a behavior points to the formation of some kind of charge ordering and/or possible orbital ordering which give rise to a low-temperature ferromagnetic insulating state in the ferromagnetic metallic phase. Due to this similarity the lightly doped manganites $La_{1-x}Sr_xMnO_3$ (LSMO) ($0.10 \leq x \leq 0.14$) can be considered as a counterpart of the present study [1–3]. In particular, in LSMO with x=0.12 the orbital degrees of freedom play a decisive role in the FM/FI transition enhancing the ferromagnetic superexchange interaction toward low temperature due to spin-orbital coupling [16–1, 7]. This leads to a stabilization of the orbital ordered state in the FI phase [8]. In the FM phase the relatively high resistivity is ascribed to diffuse scattering on orbital fluctuations [8, 9, 6]. However, *a priori* we have no reasons to believe that charge ordering must be accompanied by orbital ordering in such lightly doped LSMO and $LaMnO_{3+\delta}$. Thus, despite charge ordering, the orbital state can still be in a fluctuating state and orbital ordering may occur far below the charge ordering temperature.

Let us look at the temperature- and doping-dependence of the Raman spectra of two representative samples (M1 and M5) in Fig. 2. At room temperature we observed three pronounced phonon modes at 270,

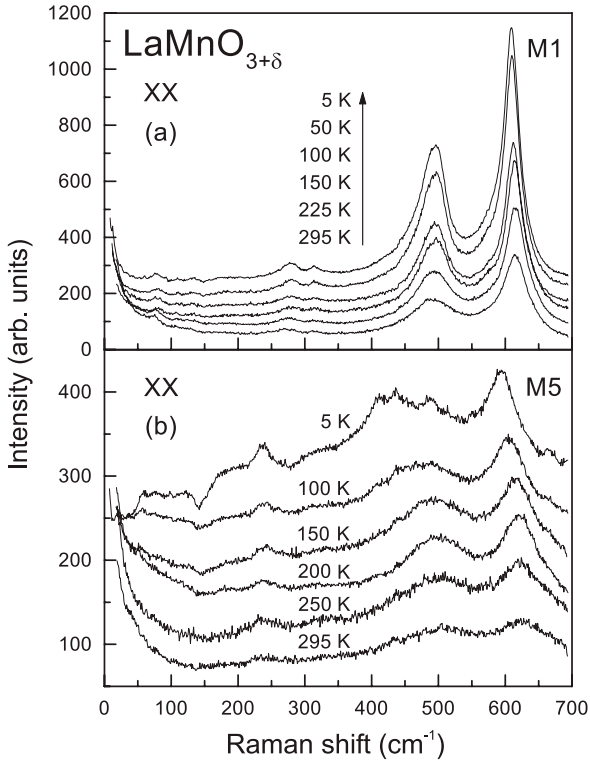

Figure 2. Polarized Raman spectra at different temperatures for (a) an antiferromagnetic sample (M1, δ =0.071) and (b) a ferromagnetic sample (M5, δ = 0.125).

490, and 620 cm^{-1} in the M1 sample. These modes are much weaker in the M5 sample. Symmetry-forbidden Raman scattering in manganites becomes allowed due to lattice distortions leading to a deviation from cubic perovskite symmetry. Therefore the pronounced Mn-O bond stretching modes at 490 and 620 cm^{-1} become weaker with increasing doping δ due to a weakening of Jahn-Teller distortions. In spite of the different doping level, however, all FM samples (M2 - M5) exhibit similar phonon spectra with a detailed fine structure appearing for T<100 K and frequencies ω <500 cm^{-1} as shown in Fig. 2(b) and 3(a). The temperature evolution of these excitations is related to the strong upturn in the resistivity toward low temperatures and indicates the nucleation of the charge ordered state. Further evidence for charge ordering and an increase of lattice distortions toward low temperatures is provided by the temperature dependence of the integrated intensity of the 620-cm^{-1} mode for samples M1 - M5 in Fig. 3b. This dependence is similar to that of the resistivity (Fig. 1).

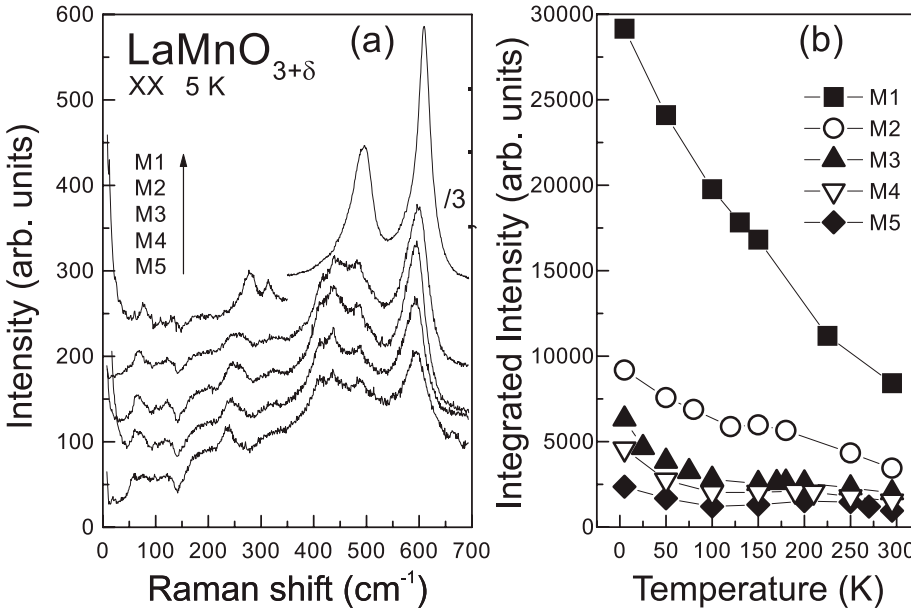

Figure 3. (a) Raman spectra at T=5 K of samples with different doping levels. (b) Temperature dependence of integrated intensity of the 620-cm^{-1} mode for all samples.

The most salient features of this study are evident in the temperature dependence of the 490- and 620-cm^{-1} modes as shown in Fig. 4. The moderate softening of the 620-cm^{-1} mode and respective hardening of the 490-cm^{-1} mode in the AF (M1) sample turns over to a giant softening of both modes by 20 to 30 cm^{-1} in all ferromagnetic samples below T_c. Please note that the softening in the ferromagnetic samples is increasing from M2 to M5 and does not scale with the upturn in the resistivity. This implies that the softening is not induced by a special type of charge ordering. Apparently, the onset of the softening starts around T_c. Furthermore, the phonon frequencies soften continuously without any obvious saturation or other anomalies down to the lowest temperatures. Magnetic ordering may lead to phonon anomalies proportional to the square of the magnetic moment of the magnetic ions [17] and should show a saturation at low temperatures. This is indeed observed for the 490-cm^{-1} and 620-cm^{-1} mode in antiferromagnetic $LaMnO_3$ (M1) for $T<T_N$ [14, 15]. We conclude that the main mechanism for the continuous and smooth softening observed here is not of magnetic origin.

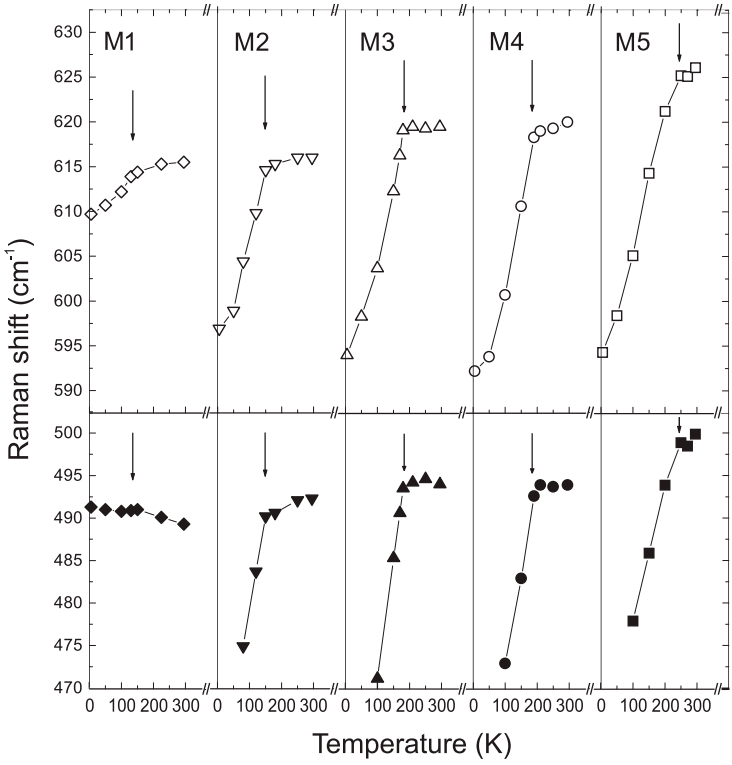

Figure 4. Temperature dependence of peak position of Mn-O stretching modes. Upper (lower) panel for the breathing mode at 620 cm^{-1} (Jahn-Teller mode at 490 cm^{-1}). Arrows indicate the magnetic ordering temperature and the lines are guides to the eye.

An alternative model for phonon anomalies is based on electron correlation effects. The transition from a FM to a FI implies that double-exchange is replaced by superexchange interaction. This results in an increase of Mn-O hybridization. In other words, the covalency is increasing due to the suppressed double exchange and reduced hopping rate with decreasing temperatures [18]. The reduced average charge of the oxygen ions leads to a lowering of phonon frequencies which involve Mn-O modes. In our experimental data, however, the observed softening continues to increase with δ despite the increasing dominance of double exchange over superexchange with increasing δ.

A probably more relevant mechanism for a large phonon softening in ferromagnetic manganites relies on a coupling of phonons to orbital degrees of freedom [19, 8, 9]. Model calculations in Refs.[19, 9] yield a renormalization of phonon frequencies in the orbital ordered phase

as a function of the symmetry of orbital order and the strength of the Jahn-Teller coupling constant. The observed softening is initiated below T_c in the orbital fluctuating state and should finally saturate if orbital ordering occurs. In the FM state such a contribution competes with the DE contribution [20] and possibly, may exceed it. Here it is worth mentioning that the pure metallic phase of $La_{0.725}Ca_{0.275}MnO_3$ and $Pr_{0.75}Sr_{0.25}MnO_3$ shows a moderate softening of the phonons for $T<T_c$ [21, 22].

A development of phase separation with decreasing temperatures is clearly observed in our spectra. Using Raman scattering lattice distorted regions with a deviation from cubic perovskite symmetry can be detected even if domains with a size comparable to a few lattice constants are involved. This is because phonon spectra are dominated by short range forces. These regions are associated with the insulating and charge ordered phase. The Raman spectra just below T_C are similar to each other and to the spectra of M1 AFM sample as shown in Fig.3(a). This can be interpreted as a presence of some insulating region or regions with a charge hopping rate smaller than the phonon frequencies in the FM phase. One can suppose that these regions become nuclei of the charge ordered FI phase and further demonstrate Raman spectra with phonon fine structure. Despite of different doping microscopic details of charge ordering must therefore be similar.

In summary, our Raman study of the lightly doped manganites $LaMnO_{3+\delta}$ reveals that the orbital ordered state in the AFI phase evolves into an orbital fluctuating state in the FM and even FI phase.

Acknowledgments

We thank J. van den Brink, B. Büchner, M. Braden, G. Khaliulin, D. Khomskii, M. Mostovoy and M.M. Savosta for useful discussions. This work was supported in part by the NATO Grant PST.ARW.979393, and PST.CLG.977766, as well as the Ministry of Education and Science of Ukraine (NATO-Ukraine subprogram).

References

[1] Y. Endoh *et al.*, Phys. Rev. Lett. **82**, 4328 (1999).

[2] B. Dabrowski *et al.*, Phys. Rev. **B 60**, 7006 (1999).

[3] Y. Yamada *et al.*, Phys. Rev. **B 62**, 11600 (2000).

[4] D.E. Cox *et al.*, Phys. Rev. **B 64**, 024431 (2001).

[5] J.-S. Zhou and J.B. Goodenough, Phys. Rev. **B 64**, 024421 (2001).

[6] Y. Tokura and N. Nagaosa, Science **288**, 462 (2000).

[7] S. Okamoto, S. Ishihara, and S. Maekawa, Phys. Rev. **B 61**, 14647 (2000).

[8] S. Ishihara, M. Yamanaka, and N. Nagaosa, Phys. Rev. **B 56**, 6866 (1997).

[9] J. Bała, A. Oleś, G. Sawatzky, Phys. Rev. **B 65**, 184414 (2002).

[10] W.H. McCarrol, K.V. Ramanujachary and M. Greenblatt, J. Solid State Chem. **130**, 327 (1997).

[11] S.N. Barilo, *et al.*, Fiz. Tverd. Tela (St. Petersburg), **45**, 139 (2003) [Physics of the Solid State, **45**, 146 (2003)].

[12] M.N. Iliev, *et al.*, Phys. Rev. **B 57**, 2872 (1998).

[13] S. Yoon *et al.*, Phys. Rev. **B 58**, 2795 (1998).

[14] V.B. Podobedov *et al.*, Phys. Rev. **B 58**, 43 (1998).

[15] E. Granado *et al.*, Phys. Rev. **B 60**, 11879 (1999).

[16] J. v.d. Brink, G. Khaliullin, D. Khomskii, Colossal Magnetoresistive Manganites, ed. T. Chatterji, Kluwer Academic Publishers, Dordrecht, Netherlands and cond-mat/0206053 (2003).

[17] W. Baltensperger and J.S. Helman, Helvetica Phys. Acta **41**, 668 (1968).

[18] J.B. Goodenough, Phys. Rev. **100**, 564 (1955).

[19] J. v.d. Brink, Phys. Rev. Lett. **87**, 217202 (2001).

[20] The DE model combined with an electron-phonon interaction predicts an increase of phonon frequencies below T_c in the FM state. For details we refer to A.J. Millis *et al.*, Phys. Rev. Lett. 74, 5144 (1995) and J.D. Lee *et al.*, Phys. Rev. **B 55**, 12454 (1997).

[21] A.E. Pantoja *et al.*, J.Phys.:Condens. Matter **13**, 3741 (2001)

[22] J-M. Liu *et al.*, J.Phys.:Condens. Matter **14**, L141 (2002)

RAMAN STUDIES OF SINGLE AND POLYCRYSTALLINE COBALTATITES $GdBaCo_2O_{5+\delta}$ WITH δ CLOSE TO 0.5

Yu.G. Pashkevich[1], V.P. Gnezdilov[2], P. Lemmens[3,4], K.-Y. Choi[4], K.V. Lamonova[1], A.A. Gusev[1], G. Güntherodt[4], S.N. Barilo[5], S.V. Shiryaev[5], and G.L. Bychkov[5]

[1]*A.A. Galkin Donetsk Phystech NASU, 83114 Donetsk, Ukraine*

[2]*B.I. Verkin Inst. for Low Temp. Physics NASU, 61164 Kharkov, Ukraine*

[3]*Max Planck Institute for Solid State Research, D-70569 Stuttgart, Germany*

[4]*2. Physikalisches Institut, RWTH Aachen, D-52056 Aachen, Germany*

[5]*Inst. of Physics of Solids & Semiconductors, Academy of Sciences, 220072 Minsk, Belarus*

Abstract: Comparative Raman scattering studies of single crystals $GdBaCo_2O_{5+\delta}$ with $\delta \sim 0.35 \div 0.5$, and polycrystalline $GdBaCo_2O_{5.5\pm0.05}$ in the temperature range 5 - 295 K have been made. $8A_g + 3B_{1g}$ modes in backscattering XX, and XY configuration from polycrystalline and single crystal samples with $\delta \sim 0.5$ have been observed. The Pmmm space group symmetry of $GdBaCo_2O_{5.5}$ has been used as a basic structure. Phonon frequencies have been estimated using a modified Thomas-Fermi electron density calculations and a frozen phonon approach. Intensities and frequency of some A_g and B_{1g} modes show a non-uniform temperature dependence in the temperature range of 100-250 K. This correlates with changes of the magnetic ground states and magnetization previously observed in $GdBaCo_2O_{5.5}$.

Key words: layered cobaltites, Co^{3+} ion spin state, Raman light scattering, phonon excitations

1. INTRODUCTION

The change of spin state of Co^{3+} ions with changing temperature or pressure is an intriguing feature of cobalt-based perovskite compounds represented mainly by $LaCoO_3$. Due to the closeness of the crystal field

E. C. Faulques et al. (eds.), Spectroscopy of Emerging Materials, 195–204.

splitting energy and Hund's coupling the population of Co^{3+} – e_g orbitals can be easily changed [1]. In this very simplified picture, three different spin states are realized: high spin (HS) state ($t_{2g}^4, e_g^2, S=2$), intermediate spin (IS) state ($t_{2g}^5, e_g^1, S=1$), and low spin (LS) state ($t_{2g}^6, e_g^0, S=0$). It was noted, that different spin states correspond to different radii of Co ions or different length of the Co-O bonding and angles in the octahedral oxygen cage in such a way that the radii increase with increasing spin [1, 2]. Thus, one can explain unusual magnetic properties of $LaCoO_3$ by a temperature's lattice shrinking which simply removes magnetic moment from Co-sites at low temperatures [2].

This behavior is not so clearly observed for $RBaCo_2O_{5.5}$ – an emergent material, which belong to a wider family of perovskite-like rare earth layered cobaltites $RBaCo_2O_{5+\delta}$ (R is rare earth ion, $0 \le \delta \le 1$) [3-13]. Co^{3+} ions in the former compounds are distributed on equal footing to closed octahedral CoO_6 coordinations and to open square pyramidal CoO_5 ones [3, 5, 6, 9-11]. Furthermore, Co^{3+} ions occupy non-central positions in the octahedral coordination [3, 5, 6] (see Fig. 1). These circumstances do not allow to directly connect the ion radii with the corresponding spin states in $RBaCo_2O_{5.5}$. Nevertheless, X-ray studies [6, 9-11] have detected changes of lattice parameters at T_{MI} – the transition temperature of a metal-insulator phase transition (T_{MI} =350 K for R= Gd and T_{MI} =340 K for R= Tb). The change in slope of the reciprocal magnetic susceptibility, simultaneously observed at T_{MI}, also evidence a spin-state transition and a connection between the Co spin state and conductivity [5,10, 11].

The magnetic phase diagram of $RBaCo_2O_{5.5}$ is characterized by the onset of ferromagnetic order below T_{MI} that exists in very narrow temperature range $\Delta T \sim 20$ K at $T_C \sim 280$ K for R= Gd, Tb. With decreasing temperatures the ferromagnetic order suddenly changes to antiferromagnetic. A further transformation of magnetic structure to another antiferromagnetic phase has been detected at lower temperatures [12-14]. This structure is rather complicated and there is no consensus on its properties [12-14]. There exists a pronounced Ising-like anisotropy of magnetic moments [15,16] that are directed along the a-axis in this phase. The properties of $RBaCo_2O_{5.5}$ connected with the unknown Co-spin states in pyramidal and octahedral coordinations, actually in the whole temperature range from 400 K to zero, are a subject of a wide and rather controversial discussion in the literature [3-18].

Raman spectroscopy can provide information about subtle changes of spin states through detecting changes in phonon spectra, which in its turn are sensitive to the length and O-Co-O bonding angles. In this paper, we report the first investigation of phonon spectra in single and polycrystalline $GdBaCo_2O_{5+\delta}$ with δ close to 0.5.

2. EXPERIMENTAL

Single crystals of $GdBaCo_2O_{5+\delta}$ layered cobaltites have been grown from a flux melt of an overstoichiometric solution of Gd_2O_3 - BaO - CoO starting oxides [16]. As grown crystals have a tetragonal symmetry (space group P4/mmm) with a well-developed (ab) plane. The crystals were annealed in oxygen flow for several days at 600 °C. This provides an oxygen content δ=0.46±0.03, close to stoichiometric δ=0.5. X-ray studies showed that properly annealed samples posses orthorhombic symmetry (space group Pmmm) with a twinning structure in the (ab) plane [16]. We used for Raman studies an as-grown single crystal of $GdBaCo_2O_{5+\delta}$ with a roughly estimated δ=0.3÷0.4 (Gd1-sample), a polycrystalline $GdBaCo_2O_{5.5\pm0.05}$ (Gd2-sample), and a properly annealed single crystal with $\delta \sim 0.5$ (Gd3-sample). The polycrystalline sample was prepared by standard ceramic techniques with the final heating for 48 h in air at 1100°C followed by a slow cooling to room temperature. It was shown by Maignan *et al.* [5] and confirmed in Refs. [7, 8] that for R = Gd the oxygen content δ under such conditions is close to 0.5. According to X-ray powder diffraction, the sample is well crystallized in a single phase.

Raman spectra were measured on fresh, chemically etched surfaces in quasi-backscattering configuration using a triple DILOR XY spectrometer, a liquid nitrogen cooled CCD detector, and a 514.5-*nm* Ar-ion laser. The laser beam of power level 20 *mW* was focused on an area of 0.1 mm^2 on the mirror-like plane (it was the (*ab*) plane of the single crystals). The measurements were performed in a cryostat with a helium gas atmosphere in the temperature range 5-295 K below temperature of metal-insulator phase transition.

3. RESULTS AND DISCUSSION

The orthorhombic structure of $RBaCo_2O_{5.5}$ is represented by rows of pyramids and octahedral running along the b-axis. [CoO_2]-layers alternate along the c-axis with [BaO]-layers and [$RO_{0.5}$] oxygen half-filled layers. $RBaCo_2O_{5.5}$ has Pmmm space group symmetry and the primitive cell contains two formula units (see Fig.1). Ions occupy the following sites: Ba - 2o (1/2,y,0); Gd - 2p (1/2,*y*,1/2); Co1 - 2r (0, 1/2, z); Co2 - 2q (0,0,*z*); O1 - 1a (0,0,0); O2 - 1e (0, 1/2 ,0); O3 - 1g (0, 1/2, 1/2); O4 - 2s (1/2,0,*z*); O5 - 2t (1/2, 1/2, *z*); O6 - 4u (0,*y*,*z*). Co1 and Co2 are located in octahedral and pyramidal oxygen environment, respectively. O6 from the 4u site share pyramidal and octahedral sites. O4 and O5 connect pyramids and octahedra along the a-axis, respectively. A factor group analysis gives $8A_g + 3B_{1g} + 5B_{2g} + 8B_{3g}$ Raman active phonon modes. In our scattering geometry, just

$8A_g + 3B_{1g}$ should be observed. The temperature evolution of Raman spectra in XX geometry for the properly annealed $GdBaCo_2O_{5.5}$ (Gd3) sample is shown in Fig.2. The X- and Y-axes were taken to be along the a- and b-crystallographic axes, respectively. Due to a twinning in the ab-plane, XX and YY spectra cannot be distinguished from each other. At low temperature, the XX spectra demonstrate more than eight lines.

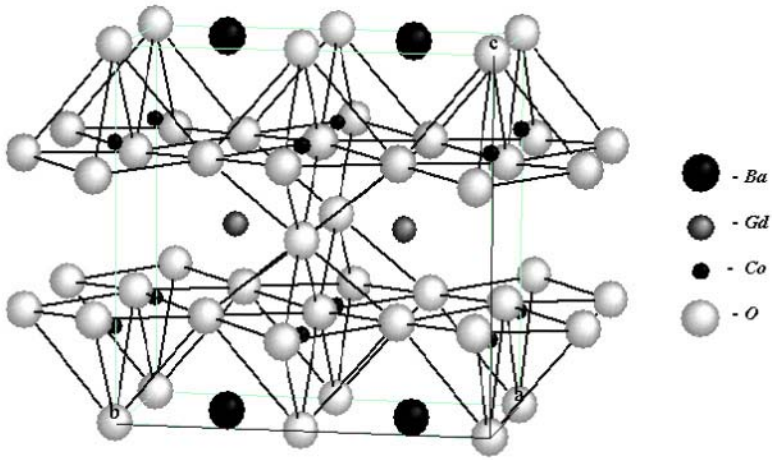

Figure 1. Crystallographic structure $GdBaCo_2O_{5.5}$.

Using a modified Thomas-Fermi electron density calculations and a frozen phonon approach, the lattice dynamic constants have been estimated. This allows us to make a preliminary attribution of A_g lines. Note that oxygen from single site positions do not participate to the A_g modes as well as vibrations of all other ions along a-axis do not contribute to A_g normal coordinates. Five normal coordinates describe vibrations of Co1, Co2, O4, O5, and O6 ions along c-axis, while Gd and Ba heavy ions and O6 ions form A_g modes oscillating along b-axis. According to the eigenvectors value, one can conclude that group of lines at 455, 537, and 596 cm^{-1} are formed primarily by O4, O5, and O6 ions bond stretching motions. A wide band at 320 cm^{-1} consists of two lines with main contribution from Co1, Co2 ions vibrations. The lines at 120 and 182 cm^{-1} are formed by the displacement of heavy ions. Due to a non central position of Co ions in the oxygen environments one expects a strong anharmonicity of their vibrations along the c-axis. Thus, the wide shoulder centered at 676 cm^{-1} can be attributed to a two-phonon repetition of the "Co modes" at 320 cm^{-1}.

The temperature evolution of XX Raman spectra demonstrate a conspicuous redistribution of intensities as well as frequency shifts of the "cobalt" and the high frequency "oxygen" modes in the 100 – 295 K range, while below 100 K our spectra do not show visible modifications. This is

consistent with the expected change of the Co spin states in these temperature regimes.

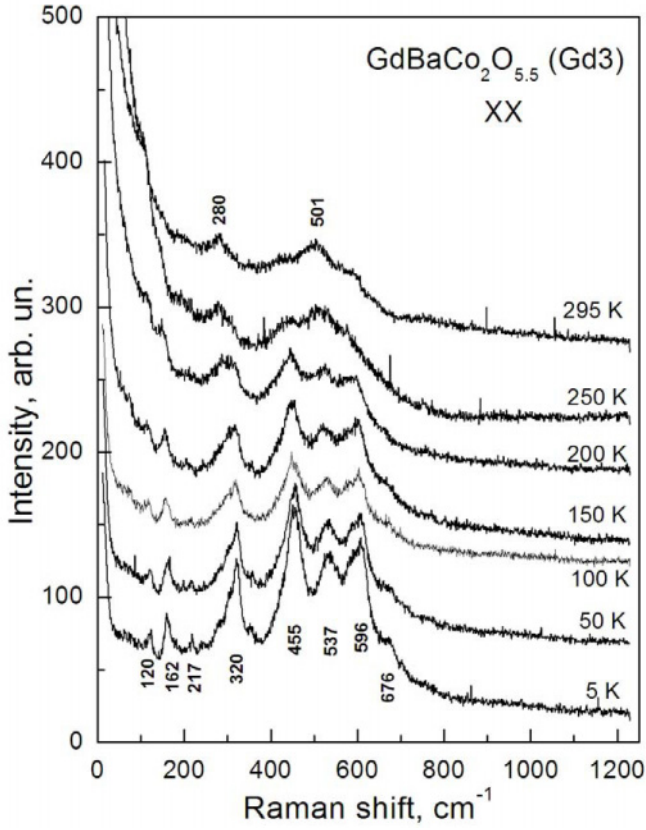

Figure 2. Temperature dependent RS-spectra for *xx* polarization of single crystal $GdBaCo_2O_{5.5}$ (Gd3 sample).

The spectra at 5 K are shown for all available polarizations in Fig.3. As follows from comparison of XX and X'Y' spectra there is a pronounced anisotropy of Raman tensor in ab-plane which can be connected to a strong polarization of phonon modes at 162 and 596 cm^{-1}. The XY spectra consist of $3B_{1g}$ modes, which are formed by motions of heavy ions and pyramidal – octahedral shared oxygen ions along x-direction. We attribute the mode at 307 cm^{-1} to a clockwise and anti-clockwise rotation of pyramids and octahedra along the c-direction. Our preliminary calculations show that a mode at 61 cm^{-1} consists mainly of Gd vibrations.

Raman spectra of an as-grown single crystal of $GdBaCo_2O_{5.3}$ (Gd1) at 5K are given in Fig.4. The intermediate oxygen content between 5.0 and 5.5 is

consistent with randomly distributed oxygen vacancies and a larger number of Co ions in pyramidal coordinations compared to octahedral ones. Therefore, almost all lines, which are characteristic of the Gd3 sample, are smeared out in the Gd1 sample.

A comparison of Raman spectra of the polycrystalline sample Gd2 shown in Fig.5 and the properly annealed sample Gd3 shown in Fig.2 for XX polarization, demonstrates a close similarity of their phonon excitations. This allows to draw conclusions about a proximity of the oxygen content of sample Gd2 and Gd3.

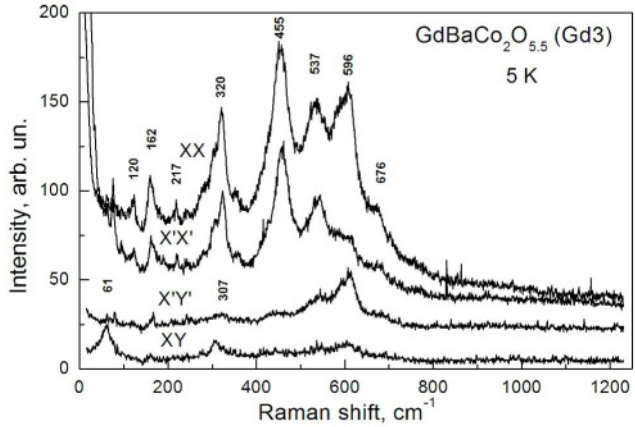

Figure 3. Raman spectra of single crystalline $GdBaCo_2O_{5.5}$ (Gd3) at 5 K.

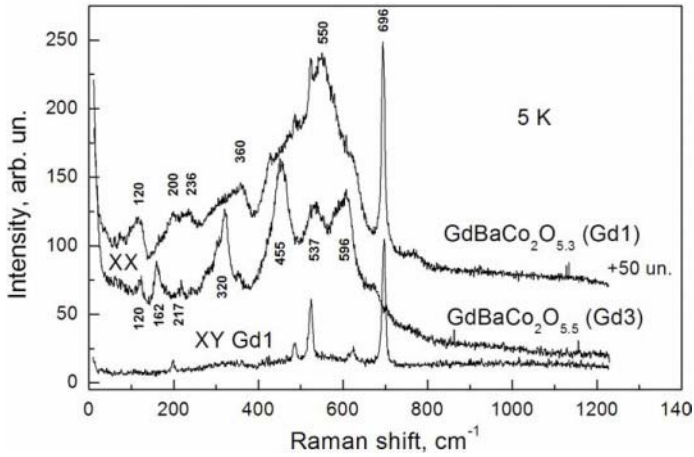

Figure 4. Comparison of Raman spectra of single crystals $GdBaCo_2O_{5.5}$ (Gd3) and $GdBaCo_2O_{5.3}$ (Gd1) at 5 K.

However, the presence of lines at 700 cm^{-1} in the Gd2 sample which are independent on scattering geometry and the existence of the same line at 696 cm^{-1} in the Gd1 spectra both evidence an impurity origin of these excitations. We propose that Co oxides like CoO and Co_2O_3 are present at inter crystallite boundaries and on the surface of the none annealed sample Gd1. Such phases could also be the reason for the luminescence observed in the polycrystalline sample G2 seen in Fig.5 as a linear increase of the scattering background.

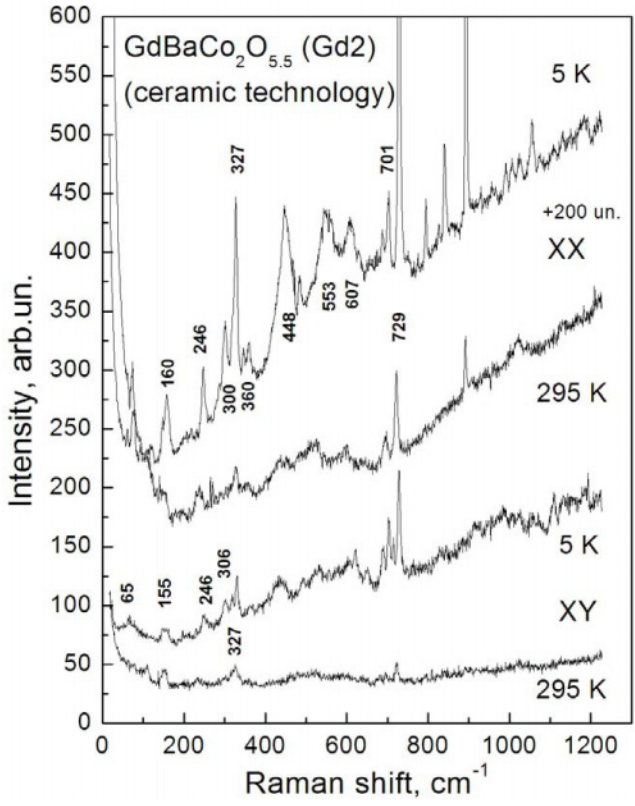

Figure 5. Raman spectra of polycrystalline $GdBaCo_2O_{5.5}$ (Gd2 sample).

The most prominent feature of the diagonal spectra of the Gd2 sample is a remarkable redistribution of Raman scattering intensities of some lines compared with the XX spectra of the single crystal Gd3. To explain this behavior we have to note that vibrations along the c-axis direction are mainly given by A_g lines. It is expected that Raman tensor elements of respective lines should demonstrate a strong anisotropy of the zz

components with respect to the xx, and yy ones, especially for the "cobalt" modes. Thus, the diagonal spectra of the polycrystalline sample are primarily given by scattering from the ZZ geometry.

The temperature dependence of the XY Raman spectra (shown in Fig.6) reveals an anomalous and non-uniform softening of a lowest energy B_{1g} mode from 73 cm^{-1} at 300 K to 62 cm^{-1} at 5 K. We connect this unusual behavior with spin phonon interactions. As previously mentioned, vibrations of Gd ions mainly contribute to this mode. Gd ions remain in the paramagnetic state in the whole temperature range investigated. One can show that all different Co ion orderings lead to nonzero local magnetic fields at the Gd sites. In this way, the induced magnetization of the Gd ions traces the change of magnetic state of the Co subsystem. Besides, Gd ions can be involved in exchange paths between spins of the Co ions from both pyramidal and octahedral sites. Spin phonon coupling includes Gd and Co ions magnetizations and renormalizes the elements of the phonon's dynamic matrix. Therefore, the softening shown in the right hands side of Fig. 6 follows for a certain temperature range a combination of the Co magnetizations in pyramidal and octahedral oxygen coordinations. Therefore, this softening resembles the non-uniform temperature dependence of the macroscopic magnetization observed in $GdBaCo_2O_{5.5}$ [16].

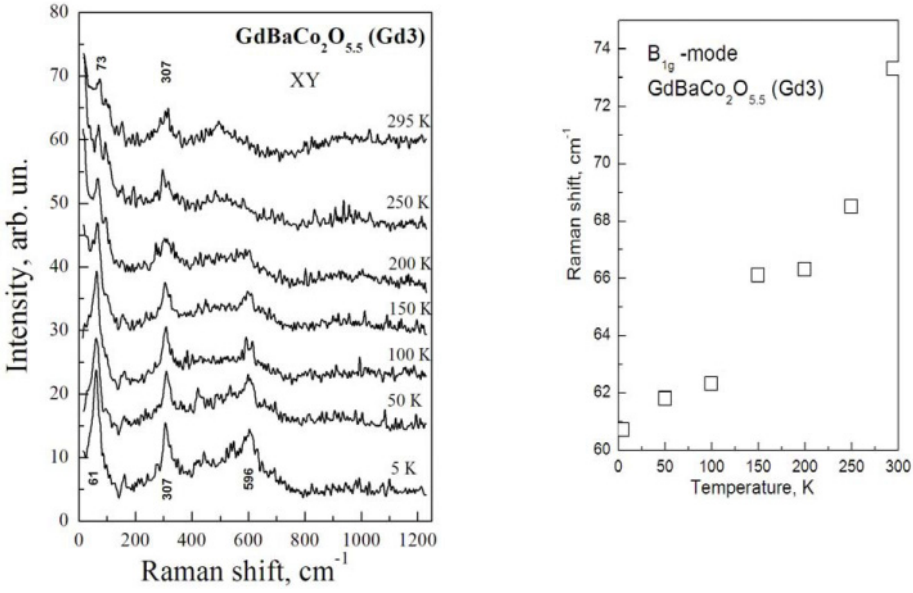

Figure 6. Temperature dependent Raman spectra for *xy* polarization (left) and temperature evolution of peak position of a low-lying B_{1g} mode (right) of single crystal $GdBaCo_2O_{5.5}$ (Gd3 sample).

4. CONCLUSION

We have studied Raman light scattering spectra of rare earth layered cobaltites $GdBaCo_2O_{5+\delta}$ prepared by different techniques with oxygen content close to 0.5. A preliminary assignment of $8A_g$ and $3B_{1g}$ phonon modes has been made for the stoichiometric compound with δ=0.5. Oxygen non-stoichiometry drastically changes the Raman spectra of the as-grown sample, smoothing almost all characteristic lines. The polycrystalline sample surprisingly demonstrates very similar Raman spectra as the properly annealed single crystal in phonon frequency region. We observe a strong anisotropy of the Raman tensors for some lines, which is expected for layered compounds. A strong non-uniform softening of a low-lying B_{1g} mode in $GdBaCo_2O_{5.5}$ has been observed. The temperature dependence of the softening correlates with the magnetization as function of temperature. We conclude, that changes of the spin state of Co^{3+} ions as well as magnetic phase transitions are reflected in the Raman scattering spectra as a modification of frequency and intensities of some characteristic lines.

This work was supported by NATO Collaborative Linkage Grant PST.CLG.977766, NATO Grant PST.ARW.979393, and INTAS Grant 01-0278.

REFERENCES

1. P. M. Raccah and J. B. Goodenough, Phys. Rev. B **155** (1967) 932.
2. K. Asai, A. Yoneda, O. Yokokura, J. M. Tranquada, and G. Shirane, J. Phys. Soc. Jpn. **67** (1998) 290.
3. C. Martin, A. Maignan, D. Pelloquin, N. Nguyen, and B. Raveau, Appl. Phys. Lett. **71 (**1997) 1421.
4. I. O. Troyanchuk, N. V. Kasper, D. D. Khalyavin, H. Szymczak, R. Szymczak, and M. Baran, Phys. Rev. Lett. **80 (**1998) 3380.
5. A. Maignan, C. Martin, D. Pelloquin, N. Nguyen, and B. Raveau, J. Solid State Chem. **142** (1999) 247.
6. Y. Moritomo, T. Akimoto, M. Takeo, A. Machida, E. Nishibori, M. Takata, M. Sakata, K. Ohoyama, and A. Nakamura, Phys. Rev. B **61** (2000) R13325.
7. M. Respaud, C. Frontera, J. L. Garcia-Munoz, M. A. G. Aranda, B. Raquet, J. M. Broto, H. Rakoto, M. Goiran, A. Llobet, and J. Rodriguez-Carvajal, Phys. Rev. B **64** (2001) 214401.
8. W. S. Kim, E. O. Chi, H. S. Choi, N. H. Hur, S. J. Oh, and H. C. Ri, Solid State Comm. **116 (**2000) 609
9. H. Kusuya, A. Machida, Yu. Moritomo, K. Kato, E. Nishibori, M. Takata, M. Sakata, and A. Nakamura, J. Phys. Soc. Jpn. **70**, (2001) 3577.
10. S. Roy, M. Khan, Y. Q. Guo, J. Craig, and N. Ali, Phys. Rev. B **65** (2002) 064437.

11. C. Frontera, J. L. Garcia-Munoz, A. Llobet, and M. A. G. Aranda, Phys. Rev. B **65** (2002) 180405R
12. D. D. Khalyavin, I. O. Troyanchuk, N. V. Kasper, Q. Huang, J. W. Lynn, and H. Szymczak, J. Mater. Res. **17 (**2002) 838.
13. E. Suard, F. Fauth, V. Caignaert, I. Mirebeau, and G. Baldinozzi, Phys. Rev. B **61** (2000) R11871.
14. M. Soda, Y. Yasui, T. Fujita, T. Miyashita, M. Sato, and K. Kakurai, J. Phys. Soc. Jpn. **72** (2003) 1729.
15. A. A. Taskin, A. N. Lavrov, and Y. Ando, Phys. Rev. Lett. **90** (2003) 227201.
16. D. D. Khalyavin, S. N. Barilo, S. V. Shiryaev, G. L. Bychkov, I. O. Troyanchuk, A. Furrer, P. Allenspach, H. Szymczak, and R. Szymczak, Phys. Rev. B **67** (2003) 214421.

Phonons and magnons in $La_{5/3}Sr_{1/3}NiO_4$ single crystal

A Raman scattering study

V. Gnezdilov,[a] V. Kurnosov,[a] Yu. Pashkevich,[b] J. Tranquada,[c]
P. Lemmens,[d,e] K.-Y. Choi,[e] G. Güntherodt,[e] A. Yeremenko,[a] K. Nakajima[f]

[a]) B.I.Verkin Instute for Low Temperature Physics&Engineering NASU, 61103 Kharkov, Ukraine; [b]) A.A.Galkin Donetsk Phystech NASU, 83114 Donetsk, Ukraine; [c]) Brookhaven National Laboratory, Upton, NY 11973, USA; [d]) MPI for Solid State Research, MPI-FKF, D-70569 Stuttgart, Germany; [e]) Physikalisches Institut, RWTH Aachen, 52056 Aachen, Germany; [f]) Neutron Scattering Laboratory ISSP, University of Tokyo, Tokai, Ibaraki, Japan.

Abstract: Electronic correlation effects in $La_{2-x}Sr_xNiO_4$ lead to spontaneous phase separation into microscopic spin/charge stripes with commensurate or incommensurate order. Raman scattering experiments on such single crystalline materials show a rich phenomenology of phonon and magnon anomalies due to the new, self-organized periodicities. These effects are observable as function of temperature.

Key words: Raman scattering, stripe ordering, phonon and two-magnon excitations

1. INTRODUCTION

Stripe ordering of charge and spin in transition-metal oxides has been of intense interest to condensed-matter physics from the theoretical and experimental point of view as an example of a nontrivial ordering phenomenon that originates from the interplay between charge hybridization and interaction. Historically, the first evidence for unusual magnetic correlations was obtained in doped nickel oxide, namely on a single crystal of $La_{1.8}Sr_{0.2}NiO_{3.96}$ in a neutron diffraction study;[1] similar magnetic ordering was also observed in $La_2NiO_{4.125}$.[2] A second set of superlattice peaks, indicative of charge order, was detected in a series of $La_{2-x}Sr_xNiO_{4+\delta}$ samples by electron diffraction.[3] Neutron diffraction studies[4,5] on a crystal of

E. C. Faulques et al. (eds.), Spectroscopy of Emerging Materials, 205–214.

$La_2NiO_{4+\delta}$ with $\delta = 0.125$ were the first to detect the magnetic and charge-order superstructure peaks simultaneously. The observed superstructure provided clear evidence for a highly correlated state in which the dopant-induced holes segregate into periodically spaced stripes that separate antiferromagnetic domains. Later a static form of this modulation has been clearly identified in the system $La_{1.6-x}Nd_{0.4}Sr_xCuO_4$,[6] in which an anomalous suppression of T_c was found for $x \sim 1/8$. A model of a dynamical form of this modulation was exploited for interpreting the spin correlations in $La_{2-x}Sr_xCuO_4$ [7] with $x \neq 1/8$ and $Yba_2Cu_3O_{6+\delta}$.[8] Note, that stripe ordering was observed in some molecular oxides e.g., dmit-based complexes, also.

Before continuing, it may be useful to briefly review some of the basic knowledge, notations, and relevant work. The structure of the parent compound La_2NiO_4 consists of NiO_2 planes separated by La_2O_2 layers. Within a NiO_2 plane, Ni ions form a square lattice with oxygen atoms bridging the nearest-neighbor sites. The unit-cell vectors $\mathbf{a}_1$ and $\mathbf{a}_2$ are parallel to nearest-neighbor Ni-O bonds within the planes, and $\mathbf{a}_3$ is perpendicular to the planes. There are two NiO_2 planes per unit cell, and they are related by the basis vector $\frac{1}{2}\mathbf{a}_1 + \frac{1}{2}\mathbf{a}_2 + \frac{1}{2}\mathbf{a}_3$. For each Ni ion there is one out-of-plane oxygen directly above and one below (along $\mathbf{a}_3$ axis) effectively completing a tetragonally distorted octahedron of oxygen ions. La ions sit above and below the centers of the squares formed by the Ni ions. The simple structure described above is known as the High Temperature Tetragonal (HTT) phase of the K_2NiF_4 structure. Upon cooling, La_2NiO_4 undergoes two structural phase transitions at 650 K and 75 K. Thus, with decreasing temperature, the phase transitions (and space groups) are

HTT ($I4/mmm$) → LTO ($Abma$) → LTT ($P4_2/ncm$).

The NiO_2 planes can be doped with holes both by Sr substitution and by addition of excess oxygen. However, contrary to conventional expectations, the material remains nonmetallic up to quite large hole concentrations.[9-11] The insulating behavior occurs because the dopant-induced holes tend to order themselves in periodically spaced stripes. Nevertheless, these is considerable evidence for one-dimensional charge transport along the charge rows in the static stripe ordered phase both for $La_{2-x}Sr_xNiO_{4+\delta}$ and $La_{2-x-y}Nd_ySr_xCuO_4$ systems.[12,13] These charge stripes run diagonally relative to the square lattice defined by the Ni-O-Ni bonds. In the essentially undoped regions between the stripes the Ni spins can order antiferromagnetically, with the charge stripes acting an antiphase domain walls.[1,2,4,5] The analysis of results on stripe order for a number of doped La_2NiO_4 shows that the charge orders at a higher temperature (T_{co}) than the spins (T_m) and that both the T_{co} and T_m increase systematically with holes concentration increasing.[4] This fact indicates the primary role of charge in driving the ordering.[14]

The average structure of the compositions under study remains in the high-temperature tetragonal (HTT) phase (space group *I*4/*mmm*) down to at least 10 K.[15] The charge and spin order are more easily described in a unit cell size $\sqrt{2}a\times\sqrt{2}a\times c$. Then, the charge density modulation is characterized by the wave vector $\mathbf{g}_{2\epsilon} = (2\epsilon,0,0,)$ and the characteristic wave vector for the spin-density modulation is $\mathbf{g}_{\epsilon} = (1 + \epsilon,0,0,)$ (in real space modulation periods are $a/2\epsilon$ and a/ϵ, respectively). In the first studies of $La_{2-x}Sr_xNiO_4$ it has been suggested that ordering of the dopant-induced holes occurs only commensurately at special values of x, such as 1/2 and 1/3.[3,16] Later it was found that a single crystal with $x = 0.2$, although not at a special value of x, shows commensurate order,[17] albeit with a short in-plane correlation length of ~ 40 Å. In contrast, the stripe order in $La_2NiO_{4+\delta}$[4,5] and $La_{1.775}Sr_{0.225}NiO_4$[15] was found to be incommensurate, with the wave vector varying significantly with temperature. Since the stripes are charged, they will repel each other. As a result, the stripes will arrange themselves so as to maintain the maximum possible spacing, with the constrain that each stripe is centered on a Ni (site-centered stripes) or O (bond-centered stripes) site. For the case of $x = 1/3$, it was shown[18] that in the temperature range $T_{co} > T > T_m$ the domain walls are bond centered. For $T < T_m$ the density of stripes decreases, and the stripes become increasingly site centered. Stripe models for $x = 1/3$ are illustrated in Fig. 1. In the real case, the spins are collinear and rotated on angle φ relatively the stripe direction.[19,20] It was found $\varphi = 53°$ at $T = 14$ K in $La_{5/3}Sr_{1/3}NiO_4$.[21] For the incommensurate stripe order, direct evidence for alternating site- and body-centered stripes within the NiO_2 plane was presented in the transmission-electron-microscopy study of $La_{1.725}Sr_{0.275}NiO_4$ crystal.[22]

Despite very intense studies in the stripe physics field, it is somewhat surprising that there are only a few Raman scattering (RS) studies of this

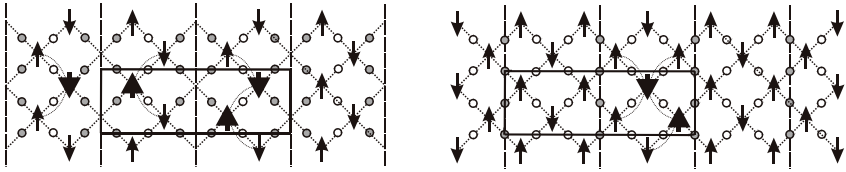

(a) Ni-centered domain walls (b) O-centered domain walls

Fig.1. Stripe models for 1/3 doping.[18] Arrows indicate correlated Ni magnetic moments; circles indicate oxygen sites; filled circles indicate locations of doped holes on oxygen sites. Bold dashed lines indicate positions of domain walls, while bold solid lines outline a magnetic unit cell. The two-magnon Raman process is shown also: bold arrows demonstrate spins on adjacent sites and curved lines indicate broken magnetic bonds.

exotic form of order[12,23-26] and some deficiencies in our knowledge of light scattering in striped phases are now evident. For example, under the discussion is the question of RS from spin waves. Another problem, which has not yet been studied, is a phonon dynamics in the direction perpendicular to the NiO_2-planes.

2. EXPERIMENT

In our RS experiments $La_{2-x}Sr_xNiO_4$ sample with $x = 1/3$ was studied. Single crystal was grown by radio frequency induction melting.[27] Measurements were performed in a backscattering configuration utilizing Raman spectrometer DILOR XY with 5145 Å laser light of 20 mW. The incident laser beam was focused onto 0.1 mm diameter spot on the mirror-like polished and chemically cleaned crystal surface. The spectra were recorded on a liquid nitrogen-cooled CCD. The laboratory coordinate system was locked to the axes of the crystal ($x \| a$, $y \| b$, $z \| c$). The x' and y' axes are rotated by 45° from x and y. The a, b, and c crystallographic axes in the $I4/mmm$ setting were determined by x-ray Laue diffraction. The measurements were performed in an optical cryostat in helium gas atmosphere.

3. RESULTS AND DISCUSSION

For the tetragonal K_2NiF_4 structure, of the total 12 zone center phonon modes, 4 ($2A_{1g} + 2E_g$) are Raman active. Figure 2 shows room temperature RS spectra in $x'x'$ scattering geometry for the sample under study. In this geometry A_{1g} lines are allowed. First of them at around 230 cm^{-1} was assigned to the La stretching mode.[28-31] The second one at around 450 cm^{-1} was identified as the oxygen stretching mode.[28-31] Above the charge ordering temperature all the observed modes are weak; the 230 and especially 450 cm^{-1} modes are broad, indicating strong polaronic effects and inhomogeneous charge

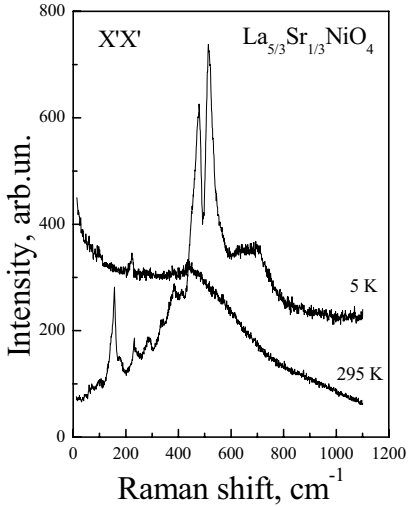

Fig. 2. The $x'x'$ Raman spectra of the single crystal $La_{5/3}Sr_{1/3}NiO_4$ at 5 and 295 K.

distribution.[23,32] Notable changes in the RS spectra are observed below T_{co}. The charge ordering gives rise to formation of a superlattice, multiplies the unit cell size, and lowers the crystal symmetry. It leads to the appearance of new Γ-point Raman-active phonon modes in the spectra. The origin of the extra lines in the stripe-ordered state and their assignment for the sample with $x = 0.225$ were made in Ref. 26.

Now we turn to the measurements in *zz* polarization configuration. For our crystal two lines of A_{1g} symmetry at 232 and 448 cm^{-1} are observed at room temperature as shown in Fig. 3. The disadvantage of the Sr-doped La_2NiO_4 system is that the dopant positions are fixed at relatively high temperature and may be random. At room temperature we do not see any dopant-induced extra features in the low frequency part of the spectra. The line shape of the Ni-O(2) bond stretching mode at 448 cm^{-1} is asymmetric. This asymmetry can be explained by a random distribution of holes on oxygen above T_{co}.

Changes in phonon spectra are observed below T_{co} – new phonon peaks appear. To explain this, we ought to analyze the stripes alignment in the neighboring NiO_2 layers. As it was supposed in earlier publications,[5] the charge stripes align themselves from one layer to the next so as to minimize the long range part of the Coulomb interaction. However, the pinning of the charge stripes to the lattice means that the shift of the stripe pattern from one layer to the next can only occur in increments of the lattice spacing. For our sample, with the stripe spacing of 3/2*a* it is possible to have a perfectly body-centered stacking. Such a symmetric stacking of the layers of stripes

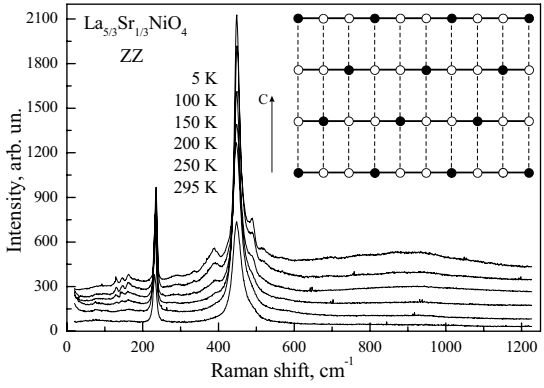

Fig. 3. Temperature dependent Raman spectra for *zz* polarization of single crystal $La_{5/3}Sr_{1/3}NiO_4$. Inset shows an idealized structure of the stripe-ordered phase in the plane perpendicular to the charge domain walls for 1/3 doping. The open circles indicate correlated in the NiO_2 layers spins at Ni^{2+} sites. The filled circles show locations of doped holes on Ni sites.

can lead to forbidden superlattice peaks corresponding to the charge order. Inset on Fig. 3 shows the possible arrangement of the charge stripes in the neighboring layers for the $x = 1/3$ crystal. In this case an additional periodicity along the *c* axis can also lead to forbidden superlattice peaks that is most likely observed in our experiments.

Two relatively strong bands at ~ 730 cm^{-1} and ~ 1120 cm^{-1} were observed in Raman spectra of $La_{2-x}Sr_xNiO_4$ at low temperature in $x'y'$ polarization.[23,24,26] These bands were interpreted as two-magnon scattering.[23,24,26] What was the reason for this attribution? Two-magnon scattering involves a simultaneous excitation of a pair of magnons with equal and opposite momenta **k** on each of the sublattices. In total, excitations from the entire Brillouin zone lead to a band of Raman frequencies that reflects the magnon density of states. Since the density is sharply peaked at the zone-boundary, Raman scattering probes preferentially local antiferromagnetic order. If two spin deviations are created on sites far apart, the excitation frequency is $2(JSz + g\mu_B B_A)$, where z is the number of nearest neighbors, B_A is the effective anisotropy field, and J is the exchange interacting constant. In the case of two spin deviations are created on adjacent sites, the excitation frequency is only $J(2Sz - 1) + 2g\mu_B B_A$ because the presence of the first spin deviation leads to a reduction in the energy required for the second spin deviation. The undoped La_2NiO_4 antiferromagnetic insulator was studied by Sugai *et al*.[33] The B_{1g} spectra exhibits a band peaked at ~ 1640 cm^{-1} that has been assigned to scattering by two-magnons. The estimated J was 240 cm^{-1} on the assumption that the peak energy is $6.7J$ for the $S = 1$ nickel oxide.

For doped $La_{2-x}Sr_xNiO_4$ a band near 1640 cm^{-1} was not observed in Raman experiments at any temperatures. Instead, two broad peaks in $x'y'$ polarization appear in the high frequency region at temperature lowering. Temperature dependent Raman spectra for $x'y'$ polarization of single crystals $La_{5/3}Sr_{1/3}NiO_4$ is shown in Fig. 4. The first band was assigned to the two-magnon excitation within the antiferromagnetic domain and the second one to the excitation across the domain wall[23,26] or to the excitation on the Ni^{2+}-Ni^{3+} bond.[24] Accurate account of the spin-1 system gives peak positions of $\omega_1 \approx 3J$ and $\omega_2 \approx 4J$ for the $x = 1/3$ Ni-centered stripes. Thus, the peak positions for the two-magnon excitations within the antiferromagnetic domain and across the domain wall are $\omega_1 = 720$ cm^{-1} and $\omega_2 = 960$ cm^{-1} for the value of $J = 240$ cm^{-1}, respectively. On the first sight it seems consistent with

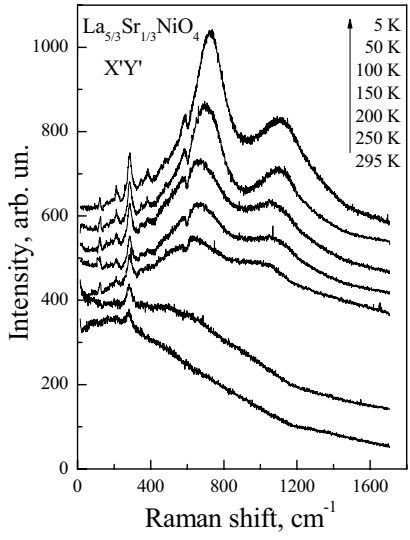

Fig. 4. Temperature dependent Raman spectra for $x'y'$ polarization of $La_{5/3}Sr_{1/3}NiO_4$ single crystal.

experiment.

Not recently this assignment was criticized in Ref. 34. It was disclosed that the band at ~730 cm^{-1} is due to a one-phonon excitation and only the ~1120 cm^{-1} excitation is due to the magnetic excitation related to the stripe structure. The 685 cm^{-1} band, which appears in $La_2NiO_{4.15}$ at temperature lowering, was attributed to phonon excitation[25] because its energy coincides with one-phonon peak in $La_2NiO_{4.0}$. There are some doubts in last motivation by the following reasons:

(i) The bands at ~730 cm^{-1} in $La_{2-x}Sr_xNiO_4$ and at 685 cm^{-1} in $La_2NiO_{4.15}$ are much broader than one-phonon lines observed in lightly doped cuprates[35] and nickelates.[25,33]

(ii) The temperature dependencies of the frequency position and integrated intensity for the ~730 cm^{-1} peak differ from those of the one-phonon peak at 684 cm^{-1} in undoped $La_2NiO_{4.0}$ and of one-phonon peaks at lower frequencies in doped nickelates and are similar to the corresponding dependences for the second wide band at ~ 1120 cm^{-1}.

(iii) In our RS spectra two sharp lines at 580 and 630 cm^{-1} are superposed on the broad band (see Fig. 4). Moreover, the Fano lineshape seen for the 580 cm^{-1} line is clearly seen in Fig. 5. It means that a coherent interaction exist between the two scattering sources. We believe that the observed effect is connected with an interaction between the phonon, which shows a Fano effect and the charge carriers excitations[12] causing the background. However, we do not exclude the possibility of an interaction with the excitation causing the wide band at ~730 cm^{-1}. The probability of the latter assumption is now analyzed theoretically.

In Ref. 34 only one band was attributed to two-magnon scattering in the case that the spin exchange occurs near the diagonal charge domain wall. However, it was examined the case of one domain wall without taking into account the width of antiferromagnetic domain that lead to incorrect calculation of nearest neighbors number.

Not any feature was observed in the single-magnon dispersion that would correlate with the lower-energy two-magnon peak in the inelastic neutron scattering measurements of the stripe-ordered nickelate $La_{1.69}Sr_{0.31}NiO_4$ also.[36]

Next we have tried to analyze the two-magnon scattering theoretically. A simple square plane array of paramagnetic ions was implemented for the calculations. The site-centered model of charge ordering was used, and thus paramagnetic ions inside the domain walls were considered to be frustrated. So, the pattern of spins for approximation of the $La_{5/3}Sr_{1/3}NiO_4$ magnetic structure was similar to those showed in Fig. 1(a) or in Ref. 21. Four exchange integrals between nearest and next-nearest neighbors were taken into account. Two of them are found to be identical to J and J' labeled

exchange integrals introduced in Ref. 21. The exact solution for two-magnon light scattering line shape was obtained with the following restrictions:

(i) zero temperature or temperature much smaller than T_N;
(ii) Heisenberg character of spin exchange;
(iii) small single-ion anisotropy, in comparison to the exchange energy.

Two-magnon band shape was calculated in the exchange approximation of the Moriya theory using real polarizability tensors connected with the respective exchange integrals.

Before the appearance of Ref. 21 values of exchange integrals were unknown. We did only estimates using the value for undoped La_2NiO_4 for an exchange integral which bonds spins inside a single antiferromagnetic domain. By the way, our previous attempts to approximate both bands failed. The calculated shapes cannot be fitted to the experimental spectra at any value of exchange integrals and respective values of polarizability constants we used.

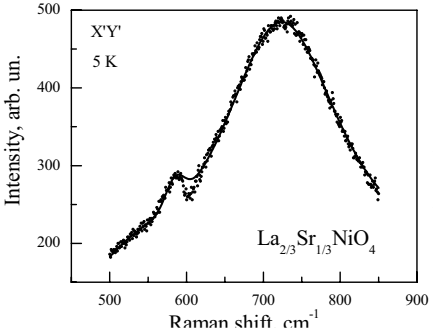

Fig. 5. Fano lineshape of the phonon at 580 cm^{-1}. Solid line represents a fit with Lorentzian lineshapes.

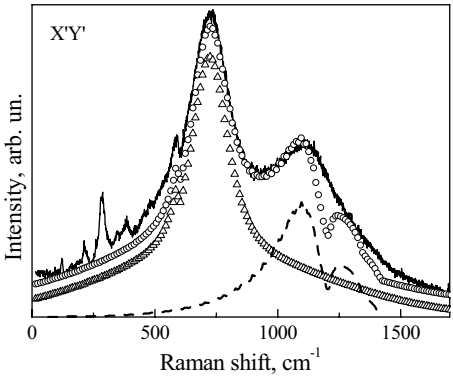

Fig. 6. Theoretical approximation of Raman spectra for *x'y'* polarization of $La_{5/3}Sr_{1/3}NiO_4$ single crystal at T = 5 K. Solid line is the experimental spectrum, dashed line is the calculated two-magnon band, dotted line is a sum of some reasonable spectral shapes to fit line at ~720 cm^{-1} and wide background, open circles represent total fitting spectrum.

Recent experimental data of neutron inelastic scattering[21] have just supplied the needed exchange integral values. Using those we have obtained a reasonably good description of the band at ~1110 cm^{-1} with the following values of the exchange integrals and respective polarizability constants relation: J = 242 cm^{-1} (30 meV), J_2 = 109 cm^{-1} (13.5 meV), P_2/P = -0.75. Our values of exchange integrals are twice higher then the respective values of J and J' from Ref. 21 due to a different kind of summation over the spin pairs in the Hamiltonians. Result of the best fit is shown in Fig. 6. It is clear that narrow decrease of intensity at ~1200 cm^{-1} in the theoretical two-magnon band (dashed curve in Fig. 6) has interference nature and probably is a result of above mentioned restrictions connected with the real type of polarizability

constants. Because of the absorption at the exciting laser wavelength in the RS experiments in $La_{5/3}Sr_{1/3}NiO_4$ it is reasonable to use complex type of these constants. Such calculations are in progress.

These results show evidence for not simple two-magnon nature of the band at ~730 cm^{-1}. Perhaps possible effects connected with the interaction between spin excitations and collective motion of charge domain-walls[21,37] are necessary to be taken into account.

4. CONCLUDING REMARKS

Although the basic nature of the charge and associated spin order in cuprates and nickelates has now been fairly well been established, many questions concerning this order remain to be answered. One of our goals here was to elucidate some problems that are under discussion at present. Unquestionable, Raman scattering will continue to be an essential tools as we try to improve our understanding of stripe ordering and other complex correlation effects.

This work was supported partially by NATO Collaborative Linkage Grant PST.CLG.977766, INTAS Grant 96-0410, STCU Grant 2276, and by Ministry of Education and Science of Ukraine (NATO – Ukraine subprogram).

REFERENCES

1. S.M. Hayden *et al*., Phys. Rev. Lett. **67,** 1061 (1992).
2. K. Yamada *et al*., Physica C **221**, 355 (1994).
3. C.H. Chen, S.-W. Cheong, and A.S. Cooper, Phys. Rev. Lett. **71,** 2461 (1993).
4. J.M. Tranquada, D.J. Buttrey, V. Sachan, J.E. Lorenzo, Phys. Rev. Lett. **73**, 1003 (1994).
5. J.M. Tranquada, J.E.Lorenzo, D.J.Buttrey, V.Sachan, Phys. Rev. B **52**, 3581 (1995).
6. J.M. Tranquada, B.J. Sternlieb, J.D. Axe, Y. Nakamura, S. Uchida, Nature **375**, 561 (1995); J.M. Tranquada, J.D. Axe, N. Ichikawa, Y. Nakamura, S. Uchida, and B. Nachumu, Phys. Rev. B **54**, 7489 (1996).
7. J.D. Axe, H. Moudden, D. Hohlwein, K.M. Mohanty, A.R. Moodenbaugh, and Youwen Xu, Phys. Rev. Lett. **62,** 2751 (1989).
8. P. Dai, H.A. Mook, F. Doğan, Phys. Rev. Lett. **80,** 1738 (1998); H.A. Mook, P. Dai, S.M. Haugen, G. Aeppli, T.G. Perring, and F. Doğan, Nature **395**, 580 (1998).
9. J. Gopalakrishnan, G. Colsmann, and B. Reuter, J. Solid State Chem., **22**, 145 (1977).
10. R.J. Cava *et al*., Phys. Rev. B **43**, 1229 (1991).
11. T. Strangfeld, K. Westerhold, and H. Bach, Physica C **183**, 1 (1993).
12. V.P. Gnezdilov, Yu. G.Pashkevich, A.V. Yeremenko, P. Lemmens, G. Güntherodt, J.M. Tranquada, D.J. Buttrey, K. Nakajima, Low Temp. Phys., **28**, 510 (2002).
13. Takuya Noda, Hiroshi Eisaki, Shin-ichi Uchida, Science **286**, 265 (1999).
14. O. Zachar, S.A. Kivelson, and V.J. Emery, Phys. Rev. B **57**, 1422 (1998).
15. J.M. Tranquada, D.J. Buttrey, V. Sachan, Phys. Rev. B **54**, 12318 (1996).

16. S.-W. Cheong *et al*., Phys. Rev. B **49**, 7088 (1994).
17. V. Sachan *et al*., Phys. Rev. B **53**, 12742 (1995).
18. J.M. Tranquada, P. Wochner, A.R. Moodenbaugh, D.J. Buttrey, Phys. Rev. B **55**, R6113 (1997).
19. H. Yoshizawa *et al*., Phys. Rev. B **61**, R854 (2000).
20. S.-H. Lee *et al*., Phys. Rev. B **63**, 060405 (2001).
21. A.T. Boothroyd *et al*., Phys. Rev. B **67**, 100407(R) (2003).
22. Jianqi Li, Yimei Zhu, J.M. Tranquada, K. Yamada, D.J. Buttrey, Phys. Rev. B **67**, 012404 (2003).
23. G. Blumberg, M.V. Klein, and S.W. Cheong, Phys. Rev. Lett. **80**, 564 (1998).
24. K. Yamamoto, T. Katsufuji, T. Tanabe, and Y. Tokura, Phys. Rev. Lett. **80**, 1493 (1998).
25. S. Sugai, N. Kitamori, S. Hosoya, and K. Yamada, J. Phys. Soc. Jpn. **67**, 2992 (1998).
26. Yu.G. Pashkevich *et al*., Phys. Rev. Lett. **84**, 3919 (2000).
27. D.J. Buttrey, H.R. Harrison, J.M. Honig, and R.R. Schartman, J. Solid State Chem., **54**, 407 (1984).
28. F.E. Bates and J.E. Eldridge, Solid State Comm. **72**, 187 (1989).
29. G. Burns *et al*., Phys. Rev. B **42**, 10777 (1990).
30. A. de Anders *et al*., J. Phys.: Condens. Matter **3**, 3813 (1991).
31. M. Udagawa *et al*., Phys. Rev. B **47**, 11391 (1993).
32. V.I. Anisimov *et al*., Phys. Rev. Lett. **68**, 345 (1992).
33. S. Sugai *et al*., Phys. Rev. B **42**, 1045 (1990); S. Sugai *et al*., Physsica C **185-189**, 895 (1991).
34. S. Sugai and N. Hauamizu, Stripes AIP Conf. Proc. **554**, 84 (2001).
35. S. Sugai, Phys. Rev. B **39**, 4306 (1989).
36. P. Bourges, Y. Sidis, M. Braden, K. Nakajima, and J.M. Tranquada, Phys. Rev. Lett. **90**, 147202 (2003).
37. J. Zaanen *et al*., Phys. Rev. B **53**, 8671 (1996).

High-resolution infrared spectroscopy of low-dimensional magnetic oxides

Marina N. Popova
Institute of Spectroscopy, Russian Academy of Sciences
142190 Troitsk Moscow region, Russia

Abstract: This paper presents a brief review of the work of the author's group on high-resolution Fourier spectroscopy of low-dimensional magnetic oxides. Recent studies of the chain nickelates $(Er_xY_{1-x})_2BaNiO_5$ and the quarter-filled ladder vanadate α'-NaV_2O_5 are described in more detail.

Key words: Fourier-transform spectroscopy, low-dimensional magnetics, oxides.

1. INTRODUCTION

Low-dimensional magnetic systems attracted attention of researches since the time when the quantum theory of solid state was created. The recent discovery of high-T_c superconductivity in copper oxides containing Cu-O chains and/or planes triggered an enormous new wave of both theoretical and experimental efforts in the field of low-dimensional magnetism. In particular, many new cuprates, nickelates, and vanadates containing different kinds of magnetic chains, ladders or planes were synthesized (some of them in the form of single crystals) and studied by a vast arsenal of physical methods.

In this presentation, I shall show that high-resolution Fourier-transform infrared spectroscopy is a useful tool for studying (i) rare-earth containing isulators, low-dimensional magnetics, in particular, and (ii) quasi-one dimensional magnetic systems with the spin-Peierls and related instabilities.

For a rare earth (RE), optical transitions take place within the f-shell, which is well screened by the outer p- and s-shells, and result in extremely

E. C. Faulques et al. (eds.), Spectroscopy of Emerging Materials, 215–228.

narrow spectral lines. Inhomogeneous width of some RE spectral lines can be as small as 0.007 cm^{-1} [1]. The most intense optical transitions, allowed for a free ion, lie in the infrared and occupy broad spectral regions for the majority of RE^{3+} ions. It is advantageous to register such spectra by a Fourier transform spectrometer (FTS) rather than by a classical one. A brief description of the method of Fourier-transform spectroscopy and its principal features can be found, e.g., in Ref [2]. Substantial gain in sensitivity of FTS compared to grating spectrometers permits to study weak spectra of RE ions introduced in a small amount as a probe into a magnetic material, even if the latter is available in a polycrystalline form only. Far-infrared (FIR) study of magnetic compounds that undergo magneto-elastic phase transition is another field where FTS can be successfully applied. High-resolution Fourier-transform spectroscopy offers new possibilities in studying magnetic phase transitions, short-range order, magnetic structures in magnetic insulators.

Review of our work on quasi-two-dimensional cuprates $R_2Cu_2O_5$, quasi-zero-dimensional compounds R_2BaCuO_5 and R_2BaNiO_5 (R=Yb or Lu) was given, e.g., in Ref.[3]. In this paper, our resent studies of the chain system $(Er_xY_{1-x})_2BaNiO_5$, the spin-Peiers cuprate $CuGeO_3$, and the quarter-filled ladder vanadate α'-NaV_2O_5 are briefly described.

2. RARE-EARTH SPECTROSCOPIC PROBE IN A MAGNETIC COMPOUNDS

The use of the RE spectroscopic probe for the studies of magnetic materials is based on a detection of splittings or shifts of spectral lines in the course of a magnetic phase transition. Fig.1 shows, as an example, the scheme of Er^{3+} levels and optical transitions in a magnetic compound. In a magnetically ordered state, magnetic interactions split the Er^{3+} Kramers doublets which results in a splitting of spectral lines. Each line splits into four components maximum. Two of them, originating from the upper sublevel of the split Kramers doublet, diminish in intensity with decreasing the temperature.

3. CHAIN NICKELATES $(Er_XY_{1-X})_2BaNiO_5$

The nickelates R_2BaNiO_5 with R=Y, Nd-Gd, Dy-Tm feature antiferromagnetic S=1 Ni^{2+} chains interconnected by either nonmagnetic (R=Y) or magnetic (R=RE) ions. Recently, they attracted a considerable attention as model systems to study the 1D magnetism, 1D to 3D crossover, and the behavior of the Haldane-gap excitations through this crossover, as

well as the interaction of Haldane-gap modes with single-ion RE excitations (for a recent review, see e.g. Ref. [4] and references cited therein). The gap in the spectrum of magnetic excitations is an intrinsic property of Heisenberg antiferromagnetic (HAF) quantum spin chains with integer value of spins [5]. R_2BaNiO_5 chain compounds differ from the earlier studied inorganic Haldane compounds like $CsNiCl_3$ in such a way that the interchain interaction in them can be changed and controlled by choosing different R-ions or by changing the composition within a given $(R_xY_{1-x})_2BaNiO_5$ system. While Y_2BaNiO_5 does not order magnetically, at least down to 1.7 K, a substitution of a RE for yttrium leads to a 3D AF ordering at temperatures ranging from T_N=12.5 K for Tm_2BaNiO_5 to T_N=61.5 K for Dy_2BaNiO_5 [6]. Er_2BaNiO_5 orders antiferromagnetically at T_N≈34 K. It is the only compound in the family of chain nickelates where the ordered magnetic moments are aligned along the chain direction [7].

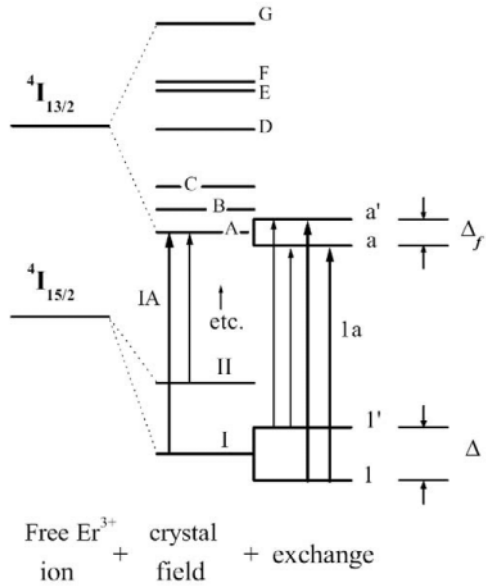

Figure 1. Scheme of Er^{3+} levels and optical transitions in a magnetic crystal. Optical transitions that remain (disappear) at low temperature are shown by thick (thin) lines.

3.1 Optical spectra in a paramagnetic state

Fig.2 shows the absorption spectrum of Er_2BaNiO_5. Optical spectra of all the members of $(Er_xY_{1-x})_2BaNiO_5$ series are very similar for the temperatures above T_N announcing a similarity of the crystal field at the Er site. The analysis of the temperature-dependent spectra of a series of samples with x=0.1, 0.2, 0.4, 0.6, 0.8, and 1.0 enabled us to determine a reliable scheme of

crystal-field sublevels for the seven lowest levels of Er^{3+}. Crystal-field calculations were performed starting from the analysis in the framework of the exchange-charge model [8].

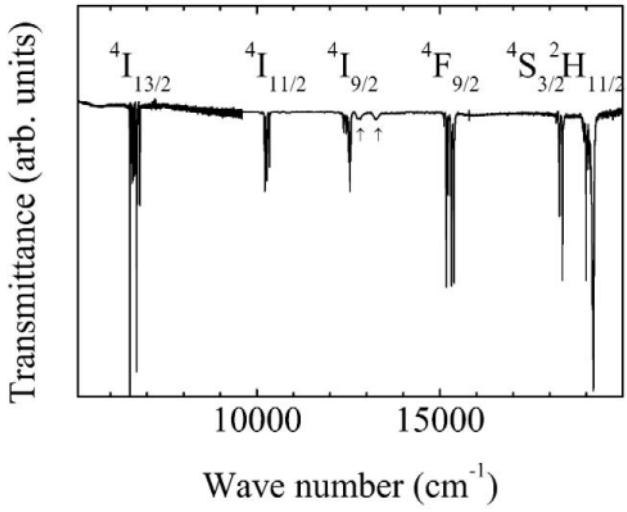

Figure 2. Transmission spectrum of Er_2BaNiO_5. The final states of the Er^{3+} transitions from the ground state $^4I_{15/2}$ are indicated. Arrows point to the lines not related to Er^{3+}.

3.2 Spectroscopic detection of magnetic ordering

Fig.3 demonstrates a splitting of the Er^{3+} spectral line in Er_2BaNiO_5 in the course of a magnetic ordering. The analysis of the spectra at different temperatures and erbium content x revealed the Er^{3+} ground-state splitting Δ and magnetic ordering temperature T_N as functions of x in the $(Er_xY_{1-x})_2BaNiO_5$ system, as shown in Fig.4. The value of T_N = (34 ± 1) K for Er_2BaNiO_5 corresponds well to T_N = 33 K [9] or to T_N = 32 K [7] as determined by neutron scattering experiments. It is worth mentioning that the data for $(Nd_xY_{1-x})_2BaNiO_5$ [10] perfectly fall to the same $T_N(x)/T_N(x=1)$ dependence as the data for $(Er_xY_{1-x})_2BaNiO_5$ (see Fig. 4b). Below T_N, the Er^{3+} spectral lines narrow drastically which points to a simultaneous ordering of both nickel and erbium magnetic subsystems.

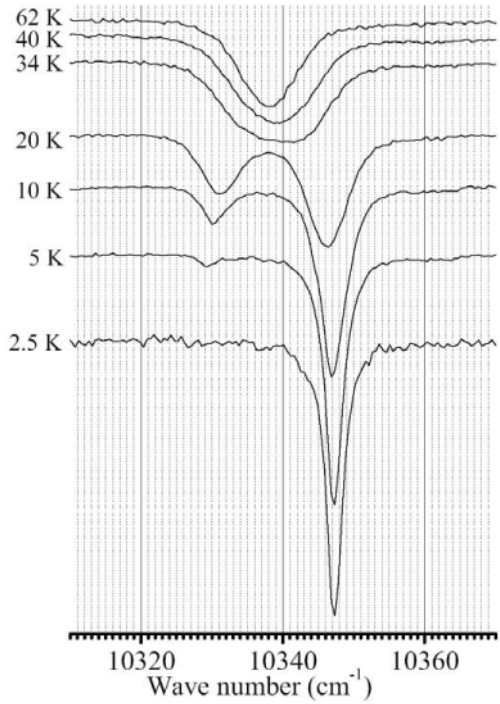

Figure 3. A spectral line of the $^4I_{15/2} \rightarrow {}^4I_{11/2}$ transition in Er_2BaNiO_5 at different temperatures. Line splitting due to magnetic ordering is seen.

3.3 Magnetic susceptibility of Er_2BaNiO_5

Though a simultaneous ordering of both nickel and erbium magnetic moments in Er_2BaNiO_5 at $T_N \approx 34$ K follows unambiguously from neutron scattering [9, 7] and spectroscopic [6] data, the magnetic susceptibility does not show any peculiarity at T_N but demonstrates a sharp maximum at a considerably lower temperature T_m=15 K (see, e.g., [8]).

This maximum does not manifest any magnetic phase transition but is connected with a depopulation of the upper component of the ground Kramers doublet of Er^{3+} split by magnetic interactions in the magnetically ordered state. Such an interpretation followed from a qualitative analysis based on the spectroscopic data [6] and was recently confirmed [8] by the results of the magnetic susceptibility calculations for Er_2BaNiO_5 using the Er^{3+} wave functions obtained from the crystal-field calculations and the experimental fact that the staggered magnetic field at erbium sites in the AF phase is proportional to the spontaneous nickel moment [6].

3.4 Molecular-field approach

Comparison of the spectroscopic data on Er_2BaNiO_5 [6, 8] with the results of neutron diffraction measurements [9] shows that the ground-doublet splitting

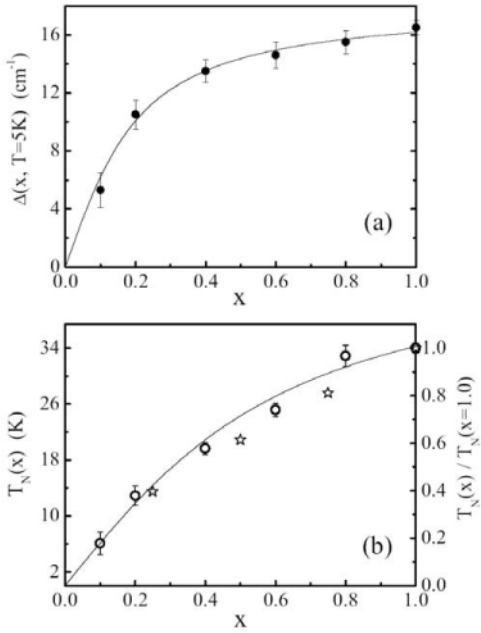

Figure 4. Dependence of the ground-state splitting at 5 K (a) and the Neel temperature (b) on the Er concentration x in $(Er_xY_{1-x})_2BaNiO_5$. The data for $(Nd_xY_{1-x})_2BaNiO_5$ from Ref. [10] are also indicated (by stars) at the $T_N(x)/T_N(1)$ scale ($T_N(1)$=48 K for Nd_2BaNiO_5 [10]). Solid lines are guides for the eye.

$\Delta(T)$ of $Er^{3+}$is proportional to the magnetic moment of the nickel subsystem (see Fig.5). This fact means that the Er^{3+} ground-sate splitting can be considered in the same way as the Zeeman splitting in a magnetic field created by ordered magnetic moments of nickel chains. In other words, a molecular field acting on a single erbium ion

$$B_{Er}(T) = \lambda m_{\mathrm{Ni}}(T) \qquad (1)$$

can be introduced to describe the behavior of the rare-earth magnetic subsystem and the ground-state splitting of Er^{3+} can be written as

$$\Delta(T) = 2m_{Er}(0)B_{Er}(T) = 2\lambda m_{Er}(0)m_{\mathrm{Ni}}(T). \qquad (2)$$

Here λ is the molecular-field constant.

The spectral measurements have shown that the energy of the first exited state in the $^4I_{15/2}$ ground CF manifold of Er^{3+} in Er_2BaNiO_5 is 66 cm^{-1} [8].

Due to the Boltzman factor, the population of this level is only 0.04 at T=30 K. Thus, in a good approximation, only the ground doublet contributes to the magnetic moment $m_{\mathrm{Er}}(T)$ of the Er subsystem at lower temperatures and the temperature dependence of m_{Er} follows the Brillouin function $B_{1/2}(x)=\tanh(x)$:

$$m_{\mathrm{Er}}(T) = m_{\mathrm{Er}}(0)\tanh\frac{\Delta(T)}{2kT}. \qquad (3)$$

Using the experimentally measured $\Delta(T)$ dependence we calculate, according to Eq. (3), the $m_{\mathrm{Er}}(T)$ dependence of the ordered Er magnetic subsystem in Er_2BaNiO_5. A good agreement with $m_{\mathrm{Er}}(T)$ measured by the neutron diffraction method [9] (see Fig. 5) confirms the validity of the used approximation of Eq.(3). A simple concept of the staggered molecular field created by antiferromagnetically ordered nickel magnetic moments of the nickel chain and acting upon a given RE ion was introduced first in Ref.6. It was emphasized there that the nickel magnetic subsystem must be treated in a more complicated way, because of strong Ni-Ni intrachain interactions and the existence of the Haldane gap for S=1 chains [6]. In Ref. 11, the staggered magnetization function for the nickel chain as a whole was introduced to describe the behavior of the nickel magnetic subsystem in the staggered magnetic field created by ordered RE magnetic moments.

Our spectroscopic study of the $(Er_xY_{1-x})_2BaNiO_5$ system ($0.1\le x\le 1$) has shown that positions of CF levels and, hence, CF parameters, wave functions, and g-factors of the Er^{3+} ion practically do not depend on x. It is physically reasonable to assume that the molecular-field constant λ of the Er-Ni interaction also does not depend on x. In this case, Eqs. (2) and (3) are valid for an arbitrary x and the ordered magnetic moments of the Er and Ni magnetic subsystems can be extracted from the experimentally measured ground-state splittings.

Following Ref. [11], we write for the staggered effective magnetic field created at the nickel chain by the staggered ordered erbium magnetic moments

$$B_{Ni}(x,T) = 2\lambda x m_{\mathrm{Er}}(x,T). \qquad (4)$$

In Fig. 6, we plot m_{Ni} versus B_{Ni} for different T and x. A good data collapse for materials with substantially different ordering temperatures supports the concept of the staggered magnetization function for a Haldane spin chain. The response of the nickel chain to the staggered field created by ordered magnetic moments of the Er^{3+} ions situated between the chains in $(Er_xY_{1-x})_2BaNiO_5$ represented by the curve of Fig. 6 has the same character as the staggered magnetization function for the $(Nd_xY_{1-x})_2BaNiO_5$ system derived earlier from neutron scattering data in Ref. [11]. However, the

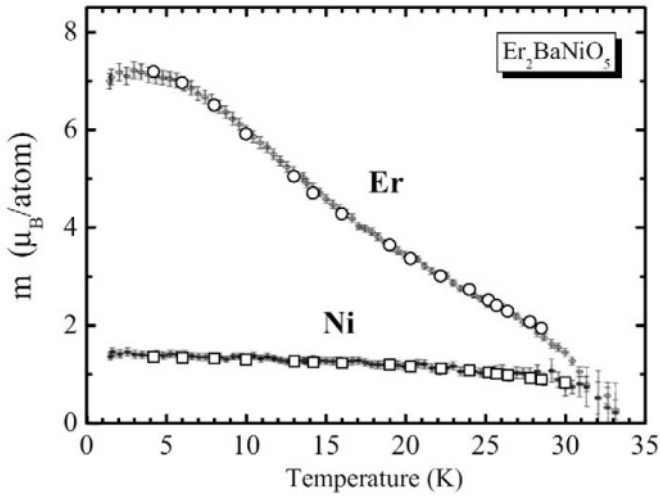

Figure 5. Temperature dependences of the ordered magnetic moments of nickel and erbium subsystems in Er_2BaNiO_5 (open circles) calculated from the measured Er^{3+} ground-state splitting $\Delta(T)$ according to Eqs. (2) and (3) with $m_{Er}(0)=7.24$ μ_B [7], $\lambda=1.81$ T/μ_B. Data from neutron scattering measurements [9, 7] are also shown.

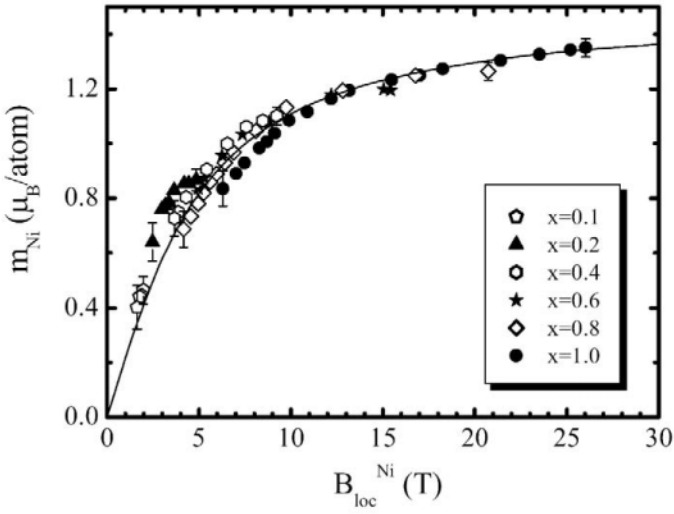

Figure 6. Ordered nickel magnetic moments vs staggered magnetic field directed along the nickel chain. Both quantities are estimated from the spectroscopically measured ground-state splitting of Er^{3+} in $(Er_xY_{1-x})_2BaNiO_5$.

scales for the staggered field B_{Ni} are different for Er and Nd families of the chain nickelates. The reason may be in the difference of their magnetic structures: while the magnetic moments in Er-nickelates are aligned along

the *a*-axis parallel to the direction of nickel chains, the magnetic moments in Nd-nickelates are aligned along the c-axis. A more detailed study of this point is necessary.

4. FAR-INFRARED SIGNATURES OF THE PHASE TRANSITIONS IN $CuGeO_3$ AND α'-NaV_2O_5

For a system of half-integer spin HAF chains interacting with 3D phonon field a gapped state is achieved through the so-called spin-Peierls transition when magnetic atoms shift and dimerize forming nonmagnetic dimers. The magnetic energy gain $\Delta E_m \approx -u_0 \left| l_n u_0 \right|$ (here u_0 is the amplitude of atomic displacements along the chain) may exceed the energy loss due to lattice distortion, $\Delta E_l \approx u_0^2$. The idea of the spin-Peierls transition appeared in 1962 [12], later the theory was built [13]. In real systems, however, a competing interchain coupling leading to the 3D AF ordering usually prevents observation of the spin-Peierls transition. It was observed for the first time in 1975 in the complicated organic compound TTF-$CuS_4C_4(CF_3)_4$ containing Cu^{2+} (S=1/2) chains [14]. This compound did not exist in the form of sufficiently big single crystals and it was difficult to study it. The same was valid for several other organic spin-Peierls compounds discovered later. So it is easy to understand why the first observation (in 1993, Ref. [15]) of the spin-Peierls transition in a relatively simple inorganic compound $CuGeO_3$ caused an enormous interest of researchers. In 1996, α'-NaV_2O_5 has been announced to be the second inorganic spin-Peierls compound [16]. It turned out later that the phase transition in α'-NaV_2O_5 has a more complicated nature and involves charge ordering.

Lattice dimerization in the course of the spin-Peierls-like transition leads to the appearance of new optically active modes folded from a boundary of the Brillouin zone to its center. Charge ordering results in a dielectric anomaly observable in the far-infrared spectral region.

4.1 Folded FIR vibrational modes in $CuGeO_3$

The detailed analysis of both high- and low-temperature structures of $CuGeO_3$ has been performed in many works, see, e.g., Ref [17].

According to the factor-group analysis, there are 18 Raman and 9 IR active new vibrational modes in the low-temperature structure of $CuGeO_3$, below the temperature of the spin-Peierls transition T_c=14 K. While two of the Raman-active folded modes were clearly observed in the very first optical experiments, no traces of the IR folded modes could be found for a long time. We have observed IR folded modes for the first time, measuring

FIR transmission spectra of very thin $CuGeO_3$ crystals by a high-resolution Fourier-transform spectrometer [18].

4.2 Dielectric anomaly at the phase transition in α'-NaV_2O_5

The structure of this vanadate consists of two-leg ladders formed by corner-sharing distorted V_2O_5 pyramids running along the orthorhombic b-axis, with their rungs along the a-axis (see Fig. 7). Neighboring ladders are linked via common edges of the pyramids to form the ab-layers. Na atoms

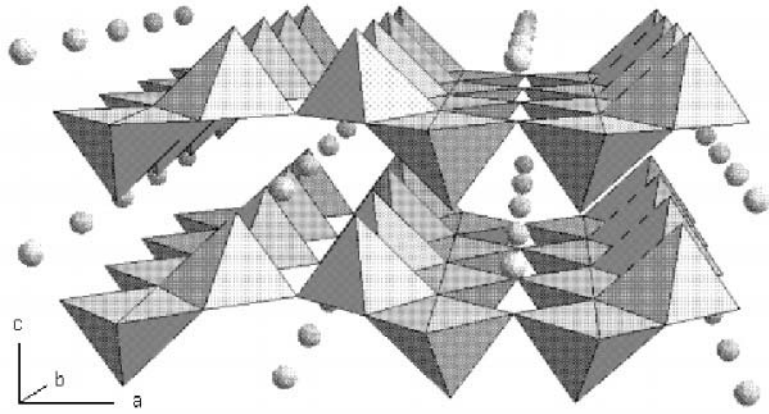

Figure 7. The crystal structure of α'-$NaVO_5$.

lie between the layers. Based on early crystallographic work [19], quasi-one-dimensional magnetic properties of α'-NaV_2O_5 were ascribed to the chains of magnetic V^{4+}(S=1/2) ions running along the b-axis, separated by nonmagnetic V^{5+} chains in the noncentrosymmetric space group $P2_1mn(C^7_{2v})$. The recent X-ray crystallographic study [20] suggested, however, the centrosymmetric space group $Pmmn(D^{13}_{2h})$ for the high-temperature phase of α'-NaV_2O_5, with only one structural position for vanadium. Raman and FIR [21] as well as NMR [22] data also pointed to the centrosymmentric structure. In this structure, vanadium has a formal valence +4.5. As a result, one electron is shared by two V atoms and is actually distributed over a V-O-V molecular orbital at the ladder rung. A quarter-filled ladder along the b-direction is formed, which explains one-dimensional magnetic properties of α'-NaV_2O_5 above T_c [20].

Below T_c, the magnetic susceptibility decreases isotropically, thus showing a spin gap formation, the lattice dimerizes and, as follows from the ^{51}V NMR data [22], a charge ordering into the V^{4+} and V^{5+} states occurs. According to the theoretical consideration of Ref [23], Coulomb repulsion

stabilizes the system of alternating V^{4+}-V^{5+} chains. However, the interaction with lattice deformations can lead to a zigzag charge distribution on each leader [24].

A rearrangement of electrons at the phase transition should cause a dielectric anomaly. It can be studied, in particular, by following the temperature shifts of Fabry-Perot fringes in the FIR spectra of samples with parallel faces. Such a study revealed a distinct anomaly of the antiferroelectric type at the phase transition in α'-NaV_2O_5, which was in agreement with the models assuming the zigzag charge ordering in the ab plane below T_c [25].

A simultaneous study (in the same spectrum) of the transition - induced dielectric anomaly announcing the charge ordering and of the folded modes of the dimerized lattice showed that both charge ordering and structural phase transitions take place at the same temperature T_c=34K [26]. Pretransitional charge fluctuations start, however, at a considerably higher temperature of ~100K [27].

4.3 Transition-induced modes in α'-NaV_2O_5.

Numerous new modes emerge below T_c in the FIR [28-32] and Raman [33-37] spectra of α'-NaV_2O_5. Fig. 8 presents FIR polarized transmittance in a spectral range from 55 to 350 cm^{-1} at temperatures above and below T_c. Arrows show new low-temperature modes. Some of them clearly split into doublets (see inset of Fig 8). The number and polarization properties of all the observed new LT modes in α'-NaV_2O_5 can be reasonably described within the conception of folded vibrational modes of the dimerized Fmm2 crystal structure. Observed FIR doublets and close frequencies in different polarizations are naturally explained by their origin from the Q-point quadruplets folded into the zone center [30].

Three lowest-frequency Raman lines (67, 107, 133 cm^{-1}) that emerge below T_c have been attributed in Refs [35, 36] to magnetic singlet bound states. These lines demonstrated an unusually large broadening, shift, and loss of intensity upon heating and their frequencies were sample-dependent. All these modes were also observed in FIR transmittance, exhibiting the same properties as their Raman counterparts [29, 30]. As an alternative interpretation to magnetic bound state, the concept of folded phonon modes that strongly interact with charge and spin excitations has been suggested in Ref [30].

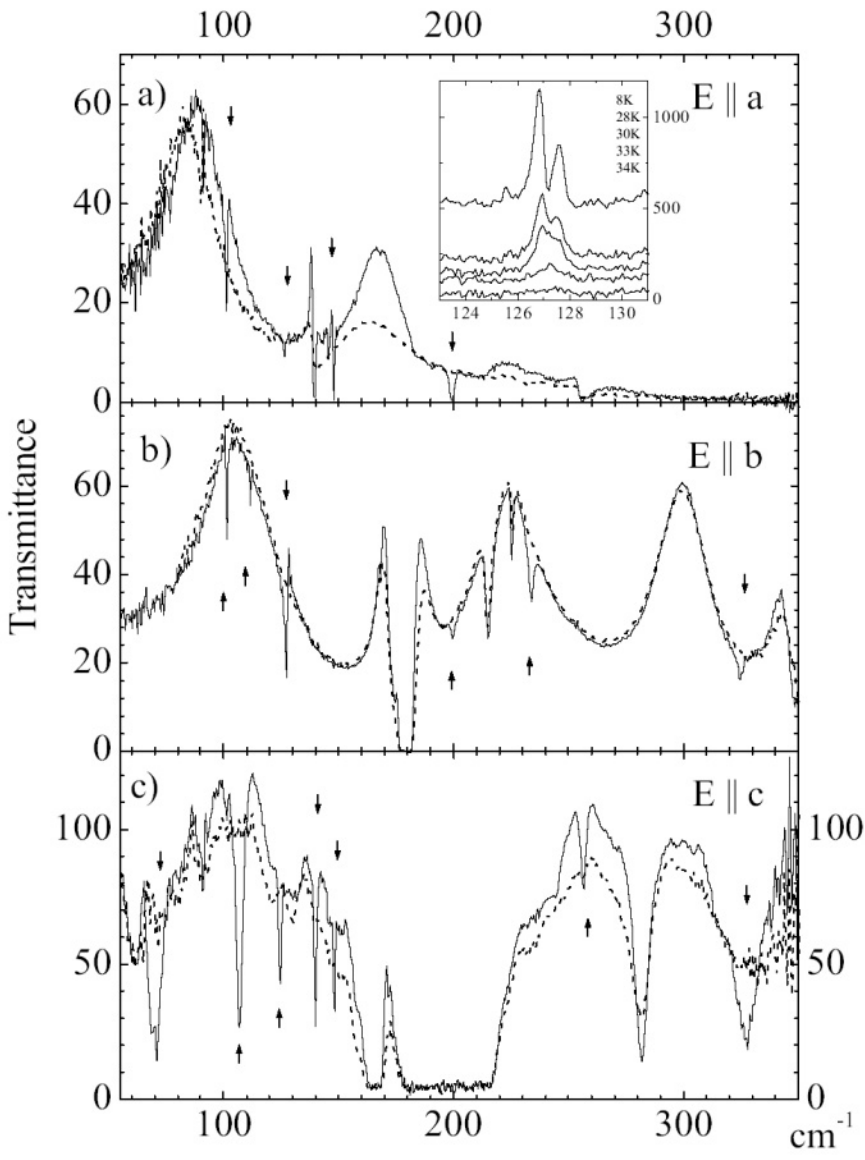

Figure 8. Transmission spectra of α'-$NaVO_5$ at T≈40K>T_C (dashed line) and T=8K<T_C (solid line) in **E**||**a**, **E**||**b**, and **E**||**c** polarizations of the incident light with **k**||**c** [(a) and (b)] and **k**||**a** (c). The sample thicknesses were 14μm [(a) and (b)] and 150μm (c). Arrows show new low-temperature modes below T_C. Inset shows the line near 127cm^{-1} at different temperatures.

ACKNOWLEDGEMENTS

The author would like to emphasize the contribution of her coworkers and students S.A. Klimin, E.P. Chukalina, A.B. Sushkov, S.A. Golubchik, and E.A. Romanov. The cooperation with B.N. Mavrin, B.Z. Malkin, R.Z. Levitin, A.N. Vasil`ev, B.V. Mill, A.I. Smirnov, and E. Antic-Fidancev was of primary importance. Valuable discussions with P.H.M. Van Loosdrecht, M.V. Mostovoy, and D.I. Khomskii are acknowledged. We are grateful to B.V. Mill, M. Isobe, and Y. Ueda for the synthesis and crystal growth. This work was supported in part by the Russian Foundation for Basic Research (grant №01-02-16329), by the Russian Ministry of Science and Technology (contract №40.020.1.1161), by the Russian Academy of Sciences under the Programs for Basic Research, by INTAS, Grant No. 99-0155, and by the RAS-CNRS (France) mutual exchange program (project №12234).

5. REFERENCES

1. N.I. Agladze, M.N. Popova, G.N. Zhizhin, V.J. Egorov, and M.A. Petrova, Phys. Rev. Lett. **66**, 477 (1991).
2. M.N. Popova. High resolution Fourier Transform Spectroscopy: Application to Magnetic Insulators, in: Encyclopedia of Materials: Science and Technology, 2001 Elsevier , p 3786
3. M. N. Popova, J. Alloys Compounds **277**, 142 (1998).
4. A. Zheludev, S. Maslov, T. Yokoo, J. Akimitsu, S. Raymond, S.E. Nagler, and K. Hirota, Phys. Rev. B **61**, 11 601 (2000).
5. F. D. M. Haldane, Phys. Rev. Lett. **50**, 1153 (1983).
6. G.G. Chepurko, Z.A. Kazei, D.A. Kudrjavtsev, R.Z. Levitin, B.V. Mill, M.N. Popova, and V.V. Snegirev, Phys. Lett. A **157**, 81 (1991).
7. E. García-Matres, J.L. Martínez, and J. Rodríguez-Carvajal, Eur. Phys. J. B **24**, 59 (2001).
8. M.N. Popova, S.A. Klimin, E.P. Chukalina, B.Z. Malkin, R.Z. Levitin, B.V. Mill, and E. Antic-Fidancev, Phys.Rev. B **68**, 155103 (2003).
9. J.A. Alonso, J. Amador, J.L. Martínez, I. Rasines, J. Rodríguez-Carvajal, and R. Sáez-Puche, Solid State Commun. **76**, 467 (1990).
10. T. Yokoo, A. Zheludev, M. Nakamura, and J. Akimitsu, Phys. Rev. B **55**, 11516 (1997).
11. T. Yokoo, S.A. Raymond, A. Zheludev, S. Maslov, E. Ressouche, I. Zaliznyak, R. Erwin, M. Nakamura, and J. Akimitsu, Phys. Rev. B **58**, 14424 (1998).
12. H. M. McConnell, R. Lynden-Bell, J. Chem. Phys. **36**, 2393 (1962).
13. E. Pytte, Phys. Rev. B **10**, 2039 (1974).
14. J. W. Bray, H. R. Hart, L. V. Interrante, I. S. Jacobs, J. S. Kasper, G. D. Watkins, S. H. Wee, J. C. Bonner, Phys. Rev. Lett. **35**, 744 (1975).
15. M. Hase, I. Terasaki, K. Uchinokura, Phys. Rev. Lett. **70**, 3651 (1993).
16. M. Isobe and Y. Ueda, J. Phys. Soc. Jap. **65**, 1178 (1996).
17. M. Braden, G.Wilkendorf, J.Lorenzana, M.Aïn, G.J.McIntyre, M.Behruzi, G.Heger, G.Dhalenne, and A.Revcolevschi, Phys. Rev. B **54**, 1105 (1996).

18. M.N. Popova, A.B. Sushkov, S.A. Golubchik, A.N. Vasil'ev, L.I. Leonyuk, Phys. Rev. B **57**, 5040 (1998).
19. A. Carpy and J. Galy, Acta Cryst. B **31**, 1481 (1975).
20. H. Smolinski, C. Gros, W. Weber, U. Peuchert, G. Roth, M. Weiden, and C. Geibel, Phys. Rev. Lett. **80**, 5164 (1998).
21. M.N. Popova, A.B. Sushkov, S.A. Golubchik, B.N. Mavrin, V.N. Denisov, B.Z. Malkin, A.I. Iskhakova, M. Isobe, and Y. Ueda, JETP **88**, 1186-1197 (1999).
22. T. Ohama, H. Yasuoka, M. Isobe, and Y. Ueda, Phys. Rev. B **59**, 3299 (1999).
23. P. Thalmeier and P. Fulde, Europhys. Lett. **44**, 242 (1998).
24. M.V. Mostovoy, and D.I. Khomskii. Solid State Commun. **113**, 159 (2000).
25. A.I. Smirnov, M.N. Popova, A.B. Sushkov, S.A. Golubchik, D.I. Khomskii, M.V. Mostovoy, A.N. Vasil'ev, M. Isobe, and Y. Ueda, Phys. Rev. B **59,** 14546-14551 (1999).
26. M.N. Popova, A.B. Sushkov, E.P. Chukalina, E.A. Romanov, M. Isobe, and Y. Ueda, Physics of the Solid State (Russia), **44**, 8, 1450–1454 (2002).
27. H. Schwenk, S. Zherlitsyn, B. Lüthi, E. Morre, C. Geibel. Phys. Rev. B **60**, 13, 9194 (1999).
28. M.N. Popova, A.B. Sushkov, A.N. Vasil'ev, M. Isobe, and Y. Ueda, JETP Lett. **65**, 743 (1997).
29. M.N. Popova, A.B. Sushkov, S.A. Golubchik, M. Isobe, and Y. Ueda, Physica B **284-286**, 1617 (2000).
30. M.N. Popova, A.B. Sushkov, S.A. Klimin, E.P. Chukalina, B.Z. Malkin, M. Isobe, and Yu. Ueda, Phys. Rev. B **65**, 144303-1 (2002).
31. D. Smirnov, P. Millet, J. Leotin, D. Poilblanc, J. Riera, D. Augier, and P. Hansen, Phys. Rev. B **57**, R11035 (1998).
32. A. Damascelli, D. van der Marel, M. Grüninger, C. Pressura, T.T.M. Palstra, J. Jegoudez, and A. Revcolevschi, Phys. Rev. Lett. **81**, 918 (1998).
33. M. Weiden, R. Hauptmann, C. Geibel, F. Steglich, M. Fisher, P. Lemmens, and G. Güntherodt, Z. Phys. B **103**, 1 (1997).
34. H. Kuroe, H. Seto, J. Sasaki, T. Sekine, M. Isobe, and Y. Ueda, J. Phys. Soc. Japan **67**, 2881 (1998).
35. P. Lemmens, M. Fischer, G. Els, G. Güntherodt, A.S. Mishchenko, M. Weiden, R. Hauptmann, C. Geibel, and F. Steglich, Phys. Rev. B **58**, 14159 (1998).
36. M. Fischer, P. Lemmens, G. Els, G. Güntherodt, E. Ya. Sherman, E. Morre, C. Geibel, and F. Steglich, Phys. Rev. B **60**, 7284 (1999).
37. M.J. Konstantinovic, J.C. Irwin, M. Isobe, and Y. Ueda, Phys. Rev. B **65**, 012404 (2002).

MAGNETIC RESONANCE IN LOW DOPED $Cu_{1-x}M_xGeO_3$ WITH DIFFERENT TYPE OF 3D AFM ORDERING

K. V. Lamonova and Yu. G. Pashkevich
A. A. Galkin Donetsk Phystech NASU, 83114 Donetsk, Ukraine

Abstract: We report a symmetry analysis and a calculation of the frequency - field dependencies of different 3D AFM states for the underdoped $Cu_{1-x}M_xGeO_3$. Our consideration based on the supposition about existence or absence of structural distortions, which result into an alternation of the AFM exchange along magnetic chains. Two types of wave vectors $k_{AF} = (0, 1, 1/2)$ and $k_{SP} = (1/2, 0, 1/2)$ were considered. The existence or absence of displacements of the copper ions does not result in appearance of Dzyaloshinskii-Moriya antisymmetric interaction along chains. However, such an interaction between chains presents in all AFM phases. It is shown that spin wave spectrum contains two acoustical and two exchange branches. Surprisingly, that frequency of exchange mode possesses the same magnitude ~20 $см^{-1}$ as the gap energy of the triplet state. The role of exchange modes for coexisting dimerized and 3D-AFM states has been discussed.

Key words: Magnetic resonance, symmetry analysis, Dzyaloshinskii-Moriya interaction, structural phase transition, 3D AFM ordering, spin-Peierls state.

1. INTRODUCTION

Competing ground states and quantum criticality present a special interest of modern physics of strongly correlated systems and most of emergent materials [1, 2]. The lightly doped $Cu_{1-x}M_xGeO_3$ has demonstrated a competition of a dimerized spin-Peierls (SP) phase and a 3D AFM phase, which replace each other under temperature decrease [3-5]. The ***microscopic mechanism*** of this replacement and phase coexistence (phase separation) could be a subject of magnetic resonance spectroscopy.

The most interesting features of the phase diagram of $Cu_{1-x}M_xGeO_3$ de-

E. C. Faulques et al. (eds.), Spectroscopy of Emerging Materials, 229–238.

velop in a region of the small doping concentration (less than 3%). In this region the 3D AFM ordering realizes on the background of the SP structure distortions (D-AFM). The SP-phase precedes its appearance so that $T_N < T_{SP}$. High level doping (more than 3%) leads to a suppression of SP-distortions and development of a U-AFM phase. Recent studies of the $Cu_{1-x}Mg_xGeO_3$ [6-9] revealed that AFM ordering changes from D-AFM to U-AFM discontinuously in the region of critical concentrations close to $x_0 = 0.027 \pm 0.001$. Such changing is typical for the first order phase transition. The ion magnetization, Néel temperature, the atomic displacements, changes discontinuously.

However, elastic neutron scattering studies show that SP-phase, for instance, in $Cu_{1-x}Si_xGeO_3$ with x less than 1% coexists with the AFM ordering at the temperatures below T_N [3, 10]. Furthermore, in the work [11] an EPR-signal in $Cu_{1-x}Mg_xGeO_3$ was observed at temperatures less than Néel one. Authors considered this fact as a manifestation of more complicated phase composition in the samples, which supposes a small admixture of the paramagnetic phase also. All of this evidences about presence of a complex phase separation in the lightly doped $Cu_{1-x}M_xGeO_3$ in the vicinity of Néel temperature under temperature decrease.

We are going to explore of high frequency properties of all type AFM phases and SP-phase to justify its participation in phase-separated regions. Triplet excitations are representatives of SP-phase and exchange modes of magnetic resonance can serve as fingerprints of AFM order.

It is necessary to make a comment about exchange modes. Onset of 3D AFM order in $Cu_{1-x}M_xGeO_3$ implies intra-chain and inter-chain spin ordering. Thus, four sub-lattices model is a minimal model for description of this type of ordering. The exchange modes of magnetic resonance are an analogue of optic phonons. These modes can appear only if magnetic cell contains more then two magnetic sublattices. Such kinds of excitations were discovered, for instance, in $CuCl_2 \cdot H_2O$ [12] a classical compound of antiferromagnetism in which for the first time in early 50-th were observed antiferromagnetic resonance and spin-flop magnetic phase transition. Spin oscillations of exchange modes violate of the 3D AFM ordering and their gaps define by production of intra- and inter-chain exchange interactions like $(J_bJ_c)^{1/2}$. One can show that such kind of excitations will destroy of boundaries between SP- and AFM-phase if they coexist in the sample.

We provide a symmetry analysis and a calculation of the frequency-field dependencies of the different 3D AFM states for the underdoped $Cu_{1-x}M_xGeO_3$. Our consideration based on the supposition about existence or absence of structural distortions, which result into an alternation of the AFM exchange along magnetic chains. Two types of wave vectors

$k_{AF} = (0,\ 1,\ 1/2)$ and $k_{SP} = (1/2,\ 0,\ 1/2)$ were considered. The existence or absence of displacements of the copper ions does not result in appearance of Dzyaloshinskii-Moriya (DM) antisymmetric interaction along chains. However, such an interaction between chains presents in all AFM phases. It shown that spin wave spectrum contains two acoustical and two exchange branches. In case of orientation AFM vector along chains (in $Cu_{1-x}M_xGeO_3$ with ($M = Si, Mg, Zn$) the magnetic resonance on exchange modes is excited in unusual polarizations - perpendicularly to easy axis. Surprisingly, that frequency of exchange mode possesses a magnitude of order ~600 GHz that coincides with the value of gap energy of the triplet state.

2. SYMMETRY ANALYSIS

The averaged crystallographic symmetry of the $Cu_{1-x}M_xGeO_3$ (M=Zn, Ni) at high temperatures both in a pure, and in a doped state can be described by *Pbmm* space group of symmetry. The primitive cell contains two formula units. The Ge-ions are in the $2f$ -position, and the oxygen ions are distributed in the following way: $2e - O(1)$ and $4j - O(2)$. The magnetic ions of divalent copper Cu^{2+} with the spin $s = 1/2$ possess C_{2h} site-symmetry (Fig.1) and create one-dimensional chains along *c*-axis of orthorhombic crystal, which are bounded by AFM type exchange interaction. The intra-chain exchange integral J_c is greatest, whereas the inter-chain exchange integrals are equal to $J_a = -0.01 J_c$, $J_b = 0.1 J_c$ [13].

Such distribution of the exchange interactions corresponds to a magnetic cell doubled along ***c*** axis. The calculations show that the exchange value for the second coordination sphere is rather significant and equals to $J_c = 0.23 \div 0.3\, J_c$ [14]. It experimentally revealed that the translation symmetry of the magnetic ground states can be described by two wave vectors either $k_{AF} = (0, 2l+1, 1/2)$ for U-AFM state or $k_{SP} = (1/2, 0, 1/2)$ for SP-state [9].

The structure of the vector k_{AF} reflects existence of an AFM ordering inside and between chains. In the absence of a doping SP phase transition is anticipated by appearance of the structural distortions, which have symmetry of the k_{SP}. It is necessary to assume, that such distortions can also exist at a weak doping. Therefore, we also considered the symmetry of homogeneous antiferromagnetic ordering on a background of structural distortions. Explicit account of these distortions lead to the *Bbcm* space symmetry group with four formula units in a primitive cell.

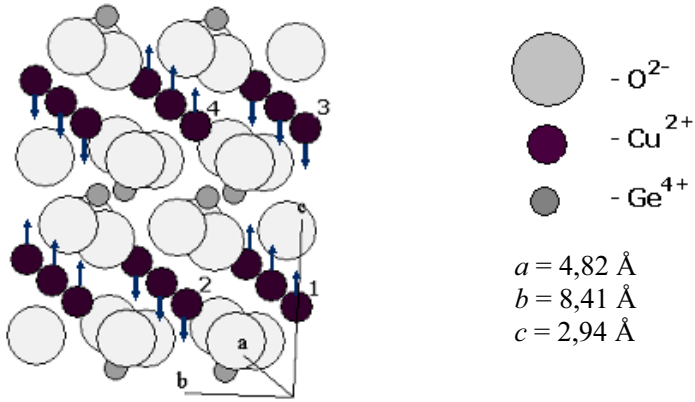

Figure 1. Crystallographic structure $CuGeO_3$.

Let's input the basic functions F, L_α $(\alpha = 1,2,3)$ which constitute the linear spin combinations of the sub-lattices of the $CuGeO_3$.

$$\begin{aligned} &\vec{F} = \vec{S}_1 + \vec{S}_2 + \vec{S}_3 + \vec{S}_4, \quad \vec{L}_1 = \vec{S}_1 + \vec{S}_2 - \vec{S}_3 - \vec{S}_4, \\ &\vec{L}_2 = \vec{S}_1 - \vec{S}_2 + \vec{S}_3 - \vec{S}_4, \quad \vec{L}_3 = \vec{S}_1 - \vec{S}_2 - \vec{S}_3 + \vec{S} \end{aligned} \tag{1}$$

Its components transform by the irreversible representations (IR) $\Gamma_1 - \Gamma_8$ of the orthorhombic symmetry (see Table). The left and right columns show the magnetic and electric field components, which transform according to the respective IR, t - is time.

The vector $L_3 \neq 0$ is the main AFM vector for the collinear AFM structure of the doped $Cu_{1-x}M_xGeO_3$ in exchange approximation (see Fig.1). It follows from allocation of the values and signs of the exchange constant. Its orientation in space (easy axes) defines by small anisotropic interactions. They found, that the easy axes directions in the AFM state depend on a doping. For instance, for *Si* [15], *Zn* [16] and *Co* [17] the easy axis directed along *c*-axis, whereas for *Ni*-doped crystals ones directed along *a* axis of the orthorhombic structure [18]. It is interesting to elucidate the next questions experimentally. Do easy axes coincide in the D-AFM and U-AFM phases, which have the same doping ion? In other words, does presence of SP-structure distortions have influence upon magnetic anisotropy value?

Table

$Pbmm$		$F,\ L_\alpha$ $(\alpha = 1,2,3)$	$Bbcm$ SP distortions already included	
-	$\Gamma_1(0)$	L_{2z}	$\Gamma_1(0)$	-
H_x	$\Gamma_2(0)$	F_x, L_{2y}	$\Gamma_2(0)$	H_x
H_y	$\Gamma_3(0)$	F_y, L_{2x}	$\Gamma_3(0)$	H_y
H_z	$\Gamma_4(0)$	F_z	$\Gamma_4(0)$	H_z
$k_{AF} = (0\ 1\ ½)$	$\Gamma_5(k_{AF})$	L_{3z}	$\Gamma_5(0)$	-
	$\Gamma_6(k_{AF})$	L_{1x}, L_{3y}	$\Gamma_6(0)$	$E_x\ t$
	$\Gamma_7(k_{AF})$	L_{1y}, L_{3x}	$\Gamma_7(0)$	$E_y\ t$
	$\Gamma_8(k_{AF})$	L_{1z}	$\Gamma_8(0)$	$E_z\ t$

3. RESULTS AND DISCUSSION

The Hamiltonian of a magnetic subsystem, which includes also an interaction with a magnetic field, H is:

$$\mathrm{H} = \sum K^{ij}_{\alpha\beta} S^i_\alpha S^j_\beta - N^{1/2} \mu_B \sum g^{ij}_\alpha H_i S^j_\alpha \ , \tag{2}$$

here g^{ij}_α is the g-factor tensor of the α-th ion, and $K^{ij}_{\alpha\beta} = \sum_m K^{ij}_{\alpha\beta}(n,\ m)$, where $K^{ij}_{\alpha\beta}(n, m)$ is the tensor of spin interactions between the α-sublattice in the n-th primitive cell and the β-sublattice in the m-th primitive cell. N - are a number of cells. Because of permutation symmetry only four interactions - K^{ii}_{11}, K^{ij}_{12}, K^{ij}_{13} and K^{ij}_{14} are independent.

Using Table data Hamiltonian (2) of the four sub-lattice orthorhombic antiferromagnet $Cu_{1-x}M_xGeO_3$ can be rewritten as follow:

$$\begin{aligned} \mathrm{H} = & \sum_i \left(J_{0i} F_i^2 + \sum_\sigma J_{\sigma i} L^2_{\alpha,i} \right) + \\ & + \ D_{01} F_y L_{2x} + D_{02} F_x L_{2y} + D_{03} L_{1y} L_{3x} + D_{04} L_{1x} L_{3y} - \\ & - N^{1/2} \left(h_y \left\{ F_y + \tau_y L_{2x} \right\} + h_z F_z + h_x \left\{ F_x + \tau_x L_{2y} \right\} \right) \ . \end{aligned} \tag{3}$$

The following denotations here are introduced: $h_i = g_{ii}\mu_B H_i$ $(i = x, y, z)$, $\tau_x = g_{xy}/g_{xx}$, $\tau_y = g_{xy}/g_{yy}$, J_{0i} and $J_{\sigma i}$ have exchange order of a magnitude and consist of the diagonal spin-spin interactions $K^{ii}_{\alpha\beta}$, D_{0i} - Dzyaloshinskii-Moriya interaction constants to which contribute antisymmetric as well as symmetric non diagonal components of the spin-spin interaction $K^{ij}_{\alpha\beta}$. Anisotropy represents as a difference $J_{\sigma i} - J_{\sigma j}$ with $i \neq j$. The connection of the J_{0i}-, $J_{\sigma i}$- and D_{0i}-constants with $K^{ij}_{\alpha\beta}$ ones are shown in Appendix A1, A2.

As follows from the Table the uniform U-AFM and D-AFM states possess quite similar symmetry. In spite of the SP-distortions nothing new appears in DM interactions. Thus, Hamiltonian (3) is suitable for both states but with slightly different constants. The strongest differences expect for the anisotropy constants.

Let us consider the symmetry of the different magnetic phases under effect of a magnetic field. For determinacy, we'll use the data available for $Cu_{1-x}Zn_xGeO_3$ [5].

$H = 0$ ($Phase\ \Gamma_5$).

The ground state of a magnetic subsystem of this crystal characterizes by only L_{3z}-component in the absence of an external magnetic field (Fig. 1). We'll be assert that magnetic ordered Γ_5-phase realizes in the absence of a magnetic field since L_{3z}-component transforms by IR Γ_5 of the *Pbmm* group. This phase is purely collinear in spite of existence of Dzyaloshinskii-Moriya interaction.

$\overline{H} \parallel a$ ($phase\ \Gamma_{25}$). An external magnetic field induces new nonzero values of basic functions. Its have the same symmetry as corresponding components of a magnetic field. For instance, the equilibrium components F_x and L_{2y} arise in an external magnetic field directed along OX axis (axis *a*, IR Γ_2 in Table). Thus, magnetic ordered phase Γ_{25} has been realized.

$\overline{H} \parallel b$ ($phase\ \Gamma_{35}$). If magnetic field is parallel to the OY axis (axis *b*, IR Γ_3), then the equilibrium values F_y and L_{2x} become nonzero and magnetic ordered phase Γ_{35} has been appeared.

$\overline{H} \parallel c$ ($H < H_{sf}$-$phase\ \Gamma_{45}$, $H > H_{sf}$-$phase\ \Gamma_{47}$, $H > H_{ex}$-$phase\ \Gamma_4$).

In that case if H || OZ (IR Γ_4) the ferromagnetic vector F_z can arise at nonzero temperatures. At the $H_{sf} \sim (g\mu_B)^{-1}(JA)^{1/2} \sim 1\,K$, spin-reorientation phase transition takes place and the basic AFM vector becomes parallel to

OX or OY axis [11]. The magnetic ordered phase Γ_{45} in the $Cu_{1-x}Zn_xGeO_3$ realizes at $H < H_{sf}$, and at $H > H_{sf}$ the spin-flop phase Γ_{47} takes place, because OX axis is the second easy axis [9]. When the magnetic field becomes $H \sim H_{ex} \sim J_c$ the second order phase transition occurs. This transition characterizes by the disappearance of a basic AFM-vector and the magnetic ordered phase Γ_4 arises.

Let us consider resonance properties of 3D U-AFM state for the $Cu_{1-x}Zn_xGeO_3$ [5]. The frequencies of the AFM resonance (AFMR) will be calculated with the help of a second-order quantization procedure [19].

The main feature of the magnetic ordering in the Zn-doped crystal is the same symmetry of exchange and acoustic modes. It follows from Hamiltonian expression (3) that does not contain such crossing items as FL_2, FL_3, L_1L_2, L_1L_3. Hence, the dynamic matrix has to break up two independent blocks each of them describe the exchange and acoustic modes. The exact expressions for the AFMR frequencies are cumbersome. Below we give some simplified version that includes just six magnetic constants:

$$w_{1,3}^{+} \approx 4S \cdot \sqrt{J_b J_c}\ ,$$

$$w_2^{-} \approx 4S\sqrt{2\ \left(J_b + J_c\right)\left(A_x - (D+d)^2 / J_c\right)}\ ,$$

$$w_4^{-} \approx 4S\sqrt{2\ \left(J_b + J_c\right)\left(A_y - (D-d)^2 / J_c\right)}\ . \qquad (4)$$

Here $J_b = K_{12}^{zz}$, and $J_c = K_{13}^{zz}$ are inter-chain and intra-chain exchange constants, respectively. Two anisotropy constants determine as $A_{x,y} = J_{3x,y} - J_{3z}$. $d = K_{13}^{yx}$, is a symmetric part of an intra-chain DM-interaction and $D = K_{12}^{yx}$ is an antisymmetric part of an inter-chain DM interaction. Note, that antisymmetric part presence in both U-AFM and D-AFM phases. A conventional Moriya estimation of DM-constants [20] in terms of the shift of the *g*-factor from its spin-only value $\Delta g = g - 2$ yield $D \cong \left(\Delta g / g\right) J_b$, as well as $d \cong \left(\Delta g / g\right)^2 J_c$. According to this estimation and ratio between J_c and J_b one can expect at least the equal significance of intra- and inter-chain DM interactions in the resonance properties of AFM states in $Cu_{1-x}M_xGeO_3$. Furthermore, DM interactions renormalize anisotropy for both acoustic modes.

The frequency-field dependency of all modes of a magnetic resonance in

Γ_{45} phase for $H_z < H_{sf}$ is shown in Fig 2. By virtue of a ground state symmetry, all modes in a non-zero magnetic field have an identical symmetry and consequently the calculation of frequency-field dependences is conducted numerically. Using our formulas for spin-waves and available data on inelastic neutron scattering [5], and AFMR [21] studies of $Cu_{1-x}Zn_xGeO_3$ with x close to 0.04 the following set of parameters were restored: $J_c = 3.5\,meV$, $J_b = 0.36\ meV$, $D = 5.1\cdot10^{-3}\ meV$, $g_c = 2.08$, $d = 1.38\cdot10^{-2}\ meV$, $A_x = 4.9\cdot10^{-4}\ meV$, $A_y = 9.5\cdot10^{-4}\ meV$.

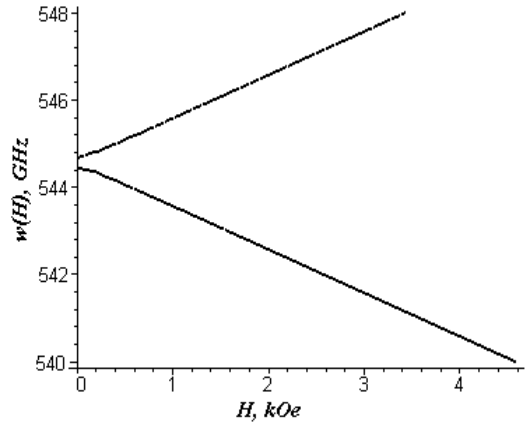

Figure 2. Frequency-field dependence of the exchange modes of a magnetic resonance.

The value of the exchange modes of the magnetic resonance has the same order of a magnitude as triplet excitations in the dimerized state [5]. These modes exist in both U- and D-AFM states. Furthermore, these modes excite by a high frequency magnetic field polarized perpendicular to easy axis. Their intensities define by the DM interactions. The spin oscillations in these modes respect to a violation of 3D AFM order along chains as well as between chains. Therefore, one can expect an amplification of their intensities under motion of boundaries between coexisting SP- and AFM states. The next experiments are necessary to make situation clear.

4. CONCLUSION

The symmetry analysis of D-AFM and U – AFM states has been done. The new kind of magnetic excitations - exchange modes in 3D AFM state of $Cu_{1-x}M_xGeO_3$ has been predicted. Furthermore, due to a coincidence of

triplets and exchange modes energy as well coexisting of dimerized state and 3D AFM state, part of previous experimental results has to be reconsidered.

APPENDIX

Here we use the following notation:

$$\begin{cases} J_{0i} = \frac{1}{4}\left\{K_{11}^{ii} + K_{12}^{ii} + K_{13}^{ii} + K_{14}^{ii}\right\},\ J_{1i} = \frac{1}{4}\left\{K_{11}^{ii} + K_{12}^{ii} - K_{13}^{ii} - K_{14}^{ii}\right\}, \\ J_{2i} = \frac{1}{4}\left\{K_{11}^{ii} - K_{12}^{ii} + K_{13}^{ii} - K_{14}^{ii}\right\},\ J_{3i} = \frac{1}{4}\left\{K_{11}^{ii} - K_{12}^{ii} - K_{13}^{ii} + K_{14}^{ii}\right\}, \end{cases}, \tag{A1}$$

$$\begin{cases} D_{01} = \frac{1}{2}\left\{\left[K_{11}^{xy} + K_{11}^{yx}\right] - \left[K_{12}^{xy} - K_{12}^{yx}\right] + \left[K_{13}^{xy} + K_{13}^{yx}\right] - \left[K_{14}^{xy} - K_{14}^{yx}\right]\right\}, \\ D_{02} = \frac{1}{2}\left\{\left[K_{11}^{xy} + K_{11}^{yx}\right] + \left[K_{12}^{xy} - K_{12}^{yx}\right] + \left[K_{13}^{xy} + K_{13}^{yx}\right] + \left[K_{14}^{xy} - K_{14}^{yx}\right]\right\}, \\ D_{03} = \frac{1}{2}\left\{\left[K_{11}^{xy} + K_{11}^{yx}\right] - \left[K_{12}^{xy} - K_{12}^{yx}\right] - \left[K_{13}^{xy} + K_{13}^{yx}\right] + \left[K_{14}^{xy} - K_{14}^{yx}\right]\right\}, \\ D_{04} = \frac{1}{2}\left\{\left[K_{11}^{xy} + K_{11}^{yx}\right] + \left[K_{12}^{xy} - K_{12}^{yx}\right] - \left[K_{13}^{xy} + K_{13}^{yx}\right] - \left[K_{14}^{xy} - K_{14}^{yx}\right]\right\}. \end{cases} \tag{A2}$$

REFERENCES

1. E. Dagotto, Springer-Verlag, Berlin, November 2002.
2. S. Sachdev, Science **288** (2000) 475.
3. L. P. Regnault, J. P. Renard, G. Dhalenne, and A. Revcolevschi, Europhys. Lett. **32**, (1995) 579.
4. Y. Sasago, N. Koide, K. Uchinokura, M. C. Martin, M. Hase, K. Hirota, and G. Shirane, Phys. Rev. B **54** (1996) R6835.
5. M. C. Martin, M. Hase, K. Hirota, G. Shirane, Y. Sasago, N. Koide, K. Uchinokura, Phys. Rev. B **56** (1997) 3173.
6. T. Masuda, A. Fujioka, Y. Uchiyama, I. Tsukada, and K. Uchinokura, Phys. Rev. Lett. **80** (1998) 4566.
7. M. Nishi, H. Nakao, Y. Fujii, T. Masuda, K. Uchinokura, and G. Shirane, J. Phys. Soc. Jpn. **69** (2000) 3186.
8. T. Masuda, I. Tsukada, K. Uchinokura, Y. J. Wang, V. Kiryukhin, and R. J. Birgeneau, Phys. Rev. B **61** (2000) 4103.
9. H. Nakao, M. Nishi, Y. Fujii, T. Masuda, I. Tsukada, K. Uchinokura, K. Hirota, and G. Shirane, J. Phys. Soc. of Japan **68** (1999) 3662.
10. S. Katano, O.Fujita, J.Akimitsu, M.Nishi, K.Kakurai, and Y.Fujii Phys. Rev. B **57** (1998) 10280.

11. V. N. Glazkov, A. I. Smirnov, K.Uchinokura, and T.Masuda, Phys. Rev. B **65** (2002) 144427.

12. V. Eremenko, V. Naumenko, Yu. Pashkevich, and V. Pishko, JETP Lett. (USA) **38** (1983) 112.

13. M. Nishi, O. Fujita, and J. Akimitsu, Phys. Rev. B **50** (1994) 6508.

14. D. Khomskii, W. Geertsma, and M. Mostovoy, Czech. J. Phys. **46** Suppl. S6, 3239 (1996); W. Geertsma and D. Khomskii, Phys. Rev. B **54** (1996) 3011.

15. H. Nojiri, T. Hamomoto, Z. J. Wang, S. Mitsudo, M. Motokawa, S. Kimura, H. Ohta, A. Ogiwara, O. Fujita, and J. Akimitsu, *J. Phys.: Condens. Matter* **9**, 1331 (1997).

16. A. I. Smirnov, V. N. Glazkov, A. N. Vasil'ev, L. I. Leonyuk, S. M. Goad, D. McK.Paul, G. Dhalenne and A. Revcolevschi JETP Lett. **64** (1996) 305.

17. P. E. Anderson, J. Z. Liu, R. N. Shelton, Phys. Rev. B **56** (1997) 11014.

18. N. Koide, Y. Sasago, T. Masuda, and K. Uchinokura, Proceedings of the 21-st International Conf. on Low Temperature Physics, Prague, 1996. Czech. J. Phys. Suppl. S4 (1981).

19. V. G. Bar'yakhtar, Yu. G. Pashkevich, V. L. Sobolev, JETF **85** (1983) 1625.

20. T. Moriya, Phys. Rev. **120** (1960) 91.

21. M. Hase, M. Hagiwara, and K. Katsumata, Phys. Rev. B **54** (1996) R3722.

HIGH-FIELD ESR SPECTROSCOPY OF LOW-DIMENSIONAL QUANTUM SPIN SYSTEMS

Review paper

S.A. Zvyagin
National High Magnetic Field Laboratory, 1800 E.Paul Dirac Drive, Tallahassee, FL 32310

Abstract: Low-dimensional antiferromagnets are excellent systems for probing many-body solid state physics in regimes where quantum fluctuations play a significant role. Here, we review our recent progress in the investigation of some low-dimensional quantum spin systems using the high-field ESR technique. The review focuses mainly on field-induced effects observed in (i) Haldane systems $Ni(C_2H_8N_2)_2NO_2(ClO_4)$ (NENP) and $Ni(C_3H_{10}N_2)_2NO_2(ClO_4)$ (NINO), (ii) antiferromagnetic S=1 chain systems with strong planar anisotropy such as $Ni(C_2H_8N_2)_2Ni(CN)_4$ (NENC), and (iii) the spin-Peierls compound $CuGeO_3$. The results offer a good possibility to test various theoretical approaches developed to describe the magnetic properties of low-dimensional materials, and they can be used for investigating quantum effects and high-field properties of other quantum spin systems.

Key words: ESR, EPR, Heisenberg chain, Haldane, spin-Peierls, large-D, low-dimensional spin systems

INTRODUCTION

Recently, a considerable amount of attention has been given to theoretical and experimental investigations of quantum low-dimensional (hereafter low-d) spin systems. Quantum effects (which can be very pronounced in spin systems with reduced dimensionality) are found to have a direct relevance to many fascinating phenomena in condensed matter

E. C. Faulques et al. (eds.), Spectroscopy of Emerging Materials, 239–250.

science (for instance, high-T_c superconductivity, heavy-fermion and non-Fermi-liquid behavior, *etc.*). To understand the role of quantum fluctuations in strongly correlated electron and spin systems with reduced dimensionality under different conditions (including high magnetic fields), it is important to explore its phenomenology in simple and well-controlled model systems.

Electron spin resonance (ESR) has proven to be an extremely powerful method to study magnetic excitations in solids [1]. Compare with inelastic neutron scattering (INS), widely considered as the most informative spectroscopic technique for studying magnetic interactions in highly-correlated electron and spin systems, ESR has several distinct and important advantages. First, it allows investigating excitation spectra in very small (of mm- and submm-size scale) samples. Second, ESR spectral resolution and sensitivity can be of several orders of magnitude better than those obtained using INS. Third, recent progress in ESR techniques shows the feasibility of ESR methods for high magnetic field (including pulsed-field up to 50 T [2-5], and higher [6]) experiments. It is generally assumed that ESR probes magnetic excitations only at zero momentum [7], whereas INS methods probe excitations in a wider range of momentum space. Even for k=0 transitions, ESR selection rules can lead to some essential limitations. But in many cases, breaking translation symmetry results in a mixture of spin states, and allows the "forbidden" transitions (see for instance [8, 9]). This might be of special importance when studying ground-state excitations, where the size of the quantum spin gap can be determined *directly*.

Using high-field ESR, frequency-field dependences of magnetic excitations, polarization parameters, ESR line width, shape and intensity can be examined in detail. Such investigations provide basic information on the nature of the ground state, magnetic structure, and peculiarities of magnetic interactions in magnetic systems.

In this paper we review our recent progress in high-field ESR studies of some spin system with reduced dimensionality. This technique was intensively used by the author for studying quantum cooperative phenomena in low-d materials at the J.-W. Goethe University (Frankfurt on Main, Germany), the National High Magnetic Field Laboratory (Tallahassee, FL, USA), and the B.I. Verkin Institute for Low Temperature Physics and Engineering (Kharkov, Ukraine) [10-17]. Here, we focus on high-field-induced phenomena revealed in some quasi-one dimensional spin systems: Haldane systems $Ni(C_2H_8N_2)_2NO_2(ClO_4)$ (NENP) and $Ni(C_3H_{10}N_2)_2NO_2(ClO_4)$ (NINO) [15], S=1 Heisenberg chain system with strong planar anisotropy $Ni(C_2H_8N_2)_2Ni(CN)_4$ (NENC) [16], spin-Peierls material $CuGeO_3$ [17].

1. High magnetic field behavior of the quantum energy gap in the Haldane spin chain systems NENP and NINO.

According to the Haldane conjecture [18] the ground state properties and the excitation spectrum of an isotropic Heisenberg chain are determined by the spin value. For integer spins the system exhibits a disordered nonmagnetic (spin liquid) ground state, which is separated from the first excited triplet by an energy gap, whereas half-integer spin systems have no gap. Using ESR, the existence of the Haldane gap has been experimentally confirmed in NENP [19-25] and the quantum spin gap was observed directly [21-25]. Transitions from the spin singlet ground state in low-d materials are normally forbidden by selection rules. It was proposed [8, 26] that a transverse staggered magnetic field (which could be induced by an external magnetic field due to the alternating tilting of the local anisotropy axes of the Ni^{2+} ions) mixes the eigenstates at q=0 and $q = /b$, and thus allows the ground state excitations in NENP and some other Haldane materials.

NENP can be described in the *Pmna* space group, whereas NINO belongs to the $Pbn2_1$ space group [27]. Both compounds are good realization of one-dimensional chains, since the intrachain exchange is about a factor of 10^4 larger than the interchain exchange and is J=-48 K and J=-53 K for NENP and NINO, respectively [28]. Both systems are characterized by non-zero planar anisotropy D, orthorhombic distortions E, and an anisotropic g tensor. A significant characteristic in NENP and NINO is the alternating tilting of the local surrounding of the Ni^{2+} ions along the chains. For NENP the tilting of the local environment is along the c direction, while the easy direction of the orthorhombic anisotropy is along a. In NINO the easy direction in the basal octahedron plane is along c. These structural peculiarities result in a significant difference in the frequency-field dependence of magnetic excitations in NENP and NINO, as we will see further.

The ESR experiments were performed in the high magnetic field laboratory at the University of Frankfurt [3]. The spectrum of magnetic excitations were studied in the 27-200 GHz frequency range in pulsed magnetic fields up to 50 T.

The frequency-field dependence for all observed ground state excitations is shown in Fig.1 (together with low-field data obtained by other groups). Since ESR involves transitions from the ground state, the resonance frequencies give a *direct* measure of the magnetic field dependence of the energy gap in NENP and NINO. Four observations are revealed: (i) for $B<B_c$ the gap in both systems decreases with a slope corresponding to the g factor (g_b=2.15 in NENP, g_b=2.17 in NINO), (ii) the gap does not close but remains

finite at the critical field B_c and increase again for $B>B_c$, (iii) the slope of the frequency-field dependence is considerably smaller than for $B>B_c$ in both substance, particularly for NENP, (iv) a drastic increase of the ESR line intensity is observed with increasing field above the critical field B_c.

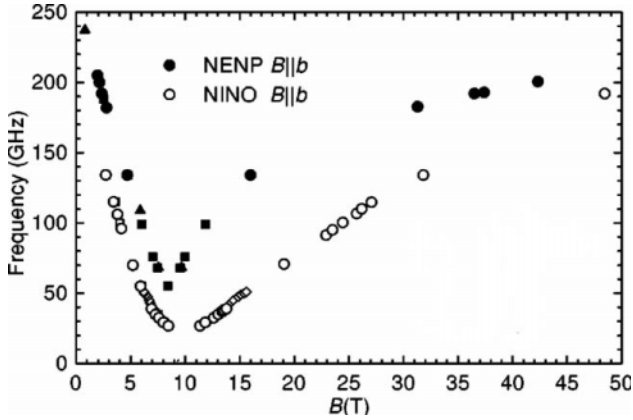

Figure 1. Frequency-field dependence of the ground state excitations in NENP and NINO (full and open symbols, respectively), T=1.5 K. Open and close circles denote the results of [15]. Diamonds, triangles and squares are data from [21, 24, 25], respectively.

The latter indicates a strongly-correlated nature of magnetic excitations for $B>B_c$ and can be explained in the framework of the staggered field concept [8, 9, 26]. On the other hand, the experimental results show a distinct deviation from theoretical expectations [8]. Because of a large staggered inclination of the Ni^{2+} surrounding in NENP, the gap in NENP was expected to be larger than that for NINO between B_c and $B=4J$. In contrast the actual field dependence of the gap energies shows a different behavior with a crossing point of the frequency-field dependences at $B\sim1.8J$.

The magnetic field dependence of the gap is calculated both with exact diagonalization for N=16 spins using the Lanczos algorithm and with the density matrix renormalization group (DMRG) method [15]. It is shown that in addition to a staggered field term the staggered anisotropy term is essential to describe the curvature of the gap as a function of field. As mentioned, the gap in NENP and NINO does not close but remains finite at the critical field B_c, which suggests a mixture of the spin states in the vicinity of B_c. Finally, the theoretical analysis also reveals that the orthorhombic anisotropy E turns out to have an unexpectedly strong effect on the energy gap for $B>B_c$.

The presented results nicely demonstrate the feasibility of the pulsed-field ESR technique for studying high-field ground state properties of low-d materials.

2. Single-ion bound excitations in *S*=1 Heisenberg antiferromagnetic chains with strong planar anisotropy.

In the previous section, we discussed the high magnetic field behavior of the quantum spin gap in the *S*=1 Heisenberg chain with strong quantum fluctuations. Generally speaking, magnetic field may be considered as a tuning parameter in the spin Hamiltonian when transforming systems from the quantum-disordered to quantum critical regime. In some cases strength of quantum fluctuations can be controlled by internal parameters as well. Crystal field (*e.g.*, single-ion anisotropy) can be one of them. A significant change in the magnetic excitation spectrum is revealed when single-ion anisotropy *D* is included in calculations for a spin-1 Heisenberg antiferromagnetic chain [29]. For the Haldane phase $D<J$, and the gap in the magnetic excitation spectrum is open. It is shown that an increased anisotropy suppresses quantum fluctuation and significantly alters the spectrum. Furthermore, it is revealed that the transition region near $D=J$ is likely to be reduced to an isolated point. Large-*D* perturbation theory is smoothly recovered as soon as $D>2J$ and the gap is open again, but it is of different nature. The size of the energy gap is determined both by the single-ion and exchange anisotropy. Due to strongly correlated nature of interactions the spectrum shows a strong dispersion. In magnetic fields the excitation spectrum may exhibit more complex and interesting peculiarities. For instance, the strong-coupling expansion approach [30] reveals the presence of single-ion bound states, apart from the common exchange-coupled bound magnons.

Here, we report on high-field ESR properties of the *S*=1 Heisenberg chain system $Ni(C_2H_8N_2)_2Ni(CN)_4$ (NENC) [16,31]. This material is characterized by strong in-plane anisotropy D/k_B=6 K, and so far can be considered as the best known candidate for a quantum *S*=1 chain in the large-*D* limit (D/J=7.5) [32].

Before going ahead with experimental data, let us briefly describe the excitation spectrum in an *S*=1 Heiesenberg chain with strong planar anisotropy and subcritical exchange interactions (hereafter large-*D* chain). The energy level scheme for the *S*=1 large-*D* system is shown in Fig. 2. For magnetic fields applied parallel to the hard axis and sufficiently low with respect to *D*, the ground state is a spin singlet characterized by an

exponential decay of the correlation function. Due to strong anisotropy a finite excitation gap appears above the ground-state energy (Fig. 2(a)). The first excited state is an $\Sigma_i S_i^z=1$ doublet corresponding to magnetic excitations called excitons and antiexcitons [33]. Higher excited states form either unbound states falling into the two-exciton continuum or bound states whose dispersion branches appear at the boundary of the Brillouin zone. In sufficiently strong magnetic field ($B>(D+4J)/g\mu_B$), the spins are flipped into the direction of the field, and ferromagnetic ground state is obtained. In this regime, magnons become the elementary excitations. Two-magnon states in the magnetic phase can be constructed either (1) by reducing the azimuthal

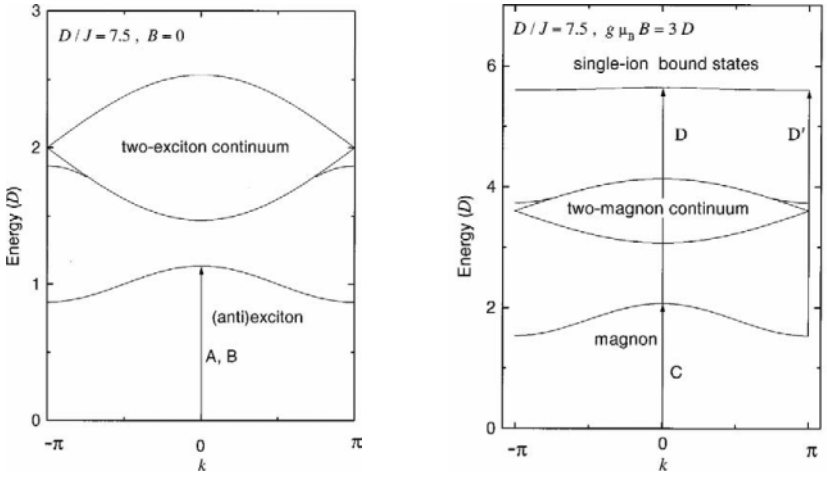

a). b).

Figure 2. (a) The energy level scheme (in units of D) for S=1 large-D chain (D/J=7.5) in zero field. A and B denote the k=0 (anti)exciton transitions. (b) The energy level scheme (in units of D) for S=1 large-D chain (D/J=7.5) in magnetic field above the spin-flop regime, $B>3D/g\mu_B$, Line C denotes the k=0 resonance transitions between the magnetic ground state and the one-magnon state, while D and D' denote the k=0 and $k=\pi$ transitions from the one-magnon to the single-ion bound states, respectively.

spin by two units at a single site, or (2) by reducing its value by one unit at two different sites. If the exchange interaction is taken into account, apart from the two-magnon continuum, two kinds of bound states will appear. States of type 1 are single-ion bound states. These states are characterized by a very weak dispersion even for intermediate values of D/J, and their dispersion branch is located above the two-magnon continuum. States of

type 2 denote common exchange-coupled bound states emerging from the continuum at the zone boundary. The corresponding energy diagram for magnetic field parallel to the hard axis, when $g\mu_B B=3D$ and $D/J=7.5$, is illustrated in Fig.2 (b).

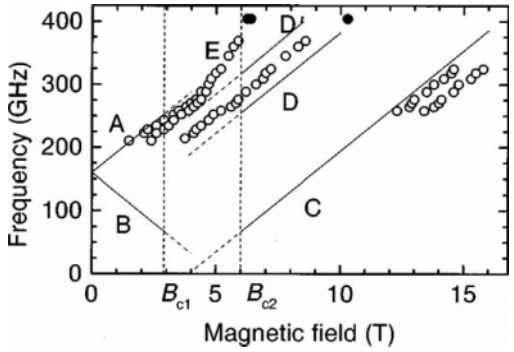

Figure 3. The frequency-field dependence of magnetic excitations in NENC. The ESR data were obtained at T=4.2 K. The theoretical predictions for the exciton and magnon regimes (lines A, B, C, D, and D') were calculated using D/k_B=6 K, D/J=7.5, and g=2.29. Full circles correspond to ESR at 404 GHz, $B\,c$.

Fig. 3 shows the resonance frequencies vs magnetic field (obtained at 4.2 K in the frequency range of ~200-400 GHz for B parallel to one of the local anisotropy axes) and the corresponding theoretical predictions for D/k_B=6 K, D/J=7.5, and g=2.29. Even though the NENC resonance spectrum possesses more complicated structure than predicted (for instance, a small tilting of the local anisotropy axes results in a double structure of the line E), the experimental data reflect the main features of the model remarkably well. The most important features of the experimental results shown in Fig. 3 is the appearance of the anomalous resonance line located in the DD' band (henceforth referred to as DD' line) and E line. Typical ESR spectra at different temperatures (lines E and DD') are shown in Fig. 4. It is revealed that the line E is formed by transitions from the ground state, while the line DD' corresponds to transitions between excited states. The field and temperature dependences of the DD' line suggest that it can be ascribed to the transitions between one-magnon states and single-ion bound states, as follows from Fig. 2 (b). Interestingly, the temperature dependence of the DD' line intensity can not be fit taking into account only excitations at k=0. The line DD' demonstrates a broad asymmetric shape, and indicates transitions within excited states (from magnon to the single-ion bound state)

which appear to occur at $k\,0$ as well. The line E corresponds to transitions from the ground to single-ion bound states which take place at k=0. Thus, the results are interpreted as the experimental evidence of single-ion bound states in an S=1 large-D Heisenberg chain.

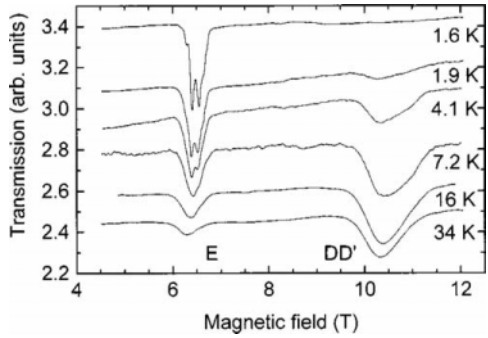

Figure 4. The excitation spectra of NENC taken at 404 GHz, $B\,c$.

ESR properties of the antiferromagnetic S=1 Heisenberg chain with strong planar anisotropy in the high-field critical phase are studied theoretically by Kolezhuk and Mikeska [34]. It is shown that transitions from the ground to the single-ion bound states (normally forbidden) can be allowed due to the tilting of the local anisotropy axes in adjacent nickel chains in NENC. More spectacularly, it is revealed that a typical feature of ESR in the critical phase is the appearance of continua with resonances being determined by power-low singularities, instead of well-defined quasiparticle peaks (seen as a broad line, DD' in our experiments). Another important feature is a characteristic change of the slope in the field dependency of the ESR frequency at B=B_c (line E, Fig. 3), which can be explained in terms of additional couplings (*e.g.*, Dzyaloshinskii-Moriya interactions or nonuniaxial anisotropies) [34]. The peculiarities of the magnetic excitation spectrum of NENC are confirmed in our experiments. To the best of our knowledge, this is the first observation of the single-ion bound states in S=1 Heisenberg antiferromagnetic chain with strong planar anisotropy and subcritical exchange interactions.

3. Field-induced structural evolution in the spin-Peierls compound $CuGeO_3$.

$CuGeO_3$ is the first known inorganic spin-Peierls material [35]. A lattice dimerization, which is one of the most characteristic features in the spin-

Peierls transition, takes place below T_{SP}~14 K. In the dimerized phase the ground state is a spin singlet, separated from the first excited triplet by an energy gap. Application of external magnetic field tends to suppress quantum fluctuations, and eventually collapses the energy gap. By increasing the magnetic field above the threshold field, B_{DI}~12.5 T, $CuGeO_3$ undergoes a transition from the dimerized spin-liquid to the incommensurate phase, where the periodicity of the spin-polarization and lattice deformation is incommensurate with respect to crystallographic lattice parameters. The low-field incommensurate region can be described by a formation of a regular array of domain walls (solitons). If the concentration of solitons is high enough, interactions between them result in a long-range ordered soliton lattice, observed experimentally [36]. A further increase in field induces a plane-wave modulated (harmonic) incommensurate state [37], where the modulation phase is a linear function of the space coordinate in the direction of the modulation. Since the dimerized-incommensurate phase transition in $CuGeO_3$ has magnetic origin, probing magnetic excitations in a broad range of magnetic fields (and frequencies) can provide important information on field-induced structural evolution of $CuGeO_3$.

The high-frequency high-field ESR technique was employed for studying magnetic excitation spectra in $CuGeO_3$ [38-43]. The first ESR investigation of the high-field, incommensurate phase in $CuGeO_3$ was performed by Palme *et al.* [43], who observed magnetic field hysteresis effects in the incommensurate phase. Drastic changes are noted on both the ESR linewidth and field, depending on the magnetic field sweep direction. A hysteresis phenomenon is a quite common feature of incommensurate structures [44], which can be explained in terms of pinning of the microscopical incommensurate superstructure on the discreteness of the crystal lattice and/or defects.

Here we present results of high-field *tunable-frequency* ESR studies of $CuGeO_3$, which were done at the National High Magnetic Field Laboratory, Tallahassee, FL. A key feature of the employed technique is a combination of a 25 T high homogeneity resistive magnet and a set of easily-tunable sources of mm- and submm- wave radiation, Backward Wave Oscillators.

In Fig.5 we show a frequency and a linewidth vs magnetic field diagrams of the ESR excitations in $CuGeO_3$ in ascending magnetic fields up to 17 T, and in a frequency range of 175-510 GHz. The Lorentzian fit of absorptions was used to calculate the ESR linewidth at half-height. The g factor of excitations remains almost constant in the entire frequency-field range, g~2.15 (which is consistent with results of [39]). However, a drastic change in the ESR linewidth is observed at the transition from the dimerized to incommensurate phase. A maximum in the linewidth is found at B_c~13.8 T.

In order to explore the nature of the ESR linewidth anomaly and the possible role of the soliton subsystem in it, ESR on $CuGeO_3$+0.8%Si samples (where a long-range-ordered incommensurate state is completely suppressed by doping [45]) is performed. Two distinguishing features in the ESR spectra are found. First, no hysteresis effects are observed in fields up to 17 T, which appears to be an evidence of the collapsing long-range ordered soliton-like lattice. Second, in contrast to that at B_c~13.8 T in the pure $CuGeO_3$ no linewidth anomaly is observed in the doped $CuGeO_3$.

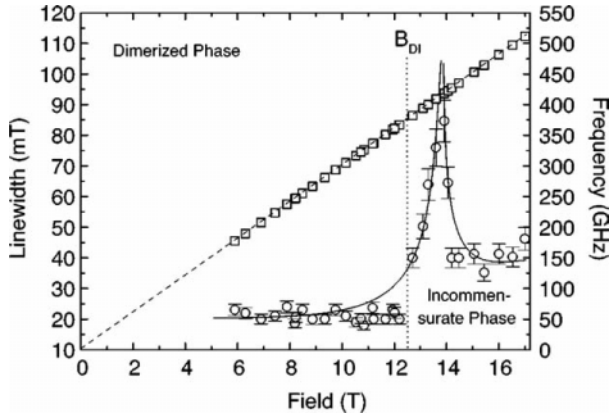

Figure 5. The frequency-field (squares) and linewidth-field (circles) dependencies of the ESR excitations in $CuGeO_3$ at T=4.2 K. The data are shown for ascending fields, $B\,a$. The dash line is a frequency-field dependence of magnetic excitations with g=2.15. The solid lines are guides for eyes. The dot line denotes the dimerized-incommensurate phase transition boundary.

Our observations reveal the essential role of the long-range-order soliton correlations in the ESR linewidth anomaly in $CuGeO_3$. Like any structural imperfection in spin systems with a collective type of elementary excitations, the soliton lattice in $CuGeO_3$ introduces additional scattering for magnons. As a result, an intensive magnon-soliton scattering manifests itself in the ESR line-broadening. A maximum of the linewidth is observed at B_c~13.8 T, that clearly indicates a pronounced development of the incommensurate soliton-like superstructure (and a corresponding enhancement of the scattering processes) close to the boundary of the dimerized-incommensurate phase transition, B_{DI}. This observation is consistent with high-field magnetostriction and thermal expansion experiments [37]. We show that the use of the high-field high-resolution frequency-tunable ESR approach

(applied for an analysis of the ESR linewidth in a broad frequency-field range) can provide important information on field-induced phase transitions in $CuGeO_3$ and other in low-d spin systems.

CONCLUSION

Our recent progress in the high-field ESR study of some low-d quantum spin systems has been reviewed. The work focused on field-induced phenomena observed in systems with reduced dimensionality: the transition from the quantum disordered spin-liquid state to the quantum critical regime in the Haldane materials NENP and NINO, the transition from the exciton to magnon regime in the S=1 large-D antiferromagnetic chain system NENC, and the dimerized-incommensurate phase transition in the spin-Peierls material $CuGeO_3$. The feasibility of high-field multifrequency ESR approaches for studying high-field properties of low-d materials has been demonstrated. The results of our high-field ESR studies offer a good possibility to test various theoretical concepts and models developed to describe magnetic properties of low-d materials, and can be used for investigating quantum effects and field-induced phenomena in other quantum spin systems.

REFERENCES

1. K. Katsumata, J. Phys. Condens. Matter **12** (2000) R589.
2. S. Kuroda *et al.*, J. Phys. Soc. Jpn. **61** (1992) 1036.
3. B. Wolf *et al.*, Physica B **294-295** (2001) 612; B. Lüthi *et al.*, Physica B **294** (2001) 20.
4. H. Nojiri *et al.*, Physica B **294-295** (2001) 14.
5. H. Ohta *et al.*, Physica B **294** (2201) 624.
6. H. Nojiri *et al.*, Phys. Rev. B **57** (1998) 10276.
7. Generally speaking, transitions with non-zero wave vector can be involved in ESR as well. See, for instance, H.-J. Mikeska, J. Phys. Soc. Jpn. Suppl. A **69** (2000) 363.
8. T. Sakai and H. Shiba, J. Phys. Soc. Jpn. **63** (1994) 867; T. Sakai *et al.*, Physica B **294-295** (2001) 26.
9. P.P. Mitra and B.I. Halperin, Phys. Rev. Lett. **72** (1994) 912.
10. H. Schwenk *et al.*, Solid State Comm. **100** (1996) 382; H. Schwenk *et al*., Physica B **237-238** (1997) 115.
11. S. Schmidt *et al.*, Solid State Comm. **108** (1998) 509.
12. M. Orendáč *et al.*, Phys. Rev. B **61** (2000) 3223.
13. S. Zvyagin *et al.*, Phys. Rev. B **66** (2002) 064424.
14. S. Zvyagin *et al.*, Physica B **392** (2003) 1211.
15. M. Sieling *et al.*, Phys. Rev. B **61** (2000) 88.

16. M. Orendáč *et al.*, Phys. Rev. B **60** (1999) 4170; S.A. Zvyagin *et al.*, Low Temp. Physics **21** (1995) 680.
17. S.A. Zvyagin *et al.*, Phys. Rev. B **67** (2003) 212403.
18. F.D.M. Haldane, Phys. Lett. A **93** (1982) 464; Phys. Rev. Lett. **50** (1983) 50.
19. M. Date and K. Kindo, Phys. Rev. Lett. **65** (1990) 1659.
20. L.C. Brunel *et al.*, Phys. Rev. Lett. **69** (1992) 1699.
21. W. Lu *et al.*, Phys. Rev. Lett. **67** (1991) 3716.
22. W. Palme *et al.*, Int. Mod. Phys. B **7** (1992) 1016.
23. T.M. Brill and J.P. Boucher, Phys. Scr. T **55** (1994) 156.
24. M. Sieling *et al.*, Z. Phys. B **96** (1995) 297.
25. M. Hagiwara and K. Katsumata, Phys. Rev. B **53** (1996) 14319.
26. H. Shiba *et al.*, J. Magn. Magn. Mater. **140** (1995) 1590.
27. A. Meyer *et al.*, Inorg. Chem. **21** (1982) 1729; T. Yisida and M.Fukui, J. Phys. Soc. Jpn. **61** (1992) 2304; T. Takeuchi *et al.*, J. Phys. Soc. Jpn. **61** (1992) 3255.
28. J.P. Renard *et al.*, Europhys. Lett. **3** (1987) 945.
29. O. Golinelli *et al.*, Phys. Rev. B **46** (1992) 10854.
30. N. Papanicolaou *et al.*, J Phys.: Condens. Matter **1** (1989) 5555; J. Condens. Matter **2** (1990) 6575; Phys. Rev. B **52** (1995) 16001.
31. S.A. Zvyagin *et al.*, Czech. J. Phys., Suppl. 4, **46** (1996) 193.
32. M. Orendáč *et al.*, Phys. Rev. B **52** (1995) 3435.
33. N. Papanicolaou *et al.*, Phys. Rev. B **56** (1997) 8786.
34. A.K. Kolezhuk and H.-J. Mikeska, Phys. Rev. B **65** (2001) 014413; Prog. Theor. Phys. Supp., **145** (2002) 85.
35. M. Hase *et al.*, Phys. Rev. Lett. **70** (1993) 3651.
36. V. Kiryukhin *et al.*, Phys. Rev. Lett. **76** (1996) 4608.
37. T. Lorenz *et al.*, Phys. Rev. Lett. **81** (1998) 148.
38. T. M. Brill *et al.*, Phys. Rev. Lett. **73** (1994) 1545.
39. H. Nojiri *et al.*, Physica B **246-247** (1998) 16.
40. H. Nojiri *et al.*, J. Phys. Soc. Jpn. **68** (1999) 3417.
41. Y. Yamamoto *et al.*, J. Phys. Soc. Jpn. **66** (1997) 1115.
42. W. Palme *et al.*, Physica B **246** (1998) 32.
43. W. Palme *et al.*, Phys. Rev. Lett. **76** (1996) 4817.
44. R. Blinc *et al.*, in *Incommensurate Phases in Dielectrics*, Edited by R. Blinc and A.P. Levanyuk (North-Holland Physics Publishing, Amsterdam, 1986).
45. B. Grenier *et al*., Europhys. Lett. **44** (1998) 511.

ACKNOWLEDGEMENTS

I am very grateful to collaborators of this work: B. Lüthi, M. Sieling, U. Löw, B. Wolf, S. Schmidt, M. Orendáč, A. M. Orendáčová, A.Feher, V.V. Pishko, M.W. Meisel, J. Krzystek, P.H.M. van Loosdrecht, G. Dhalenne, and A. Revcolevschi. It is a pleasure to thank J.L. Musfeldt and B. Lüthi for reading the manuscript and many interesting discussions.

METAL-ORGANIC COMPLEXES OF CU (II): GROUND STATE AND EXCHANGE INTERACTIONS IN MAGNETIC SUBSYSTEM

Metal-organic complexes of Cu(II)

A.Anders[a)], O.Kravchyna[b)], A.Kaplienko[b)], M. Orendach[c)], A. Orendachova[c)], M. Kajnakova[c)], A. Feher[c)]

[a)]Kharkov National University, 4 Freedom Sq., 61023 Kharkov, Ukraine; [b)] B.Verkin Institute for Low Temperature Physics and Engineering, 47 Lenin Ave., 61103 Kharkov, Ukraine; [c)] Department of Experimental Physics, Faculty of Sciences, P. J. Safarik University, 04154 Kosice, Slovakia

Abstract: The EPR spectra of powder samples for series of metal-organic compounds of Cu^{2+}ion have been investigated. These compounds are characterized by presence of identical chains of octahedrons of local surrounding for Cu^{2+} but ligand structures between chains are very different. Resonance absorption bands allow the determination of components of effective g-factor and linewidth of individual powder particles and their temperature dependence. It is established that the orbital singlet $|x^2-y^2>$ is the ground state of copper ion for all compounds. The parameters of exchange interaction had been also determined for these compounds. System with the simplest geometry of structure between chains in investigated series show the highest energy of exchange interactions.

Key words: EPR, powder sample, g-factor, Cu^{2+} ion, local surrounding, ground state, exchange interaction.

E. C. Faulques et al. (eds.), Spectroscopy of Emerging Materials, 251–260.

1. INTRODUCTION

The metal-organic compounds are interesting for coordination chemistry, biological, biochemical investigations, *etc*. The often case of the structure of metal-organic compounds is evident chains or planes of metal ions. If these ions belong to transition elements groups then the quasi-one- or quasi-two-dimensional magnets may be realized being very interesting object for magnetism of low-dimensional systems. But real interior exchange paths in metal-organic compounds are rather difficult for forecasting because of their intricacy, than it must be determined from experiments. The analysis of possible exchange bonds in magnetic subsystem may be simplified considerably if the wave function of ground orbital state of magnetic ion is known.

Electron paramagnetic resonance (EPR) is very useful tool for providing of such information because main parameters of resonance spectrum are determined appreciable by properties of crystal structure of the compound and exchange interactions in system. In particular, the value and anisotropy of effective g-factor are connected with type of local surrounding of magnetic ion which forms the arrangement of ion orbital electron levels[1]. Exchange interaction value may be determined from temperature dependence of linewidth. But as a rule the metal-organic compounds are synthesized in a powder form and the treatment of experimental results for powder sample presents some difficulties in comparison with single crystal spectrum.

In this report the series of metal-organic compounds of copper is investigated by EPR. These compounds are synthesized as a powder, they have common structural formula $[Cu(SO_4)L(H_2O)_2]$ with L = $C_2H_8N_2$ - ethylendiamine, abbreviated as Cu(en); $C_6H_6N_2O$ - nicothynamide - Cu(nad); and $C_{12}H_8N_2$ – phenanthroline – Cu(phen). These compounds have very similar local surrounding of magnetic ion and strongly different construction of organic ligands. Recent investigations of magnetization and heat capacity[2,3] revealed that for these compound the magnetic ordering temperatures being the measure of exchange interactions in system are strongly different. For Cu(en) heat capacity peak corresponds to Néel point $T_N = 0.8$ K, for Cu(nad) and Cu(phen) T_N is below 0.1 K. Analysis of magnetic resonance data of this series permits both to pick out the common features of EPR spectra formed by local surrounding and to find the correlations between structure peculiarities and magnetic characteristics.

So, the goal of this study is the elucidation of the reasons of considerable variations of exchange interactions in this series where common structural elements are present. This investigation permits to trace both the influence of local surrounding on the resonance spectra parameters

and the role of ligand structures in forming of the interactions between magnetic centers.

In next parts are presented more detailed description of structural peculiarities of investigated compounds, the treatment of spectrum for powder samples, results of low temperature EPR measurements and their discussion.

2. STRUCTURAL PARAMETERS OF INVESTIGATED SYSTEMS AND EXPERIMENTAL PROCEDURE

All investigated compounds exhibit a common structural element. They contain the chains of octahedra which present the local surrounding of two-valence copper ions. Chains are arranged along minimal cell parameter in each compound. Octahedra are connected in chain by apical oxygen atoms O2 belonging to tetrahedral sulfur groups SO_4^{2-} too. The octahedral basal plane is formed by two oxygen atoms O1 belonging to two water molecules and two nitrogen atoms from the ligands. Atomic arrangement in unite cell of Cu(en) is shown on fig.1 and structural parameters for investigated compounds are presented in Table 1.

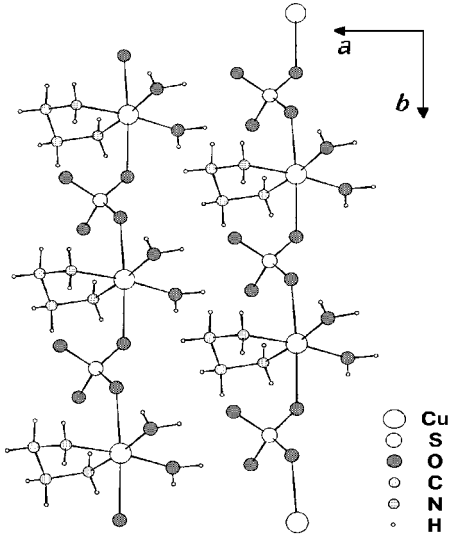

Figure 1. Projection of the crystallographic structure of compound Cu(en) into the *ab* plane.

Table 1. Structural characteristics of the investigated copper-organic complexes.

	a, Å	*b*, Å	*c*, Å	β, deg.	Space group	r_{Cu-N}	r_{Cu-O1}	r_{Cu-O2}	Ref.
Cu (nad)	11.01	6.844	21.42	93.80	$P2_1/c$	2.016	1.986	2.418	4
						2.018	1.989	2.421	
Cu(phen)	14.88	13.84	7.019	108.6	C2/c	2.009	1.970	2.486	5
Cu (en)	7.232	11.72	9.768	105.5	C2/c	1.984	1.976	2.498	6

The octahedral basal plane has the nearly square configuration with the distance from central ion about 2Å whereas the distance to apical atoms O2 is about 2.45Å. The significant elongation of octahedra must result in essential axial component of the crystal field then the EPR spectra of copper ion for these compounds must possess axial anisotropy.

In contrast with simple geometry of octahedral chains the interchain space in these compounds has rather complex arrangement. It is filled by molecular fragments with five- or six–membered rings of organic ligand groups. In these conditions the interchain interaction may be realized most likely by the hydrogen bonds through complex ways including water molecules and hydrogen atoms belonging to these ligand groups.

EPR spectra were investigated in wave-length range $\lambda \approx 4$ mm in order to increase the resolving power of the spectrometer with respect to g-factor. The significant signal intensity permits to record the integral form of the resonance absorption band. The temperature range of measurements was ~ 2 – 25 K in order to avoid the linewidth broadening due to of spin-lattice relaxation processes. It permits to trace the most interesting features of low-temperature behaviour of resonance spectra related to interior interaction processes. The accuracy of temperature stabilization was 0.1 K in 2.3 – 15 K region and ~0.5 K at T>15 K.

3. SOME COMMON FEATURES OF RESONANCE SPECTRA OF POWDER SAMPLES

The EPR line shapes produced by powder samples was calculated in many papers[1,7,8]. The spectrum of powder sample is considered as the superposition of spectra of large number small single crystals with chaotic orientation with respect to direction of external magnetic field. The sum intensity in each point of absorption band is determined by both the number of particles with given orientation and transition probability for this orientation.

The angle dependence of effective g-factor is

$$g^2=g^2_{\parallel}\cos^2\Theta+g^2_{\perp}\sin^2\Theta, \qquad (1)$$

for axial symmetry of crystal field of particles and their resonance spectra. Here $g_{\|} = g_z$, $g_{\perp} = g_x = g_y$, Θ is angle between external field direction and axis of anisotropy. The transition probability for linear polarization of high-frequency field is proportional to

$$K \sim g^2_{\perp}[(g_{\|}/g)^2+1]. \quad (2)$$

The number of particles with axis anisotropy oriented at angle Θ is

$$dN = N_0 2\pi \sin\Theta d\Theta, \quad (3)$$

where N_0 is the total number of particles in sample.

When spin value S = ½ one may introduce fields

$$H_{\|} = h\nu/g_{\|}\mu_B \quad \text{and} \quad H_{\perp} = h\nu/g_{\perp}\mu_B \quad (4)$$

determining the field boundaries for external field orientations $\Theta = 0$ and $\Theta = \pi/2$ accordingly. Here h is Planck constant, ν – work frequency, μ_B – Bohr magneton.

Then considering equations (2) and (3) the field dependence of signal intensity in absorption band where all orientation are present will be

$$I(H) \sim \int_0^{\frac{\pi}{2}} K f(H) \sin\Theta d\Theta, \quad (5)$$

where the Lorenz form of resonance line

$$f(H) \sim [(H-H`)^2+(\Delta H/2)^2]^{-1} \quad (6)$$

for individual particle is supposed. Here $\Delta H/2$ is the half-width on the half of maximum, H` is resonance field in given orientation. Substituting the integration variables in (5) and considering (1) and (2) one gets for $H_{\|} < H_{\perp}$ case

$$I(H) \sim \int_{H_{\|}}^{H_{\perp}} \frac{(1 + H_{\|}^2 H'^2) dH'}{\left[(H - H')^2 + \left(\Delta H/2\right)^2 \right] H'^2 \left(H_{\perp}^2 H'^2\right)^{1/2}} \quad (7)$$

According to this the absorption band has the specific form. As one can see from (3) the main part of particles is oriented normally to the field

direction. Then on the band end in region of $H_\perp$ the narrow peak is formed whereas in region of $H_\parallel$ the absorption intensity will be minimal and form the step with following small height shelf if ΔH is small. Growth of ΔH increases the width of peak at $H_\perp$ masking the bend at $H_\parallel$ and following shelf by peak wings. Then one must use in experiment the work frequencies as high as possible because the $H_\parallel$ - $H_\perp$ distance is proportional to ν value.

For all investigated systems the form of absorption band corresponds to the sketched above. As an example on fig. 2 the absorption band for Cu(phen) at T = 6 K and ν = 72.81 GHz is represented. The band form is computed in accordance with Eq.(7).

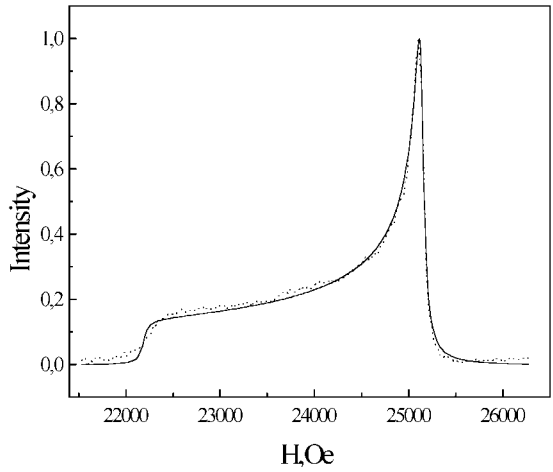

Figure 2. Low-temperature EPR spectrum of powder sample Cu(phen) for frequency ν = 72.81 GHz. Solid line is the calculation result in accordance with eq.(7) at values of parameters $g_\parallel = 2.067$, $g_\perp = 2.342$, $\Delta H = 38.35$ Oe.

4. EXPERIMENTAL RESULTS

For all investigated systems the equation (7) was used for calculations of absorption band form with $g_\parallel$, $g_\perp$ and ΔH as a fitting parameters. The temperature dependence of these parameters was also determined.

Results of experiments as follows:

Cu(en), Fig. 3a. Effective g-factor components are $g_\parallel = 2.31$, $g_\perp = 2.06$, these do not show the temperature dependence whereas the resonance line width sharply increases when temperature is reduced to T < 15 K. Such

behaviour of resonance absorption parameters of powder sample is in accordance with results for single crystal of this compound[9] where in this temperature range only small (about 1 per cent) variation of $g_{\|}$ and about 0.5 per cent variation of $g_{\perp}$ were observed. These variations are due to Jahn-Teller effect.

At same time the low-temperature broadening of resonance line at $T < 15$ K is reproduced completely in powder case. For single crystal this broadening was related to the short-range magnetic order when temperature is approached to Néel point.

Cu(nad), Fig.3b. For this compound g-factor components are $g_{\|} = 2.35$, $g_{\perp} = 2.065$; they do not show the temperature dependence. There is the noticeable low-temperature broadening of resonance line at $T < 6$ K. It may be related to the short-range magnetic order near Néel point.

Cu(phen), Fig.3c. g-factor components values are close to these for preceding compounds, they are $g_{\|} = 2.34$ and $g_{\perp} = 2.07$. Their temperature dependence is absent. The resonance linewidth have appreciable weak temperature dependence in comparison with preceding compounds.

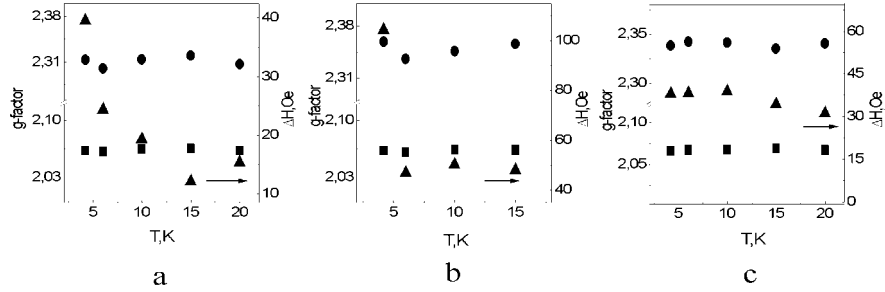

Figure 3. Temperature behaviour of effective g-factors components $g_{\|}$(•) and $g_{\perp}$ (!) and resonance linewidth ΔH(▲) for compounds: a) Cu(en); b) Cu(nad); c) Cu(phen).

From results presented on Fig.3 it follows that:

i) the closeness of g-factor components values for these compounds corresponds to similarity of local surrounding of Cu^{2+} ion in these structures;

ii) the temperature dependence for g-factor components in investigated temperature range is absent then the low-temperature broadening of ΔH for Cu(en) and Cu(nad) compounds is associated with exchange interaction rather than structural phase transition in systems;

iii) in Cu(phen) compounds the spin-spin interactions are the weakest in this series and possible region of broadening of resonance line must be displaced to temperatures lower than 2 K.

5. DISCUSSION

It is known[1] that in octahedral crystal field the ground orbital D-term of Cu^{2+} ion is split on doublet and triplet where doublet is the lowest level. The doublet degeneration is lifted by joint influence of both axial component of crystal field and spin-orbital interaction. The sign of axial distortion determines what orbital state $|z^2>$ or $|x^2-y^2>$ (they are Kramers doublets) will be the lowest. For spin doublet $|z^2>$ effective g-factor components are

$$g_{\|} = 2;\ g_{\perp} = 2 - 6\lambda/\Delta,$$

where λ- spin-orbital interaction parameter (for free Cu^{2+} ion $\lambda = -830\ cm^{-1}$), Δ – term splitting by cubic component of crystal field. For typical value $\lambda/\Delta = -0.05$ it gives $g_{\|} < g_{\perp}$ and $g_{\perp} \approx 2.3$.

For Kramers doublet $|x^2-y^2>$ g-factor components will be

$$g_{\|} = 2 - 8\lambda/\Delta;\ \ g_{\perp} = 2 - 2\lambda/\Delta,$$

and the opposite inequality $g_{\|} > g_{\perp}$ must be performed with $(g_{\|}-2)/(g_{\perp}-2) \approx 4$.

As can be seen from our experimental results the relationship between effective g-factor components values are close to latter version for all investigation system. Therefore orbital singlet $|x^2-y^2>$ is a ground state for all cases.

For this orbital state angular distribution of electron density is placed in basal plane of octahedron with maxima in the directions of ligand atoms. This distribution must contribute to realization of indirect exchange interactions between copper ions mainly in the directions which are transverse to chains. As mentioned above, it is difficult to calculate the exchange interaction in interchain directions because of complicated structure of ligands configurations. But rough estimation for these interactions may be obtained from equation connecting exchange field H_e with second moment of resonance line M_2 and linewidth ΔH observed in experiment[10]:

$$H_e = 2M_2/\Delta H.$$

Second moment of line for powder sample may be computed numerically[11]

$$M_2 = (3/5)g^4\mu_B{}^4h^{-2}S(S+1)\sum r_{ik}{}^{-6}$$

from the interior distances in lattice.

Results of calculation of second moment line for analyzed systems were obtained by summation over 10^6 cells in lattice, they are presented in Table 2. The Lorentzian linewidth calculated from these M_2 values

$$\Delta H_{dip} \approx (M_2)^{1/2},$$

for each compound is presented in Table 2 too. ΔH_{dip} is measure of magnetic dipole-dipole interaction in system if the exchange interaction is absent. But calculated ΔH_{dip} values exceeds considerably the linewidth observed in experiment, then there is exchange interaction for all investigated systems and H_e values are reflected in Table 2.

Table 2. Parameters of resonance spectra and exchange interaction of investigated systems

	$g_{\|\|}$	$g_{\perp}$	ΔH, Oe	M_2, Oe^2	ΔH_{dip}, Oe	H_e, Oe	T_k, K
Cu(en)	2.31	2.06	12.13	$3.2*10^4$	180	$5.35*10^3$	0.359
Cu(nad)	2.35	2.06	50.2	$3.64*10^4$	191	$1.45*10^3$	0.098
Cu(phen)	2.34	2.07	34.4	$8.63*10^3$	93	$5.02*10^2$	0.034

The reduction of exchange interactions from Cu(en) to Co(phen) compound in investigated series is evident from results of Table 2. The temperature dependence of the linewidth correlates well with this sequence.

As mentioned above the linewidth broadening at low temperatures corresponds to critical region of short-range magnetic order preceding to magnetic ordering point. Critical temperature values are calculated as $kT_k = g\mu_B H_e$ and presented in Table 2. Cu(en) compound with the greatest T_k value displays the widest range of critical broadening whereas minimal T_k value for Cu(phen) leads to absence of critical broadening in investigated temperature region.

As was pointed above the crystal structure for these three compounds contains similar chains of local surrounding octahedra. It must form identical intrachain interaction. Then remarkable differences of H_e values observed in this series must be related with the peculiarities of interchain interactions rather than interchain ones. The hydrogen bonds may take part in realization of interchain exchange. This conclusion accords qualitatively with both the symmetry of ground state of copper ion promoting to interchain exchange, and correlation between simplification of interchain structure geometry and increasing of exchange interactions in investigated series.

6. CONCLUSIONS

1. EPR spectra of powder and polycrystalline samples with spin S=1/2 are quite informative when rather high work frequency is used. They allow

deviation of numerical values of fundamental spectroscopic parameters and their anisotropy and the study dependence of these parameters from external conditions, for example the temperature dependence.

2. For Cu(en) and Cu(nad) compounds the short-range magnetic order is achieved in low-temperature part of the investigated temperature region. At these temperatures the effective g-factor components are nearly constant whereas the resonance line width increases dramatically when the temperature decreases.

3. The ground state of copper ion in investigated series of metal-organic compounds with octahedral local surrounding is the orbital singlet $|x^2-y^2>$. Angular distribution of electron density for this state promotes the realization of interchain exchange interactions. As a result Cu(en) compound with the simplest geometry of interchain bonds in investigated series obtains the greatest value of exchange interaction.

REFERENCES

1. A. Abragam, B.Bleaney, Electron paramagnetic resonance of transition ions, Clarendon Press, Oxford (1970).
2. M.Kajnakova, A.Orendachova, M.Orendach, J.Cernak, A.Feher, Phys.Stat.Sol. **196**, 282 (2003).
3. M.Kajnakova, A.Orendachova, M.Orendach, J.Cernak, M.W.Meisel, A.Feher, Proceeding from 14th Conference of Chech and Slovak Physicists, Plzen, (2002), p.270
4. B. Kozlevcar , I.Levan, J.Sieler, P.Segedin Acta. Cryst. **C 54**,39 (1998).
5. P.C. Healy, J.M.Patrick, A.H.White Aust. J. Chem. **37**, 1111-5 (1984).
6. V. Manriquez, M. Campos-Vallette, N. Lara, N. Gonzalez-Tejeda, O. Wittke, G. Diaz, S. Diez, R. Munoz, L. Kriskovic, J. Chem. Crystallogs. **26**, 15 (1996).
7. J.A. Ibers, J.D. Swalen, Phys. Rev. 127, 1914 (1962). T.S. Al'tshuler, JETP (in Russian) **55**, 1821 (1968).
8. F.K. Kneubuhl, J. Chem. Phys. **33**, 1074 (1960).
9. A.G.Anders, A.I.Kaplienko, O.V.Kravchyna, V.S.Bondarenko, A. Feher M. Orendach, A. Orendachova, M. Kajnakova, J. Cernak, Low Temp. Phys. **28**, 642 (2002).
10. P. W. Anderson, P. R. Weiss, Rev. Mod. Phys. **25**, 269 (1953).
11. J.H.Van Vleck, Phys. Rev., **73**, 1249 (1948).

SOLID-STATE NMR STUDIES OF NOVEL POROUS SOLIDS: STRUCTURE AND DYNAMICS

Yaroslav Z. Khimyak
Molecular Materials Centre, Department of Chemistry, The University of Liverpool, Liverpool L69 7ZD, United Kingdom, e-mail: khimyak@liverpool.ac.uk

Abstract Solid-state NMR is ideally suited to characterise solids lacking long-range periodicity such as molecular sieves, glasses, inorganic/organic hybrids, polymers and solid proteins. Recent advances in solid-state NMR spectroscopy have made it possible not only to elucidate the structure of such solids but also to characterise their dynamics. Rapid developments in instrumentation and pulse-programming methodology resulted in the measurements of the solid-state NMR spectra with the resolution comparable to that in solution-state NMR as well as the extraction of the unique structural and dynamic information on the basis of different anisotropic magnetic interactions as the latter can be reintroduced under the Magic-Angle Spinning (MAS) to measure distances or establish correlations based on proximity. We have used various double-resonance and two-dimensional solid-state NMR methods (*e.g.* cross-polarisation (CP), CP dynamics, 2D Wide-line correlation spectroscopy (WISE), Heteronuclear correlation spectroscopy (HETCOR)) to study novel porous solids with different structures and chemical compositions *e.g.* mesoporous molecular sieves, surfactant containing mesostructured solids, supported porous catalysts, and periodic mesoporous organosilicas. The synthesis pathway to these materials is based on the complex supramolecular and colloidal interactions of the inorganic precursors with surfactant micellar templates leading to complex functional materials with low structural ordering but relatively well-arranged system of uniform pores. Main focus of these studies was to identify structural and dynamic heterogeneities in the complex multi-component solids, and to gain a better insight into the understanding of the structure of the inorganic/organic interface through investigating the intermolecular interactions responsible for a particular overall structural arrangement. Several novel solid-state NMR techniques, which can be used for elucidation of the domain sizes in the complex solids, for measurements of distances and studying intermolecular interactions in supramolecular solids, are also being reviewed.

E. C. Faulques et al. (eds.), Spectroscopy of Emerging Materials, 261–272.

1. Introduction

Solid-state NMR spectroscopy has advanced rapidly over last decades and become a unique tool for structural research in various fields of modern science i.e. materials chemistry, polymer science, catalysis, structural biology. Being ideally suited for analysis of solids on the basis of the information on local ordering, this method is particularly successful for studies of solids lacking the long-range ordering and provides important information on their arrangement on different levels of their organisation.[1-3] One of the most valuable advantages of solid-state NMR compared with other structural methods, lies in the fact that it can also assess molecular dynamics of solids.[4,5]

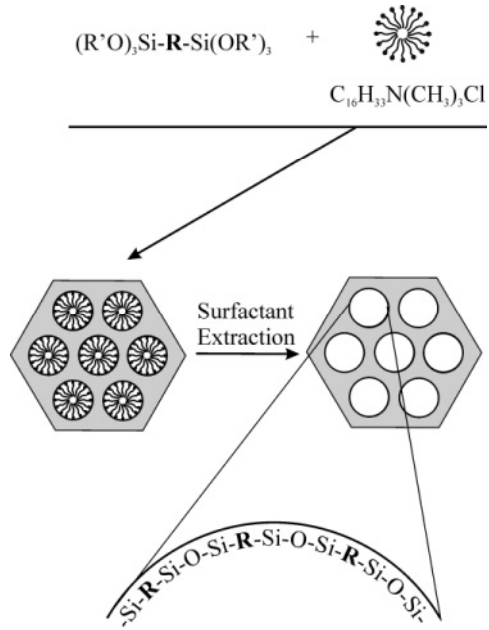

Figure 1. Periodic mesoporous organosilicas

Recent advances in the field of solid-state NMR are related both to the development of new NMR "hardware" as well as significant progress in pulse-programming methodology. Thus, use of high-speed magic-angle spinning combined with the modern heteronuclear decoupling pulse sequences and/or strong static magnetic field resulted in a possibility of recording the NMR spectra with resolution comparable to that of the solution high-resolution NMR.[4,6] While anisotropic magnetic interactions (dipolar

interacation, chemical shift anisotropy, quadrupolar interactions) were the main obstacle to obtain spectra of sufficient quality in the early years of solid-state NMR, modern experiments often aim to the use of unique structural information which can be derived from the respective anisotropic interactions. For instance, using Rotational Echo Double-Resonance (REDOR) experiment the internulclear distances between different spins can be derived on the basis of the heteronucleal dipolar couplings.[7] This method has been widely used for different spin-systems (*e.g.* ^{13}C-^{15}N couplings have been used for structural characterisation of solid proteins).[8] For quadrupolar nuclei several modified experiments were proposed and used for characterisation of ^{29}Si-^{27}Al connectivities in zeolites or ^{31}P-^{27}Al connectivities in aluiminophosphate molecular sieves.

In this work several NMR methods applicable for characterisation of novel porous inorganic/organic hybrids are reviewed. Over the resent years there have been significant advances in the synthesis and design of novel materials using advanced templating techniques.[9] One of those is based on the use of the supramolecular arrays of surfactant species to induce ordered porosity of the inorganic arrays formed around them.[10,11] Removal of the surfactant via calcination or extraction results in the formation of mesoporous solids with ordered hexagonal (*e.g.* MCM-41) or cubic (*e.g.* MCM-48) system of pores. Since their discovery in 1992, these solids have been widely used in catalysis, separation, molecular recognition etc. mostly due to the presence of the active silanol (Si-OH) groups and extremely large surface area. The synthesis methodology has been successfully applied to other inorganic oxides.[12-15] Formation of mesostructured solids is a complex process governed by different intermolecular forces (hydrogen bonding, electrostatic interactions, hydrophobic/hydrophilic balance *etc.*). Understanding of intermolecular forces responsible for the self-assembly is crucial for the design of the solids for targeted application as well as modelling of formation of inorganic/organic hybrids in nature.[10,11]

Novel composite materials must combine precise functionality with the long-range periodicity. In order to produce complex structures comprising several spatially separated domains with distinctly different properties nature resorts to a string of self-assembly processes governed by the intermolecular interactions with different strengths. One of the major advances in the area of supramolecular solids was a recent discovery of periodic mesoporous organosilicas (PMO) formed using bridged organosilane ($(R'O)_3Si$-**R**-$Si(OR')_3$) precursors (Figure 1).[16] The advantages of these solids over the earlier generations of porous silicas and organosilicas are related to the organic group being a part of the material "backbone" which allows tailoring of the pore wall density and flexibility as well as introduction of other functional groups. Despite a significant interest in synthesis of such solids

and widening of the range of both the templates and organosilane precursors the mechanism of the self-assembly is far from being understood.

Moreover, very little is known about their structure in terms of the distribution of organic functional groups in the pores, molecular arrangements at the inorganic/organic interface in both the porous products and their surfactant containing precursors.

We have synthesised bifunctional PMO containing $–CH_2-CH_2–$ (BTSE) and –CH=CH– (BTSEY) bridges incorporated in the hybrid walls. These materials show superior properties when compared to mono-functionalised $–CH_2-CH_2–$ or –CH=CH– PMO.[17]

2. Analysis of structure and connectivites in hybrid solids

One of the major advantages of solid-state NMR compared with powder X-ray diffraction is possibility of identifying different units in essentially amorphous inorganic or inorganic/organic hybrid walls. Thus, ^{29}Si MAS NMR spectra of BTSE- and BTSEY-PMOs show the presence of T^3 ($R-Si(OSi)_3$) and T^2 ($R-Si(OSi)_2$) organosilicate units (Figure 2). Deconvolution of the spectra allows the quantitative determination of the content of the structural units. For BTSE/BTSEY bifunctional PMO the deconvolution proves incorporation of both $Si–CH_2-CH_2–Si$ and Si–CH=CH–Si units in the structure. Analysis of the T^3/T^2 ratio shows the preference of –CH=CH– bridges to be located near the hybrid wall/surfactant interface for composites with BTSE/BTSEY = 5:1.

Incorporation of both functionalities is also confirmed by $^{13}C\ \{^1H\}$ MAS NMR. $–CH_2-CH_2–$ bridges are represented by the broad resonance at 2-5 ppm, while –CH=CH– units are found at 147 ppm. Importantly, $^{13}C\{^1H\}$ MAS NMR spectra also indicate the template in the BTSE-silica and BTSEY-silica mesophases is in the disordered gauche conformation as the peak attributable to the inner chain methylenes is observed at 31.0 ppm. $^{13}C\{^1H\}$ MAS NMR spectra of the extracted PMOs show only the broad resonances corresponding to $–CH_2-CH_2–$ or –CH=CH– units proving the removal of surfactant template.

3. Cross-polarisation dynamics

Cross-polarisation (CP) is a solid-state NMR experiment designed to achieve a higher sensitivity for the rare nucleus through the transfer of polarisation, driven by the heteronuclear dipolar interaction, from an abundant (^1H) to a dilute spin (^{13}C).[1,18] Transfer of magnetisation is possible

when the Hartman-Hahn condition is achieved. Since cross-polarisation relies on the heteronuclear dipolar interactions its efficiency depends on the distance between the source (abundant) and target (rare) spin. Therefore it is also sensitive towards molecular motions and can serve as an indication of dynamics in a solid under investigation. Variable contact time (VCT) experiments allow us to study the dynamics of the polarization transfer. In general, the intensity initially increases with the contact time (t_m) but a decay is observed for longer t_m due to the relaxation of ^1H and ^{13}C in the rotating frame ($T_{1\rho}$). For an abundant-to-rare nuclei transfer the intensity of the polarised peak can be described by equation (1).[5]

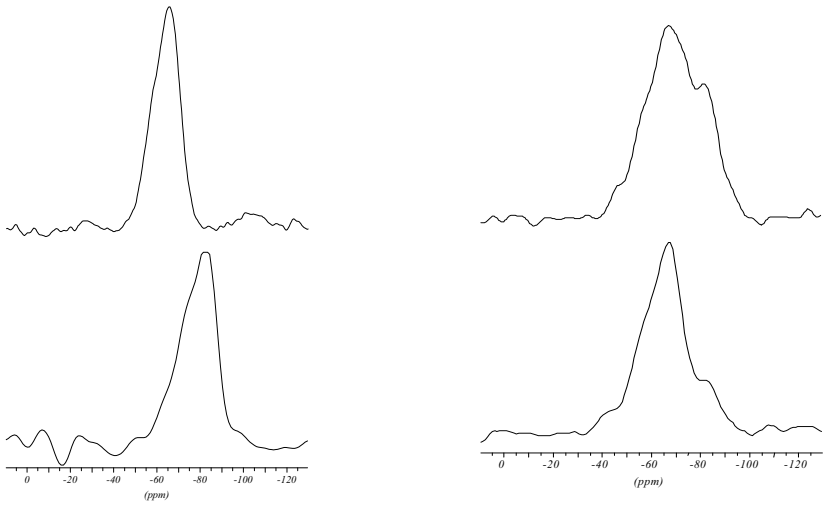

a) b)

Figure 2. ^{29}Si MAS NMR spectra of as-synthesised PMO: a) BTSE-PMO, a) bottom – BTSEY-PMO, b) top: BTSE/BSTE-PMO (1:1), b) bottom BTSE/BTSEY-PMO (5:1).

$$M(t_m) = M_0\left(1-T_{CH}/T_{1\rho H}\right)^{-1}\left[\exp(-t_m/T_{1\rho H}) - \exp(-t_m/T_{CH})\right] . \qquad (1)$$

I_0 is the maximum intensity, T_{CP} is the cross polarization time constant and $T_{1\rho H}$ and $T_{1\rho C}$ are the relaxation times for ^1H and ^{13}C in the rotating frame. The cross polarization rate ($1/T_{CP}$) depends on the square of the dipolar interaction while the relaxation time in the rotating frame provides

important information on the mobility of the molecular fragments. Relaxation times in the rotating frame can be also determined using separate solid-state NMR experiments based on the modified CP-pulse sequence.[18]

For inorganic/organic hybrids CP dynamics can provide valuable information on the structure of the inorganic framework as well as the dynamics of the organic part in form of the incorporated functional groups or surfactant template.[3,19,20] The ^{1}H – ^{13}C VCT CP/MAS spectra for the CH_2-CH_2-PMO/$C_{18}H_{37}N(CH_3)_3Br$ hexagonal mesophase indicate different mobility of the incorporated –CH_2-CH_2– groups and surfactant aliphatic chains as the broad resonance the *ca.* 2 ppm attributable to the former show significantly faster CP-dynamics than any carbon resonances of the surfactant.

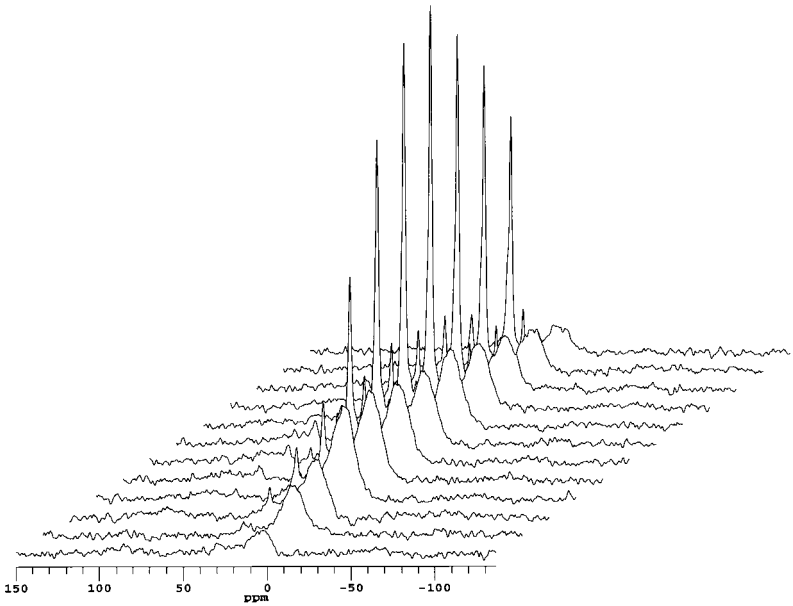

Figure 3. VCT ^{1}H- ^{13}C CP/MAS spectra of CH_2-CH_2-PMO.

Based on the analysis of T_{cp} and $T_{1\rho C}$, different segments of the surfactant show various mobility with the most mobile part located at the end of aliphatic chains.[3]

Detailed analysis of the CP dynamics can be also used for identification of structural heterogeneities. Thus, very unusual CP-dynamics curves of incorporated –CH_2–CH_2– and –CH=CH– functional groups in mono- or

bifunctional PMO can be simulated only when two component with different mobilites are considered. The rigid component shows extremely short T_{cp}, $T_{1\rho H}$ and $T_{1\rho C}$ (Table 1). Analysis of the CP-dynamics curves in this case enables the determination of the ratio between two different components in the structure. We note that such information is unique to solid-state NMR. Most probably, the mobile component can be associated with the organic bridges located at the surface of the hybrid walls while the rigid component represents functional groups incorporated in the hybrid walls. Moreover, the fact that the mobile components of bifunctional $–CH_2-CH_2–$/–CH=CH– organosilica show different $T_{1\rho H}$ times can be interpreted as an indication of the heterogeneous structural arrangements with the domains consisting of functionalities of a particular type.

Table 1. ^{1}H-^{13}C CP dynamics parameters for the extracted BTSE/BTSEY PMO (1:1)

Functional group	Component	T_{cp}, ms	$T_{1\rho H}$, ms	$T_{1\rho C}$, ms	I_m/I_r
$-CH_2-CH_2-$	mobile	0.980	50.6	27.0	1.15
	rigid	0.0230	0.435	2.79	
-CH=CH-	mobile	0.546	23.6	20.8	1.14
	rigid	0.0346	5.25	0.676	

CP dynamics has also been very useful technique for estimation of the connectivities in the porous solids. Classic example in this case would be a clear distinction between Q^2, Q^3 and Q^4 silicate sites in the molecular sieves on the basis of not only the chemical shift but also T_{cp} times which, as a result of no protons connected directly are much longer for Q^4 sites ($Si(OSi)_4$). Introduction of guest species in the pores has a dramatic effect on the CP-dynamics of the different silica sites. Thus, in the MCM-41 impregnated with the mixed metal clusters/counter-cation species, presence of embedded organic counter-cation lead to a significant reduction of T_{cp} and $T_{1\rho H}$ due to the presence of a different source of protons at the porous silica surface.[21]

While the original CP experiments were designed for the proton-to-rare spin polarization transfer, cross-polarisation in the spin system which do not involve protons (i.e. $^{31}P \rightarrow {}^{27}Al$ or even $^{27}Al \rightarrow {}^{31}P$) have also been described.[22,23] These experiments have been widely applied for characterization of the structure of molecular sieves as well as the catalytic activity of their acidic sites.[5,22]

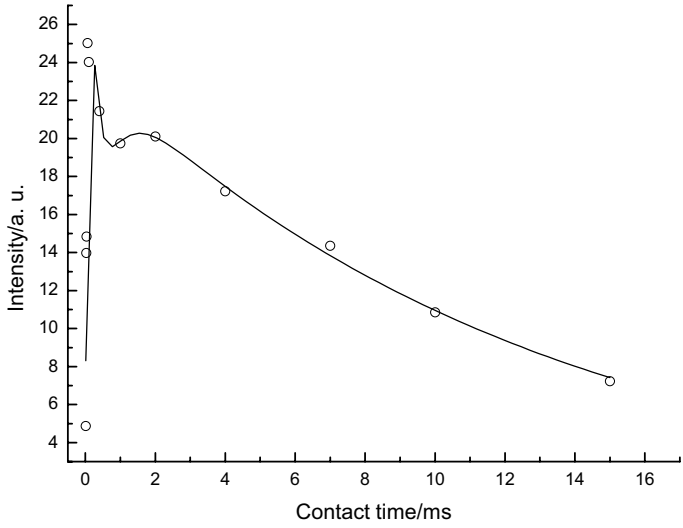

Figure 4. CP dynamics curve of $–CH_2-CH_2–$ peak in CH_2-CH_2-PMO.

4. Heteronuclear correlation

Heteronuclear correlation (HETCOR) is an experiment establishing a correlation between the chemical shift of proton and that for another nucleus (*i.e.* ^{13}C, ^{31}P, ^{15}N or ^{29}Si). The experiment relies on the heteronuclear dipolar interactions and uses a CP to transfer magnetization from protons to a rare spin.[4,6] We have used 2D HETCOR experiment to characterize support/counter-cation/cluster interaction in the supported mesoporous catalysts.[21]

It is clear that silicate units derive very significant proportion of their resonances from the $[N(C_2H_5)_4]^+$ countercation species. This implies that counteraction is located at the silica surface. Moreover, chemical shift of Q^4 species correlates with the protons of the $-CH_3$ group of the counter-cation species rather than with the Q^3 or Q^2 indicating that upon deposition of the mixed-metal cluster the contercation is embedded in the porous walls of the support.[21]

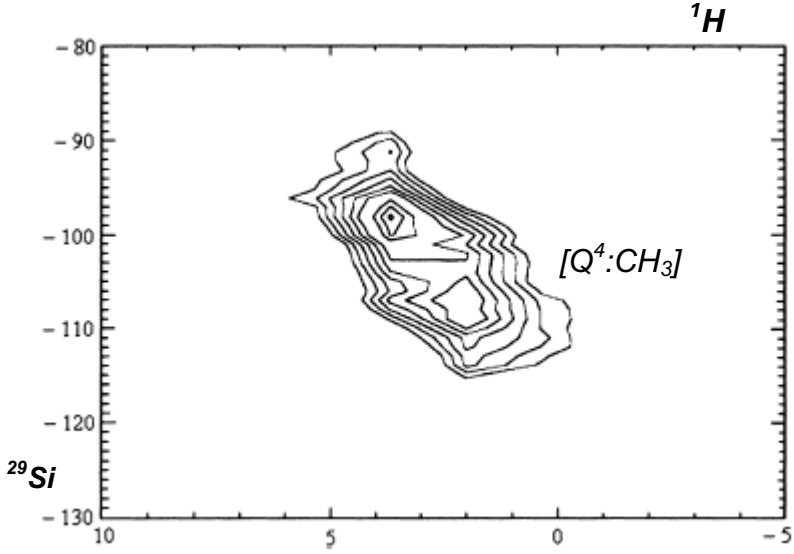

Figure 5. Two-dimensional correlation spectrum between ^{29}Si (vertical axis) and ^1H (horizontal axis) sites for MCM-41 impregnated with $[Pd_6Ru_6(CO)_{24}][NEt_4]_2$.

5. Correlation between the local structure and mobility

Among several indicators of motional state of organic solids ^1H linewidths has been used from very beginning of solid-state NMR. However, inherently low resolution of ^1H MAS NMR spectra caused by the very strong homonuclear interactions and relatively low MAS speed lead to a very limited application of ^1H MAS NMR for studies of mobility.[1] A 2D wideline separation (WISE) experiment correlates carbon chemical shifts recorded under MAS with broad ^1H lines.[1,24] As a result a broad ^1H lines are separated in the components corresponding to the ^{13}C sites in their close proximity. For mobile domains in a sample, the ^1H – ^1H coupling are relatively weak which leads to relatively narrow ^1H static lines. The opposite is observed for the rigid domains.

For mesostructured aluminophosphates with lamellar structure WISE spectra indicate that template surfactant species have very restricted mobility as the ^1H wide lines are very broad.[3] This is also consistent with the *trans*-conformation of the aliphatic chains. Other representatives of mesoporous AlPO exhibited template species with much narrower ^1H resonances.[2]

WISE NMR spectra are recorded using very short contact times in order to ensure that only the directly bound protons contribute to the ^{13}C magnetization and influence of ^1H spin-diffusion is eliminated. The WISE

experiment can be extended so that it exploits the ^{1}H spin-diffusion. In this case the experiment can not only identify the domains with different mobilities but also be used to determine their sizes.[1]

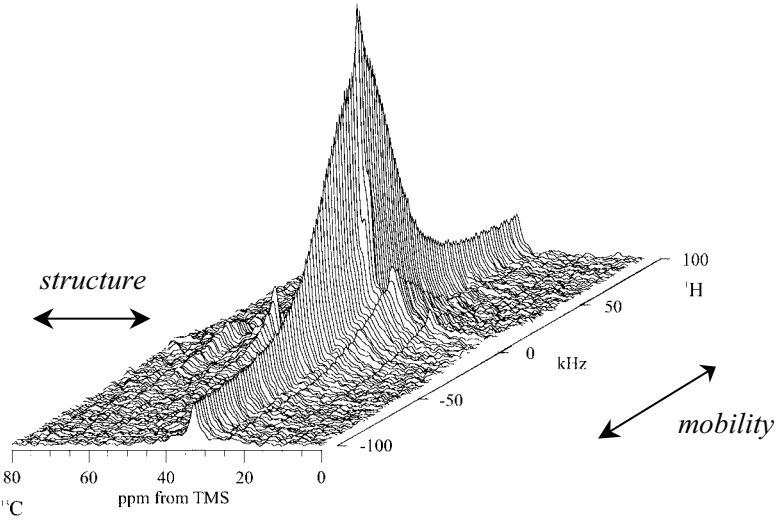

Figure 6. WISE spectra of mesostructured AlPO with lamellar structure

6. Advanced solid-state NMR techniques

Recently several new solid-state NMR techniques based on the reintroducing structural information lost due to MAS have been proposed. One of the most important examples of those is the *Rotational Echo Double Resonance* (REDOR).[7] Using this experiment one can easily determine the interatomic distances. The experiment is based on the manipulation of the heteronuclear dipolar Hamiltonian in synchrony with the MAS. As a result an effect of MAS leading to averaging out the heteronuclar dipolar interaction can be ousted. To achieve this a RF pulse is applied in synchronisation with the rotation period. If a π pulse is applied to the S spin the sign of its magnetisaion is changed. By using two π pulses per rotor period one can recouple about 70% of heteronuclear dipolar coupling.[6] Experimentally REDOR employs the following pulse sequence. For a ^{13}C-^{15}N spin system, during the first step the ^{13}C magnetisation is created using CP step (from ^{1}H). During the dephasing step two ^{15}N π pulses are used in such a way that the first one is applied at a half-period of rotor and the other one at the time of a rotor period. Use of a π pulse in the ^{13}C channel at the

half-dephasing time ensures that the heteronuclear couplings involving third species are avoided. By measuring the signal decay as function of dephasing time with and without ^{15}N π pulses and calculating the dephasing curve incorporating "natural" decay of ^{13}C magnetisation one can determine the heteronuclear dipolar coupling constant and hence the distance between the ^{13}C and ^{15}N. This technique has been extensively applied for analysis of the structure of both organic and inorganic solids.[8] The method has been extensively modified for more specific applications involving quadrupolar nuclei and TRAPDOR and REAPDOR experiments were introduced.[25]

Another very promising direction of modern solid-state NMR follows the path of employing fast MAS to obtain ^{1}H spectra and combine MAS with double-quantum (DQ) spectroscopy to extract the structural information from the ^{1}H-^{1}H homonuclear dipolar couplings.[4] Spiess *et al.* have used this method to assess the ^{1}H-^{1}H connectivities in hydrogen-bonded supramolecular structures as well as to identify the π-π stacking arrangements.[26,27] Presence of DQ cross-peaks in the spectrum can be considered as an indication of proton-proton sites in the structure. Analysis of rotor encoded ^{1}H DQ MAS NMR spinning sidebands patterns was shown to give the information on the ^{1}H-^{1}H distances for an isolated pair of aromatic protons in the organic solids. The details of DQ experiments are presented in an excellent recent review by Spiess and Brown.[4]

ACKNOWLEDGEMENTS

Financial support of this work by the EPSRC (UK) is gratefully acknowledged. We are also grateful to Dr. M. J. Duer and Prof. J. Klinowski for fruitful discussions.

References

(1) Schmidt-Rohr, K.; Spiess, H. W. *Multidimensional Solid-State NMR and Polymers*; Academic Press Ltd.: London, 1994.
(2) Khimyak, Y. Z.; Klinowski, J. *Phys. Chem. Chem. Phys.* **2001**, *3*, 2544-2551.
(3) Khimyak, Y. Z.; Klinowski, J. *Phys. Chem. Chem. Phys.* **2001**, *3*, 616-626.
(4) Brown, S. P.; Spiess, H. W. *Chem. Rev.* **2001**, *101*, 4125-4155.
(5) Kolodziejski, W.; Klinowski, J. *Chem. Rev.* **2002**, *102*, 613-628.
(6) Laws, D. D.; Bitter, H.-M. L.; Jerschow, A. *Angew. Chem. Int. Ed.* **2002**, *41*, 3096-3129.
(7) Gullion, T. *Conc. Magn. Res.* **1998**, *10*, 277-289.
(8) Watts, J. A.; Watts, A.; Middleton, D. A. *J. Biol. Chem.* **2001**, *276*, 43197-43204.

(9) Beck, J. S.; Vartuli, J. C.; Roth, W. J.; Leonowicz, M. E.; Kresge, C. T.; Schmitt, K. D.; Chu, C. T. W.; Olson, D. H.; Sheppard, E. W.; McCullen, S. B.; Higgins, J. B.; Schlenker, J. L. *J. Am. Chem. Soc.* **1992**, *114*, 10834-10843.

(10) Mann, S.; Burkett, S. L.; Davis, S. A.; Fowler, C. E.; Mendelson, N. H.; Sims, S. D.; Walsh, D.; Whilton, N. T. *Chem. Mater.* **1997**, *9*, 2300-2310.

(11) Mann, S.; Ozin, G. A. *Nature* **1996**, *382*, 313-318.

(12) Khimyak, Y. Z.; Klinowski, J. *J. Chem. Soc., Faraday Trans.* **1998**, *94*, 2241-2247.

(13) Khimyak, Y. Z.; Klinowski, J. *Phys. Chem. Chem. Phys.* **2000**, *2*, 5275-5285.

(14) Khimyak, Y. Z. Ph. D., University of Cambridge, 2000.

(15) Burkett, S. L.; Sims, S. D.; Mann, S. *Chem. Commun.* **1996**, 1367-1368.

(16) Inagaki, S.; Guan, S.; Ohsuna, T.; Terasaki, O. *Nature* **2002**, *416*, 304-307.

(17) Treuherz, B.; Khimyak, Y. Z., Synthesis of bifunctionalPMO.

(18) Michel, D.; Engelke, F. In *NMR Basic Principles and Progress*; Springer-Verlag: Heidelberg, 1994; Vol. 32.

(19) Wang, L. Q.; Liu, J.; Exarhos, G. J.; Flanigan, K. Y.; Bordia, R. *Journal of Physical Chemistry B* **2000**, *104*, 2810-2816.

(20) De Paul, S. M.; Zwanziger, J. W.; Ulrich, R.; Wiesner, U.; Spiess, H. W. *J. Am. Chem. Soc.* **1999**, *121*, 5727-5736.

(21) Jones, M. D.; Duer, M. J.; Hermans, S.; Khimyak, Y. Z.; Johnson, B. F. G.; Thomas, J. M. *Angew. Chem. Int. Ed.* **2002**, *41*, 4726-4729.

(22) Ashbrook, S. E.; McManus, J.; MacKenzie, K. J. D.; Wimperis, S. *J. Phys. Chem. B* **2000**, *104*, 6408-6416.

(23) Schulz, M.; Tiemann, M.; Froba, M.; Jager, C. *Journal of Physical Chemistry B* **2000**, *104*, 10473-10481.

(24) Spiess, H. W. *Chem. Rev.* **1991**, *91*, 1321-1338.

(25) Gougeon, R. D.; Bodart, P. R.; Harris, R. K.; Kolonia, D. M.; Petrakis, D. E.; Pomonis, P. J. *Phys. Chem. Chem. Phys.* **2000**, *2*, 5286-5292.

(26) Brown, S. P.; Schnell, I.; Brand, J. D.; Mu1llen, K.; Spiess, H. W. *J. Am. Chem. Soc.* **1999**, *121*, 6712-6718.

(27) Schnell, I.; Langer, B.; Sontjens, S. H. M.; Sijbesma, R. P.; van Genderenb, M. H. P.; Spiess, H. W. *Phys. Chem. Chem. Phys.* **2002**, *4*, 3750–3758.

POINT-CONTACT SPECTROSCOPY OF TWO-BAND SUPERCONDUCTOR MgB_2

I. K. Yanson and Yu. G. Naidyuk
B. Verkin Institute for Low Temperature Physics and Engineering, National Academy of Sciences of Ukraine, 47 Lenin Ave., 61103, Kharkiv, Ukraine
yanson@ilt.kharkov.ua

Abstract The progress in the investigation of the two-band superconductor MgB_2 by point-contact spectroscopy (PCS) is reported. Results of the study of superconducting gap temperature and magnetic field dependence for two-dimensional σ and three-dimensional π band and electron-phonon-interaction spectral function are presented. The correlation between the gap value and the intensity of the high T_c driving force – E_{2g} boron vibration mode is provided. PCS data on some nonsuperconducting transition metal diborides are surveyed for comparison.

Keywords: point-contact spectroscopy, MgB_2, two-band/gap superconductivity, electron-phonon interaction

1. Introduction

Magnesium diboride, like other diborides MeB_2 (Me=Al, Zr, Ta, Nb, Ti, V etc.), crystalizes in a hexagonal structure, where honeycomb layers of boron are separated by magnesium ions located above and below the centers of boron hexagons. The hallmark of MgB_2 is that it becomes superconducting (SC) at the high critical temperature of T_c ($\approx 40\,K$) [1], which is a record breaking value among the *s-p* metals and alloys. The outstanding property of MgB_2 is that this material represents a rare example of multi-band (2-D σ-band and 3-D π-band) electronic structure, the bands of which are weakly connected with each other. These bands lead to very uncommon properties. For example, T_c has very little dependence on elastic scattering, unlike other two-band superconductors [2]. The maximal upper critical magnetic field they can achieve has a much higher value than that for a one-band, dirty superconductor [3]. The properties of MgB_2 have been comprehensively calculated by mod-

E. C. Faulques et al. (eds.), Spectroscopy of Emerging Materials, 273–288.

ern theoretical methods, which lead to a more complete understanding of their behavior in various experiments.

The electron band structure of MgB_2 was calculated in great detail using different *ab initio* methods [4–8]. First and foremost, two incompletely filled σ bands have weak k_z dispersion forming two nearly cylindrical sheets of the Fermi surface around ΓA (Δ). In addition, they retain their covalent structure representing a unique case of conducting covalent bands which contribute to the strong electron-phonon coupling. Thus, the hole branch along ΓA experiences huge interaction with the phonon E_{2g} mode for carriers moving along the *ab* plane, although its manifestation is screened effectively by the much faster hole mobility in π-bands [2], which form two 3-D tubular networks. Appropriate electron transport is very anisotropic ($\rho_c/\rho_{ab} \simeq 3.5$ [10]) with a plasma frequency (and Fermi velocity) for the σ band along the *c* axis being an order of magnitude smaller than that in the *ab* direction [11].

The inelastic *X*-Ray scattering measurements [12] demonstrated a weak dispersion branch between 60 and 70 meV in the ΓA direction with E_{2g} symmetry at the Γ point. The linewidth of this mode is about $20 \div 28$ meV along the ΓA direction, while along the ΓM direction it is below the experimental resolution. This points to the very strong electron-phonon interaction (EPI) for this particular lattice vibration mode.

The SC energy gap distribution on the Fermi surface of MgB_2 [13] shows maximum gap value along the ΓA direction which is due to a very strong EPI. Just in this direction, the 2D σ band (cylinders along the ΓA direction) is located. The 3D π band has a much smaller EPI, and, correspondingly, an energy gap which is nearly 3 times smaller. In Ref. [13] it is shown that the average λ value on the σ band amounts up to $2 \div 3$. Moreover, λ_σ can be separated into different phonon modes, and it appears that only the E_{2g} phonon mode along the ΓA direction plays a major role with a partial λ_σ value of about $\simeq 25$ [14], though concentrated in a very restricted phase space.

The driving mechanism for the high T_c in MgB_2 is connected with the strong interaction between charge carriers and the E_{2g} phonon modes, corresponding to antiparallel vibration of the atoms in the boron planes. The electron band structure of MgB_2 along the ΓA direction is such that the Fermi energy of hole carriers is only $0.5 \div 0.6$ eV, which shrinks even more while boron atoms deviate from the equilibrium positions. Together with the 2D structure of the corresponding sheet of the Fermi surface, this leads to constant density of states at the Fermi energy and, correspondingly, to a very strong EPI. Cappelluti *et al.* [15] point out that the small Fermi velocity for charge carriers along the ΓA direction

leads to a large nonadiabatic correction to T_c (about twice as much compared with adiabatic Migdal-Eliashberg treatment). Although this interaction is a driving force to high T_c in this compound, it does not lead to crystal structure instability, since it occupies only a small volume in the phase space.

According to theoretical models, the π and the σ bands in MgB_2 are weakly connected. However, the energy gap of the π band goes to zero at the same T_c as in the bulk, and correspondingly the $2\Delta_\pi(0)/kT_c = 1.4$, which is much less than the weak coupling BCS theory predicts. One can think of the π band as having intrinsically lower $T_c \approx 10\,\mathrm{K}$ than the bulk [16] and at higher temperatures its superconductivity is induced by the proximity effect in the **k**-space from the σ band [17]. This proximity effect is very peculiar. From one side, this proximity is induced by the interband scattering between the π and the σ sheets of the Fermi surface. On the other side, the charge carriers connected with the π band are mainly located along the magnesium planes, which can be considered as a proximity effect in the coordinate space for alternating layers of the $S - N - S$ structure, although on a microscopic scale. Thus, MgB_2 is a good example to study the crossover between two-band superconductivity and the simple proximity effect structure.

2. Samples and measurements

In this work the results for two kinds of samples are surveyed. The first type of sample is thin c-axis oriented films with a thickness of about several hundred nanometers [18]. The residual resistance is about several tens of $\mu\Omega\,\mathrm{cm}$ with the residual resistance ratio (RRR) of $\simeq 2.2$ pointing out that films have a disorder between crystallites. This does not preclude the fact that, on some spots, the films contain clean, small, single crystals on which we occasionally may fabricate a point contact (PC). Normally, the contacts were prepared by touching the film surface with a noble metal counter electrode (Cu, Au, Ag) in the direction perpendicular to the substrate. Thus, nominally, the preferential current direction in the PC is along the c axis. Nevertheless, since the surface of the films contains terraces with small crystallites, a PC to the ab plane of these crystallites is also possible.

The second type of sample is composed of single crystals [19]. The crystals are plate-like (flakes) and have sub-millimeter size. They were glued by silver epoxy to the sample holder by one of their side faces. The opposite face of the flakes was used as a "needle" to gently touch the noble metal counter electrode in liquid helium. In this way we tried to make, preferentially, a contact along the ab plane. On average in

the bulk, the single crystals were cleaner than the films, but one had to be cautious, since the properties of the crystal surface differ from the properties of the bulk, and the fabrication of a PC may introduce uncontrolled further defects in the contact area.

Thus, *a priori* one cannot define the structure and composition of the obtained contacts. Nevertheless, many of the issues concerning the composition and structure of contacts can be resolved by measuring various characteristics of a contact. Among these, the most important is the Andreev-reflection-non-linearities of the $I-V$ curves in the SC energy-gap range. The magnetic field and temperature dependencies of the SC non-linearities provide us with additional information. In addition, much data can be extracted from the $I-V$ nonlinearities in the normal state (the so called PC spectra). The more information about the electrical conductivity at different conditions of the particular contact one can collect, the more detailed and defined picture of it emerges. Doing this, however, is not an easy task, since a contact has a limited life time, due to electrical and mechanical shocks.

Here is a rough estimation of the distance scales involved in the problem. The crystallite size of the films is of the order of 100 nm (see [18]). The contact size d in the ballistic regime equals $d \simeq \sqrt{\rho l/R}$ (the Sharvin formula). Taking $\rho l \cong 0.7\times10^{-6}\Omega\,\mathrm{cm}\times7\,10^{-6}\mathrm{cm}\cong 0.5\times10^{-11}\Omega\,\mathrm{cm}^2$ [10], one obtains $d \simeq 7$ nm both along the ab and the c directions for a typical resistance of 10 Ω. If one supposes that a grain is dirty (with a very short mean free path), then one can apply the Maxwell formula $d \sim \rho/R$ with the results for d of about 0.7 nm and 2.6 nm for the ab and c directions, respectively, taking ρ for corresponding directions from the same reference [10]. Thus, the contact size can be of the order or smaller than the electronic mean free path ($l_{ab} = 70$ nm and $l_c = 18$ nm, according to [10]), which means that one is working in the spectroscopic regime, probing only a single grain.

Rowell [20], analyzing a large amount of experimental data for resistivity and its temperature dependence, came to the conclusion that for highly resistive samples only a small part of the effective cross section should be taken into account. The reason for this is that the grains in MgB_2 are disconnected by oxide of magnesium and boron to a great extent. For PCS, previous analysis leads one to the conclusion that the contact resistance is frequently measured only for a single grain or for several grains, with their intergrain boundaries facing the contact interface. This is due to the current spreading with a scale of the order of the contact size d near the constriction.

3. Theoretical background of PCS

The non-linearities of the $I - V$ characteristic of a metallic contact, when one of the electrodes is in the SC state, can be written as [21]

$$I\,(V) \simeq V/R_0 + \delta I^N_{ph}(V) + I_{exc}(V) \tag{1}$$

Here R_0 is the contact resistance at zero bias in the normal state. $\delta I^N_{ph}(V)$ is the backscattering inelastic current which depends on the electron mean free path (mfp) l. For the ballistic contact this term amounts to

$$\delta I^N_{ph}(V) \sim (d/l_{in}) I(V) \tag{2}$$

where l_{in} is the inelastic electron mfp, and d is the characteristic contact diameter. If the electron flow through the contact is diffusive ($l_{el} \ll d$, l_{el} being an elastic mfp) but still spectroscopic, since $\sqrt{l_{in} l_{el}} \gg d$, then the expression (2) should be multiplied by l_{el}/d. This decreases the characteristic size, where the inelastic scattering, being essential, is from d to l_{el} ($d \to l_{el}$), and for short l_{el} makes the inelastic current very small. We notice that the inelastic backscattering current $\delta I^N_{ph}(V)$ in the SC state is approximately equal to the same term in the normal state. Its second derivative turns out to be directly proportional to the EPI function $\alpha^2(\omega)\, F(\omega)$ [22, 23]

$$-d^2 I/dV^2 \simeq (8\, ed/3\, \hbar v_{\mathrm{F}}) \alpha^2(\omega)\, F(\omega) \tag{3}$$

where α describes the strength of the electron interaction with one or another phonon branch, and $F(\omega)$ stands for the phonon density of states. In the PC spectra, the EPI spectral function $\alpha^2(\omega)\, F(\omega)$ is modified by the transport factor, which increases strongly the backscattering processes contribution.

In the SC state the excess current $I_{exc}\,(1)$, which is due to the Andreev reflection of electron quasiparticles from the $N - S$ boundary in a $N - c - S$ contact (c stands for "constriction"), can be written as

$$I_{exc}\,(V) = I^0_{exc} + \delta I_{exc}\,(V) \tag{4}$$

where $I^0_{exc} \approx \Delta/R_0 \approx const$ for $eV > \Delta$ (Δ being the SC energy gap).

The nonlinear term in the excess current (4) in its turn can be separated into two parts, which depend in a different way on the elastic scattering of electron quasiparticles:

$$\delta I_{exc}\,(V) = \delta I^{el}_{exc}\,(V) + \delta I^{in}_{exc}\,(V) \tag{5}$$

where $\delta I^{el}_{exc}\,(V)$ is of the order of $(\Delta/eV)\, I^0_{exc}$, and $\delta I^{in}_{exc}\,(V) \sim (d/l_{in})\, I^0_{exc}$. One should note that the latter behaves in a manner which is very similar to the inelastic backscattering current $\delta I^N_{ph}(V)$; namely, it disappears

if $l_{el} \to 0$, while the first term in the right hand side of the expression (5) does not depend on l_{el} in the first approximation . This enables one to distinguish the elastic term from the inelastic term. Finally, all excess current terms disappear when destroying the superconductivity, while $\delta I^N_{ph}(V)$ remains very similar in both SC and normal states.

From the expressions (1), (2), (4) and (5), it becomes clear that only on the relatively *clean* spots, can one observe the inelastic backscattering current $\delta I^N_{ph}(V)$ provided the excess current term $\delta I^{in}_{exc}(V)$ is negligible. The latter can be cancelled by the suppression of superconductivity either by a magnetic field or temperature. On the other hand, in the SC state, for *dirty* contacts, all the inelastic terms are very small, and the main non-linearity is provided by the $\Delta(eV)$-dependence on the excess current.

Brinkman *et al.* [11] have shown that even along the *ab*-plane the contribution of a σ band for MgB_2 is less than that of a π band, to say nothing of the direction along the c axis, where it is negligible. The calculation predicts that if the "*tunneling cone*" is several degrees from the precise *ab* plane, then two SC gaps should be visible in tunneling characteristics. In the other directions, only a single gap, corresponding to the π band, is visible. Below, it is shown that this prediction is fulfilled in the PC experiment as well.

Things become more difficult when one tries to measure the anisotropic Eliashberg function by means of the SC tunneling. The single-band numerical inversion program gives uncertain results, as was shown in Ref. [25].

Point-contact spectroscopy in the normal state can help clarify this situation. It is known that the inelastic backscattering current is based on the same mechanism as that of an ordinary homogeneous resistance, provided the maximum energy of the charge carriers is controlled by an applied voltage. The electrical conductivity of MgB_2 can be considered as the parallel connections of two channels, corresponding to the π and σ bands [2]. The conductivity of a π band can be blocked by Mg-atoms disorder. This situation has been observed by experiment when the temperature coefficient of resistivity increases simultaneously with increase of residual resistivity, which leads to the violation of the Matthiessen's rule (see Fig. 3 in [2]). In this case, one can obtain direct access to the σ-band conductivity, and the measurements of PC spectra of EPI for the σ band are explicitly possible in the normal state. Below, one can see that this unique situation happens in single crystals along the *ab* plane.

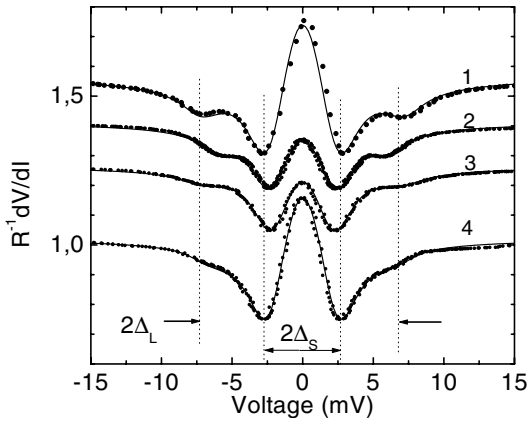

Figure 1 dV/dI (experimental dots) for 4 contacts between a MgB_2 thin film and Ag with corresponding BTK fitting (lines) [27]. $\Delta_{L(S)}$ stands for large (small) SC energy gap. After Naidyuk et al. [27].

4. Experimental results

4.1 Superconducting energy gaps

Typical shapes of dV/dI with Andreev reflection features are shown in Fig. 1. The dV/dI curves exhibit two sets of energy gap minima distributed as shown in Fig. 2 (upper panel), at 2.4± 0.1 and 7.1±0.4 meV. These curves are nicely fitted by the BTK [26] theory (with a small Γ parameter) for two conducting channels with an adjusted gap weighting factor [27]. The second kind of dV/dI represents only one gap structure and is better fitted with a single gap giving an increased depairing parameter Γ (Fig. 2, inset). According to the calculation in [11] strong impurity scattering will cause the gaps to converge to $\Delta \simeq 4.1$ meV and T_c to 25.4 K. Therefore the single gap spectra reflect a strong interband scattering due to impurities, which likely causes a "semiconducting-like" behavior of dV/dI above T_c. These two kinds of gap structure constitute almost equal parts of about one hundred junctions. Usually the contribution of the large gap in the double-gap spectra is an order of magnitude lower than that of the small one, which is in line with the small contribution of the σ band to the conductivity along the c axis [11].

In the lower panel of Fig. 2 the theoretical prediction of the energy gap distribution [13] is shown. One can see that the theoretical positions of distribution maxima approximately coincide with the experimental values. Only the low-lying maximum is not seen in the experiment.

The same variety of energy gap structure is observed for single crystals as well, but with some peculiarity due to the preferential orientation along the *ab* plane. The most amazing of them is the observation of a dV/dI gap structure in [37] with visually only the larger gap present. This kind of spectra was not observed in thin films. This means that

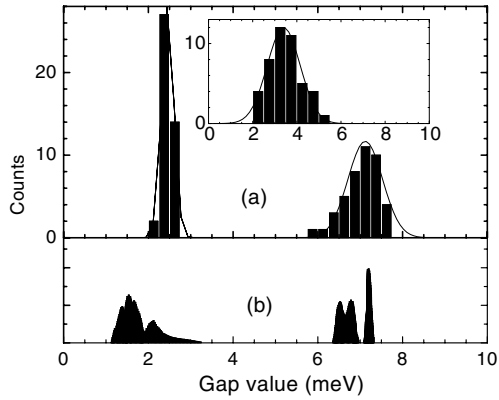

Figure 2 (a) Superconducting energy gap distribution for about one hundred different junctions prepared on a MgB_2 film [27]. The inset shows the single gap distribution. (b) Theoretical gap distribution after [13].

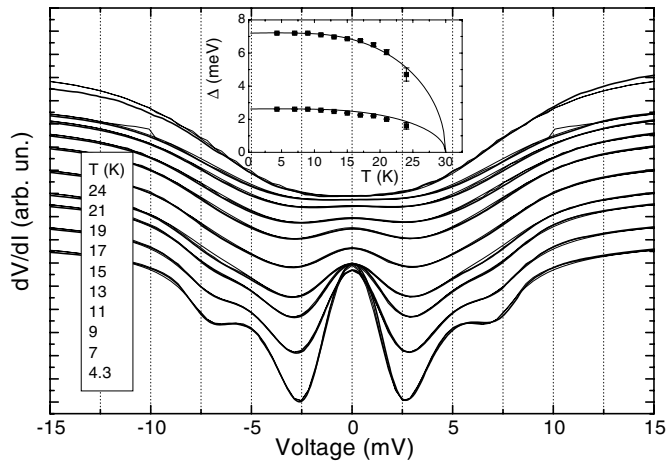

Figure 3. dV/dI curves (solid lines) at different temperatures for the same junction as in Fig. 4 with their BTK fittings (thin lines). Inset: Temperature dependencies of large and small SC energy gaps obtained by BTK fitting. Solid lines represent BCS-like behavior.

the conductivity is governed only by the σ band. This may be because the π band is blocked completely by Mg disorder or by oxidation of Mg atoms on the *ab*-side surface of the crystal. At the same time, in the single crystal, there is much less scattering in the boron planes, due to the robustness of the B-B bonds. One will see below that just this case enables one to observe directly the most important E_{2g} phonon mode in the electron-phonon interaction within the σ band.

Figs. 3 and 4 display the series of temperature and magnetic field dependencies of the dV/dI curves with their BTK fittings, respectively. Here at low field (temperature), the two separate sets of the gap minima

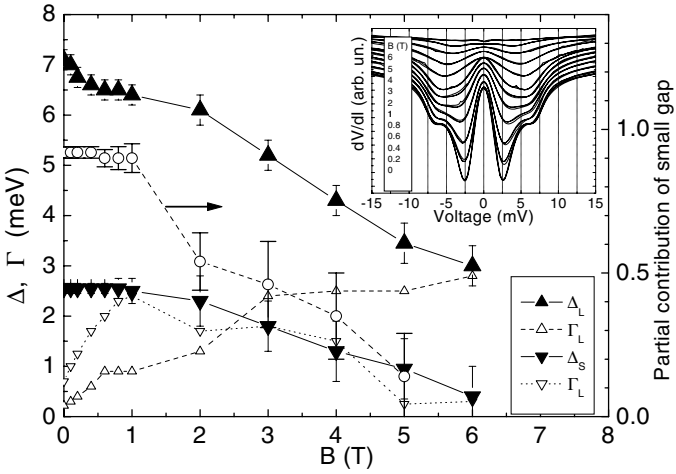

Figure 4. Magnetic field dependencies of large and small SC energy gaps (solid triangles) obtained by BTK fitting of the dV/dI curves from inset. Open triangles show Γ value for large and small gap, correspondingly. Circles demonstrate the depressing of the small gap contribution to the dV/dI spectra by the magnetic field. The lines connect the symbols for clarity. Inset: dV/dI curves (solid lines) at different magnetic field for a single crystal junction MgB_2-Cu 2.2 Ω along the *ab* plane with their BTK fittings (thin lines).

are clearly seen. The temperature dependence of both gaps follows the BCS prediction (see inset in Fig. 3). For temperatures above 25 K their behavior is unknown because this particular contact did not survive during the measurements likely due to thermal expansion of the sample holder.

Fig. 4 shows the magnetic field dependencies of large and small gaps. Surprisingly, the small gap value is not depressed by a field of about 1 T, and the estimated critical field of about 6 T is much higher as stated in [28, 29]. The intensity of small gap minima is suppressed rapidly by a field of about 1 T. Correspondingly, the small gap contribution w (w inversely depends on the Γ value, therefore the nearly constant w value between 0 and 1 T is due to the fact that Γ rises by a factor of 4 at 1 T) to the dV/dI spectra decreases significantly versus magnetic field from 0.92 to 0.16 (see Fig. 4), while w versus temperature even slightly increases from 0.92 at 4.3 K to 0.96 at 24 K (not shown). Theoretical investigation of the field dependence of the maximum pair potential in a two band superconductor MgB_2 by Koshelev and Golubov [30] shows that for both gaps, the critical field is the same. Additionally, in a recent experimental publication, Bugoslavsky *et al.* [31] reported that both order parameters survive to a common magnetic field, while Gonnelli *et al.* [32] corrected

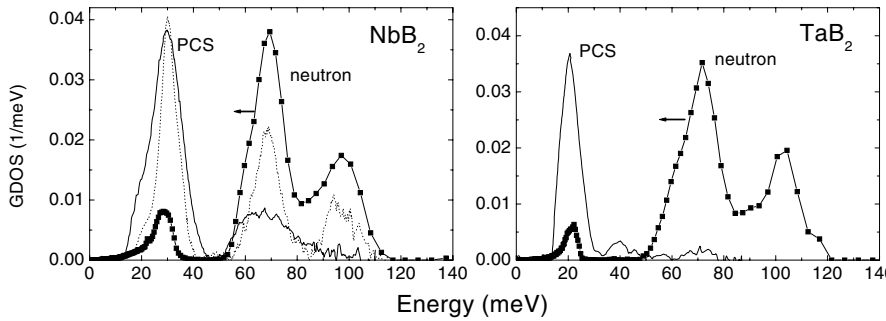

Figure 5. Comparison of phonon DoS neutron measurements [34] (symbols) with PC spectra for NbB_2 and TaB_2 [33] after subtraction of the rising background (solid curves). The dotted curve in the left panel shows the PC spectrum of ZrB_2 [33] for comparison.

their previous claims. They mentioned that the critical magnetic field, for which the π band features in dV/dI visually disappears, might not be correct.

4.2 Electron-Phonon interaction

4.2.1 PC EPI spectra of non-SC diborides. In Fig. 5 the PC EPI spectra $d^2V/dI^2 \propto -d^2I/dV^2$ (see also Eq. (3)) of non-SC diborides MeB_2 (Me=Zr, Nb, Ta) [33] are shown. The cleanest sample studied was a ZrB_2 single crystal, and its PC EPI spectrum demonstrated more pronounced features (see Fig. 5, left panel). One recognizes a classical PC EPI spectrum from which one can estimate the position of three main phonon peaks (for ZrB_2) and obtain the lower limit of the EPI parameter $\lambda_{PC} \leq 0.1$ [33].

Essentially similar spectra were observed for other diborides. The only difference was a degradation of maxima with bias rise , taking into account their purity and increased EPI, which leads to the transition from the spectroscopic to the non-spectroscopic (thermal) regime of the current flow [33]. The positions of the low-energy peaks are proportional to the inverse square root of the masses of the d metals [33], as expected. For NbB_2 and TaB_2 the phonon density of states (DoS) is measured by means of neutron scattering [34]. The position of phonon peaks corresponds to the PC spectra maxima (Fig. 5). Because Nb and Zr have nearly the same atomic mass, it is suggested that they should have similar phonon DoS.

4.2.2 PC EPI spectra of MgB_2 in c-oriented films. Unexpectedly, the stronger we suppress the superconductivity by either mag-

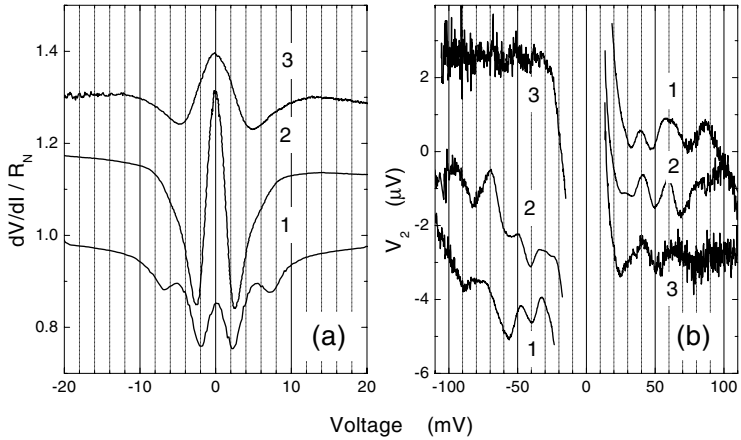

Figure 6. Superconducting gap minima (left panel) and phonon structure (right panel) in the spectra of thin film MgB_2-Ag PCs with different resistances at $T = 4.2K$, $B = 0$ with R_0=45, 43, and 111 Ω for curves 1,2 and 3, respectively. The modulation voltage V_1 when measuring the V_2 signal is 3.31, 2.78, and 2.5 mV, for curves 1,2 and 3, respectively. The numbers of curves in (b) are the same as in (a). The curves in (a) are offset for clarity. After Yanson et al. [17].

netic field or temperature in MgB_2, the fewer traces of phonon structure remain in the d^2V/dI^2 derivative [17]. This is at odds with the classical PCS, since the *inelastic* phonon spectrum should not depend on the state of electrodes in the first approximation (see section **Theoretical background of PCS**). Instead, most of the MgB_2 spectra in the SC state show a reproducible structure in the phonon energy range (Fig. 6) which was not similar to the expected phonon maxima superimposed on the rising background. This structure disappears by transition to the normal state. Interestingly, the intensity of this structure increases with the increase of the value of the small gap, which means that the gap in the π band and the observed phonon structure are connected [17]. Based on the theoretical consideration mentioned above, one can conclude that the disorder in the π band is so strong that it precludes the observation of the *inelastic current*, and the phonon non-linearities of excess current [17, 24] play the major role, which does not depend on the scattering.

Very rarely, (see [35]) the structure in d^2V/dI^2 which corresponds reasonably in shape to the phonon DoS (above 30 meV) was obtained. Thus, for this contact one can assume the observation of the *inelastic* PC spectrum for the π band, which is comparable to the Eliashberg EPI function for the same band calculated in Ref. [36]. Both experimental spectrum and π band Eliashberg function do not show the anomalously

high intensity of the E_{2g} phonon mode, since only the Eliashberg function for the σ band is the principal driving force for the high T_c in MgB_2. The same conclusion should be ascribed to the excess-current phonon structure, since it also corresponds to the π band. This band has much larger Fermi velocity and plasma frequency along the c-axis compared to the σ band [11]. Thus, in order to record the main EPI with the E_{2g} phonon mode, the PC spectra along the ab plane should be measured.

4.2.3 PC EPI spectra in ab-direction. In Ref. [37], the PC EPI spectra for a single crystal oriented in the ab plane were measured. As was mentioned above, the nominal parallel orientation of the contact axis to the ab plane is not sufficient to be sure that this situation occurs in reality. Moreover, even if one establishes the necessary orientation (i.e., the contact axis parallel to the ab plane) the spectra should reflect both bands with a prevalence of the undesired π band, because due to the spherical spreading of the current, the orientational selectivity of the metallic PC is much worse than that for the plane tunnel junction, where it goes exponentially. The large mixture of the π-band contribution is clearly seen from the gap structure in Fig. 7 (b), inset. Beyond the wings at the biases corresponding to the large gap (supposed to belong to the σ-band gap), the deep minima located at the smaller gap (corresponding to the π-band gap) are clearly seen. The EPI spectrum of the same junction is shown in the main panel. One can see that the non-linearities of the $I-V$ characteristic at phonon biases are very small, and the reproducible structure roughly corresponding to the Eliashberg EPI function of the π band [25, 36] appears in the bias range $20 \div 60$ mV. Above 60 mV, the PC spectrum broadens noticeably, sinking the higher lying phonon maxima. No remarkable contribution of the E_{2g} phonon mode is observed, like a big maximum of EPI at $\approx 60 \div 70$ meV or a kink at $T \geq T_c$ for these biases.

A quite different spectrum is shown in Fig. 7(a), which is the key result. Consider first the $dV/dI(V)$ characteristics (see inset). The energy gap structure shows gap minima corresponding to the large gap (σ-band gap). The increase of $dV/dI(V)$ at larger biases is noticeably larger than in the previous case.

Before the saturation at biases ≥ 100 meV, where the phonon DoS ends, a well resolved, wide bump, occurs in the PC spectrum, which is located at about 60 meV. One can show that this bump is of spectroscopic origin, that is to say, the regime of the current flow through the contact is not thermal, although the background at large biases ($V \geq 100$ meV) is high. To do so, one can compare this bump with a PC spectrum in thermal regime for a model EPI function, which is

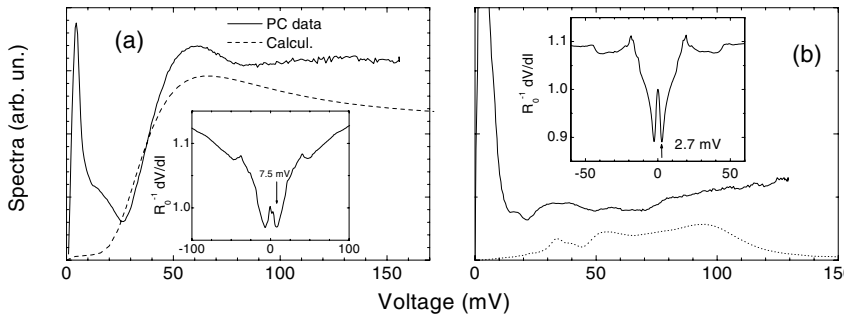

Figure 7. (a) Comparison of the PC spectrum for the σ band with the thermal spectrum using a Lorentzian model spectral function at 60 meV with a width of 2 meV (dashed line). The inset shows large gap minima. (b) PC spectrum for π band. The dashed curve is the smeared theoretical Eliashberg function [36]. The inset shows small gap minima. After Naidyuk et al. [37].

Lorentzian at 60 meV with a small (2 meV) width. According to Kulik [38], the thermal PC EPI calculated spectrum, shown in Fig. 7(a) as a dashed line, is much broader. Any further increase of the width of the model spectra will broaden the curve obtained. Comparing the experimental and model spectra enables one to conclude that in spite of its great width, the maximum of the experimental spectra still corresponds to the spectroscopic regime. Introducing greater disorder in the boron plane by a fabrication procedure or trying other spots on the side-face surface leads to the observation of smeared, thermal-like spectra, coinciding in shape with the dashed curve in Fig. 7(a) which, together with the corresponding energy-gap structure, can be ascribed to the thermal limit mainly in the π band, despite the low bath temperature.

The PC spectrum with broad maxima including one at about 60 mV, were observed by [29] on polycrystalline MgB_2 samples driven to the normal state by applying magnetic field and increasing the temperature.

The large width of the EPI peak connected with the E_{2g} phonon mode was not surprising. Shukla *et al.* [12] measured the phonon dispersion curves along ΓA and ΓM directions by means of inelastic X-ray scattering. The full width at half maximum (FWHM) for the E_{2g} mode along the ΓA direction amounts to about 20-28 meV, which corresponds well with what was observed in the PC spectrum. If the phonon life time corresponds to this (inverse) energy, then the phonon mean free path is about the lattice constant [37], and due to phonon reabsorption by nonequilibrium electrons, one should anticipate a large background in the PC spectra as observed.

For a contact with E_{2g} phonon modes in Fig. 7(a) the nonlinearity of the $I-V$ curves due to electron-phonon interaction can be estimated from the dV/dI curves by about 10%. This is comparable with the nonlinearity observed for non-SC diborides [33] with small electron-phonon coupling constant $\lambda_{PC} \leq 0.1$. The reason for the relatively low nonlinearity of the $I-V$ curves and the small intensity of the main E_{2g} phonon modes in the spectra for MgB_2 contacts can be due to the fact that an anomalous strong interaction is characteristic for a restricted group of phonons with sufficiently small wave vector [9], whereas in PCS, the large angle scattering is increased.

5. Conclusions

Comprehensive PCS investigations of c-axis oriented thin films and single crystals of MgB_2 lead to the following conclusions:

- The observed Andreev-reflection-SC gaps in MgB_2 are grouped at 2.4 and 7.0 meV and show basically a BCS-like temperature dependence. The two-gap structure merges together in the case of strong elastic scattering, and remains a single gap at about 3.5 meV.

- Anomalous magnetic field dependencies of the gap structure in PCs reflect the peculiarity of the two band structure of the SC order parameter in MgB_2. In particular, a small gap survives up to a magnetic field, which is close to the critical one for a large gap.

- The phonon structure in the PC spectra of MgB_2 can be revealed by: i) the inelastic backscattering current, like for ordinary PCS, and ii) by the energy dependence of the excess current. They can be discriminated after destroying the superconductivity by magnetic field and/or temperature, and by varying the electron mean free path.

- The prevailing appearance in the PC spectra of the E_{2g} boron mode, which mediates the creation of Cooper pairs, is seen for PC with a large gap that is along the $a-b$ direction, in accordance with the theory. The relatively small intensity of this mode in the PC spectra is likely due to their small wave vector and restricted phase volume.

- Related diborides (ZrB_2, NbB_2, and TaB_2) have PC spectra proportional to the electron-phonon-interaction spectral function, like

in common metals and a small EPI constant corresponding to their non-SC state at helium temperature.

Acknowledgements

The authors are grateful to N. L. Bobrov, P. N. Chubov, V. V. Fisun, O. E. Kvitnitskaya, L. V. Tyutrina for collaboration during MgB_2 investigation and S.-I. Lee and S. Lee for samples providing. The work in Ukraine was supported by the State Foundation of Fundamental Research under Grant Φ7/528-2001.

References

[1] J. Nagamatsu, N. Nakagawa, T. Muranaka, Y. Zenitani, J. Akimitsu, Nature **410**, 63 (2001).

[2] I.I. Mazin, O.K. Andersen, O. Jepsen, O.V. Dolgov, J. Kortus, A.A. Golubov, A.B. Kuz'menko, and D. van der Marel, Phys. Rev. Lett. **89**, 107002 (2002).

[3] A. Gurevich, Phys. Rev. B **67**, 184514 (2003).

[4] J.M. An and W.E. Pickett, Phys. Rev. Lett. **86**, 4366 (2001).

[5] Y. Kong, O.V. Dolgov, O. Jepsen, and O.K. Andersen, Phys. Rev. B **64**, 020501(R) (2001).

[6] J. Kortus, I.I. Mazin, K.D. Belashchenko, V.P. Antropov, and L.L. Boyer, Phys. Rev. Lett **86**, 4656 (2001).

[7] Amy Y. Liu, I.I. Mazin, and Jens Kortus, Phys. Rev. Lett. **87**, 87005 (2001).

[8] T. Yildirim, O. Gülseren, J.W. Lynn, C.M. Brown, T.J. Udovic, Q. Huang, N. Rogado, K.A. Regan, M.A. Hayward, J.S. Slusky, T. He, M. K. Haas, P. Khalifah, K. Inumaru, and R.J. Cava, Phys. Rev. Lett. **87**, 037001 (2001).

[9] I.I. Mazin, V.P. Antropov, Physica C **385**, 49 (2003).

[10] Yu. Eltsev, K. Nakao, S. Lee, T. Masui, N. Chikumoto, S. Tajima, N. Koshizuka, M. Murakami, Phys. Rev. B **66**, 180504(R) (2002).

[11] A. Brinkman, A.A. Golubov, H. Rogalla, O.V. Dolgov, J. Kortus, Y. Kong, O. Jepsen, and O.K. Andersen, Phys. Rev. B **65**, 180517 (2002).

[12] A. Shukla, M. Calandra, M. d'Astuto, M. Lazzeri, F. Mauri, Ch. Bellin, M. Krisch, J. Karpinski, S.M. Kazakov, J. Jun, D. Daghero, and K. Parlinski, Phys. Rev. Lett. **90**, 095506 (2003).

[13] Hyoung Joon Choi, David Roundy, Hong Sun, Marvin L. Cohen, Steven G. Louie, Nature **418**, 758 (2002); Phys. Rev. B **66**, 020513(R) (2002).

[14] J.M. An, S.Y. Savrasov, H. Rosner, and W.E. Pickett, Phys. Rev. B **66**, 220502(R) (2002).

[15] E. Cappelluti, S. Ciuchi, C. Grimaldi, L. Pietronero, and S. Strässler, Phys. Rev. Lett. **88**, 117003 (2002).

[16] F. Bouquet ,Y. Wang, I. Sheikin, P. Toulemonde, M. Eisterer, H.W. Weber, S. Lee, S. Tajima, A. Junod, Physica C **385**, 192 (2003).

[17] I.K. Yanson, V.V. Fisun, N.L. Bobrov, Yu.G. Naidyuk, W.N. Kang, Eun-Mi Choi, Hyun-Jung Kim, and Sung-Ik Lee, Phys. Rev. B **67**, 024517 (2003).

[18] W.N.Kang, Eun-Mi Choi, Hyeong-Jin Kim, Hyun-Jung Kim, Sung-Ik Lee, Physica C **385**, 24 (2003).

[19] Sergey Lee, Physica C **385**, 31 41 (2003); S. Lee, H. Mori, T. Masui, Yu. Eltsev, A. Yamanoto and S. Tajima, J. Phys. Soc. of Japan, **70**, 2255 (2001).

[20] J.M. Rowell, Supercond. Sci. Technol. **16**, R17-27 (2003).

[21] V.A. Khlus and A.N. Omel'yanchuk, Sov. J. Low Temp. Phys. **9**, 189 (1983); V.A. Khlus, Sov. J. Low Temp. Phys. **9**, 510 (1983).

[22] I.O. Kulik, A.N. Omelyanchouk, and R.I. Shekhter, Sov. J. Low Temp. Phys. **3,** 840 (1977).

[23] I.K. Yanson, in book I.O. Kulik and R.Ellialtioglu (eds.)*, Quantum Mesoscopic Phenomena and Mesoscopic Devices in Microelectronic,*, (Kluwer Acad. Publ., 2000) p. 61-77. (see also: cond-mat/0008116).

[24] A.N. Omel'yanchuk, S.I. Beloborod'ko, and I.O. Kulik, Sov. J. Low Temp. Phys. **14**, 630 (1988).

[25] O.V. Dolgov, R.S. Gonnelli, G.A. Ummarino, A.A. Golubov, S.V. Shulga, and J. Kortus, cond-mat/0301542.

[26] G.E. Blonder, M. Tinkham and T.M. Klapwijk, Phys. Rev. B **25**, 4515 (1982).

[27] Yu.G. Naidyuk, I.K. Yanson, L.V. Tyutrina, N.L. Bobrov, P.N. Chubov, W.N. Kang, Hyeong-Jin Kim, Eun-Mi Choi, and Sung-Ik Lee, JETP Lett. **75**, 283 (2002).

[28] R.S. Gonnelli, D. Daghero, G.A. Ummarino, V.A. Stepanov, J. Jun, S.M. Kazakov and J. Karpinski, Phys. Rev. Lett. **89** 247004 (2002).

[29] P. Samuely, P. Szabo, J. Kacmarcik, T. Klein, A.G.M. Jansen, Physica C **385** 244 (2003).

[30] A. E. Koshelev and A. A. Golubov, Phys. Rev. Lett. **90**, 177002 (2003).

[31] Y.Bugoslavsky, Y.Miyoshi, G.K. Perkins, A.D. Caplin, L.F.Cohen, A.V. Pogrebnyakov, X.X. Xi, cond-mat/0307540.

[32] R.S. Gonnelli, D. Daghero, G.A. Ummarino, V. Dellarocca, V.A. Stepanov, J. Jun, S.M. Kazakov and J. Karpinski, cond-mat/0308152.

[33] Yu.G. Naidyuk, O.E. Kvitnitskaya, I.K. Yanson, S.-L. Drechsler, G. Behr, and S. Otani, Phys. Rev. B **66**, 140301 (2002).

[34] R. Heid, B. Renker, H. Schober, P. Adelmann, D. Ernst, and K.-P. Bohnen, Phys. Phys. B **67**, 180510(R)(2003).

[35] N.L. Bobrov, P.N. Chubov, Yu.G. Naidyuk, L.V. Tyutrina, I.K. Yanson, W.N. Kang, Hyeong-Jin Kim, Eun-Mi Choi, C.U. Jung, and Sung-Ik Lee, in book *New Trends in Superconductivty*, Vol.67 of NATO Science Series II: Math. Phys. and Chem., ed. by J. F. Annett and S. Kruchinin, (Kluwer Acad. Publ., 2002), p.225.

[36] A.A. Golubov, J. Kortus, O.V. Dolgov, O. Jepsen, Y. Kong, O.K. Andersen, B.J. Gibson, K. Ahn, and R.K. Kremer, J. Phys.: Condens. Matter **14**, 1353 (2002).

[37] Yu.G. Naidyuk, I.K. Yanson, O.E. Kvitnitskaya, S. Lee, and S. Tajima, Phys. Rev. Lett., **90**, 197001 (2003).

[38] I.O. Kulik, Sov. J. Low Temp. Phys. **18**, 302 (1992).

MODERN APPROACHES IN POINT-CONTACT SPECTROSCOPY AND THEIR APPLICATION TO PROBE NANOCLUSTERS IN MESOSCOPIC MATERIALS

GENNADIY V.KAMARCHUK[1], PAVEL N.CHUBOV[1], VASILIY A.GUDIMENKO[1], PHILIPPE MOLINIE[2], ANNIE LEBLANC-SOREAU[2], ERIC C.FAULQUES[2]

1 – B.Verkin Institute for Low Temperature Physics & Engineering of NAS of Ukraine, 47 Lenin Ave., Kharkov, 61103 Ukraine.

2 – Institut des Matériaux Jean Rouxel, 2 rue de la Houssinière, BP 32229, F-44322 Nantes, France

Abstract: Modern approaches in point-contact spectroscopy were used for the identification of nanoclusters in mesoscopic materials. The conductive properties of a new layered mesoscopic superconductor $SnNb_5Se_9$ were studied. The investigation has been carried out with Ag(Cu)/$SnNb_5Se_9$ heterocontacts. Temperature dependence of heterocontact current-voltage characteristic derivatives gave the opportunity to study the superconducting behavior of the samples. Nanoclusters of the initial substances $NbSe_2$ and Nb_3Sn have been revealed. Their volume concentration is less than 10^{-7} in the host matrix. The value of the superconducting energy gap for $SnNb_5Se_9$ and its temperature dependence have been determined.

Key words: Point contact spectroscopy, layered compounds, nanoclusters, superconductivity.

E. C. Faulques et al. (eds.), Spectroscopy of Emerging Materials, 289–298.

1. INTRODUCTION

Contemporary research trends related to the development of mesoscopic materials, which contain nanosized inclusions of guest compounds and phases in a host matrix, are among the most prospective fields for technological applications. The physical characteristics of nano-objects in such materials can substantially differ from those of their macroscopic analogs. As a result there is a strong need to investigate both the properties of individual nano-objects and their parameter modifications when they interact with their environment.

A new family of ternary compounds BM_5Se_9 (B = Sn, Ga, and M = Nb, V), which is synthesized by dissolution of A15 superconductors in metallic dichalcogenides [1], can serve as an example of such materials. These compounds demonstrate superconducting and ferromagnetic properties at low temperatures. New local mesoscopic phase states are expected because of the complexity and possible inhomogeneity of their structure. For this reason it is necessary to investigate the physical parameters of the new compounds both on the microscale [2,3] and nanoscale levels. In this work we studied the conductive properties of $SnNb_5Se_9$ crystals, which is one of the representatives of these ternary compounds. The investigation was carried out by a nanocontact technique demonstrating the advanced possibilities of point-contact spectroscopy (PCS).

The key tool of PCS is a point contact with a diameter d much smaller than the mean free path l of the charge carriers [4]. As a rule the size of point contacts ranges from the meso- to the nanoscale up to the atomic size. In the classical case of ballistic current regime, the electrons flow through a contact of diameter $d<<l$ and get an excess energy of eV value, which is sufficient to induce atomic vibrations in the constriction area (e – electron charge, V – bias applied to the contact). Due to electron and phonon large mean free paths charge carriers can scatter on lattice vibrations without thermal heating effects in the contact material. All the thermal energy goes effectively to the banks-electrodes, forming the contact, and the initial nature of the electron-phonon interaction (EPI) is not distorted. As a result, nonlinearities caused by nonelastic energy-transfer processes from electrons to phonons appear in the current-voltage characteristic (IVC) of the contact. The energy-scale positions of the IVC nonlinearities correspond to the spectral lines of the phonon-density-of-states function $F(\omega)$ and the EPI function $g(\omega)$ for the material under investigation. One can clearly observe this process when studying the point-contact IVC second derivative which is directly proportional to the EPI point-contact function $g_{pc}(\omega)$ [5]:

$$\frac{d^2I}{dV^2}(eV) = -\frac{\pi e^3}{\langle K \rangle}\Omega_{eff} N(\varepsilon_F) g_{pc}(\omega)\Big|_{\omega=eV} .$$

Here $N(\varepsilon_F)$ is the electron density of states on the Fermi surface for one direction of spin, Ω_{eff} is the effective volume of phonon generation, $\langle K \rangle$ is the point contact form factor, averaged over the Fermi surface. It should be noted that point contacts of sizes $d \geq l$, $d >> l$ can work also in diffusive or thermal current regimes [5] and are used for the study of EPI, phase transitions, superconductivity and other interesting physical phenomena.

Initially PCS was developed as a powerful method for classical conductors investigations, in particular, for the direct determination of EPI of normal metals [6]. Further improvements of the PCS have permitted advanced investigation of physical parameters such as, for instance, EPI and energy gap in superconductors [7, 8, 9], quantization of conductivity in atomic objects [10], spin polarization in ferromagnets and their junctions with superconductors [11, 12], etc. In addition to the above-mentioned phenomena PCS allows to solve another type of problems connected with cluster physics. For this purpose one can use the displacement technique [13] in the point contact experiment. This device is described in [14] and allows a number of point contacts on the sample surface with linear dimensions up to 25-30 mm and more during the experiment. Thus, the displacement technique gives the opportunity to obtain during the investigation cycle many contacts suitable for PCS and to probe the object surface. Point contacts used have diameters of nanometer size or less and can serve as a nano-probe, that detects and records nano-objects whose physical properties differ from those of the matrix material. For example, tiny superconducting clusters which could not be characterized by other methods have been revealed by using this technique [15]. Taking into consideration these technical peculiarities, the present work is aimed at the investigation of conductive and superconducting properties of $SnNb_5Se_9$ by probing crystal surfaces with PCS.

2. EXPERIMENTAL TECHNIQUE

The crystals of $SnNb_5Se_9$ were obtained by dissolution of the A15 Nb_3Sn superconductor in the dichalcogenide 2H-$NbSe_2$ according to the method described in [1]. The crystal sizes ranged from 1×1×0.5 to 3×3×1 mm^3. Preliminary susceptibility study of the compound by SQUID technique demonstrated temperature superconductivity transition at T = 17.5 K [1-3].

The heterocontacts between layered compound and noble metals – silver and copper – were studied. The standard chemical and electrochemical treatment of silver and copper electrode surfaces [6] was performed before the experiment. To avoid any selective etching and breaking of the surface layer, the $SnNb_5Se_9$ crystals were not chemically treated.

To create point contacts and to probe the conductive properties on the surface of the samples under investigation we used the displacement technique and the special device described in Ref. [14]. The experiments were carried out on the original point contact spectrometer designed at the B.Verkin ILTPE. The cryogenic equipment of the set up allowed measurements at temperatures of 0.8 – 300K and for magnetic fields in the 0-5 T range. The IVC *I(V)* of heterocontacts, the first derivative *dV/dI(V)* and the second derivative of *I(V)* were studied. The *I(V)* derivatives were measured by a standard scheme detecting the harmonics of the alternating signal when the spectrometer works in the current source regime [6]. In this case harmonics of the alternating voltage arising at the contact are proportional to the *I(V)* derivatives of the contact and can be recorded with high accuracy.

3. RESULTS AND DISCUSSION

In this article we will present a fraction of the numerous data obtained for more than 200 contacts of $SnNb_5Se_9$. First of all let us note that the crystals studied were tested to obtain information about the electron mean free path and the spectral current regime. For this purpose we measured the electrical resistance of samples and determined the value of the resistance correlation $R_{300}/R_{4.2}$ at room and liquid helium temperature. This ratio is a good test for the evaluation of the sample quality and for choosing the crystals most amenable for future investigation. For all the samples studied the correlation $R_{300}/R_{4.2}$ was not higher than 1.5. This value indicates a rather short mean free path of the charge carriers in these objects. Taking into account the fact that high quality crystalline phase was observed in Ref. [2, 3] at the micrometer scale, one can suppose that such short mean free paths could be connected in particular with carrier scattering on guest nanosized clusters in the host matrix. Thus, there is a small probability that the spectral-regime correlation $d<<l$ holds in these samples. However, this does not exclude the possibility to find areas where contacts suitable for investigation could be obtained. Such a conclusion was confirmed in the following. To create higher quality point contacts we used pure noble metals (silver and copper). As shown in [16, 17], noble metals practically do not give any essential contribution to dichalcogenide point-contact spectra. In this case

the IVC nonlinearity is determined with an electrode made of the layered compound.

When point contacts were established at the $SnNb_5Se_9$ crystal surfaces, different types of contacts were observed – such as normal metal-normal metal (N-c-N), normal metal-superconductor (N-c-S) and a few kinds of contacts with superconductive clusters of different phases. This diversity shows a wide variety of conductive properties on the surface of samples under investigation. This is not surprising, because, as a rule, the crystal surface has an increased concentration of lattice defects. Different microedges, stairs and other defects often located in sample surface layers generate a higher density of dislocations. The elastic fields trapped at these defects promote the formation of stabilized metastable phases [18]. Besides we cannot exclude the formation of metastable superconducting clusters through the strain-force field occurring at electrode contact [19]. In the compound matrix inclusions of non-interacted starting substances and parent phases may take part. In our PCS configuration we probe sample surfaces where the highest concentration of clusters (likely formed from compounds used in the synthesis) may be present. The probability of discovering such objects is thus high. This technique is furthermore well adapted for samples containing a low density of guest inclusions. The device applied in this research [14] can create contacts with a step of 25 nanometers along the whole sample surface. It was therefore possible to discover and to investigate inclusions of the same size.

Let us consider contacts of the N-c-S type. The temperature dependences of the IVC derivatives vs. voltage yields the opportunity to identify the superconductive behavior of heterocontacts formed from $SnNb_5Se_9$ crystal faces. If we consider the curves for an $Ag/SnNb_5Se_9$ contact presented in Fig.1 we can see that their overall dependences correspond to the IVC first derivatives of contacts with well-expressed gap peculiarities [20]. This type of curves is usually observed for high quality point contacts fulfilling the condition $d<<l,\xi$, where ξ is the coherence length. The amount of contacts displaying the characteristics of Fig.1 should be small as determined from the above-mentioned values of the $R_{300}/R_{4.2}$ ratio found for $SnNb_5Se_9$ crystals. In our investigation less than 5% were found.

In N-c-S contacts an excess current I_{exc} [21] which results from the contribution of quasiparticles is observed with energy $eV<2\Delta$ (Δ - half width of the superconductor energy gap). The occurrence of I_{exc} originates from the Andreev reflection of the electrons at the normal metal-superconductor boundary. The IVC of such contact deviates from the ohmic law and can be expressed by the relation $I = V/R_N + I_{exc}$. One should note that the excess current varies nonlinearly against the contact bias and reaches a constant level when its energy is of Δ order. This allows to determine the energy gap magnitude in the material and to study its temperature dependence. In the

contact studied in this work the I_{exc} value is lower than that of the dirty limit [21]. This excess-current drop can be explained by the presence of a half transparent contact barrier arising from imperfections of the contact material structure in the presence of impurities and defects. The contact barrier induces a current tunnel component and a decrease of I_{exc}.

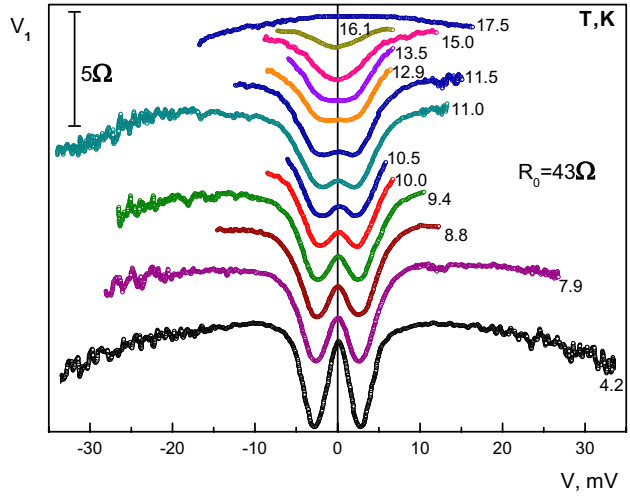

Fig.1. Dependences of V_1(V) for an Ag/$SnNb_5Se_9$ point contact.

The first derivatives of IVC (Fig.1) have maxima at zero bias and gap minima corresponding the excess current reaching to a constant level [21]. When raising the temperature, the amplitude of these features decreases, and the position of the gap minima moves to the lower energy area until they disappear at the superconducting transition of the material constituting the point contact. As we can see from Fig.1 the point contact reaches the normal state at a temperature of about 17.5 K, which agrees with the temperature of the critical superconducting temperature determined in $SnNb_5Se_9$ [1].

A number of experiments, shown in Fig.1, were used to determine the value of the energy gap parameter and its temperature dependence according to the modified model of Blonder, Tinkham, and Klapwijk [22]. This model takes into consideration the finite lifetime of quasiparticles as a result of inelastic scattering processes. In this way we got a value Δ_0 = 3 meV which is close to from the value 3.4 meV found in Nb_3Sn [23]. The BCS model describes quite well the dependence $\Delta(T)$ (Fig.2) obtained from the experimental results.

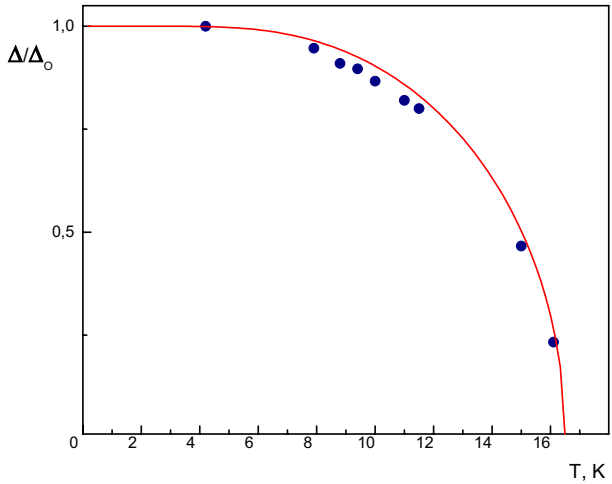

Fig.2. Temperature dependence of the superconducting energy gap for the $SnNb_5Se_9$ compound.

Among the variety of contacts created with different superconducting phases let us consider those for which the temperature dependence suggests the presence of tiny inclusions of initial substances used for the synthesis of the ternary phase. Indeed, the possibility to identify clusters by means of PCS technique depends on the character of point contact conductivity. Since the point contact resistance is in a volume of about d^3 in size the contribution to its value for a superconducting area far from the contact is small enough to be neglected because of fast running currents at distances $>d$ [6]. Conversely, if the superconducting area is close to the contact center (for a distance $\leq d$), then even minimal changes of its conductivity, caused by destruction of superconducting states, will lead to the appearance of special features in the IVC contact derivatives. As a result the characteristics of the point contacts drastically differ depending on the nature of their inclusions. Thus, it is effectively possible to detect clusters embedded in the host matrix. In addition a qualitative evaluation of the size of detected inclusions can be performed since we know the diameter of the point contact [15] is known.

The nonlinearities in the curves of Fig.3 can be explained by current flowing processes through superconducting areas in the contact region. The behavior of the curves conforms to that of superconducting inclusions in dirty contacts when the system reaches the critical current density and when the temperature increases [15].

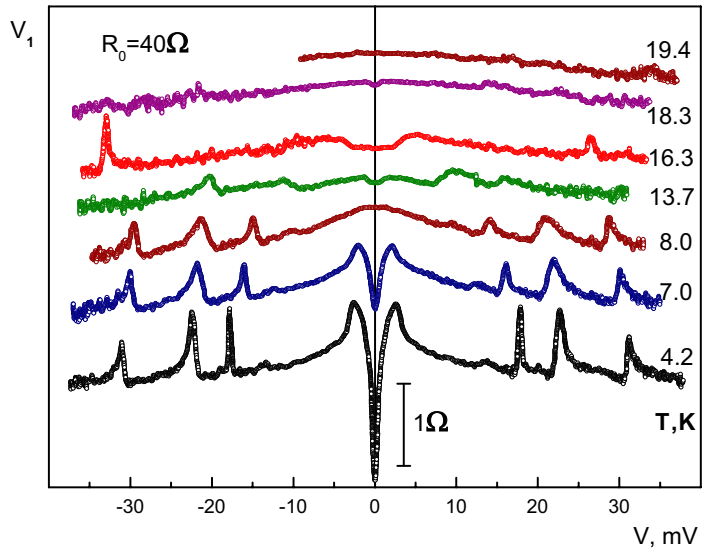

Fig.3. Dependences of V_1(V) for an Ag/$SnNb_5Se_9$ point contact.

Let us consider the differential resistivity minimum at V = 0 in curve 1 (T = 4.2K). The intensity of this minimum decreases, when the temperature increases, and it vanishes at T > 7.2K. It is known that $NbSe_2$ has practically the same superconducting transition temperature than that of this minimum disappearance. It is therefore possible to connect the observed nonlinearity with $NbSe_2$ clusters. The intensity of the high-energy maxima in the given curves also decreases at higher temperatures. Further, their position is shifted towards lower energy because the critical density current decreases as temperature increases. Moreover, the observation of several similar peculiarities in these curves can be explained by the contribution of other clusters in the contact region. The full transition of the contact to the normal state happens at T ≥ 18.3K which is higher than the Nb_3Sn superconducting critical temperature. Thus, the curves presented in Fig.3 testify that clusters of $NbSe_2$ and Nb_3Sn should exist in the contact area. The diameter evaluation of the studied contacts allows us to estimate the size of clusters observed to be in the range 5-200 nanometers.

Taking into consideration the large statistics of similar peculiarities recorded in the characteristics of different contacts, we can confidently confirm that clusters of initial substances, used for the synthesis of the $SnNb_5Se_9$ compound, are observed in the host matrix. We should also note that the total volume of such inclusions is rather low since their presence was not detected by means of SQUID investigations [1-3]. Knowing the

sensitivity of magnetic susceptibility measurements [15], we conclude that the nanocluster concentration amounts 10^{-7} in the host matrix volume.

The PCS technique has demonstrated an ultra-sensitive ability to probe the conductive properties of the layered superconductor $SnNb_5Se_9$. We have shown that PCS is a unique tool for the detection of nanoclusters which in our case were likely formed by a small fraction of unreacted initial substances (A15 and dichalcogenide) used to synthesize the ternary compound. Finally, we have determined the value and the temperature dependence of the energy gap parameter in the $SnNb_5Se_9$ phase.

ACKNOWLEDGEMENTS

The authors thank L.Tyutrina for help in calculation.

This work was partly supported by STCU (grant #2276) and NATO (grant PST.CLG.979685).

REFERENCES

1. P.Molinie, A.Leblanc, E.Faulques, Z.Ouili, J-C.Jumas, and C.Ayache, in: *Spectroscopy of Superconducting Materials*, ed. by E. Faulques (ASC Symposium series **730**, Oxford University Press, Washington D.C., 1999) ch.2, p.21.

2. A.Leblanc-Soreau, P.Molinié, To be published in: Journal de Physique IV (2004).

3. A. Leblanc-Soreau, P. Molinié, and J.C. Jumas, To be published in: Phys. Stat. Solidi C (2004).

4. I.K.Yanson, JETP **66**, No.3 (1974) 1035.

5. I.O.Kulik, A.H.Omelyanchuk, R.I.Shekhter, Sov. J. Low Temp. Phys. **3** (1977) 1543

6. A.V.Khotkevich and I.K.Yanson. Atlas of Point Contact Spectra of Electron-Phonon Interactions in Metals. - Kluwer Academic Publishers: Boston/Dordrecht/London, 168 p (1995).

7. V.A.Khlus, Sov. J. Low Temp. Phys. **9** (1983) 985.

8. I.K. Yanson, G.V. Kamarchuk, A.V. Khotkevich, Sov. J. Low Temp. Phys. **10** (1984) 423.

9. G.E.Blonder, M.Tinkham, and T.M.Klapwijk, Phys. Rev. B **25**, N 7 (1982) 4515.

10. C.J.Muller, J.M. van Ruitenbeek, and L.J. de Jongh, Phys. Rev. Lett. **69**, N 1 (1992) 140.

11. R.J.Soulen Jr., J.M.Byers, M.S.Osofsky, B.Nadgorny, T.Ambrose, S.F.Cheng, P.R.Broussard, S.T.Tanaka, J.Nowak, J.S.Moodera, A.Barry, J.M.D.Coey, Science **282** (1998) 85.

12. S.K.Upadhyay, A.Palanisami, R.N.Louie, and R.A.Buhrman, Phys. Rev.Lett. **81**, N 15 (1998) 3247.

13. P.N.Chubov, I.K.Yanson, A.I.Akimenko, Sov. J. Low Temp. Phys. **8** (1982) 64.

14. N.L.Bobrov, L.F.Rybal'chenko, A.V.Khotkevich, P.N.Chubov, I.K.Yanson, Pat. No. 1631626 (USSR), Device for creation of a cooled point contact between metal electrodes, Published in B.I., N 8 (1991) p.168.

15. O.I.Shklyarevski, I.K. Yanson, N.N.Gribov, Sov. J. Low Temp. Phys., **14** (1988) 479.

16. N.L.Bobrov, L.F.Rybal'chenko, M.A.Obolenski, V.V.Fisun, Sov. J. Low Temp. Phys. **11**, (1985) 925.

17. G.V.Kamarchuk, A.V.Khotkevich, V.M.Bagatsky, V.G.Ivanov, P.Molinie, A.Leblanc, and E.Faulques, Phys.Rev. B **63** (2001) 073107

18. A.V.Khotkevich, I.K.Yanson, M.B.Lazareva, V.I.Sokolenko, Ya.D.Starodubov, Physica B (1990) 1589.

19. G.V.Kamarchuk, A.V.Khotkevich, V.M.Bagatskii, and A.V.Kravchenko, in *Spectroscopy of Superconducting Materials*, ed. by E.Faulques, American Chemical Society Symposium Series, Vol. **730**, (Oxford University Press. Washington, D.C., 1999) ch.14, p. 196.

20. Yu.G.Naidyuk, H.V.Lohneysen, I.K.Yanson, Phys Rev. B **54** (1996) 16077

21. S.N.Artemenko, A.F.Volkov, A.V.Zaitcev, JETP **76**, No.5 (1979) 1816

22. A. Plecenik, M. Grajacar, S. Benacka P. Seidel, A. Pfuch, Phys. Rev. B **49**, 10016 (1994).

23**.** E.L.Wolf. Principles of Electron Tunneling spectroscopy. Oxford University Press. New York, Clarendon Press. Oxford,1985.

INFRARED AND RAMAN SPECTRA OF MAGNESIUM AMMONIUM PHOSPHATE HEXAHYDRATE (STRUVITE) AND ITS ISOMORPHOUS ANALOGUES

II. The O–H/N–H stretching region

Bojan Šoptrajanov[1,2], Viktor Stefov[1], Heinz Dieter Lutz[3] and Bernward Engelen[3]

[1] *Institut za hemija, PMF, Univerzitet "Sv. Kiril i Metodij", Skopje, Macedonia*

[2] *Makedonska akademija na naukite i umetnostite, Skopje, Macedonia*

[3] *Anorganische Chemie, Universität Siegen, 57068 Siegen, Deutschland*

e-mail: bojan@manu.edu.mk

Abstract: The three investigated compounds – $KMgPO_4 \cdot 6H_2O$ (KMP), $NH_4MgPO_4 \cdot 6H_2O$ (NMP) and $NH_4MgAsO_4 \cdot 6H_2O$ (NMA) – are characterized by the existence, in their structure, of quite strong $O_w \cdots O$ hydrogen bonds (of which some are among the shortest of this type ever found in crystalline hydrates, the $O_w \cdots O$ distances being slightly above 260 pm). Reflecting the strength of the hydrogen bonds, a broad and structured feature extending from ≈ 4000 down to ≈ 2000 cm^{-1} is found in the infrared spectra. Although not as rich in detail as the infrared spectra, the Raman ones are similar in appearance. Rather surprisingly, the spectral picture is not very different in the case of the two phosphate compounds ($KMgPO_4 \cdot 6H_2O$ and $NH_4MgPO_4 \cdot 6H_2O$) although N–H stretching bands are expected in the same region of the spectrum of NMP. Thus, obviously, the intensity of the feature in the O–H/N–H stretching region is due mainly to modes of the water molecules whereas the NH_4 stretches contribute to a lesser degree to the shape and intensity. The comparison of the spectra in the O–D/N–D stretching region confirms this.

Key words : metal(I) magnesium phosphate hexahydrates; ammonium magnesium arsenate hexahydrate, infrared spectra, Raman spectra, potential protonic conductors.

E. C. Faulques et al. (eds.), Spectroscopy of Emerging Materials, 299–308.

1. INTRODUCTION

Ammonium magnesium phosphate hexahydrate, $NH_4MgPO_4 \cdot 6H_2O$ (its mineralogical name is *struvite* and this name is also used to denote its *synthetic* analogue) is a biomineral present in human urinary and renal calculi [1] and is the compound that is precipitated in the course of the gravimetric determination of phosphates. Potassium magnesium phosphate hexahydrate, $KMgPO_4 \cdot 6H_2O$ (abbreviated as KMP[1]) and ammonium magnesium arsenate hexahydrate (NMA or arsenstruvite), $NH_4MgAsO_4 \cdot 6H_2O$ are isomorphous with struvite [2–6]. They all crystallize in the orthorhombic space group $Pmn2_1$ (C_{2v}^7) with $Z = 2$ [2–6]. All ions and two of the four crystallographically different types of water molecules occupy special positions with C_s symmetry, while the H_2O molecules of the other two types are located at general positions. The pertinent portion of the crystal structure is shown in Fig. 1 which is produced using the neutron-diffraction data given in the paper by Ferraris, Fuess and Joswig [6][2]. In order to add to the clarity of the presentation, omitted are the univalent cations, the E atoms of the EO_4^{3-} (E = P or As) anions and the oxygen atoms of these anions that are not involved in the hydrogen-bond network.

The H_2O molecules act as donors in hydrogen bonds that are among the shortest ones ever found in crystalline hydrates [7]. Thus, the $O_w \cdots O$ distances range from 263.0 to 269.5 pm in NMP (cf. Fig. 1), from 262.3 to 270.1 pm in KMP[3] and from 261.9 to 269.8 pm in NMA where the acceptors are, understandably, arsenate oxygens. For the H_2O molecules labelled $O_w(1)$ there is an additional type of contact, this time with another water molecule, which corresponds to a weak hydrogen bond (the $O_w \cdots O_w$ distances are 314.1 pm in struvite [6] (cf. Fig. 1), 314.2 pm in its potassium analogue [2] and 314.9 pm in the case of $NH_4MgAsO_4 \cdot 6H_2O$ [3]. All $O_w \cdots O$ distances for the three studied compounds are listed in Table 1.

It should be noted that there is an important difference concerning the two H_2O molecules located on the mirror planes. Namely, the H1–$O_w(1)$–H2 molecules have all three atoms *on* the plane, whereas the mirror plane bisects the H3–$O_w(2)$–H3 molecules. As a consequence, the two hydrogen bonds formed by the molecules of the latter type are equivalent, whereas those of the former type of water molecules are not only non-equivalent but

[1] Ammonium magnesium phosphate hexahydrate will be abbreviated as NMP.

[2] It should perhaps be noted that the crystal structure of struvite has been determined or refined on the basis of X-ray diffraction data by Whitaker and Jeffery [4] and by Abbona, Calleri and Ivaldi [5].

[3] The acceptors, in both cases, are phosphate oxygens.

are in fact grossly different in length – in struvite the $O_w \cdots O$ distances are 264.7 and 314.1 pm, the latter being already mentioned above.

Table 1. $O_w \cdots O$ distances (in picometers) in the structures of KMP [2], NMP [6] and NMA [3]

	KMP	NMP	NMA
$O_w(1) \cdots O_w(2)$	314.2	314.1	314.9
$O_w(1) \cdots O2$	264.0	264.7	266.5
$O_w(2) \cdots O3$ (2×)	264.2	264.7	264.9
$O_w(3) \cdots O3$	264.9	264.9	263.6
$O_w(3) \cdots O1$	270.1	269.5	269.8
$O_w(4) \cdots O2$	262.3	263.0	261.9
$O_w(4) \cdots O3$	263.1	264.7	264.4

It should be noticed that each O3 oxygen atom serves as a proton acceptor for *three* water molecules – those of the $O_w(2)$, $O_w(3)$ and $O_w(4)$ types. As a consequence, an extensive network of hydrogen-bonded water molecules sharing acceptor atoms is formed.

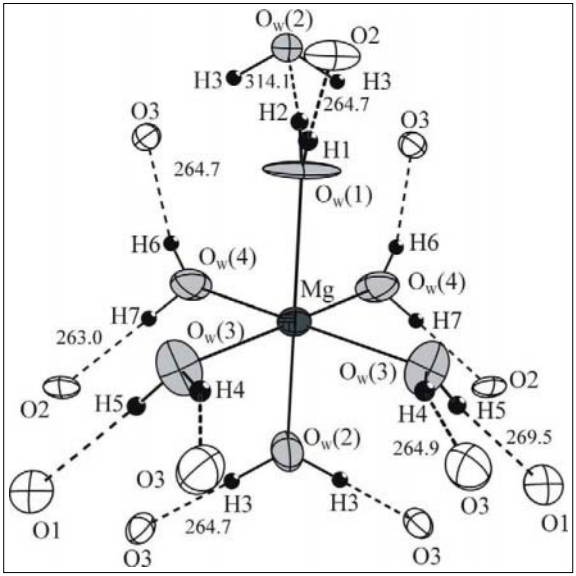

Figure 1. Part of the structure of struvite according to Ferraris, Fuess and Joswig [6]. Only the water molecules and the atoms to which they are bound are shown; the numbers refer to the O···O distances measured in picometers

The infrared spectra of ammonium magnesium phosphate hexahydrate and its potassium analogue recorded at room temperature have already been studied [8] and the RT Raman spectrum of struvite has also been reported [9]. In addition to that, our results of the study of the spectra of $KMgPO_4 \cdot 6H_2O$ will be published shortly [10]. To the best of our knowledge, the vibrational spectra of arsenstruvite and its deuterated analogues and also the vibrational spectra of the whole series of deuterated analogues of either of the three compounds have not been reported yet.

Since, as mentioned, the detailed analysis of the spectra of $KMgPO_4 \cdot 6H_2O$ [10] is about to be published and that of struvite and arsenstruvite will follow, the present paper will deal mainly with the spectra in the O–H/N–H region of the protiated compounds and in the O–D/N–D region of compounds with a low deuterium content (≈ 3–5 % D). Needless to say, no N–H or N–D modes are present in the case of $KMgPO_4 \cdot 6H_2O$ and its deuterated analogues.

The aim of this investigation is twofold. On the one hand, it fits into our extensive studies of hydrates of compounds of the $M^{I}M^{II}EO_4 \cdot nH_2O$ (n = 1 or 6) [10–14] and, on the other hand, serves as a check whether the vibrational spectra lend support to the idea (based on the structural properties) that the studied compounds might be potential protonic conductors.

2. EXPERIMENTAL

The investigated compounds were synthesized according to methods given in the literature [2,3,5]. The synthesis of the partially deuterated analogues was accomplished analogously, but using as solvents H_2O–D_2O mixtures with appropriate compositions.

The Fourier transform (FT) infrared spectra were recorded, from both mulls and pressed KBr disks, on a Perkin-Elmer System 2000 infrared interferometer. The spectra were recorded at room and liquid-nitrogen temperature (RT and LNT, respectively). In the latter case, the variable-temperature cell P/N 21525 (Graseby Specac) with KBr windows was used. To obtain a good signal-to-noise ratio, 64 scans were collected and averaged at LNT (32 scans were sufficient at RT). The working resolution of the instrument was 4 cm^{-1}. The FT Raman spectra were recorded (with a resolution of 2 cm^{-1}) on a Brucker RFS 100\s FT Raman equipped with a Nd : YAG laser emitting at 1064 nm. To achieve good signal-to-noise ratio 500 scans were accumulated and averaged. The GRAMS ANALYST 2000 [15] software package was used for acquisition of the spectra which were then treated with the GRAMS 32 [16] package.

3. RESULTS AND DISCUSSION

The RT and LNT infrared spectra of synthetic struvite are shown in Fig. 2. As seen, the lowering of the temperature does not produce dramatic changes in the spectral picture, although some of the bands become sharper and the substructure of the high-frequency feature is more apparent. In addition to that, the bands originating from water librations (hindered rotations) become more intense and shift towards higher frequencies.

In what follows, the LNT spectra will mainly be considered and the attention will be focused on the high-frequency region where bands due to the X–H (O–H or N–H) stretching vibrations are expected to appear.

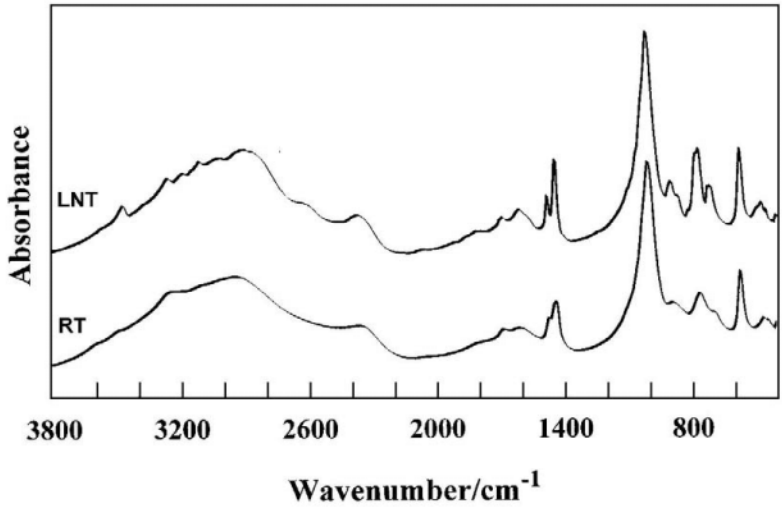

Figure 2. The RT and LNT infrared spectra of $NH_4MgPO_4 \cdot 6H_2O$ (NMP)

Reflecting the strength of the hydrogen bonds, a broad and structured feature extending from ≈ 4000 cm^{-1} down to ≈ 2000 cm^{-1} is found in the infrared spectra of all three compounds (Fig. 2 and Fig. 3).

As seen, in addition to the strong bands centered around 3000 cm^{-1}, a rather prominent peak is present around 2400 cm^{-1}. The whole picture is reminiscent of the A and B bands of the ABC trio [17] and is indicative of the presence of easily polarizible bonds in the structure. This, in turn, is a prerequisite to qualify the studied compounds as potential protonic conductors although by no means it is a sufficient guarantee that such is indeed the case.

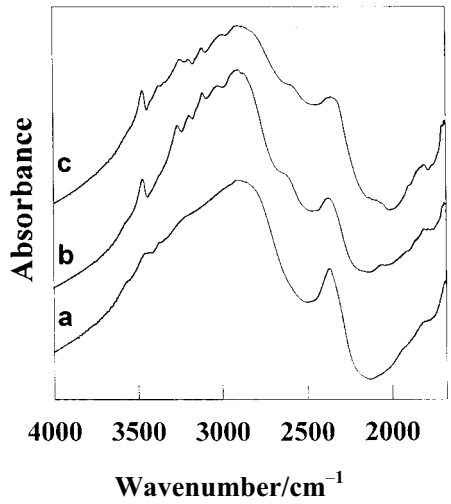

Figure 3. The X–H stretching region in the LNT infrared spectra of KMP (a), NMP (b) and NMA (c)

Somewhat surprisingly, the spectral picture is not very different in the case of the two ammonium compounds (b and c) as compared with the spectrum of $KMgPO_4 \cdot 6H_2O$ (a) despite the fact that in the case of NMP and NMA bands due to N–H stretches are also expected in the same spectral region.

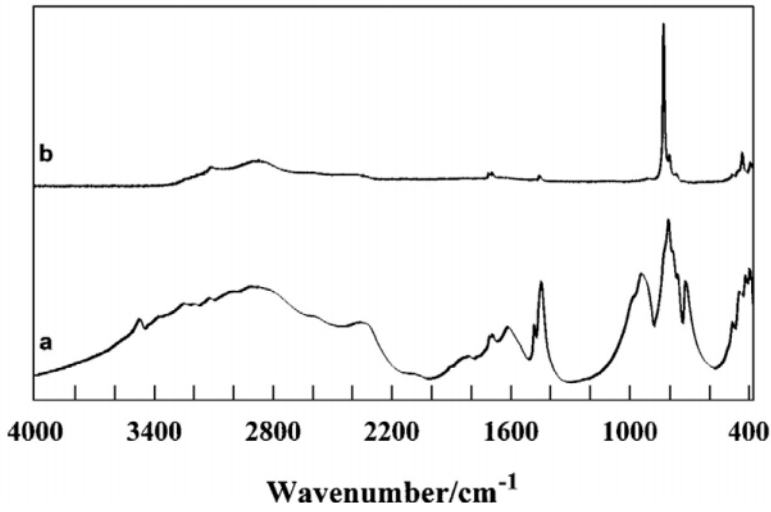

Figure 4. The infrared (a) and Raman spectra (b) of synthetic arsenstruvite (NMA)

In principle, the bands originating from the vibrations of the H_2O molecules and NH_4^+ ions the Raman spectra are weaker than those arising from the vibrations localized in the EO_4^{3-} ions (of these, the strongest band is due to the totally symmetric EO_4 stretch). This is clearly seen in the case of the Raman spectrum of synthetic arsenstruvite (Fig. 4). On the other hand, the X–H stretching bands are rather prominent in the Raman spectra of struvite itself (Fig. 5).

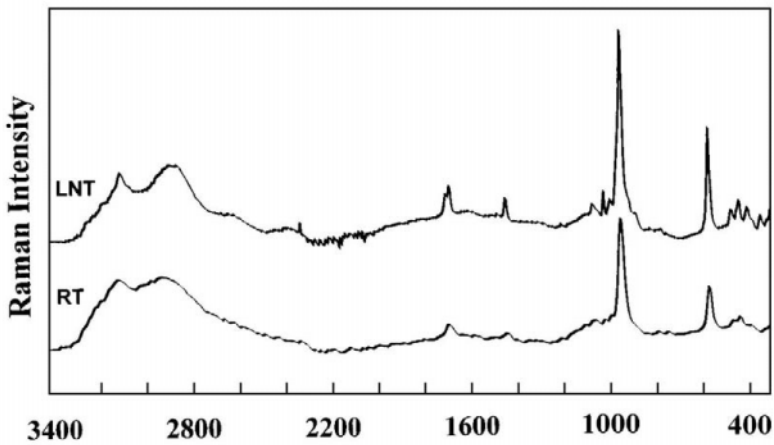

Figure 5. The RT (a) and LNT (b) Raman spectra of synthetic struvite (NMP)

One of the advantages of the Fourier transform spectra is the ease with which they can be expanded (or, for that matter, manipulated in many different ways). When the high-frequency portion of the Raman spectra of NMP, KMP and NMA is made comparable in intensity, it becomes apparent that broad and structured bands, similar to those found in the infrared spectra, are present in the Raman spectra of all three investigated compounds as well (Fig. 6). The spectral picture is somewhat less rich in detail than that in the case of the infrared spectra but is, nevertheless, essentially identical in the two cases.

The infrared spectra of slightly deuterated KMP, NMP and NMA in the O–D/N–D stretching region are also alike (Fig. 7) although the intensities in the spectrum of NMA are different from those in the spectra of the two other compounds.

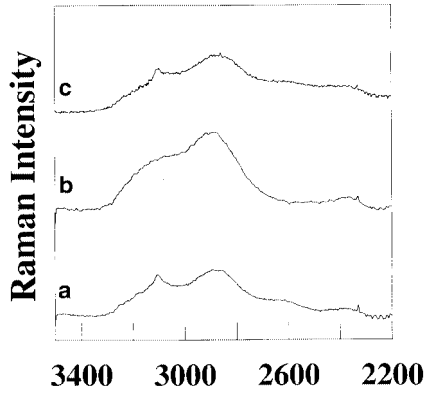

Figure 6. The X–H stretching region in the Raman spectra of NMP (a), KMP (b) and NMA (c)

It is presently hard to give a definitive explanation of the unexpected appearance of the spectrum of slightly deuterated NMA, although one is tempted to suspect a Fermi resonance interaction giving rise to an Evans hole centered around 2300 cm^{-1}.

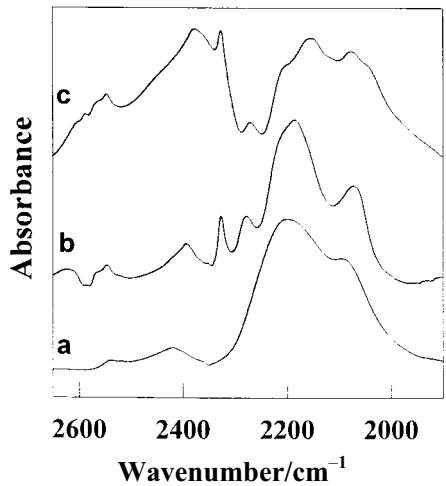

Figure 7. The X–D stretching region in the infrared spectra of slightly deuterated KMP (a), NMP (b) and NMA (c)

Since such a picture is present only in the spectrum of arsenstruvite, it is reasonable to assume that the mode interacting with the X–D stretching vibrations is a second-order transition involving the stretching mode(s) of

the AsO_4^{3-} ions. The frequencies of these modes are ≥ 800 cm^{-1} and since bands are present above 1400 cm^{-1} as well (cf. Fig. 4) it is possible to find a suitable summation frequency which would be responsible for the apparent Evans hole.

On the other hand, the weak bands centered around 2270 cm^{-1} in the spectra of deuterated NMP are probably due to N–D stretches of the isotopically isolated NH_3D^+ ions.

The results presented above show that the intensity of the features in the O–H/N–H and O–D/N–D stretching regions is due mainly to modes of the water molecules whereas the N–H(D) stretches contribute to a lesser degree to the shape and intensity of the complex bands. In view of the fact that the hydrogen bonds formed by the water molecules are *stronger* than those in which the ammonium ions take part and thus the O–H···O bonds are easier to polarize, the above result finds a logical explanation. As is well known, namely, the strength of the X–H···Y hydrogen bonds and the intensity of the X–H stretching bands are proportional (the stronger the hydrogen bond, the greater is the intensity of the ν(X–H) bands).

For our present purposes the most important point is that the vibrational (infrared and Raman) spectra show beyond doubt that quite strong and, hence, easily polarizible O–H···O bonds are present in the three investigated systems and that, consequently, the $M^IMgEO_4 \cdot 6H_2O$ compounds can be considered as potential protonic conductors.

ACKNOWLEDGEMENTS

The research the results of which are presented in the present communication was supported by funds from the project MAK-002-97 by the German Federal Ministry of Education and Research, Federal Republic of Germany and by the Ministry of Education and Science, Republic of Macedonia. The authors are sincerely grateful for the financial assistance.

REFERENCES

1. F. Abbona, R. Boistelle, *J. Cryst. Growth*, **46** (1979) 339.
2. M. Mathew, L.W. Schroeder, *Acta Crystallogr.,* **B35** (1979) 11.
3. G. Ferraris, M. Franchini-Angela, *Acta Crystallogr.*, B**29** (1973) 859.
4. A. Whitaker, J. W. Jeffery, *Acta Crystallogr.*, B**26** (1970) 1429.
5. F. Abbona, M. Calleri, G. Ivaldi, *Acta Crystallogr.*, **B40** (1984) 223.
6. G. Ferraris, H. Fuess, W. Joswig, *Acta Crystallogr.*, B**42** (1986) 253.

7. G. Chiari, G. Ferraris, *Acta Crystallogr.*, B**38** (1982) 2331.
8. E. Banks, R. Chianelli, R. Korenstein, *Inorg. Chem.*, **14** (1975) 1634.
9. N.Q. Dao, M. Daudon (Eds.), *Infrared and Raman Spectra of Calculi*, Elsevier, Paris, 1997.
10. V, Stefov, B. Šoptrajanov, F. Spirovski, I. Kuzmanovski, H.D. Lutz, B. Engelen, *J. Mol. Struct.* (accepted for publication).
11. B. Šoptrajanov, *J. Mol. Struct.*, **555** (2000) 21.
12. Lj, Pejov, B. Šoptrajanov, G. Jovanovski, *J. Mol. Struct.*, **563**–**564** (2001) 321.
13. B. Šoptrajanov, G. Jovanovski, Lj. Pejov, *J. Mol. Struct.*, **613** (2002) 47.
14. B. Šoptrajanov, V. Stefov, I. Kuzmanovski, H.D. Lutz, B. Engelen, *J. Mol. Struct.*, **613** (2002) 7.
15. GRAMS ANALYST^{TM} for PE-2000 FT-IR, Version 3.01B Level II, Galactic Industries, 1994.
16. GRAMS/32 Spectral Notebase, Version 4.10, Galactic Industries Corporation, 1996.
17. D. Hadži, *Pure Appl. Chem.,* **11** (1965) 435.

TRANSPORT, MAGNETIC AND OPTICAL PROPERTIES OF A QUASI-TWO-DIMENSIONAL ORGANIC METAL BASED ON BEDO-TTF (BIS-(ETHYLENEDIOXY)TETRATHIAFULVALENE)

R.B.LYUBOVSKII[a,e*], S.I.PESOTSKII[a,e], M.GENER[b], R.ROUSSEAU[c], E.CANADELL[b], N.V.DRICHKO[d], R.M.VLASOVA[d], V.N.SEMKIN[d], O.A.BOGDANOVA[a], E.I.ZHILYAEVA[a], R.N.LYUBOVSKAYA[a]

[a] *Institute of Problems of Chemical Physics, Russian Academy of Sciences, 142432 Chernogolovka, MD, Russia*
[b] *Institut de Ciència de Materials de Barcelona (CSIC), Campus de la U. A. B., 08193 Bellaterra, Spain*
[c] *Steacie Institute for Molecular Sciences, National Research Council of Canada, Ottawa, Ontario, Canada K1A 0R6*
[d] *A.F.Ioffe Physico-Technical Institute, Russian Academy of Sciences, Politekhicheskaya 26, 194021 St.Peterburg, Russia*
[e] *International High Magnetic Fields and Low Temperatures Laboratory, 53-529 Wroclaw, Poland*
E-mail: <rustem@icp.ac.ru>

Abstract.

Polarized reflectivity spectra, tight binding band structure calculations as well as magnetoresistance and magnetization measurements have been carried out for the new quasi-two-dimensional organic conductor β''-$(BEDO\text{-}TTF)_5[CsHg(SCN)_4]_2$. Polarized reflectivity and optical conductivity spectra have shown that at low temperatures this salt exhibits metallic behaviour in the direction perpendicular to the BEDO-TTF stacks, but non-metallic behaviour in the direction parallel to the stacks. It is supposed that the non-metallic behaviour is due to the dimerization of BEDO-TTF molecules in the stacks at low temperatures. Tight binding calculations suggest that the Fermi surface can be described as containing two contributions: a closed two-dimensional portion associated with holes and a open, pseudo-one-dimensional portion associated with electrons. Shubnikov-de Haas and de Haas-van Alphen oscillations have shown that some frequencies of their complicated Furie spectra are in good agreement with the calculated Fermi surface. The other frequencies of the spectra can be well understood in the frame of the quantum interference effect.

1. Introduction

Last decades quasi-two-dimensional charge-transfer salts have attracted a growing interest for the physics community because their electronic properties are often

E. C. Faulques et al. (eds.), Spectroscopy of Emerging Materials, 309–318.

beautifully simple [1,2]. They can provide a great deal of information about very basic phenomena like electronic band structure formation, magnetism and superconductivity. They can be excellent model objects to study the effects of electron-electron correlations and different types of charge ordering in case of two dimensions. The crystal structures of these salts are formed by an alternation of conducting cation layers of BEDT-TTF (bis(ethylenedithio)thetrathiafulvalene) or their derivatives and of isolating anion layers. Physical properties of these salts can be tuned by small changes of the chemical composition or structure of the layers. Depending on the arrangement of the molecules in the conducting cation layers and the chemical composition of the anions, these charge transfer salts display a large variety of electronic properties from dielectric to superconductors including different types of instabilities. To understand the nature of these states a key question is connected with the electronic band structure and the shape of the Fermi surface of the studied compounds. Fermi surface quantum oscillations of magnetoresistance and magnetization connected with magnetic breakdown at high magnetic field can play an important role in this investigation. If the studied compound has a simple Fermi surface at weak magnetic fields there are visible oscillations which correspond to extremal cross section of semiclassical closed orbits perpendicular to the field direction. In case of several bands there are frequencies which correspond to each closed orbit but not to those orbits which cross the first Brillouin zone and are open. As magnetic field increases in a multi-band system there may be magnetic field-induced tunneling from band to band. This gives rise to larger orbits with frequencies that are combinations of the original frequencies or which may include portions of Fermi surface open parts yielding new frequencies. Oscillatory spectra in this case can be very complicated [3]

The aim of this article is to show that the new quasi-two-dimensional organic conductor β''-$(BEDO\text{-}TTF)_5[CsHg(SCN)_4]_2$ [hereafter called (BEDO)CsHg] (BEDO-TTF - bis-(ethylenedioxy)tetrathiafulvalene) which contains closed and open orbits displays rather complicated oscillatory spectra associated with magnetic breakdown (MB) and quantum interference (QI) effects. Tight binding band structure calculations for this compound are proposed to characterise its Fermi surface. The aim of the article includes also an investigation of the optical conductivity anisotropy with polarized infrared reflectance spectra.

2. Experimental

Synthesis.

Single crystals of β''-$(BEDO\text{-}TTF)_5[CsHg(SCN)_4]_2$ were prepared by electrochemical oxidation of BEDO-TTF as described in [ ] In the β''-phase BEDO-TTF molecules form conducting layers in *ab*-plane. In this plane BEDO-TTF molecules stack parallel to 2*a*-*b* direction. The distance between the planes of the neighbouring molecules in the stacks are nearly equal. According to the stoichiometry each BEDO-TTF molecule carries an average charge +0.4, thus the conductance band is 1/5 filled. The crystals grows as parallelogram-shaped plates, some of them reached 2*1 mm^2 in size. The largest extension of the crystals is parallel to the stacking direction of the BEDO-TTF molecules in the conducting layer, i.e. 2*a*-*b* direction.

Infrared reflectance spectra

The IR reflectivity measurements were performed on single crystals of 2*0.5*0.3 mm^3 in size. A FT-IR Perkin-Elmer 1725X spectrometer equipped with microscope and a helium cryostat was used. Polarized reflectivity spectra (R(ω)) were measured from the conducting plane in two principal directions. Optical conductivity σ(ω) was obtained by Kramers-Kronig transformation.

Resistance and magnetoresistance.

The resistance was measured with the standard dc four-probe method with 10μm platinum wire and graphite paste, 10-100μA current and temperatures down to 1.5K. The Shubnikov-de Haas oscillations were observed by ac (337Hz) method with current (I=100μA) directed parallel to the c^*-axis. The de Haas-van Alphen oscillations were studied with cantilever torquemeter [4]. The magnetic fields used were up to 14 T for both types of experiment and the temperature range was 1.5-4.2K.

Band structure calculations.

The tight-binding band structure calculations were based upon the effective one-electron Hamiltonian of the extended Huckel method.[5] The off-diagonal matrix elements of the Hamiltonian were calculated acording to the modified Wolfsberg-Helmholtz formula. All valence electrons were explicitly taken into account in the calculations and the basis set consisted of double-ζ Slater-type orbitals for C, O and S and a single-ζ Slater-type orbitals for H. The exponents, contraction coefficients and atomic parameters were taken from previous work [6].

3. Results and discussion.

The crystal structure of (BEDO-TTF)$_5$[CsHg(SCN)$_4$]$_2$ is built from BEDO-TTF layers which alternate along the *c*-direction with inorganic layers wherein Cs^+ cations and $[Hg(SCN)_4]^{2-}$ anions form an extended two-dimensional network [7].

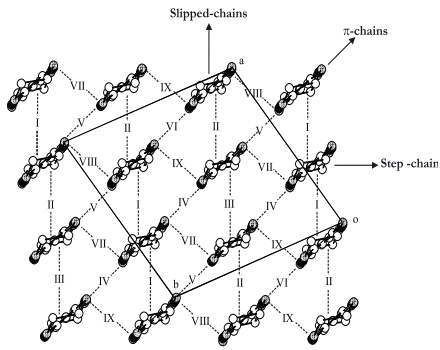

Figure 1. Donor layers of (BEDO-TTF)$_5$ [CsHg(SCN)$_4$]$_2$ where the different types of chains and donor…donor interactions have been labelled.

This structure differs from those of α-(BEDT-TTF)$_2$MHg(SCN)$_4$ salts with respect to both the donor and acceptor sublattices [7]. The donor layers in the present salt have a β''-type arrangement (Fig. 1) and are built from three different BEDO-TTF donors (A, B and C). There are three different types of intermolecular interactions with the slab of organic molecules, the relative orientation of which allows us to describe this layer as being composed of a series of parallel stacks of slipped donors along the (2*a*-*b*)-direction, as a series of step-chains along the (*a*+2*b*)-direction, or as a series of parallel

chains of donors making lateral contacts along the (*a*-3*b*)-direction. The three types of chains have been labelled as 'slipped-chains', 'step-chains' and 'π-chains' in Fig. 1. Note that the slipped-chains are associated with interactions I to III, the π-chains with interactions IV to VI and the step-chains with interactions VII to IX. Infrared spectra which are discussed below were studied for two directions: along slipped chains (E ‖ L) (L is BEDO-TTF stack direction) and step-chains (E⊥L).

The polarized reflectivity spectra of the (BEDO)CsHg at T = 300, 200, 100, and 10 K are shown in Fig.2. The spectra of the studied salt for E ⊥ L over the whole temperature range and for E || L down to 200 K correspond to a metallic behaviour. A qualitative change in the spectra for E || L is observed at T < 200 K. The reflectivity below 2000 cm^{-1} becomes so high that the anisotropy of the reflectivity for the 700–1600 cm^{-1} range changes: R(E||L) becomes greater than R(E⊥L) (see inset of Fig. 2).

Some weak features attributed to the BEDO-TTF intramolecular vibrations are observed below 1600 cm^{-1} and a narrow double band near 2100 cm^{-1} is assigned to the CN stretching vibration of the anion. Below 200 K the qualitative change in the reflectivity spectra for E || L is accompanied by the appearance of new vibrational features at 862 and 1012 cm^{-1}.

The optical conductivity spectra of the (BEDO)CsHg are shown in Fig.3. The temperature behaviour of σ(ω) is qualitatively different for E ⊥ L and E || L. For E ⊥. L, the changes of σ(ω) with temperature decrease are of metallic character. For E || L, the optical conductivity decreases on cooling within 700–2000 cm^{-1}, and a wide asymmetric band appears near 4000 cm^{-1}; these changes manifest a non-metallic behaviour of the electron system and can occur due to the development of the metal–semiconductor transition in the L direction. The new vibrational features at 864 and 1015 cm^{-1} appearing below 200 K are shown by arrows in Fig.3.

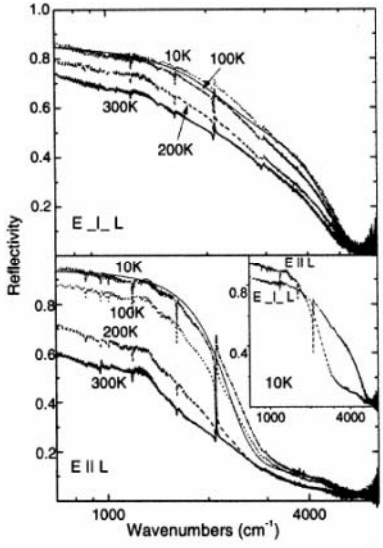

Figure 2.. Polarized reflectivity spectra of β"-BEDO-TTF)$_5$[CsHg(SCN)$_4$]$_2$ for **E** ⊥ **L** and **E** ‖ **L** at 300, 200, 100 and 10 K (**L** is BEDO-TTF stack direction). The fit with Drude-Lorenz model for T=10 K is shown by thin solid line.

To describe the optical properties of the crystals over a wide temperature range and to derive the basic phenomenological parameters of the electronic transition, we fitted the R(ω) and σ(ω) spectra using the Drude–Lorentz model. The Drude part describes the intraband transition of free carriers,

and the sum of Lorentz oscillators phenomenologically describes interband transitions. The complex dielectric constant for this model is written as

$$\varepsilon(\omega) = \varepsilon_\infty - \frac{\omega_p^2}{\omega(\omega + i\Gamma)} + \sum_{l=1}^{n} \frac{\omega_{Ll}^2}{\omega_{Tl}^2 - \omega^2 - i\gamma_l\omega}, \quad (1)$$

where ω_p is the plasma frequency, Γ is the relaxation constant of free carriers, ω_{Ll} is the oscillator strength, ω_{Tl} is the resonance frequency, and γ_l is the relaxation constant for the Lorentz oscillators. The Drude–Lorentz analysis was performed by fitting simultaneously R(ω) and σ(ω) spectra. It enables one to find reliable sets of parameters. We found that the Drude–Lorentz model with one Lorentz oscillator (n=1)

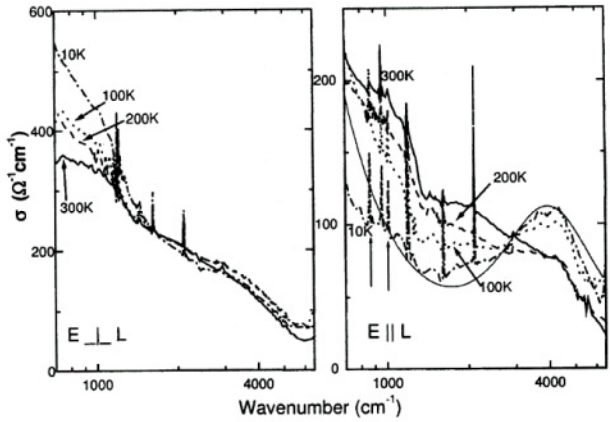

Figure 3. Optical conductivity spectra of β˝-BEDO-TTF)$_5$[CsHg(SCN)$_4$]$_2$ for **E** ⊥ **L** and **E** ‖ **L** at 300, 200, 100 and 10 K (**L** is BEDO-TTF stack direction). The fit with Drude-Lorenz model for T=10 K is shown by thin solid line.

fits sufficiently well R(ω) and σ(ω) for the E ⊥ L spectra of the (BEDO)CsHg at all measured temperatures (Figs. 2-3). On the contrary, the temperature changes of R(ω) and σ(ω) spectra for E || L cannot be fitted by Eq. (1) with one Lorentz oscillator (n=1). This case can describe sufficiently well the rise of R(ω) at 700–2000 cm $^{-1}$ below 200 K by a decrease of Γ, but these parameters do not fit the corresponding σ(ω) spectra, and are in contradiction with the non-metallic behaviour of dc conductivity for E || L [8]. To describe the sharp increase of the reflectivity and the simultaneous decrease of optical conductivity within the 700–2000 cm $^{-1}$ range below 200 K following the model of Eq. (1), it is necessary to suppose the appearance of an additional oscillator in the low-frequency range. The best fit is achieved by introducing a low-frequency oscillator at 200 cm $^{-1}$. Figs.2 and 3 show that the calculated R(ω) and σ(ω) spectra for T = 10 K with the Drude parameters ω_p = 2000, Γ = 400, ε_∞ = 3, and two Lorentz oscillators (l = 1, 2) with parameters ω_{T1} = 4000, ω_{L1} = 5300, γ_{L1} = 4400, ω_{T2} = 200, ω_{L2} = 5200, γ_{T2} = 140 cm^{-1} are in a good agreement with the experimental spectra. The intensity of the wide asymmetric band at about 4000 cm $^{-1}$ increases by 20% when the temperature decreases from 300 to 10 K, pointing to the appearance of a corresponding energy gap

for E || L. The necessity of an additional low-frequency oscillator in the calculated spectra suggests the appearance of a low-frequency gap in the energy spectrum of the charge carriers at low temperatures. The occurence of the gaps is consistent with the non-metallic temperature dependence of the dc electrical resistance [8] and microwave resistivity [9] in the L direction.

Based on the structure of the donor layers (Fig.1) of (BEDO-TTF)CsHg, the band structure for these layers was calculated near the Fermi level (Fig.4). As shown in Fig. 1, there are five donors per repeat unit of the layer so that the five bands of Fig. 4 are mainly built from the HOMO (highest occupied molecular orbital) of the BEDO-TTFs. The HOMO of donors A, B and C are quite similar in energy (-8.43, -8.44

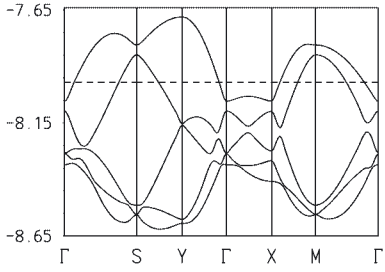

Figure 4. Calculated dispersion relations of the HOMO bands in $(BEDO\text{-}TTF)_5[CsHg(SCN)_4]_2$

and –8.37 eV, respectively) so that they strongly mix and lead to the quite dispersive bands of Fig. 4. According to the usual oxidation states, the average charge of the donors is +0.4 and consequently, there should be two holes in the HOMO bands. In principle, the salt could be either a semiconductor (if there is a band gap between the two upper HOMO bands) or a metal (if the two upper bands overlap). As shown in Fig. 4, the system is predicted to exhibit a metallic behaviour in agreement with the resistivity measurements.

The Fermi surface associated with the band structure of Fig. 4 is shown in Fig. 5. This Fermi surface can be described as having two contributions: a) a closed two-dimensional (2D) portion centred at M which is associated with holes, and b) an open pseudo-one-dimensional (pseudo-1D) portion which is warped and parallel to the a^*-direction, which is associated with electrons. However, the Fermi surface of Fig. 5 can be seen as a superposition of ellipses if we disregard the band hybridization, i.e., the creation of gaps at the regions of interaction. This suggests that the system is a typical 2D metal despite the presence of open lines in the Fermi surface.

The important result is that the interactions along the step-chains and π-chains are comparable while those along the slipped-chains are considerably weaker (by a factor of two or three). That the interactions along the step-chains are among the strongest and that those along the slipped-chains are considerably smaller is hardly surprising in

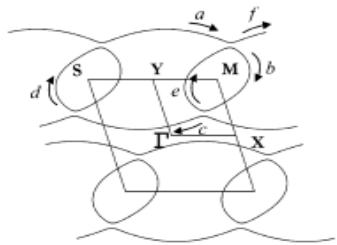

Figure 5. Calculated Fermi-surface for the donor layers in $(BEDO\text{-}FFT)_5[CsHg(SCN)_4]_2$.

view of past experience concerning the analysis of the intermolecular interaction strength in

many BEDT-TTF salts. Most surprisingly, and in sharp contrast to the BEDT-TTF salts, the interactions along the π-chains, which result from a π-type overlap between the HOMOs, are comparable (if not even somewhat stronger) than those along the step-chains where the intermolecular overlap is of the more favourable σ-type. This is a result of the very short S···S intermolecular contacts within the π-chains which override the intrinsic weakness of the π-type interactions with respect to the σ-type ones. These short contacts are a consequence of the smaller size of the oxygen atoms with respect to the sulphur ones, which allows for closer lateral contacts between the two almost coplanar donors. This is an important difference with the β''-type BEDT-TTF layers which of course influences the shape of the respective Fermi surfaces.

On the basis of the Fermi surface of Fig. 5, it is predicted that at least one Shubnikov-de Haas frequency corresponding to an approximately cross sectional area of 19 % of the first Brillouin zone should be observable in the magnetoresistance experiments (remind that the calculations have been carried out using the room temperature structure). In view of the weakly avoided crossings in Figure 5, a second frequency corresponding to the full ellipse (i.e., due to the magnetic breakdown effect) should also be observable. Since the magnetic breakdown orbit corresponds to the ellipse of the unfolded Fermi surface and given the average charge of the donor (+0.4) which corresponds to one-fifth of the 2D unfolded first Brillouin

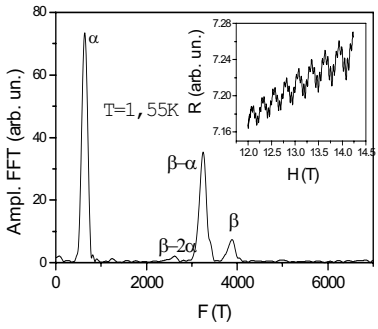

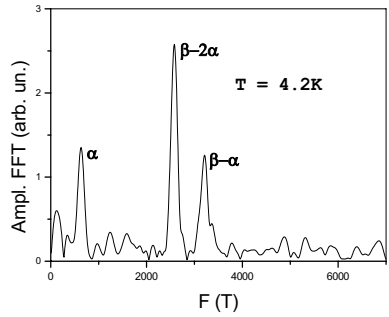

Figure 6. FFT spectrum for Shubnikov-de Haas oscillations (inset) for $(BEDO\text{-}TTF)_5[ScHg(SCN)_4]_2$ at T=1.55K and the field direction parallel to the c^*-axes ($\theta=0^o$). Four different frequencies F_1~650T, F_2~2600T F_3~3200T and F_4~3850T are clearly seen.

Figure 7. FFT spectrum for SdH oscillations at T=4.2K and $\theta=0^o$. The frequency F_4 is absent and frequency F_2 assosiated with QI effect dominates.

zone) this frequency should correspond to a cross section area of 100 % of the first Brillouin zone.

Shubnikov - de Haas (SdH) and de Haas – van Alphen (dHvA) quantum oscillations were observed in the crystals studied at different magnetic field directions and temperatures. Fig. 6 (inset) shows an example of these SdH oscillations. It should be noted that no beating node occurs in these oscillations, suggesting again a strong 2D

electronic character with a negligible warping of the Fermi surface. The Furie spectrum of these oscillations contains four frequencies: $F_1 \approx 650$ T, $F_2 \approx 2600$ T, $F_3 \approx 3200$ T, $F_4 \approx 3850$ T for the field direction perpendicular to the conducting plane (Fig. 6). The dependence of these frequencies on the angle θ between the field direction and the perpendicular to the conducting plane can be described by the relation $F_i(\theta) = F_i(0)/\cos\theta$, which is the expected one for quasi-2D Fermi surface sections (i.e., cylinder-like Fermi surfaces). The frequency F_1 corresponds to a cross sectional area of 16% of the first Brillouin zone and originates from the closed part of the Fermi surface (see Fig. 5). The frequency F_4 corresponds to an area of 100% of the first Brillouin zone and most likely results from a magnetic breakdown orbit including parts of the closed and open portions of the Fermi surface (see Fig. 5). Consequently, the F_1 and F_4 frequencies are in good agreement with the results of our theoretical study. Two additional frequencies, $F_2 \approx F_4 - 2F_1$ and $F_3 \approx F_4 - F_1$, correspond to the forbidden orbits. From a quantum-mechanical point of view there is no semiclassical closed orbit to explain these frequencies. However, they can be understood in the frame of the quantum interference (QI) model [10] as two-arms Stark interferometers [11]. Within the QI model [10] the temperature damping of the oscillation amplitude is given by the energy derivative of the phase difference ($\varphi_i - \varphi_j$) between two different routes *i* and *j* of a two-arms interferometer. This model states that $\partial(\varphi_i - \varphi_j) / \partial\varepsilon = (/eB) \partial S_k / \partial\varepsilon$, where S_k is the reciprocal space area bounded between two arms. Since $\partial(\varphi_i - \varphi_j) / \partial\varepsilon$ is proportional to the difference between the effective masses of the two arms of the interferometer, the associated effective mass is given by $m^* = | m_i^* - m_j^* |$, where m_i^* and m_j^* are the partial effective masses of the routes i and j. In our case an interferometer connected with the frequency F_3 consists of two routes, *abcdaf* and *abef,* and another interferometer, connected with the frequency F_2, includes two cyclotron orbits, *abcdaf* and *abebef* (see Fig 5).

According to Falicov and Stahowiak [12] the contribution of every segment of the cyclotron orbit to the cyclotron mass parameter is proportional to the subtended angle of this segment, and the total cyclotron mass parameter equals the sum of the partial cyclotron mass parameters. We have estimated the effective mass parameters from the temperature dependence of the SdH oscillation amplitude using the standard formula

$$R_T = \frac{\alpha r \mu_c T / B}{\sinh(\alpha r \mu_c T / B)} \qquad (2)$$

where $\alpha = 14{,}69$ T/K and μ_c is the cyclotron effective mass (relative to the free electron mass m_e). The field window 12-14 T and temperature range 1.5-4.2 K were used for the fast Fourier transform (FFT) analysis of the amplitudes. We have obtained the following values for the effective mass parameters: $m_1 = (1.6\pm0.1)m_e$, $m_2 = (0\pm0.3)m_e$, $m_3 = (1.5\pm0.1)m_e$ and $m_4 = (3.0\pm0.1)m_e$. This
estimation shows that $m_3 \sim m_4 - m_1 = m_{abcdaf} - m_{abef}$ and $m_2 \sim m_4 - 2m_1 = m_{abcdaf} - m_{abebef}$, where m_{abcdaf}, m_{abef} and m_{abebef} are the partial effective masses of the routes *abcdaf, abef* and *abebef*, respectively.

It is interesting to compare the temperature dependence of the amplitude for all frequencies (see Fig. 6 for T = 1.5 K and Fig. 7 T = 4.2 K). At 1.5 K the α and (β-α) oscillation amplitudes dominate whereas the (β-2α) amplitude oscillation is very small. However, the (β-2α) amplitude oscillation dominates and the β one disappears completely at 4.2 K. These results are in agreement with the effective mass values corresponding to these oscillation frequencies and satisfy the necessary relations between effective masses for the QI effect. Noting that below 4.2 K the oscillation amplitude connected with the (β-2α) frequency is constant within the experimental error (i.e., a zero cyclotron mass), we may assume that this oscillation can survive to considerably higher temperatures. An analogous situation has been previously found for the (κ-BEDT-TTF)$_2$Cu(NCS)$_2$ salt [13].

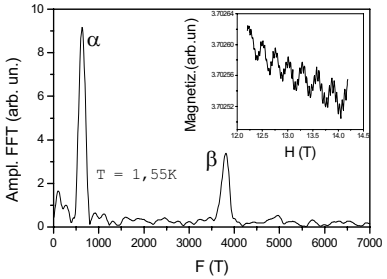

Figure 8. FFT spectrum for de Haas-van Alphen oscillations (inset) at T=1.5K and θ=14°. Only two frequensies F_{-1} and F_4 are visible.

It is well known [14] that the Stark QI effect should not contribute to the free energy and does not manifest itself in the thermodynamical properties of the system. So it cannot contribute to the magnetic oscillations giving rise to the de Haas-van Alphen effect. Fig. 8 (inset) shows the dHvA oscillations for the present salt at 1.5 K and the FFT is shown in Fig. 8. Only two frequencies, α and β, can be seen so that this can be taken as an additional confirmation of the fact that the (β-α) and (β-2α) frequencies are really connected with a QI effect.

4. Conclusion.

The behaviour of the polarized reflectivity and optical conductivity spectra of new quasi-two-dimensional organic conductor β"-(BEDO-TTF)$_5$[CsHg(SCN)$_4$]$_2$ versus temperature for E || L and E ⊥. L are quite different. For E ⊥. L, the temperature changes of R(ω) and σ(ω) are due to the decrease of the optical relaxation constant of the free carriers as expected for a metal. For E || L at temperatures below 200 K, the energy gaps in the σ(ω) spectra at about 4000 cm^{-1} and at frequencies below 700 cm^{-1} appear simultaneously with the two new bands of a_g vibrations of the BEDO-TTF molecule activated by EMV coupling. This suggests a dimerization of the BEDO-TTF molecules in the stacks, which leads to a metal–semiconductor transition.. In the direction perpendicular to L, the studied salt shows metallic properties due to a very favourable overlap of the BEDO-TTF molecular orbitals.

The behaviour of the quantum oscillations in (BEDO-TTF)$_5$[CsHg(SCN)$_4$]$_2$ seems to be in good agreement with the predictions of tight binding band structure calculations. The additional frequencies in the SdH oscillations spectrum are most probably caused by the quantum interference effect. Thus, we propose that Fig. 5 provides an adequate description of the Fermi surface of (BEDO-TTF)$_5$[CsHg(SCN)$_4$]$_2$ and that the

frequencies (β-α) and (β-2α) are connected with magnetic breakdown and the quantum interference effect.

Acknowlegement.

This work was supported by RFBR 03-02-16606.

References

1. .Ishiguro T. , Yamaji K., and Saito G., "*Organic superconductors*" Springer-Ferlag, Berlin, 1998.
2. Singleton J., 2002, Why do Physics Love Charge-Transfer Salts, *J. .Solid State Chem* –**168,** 675-689.
3. Proust C., Audouard A., Brossard L., Pesotskii S.I., Lyubovskii R.B. and Lyubovskaya R.N. (2002) On competing types of quantum oscillations in the 2D organic conductor $(ET)_8[Hg_4Cl_{12}(C_6H_5Cl)_2]$ *Phys. Rev. B65, 155106.* .
4. Brooks J.S., Naughton M.J., Ma J.P., Chaikin P.M., Chamberlian R.V., (1987) *Rev.Sci.Instrum.* **58,** 117
5. Whangbo M.-H., and Hoffmann R. (1978) *J. Am. Chem. Soc.***100,** 6093.
6. Lyubovskii R.B., Pesotskii S.I., Cener M., Rouseau R., Canadell E., Perenboom J.A.A.J., Nizhankovskii V.I., Zhilyaeva E.I., Bogdanova O.A.,and Lyubovskaya R.N. (2002). Characterization of the Fermi surface of $(BEDO\text{-}TTF)_5[CsHg(SCN)_4)_2]$ by magnetoresistance measurements and tight-binding band structure calculations. *J.Mater. Chem.* **12,** 483-488.
7. Zhilyaeva E.I., Bogdanova O.A., Lyubovskaya R.N., Lyubovskii R.B, ., Lyssenko K.A. and Antipin N.Yu. (1999). New Organic conductors $(BEDO\text{-}TTF)_mMHg(SCN)_4$, *Synth. Met.* **99**, 169-174.
8. Drichko N.V., Vlasova R.M., Semkin V.M., Bogdanova O.A., Zhilyaeva E.I., Lyubovskaya R.N., Lyubovskii R.B.,Graja A..(2003) Electr5onic properties of new quasi-two-dimensional organic conductors $(BEDO\text{-}TTF)_5[MHg(SCN)_4]_2$ (M=Rb, Cs) studied by IR reflectance spectroscopy at temperatures down to 10 K. *Phys. Status sol. (b)* **236,** 668-677
9. Drichko N., Dressel M., Petukhov K., Bogdanova O., Zhilyaeva E., and Lyubovskaya R., (2003) Low-Frequencies Optical Properties of β''-$(BEDO\text{-}TTF)_5[CsHg(SCN)_4]_2$. (*in press)*
10. Stark R.W. and Freidberg C.B. (1974) Interfering Electronic Quantum States in Ultrapure Magnesium, *J. Low Temp. Phys.* **14**, 111-144.
11. Shoenberg D. (1984) *Magnetic Oscillations in Metals,* Cambridge University Press, London.
12. Falicov L.M. and Stachowiak H. (1966) The Theory of de Haas-van Alphen Effect in a system of Coupled Orbits. Application to Magnesium, *Phys. Rev.* **147,** 505-515.
13. Kartsovnik M.V., Logvenov G.Yu., Ishiguro T., Biberacher W.., Anzai H. and Kushch . (1996) Direct Oscillation of the Magnetic-Breakdown Induced Quantum Interference in Quasi-Two-Dimensional Organic Metal k-$(BEDT\text{-}TTF)_2Cu(SCN)_2$ *Phys. Rev. Lett.* **77,** 2530-2533.
14. Stark R.W. and Reifenberg R. (1977) Quantitative Theory of Quantum Interference Effect *J. Low Temp. Phys.* **26,** 763.

SPECTRAL AND ELECTROPHYSICAL PROPERTIES OF ANION-RADICAL SALTS OF TCNQ AND METHYL-TCNQ WITH N-ALKYLPIRAZINIUM CATIONS

ANDREY V.KRAVCHENKO[1], VLADIMIR A.STARODUB[1], ALEXANDER R.KAZACHKOV[1] , ANDREY V.KHOTKEVICH[2], OLEG S.PYSHKIN[2] , GENNADIY V.KAMARCHUK[2]

1 – V.Karazin National University, 4 Svobody Sq., Kharkov, 61077 Ukraine.

2 – B.Verkin Institute for Low Temperature Physics & Engineering of NAS of Ukraine, 47 Lenin Ave., Kharkov, 61103 Ukraine.

Abstract: Anion-radical salts (ARS) of 7,7,8,8-tetracyanoquinodimethane (TCNQ) and methyl-TCNQ (MTCNQ) of composition [N-(C_nH_{2n+1})-Pz](TCNQ)$_m$ and [N-(C_nH_{2n+1})-Pz](MTCNQ)$_m$, with Pz for pirazinium, n = 1, 2,…5 and m = 1, 2 have been synthesized and investigated. The IR absorption spectra of these compounds have been studied at room temperature. For single crystal and pellet samples of the synthesized salts**,** electric conductivity has been measured in the temperature range of 77 – 300 K, and the basic electrophysical characteristics were determined. The [N-CH_3-Pz](TCNQ) compound was revealed to be an organic metal undergoing a metal-dielectric transition when cooled below 120 K, the lowest temperature which has ever been achieved for ARS of TCNQ with close-type cations. The conductivity of [N-(C_nH_{2n+1})-Pz](MTCNQ)$_m$ salts has

E. C. Faulques et al. (eds.), Spectroscopy of Emerging Materials, 319–330.

been found to be substantial and comparable with that of analogous TCNQ-based compounds. In this**,** the above compounds are noticeably distinguished from the ARS with cations based on other nitrogen-containing heterocycles. In crystals of the [N-C_2H_5-Pz](MTCNQ)$_2$ salt**,** the existence of a highly quasi-two-dimensional conducting state is expected, despite this being atypical for TCNQ-based ARS.

Key words: 7,7,8,8-tetracyanoquinodimethane (TCNQ), methyl-TCNQ, anion-radical salts, IR absorption spectra, electron-phonon interaction, electric conductivity.

1. INTRODUCTION

Due to the variety of their properties and the prospects for extensive high-tech applications, organic molecular compounds are among the more actively and comprehensively studied materials. Interest in that sort of materials was generated, in particular, by the search to discover new mechanisms of superconductivity. Specifically, Little's consideration [1] has given us reason to believe in the possibility of obtaining one-dimensional systems presenting superconductivity based on an exciton mechanism. Ion-radical salts (ARS) of 7,7,8,8-tetracyanoquinodimethane (TCNQ), highly conducting at room temperatures, were considered to be among the materials which could most likely manifest the above property. They have been found, additionally, to undergo a metal-dielectric transition upon cooling [2]. In particular, crystals of NMP-TCNQ (where NMP is for N-methylphenazinium-ion) – one of the first comprehensively studied ARS organic metals – were discovered to undergo a Mott dielectric transition below $T_M \approx 220$ K [2].

The synthesis of novel organic conductors with physical properties for prospective technological applications has given a new impetus to the studies of conducting organic compounds. In particular, magnetic ordering was discovered in some organic and metal-organic compounds [3], including ARS of TCNQ [4-6]. Importantly, the coexistence of magnetic ordering and a conducting phase has been observed in some molecular materials, making them potential materials to be utilized in measuring devices based on the ability of magnetic metals to conduct spin-polarized current [7].

Another interesting application of the organic conductors was promoted by the discovery of a TCNQ-based class of ARS which is able to melt without destruction [8, 9]. This property is indeed highly atypical for organic metals. Compounds of this type may be used in the production of novel

electrolytic metal-oxide capacitors [10, 11] with advanced work characteristics and unique properties like self-healing of oxide layer defects [12]. Results of electrophysical and optical studies [13] support the assumption that the melted phase of TCNQ ARS behaves as a conducting liquid crystal retaining stack structure typical for solid conducting TCNQ-based compounds. Recently, evidence for the high sensitivity and selectivity of conducting TCNQ-based compounds to the action of external agents of a different nature has been obtained, which has led to the design of new sensor devices [14].

Taking all these facts into account, we have proceeded to the synthesis and the investigation of new TCNQ salts aimed at obtaining materials whose properties might be applied in modern high-tech devices. In the present study, we have first synthesized and investigated a series of compounds of TCNQ and methyl-TCNQ (MTCNQ) with N-alkilpyrazinium (N-Alk-Pz) as cations.

It should be noticed that the use of bi-functional organic cations is by itself of great experimental and theoretical interest. The second nitrogen atom present in the cationic structure is able – due to a lone pair of electrons – to mediate an additional inter-molecular interaction producing novel, unusual types of TCNQ. On the other hand, the presence of such a pair of electrons is a prerequisite for the adhesion of the considered materials to the surface of metals resulting in the formation of stable complexes with nitrogen-containing ligands. Also, the use of an alkyl-substituted TCNQ, e.g., MTCNQ, may result in the decrease of the ARS melting temperature due to a weakening of the inter-stacking interaction along the anion-radical stacks.

2. EXPERIMENTAL TECHNIQUE

In the present study, [N-Alk-Pz](TCNQ)$_m$ and [N-Alk-Pz](MTCNQ)$_m$ salts have been synthesized, with Alk for C_nH_{2n+1}; n = 1, 2,…5; m = 1, 2. *Aldrich*-produced pyrazine was used without any additional purification, while TCNQ and MTCNQ were refined by vacuum zone sublimation. Iodide alkyls were synthesized by the reaction of corresponding alcohols with phosphate tri-iodide followed by a distillation in inert atmosphere. To obtain alkylpyrazinium iodides, the quaternization reaction was used:

$$Pz + AlkI \rightarrow (N\text{-}Alk\text{-}Pz)I\ .$$

ARS of TCNQ and MTCNQ of simple and complex composition were produced by the following reaction:

$$1.5(N\text{-}Alk\text{-}Pz)I + mA \rightarrow (N\text{-}Alk\text{-}Pz)A_m\downarrow + 0.5(N\text{-}Alk\text{-}Pz)(I_3),$$

where m = 1 or 2; A is for TCNQ or MTCNQ; Alk is for CH_3, C_2H_5, iso-C_3H_7, iso-C_4H_9 and iso-C_5H_{11}.

Sediments of the obtained ARS were filtered, washed with butanol and ether, and vacuum dried. For further refining, double re-crystallization from acetone or methanol was performed.

The composition of the synthesized ARS was determined spectrophotometrically. The optical density D of their solutions in acetonitrile was measured in the absorption range of both the anion-radicals – $TCNQ^{\cdot -}$ and $MTCNQ^{\cdot -}$ – and of the acceptor molecules – TCNQ (394 nm) and MTCNQ (393 nm). Also, the optical density was determined at 840 nm where anion-radicals are the only absorbing species**.**

Then, the composition of salts dissolved in acetonitrile is calculated from the ratio [13]:

$$\frac{[TCNQ]}{[TCNQ^{-}]} = 0.74\frac{D_{394}}{D_{840}} - 0.35,$$

$$\frac{[MTCNQ]}{[MTCNQ^{-}]} = 0.87\frac{D_{393}}{D_{840}} - 0.46,$$

here D_λ is the optical density of the solution at the corresponding wavelength. Synthesized compounds were investigated by two experimental techniques: measurement of their infrared (IR) absorption and of their electrical conductivity.

For IR absorption, the samples were grown with KBr to produce pellets, and the spectra were recorded at room temperature on a Specord-75 IR spectrophotometer, from 400 to 4000 cm^{-1}.

The DC conductivity of single crystals and the pressed powder of the synthesized salts has been measured in the temperature range of 77-300 K by four-contact technique. Table 1 presents the values of specific electrical conductivity at room temperature σ_{RT} and of conductivity activation energy Δ calculated on the basis of resistive measurements at various temperatures. Conductivity models applied for the calculation of the Δ value in each compound are presented and discussed in the next section.

3. RESULTS AND DISCUSSION

In our optical studies, two types of IR spectra have been obtained. The first one was measured for ARS with cations including the shortest alkyl radicals, namely, methyl-, ethyl- and iso-propyl-radicals (Fig.1, 2). For this

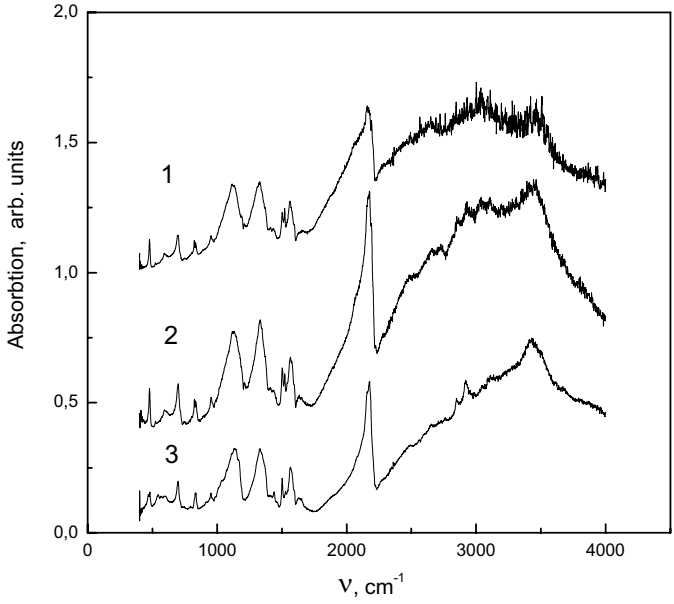

Fig 1. IR absorption spectra of the conducting salts of TCNQ: 1 - [N-CH_3-Pz](TCNQ)$_2$, 2 - [N-CH_3-Pz](TCNQ), 3 - [N-iso-C_3H_7-Pz](TCNQ)$_2$.

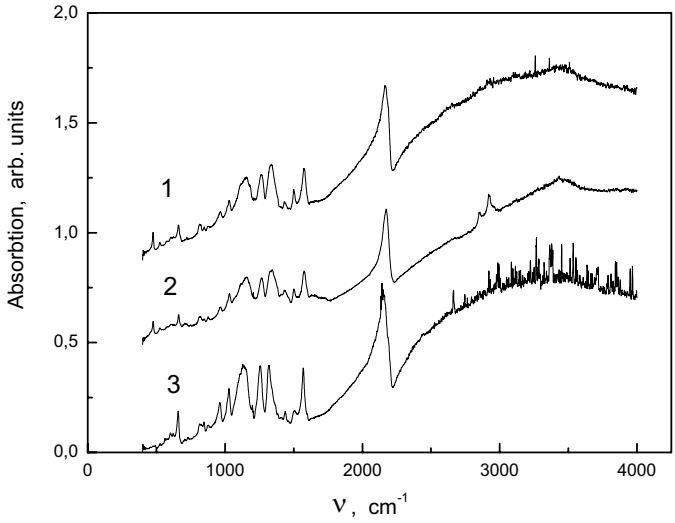

Fig 2. IR absorption spectra of the conducting salts of MTCNQ: 1 - [N-CH_3-Pz](MTCNQ), 2 - [N-CH_3-Pz](MTCNQ)$_2$, 3 - [N-C_2H_5-Pz](MTCNQ)$_2$.

group of spectra, we observe a characteristic broadening of the absorption lines (up to 250-300 cm^{-1}), obviously caused by the electron-phonon interaction (EPI) [15, 16]. Spectra of that kind are known to indicate well conducting materials [see, e.g., 17]. Broadened lines in the spectra of the considered group of salts are observed in the ranges of 1115 – 1140 cm^{-1}, 1320 – 1330 cm^{-1} and 2140 – 2180 cm^{-1}. The later range corresponds to ν(C≡N) covalent vibrations of the nitrile group. The increasing length of the alkyl-radical part of the cation results in a shift of the line towards smaller wavenumbers. In the MTCNQ-based ARS absorption spectra, a broadening of the spectral lines is also observed in the range of methyl group ν(CH) covalent vibrations (2920 – 2990 cm^{-1}). This indicates a noticeable contribution of methyl groups into the transfer processes, possibly due to a superconjunction phenomenon.

Broadened lines in the spectra presented in Fig.1, 2 are observed on the background of the continuous absorption caused by the excitation of conductivity electrons. The absorption edge corresponds to the gap width. Also, from the decrease of continuous absorption at wavelengths exceeding 3500 cm^{-1}, the conductivity bandwidth of the considered ARS could be estimated as close to 0.4 eV.

Back to the beginning of continuous absorption v_{min} we have estimated the conductivity activation energy Δ for all the studied compounds. In particular, $v_{min} \approx 500$ cm^{-1} for [N-CH_3-Pz](TCNQ) salts, so $\Delta \approx 0.06$ eV there. All the first synthesized ARS of MTCNQ continuously absorb beginning from $v_{min} \approx$ 400 cm^{-1} which yields $\Delta \approx 0.05$ eV. The results obtained lead one to expect the discussed compounds to be either metals or narrow-band semiconductors. This sets the ARS of simple composition [N-CH_3-Pz](TCNQ), [N-CH_3-Pz](MTCNQ) and [N-C_2H_5-Pz](MTCNQ) well apart from the earlier studied analogous compounds with the piridinium-, quinolinium- and isoquinolinium-based cations [11, 12]. The conductivity of the latter salts is 2-3 orders smaller than that of their analogs of complex composition. High conductivity of simple pyrazinium-based ARS may be explained by charge transfer interaction between the corresponding cations and anion-radicals [18]. We should mention that substitution of TCNQ by MTCNQ in the studied ARS has never caused a decrease of conductivity, as it was in the case of the compounds investigated in Refs. [11, 12].

Fig.3 presents IR absorption spectra of TCNQ ARS, the cations of which include longer alkyl radicals iso-C_4H_9- and iso-C_5H_{11}. Here essential distinctions from the above-discussed spectra of conducting ARS (Fig. 2) are obvious. In particular, no EPI-caused peculiarities are observed since no lines are broadened in the range of pyrazinium skeleton vibrations and ν(C≡N) vibrations. Continuous absorption is also absent in all the studied range. This suggests the existence of a dielectric ground state in the [N-iso-

C_4H_9-Pz](TCNQ), [N-iso-C_4H_9-Pz](TCNQ)$_2$ and [N-iso-C_5H_{11}-Pz](TCNQ) salts.

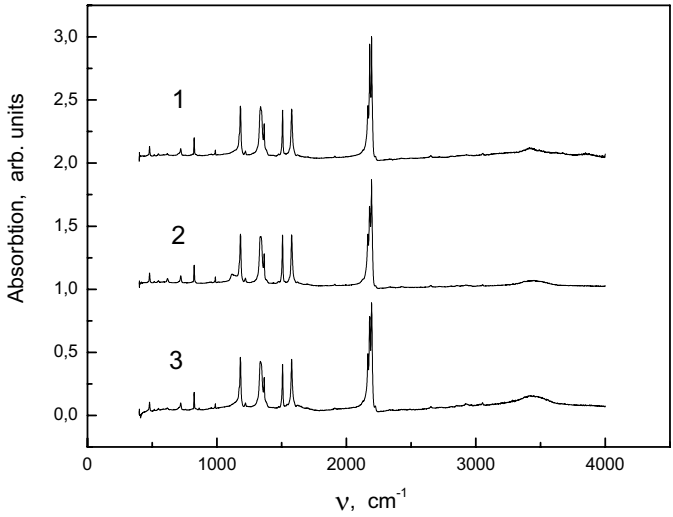

Fig 3. IR absorption spectra of the conducting salts of TCNQ: 1 - [N-iso-C_5H_{11}-Pz](TCNQ), 2 - [N-iso-C_4H_9-Pz](TCNQ), 3 - [N-iso-C_4H_9-Pz](TCNQ)$_2$.

Results of the resistive measurements presented in Table 1 confirm the conclusions based on the optical investigations. Room temperature conductivity σ_{RT} of the complex ARS of MTCNQ is approximately 4 times higher than that of the simple ARS with the same cations, and it slightly decreases when the alkyl radical length increases. Room temperature conductivity of MTCNQ salts synthesized in our studies is an order or two higher than the σ_{RT} of analogous ARS of TCNQ. It should be noticed that for the earlier investigated ARS of TCNQ and MTCNQ based on of N-alkylpiridinium, N-quinolinium and N-isoquinolinium cations, transition from the TCNQ salts to their MTCNQ analogs has yielded a decrease of conductivity explained in Ref. [11] by the loosening action of the methyl group of MTCNQ on the stack structure of the above ARS. Meanwhile, in the case of [N-(C_nH_{2n+1})-Pz](MTCNQ)$_m$ compounds, their electric conductivity is higher than that of analogous ARS of TCNQ and may be caused by the supposed stereo-regular orientation of methyl groups and by the specific influence of the pyrazine-based cations. Such an orientation of methyl groups should be expected to result in the additional ordering of the stack structure of MTCNQ$^{\cdot -}$ anion radicals. Presence in the cation of the second nitrogen atom with a free lone pair of electrons is able to cause an enhancement of the interaction between the anion-radical stacks and the cations. Such an interaction may be finalized in the formation of the quasi-

two-dimensional electronic structure instead of the quasi-one-dimensional one typical for ARS.

Table 1. Properties of anion-radical salts of TCNQ and MTCNQ:
ν_{min} – beginning of the continuos absorption in IR spectrum; Δ – the values of conductivity activation energy obtained from the data of resistive measurements; σ_{RT} – specific conductivity at room temperature.

ARS	ν_{min}, cm^{-1}	Δ, eV	σ_{RT}, $\Omega^{-1}cm^{-1}$
[N-CH_3-Pz](TCNQ)	500	0.055	$1.1 \cdot 10^{-2}$
[N-CH_3-Pz](TCNQ)$_2$	500	0.090	$1.5 \cdot 10^{-2}$
[N-C_2H_5-Pz](TCNQ)	1700	0.260	$2.36 \cdot 10^{-3}$
[N-C_2H_5-Pz](TCNQ)$_2$	1700	0.340	$1.26 \cdot 10^{-2}$
[N-iso-C_3H_7-Pz](TCNQ)	1700	0.680	$1.32 \cdot 10^{-4}$
[N-iso-C_3H_7-Pz](TCNQ)$_2$	1700	0.500	$1.68 \cdot 10^{-4}$
[N-iso-C_4H_9-Pz](TCNQ)	-	-	$2.6 \cdot 10^{-6}$
[N-iso-C_4H_9-Pz](TCNQ)$_2$	-	-	$3.4 \cdot 10^{-6}$
[N-iso-C_5H_{11}-Pz](TCNQ)	-	-	$1.7 \cdot 10^{-6}$
[N-CH_3-Pz](MTCNQ)	400	0.051	0.38
[N-CH_3-Pz](MTCNQ)$_2$	400	-	1.38
[N-C_2H_5-Pz](MTCNQ)	400	0.052	0.34
[N-C_2H_5-Pz](MTCNQ)$_2$	400	-	1.34

Results obtained in the studies of temperature dependencies of electric conductivity of the synthesized ARS support the above assumptions.

For single crystals of the [N-CH_3-Pz](TCNQ) compound, no increase of electric conductivity is observed when cooling from 300 to 120 K (Fig.4). In the case of MTCNQ salts, changes of conductivity are also small in the $300 < T < 140$ K interval. This allows one to suspect that in the above temperature range, there is an interesting case of coexistence of metallic electrical conductivity along the anion-radical stacks and semiconducting behavior in the perpendicular direction. A similar temperature dependence of electric conductivity was earlier observed in polymer materials [19], where motion of charge carriers occurs along the polymeric conjugated chain.

Further cooling yields a sharp increase of the resistivity of the studied compounds, caused by a transition towards the dielectric state. It should be noticed that the [N-CH_3-Pz](TCNQ) salt becomes dielectric at a temperature of T ≈ 120 K which is the lowest ever recorded for TCNQ ARS with "close" type cations.

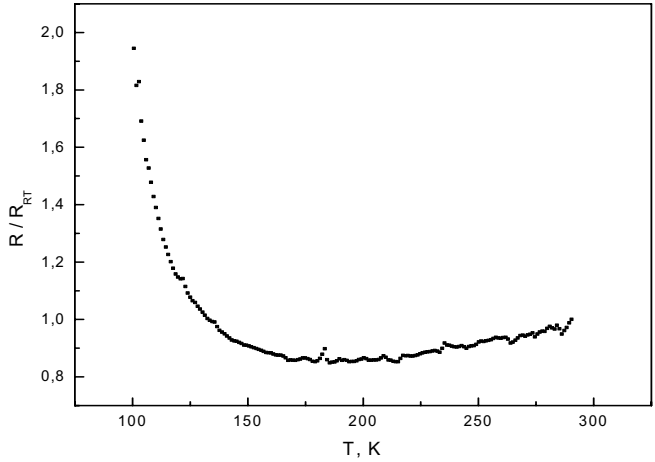

Fig 4. Temperature dependence of the electric conductivity of [N-CH_3-Pz](TCNQ) compound.

Below 120 K, the temperature dependence of electric conductivity of [N-CH_3-Pz](TCNQ) is well approximated by a theoretical curve obtained in the frame of the simple activation energy model:

$$R(T) = R_\infty exp(\Delta/2T),$$

(here R_∞ is the minimum value of electric resistance). This allows one to determine the value of the energy of conductivity activation Δ (see Table 1).

For the ARS of MTCNQ, temperature dependence of electric resistance (Fig. 5) is best described in the frame of a model taking into account the scattering of conductivity electrons possibly caused by the narrowness **of** the small amplitude of the energy gap [20]:

$$R(T) = AT^n\, exp(\Delta/2T).$$

Procession of experimental data in the frame of this model (by least square root technique) yields the following expressions for the temperature dependence of the reduced resistance R/R_{RT} of the investigated salts (R_{RT} is the resistivity at room temperature):

$$ln(R/R_{RT}) = 16.34 - 3.08\, lnT + 595.7/T$$

for [N-CH_3-Pz](MTCNQ) and

$$ln(R/R_{RT}) = 17.08 - 3.36\, lnT + 604.9/T$$

for [N-C_2H_5-Pz](MTCNQ). Here and below all the coefficients are of the corresponding dimension have the same dimensions.

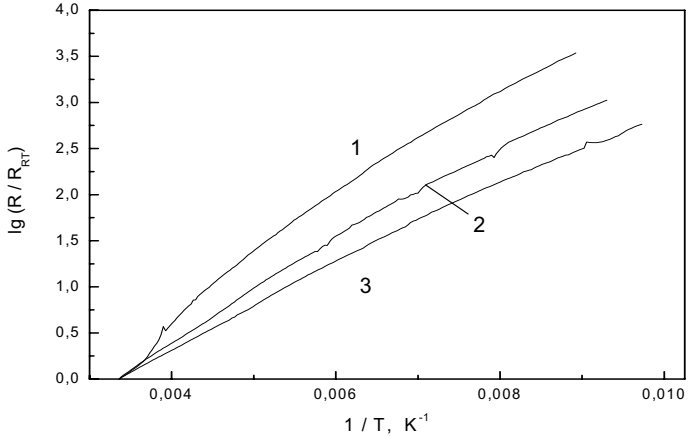

Fig 5. Temperature dependence of the electric resistivity of MTCNQ salts: 1 - [N-C_2H_5-Pz](MTCNQ)$_2$, 2 - [N-C_2H_5-Pz](MTCNQ), 3 - [N-CH_3-Pz](MTCNQ)$_2$.

Using these expressions, it is possible to determine gap energy. In the case of [N-CH_3-Pz](MTCNQ) its value is 0.051 eV, which corresponds to the beginning of the continuous optical absorption band edge at 414 cm^{-1}. For [N-C_2H_5-Pz](MTCNQ) calculations give 0.052 eV and 419 cm^{-1}. The above estimations closely agree with IR absorption spectra of the investigated compounds.

For an adequate description of the temperature behavior of electric resistivity of complex salts [N-CH_3-Pz](MTCNQ)$_2$ and [N-C_2H_5-Pz](MTCNQ)$_2$ we use a model based on a conductivity hopping mechanism possibly conditioned by the structural peculiarities of the ARS:

$$R(T) = A\exp[(\frac{T_0}{T})^{\frac{1}{\alpha+1}}].$$

Here $\boldsymbol{\alpha}$ is the dimensionality of the system, $\boldsymbol{T_0}$ and $\boldsymbol{A}$ are the parameters of the model.

For the [N-CH_3-Pz](MTCNQ)$_2$ compound, the best fit of the experimental and theoretical $R(T)$ dependencies occurs for $\alpha = 1$, which corresponds to the one-dimensional case. The logarithm of the reduced electric resistivity R/R_{RT} is expressed as:

$$ln(R/R_{RT}) = -9.32 + \frac{158.59}{\sqrt{T}}.$$

Meanwhile, the fit of the experimental $R(T)$ dependence for [N-C_2H_5-Pz](MTCNQ)$_2$ salt by varying the α parameter yields an estimate value of α

= 2 which is typical of a two-dimensional conductivity. In this case $ln(R/R_{RT})$ is expressed as:

$$ln(R/R_{RT}) = -21.44 + \frac{143.48}{\sqrt[3]{T}}.$$

A direct verification of a quasi-two-dimensional electric conductivity, which is so unusual for TCNQ-based ARS, can be performed by studying the electric resistance anisotropy of $[N\text{-}C_2H_5\text{-}Pz](MTCNQ)_2$ single crystals.

For all the studied compounds, values of conductivity activation energy Δ calculated from the data of resistive measurements (Table 1) exceed those estimated in the analysis of IR absorption spectra. This difference may be due to the quality of crystals and to that of the electric contacts used for conductivity measurements.

4. CONCLUSIONS

In the present study, anion-radical salts of TCNQ and MTCNQ with composition $[N\text{-}(C_nH_{2n+1})\text{-}Pz](TCNQ)_m$ and $[N\text{-}(C_nH_{2n+1})\text{-}Pz](MTCNQ)_m$ have been first synthesized and investigated. All the above compounds can be classified into two groups. The first group includes ARS with the cations including short alkyl (methyl-, ethyl- and propyl-) radicals, all being either narrow-band semiconductors or metals. The second group is composed of salts with larger (iso-C_4H_9- and iso-C_5H_{11}-) alkyl radicals in the cation, which typically display dielectric properties. Characteristically, the conductivity of $[N\text{-}(C_nH_{2n+1})\text{-}Pz](MTCNQ)_m$ salts is considerable, and it is similar to that of the analogous TCNQ-based compounds. Such a property sharply distinguishes the above salts from the ARS with cations designed on other nitrogen-containing heterocycles. Analysis of IR absorption spectra and of the temperature dependence of electric resistivity performed by using different conductivity models points to the probability of a quasi-two-dimensional conducting state in $[N\text{-}C_2H_5\text{-}Pz](MTCNQ)_2$ crystals. Such an unusual, atypical conductivity behavior for most of the ARS is of special interest. These results are good prerequisites for technological applications of these TCNQ-based materials, particularly as sensor devices.

These studies were supported by the STCU grant #2276 and by The Ministry of Education and Science of Ukraine.

REFERENCES

1. W.A.Little, Phys. Rev. A, **134** (1964) 1416.
2. T.F.Schegolev, Phys. Stat. Sol. Ser.a, **12** (1972) 9.

3. J.S.Miller, A.J.Epstein. Angew. Chem. Int. Ed. Engl., **33** (1994) 385.

4. W.E.Broderick, J.A.Thompson, E.P.Day, B.M.Hoffman, Science, **249** (1990) 401.

5. K.Mukai, S.Jinno, Y.Shimode, N.Azuma, Y.Hosokoshi, K.Inoue, M.Taniguchi, Y.Misaki, K.Tanaka. Polyhedron. **20** (2001) 1537.

6. L.Ballester, A.M.Gil, A.Guttierez, M.F.Perpinan, A.E.Sanchez, M.Fonari, K.Suwinska, V.Belsky. Eur. J. Inorg. Chem. (2003) 3034.

7. G.A.Prinz, Spin-Polarized Transport, Phys. Today **48** (1995) 58.

8. Patent 60-139832 Japan, MKI 07 D 215/10 C 07D 217/10. Organic electroconducting complexes / M.Tanaka, F.Urano, M.Nakabata. - Publ. 06.01.87.

9. Patent 1389226 USSR, subm. 4091791 prior. from July 10, 1986, regist. December 15, 1987 // 7,7,8,8-tetracyanoquinodimethanids of N-alkylquinaldinium as melting narrow-zone organic semiconductors // V.A.Starodub, V.V.Barabashova, Ye.M.Gluzman *et al.*

10. Patent 458055 USA, MKI H 016 9/5. Condenser with solid electrolyte / Sanyo Electric Co., LTD (Jap). - Publ. 08.04.86

11. Patent 1696428 USSR, subm. 4706057 prior. from June 15, 1989, regist. August 8. 1991 // Anion-radical salt of 2-methil-7,7,8,8-tetracyanoquinodimethane as an addend to organic conducting materials // V.A.Starodub, Ye.M.Gluzman, K.V.Krikunov *et al.*

12. V.A.Starodub, Ye.M.Gluzman, K.I.Pokhodnya, M.Ya.Valah, Theor. Exp. Chem., **29** (1993) 361.

13. V.A.Starodub, Ye.M.Gluzman, Yu.A.Kaftanova, I.Olejniczak, Theor. Exp. Chem. **33**, No. 2 (1997) 111.

14. A.P.Pospelov, M.V.Ved, N.D.Sakhnenko, Yu.L.Alexandrov, V.V.Shtefan, A.V.Kravchenko, G.V.Kamarchuk, Materials Science, Vol.20, No.3 (2002) 65.

15. C.C.Homes, J.L.Musfeldt, D.B.Tanner, Phys. Rev. B, **48**, (1993-II) 16799.

16. A.Graja, I.Olejniczak, J. of Molecular Structure, **325**, (1994) 37.

17. G.C.Papavassiliou, A.Terzis, P.Delhaes. Tetrachalcogenafulvalenes, Metal 1,2-Dichalcogenolenes and Their Conducting Salts. In: Handbook of Organic Conductive Molecules and Polymers. Vol. 1. Edited by H.S.Nalwa. John Wiley and Sons Ltd., 1997. ch. 3, p. 152.

18. V.E.Klimenko, V.Ya.Krivnov, A.A.Ovchinnikov, I.I.Ukrainskiy, Theor. Exp. Chem. **13**, (1977) 614.

19. A.J.Heeger. Angew. Chem., **113**, (2001) 2660.

20. J.M.Ziman. Models of disorder. Cambridge University Press. Cambridge, London, New York, Melbourne. 1979.

NEW DEVELOPMENT OF IMPEDANCE SPECTROSCOPY

A.POSPELOV[1], G.KAMARCHUK[2], YU.ALEXANDROV[1], A.ZAIKA[2], E.FAULQUES[3]
[1]National Technical University " Kharkov Polytechnical Institute ", Kharkov, Ukraine; [2]B.Verkin Institute for Low Temperature Physics and Engineering, Kharkov, Ukraine;
[3]Institute des Materiaux Jean Rouxel, Nantes, France
E-mail: pospelow@kpi.kharkov.ua <mailto:pospelow@kpi.kharkov.ua>

Abstract: We propose a modification of the impedance spectroscopy technique based on a new electrode system design. The experiment is carried out in an electrolytic cell with an extended conductor immersed into electrolyte. The ends of the conductor are connected directly to the plugs of a measuring device. Thus, the conductor develops two identical and electrochemically conjugated electrodes fed with a variable polarity. The electrode polarization occurs in conditions of linearly distributed potential along the conductor. Water solutions of sulfuric acid, potassium sulfate, ferry- and ferrocyanide were used as a liquid electrode phase. The possibilities and advantages of this updated impedance spectroscopy are described.

Key words: Electrochemical impedance, electrode, distributed potential, solution, polarization.

Impedance spectroscopy is one of the most informative methods in electrochemistry research [1, 2]. The essence of the method consists in investigating the response of a target taking place in stationary conditions to weak influences of a variable voltage or to an electric current in a wide range of frequencies. It is possible

E. C. Faulques et al. (eds.), Spectroscopy of Emerging Materials, 331–338

to determine the structure and the systems properties by the character of an impedance's frequency dispersion. In the target's complex impedance research, modelling is applied widely. In this model, the target is considered as a system including a structured set of discrete electrotechnical elements. The base structure for modelling of all the electrochemical systems is the circuit including a resistance of electrolyte Re, a capacity of double electric layer C_d and an impedance Z_R reflecting the final rate of the processes of diffusion, adsorption, and electron transfer through the phase surface, as well as the interaction of these processes (Fig.1).

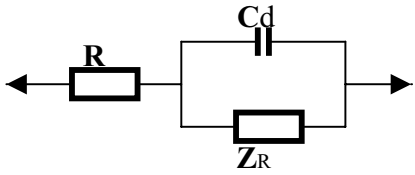

Fig. 1.The block diagram of the equipotential electrode to be forced by an alternating electric current.

On the basis of such a model, it is possible to calculate the thermodynamic and kinetic parameters of an electrode as well as electrode reactions.

In the last few decades, researchers have been actively working to update the classical impedance method [3]. Among the achievements in this area, advances such as non-linear and non-stationary impedance analysis, combined optical impedance, and impedance measurements using a rotating disk electrode should be mentioned. However, these innovations have not altered the configuration of the target electrode under investigation. Views of the basic device of a measuring cell have been mostly conservative. Up to now the electrode system in impedance measurements still involves two electrodes separated by an electrolyte layer. One of the electrodes is the direct target of research while the other one is an auxiliary device closing the electric circuit. The direct or alternating current forces the circuit and polarizes the target electrode in order to vary its potential. In such electrode systems, there are two ways to derive the target electrode impedance from the total measured value of the input impedance Z_c which includes the electrolyte resistance and the impedances of both electrodes [4]. One of the ways involves the design of a target electrode having a surface essentially smaller than that of the auxiliary electrode ($S_1 << S_2$), which allows the researcher to neglect the impedance contribution of the auxiliary electrode. Namely,

$$Z_c = Re + (Z/ S_1)(1 + S_1/S_2) \approx Re + Z/ S_1,$$

where Z is the specific electrode impedance, S_1 and S_2 are the surface square values of the target and auxiliary electrodes, respectively, and Re is the electrolyte resistance. The second way involves the use of a cell in which the electrodes have a similar size ($S_1 = S_2 = S$). Consequently, $Z_c = Re + 2Z/S$, which means that the target electrode impedance is defined as half the input impedance minus the electrolyte resistance.

The authors of this paper propose for the first time an updated, prospective method for impedance spectroscopy based on an essentially new design of the electrode system. In this case, the electrode system is replaced by an extended electric conductor immersed into the electrolyte. An alternating voltage is applied to the ends of the conductor connected directly to a measuring device. This signal induces two identical and electrochemically conjugated electrodes at the both ends of the conductor. The polarity of these electrodes is variable by fed frequency. They come in contact at the non-polarized centre of the extended conductor. The linear coordinate of the non-polarized centre is estimated on the condition of a conjugation of cathodic and anodic process:

$$\int_{x_0}^{x_k} \left[\frac{(\partial u / \partial x) S}{(\partial(\Delta E) / \partial j)} \right] (x)dx = -\int_{x_0}^{x_a} \left[\frac{(\partial u / \partial x) S}{(\partial(\Delta E) / \partial j)} \right] (x)dx$$

where $(\partial u/\partial x)$ is the potential gradient along the conductor, $\partial(\Delta E)/\partial j$ the polarizing resistance, x_k and x_a are the coordinates of the maximal cathodic and anodic polarization points along the conductor, respectively, and x_0 is the coordinate of the point where the polarization is zero. In the second classical way, the impedance contribution of the target electrode is defined as a half of the input impedance. However, the design of two identical electrodes which are identical in shape and which have a common chemical composition is a rather complex technical problem. In our case, such a design is properly achieved when the voltage is switched on at the ends of the conductor.

The basic difference between the conventional electrodes and our electrode design is that of the distribution of potentials along the conductor. While conventional electrodes have a similar potential [4], in our electrode, the potentials are distributed monotonously, and can be described by the so-called Voit's model (Fig. 2) [3].

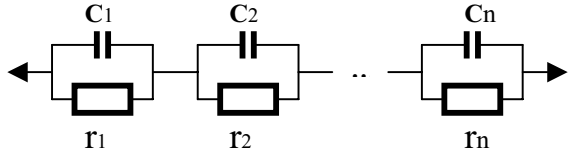

Figure 2. The block diagram of Voit's model

The Voit's impedance model is defined by

$$Z_V = \sum_{i=1}^{n} \left[r_i^{-1}(x) + j\omega c_i(x) \right]^{-1}$$

where $r_i(x)$ and $c_i(x)$ are elementary components of the resistance and capacitance of conductors which are functionally related to a linear coordinate.

Experiments using electrodes under monotonous potential distribution and constant voltage combined with alternating-current-impedance measurements give us the opportunity to study the potential area of electrode activity for synthesized products i.e. to optimize conditions of their electrochemical synthesis. Moreover, the length of the electrode part immersed in the electrolyte is correlated to the polarizing voltage amplitude. This allows us to pinpoint the limits of the electrode processes reversibility.

Thus, the electrode system designed in the present work possesses an additional degree of flexibility. Besides, the measurements may be carried out on a conventional pattern. Another advantage is that the experimental simplicity provides reliable results.

Experiments were carried out in a cell filled with electrolyte into which a platinum wire of 0.2 mm diameter and of 1.1 m length was immersed. A 1 mm pitch spiral-shaped wire was coiled on a teflon core of 14 mm diameter. A special device allowed us to change the length of the immersed part of the platinum conductor.

Several electrode types can be achieved by choosing the proper electrolyte solutions. When platinum interacts with a ferri-ferrocianide solution, a low polarization occurs as a result, e.g., of the follow reaction

$$[Fe(CN)_6]^{3-} + e \leftrightarrow [Fe(CN)_6]^{4-}.$$

Platinum ranks among the metals with the highest hydrogen adsorption energy and with low overvoltage of protons reduction [5]. Because of this, it is necessary improve the preparation of electrodes' surface. To obtain reliable and reproducible resultss, the platinum surface is electrochemically cleaned by consecutive anodic and cathodic polarization in H_2SO_4 before each experiment run. Gaseous impurities dissolved in the electrolyte were removed by de-gassing with argon for 30 minutes. Since the ferri-ferrocianide solution is neutral, i.e. the concentration of protons is insignificant, and since impurities have been removed from the surface of the platinum wire, the probability that the reaction $H_{ads} \leftrightarrow H^+ + e$ will influence the velocity of the electrode processes is reduced to a minimum. When the platinum is immersed into a K_2SO_4 solution at neutral pH, a well polarized electrode is formed, on which minor alterations in the process velocity induce strong potential shifts with respect to the stationary value. Adsorption processes on the platinum in this solution are also insignificant. The H_2SO_4 solution in contact with platinum provides a so-called hydrogen electrode with the reversible protons reaction $H^+ + e^- \rightarrow H_{ads}$. In view of the above mentioned reasons, the balance of this reaction is shifted to the

right. Therefore, atomic layers of hydrogen are adsorbed onto the platinum surface, which influences the kinetics of the electrode processes.

A bridge of alternating current (R 5083 type) was used as a measuring device, and its polarizing plugs were switched with the target electrode by connecting them directly to the ends of the platinum wire. The frequency range of supplied voltage was 0.1 – 100 kHz. Before each experiment, the impedance measurements of the non-immersed (dry) conductor were carried out. The entering impedance of the cell was simulated by serial connection of active (R_s^{Σ}) and reactive (X_s^{Σ}) components. This impedance was considered as a parallel connection of impedances of the non immersed conductor and the immersed electrode. Thereby, both the active (R_S) and the reactive (X_S) component of electrode impedance were defined as

$$R_S = \frac{(R_s^{\Sigma}R_s^0 - X_s^{\Sigma}X_s^0)(R_s^0 - R_s^{\Sigma}) + (R_s^{\Sigma}X_s^0 + R_s^0X_s^{\Sigma})(X_s^0 - X_s^{\Sigma})}{(R_s^0 - R_s^{\Sigma})^2 + (X_s^0 - X_s^{\Sigma})^2},$$

$$X_S = \frac{(R_s^{\Sigma}X_s^0 + R_s^0X_s^{\Sigma})(R_s^0 - R_s^{\Sigma}) - (R_s^{\Sigma}R_s^0 - X_s^{\Sigma}X_s^0)(X_s^0 - X_s^{\Sigma})}{(R_s^0 - R_s^{\Sigma})^2 + (X_s^0 - X_s^{\Sigma})^2},$$

where R_s^0 and X_s^0 are active and reactive components of the impedance of the non-immersed conductor.

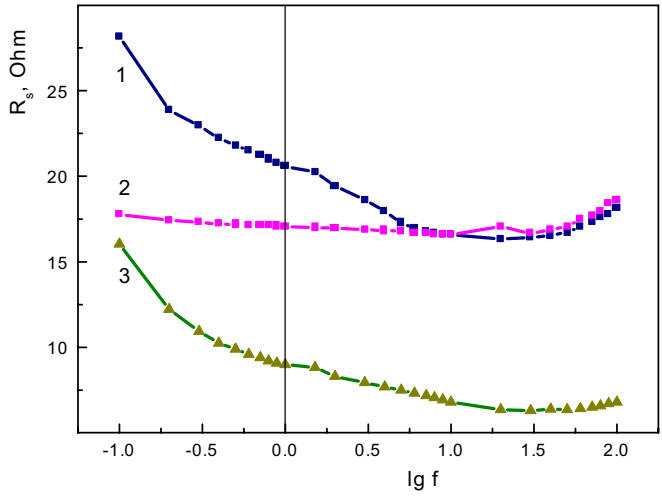

Fig. 3. The frequency dependence of Pt | L electrode impedance active component. L: 1- 0.5M K_2SO_4; 2- 0.1M $K_3Fe(CN)_6$ / 0.1M $K_4Fe(CN)_6$; 3- 0.5M H_2SO_4.

At the present time, the theory of electrochemical impedance of electrodes with distributed potentials is not yet completed, and algorithms of parametrical and structural identification procedures are not available. In addition, the interpretation of the results is very complicated. For this reason, in this work we analyzed only the frequency characteristics of impedance's components in the modified electrode system. As a result, we obtained a set of response peculiarities in the frequency range under investigation. Rather low frequency dispersion was observed in a solution containing a ferri-ferrocyanide system for both active (Fig.3, curve 2) and reactive (Fig.4, curve 3) components. In our opinion, this fact confirms that the independent on frequency resistance of charge transfer determines the main contribution to the impedance.

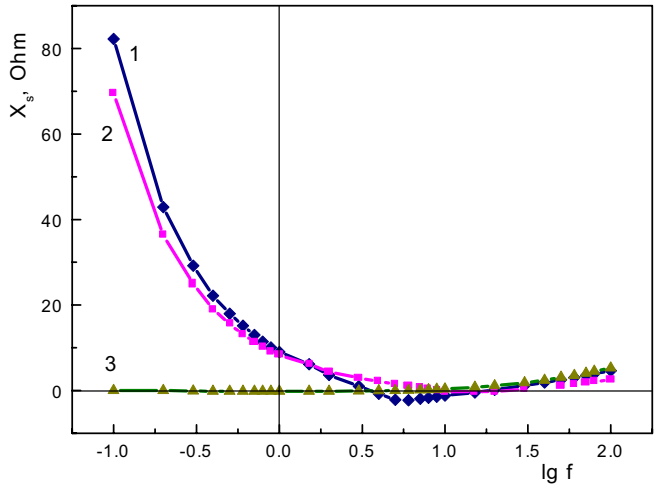

Fig. 4. The frequency dependence of Pt | L electrode impedance reactive component. L: 1- 0.5M K_2SO_4; 2- 0.5M H_2SO_4; 3-0.1M $K_3Fe(CN)_6$ /0.1M $K_4Fe(CN)_6$.

The limiting electrode processes in solutions of K_2SO_4 and H_2SO_4 have other and more complicated natures. Curve 3 (Fig.3) corresponds to a higher specific electrical conduction in sulfuric acid solution. The rather insignificant value of the reactive component in a solution of the ferri-ferrocyanide system (Fig.4) allows one to conclude that the capacity of the double electric layer on the platinum in this solution has an essentially higher value. It is well known that this capacity is defined, first of all, by the distance between centers of opposite charges on a phase surface. Atoms and ions that are adsorbed on a solid electrode phase create structures which can be described, in particular, by equivalent circuits with negative

capacitance elements. Positive values of X_s for K_2SO_4 and H_2SO_4 solutions in the range of low frequencies are evidence of the formation of such structures. At frequencies of more than 5 kHz, the frequency dependence of the reactive component in these solutions is characterized by a minimum. The absolute value of this minimum increases when the amplitude of the polarizing variable voltage decreases. Upon reduction of this amplitude, the frequency of the minimum is displaced toward lower values (Fig.5). Because the length of the electrode part of the immersed platinum wire is directly proportional to the amplitude of the polarizing voltage, the obtained data allow one to estimate the character of the resistivity dependence versus the polarization of the electrode. The increase of the active component of the impedance when the amplitude of the polarizing voltage inside a ferri-ferrocyanide system solution (Fig. 6) decreases can be caused by an activation nature of electrode processes of the system under investigation.

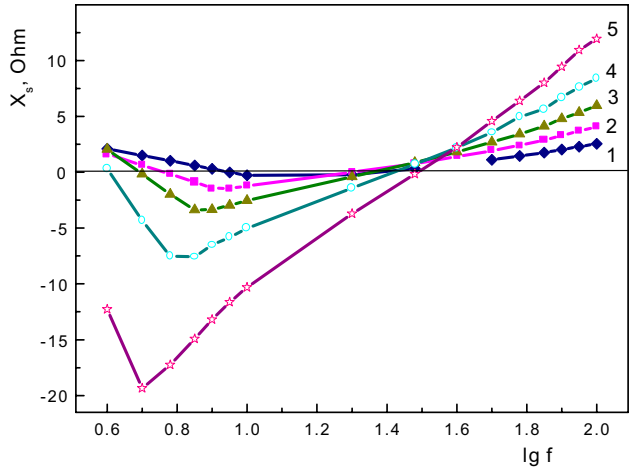

Fig. 5. The frequency dependence of Pt|0.5M H_2SO_4 electrode impedance reactive component at relative length of extended conductor electrode parties equal to 1- 1.0; 2- 0.8; 3- 0.64; 4- 0.52; 5- 0.40.

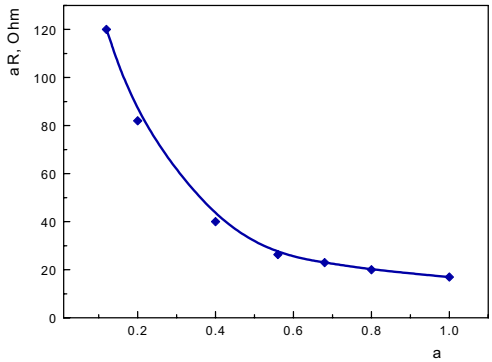

Fig. 6. The dependence of the specific value of Pt | 0.1M $K_3Fe(CN)_6$ /0.1M $K_4Fe(CN)_6$ electrode impedance active component depending on the relative length of the extended conductor electrode.

In summary, we have described in this study a novel approach of impedance spectroscopy which should be useful for expanding the field of electrochemical synthesis. The method needs, of course, some theoretical improvements. For instance, by varying electric potentials, a wide variety of potential distribution laws might be derived, provided that the electrochemical cell is assimilated to serial resistors.

The developments of impedance spectroscopy described in this paper highlight that precise investigations of polarization effects under conditions of monotonously distributed potentials are possible. Further development of experimental and theoretical bases of the method will allow direct studies of discontinuity surface states that are of great fundamental and applied interest.

This work was partly supported by STCU (grant #2276).

REFERENCES

1. A.J. Bard, L.Faulkner. Electrochemical Methods. J. Wiley, New York, 2001.

2. G.K. Budnikov. Modern electrochemical analysis. M.:Mir: Binom LZ, 2003.

3. Z.B. Stoynov, B.M. Grafov, B.S. Savova-Stoinov, V.V. Elkin. Electrochemical impedance. M.: Nauka publ., 1991.

4. J.R. Macdonald. Impedance spectroscopy. Wiley, New York, 1987.

5. A.N. Frumkin. Zero-charge potentials. M.: Nauka, 1979.

THE SCALED QUANTUM-MECHANICAL FORCE FIELD

A Promising Approach to the Molecular Vibrational Dynamics

Victor G. Ivanov
Sofia University, Faculty of Physics
5 James Bourchier Blvd., 1164 Sofia, Bulgaria
vgi@phys.uni-sofia.bg

Sophie Quillard
Institut des Matériaux Jean Rouxel, Laboratoire de Physique Cristalline
2 rue de la Houssinière, BP 32229, 44322 Nantes Cedex 3, France
Sophie.Quillard@cnrs-imn.fr

Abstract We present the physical backgrounds of the Scaled Quantum-Mechanical Force Field (SQMF) approach to the vibrational dynamics of molecules. SQMF is a semi-empirical method, which is based on a preliminary quantum-mechanical calculation of the equilibrium geometry of the molecule together with its normal modes and eigenfrequencies. Subsequently a specific scaling transformation is applied to the as determined molecular force-constants in order to reproduce a set of empirically observed vibrational frequencies. SQMF being based on the realistic electronic structure of the molecule removes many of the ambiguities specific to the purely empirical valence force field approaches. We discuss also the problem of attribution of the experimentally observed frequencies to the calculated normal modes. In this context we propose a new technique, the so-called Maximum Spectral Overlap (MSO), which is especially helpful in the analysis of the Raman and IR spectra of multicomponent samples or molecules with low symmetry. The SQMF technique is illustrated with two sample systems: the B3 polyaniline oligomer and its ionized form $B3^{+\cdot}$.

Keywords: molecular vibrations, force-constants, scaled force field, vibrational spectra

1. Introduction: the Valence Force Field (VFF) model

The assignment of the vibrational bands of molecules is an essential step in the structural characterization of materials. For this purpose a large variety

E. C. Faulques et al. (eds.), Spectroscopy of Emerging Materials, 339–350.

of calculation methods, ranging from purely empirical to *ab initio*, has been developed. It is currently clear that the most successful theoretical approaches are based on preliminary determination of the molecular vibrational modes by means of parameter-free quantum-mechanical methods followed by fine adjustment of the corresponding force constants according to different schemes. This short review is devoted to one of those methods known as Scaled Quantum-mechanical Force Field (SQMF).

The advantages of SQMF however can be understood only in comparison with the purely empirical schemes for normal mode calculations. Despite of their wide diversity VFF is always present as a compulsory element, as far as compounds with well pronounced covalent bonding are considered (isolated molecules, molecular crystals, polymers, etc.). In the context of the SQMF technique VFF is also an important model from a conceptual point of view. For this reason in the Introduction we will consider the main ideas which underlie the VFF model. The SQMF method itself will be considered in the following sections.

In VFF the molecular vibrations are considered in terms of **internal coordinates** q_s ($s = 1..3N-6$, where N is the number of atoms), which describe the deformation of the molecule with respect to its equilibrium geometry. The advantage of using internal coordinates instead of Cartesian displacements is that the translational and rotational motions of the molecule are excluded explicitly from the very beginning of the vibrational analysis. The set of internal coordinates $\mathbf{q} = \{q_s\}$ is related to the set of Cartesian atomic displacements $\mathbf{x} = \{x_i^\alpha\}$ by means of the Wilson's **B**-matrix [1]: $\mathbf{q} = \mathbf{B}\mathbf{x}$. In the harmonic approximation the **B**-matrix depends only on the equilibrium geometry of the molecule.

It is assumed in VFF model that the potential energy of the molecule consists mainly of **spatially localized** contributions, which arise from four basic types of deformations: valence bond stretching Δr, modulation $\Delta\phi$ of the angle between two adjacent valence bonds (bending), relative twist (torsion) $\Delta\tau$ of the two bonds 12 and 34 about the bond 23, and inclination (wagging) $\Delta\theta$ of the bond 12 with respect to the plane defined by the bonds 23 and 24. Thus in a crude approximation the potential energy V is a diagonal quadratic form of the internal coordinates corresponding to the those deformations:

$$2V \approx \sum_r f_{rr}(\Delta r)^2 + \sum_\phi f_{\phi\phi}(\Delta\phi)^2 + \sum_\tau f_{\tau\tau}(\Delta\tau)^2 + \sum_\theta f_{\theta\theta}(\Delta\theta)^2. \quad (1)$$

Physically Eq. (1) implies that the valence electron wave functions are strongly localized within the space between the bonded atoms, and that electrons belonging to spatially separated valence bonds do not interact with each other. In practice this condition is never fulfilled and the deformation of a given bond results in charge-density redistribution over the entire molecule, which is man-

ifested as mechanical strain on the other valence bonds. For example this effect is well pronounced in the π-conjugated systems, where due to the delocalized nature of the π electronic wave functions long range interactions may take place between distant valence bonds. Formally the interaction is accounted for by adding off-diagonal terms to the potential energy (1):

$$2V_{\text{int}} = \sum_{s \neq s'} f_{ss'} q_s q_{s'} \tag{2}$$

for every pair of internal coordinates s and s'.

Provided that the full matrix of force-constants $\mathbf{F} = \{f_{ss'}\}$ is specified, the problem of determination of normal vibrations of the molecule is reduced to the solution of the following secular equation:

$$z_i \mathbf{q}_i = \mathbf{GF}\mathbf{q}_i, \tag{3}$$

where $\mathbf{q}_i$ is the vector of i-th normal vibration in terms of internal coordinates, the frequency parameter $z_i = \omega_i^2$ is the square of the corresponding vibrational frequency ω_i, and $\mathbf{G}$ is the matrix of reciprocal masses in the basis of internal coordinates (also called the matrix of kinematic coefficients) [1].

In practice, however, one has to solve the **inverse vibrational problem** (IVP), i.e. on the basis of known experimental frequencies ω_i^{exp} for a given molecule to extract the values of the force-constants $\{f_{ss'}\}$ and thereby to ascribe specific normal vibration to every observable frequency. This task requires minimization of the functional:

$$R[\mathbf{F}] = \sum_{i=1}^{m} \left(z_i^{\text{cal}} - z_i^{\text{exp}}\right)^2 \tag{4}$$

with respect to the elements of the force-constant matrix $\mathbf{F}$. The frequency parameters z_i^{cal} correspond to the calculated values of frequencies.

At this point it has to be stressed that the minimization of the functional (4) is an ill-posed problem [2]. This is due to the fact that the number of normal frequencies n for a given polyatomic molecule is less than the number of independent adjustable force-constants, which is given by $n(n+1)/2$. The situation is even worse since the number m of vibrations accessible by spectroscopic techniques is smaller than the total number of normal vibrations. It is obvious that additional restrictions have to be applied on the set of force-constants in order to obtain a well defined molecular force field.

It is a common practice to neglect systematically in the VFF model all the off-diagonal interaction terms in $\mathbf{F}$ except those, which correspond to internal coordinates sharing common atom or the interaction terms within the aromatic rings [3]. Additionally some of the force-constants are set equal by symmetry. This effectively reduces the number of adjustable parameters.

Another specific VFF feature is that it relies on the **transferability** of the force-constants from one molecule to chemically and structurally related systems. Thus a set $\{f^{\text{tr}}_{ss'}\}$ optimized for simpler and well studied substances is used as a trial force field for the system under consideration. Due to the ill-conditioned nature of IVP special measures have to be taken in order to keep the adjustable force-constants as close as possible to the initial trial set. One possible approach is to restrict them in a physically meaningful interval of say $\pm 10\%$ around the starting values. Alternatively a penalty function can be added to the minimized functional (4) [4]:

$$M\left[\mathbf{F}\right] = \alpha \sum_{ss'} \left(f_{ss'} - f^{\text{tr}}_{ss'}\right)^2 \tag{5}$$

so that the large deviations of the adjustable parameters with respect to the trial set are payed out by an increase of the minimized functional and are therefore disregarded. The technique of adding penalty functions to the functional (4) is known as **regularization** and is intended to make the IVP a well-defined problem.

Apart from the ill-definitiveness of the inverse vibrational problem two principal objections are usually posed against the standard VFF model [5]. First, the neglect of the long range interactions is not always physically justified and often contradicts with the real electronic structure of the molecule under study. Second, the transferability of force-constants is still a disputable topic, especially when the force-constants are transferred between neutral molecules and the corresponding ionized forms, or between conformational isomers [6, 7].

2. The quantum-mechanical force fields

Nowadays a wide variety of quantum-chemical programs are disposable, which permit to calculate with high accuracy the equilibrium geometry of the molecules and their energy of formation. Theoretical methods have been developed for analytical calculation of the first and second derivatives of energy [8, 9], so that the force-constant matrix $\mathbf{F}^{\text{q-m}}$ and the harmonic frequencies can be extracted from the quantum-mechanical calculations. Since as a rule the molecular orbitals (MO) obtained by the quantum-mechanical methods are spread around the entire molecule, the corresponding quantum-mechanical force fields incorporate the important effects of the off-diagonal interactions.

One modern theoretical approach consists in using the quantum-mechanical force-constants $f^{\text{q-m}}_{ss'}$ as a trial force field in the regularization functional (5), instead of empirical force-constants [2, 10]. It is obvious that the reliability of this method depends crucially on the choice of a realistic quantum-mechanical force field. Unfortunately even the advanced quantum-chemical methods often fail to reproduce the molecular frequencies with sufficient accuracy to assign the experimental spectroscopic features to the corresponding normal vibrations.

The reasons for this discrepancies will be discussed shortly in the following sections. As a rule frequencies calculated on the Hartree-Fock (HF) or density functional theory (DFT) levels are upshifted with respect to the experimental values, and differences sometimes overwhelm 100 cm^{-1} [11–13]. This makes the pristine quantum-mechanical force fields inadequate as a trial approximations in the regularization technique. Consequently some empirical corrections to the quantum-mechanical force-constants are unavoidable when analyzing the normal vibrations of the molecules.

3. Scaling of the quantum-mechanical force fields

The principal idea, which underlies different schemes of empirical corrections to $\mathbf{F}^{\text{q-m}}$ is that even if the quantum mechanical force fields fail to reproduce the experimental vibrational frequencies in absolute scale, they still keep the right information about the **relative** magnitude and sign of the different elements in the force-constant matrix.

One of the simplest approaches is to scale by the same factor all the calculated frequencies in order to obtain the least mean-squared deviation between the experimental and the theoretical frequencies [14]. This procedure is equivalent to homogeneous scaling of all the elements in $\mathbf{F}^{\text{q-m}}$. The advantage of this method is that it uses only one adjustable parameter. However, this is payed out by the necessity of very extensive quantum-mechanical calculations: large atomic basis sets, and appropriate account for the electron correlation effects. If simpler theoretical schemes are used the homogeneous scaling may result in improper assignment of the experimental frequencies.

A more flexible method was proposed by Blom and Altona [15], where the diagonal matrix elements in $\mathbf{F}^{\text{q-m}}$ are scaled by different factors but all the off-diagonal elements with the same factor.

However, the most reliable and widely used is the method developed by Puley [16], which is now referred to as Scaled Quantum Mechanical Force Field (SQMF). In SQMF a scale constant λ_s is ascribed to each internal coordinate q_s such that the corrected (scaled) force-constants $f_{ss'}^{\text{scal}}$ are calculated according to the equation:

$$f_{ss'}^{\text{scal}} = \lambda_s \lambda_{s'} f_{ss'}^{\text{q-m}}. \tag{6}$$

It can be easily seen that the scale factors for the off-diagonal elements are geometric mean of the scale factors for the corresponding diagonal elements. The homogeneous scaling scheme is recovered as a special case when all the λ-factors are set equal. Geometrically this type of scaling is equivalent to elongation or squeezing of the potential energy hypersurface along its principal axes together with its rotation in the configuration space [5]. The scaling parameters are adjusted in a way to obtain the least squared deviation (4) between

the experimental frequencies and the frequencies calculated with the scaled force-constant matrix (6).

A theoretical justification of the scaling procedure was given by Pupyshev *et al* [14]. They compared the force field $\mathbf{F}_{\mathrm{HF}}$ obtained in the Hartree-Fock (HF) limit with the force-field $\mathbf{F}_{\mathrm{CI}}$ obtained in the configuration interaction (CI) technique, where the electron correlation effects are taken into account by mixing the HF ground state function with electronic excitations from the occupied one-electron HF states to the virtual (unoccupied) HF states. It was assumed that the force constants $\mathbf{F^{CI}}$ obtained in the CI approximation simulate the exact harmonic force field while those, extracted from the HF approximation $\mathbf{F^{HF}}$ cast the quantum-mechanical force field $\mathbf{F}^{\mathrm{q-m}}$. It was demonstrated that under conditions listed below:

1 large energy gap between the highest occupied molecular orbital (HOMO) and the lowest unoccupied molecular orbital (LUMO);

2 relatively localized wavefunctions of the one-electron occupied states;

3 singlet stability of the HF ground state

the "exact" harmonic force field is related to the HF-level force field by a homogeneous scaling relation:

$$\mathbf{F^{CI}} = C\mathbf{F^{HF}}. \tag{7}$$

Therefore the scaling transformation of the quantum-mechanical force field is an empirical way to account for the electronic correlation effects. As far as the conditions listed above are not always satisfied (e.g. in the presence of delocalized π-electron wavefunctions) the real transformation is not exactly homogeneous but rather of Puley's type, involving n different scale constants. The need of inhomogeneous Puley's scaling also arises due to the fact that the quantum-mechanical calculations are never performed in the perfect Hartree-Fock level. The realistic calculations employ incomplete basis sets and often are based on different calculation schemes, e.g. semiempirical hamiltonians or methods which account for the electronic correlations like CI and density-functional techniques. In this context we want to stress that the set of scale factors for the molecule under consideration is specific for a **given set of internal coordinates** and a **given quantum-mechanical method**.

As a rule the quantum-mechanical force-fields and the corresponding normal frequencies are calculated in a harmonic approximation, while the experimentally accessible frequencies are influenced by anharmonic contributions. The Puley's scaling factors are also found to incorporate the relevant empirical corrections for the vibrational anharmonicity.

4. Determination of the scaling factors

Normally the scaling factors are extracted by minimizing the squared deviation (4) considered as a functional $R(\lambda)$ of the variable set $\{\lambda_s\}$. The frequency parameters z_i^{calc} now correspond to the harmonic normal frequencies calculated with the scaled quantum-mechanical force-field (6). The first and second derivatives of $R(\lambda)$ with respect to the scaling factors can be calculated analytically [17, 18], which permits to implement rapidly converging minimization procedures of the Newton-Gauss type. Alternative iterative minimization methods were also proposed [19].

Minimization of the squared deviation $R(\lambda)$ is based on a premeditated assignment of the experimental frequencies ω_i^{exp} to the calculated normal vibrations. This assignment can be reliably performed in the case of pure substances with high molecular symmetry, or if isotopic substitution experiments are available. Unfortunately often the vibrational spectrum of the compound under study is superimposed on the spectrum of a solvent or the fundamental vibrations of the molecule overlap with bands, which stem from the vibrational overtones. In a recent work [13] a new mathematical technique, which we will call Maximum Spectral Overlap (MSO) was proposed, which avoids the necessity of the preliminary attribution of the experimental lines to normal vibrations. In the MSO method a square-normalized Gaussian function $G(\omega - \omega_i)$ is ascribed to each experimentally observed or theoretically calculated frequency ω_i. The width of the Gaussian is usually taken between 10 and 20 cm^{-1}. Thus the experimental and calculated vibrational spectra are represented by a superpositions of the corresponding Gaussian functions:

$$y^{\mathrm{exp(calc)}}(\omega) = \sum_i G(\omega - \omega_i^{\mathrm{exp(calc)}}). \tag{8}$$

The spectral overlap :

$$S = \int_{-\infty}^{+\infty} y^{\mathrm{exp}}(\omega) y^{\mathrm{calc}}(\omega) d\omega, \tag{9}$$

is a convenient measure for the number of experimental frequencies that coincide with some calculated ones. Indeed the integral of any two Gaussians, one experimental and one calculated, that overlap completely, is equal to one due to their normalization. The scale factors are varied until the overlap S is maximized, i.e. the best correspondence between the calculated frequencies and a group of experimental values is achieved.

5. Transferability of the scaling factors

The wide applicability and predictive power of the SQMF method is based on the fact that the scale factors obtained on a simpler and well studied compound

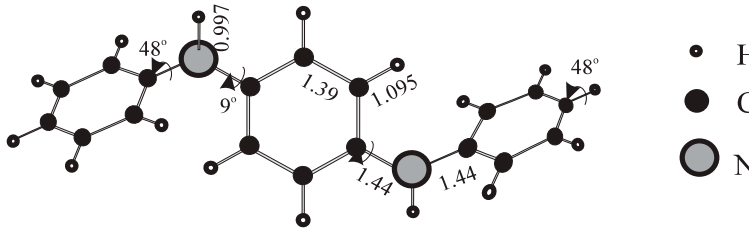

Figure 1. Optimized structure of the isolated B3 molecule. The interatomic distances are in Å; the tilt angles are in degrees.

can be transferred with minor changes to chemically and structurally related compounds. It has to be stressed however that the transferability is granted under the following conditions:

1 The quantum-mechanical force fields of the two different molecules are obtained by means of the same method (the same level of theoretical approximation and the same basis set of one-electron wavefunctions).

2 The same set of internal coordinates is used for the similar structural units in the molecules under consideration.

For example the SQMF was found very efficient in predicting the vibrational spectra of rotational isomers (e. g. cis and trans) of several molecules, provided the scale factors for the ground-state isomer are known [6, 7, 20–22]. The transferability of the scale factors has been proven also for a large variety of molecules containing equivalent structural units like piridizine and dichloropyridazine [23], different polyenes and the corresponding oligoenes [24], naphthalene and anthracene [25] as well as many other systems.

The transferability of the scale factors is based on the fact that a given quantum-mechanical method produces **almost equivalent relative errors** of the quantum-mechanical force constants for a series of related molecules, and hence equivalent scale factors [5].

6. Example: vibrations of the B3 molecule

B3 is a short notation for N,N'-diphenyl-1,4-phenylenediamine, which is known also as "phenyl-end-capped-dimer" of the polyaniline chain [26]. B3 consists of three phenyl (benzene-like) rings connected by C-N links as shown in Fig. 1. The interest in this molecule was stimulated by its luminescence properties [27] as well as by the potential applications in the field-effect transistors [28].

The vibrational spectra of different polyaniline oligomers, including B3, have been studied earlier by means of Raman and infrared spectroscopy, and

modelled in terms of VFF [3, 29]. The aim of our present work was to verify the mode assignment in B3 in the frame of the SQMF approach, and to use the extracted scale factors in order to characterize the vibrational spectrum of the oxidized form $B3^{+\cdot}$.

As a first step we determined the equilibrium geometry of the neutral B3 molecule by means of the semiempirical PM3 method, implemented in the MOPAC7 package. In full agreement with the experiment we found that the ground state of the molecule is of C_i symmetry and that all the C-N-C bridges lie in the same plane. The optimized interatomic distances are noted in Fig. 1. The outer phenyl rings are tilted in a same direction with respect to the C-N-C plane at an angle of $\approx 48°$. The central ring is tilted in the opposite direction at $\approx 9°$. The dihedral angle between the central ring and the outer rings was found to be around 57°, a value which is also very close to the experimental one.

In the same PM3 approximation the harmonic frequencies of the molecule were calculated and the quantum-mechanical force-field was extracted. Fig. 2(c) shows infrared (IR) absorption spectrum of an orthorhombic B3 crystal while Fig. 2(d) represents Raman spectrum taken on B3 solution in dimethylformamide. Shown in Fig. 2(a) is the set of harmonic frequencies, calculated with the unscaled force constants. Calculated frequencies are represented in terms of overlapping Gaussians. The more intense bands correspond to superimposed, nearly degenerated pairs of IR and Raman modes. It can be seen that the correspondence between the sets of calculated and experimental frequencies is not satisfactory. The largest discrepancy is met for the totally symmetric breathing mode of the internal phenyl ring, which is detected experimentally at 993 cm^{-1} while the unscaled frequency is calculated at 1228 cm^{-1}. Largely overestimated are also the carbon E_{2g} (in terms of D_{6h} symmetry of the phenyl rings) vibrational modes. Their unscaled frequencies overwhelm 1700 cm^{-1}, while the experimental values lie between 1580 and 1620 cm^{-1}.

Due to these large deviations the direct application of the SQMF method to the B3 molecule may lead to incorrect assignment of the vibrational modes. Therefore we performed a preliminary SQMF calculation on the benzene molecule, where the normal modes are well ascribed [1] and discriminated by symmetry. The extracted scale factors correspond to the set of symmetry-adapted internal coordinates, as introduced by Wilson [1]. The same scale factors were then applied to the B3 molecule, which was considered as a system constructed by three benzene molecules. The single C-N bonds in B3 were treated with the same scale factors as the single C-H bonds in the benzene molecule. The scale factors corresponding to the N-H bonds were initially set equal to 1. The as-obtained scaled force-field, after minor adjustment of the scaling factors, was employed to calculate the normal frequencies of B3. Fig. 2(b) shows the corresponding pattern of the calculated scaled frequencies. It can be seen that there

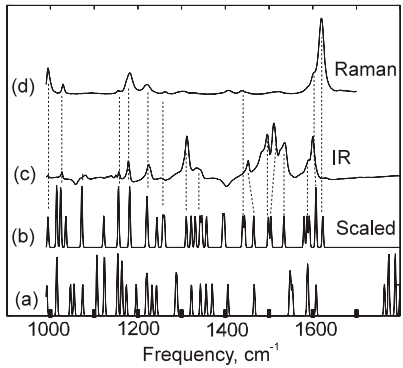

Figure 2. Normal mode frequencies for the neutral B3 molecule: calculated unscaled (a), calculated scaled (b), IR absorption (c), and Raman (d).

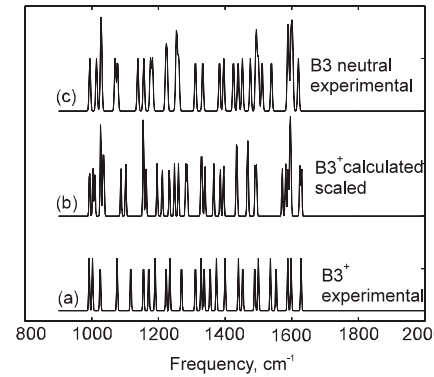

Figure 3. Frequency patterns for the free $B3^{+\cdot}$ radical: experimental (a), calculated scaled (b). The neutral B3 spectrum is given for comparison (c).

is a fairly good correspondence between the main bands in the IR and Raman spectra, and the set of scaled frequencies.

Next we calculated the equilibrium geometry of the oxidized $B3^{+\cdot}$ form and its unscaled vibrational modes by making use of the same quantum-chemical method, the restricted Hartree-Fock in a PM3 approximation. Some important structural changes were observed in the radical compared to the neutral molecule. First, the tilt angles of the carbon rings are reduced to 37° for the external rings and to 2° for the central ring. Second, the nitrogen links to the central ring are shortened from 1.44 Åto 1.37 Å, which can be attributed to the formation of double N=C bonds. Finally, the bond lengths in the central ring are modulated in a quinoid manner, characteristic for the deprotonated pernigraniline base of the polyaniline chain [26].

Obviously, these structural changes make the transfer of force-constants from the neutral B3 molecule to the $B3^{+\cdot}$ radical inadequate. Instead, we tentatively transferred the scale factors optimized for the neutral molecule to the quantum-mechanical force-field of $B3^{+\cdot}$ and calculated the corresponding scaled normal frequencies. We obtained a clear correspondence between many of the frequencies experimentally observed in Cl doped B3 crystals (Fig. 3(a)) and the calculated scaled frequencies (Fig. 3(b)). We also observed that some of the calculated scaled frequencies in the neutral B3 molecule are present in the spectra of the Cl doped crystals (Fig. 3(c)). This fact tells us that there is some portion of unoxidized B3 molecules in the sample and gives additional proof for the validity of the SQMF calculations performed on the neutral B3 molecule.

The results presented above once again demonstrate the transferability of the scale factors between molecules containing similar structural elements (benzene and B3) as well as between different states of oxidation of a given molecule (neutral B3 and the $B3^{+\cdot}$ radical). The detailed results of the SQMF analysis (normal mode assignment and the scaled factors) will be published elsewhere.

7. Summary and conclusions

In summary, the SQMF technique proposes several important advantages over the traditional empirical approaches to the vibrational dynamics. The relative magnitudes and signs of all the elements in the force-constant matrix are calculated by means of realistic quantum-mechanical calculations. The Puley's scaling scheme is based on a small number of adjustable parameters and therefore the inverse vibrational problem is well defined, contrary to the VFF model, where additional conditions on the adjustable force constants have to be imposed. The scale factors are transferable in a much wider classes of molecules than the force constants themselves. This makes SQMF a powerful predicting tool for the vibrational assignment of novel materials.

8. Acknowledgments

The authors would like to thank Dr. Eric Faulques from the Institut des matériaux Jean Rouxel in Nantes for the useful discussions.

This work was partially supported by NATO (Grant No PST.CLG.979685).

References

[1] Bright E. Wilson, Jr., J. C. Decius and Paul C. Cross, *Molecular Vibrations: The Theory of Infrared and Raman Vibrational Spectra.* New York: Dover Publications Inc., (1955).

[2] I.V. Kochikov, G.M. Karamushina, Yu.A. Pentin, and A.G. Yagola, *Inverse Problems in Vibrational Spectroscopy*. Zeist: VSP, (1999).

[3] This is just an arbitrary example of a typical VFF analysis of the different forms of polyaniline: S. Quillard, G. Louarn, S. Lefrant, and A.G. MacDiarmid, Phys. Rev. B. **50** (17): 12 496, (1994).

[4] T.-K. Ha, R. Meyer, and Hs.H. Günhard, Chem. Phys. Lett. **59**: 17, (1978).

[5] Yu. N. Panchenko, J. Mol. Struct. **567-568** : 217-230, 2001.

[6] G. R. DeMaré, Yu. N. Panchenko, and Ch. W. Bock, J. Phys. Chem. **98**: 1416, (1994).

[7] G. R. DeMaré and Yu. N. Panchenko, J. Phys. Chem. **98**: 8315, (1994).

[8] P. Puley, Mol. Phys. **17**: 197, (1969).

[9] P. Puley, J. Chem. Phys. **78(8)**: 5043, (1983).

[10] I. V. Kochikov, Y. I. Tarasov, G. M. Karamushina, V.P. Spiridonov, A.G. Yagola, and T.G. Strand, J. Mol. Struct. **445**: 243, 1998.

[11] A. Bérces and T. Ziegler, J. Chem. Phys. **98**: 4793, (1993).

[12] J. Florián and B. G. Johnson, J. Phys. Chem. **98**: 3681, (1994).

[13] F. Ragot, V. Ivanov, J. Wéry, A. Garcia, D.L. Perry, G. Ouvrard, and E. Faulques, Synth. Met. **120**: 773, (2001).

[14] V. I. Pupyshev, Yu. N. Panchenko, Ch. W. Bock, and G. Pongor, J. Chem. Phys. **94**: 1247, (1991).

[15] C. E. Blom and C. Altona. Mol. Phys. **31**: 1377, (1976).

[16] P. Puley, G. Fogarasi, G. Pongor, J. E. Boggs, and A. Vargha, J. Am. Chem. Soc. **105**: 7037, (1983).

[17] W.D. Allen, A.G. Császár, and D.A. Horner, J. Am. Chem. Soc. **114**: 6834, (1992).

[18] T. Sundius, Vibrational Spectroscopy **29**: 89, (2002).

[19] J.F. Arenas, S.P. Canteno, J.I. Marcos, J.C. Otero, and J.Soto, J. Chem. Phys. **113**: 8472, (2000).

[20] Ch.W. Bock and Yu.N. Panchenko, J. Mol. Struct. **221**: 159, (1990).

[21] Ch.W. Bock, Yu.N. Panchenko, and S.V. Krasnoshchikov, Chem. Phys. **147**: 65, (1990).

[22] Y. Hase, Spectrochimica Acta A, **51A(14)**: 2561, (1995).

[23] J. Vázquez, J.L. González, F. Márquez, E.M. Torres, and J.E. Boggs, J. Phys. Chem. A **105**: 9354, (2001).

[24] S. Hirata, H. Torii, and M. Tasumi, Bull. Chem. Soc. Jpn. **69**: 3089, 1996.

[25] D. Chakraborty, R. Ambashta, and S. Manogaran, J. Phys. Chem. **100(33)**: 13963, (1996).

[26] A.G. MacDiarmid, Y. Zhou, and J. Feng, Synth. Met. **100**: 287, (1999).

[27] E. Faulques, *et.al.*, to be published.

[28] S. Quillard, B. Corraze, M. Poncet, J.Y. Mevellec, J.P. Buisson, M. Evain, W. Wang, and A.G. MacDiarmid, Synth. Met. **137**: 921, (2003).

[29] J.-Y. Mevellec, S. Quillard, M.I. Boyer, and J.-P. Buisson, J. Raman Spectrosc. **32**: 710, (2001).

Vibration-Induced Excited State Decay

Miroslav Menšík, Stanislav Nešpůrek
Institute of Macromolecular Chemistry, Academy of Sciences of the Czech Republic, Heyrovský Sq. 2, 162 06 Prague 6, Czech Republic, e-mail:mensik@imc.cas.cz

Abstract: Time evolution of excited state population was studied theoretically for the system of two electronic levels coupled to two vibrational modes, which are also attached to a heat bath. In the excited state, the mutual coupling of the vibrational modes was included. It was demonstrated that excited state population relaxes faster if interacting vibrational mode dissipates its energy via vibrational mode of a smaller eigenfrequency. It was also demonstrated that fast component of excited state depopulation cannot be achieved via coherent mode-mode coupling, if the second mode is not directly coupled to the electronic inter-state transition.

Key words: excited state relaxation, electron-vibrational interaction, vibrational coherence

1. INTRODUCTION

The development of femtosecond spectroscopy made it possible to study the time dynamics of excited states in great details with time resolution sufficiently better than characteristic times of vibrational periods. It enabled to investigate the vibrational structure of breathing electronic distribution. Originally, the vibrational coherence could be observed on diatomic molecules in the gas phase, with only one vibrational frequency included [1,2]. Later, the coherent oscillations were observed in polyatomic molecules [3-12]. In 90´s, the complicated coherent motions with different frequencies were observed in complex biological systems, in proteins. In the Ref. 13, the authors demonstrated the vibrational coherence in various electron donor-acceptor (EDA) complexes formed by relatively large organic molecules in the liquid phase. Even though such complexes have many inter- and intramolecular vibrational modes, the oscillations with only one frequency were dominantly observed. The fluorescence data were fitted by the function $f(t)$ convoluted with the instrument response function obtained from the time-resolved Raman scattering signal.

E. C. Faulques et al. (eds.), Spectroscopy of Emerging Materials, 351–362.

$$f(t) = A_1 \exp(-t/\tau_1) + A_2 \exp(-t/\tau_2) + A_3 \cos(\omega t + \phi) \exp(-t/\tau_{\text{damp}}) \quad (1)$$

In Eq. (1), ω is the eigenfrequency and τ_{damp} is the life-time of the coherent oscillation. The frequency ω was determined to correspond to the out-of-plane vibrational mode of the acceptors, having b_{3u} symmetry. The first exponential in Eq. 1 corresponds to a fast decay component and it was argued in Ref. (13), that it represents the intramolecular vibrational energy redistribution in a subpicosecond regime (about 100 fs). The second component was one order of magnitude slower. Very similar behaviour of the excited state decay consisting of two decay components can be found, e.g., in the work of Wolfseder and Domcke [14]. The authors studied relaxation in the system of two diabatic electronic states coupled with three independent harmonic oscillators. They assumed: a) the inter-state coupling to be independent of vibrational modes (Franck-Condon approximation) b) non-zero Stokes shift of vibrational modes in the excited state c) different eigenfrequencies of respective vibrational modes d) either coherent (non-dissipative) or dissipative regime due to the coupling of vibrational modes to a heat bath. For the case of coherent system the fast transition for very short time was found, while for longer times, oscillations around a constant value were found. The fact that the amplitude of these oscillations are smaller than the initial fast decay can be associated to the fact that, after a short time, the destructive interference, resulting from different eigenfrequencies and values of the Stokes shift, blocks the back transfer of the population probability to the values close to unity. On the other hand, for the dissipative system, the fast transition was the same as in the coherent case but for longer times the oscillations were damped and probability curves decayed to the ground state (temperatute T was set to zero). Physical interpretation of this behaviour is as follows: First, the electronic excited energy is redistributed to vibrational modes in a fast coherent process. Second, the excess vibrational energy is dissipated to the heat bath formed by other modes (particularly those of lower eigenfrequencies) and ambient molecules. Another very important conclusion of the authors of Ref. 14 was that models with a single-vibrational mode approximations cannot provide results containing various components, particularly, that of fast energy redistribution. Concerning the vibrational structure manifold theoretical simulations of excited state population probability were published in the literature. To the knowledge of authors, practically without exceptions, the assumption of vibration-independent inter-state coupling is assumed, e.g. [14-17]. It was found recently [18] that considering general dependence of inter-state coupling $W(Q)$ on the set of vibrational displacement Q a very rich structure of coherent oscillation is found. The authors of Ref. 18 checked the model of two electronic levels coupled to a single-vibrational mode. For the case of

constant coupling $W(Q)$ = const they found that the almost exponential decay was superimposed with oscillations with frequency corresponding to the difference between excited and ground states. The amplitude of the oscillations was slightly modulated with the frequency ω of vibrational motion. The situation completely changed for the linear (quadratic) coupling $W(Q) \sim Q$ (Q^2). The modulation became so strong that it was even overwhelming fast oscillations. The theoretical simulations gave vibration-dependent characteristics completely similar to that of experimental measurement of Yoshihara and Rubtsov [13]. It was also proved that the vibration-dependent modulation increases with increasing value of the Stokes shift in complete agreement with considerations of the authors of Ref. 13. In the Ref. 19 it was shown that the proportionality constant Δ in the relation

$$W(Q) = \Delta Q \tag{2}$$

is proportional to the derivative of the excited adiabatic state with respect to the vibrational coordinate Q, i.e., to the Herzberg-Teller correction. In Ref. 18 it was also shown that the vibrational modulation strongly increased with the constant Δ (Hezberg-Teller correction), while the electronic states $\varphi_m(r)$ were defined in the folowing way [19]

$$\varphi_m(r) = \psi_m^{\text{adiab}}(r, Q = 0) \tag{3}$$

The wave functions on the right side are adiabatic states for fixed vibrational coordinate $Q = 0$ corresponding to the minimum position of the ground state potential energy surface. The electronic distributions on the left side are static, so measuring the population of these states provide us a suitable information about the breathing of the excited state. For $Q = 0$ they correspond to the adiabatic states (so they are orthogonal) and they are suitable for studying the process of vertical excitation. As a result of that the decay curves of the occupation probability $p(t)$ of the static excited state $\varphi_1(r)$ correspond (to a good approximation) to the decay curves of the occupation probability of excited adiabatic state (energy dissipation). The coherent structure in these occupation probabilities $p(t)$ reflects, on the other hand, contrary to adiabatic states, the breathing of electronic distribution. It should be visible in the optical spectroscopy measurement through a dependence of dipole moments on breathing electronic states. An illustrative example of such a dependence for the linear case is shown in Fig.1. Charac-

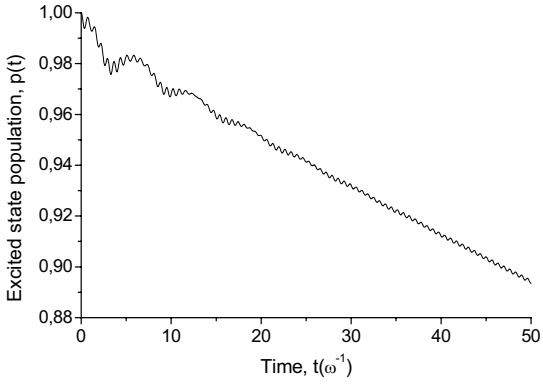

Figure 1. Excited state populations for the linear case of the inter-state coupling in the single-mode model

teristics of the coherent structure with respect to the parameters of the model were analysed in great details in Ref.18 and they were compared with coherent oscillations in a simple dimer model. Relations determined numerically for the constant, linear and quadratic cases were in surprisingly high agreement with analytical expressions for the dimer model. The amplitude of vibration-induced oscillations were, e.g., proportional to Δ^2. Next very important feature was the fact that results for the linear and quadratic cases were very similar indicating that, in general, higher order terms in the Herzberg-Teller approximation cannot be neglected. The life-time of the vibration-induced oscillation modulation was the same as the life-time of vibrational states given by the relaxation tensor.

2. THEORY

In this paragraph we will outline a general theory of non-radiative energy transfer with special interest to the vertical processes. First of all we define adiabatic levels for the total number of vibrational modes $\{\lambda\}$. For the ground state minimum we define point $\{\lambda\} = \{0\}$ and we define the static "vertical" electronic basis through the relation

$$\varphi_m(r) = \psi_m^{\text{adiab}}(r, \{\lambda\} = 0). \tag{4}$$

After projection of the total Hamiltonian to the ground static state we perform the expansion of Hamiltonian in the vibrational displacements and diagonalization of the quadratic form. This procedure defines the set of normal vibrational modes $\{\lambda\}$. Next, the total Hamiltonian will be projected to the first excited static state. The quadratic vibrational form will have, in general, both diagonal as well as off-diagonal terms. Modes, giving in diagonal terms higher values of the Stokes shift (in combination with linear terms) and those contributing significantly to the Herzberg-Teller correction,

will be called relevant and denoted $\{Q\}$. Other modes will form a heat bath and will be denoted $\{Z\}$. The total Hamiltonian H can be written as

$$H = \sum_m |m\rangle\langle m|(H_m^{\mathrm{S}}(Q,\partial Q) + H_m^{\mathrm{B}}(Z,\partial Z) + H_m^{\text{S-B}}(Q,Z)) +$$

$$+ \sum_{m,n}(1-\delta_{mn})|m\rangle\langle n|V_{mn}(Q,Z) \tag{5}$$

Here H^{S} is the Hamiltonian of the relevant system S, H^{B} is that of the heat bath B, while $H^{\text{S-B}}$ denotes the system-bath coupling. Subscribe m describes the projection onto $\varphi_m(r)$ states. The inter-state coupling $V_{mn}(Q,Z)$ can be written as

$$V_{mn}(Q,Z) = \sum_k \Delta_{mn}^{1k} Q^k + \sum_l \Delta_{mn}^{2l} Z^l + \text{higher order terms} \tag{6}$$

It is worth mentioning that constant term disappears in Eq. (6) because of the suitable choice of the basis in the form (4). In the following, the evolution of the density matrix of the relevant system will be examined by means of the standard projection technique. The matrix elements $\rho_{\alpha\beta}(t)$ of the reduced density matrix operator are defined as follows

$$\rho_{\alpha\beta}(t) \equiv \mathrm{Tr}_{\mathrm{bath}}\langle\alpha|S_a^+\rho(t)S_b|\beta\rangle \tag{7}$$

where $\alpha \equiv a,A$ numerates electronic, respectively vibrational levels and unitary operator S_a are defined through the relation

$$H_a^{\mathrm{B}}(Z,\partial Z) = S_a H_{\mathrm{g}}^{\mathrm{B}}(Z,\partial Z)S_a^+ \tag{8}$$

with Hamiltonian $H_{\mathrm{g}}^{\mathrm{B}}$ defined as the projection of H^{B} onto ground static state. Unitary transformations S_a thus describe a transformation of vibrational modes of the bath for general electronic potential energy surface a. They contain, in general, the Stokes shift and change of eigenfrequencies as well. In the quantum master equation we use the standard Nakajima - Zwanzig equation, perform the Markovian approximation in the interaction picture and hold terms up to the second order in the perturbation parameter γ. We assume that $H_m^{\text{S-B}}$, V_{mn}, S_m- $1 \sim \gamma$. The projector P will be choosen in the form

$$PA = \sum_{\mu,\nu} S_m \left|\mu\right\rangle \rho^{\mathrm{BOL}} \left\langle \nu\right| S_n \mathrm{Tr}_{\mathrm{Bath}} \left\langle \mu\right| S_m^{+} A S_n \left|\nu\right\rangle \tag{9}$$

where ρ^{BOL} describes the Boltzmann distribution of the vibrational modes in the ground state. After a lengthy algebra and above mentioned approximation we get the quantum master equation

$$\frac{\partial}{\partial t}\rho_{\alpha\beta}(t) \approx -\frac{i}{\hbar}\left\langle \alpha\right| H^{\mathrm{Ren}}\rho - \rho H^{\mathrm{Ren}}\left|\beta\right\rangle - \sum_{\gamma,\delta} D^{\mathrm{Dis}}_{\alpha\beta\gamma\delta}(t)\rho_{\gamma\delta}(t) \tag{10}$$

The tensor $D_{\alpha\beta\gamma\delta}{}^{\mathrm{Dis}}(t)$ contains, in general, both the real and imaginary parts. For long times it approaches to a constant value under implicit assumption of internal relaxation processes in the bath. The change of relaxed equilibrium positions of vibrational modes for the electronic excited states in the bath are given by the unitary operator S_m, which appears in the definition of the projector P. In this way, the decay of the memory in the master equation cannot be separated from the choice of the projector. The real part of $D_{\alpha\beta\gamma\delta}{}^{\mathrm{Dis}}(t)$ describes the dissipation process, while the imaginary part contributes to general eigenenergy renormalization of the second order, leading to the deviation from the Boltzmann distribution [20, 21]. The renormalized Hamiltonian H^{ren} can be written in the form

$$H^{\mathrm{Ren}}(Q,\partial Q) = H^{\mathrm{S}}(Q,\partial Q) + \sum_{m,n}\Delta^{1k(\mathrm{Ren})}_{mn}(1-\delta_{mn})\left|m\right\rangle\left\langle n\right|Q^{k} +$$

$$+ \sum_{m,n} V^{\mathrm{Con}}_{mn}(1-\delta_{mn})\left|m\right\rangle\left\langle n\right| \tag{11}$$

with

$$\Delta^{1k(\mathrm{Ren})}_{mn} = \Delta^{1k}_{mn}\mathrm{Tr}_{\mathrm{Bath}}\{S_m^{+}S_n\rho^{\mathrm{Bol}}_{\mathrm{Bath}}\} \tag{12}$$

$$V^{\mathrm{Con}}_{mn} \approx -\sum_{l}\Delta^{2l}_{mn}\frac{(D^{l}_{m}+D^{l}_{n})}{2} \tag{13}$$

The renormalized contributions come from the influence of bath. The terms $D_m{}^l$ represents the shift of the l-th mode in the bath for the m-th electronic level. The master equation (10), as it stands, holds true after relaxation process in the bath appears, so the contribution from the bath corresponds to relaxed bath states. It is worth mentioning that although the constant term disappears in the interaction term (6) for the vertical transition, it is

introduced as an effective "field" from the bath. This "field" is formed by the product of the Herzberg-Teller correction (~ Δ) and shift of the vibrational positions of bath modes (contributing to the Stokes shift). For short time the master equation is an approximation so these renormalized terms are also the approximation. They should be understood as an effective mean values around which exact terms are oscillating until they relax to the equilibrium values.

3. NUMERICAL SIMULATIONS OF TWO COUPLED MODES

In the present simulation we apply a simple model consisting of two vibrational modes in the relevant system. The first one will contribute to the Stokes shift as well as to the Herzberg-Teller correction, while the second one only to the Stokes shift. Next, we will assume a mutual coupling of the modes in the bilinear form ~ Q_1Q_2 for the excited state. This type of coupling is usually omitted in literature. The Hamiltonian H^S is written as

$$H^S = \omega_1[|1\rangle\langle 1|(2\varepsilon + \frac{Q_1^2}{2} + \frac{P_1^2}{2} + D_1Q_1 + f\{\frac{Q_2^2}{2} + \frac{P_2^2}{2} + D_2Q_2\} + TQ_1Q_2) +$$

$$+ |2\rangle\langle 2|(\frac{Q_1^2}{2} + \frac{P_1^2}{2} + f\{\frac{Q_2^2}{2} + \frac{P_2^2}{2}\}) + \{|1\rangle\langle 2| + |2\rangle\langle 1|\}\Delta_1Q_1] \qquad (14)$$

In Eq. (14), $2\hbar\omega_1\varepsilon$ is the vertical excitation energy, ω_1 ($f\omega_2$) is the eigenfrequency of the first (second) mode. D_i is the shift of the vibrational position of the i-th mode for the excited state. Δ_1 is the inter-state coupling constant of the first mode and T is the coupling constant of the modes in the excited state. Other parameters denote harmonic oscillator potentials. Both of the modes are also attached to a heat bath. This process is modelled by the so called diabatic damping method [16], the rate of vibrational relaxation was chosen $k_1 = 0.1\omega_1$($k_2 = 0.1\omega_1/f$) for the first (second) mode. We performed the numerical simulation in the short-time interval $t \in (0, \pi/\omega)$. We change the following parameters: $T = 0.1, 0.2$, $D_2 = 0, 0.3$, $f = 1, 0.7, 0.4, 0.1$ Other parameters were fixed: $2\hbar\omega_1\varepsilon = 2.5$ eV, $\hbar\omega_1 = 0.25$ eV, thermal energy $K_BT_B = 0.025$ eV, $D_1 = 1$, $\Delta_1 = 1$. The vibrational cut-off was $N = 8$. The results of the excited state populations for different values of the ratio of eigenfrequencies f are shown in Fig. 2-5. It is apparent that excited state population deviates more from other cases when the value $f = 0.1$, i.e., the eigenfrequency of the second mode is at least one order of

magnitude lower. The deviation increases with increasing time *t*. In Fig. 6 the influence of mode-mode coupling is demonstrated for the case of the ratio $f = 0.1$ and non-zero shift of the second vibrational mode $D_2 = 0.3$. For

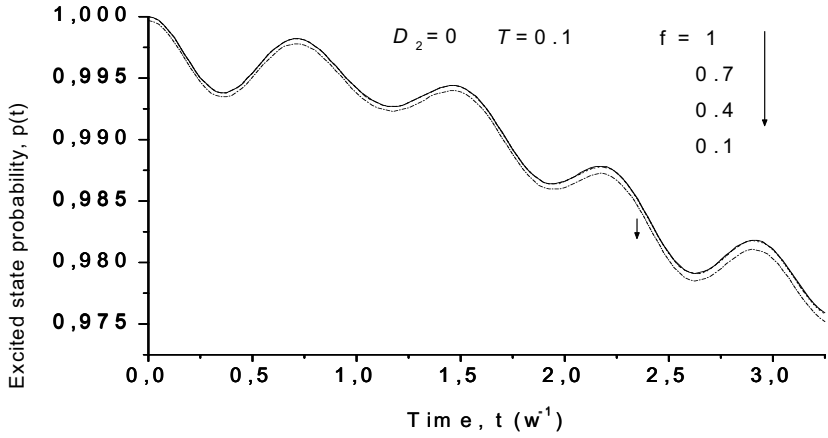

Figure 2. Excited state probability for different ratio of eigenfrequencies *f*. For $f = 1$, 0.7, 0.4 (solid, dashed and dotted curves) almost equivalent results are obtained. For $f = 0.1$ (dash-dotted curve) population deviates more.

stronger values of the mode-mode coupling *T* the relaxation process is faster. The delayed influence of the second mode is apparent. In Fig.7 it is shown that the Stokes shift of the second mode also causes faster relaxation but the influence is delayed again.

4. SUMMARY

We studied the system of two electronic levels coupled to two mutually interacting vibrational modes. The first mode contributed to the Stokes shift and Herzberg-Teller correction (inter-state coupling), while the second mode only to the Stokes shift. In this sense the influence of the second mode to the electronic state transition is indirect. We proved that the second mode increases the excited state decay for increasing value of the Stokes shift,

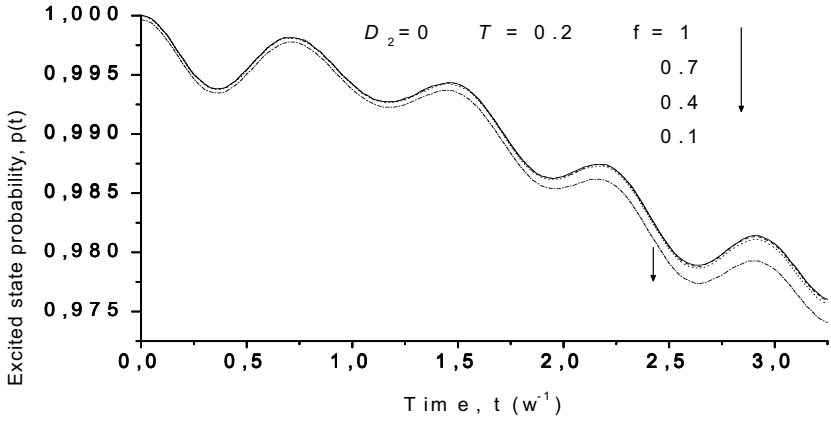

Figure 3. Excited state probability for different ratio of eigenfrequencies *f*. For $f = 1, 0.7, 0.4$ (solid, dashed and dotted curves) almost equivalent results are obtained. For $f = 0.1$ (dash-dotted curve) population deviates more. For the mode coupling $T = 0.2$ the effect is stronger.

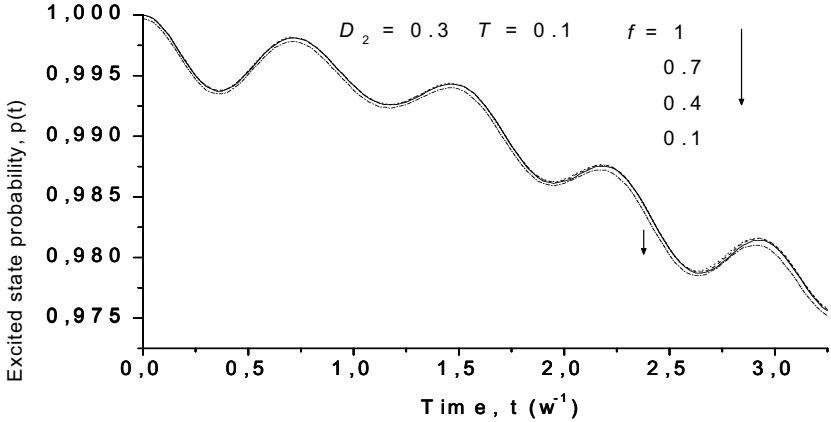

Figure 4. Excited state probability for different ratio of eigenfrequencies *f*. For $f = 1, 0.7, 0.4$ (solid, dashed, dotted curves) almost equivalent results are obtained. For $f = 0.1$ (dash-dotted curve) population deviates more. For the shift $D_2 = 0.3$ of the second mode the effect is slightly pronounced even for higher values of *f*.

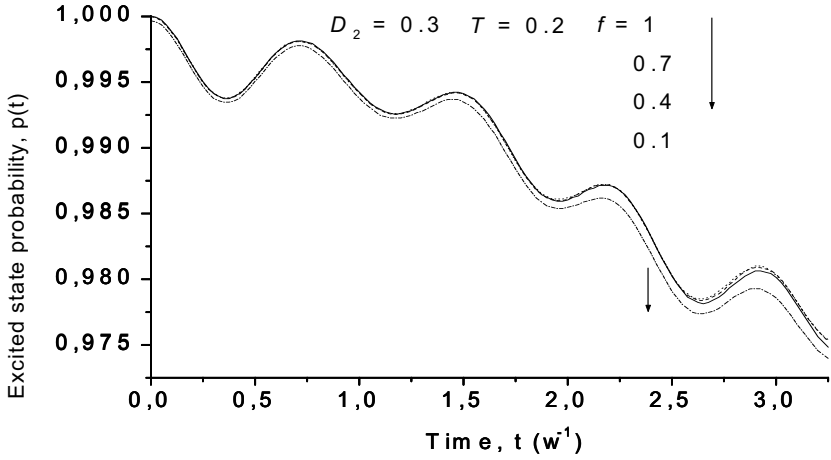

Figure 5. Excited state probability for different ratio of eigenfrequencies *f*. For $f = 1$, 0.7, 0.4 (solid, dashed and dotted curves) almost equivalent results are obtained. For $f = 0.1$ (dash-dotted curve) population deviates more. For the shift $D_2 = 0.3$ of the second mode and mode-mode coupling $T = 0.2$ the effect is slightly pronounced even for higher values of *f*.

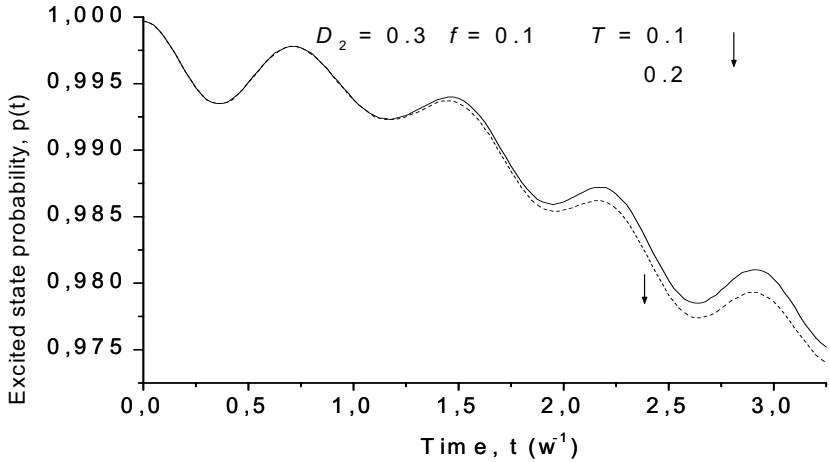

Figure 6. Excited state probability for different values of mode-mode coupling $T = 0.1$, 0.2 (solid and dashed curves). The increasing value of the coupling increases the excited state decay but with delayed influence. The shift of the position of the second mode $D_2 = 0.3$. The eigenfrequency ratio $f = 0.1$.

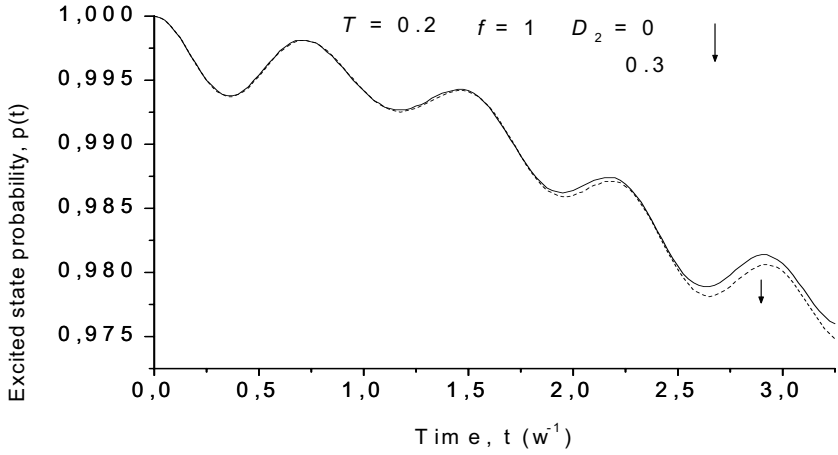

Figure 7. Excited state probability for different values of the position shift of the second mode D_2 = 0, 0.3 (solid and dashed curves). The eigenfrequency ratio f = 1 and mode-mode coupling T = 0.2.

mode-mode coupling and for eigenfrequency lower by the order of magnitude than that of the first mode. In all investigated cases the coherent regime was only slightly changed and influence of the second mode in the excited state decay was delayed. We conjecture that vibrational modes with a small (or zero) contribution to the Herzberg-Teller correction (vibration-induced electronic inter-state coupling) cannot contribute to a fast decay component of the electronic excited state. Modes contributing to the Herzberg-Teller correction, but with lower values of the vibrational displacements (Stokes shift), are expected to contribute to the fast initial decay compenent. They will thermalize faster than the mode with a strong coherent character (with significant values of the Herzberg-Teller correction and Stokes shift in the excited state). These effects will be studied by the authors in next publications.

ACKNOWLEDGEMENT

This research was supported by the Grant Agency of the Academy of Sciences of the Czech Republic (project AV0Z4050913) and by the grant NATO PST.ARW 979393.

REFERENCES

1. T.S. Rose, M.J. Rosker, A. H. Zewail, J.Chem. Phys., **88**, 6672 (1988)
2. A. H. Zewail, Science, **22**, 1645, (1988)
3. J. Chesnoy, A. Mokhtari, Phys. Rev A, **38**, 3566 (1988)
4. H. Okamoto, K.Yoshihara, Chem. Phys. Lett., **177**, 568 (1991)
5. E. Lenderink, K. Duppen, D. A. Wiersma, J. Phys. Chem., **99**, 8972 (1995)
6. A. Mokhtari, A. Chebira, J. Chesnoy, J. Opt. Soc. B, **7,** 1551 (1990)
7. P. Voringer, R. A. Westervelt, T. S. Yang, D. C. Arnett, M. J. Feldstein, N. F. Scherer, J. Raman Spectrosc., **26**, 535 (1995)
8. Q. Hong, I. A. D. Pexton, G. Porter, D. R. Klug, J. Phys. Chem. **97**, 12561 (1993)
9. M. Seel, S. Engleitner, W. Zinth, Chem. Phys. Lett., **275**, 363 (1997)
10. K. Wynne, C. Galli, R. M. Hochstrasser, J. Chem. Phys., **100**, 4797 (1994)
11. K. Wynne, G. Reid, R. M. Hochstrasser, J. Chem. Phys. **105**, 2287 (1996)
12. I. V. Rubtsov, K. Yoshihara, J. Phys. Chem., **101**, 6138 (1997)
13. I. V. Rubtsov, K. Yoshihara, J. Phys. Chem., **103**, 10202 (1999)
14. B. Wolfseder, W. Domcke, Chem. Phys. Lett., **259**, 113 (1996)
15. D. Egorova, A. Kühl, W. Domcke, Chem. Phys., **268**, 105 (2001)
16. O. Kühn, V. May, M. Schreiber, J. Chem. Phys., **101**, 10404 (1994)
17. U. Kleinekathöfer, I. Kondov, M. Schreiber, Chem. Phys., **268**, 121 (2001)
18. M. Menšík, S. Nešpůrek, Accepted to Macromol. Symp.
19. M. Menšík, S. Nešpůrek, Czech J. Phys., **52**, 945 (2002)
20. V. Romero-Rochin, I. Oppenheim, Physica A, **155**, 52 (1989)
21. E. Geva, E. Rosenman, D. J. Tannor, J. Chem. Phys., **113**, 1380 (2000)

ADVANCES IN TIME-RESOLVED SPECTROSCOPY

Eric Faulques
Institut des Matériaux Jean Rouxel, Laboratoire de Physique Cristalline
2 rue de la Houssinière, BP32229, 44322 Nantes, France
faulques@cnrs-imn.fr

Abstract Time-resolved optical spectroscopies are now routinely used in condensed matter sciences to scrutinize the temporal physics of semiconductors, nanostructures, organic molecules and supramolecular assemblies. We will confine ourself to a brief outline of the techniques in this discipline with a focus on emerging materials.

Keywords: ultrafast processes, photo-induced absorption, photoluminescence, organic materials, nanomaterials, excitons.

1. Introduction

What we are mainly concerned with here is to exemplify three typical techniques of time-resolved spectroscopy based on the advent of ultrashort laser pulses in the femtosecond time domain : pump-probe photo-induced absorption (PIA), photoluminescence up-conversion (PL, UCP), and photoluminescence imaging. In the last few years, these techniques have been tremendously exploited to probe exciton dynamics, energy transfer and radiative decay channels in organic materials and nanomaterials with attractive properties such as luminescence and quantum confinement. Among the substances studied we can cite short organic molecules deposited on substrates, electroluminescent polymers, natural pigments, nano-objects and nanocomposites. These materials are of interest for organic electroluminescent diodes (OLED), field effects transistors (FET), transport layers, non linear optical applications, and photovoltaïc cells. Optical processes like absorption and emission which take place in semiconductors (SC) upon illumination can be interpreted on the basis of the exciton concept. Basically, an exciton is a neutral quasi-particle which is formed by an excited Coulomb bound state of an electron and a hole. Excitons can be singlet (S^*) or triplet (T^*) states as shown in Fig. 1. Depending on the nature of the electron-hole interaction, excitons can be more or less tightly bound on a single molecule or on few atomic sites. These are the so-called Frenkel and charge-transfer excitons with binding energies from some eV's to

E. C. Faulques et al. (eds.), Spectroscopy of Emerging Materials, 363–378.

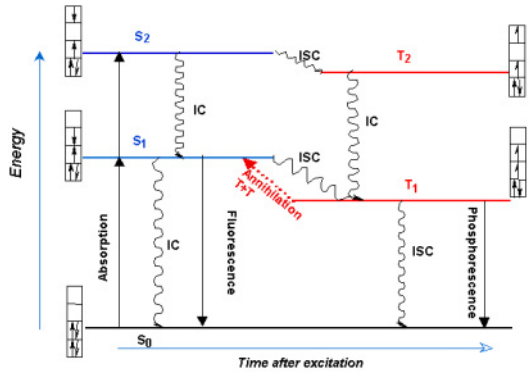

Figure 1. Jablonski diagram for a four-level system depicting absorption, non-radiative (wavy arrows) and radiative processes between singlet (total spin S = 0) and triplet (total spin S = 1) states. Emissions respect Kasha's rule. IC : internal conversion. ISC : intersystem crossing.

0.1 eV which are created in organic SC's. Weakly bound excitons (tens of meV's) with much larger radii are known as Wannier-Mott excitons typical for inorganic SC's. When interacting with the surrounding atomic framework, the exciton can move or be trapped at defects, is able to transfer energy, and has a limited lifetime. It is worth stating at this point that time-resolved optical probes are therefore adequate tools to investigate the relaxation processes of the excitons (i.e. the recombinations of the electron-hole pair) towards the ground state. Ultimately, then, such mechanisms are governed by rate equations which are relevant to interpret transient optical data. The following section gives some of them. Additionally, tutorials on exciton physics can be found in Refs. [1–3] and in the present volume while more technical details concerning the principles of time-resolved experiments are available in Ref. [4].

2. Excited-states population dynamics

Various models are used in the literature to account for the kinetics of the excitons involved in optical processes. In the simplest cases, the signal evolution $n(t)$ can be reproduced by considering either a single exponential or multi-exponential time dependences. This model is well suited for solutions or solids in which monomolecular mechanisms happen alone. Since in most transient experiments the temporal response is a convolution of a Gaussian-shaped pulse and of the intrinsic kinetics, the rate of change with time of the excited-state population decaying exponentially is given by

$$\frac{dn(t)}{dt} = G(t) - \beta n(t) \tag{1}$$

where $\beta = 1/\tau$ is the inverse relaxation time. The term $G(t)$ is intended to describe the laser pulse. Ideally, $G(t)$ is a Gaussian function with maximum

position t_0 (origin of decay times), integrated intensity I and width σ:

$$G(t) = \frac{I}{\sigma\sqrt{2\pi}} \exp\Big[-\frac{(t-t_0)^2}{2\sigma^2}\Big]$$

Similarly, when two excited-states are involved, their kinetics can be modeled by

$$\begin{aligned} \frac{dn_1(t)}{dt} &= G(t) - \beta_1 n_1(t) \\ \frac{dn_2(t)}{dt} &= \beta_1 n_1(t) - \beta_2 n_2(t) \end{aligned} \tag{2}$$

The solutions of Eqs. 1- 2 are respectively

$$n_1(t) = \frac{I}{2} \exp\Big[\beta_1(t_0 - t) + \frac{(\beta_1\sigma)^2}{2}\Big] \times \operatorname{erfc}\Big[\frac{\beta_1\sigma^2 + t_0 - t}{\sigma\sqrt{2}}\Big] \tag{3}$$

$$\begin{aligned} n_2(t) = \frac{I}{2}\frac{\beta_1}{\beta_2 - \beta_1}\Bigg\{ &\exp\Big[\beta_1(t_0 - t) + \frac{(\beta_1\sigma)^2}{2}\Big]\operatorname{erfc}\Big[\frac{\beta_1\sigma^2 + t_0 - t}{\sigma\sqrt{2}}\Big] \\ &- \exp\Big[\beta_2(t_0 - t) + \frac{(\beta_2\sigma)^2}{2}\Big]\operatorname{erfc}\Big[\frac{\beta_2\sigma^2 + t_0 - t}{\sigma\sqrt{2}}\Big]\Bigg\} \end{aligned} \tag{4}$$

Here, the responses are normalized to the maximum concentration n_0 of excitations. The signal evolution in a bi-exponential decay is therefore $n(t) = An_1(t) + Bn_2(t)$, where A and B are proportional to the radiative (or non-radiative) rates of the two levels. For solids, a monoexponential PL decay can be explained by the thermally activated recombination of highly mobile electrons and holes trapped onto radiative defects. Such a mechanism requires that the spatial separation of the trapped charge carriers be small.

In actual fact it would be more accurate to say that the population evolution in condensed matter (thin films, crystals, amorphous solids) often follows non-exponential decays. This behavior may be governed by several factors such as disorder (grain boundaries, polycristallinity, surface defects), energy relaxation within the excited electronic state, or direct interaction of excitations, especially in molecular systems. In a number of situations, as soon as the energy density of the exciting light significantly increases, one can observe that:

- The transient PL intensity experiences a strong quenching when the time delay increases.
- The time-dependent decay of the differential transmittance ($-\Delta T/T$) corresponding to an induced absorption resulting from photoexcitation is nonexponential.

In case of interaction between excitations, exciton-exciton annihilations (or fusion) are the most likely mechanisms to be employed for an energy density dependence of the transient decays. The dynamics is reflected in a Riccatti rate equation including simultaneous monomolecular and bimolecular processes,

$$\frac{dn(t)}{dt} = G(t) - \beta n(t) - \gamma n(t)^2 \tag{5}$$

where γ is the exciton-exciton annihilation rate constant. The simplified solutions of this equation, when $G(t)$ is a $\delta-$function are

$$n(t) = n_0 \times (1 + \gamma n_0 t)^{-1} \tag{6}$$

if the decay is simply bimolecular ($\beta = 0$), and

$$n(t) = n_0 \exp(-\beta t) \times \left[1 + \gamma n_0 \beta^{-1} \times (1 - \exp(-\beta t)\right]^{-1} \tag{7}$$

if the exciton recombination involves simultaneously a monomolecular process ($\beta \neq 0$), a case to be used in real events at high laser densities with nonexponential decays.

For a critical concentration of excitons $n_c = \beta/\gamma$, the critical radius R_c below which bimolecular annihilation process predominates over singlet exciton recombination can be expressed as [5],

$$R_c = \left(\frac{3\gamma}{4\pi\beta}\right)^{1/3} \tag{8}$$

The γ constant (in $\mathrm{cm^3 s^{-1}}$) of mobile excitons is directly related to the exciton diffusion constant D : $\gamma = 8\pi D R_c$ (in $\mathrm{cm^2 s^{-1}}$).

Added to that, kinetics can also be simulated with time-dependent decay rate parameters. Dexheimer *et al.* and Lanzani *et al.* have identified such dynamics in C_{60} (ps regime) and α-sexithienyl thin films (fs regime) from pump-probe experiments [6, 7]. They implemented a Förster rate equation with a $\delta-$ function pulse

$$\frac{dn(t)}{dt} = -\beta n(t) - \gamma t^{-1/2} n(t)^2 \tag{9}$$

The solution of this rate equation is

$$n(t) = n_0 \exp(-\beta t) \times \left\{1 + \left(\frac{\pi^{1/2}\gamma n_0}{\beta^{1/2}}\right) \times \mathrm{erf}\left[(\beta t)^{1/2}\right]\right\}^{-1} \tag{10}$$

In the Förster mechanism, the energy transfer upon excitation may take place between excited molecular entities separated by distances R, which are considered as spatially fixed Frenkel excitons. It is described in terms of resonant interaction between their transition dipole moments, which decreases as R^{-6}.

As far as the concentration of excitons decreases with time, the average distance R increases, which results in a peculiar $t^{-1/2}$ dependence of the annihilation constant γ. A time-dependent annihilation rate may also be found for mobile excitons in molecular aggregates which depends on their effective dimensionnality d. In this case, $\gamma \sim 1/\ln t$ if $d = 2$ and $\gamma \sim t^{-d/2}$ if $d < 2$ [6–8]. Ivanov [9] has proposed a simple procedure to check the time dependence of $\gamma(t)$ by plotting the logarithmic derivative of the experimental data $n(t)$,

$$\frac{\dot{n}(t)}{n(t)} = -\beta - \gamma(t)n(t) \tag{11}$$

It is clear that linearity of $\dot{n}(t)/n(t)$ should imply a process in which $\gamma(t)$ is constant. Further, direct estimate of β and γ from Eq. 11 is made possible without integrating Eq. 5.

Quenching centers are often relevant for nonexponential PL processes in disordered materials. At low pump power, the density of quenching centers is low while the density of recombining radiative excitons is high. At high energy density, the number of quenching centers increases and the population of radiative excitons is depleted. These centers can be photogenerated and extrinsic in nature or be located at grain boundaries.

The kinetics captured in disordered systems like polymers, glasses and polycristalline structures has been often described in terms of continuous relaxation times and exciton diffusion at recombination centers [10]. Assuming a $\delta-$ pulse function, the temporal data are best fitted by a monomolecular kinetic equation,

$$\frac{dn(t)}{dt} = -k(t)n(t) \tag{12}$$

in which $k(t)$ is a *time-dependent* decay rate constant. Thus, in this model, the population of the surviving excitons at time t obeys the stretched-exponential Kohlrausch function,

$$n(t) = n_0 \exp\left[-\left(t/\tau_k\right)^{\beta_k}\right], \tag{13}$$

where τ_k is the characteristic Kohlrausch time of the relaxation and $0 < \beta_k \leq 1$ is a shape parameter of the relaxation function.

Physically, Eq. 13 means that a dispersive diffusion of the excitons takes place with a time dependent hopping rate towards recombination centers. The β_k exponent is a temperature-dependent parameter directly related to the disorder and distribution of traps. β_k is linked to the dimensionnality d of the system through the relation $\beta_k = d/(d+2)$. It is seen that in the 1-D case $\beta_k = 1/3$. Taking a wide range of representative examples of relaxation processes in disordered systems, Phillips [11] has shown that when $\beta_k = \beta_s = 3/5$ (for $d = 3$) short-range interactions are involved as opposed to the case $\beta_l = 3/7$ (for $d = 3/2$) which characterizes long-range interactions.

This kinetics was additionally employed in Ref. [7] to discuss PIA exciton dynamics in α-sexithienyl thin films in the ps regime. The data were fitted with $\beta_k = 0.35$, close to 1/3 and τ_k = 6.5 ps.

In thin films of electroluminescent conjugated polymers, Kanner *et al.* [12] and Yan *et al.* [13] explained the quenching of PL by invoking an exciton migration mechanism to nonradiative traps based on the Balagurov-Vaks model [14]. The survival probability of an exciton on a 1-D lattice ($\beta_k = 1/3$) is characterized by a diffusion time τ_d. For times $t \gg \tau_d$, the PL intensity follows a stretched-exponential dependence, corresponding to a fast decay of highly mobile excitons. However, in those polymers, the decay dynamics show an additional much slower regime ascribed to localized, immobile excitons with lifetime τ_h. The PL intensity decay $I(t)$ was therefore expressed by a two-regime equation

$$I(t) = \left[I_d \sqrt{\frac{t}{\tau_d}} \exp\left(-\left[\frac{t}{\tau_d} \right]^{1/3} \right) + I_h \exp\left(-\left[\frac{t}{\tau_h} \right]^{n} \right) \right] \exp\left(-\frac{t}{\tau_c} \right) \qquad (14)$$

where I_d and I_h are the amplitudes of the short- and long-lived components, respectively, and τ_c accounts for a constant natural lifetime of the exciton. This relation was applied also by Herz *et al.* to study the exciton diffusion in chiral stacks of p-phenylene vinylene (PPV) oligomer assemblies [15].

3. Femtosecond optical spectroscopies

Pump-probe techniques are the most widely used to study transient phenomena. Their success comes from the fact that they need only simple optical pathways and detection with the advantage to probe transients up to the laser pulse width. The techniques use two femtosecond beams: a pump to initiate chemical reaction or absorption in the sample, and a probe beam which is a fraction of the pump at a different wavelength entering the sample at a later time delay. In transient absorption, the probe beam contains a continuum of visible-light wavelengths called the white light continuum (WLC, 300-800 nm typically), as to detect the changes in optical absorption. The WLC is generated by entering the probe beam into some transparent media; for example, a rotating disk of fused silica. In order to obtain WLC, one should dispose of sufficient laser power which is given by a regenerative amplifier placed in front of the femtosecond oscillator. The wavelength of the excitation pulse (pump) is choosen by adjusting the nonlinear crystal of an optical parametric amplifier (OPA). The time delay between pump and probe is obtained by a variable optical delay line placed on the pump beam optical pathway. In femtosecond experiments, the delay line should be motorized since 1 ps represents only 300μm of light travel.

The signal measured versus time delay changes Δt reflects the transient chemical changes or the absorption- transmittance variations (ΔA or $-\Delta T$) inside the sample. The energy losses through the sample are analyzed with a

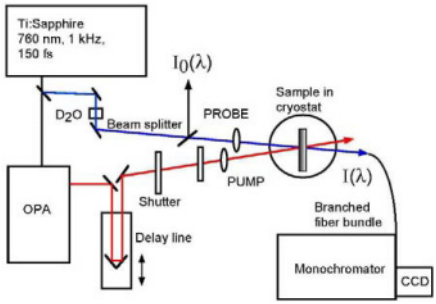

Figure 2. Transient photoabsorption set-up.

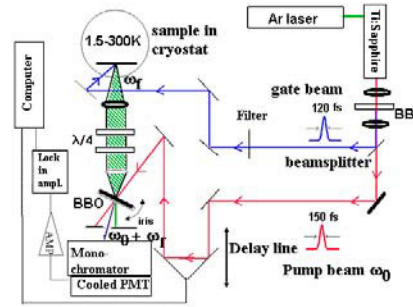

Figure 3. Photoluminescence up-conversion set-up.

monochromator coupled to a charge-coupled device (CCD) detector in order to acquire the full spectrum at once. If more sensitivity is needed, the spectrum is acquired by rotating the gratings of the monochromator and detected with a photomultiplier (PM). In pump-probe photoabsorption (sometimes called photobleaching) only transitions between states of the same spin multiplicity are allowed, while $S_0 \rightarrow T^*$ transitions are, in principle, forbidden. There are many different experimental configurations for time-resolved absorption. Fig. 2 details a very common set-up. In such an experiment, the physical quantities to be measured are the absorption coefficient α which provides for the absorption spectrum on the spectral region of interest for a given Δt, and the population evolution of the excited states $n(t)$ which is obtained by varying Δt at a given wavelength λ. Measurements are made considering the time-dependent Beer-Lambert law

$$I(\lambda, t) = I_0(\lambda) exp\big[- \alpha(\lambda, t) n(t) l\big] \tag{15}$$

where I_0 and I are the intensities measured before and after perturbation, respectively, and l the thickness of the excited sample. The relative change of transmittance T during time t is given by

$$-\frac{\Delta T}{T_0}(\lambda, t) \sim exp\big[- \Delta\alpha(\lambda, t) n(t) l\big] \sim exp\Big[- \frac{t}{\tau(\lambda)}\Big] \tag{16}$$

where τ is the decay time of the excited states population assuming an exponential decay at wavelength λ.

The technique of up-conversion photoluminescence allows one to record the transient PL of a system at the temporal resolution of the laser pulse. It is used to study very fast processes below the picosecond time domain. A typical set-up for this experiment is shown in Fig. 3. The sample is excited at frequency ω_0 by a femtosecond laser pulse and its PL at ω_f is mixed with that of an optically

delayed, femtosecond gate-beam laser pulse in a sum-frequency generating, optical nonlinear crystal ($LiIO_3$, LBO, BBO) which acts as an optical gate opening only when the laser pulse impinges in the crystal. The frequency mixing (up-conversion) produces light pulses at the sum-frequency of the gate beam and PL, $\omega_m = \omega_0 + \omega_f$. Light intensity is measured using a fast photomultiplier at this sum-frequency, which is determined by the monochromator and the nonlinear crystal adjustments. The dynamics of PL is observed by varying the time delay between the gate-beam and the PL signal. In its original design, this is a single-channel, stroboscopic technique, which necessitates high-repetition rate lasers (4 kHz-100 MHz) with low energy. The obtention of a spectral kinetics is rather slow since one should measure it at each ω_m by spanning the desired spectral domain.

To illustrate these femtosecond techniques, we shall give several examples. The first one is a PIA/UCP combined study of N,N− dimethyl- aminobenzylidene $-1,3-$ indandione films (DMABI) [16]. This compound is promising for photoconductivity and nonlinear optical properties to possible applications in molecular optoelectronics. The study concluded that the enhanced nonradiative relaxation of the excitons took place in the femtosecond timescale due to localization and thermalization of self-trapped excitons (STE). At high energy-density, one-dimensional exciton-exciton annihilation was observed. The main results are shown in Fig. 4. In the upper panel, there is an instantaneous rise of PL just after excitation attributed to STE trapping in less than 100 fs. The rapid, highly nonexponential decay shows two kinetics: the first one is ultrafast (500 fs) and corresponds to localization of excitons; the second one is slow (23 ps) and indicates PL quenching of relaxed STE by nonradiative decay to lower states. In the lower panel, it seen that high-density impinging energy induces strong nonexponential decay which reduces considerably at lower laser energies. The decay can be fitted with $n(t) = (1/n_0 + 2\gamma t^{0.5})^{-1}$ which describes exciton annihilation with annihilation rate $\gamma = 4.5 \times 10^{-15}\mathrm{cm}^3\mathrm{s}^{-1/2}$.

An interesting application of UCP to the ultrafast light emission from novel metal-dendrimer nanocomposites was reported in Ref. [17]. The interaction of metallic nanoparticles (silver and gold) with macromolecules yields specific optical properties strongly dependent on their size and shapes. It was observed that the PL of embedded metal nanoclusters (larger than 3 nm in size) in polyaminoamine was enhanced in those systems (quantum efficiency around 10^{-7}) with respect to that reported for bulk metals (10^{-10}) or metal nanoparticles alone. The relaxation of PL in UCP experiments was found to follow multi-exponential, ultrafast decay regimes with time constants τ = 75 fs − 5.5 ps and 70 fs − 700 fs − 5.3 ps in gold and silver nanocomposites, respectively (Fig. 5).

The field of luminescent conjugated polymers and molecules is also representative of current research carried out to identify the nature of photoexcitations

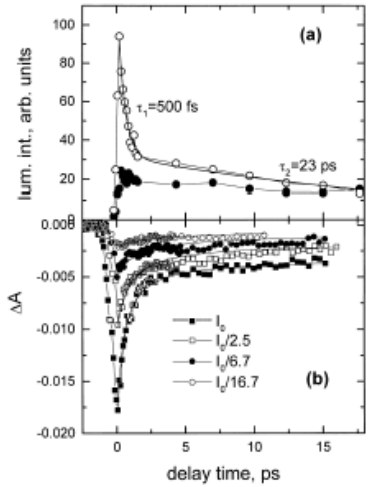

Figure 4. Transients of DMABI films. (a) Up-conversion PL intensity decays of two self-trapped exciton states of DMABI at excitation energy 3.14 eV.(b) Time-dependence of photoinduced absorption monitored at 1.93 eV for different energy densities. Excitation at energy 2.15 eV. Reprinted with permission from Ref. [16].

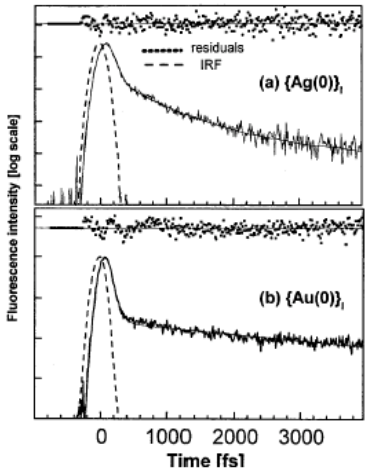

Figure 5. Up-conversion photoluminescence dynamics of : (a) Ag- and (b) Au-dendrimer nanocomposites, for emission at 2.58 eV and 2.17 eV, respectively. Excitation at 3.14 eV. Reprinted with permission from American Institute of Physics Ref. [17].

in prospective compounds. The luminescence efficiency of such polymers is strongly diminished by energetic disorder and structural defects of the chains. It is known that photoexcitations result in the existence of intrachain and interchain singlet and triplet states with spin statistics giving a singlet to triplet ratio of 1-to-3. Triplets are non-emissive states and then reduce the light efficiency of polymer-based devices, since the $T_1 \rightarrow S_0$ transition is spin-forbidden. Thus, the tailoring of polymer backbone appears to be one of the solutions to improve efficient phosphorescence from the triplet state, by altering the chain length, by incorporating heavy atoms enhancing spin-orbit coupling, or dye molecules to favor the energy transfer from the polymer to the chromophore. Delayed, red-shifted fluorescence is one of the signatures of triplet generation in molecular crystals and polymers. The most probable mechanism for this is $T-T$ exciton annihilation into singlet excitons ($T_1 + T_1 \rightarrow S_1^* \rightarrow S_0 + h\nu_F$ + phonons) as evidenced in polyfluorene, PPV and poly-p-phenyleneethynylene (PPE) [19, 18]. The nature of photogenerated states (S or T) can be probed with PIA. For instance, triplets and singlets formation rates were measured in a polyfluorene-based OLED and in $\alpha-$sexithienyl (6T) crystals (used for FET and photovoltaic cells), respectively [20, 21]. Figs. 6- 7 show the dynamics of the photoexcitations in 6T at ultrashort and longer time delays.

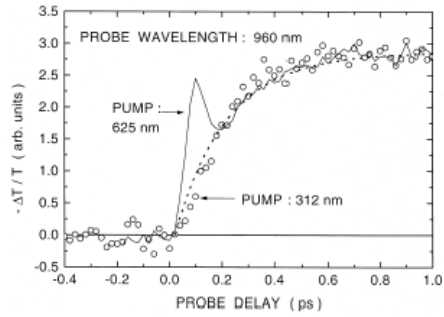

Figure 6. Temporal variation of photoinduced absorption in sexithienyl (femtosecond range) with exponential fit $\tau = 200$ fs [21].

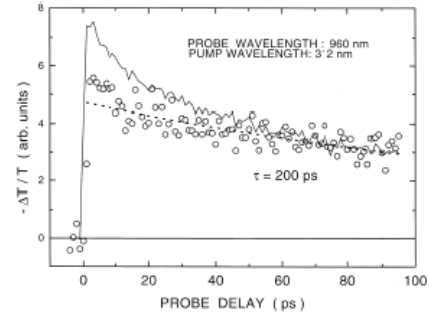

Figure 7. Decays of photoinduced absorption in sexithienyl at pump intensities I_0 and $I_0/2$ (picosecond range). Bimolecular exciton-exciton annihilation is evidenced [21].

Very recently, time-resolved spectroscopy was considered indispensable to pinpoint excitations in nano-objects such as single-walled carbon nanotubes (SWNT). The 1-D physics of SWNT is extensively investigated because they have demonstrated very interesting optical properties such as PL (radiative exciton recombination) when they are isolated or PL quenching (non-radiative exciton decay processes) when they aggregate into bundles. These properties arise from their tubular structure which shows a wide variety of diameters (typically 0.8 to 1.3 nm) and chiralities. The chirality is described by the Hamada vector (n, m) and determines the electronic properties of SWNT; armchair (n, n) SWNT are metallic, while chiral (n, m) and zigzag $(n, 0-0, m)$ SWNT are semiconducting or semiconducting and metallic [22, 23]. Bright bandgap PL has been observed from unprocessed, isolated SWNT of about 1 nm in diameter, in the near infrared region, and each (n, m) nanotube emits at a specific wavelength (1.0 to 1.6 μm) [24]. Pump-probe techniques are of primary importance to unravel the 1-D exciton dynamics in these nano-objects. A recent ultrafast dynamical study in the near infrared [0.853 eV (1.45 μm) to 1.6 eV (0.775 μm)] has reported that two relaxation regimes take place in micelle solutions of (n, m) semiconducting SWNT [25]. The observed lifetimes extracted from exponential decays of the pump-probe absorption were $\tau_1 = 0.3 - 1.5$ ps and $\tau_2 = 5 - 20$ ps, corresponding to a fast and a slow component, respectively.

4. Imaging of transient luminescence

The imaging of ultrafast photoluminescence or slower processes (fluorescence, phosphorescence) can readily be carried out with special optoelectronic equipment. The technique allows one to record simultaneously the intensity, the spectral and the temporal responses of fluorescence by using ultrafast streak cameras.

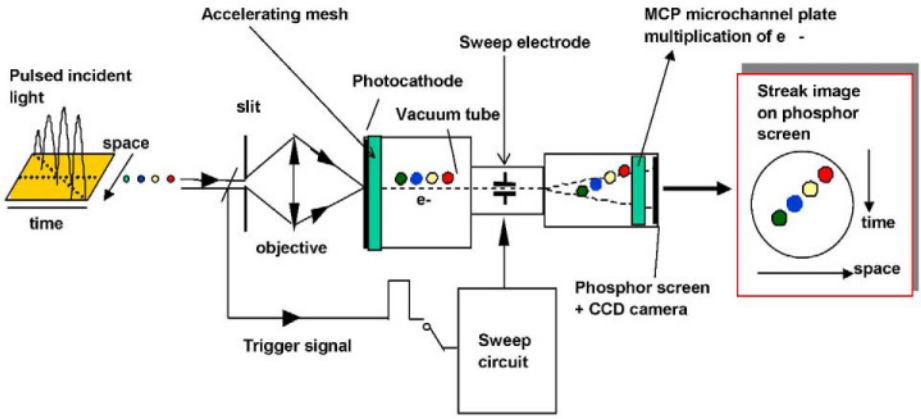

Figure 8. Schematic of a streak camera.

A streak camera is an optoelectronic device for detection of ultrafast optical events nominally at the ps resolution, whereas the temporal resolution can drop down to 200 fs with newer equipment, but not below, due to physical constraints inherent to the device. It should be pointed out that no other device devoted to the direct detection of light has better temporal resolution than a streak camera. The device can be considered as a time-space converter. The streak camera works as follows (Fig. 8) [26]. The light being measured is focused through a slit on the streak tube's photocathode which emits a number of photoelectrons proportional to the light intensity. The emitted photoelectrons are then accelerated through an accelerating mesh. They enter a pair of deflection plates to which a high-speed voltage sweep has been applied. Since they arrive between the sweep electrodes at slightly different times, they are deflected by the applied electric field at different angles in the vertical direction. The sweep is linear and is synchronized with the light pulse via a synchronization signal applied to the camera. The photoelectrons are multiplied as they pass a microchannel plate and then impact a phosphor screen where they are converted back into light. The image obtained on the phosphor screen thus represents the time-intensity or time-wavelength variations along the vertical deflection axis of the device. The signal is finally read by a high-sensitivity CCD detector (1024×1024 or 2048×2048 pixels).

An illustrative example of transient PL experiments using a streak camera is the study of a nano-structured material, opal [27]. This natural substance

provides information on optophysical properties of micro-to nanostructured SiO_2 polymorphs bearing a resemblance to those of oxidized porous silicon or damaged silicas [28]. Two kinds of opals were investigated : a "common" opal CT composed of disordered cristobalite and trydimite crystals, built up of nanograins about 20 nm in diameter, and a "noble" opal A (play-of-color opal) which presents extensive areas with long-range order and regular stacking of nanospheres about 200 nm in diameter. In Fig. 9 the transient PL images obtained from opals CT and A in the 50 ns range show strong blue emission extending between 375 and 600 nm possibly compatible with surface defect recombinations.

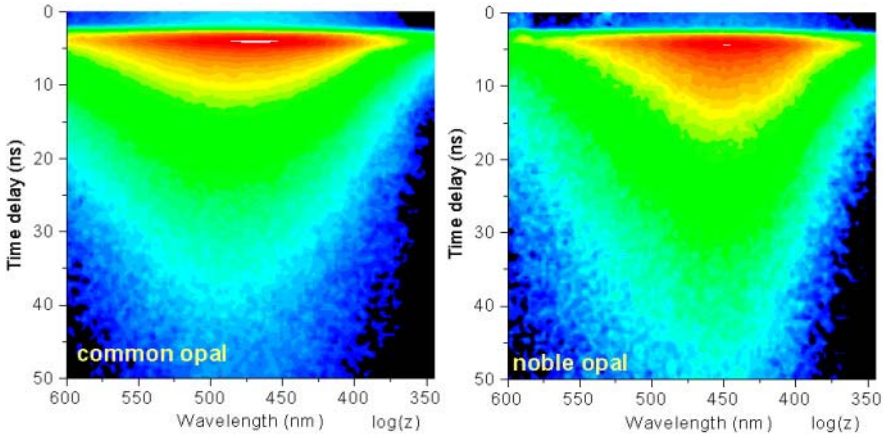

Figure 9. Picosecond photoluminescence maps of opal CT (left pannel) and opal A (right pannel). The PL intensity z is plotted in logarithmic scale and increases from blue colors to red colors. Zero-time delay corresponds to the beginning of the streak camera sweep. Opal CT "common" is from Mapimi, Mexico; opal A "noble" is from Lightning Ridge, Australia.

In Fig. 10, the transients exhibit quite different behavior from opal A to opal CT. In particular, a bi-exponential decay (Eq. 2) failed to reproduce the kinetics of opal CT. In this material, the emission is red-shifted towards 2.6 eV and the PL is strongly quenched at shorter time delays, with an unusual, non-linear kinetics in semi-log scale, indicating a complex decay channel either involving multi-exponential relaxation or exciton-exciton annihilations. Runge-Kutta integration of Eq. 5 seems to confirm the latter assumption with satisfactory reproduction of the observed decays. The lifetimes and annihilation rates are $\tau_{CT} = 9.3$ ns, $\tau_A = 13.5$ ns, $\gamma_{CT} n_0 = 650$ ps^{-1} and $\gamma_A n_0 = 241$ ps^{-1}, for opal CT and opal A, respectively.

Relations between structural properties (nanostructure and texture) and optophysical processes were also established in oligomer thin films. Oligomers of π-conjugated polymers with non-degenerate ground state are good computer-

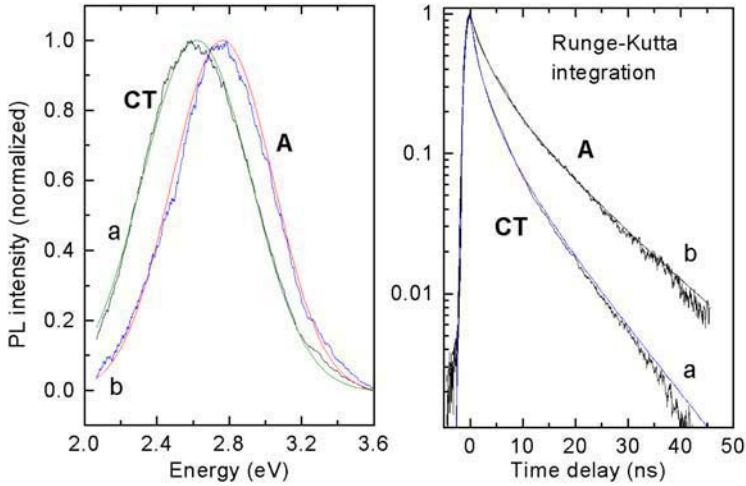

Figure 10. Transient photoluminescence of opal CT (a) and opal A (b) and kinetics at maximum emission fitted with the annihilation model.

tractable model compounds for studying the electrodynamics of electroluminescent polymers such as PPV [29, 30]. These short, ordered molecules present specific advantages from the experimental standpoint. Well-organized, crystalline phases and low-dimensional layers can be grown, whereas polymers are known to be poorly structured and disordered systems. Further, the technological flexibility of oligomeric materials has been readily demonstrated by the realisation of devices based on e.g. polythiophene, poly-*p*-phenylene and polyaniline oligomers. For instance, materials based on the six-phenyl-ring *para*-hexaphenyl molecule (PHP or Φ_6) and on three-to-five aniline rings, such as N,N'-diphenyl-1,4-phenylenediamine (DPPD) are interesting for prospects of engineered blue-light-OLED, FET, and memory type devices, respectively [31–34]. In addition, several PL studies of electroluminescent polymers have clearly substantiated that effective conjugation length, and chain alignment sharply control the exciton evolution in these systems [35]. Therefore, oligomer systems in which chain length is actually fixed should yield more clues on exciton evolution. Thin layers can grow with molecules lying parallel or standing perpendicular to various substrate surfaces [33, 36–38]. The textures of these layers strongly influence their optical performances [9, 39–41]. As an example, while the PL response of a standing PHP film is ultrafast ($\tau \leq 2$ ps), that of a lying film is delayed and red-shifted with concomitant PL quenching when time delay and energy density increase (Figs. 11- 12). Such behavior can be explained by rapid recombination of localized intramolecular, singlet

Frenkel excitons in the standing film and, in the lying film, by short-range intermolecular annihilation of singlet excitons highly mobile between adjacent PHP molecules ($R_c \approx 0.8$ nm). A fit to the experimental data (from Eq. 5) yields $\beta = 10.8 \times 10^8$ s^{-1} and $\gamma n_0 = 1.3 \times 10^{10}$ s^{-1}, values close to those determined from Eq. 11 (see Fig. 12).

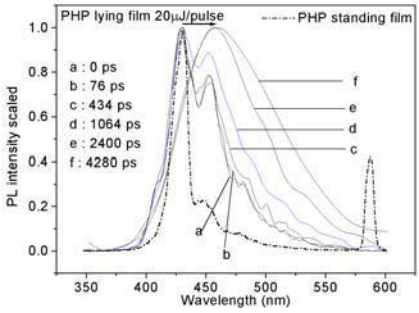

Figure 11. Transient photoluminescence of a $para$-hexaphenyle layer with molecules lying on the substrate, for increasing time delays. The dotted curve corresponds to the ultrafast response of a film with molecules standing almost perpendicular to the substrate.

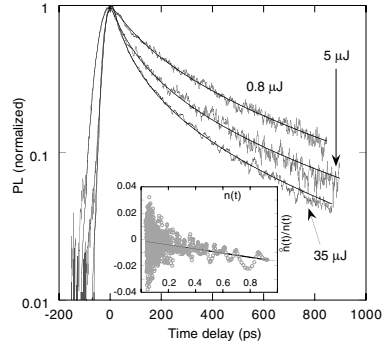

Figure 12. Normalized kinetics vs different energy densities for a $para$-hexaphenyle film with molecules lying on the substrate fitted with Eq. 5. In inset, logarithmic derivative of the decay at 35 μJ per pulse in this film. The linear regression fits the data with $\gamma n_0 = 1.5 \times 10^{10}$ s^{-1}, and $\beta = 9.7 \times 10^8$ s^{-1}. From Ref. [9].

5. Summary

The most sensible conclusion we can come to is that the optimization of optical characteristics in devices strongly depends on exciton dynamics, dimensionnality, and textures of the systems. In particular, the interpretation of transient data with realistic models is of utmost importance. In the forthcoming years, microscopic mechanisms underlying optical phenomena in nanostructural materials will remain subject to intense investigations for innovative optoelectronic properties. Some of these key issues can be solved with techniques described in this paper. In organic light emitting devices, for example, non-radiative triplet relaxation channels compete with intrinsic radiative decays produced by singlet states and, therefore, lower the radiative efficiency. Substantial progress, using time-resolved spectroscopy, is currently performed to understand these processes in electroluminescent organic systems [42–44].

Acknowledgments

The author thanks V. Ivanov, G. Jonusauskas, S. Quillard, B. Corraze, L. Athouël, J. Wéry, A. Kazachkov, E. Fritsch and S. Lefrant for useful discussions.

This work was partially supported by NATO (Grant No PST.CLG.979685). Fig. 4 and Figs. 6-7 are reprinted with permission from Elsevier from Synthetic Metals, 109, Jursenas *et al.*, *Femtosecond excited-state dynamics in N,N-dimethylaminobenzylidene-1,3-indandione DMABI films*, p. 171, 2000, and from Chemical Physics Letters, 320, G. Klein, *Transient femtosecond spectroscopy in α-sexithiophene single crystals*, p. 67, 2000, respectively.

References

[1] D. L. Dexter, and R. S. Knox, *Excitons* (Interscience Publishers, Wiley, New York, 1965).

[2] S. P. McGlynn, T. Azumi and M. Kinoshita, *Molecular Spectroscopy of the Triplet State* (Prentice-Hall, Englewoods Cliffs, N. J., 1969).

[3] H. van Amerongen, L. Valkunas and R. van Grondelle. *Photosynthetic Excitons.* Singapore, New Jersey, London, Hong Kong: World Scientific (2000).

[4] C. Rullière (Ed.). *Femtosecond Laser Pulses. Principles and Experiments*. Berlin, Heidelberg, New York: Springer-Verlag (1998).

[5] T. Kobayashi and S. Nagakura, Mol. Phys. **24**, 695 (1972).

[6] S.L. Dexheimer, W.A. Vareka, D. Mittleman, A. Zettl, and C.V. Shank, Chem. Phys. Lett. **235**, 552 (1995).

[7] G. Lanzani, M. Nisoli, S. De Silvestri, F. Abbate, Chem. Phys. Lett. **264**, 667 (1997).

[8] L. Peliti, J. Phys. A: Math. Gen. **19**, L365 (1986).

[9] E. Faulques, J. Wéry, S. Lefrant, V.G. Ivanov, G. Jonusauskas, Phys. Rev. B **65**, 212202-1-212202-4 (2002).

[10] R. Chen, J. Lumin. **102-103**, 510 (2003) and references therein.

[11] J.C. Phillips, Phys. Rev. B **52**, R8637 (1995); Rep. Prog. Phys. **59**, 1133 (1996).

[12] G.S. Kanner, X. Wei, B.C. Hess, L.R. Chen, and Z.V. Vardeny, Phys. Rev. Lett. **69**, 538 (1992).

[13] M. Yan, L.J. Rothberg, F. Papadimitrakopoulos, M. E. Galvin, and T.M. Miller, Phys. Rev. Lett. **73**, 744 (1994).

[14] B.Y. Balagurov and V.G. Vaks, Zh. Eksp. Teor. Fiz. **65**, 1939 (1973) [Sov. Phys. JETP **38**, 968 (1974)].

[15] L.M. Herz, C. Daniel, C. Silva, F.JM. Hoeben, A.P.H. Schenning, E.W. Meijer, R.H. Friend, and R.T. Phillips,Phys. Rev. B **68**, 045203 (2003).

[16] S. Jursenas, V. Gulbinas, Z. Kuprionis, R. Kananavicius, G. Kodis, T. Gustavsson, J.C. Mialocq, L. Valkunas, Synth. Met. **109**,169 (2000).

[17] O. Varnavski, R.G. Ispasoiu, L. Balogh, D. Tomalia, and T. Godson III, J. Chem. Phys. **114**,1962 (2001).

[18] J. Partee, E. L. Frankevich, B. Uhlhorn, J. Shinar, Y. Ding, and T. J. Barton, Phys. Rev. Lett. **82**, 3673 (1999).

[19] D. Hertel, H. Bässler, R. Guenter, U. Scherf, J. Chem. Phys. **115**, 10007 (2001).

[20] A. Köhler and J. Wilson, Organic Electronics, in press (2003).

[21] G. Klein, Chem. Phys. Lett. **320**, 65 (2000).

[22] N. Hamada, S. Sawada, A. Oshiyama, Phys. Rev. Lett. **68**, 1579 (1992).

[23] R. Saito, M. Fujita, G. Dresselhaus, M.S. Dresselhaus, Phys. Rev. B**46**, 1804 (1992).

[24] J. Lefebvre, Y. Homma, and P. Finnie, Phys. Rev. Lett. **90**, 217401 (2003).

[25] G.N. Ostojic, S. Zaric, J. Kono, M.S. Strano, V.C. Moore, R.H. Hauge, and R.E. Smalley, cond-mat/0307154 (2003).

[26] Hamamatsu 1996 *Guide to Streak Cameras* Cat. No SSCS1035E02 pp 4-5.

[27] E. Fritsch, J. Wéry, G. Jonusauskas, and E. Faulques, Phys. Chem. Minerals **30**, 393 (2003).

[28] E. Fritsch, L. Mihut, M. Baibarac, I. Baltog, M. Ostrooumov, S. Lefrant, and J. Wéry, J. Appl. Phys. **90**, 4777 (2001).

[29] D.D.C. Bradley , R. H. Friend, H. Lindenberger, and S. Roth, Polymer **27**, 1706 (1986).

[30] J.H. Burroughes, D.D.C. Bradley, A.R. Brown, R.N. Marks, K. Mackay, R.H. Friend, P.L. Burns, A.B. Holmes, Nature **347**, 539 (1990).

[31] A. Dodabalapur, L. Torsi, and H.E. Katz, Science **268**, 270 (1995).

[32] S. Tasch, C. Brandstätter, F. Meghadi, G. Leising, G. Froyer, and L. Athouël, Adv. Mater. **9**, 33 (1997).

[33] S. Quillard, B. Corraze, M. Poncet, J.Y. Mevellec, J.P. Buisson, M. Evain, W. Wang, and A.G. MacDiarmid, Synth. Met. **137**, 921-922 (2003).

[34] A.K. Flatt and J.M. Tour, Tetrahedron Lett. **44**, 6699–6702 (2003).

[35] G. R. Hayes, I. D. W. Samuel, and R. T. Phillips, Phys. Rev. B **52**, R11569 (1995).

[36] L. Athouël, G. Froyer, M.T. Riou, and M. Schott, Thin Sol. Films **274**, 35 (1996).

[37] R. Resel, N. Koch, F. Meghadi, G. Leising, W. Unzog, and K. Reichmann, Thin Sol. Films **305**, 232 (1997).

[38] R. Resel, N. Koch, F. Meghadi, G. Leising, L. Athouël, G. Froyer, and F. Hofer, Cryst. Res. Technol. **36**, 47 (2001).

[39] A. Niko, E. Zojer, F. Meghadi, C. Ambrosch-Draxl, and G. Leising, Synth. Met. **101** 662 (1999).

[40] M. Ariu, G. Bongiovanni, M. A. Loi, A. Mura, A. Piaggi, L. Rossi, W. Graupner, F. Meghadi, and G. Leising, Chem. Phys. Lett. **313**, 405 (1999).

[41] C. Zenz, G. Cerullo, G. Lanzani, W. Graupner, F. Meghadi, G. Leising, and S. De Silvestri, Phys. Rev. B **59**, 14336 (1999) and references therein.

[42] M. Segal, M.A. Baldo, R.J. Holmes, S.R. Forrest, and Z.G. Zoos, Phys. Rev. B**68**, 075211 (2003).

[43] J. De Ceuster, E. Goovaerts, A. Bouwen, and V. Dyakonov, Phys. Rev. B**68**, 125202 (2003).

[44] A.Yu. Kobitski, R. Scholz, D.R.T. Zahn, and H.P. Wagner, Phys. Rev. B**68**, 155201 (2003).

LINEAR AND NONLINEAR LIGHT SCATTERING BY EMERGING MATERIALS

Koen Clays
Department of Chemistry, University of Leuven, Celestijnenlaan 200D, B-3001 Leuven, BELGIUM

Abstract: Second-order nonlinear light scattering, or hyper-Rayleigh scattering (HRS) was originally conceived as a simple screening technique for neutral, dipolar second-order nonlinear optical chromophores. It was realized early on that this incoherent scattering technique was, unlike the more conventional coherent electric-field-induced second-harmonic generation (EFISHG), uniquely suited to address new molecular symmetries. Since the advent of HRS, octopolar design strategies at the molecular and supramolecular level emerged as alternatives to the dipolar paradigm. Also ionic molecules, organometallic complexes and chiral helicenes could be studied at the molecular level. For improved accuracy and precision, HRS has been implemented with high repetition rate femtosecond laser pulses in combination with phase and demodulation measurements. Through rational design of optimized chromophores in the right environment, large first hyperpolarizability values have been obtained in accordance with a limiting theory. Photonic crystals have recently emerged as interesting linear and nonlinear optical materials. We have demonstrated that the natural protein bacteriorhodopsin is, in fact, a nonlinear photonic crystal.

Key words: nonlinear optics, hyperpolarizability, hyper-Rayleigh scattering, photonic crystals, photonic bandgap materials

1. INTRODUCTION

Photonics is playing an ever-increasing role in our modern information society. Information is now distributed over long distance mainly over optical fiber. The carrier of the information is then the elementary particle in photonics, *i.e.*, the photon. This photon is gradually replacing the electron, the elementary particle in electronics. At this time, it is only the distribution of information that is done all-optically. The information itself is still electronic in origin, *e.g.*, video or audio, or digital information. For the information transfer, the electro-optic (EO) effect transforms the electronic information to optical modulation. At the end of the optical fiber, a photodetector back-transforms the optical information to electronic signals that then can be processed or stored, again electronically.

E. C. Faulques et al. (eds.), Spectroscopy of Emerging Materials, 379–393.

The EO effect is a second-order nonlinear optical (NLO) effect. Only non-centrosymmetrical materials exhibit second-order NLO effects. This non-centrosymmetry is a condition, both at the macroscopic level of the bulk arrangement of the material and at the microscopic level of the individual molecule. All electro-optic modulators that are presently used by telecom operators are ferro-electric inorganic crystals. The optical nonlinearity in these materials is to a large fraction caused by the nuclear displacement in the applied electric field, and to a smaller fraction by the movement of the electrons. This limits the bandwidth of the modulator. The nonlinear response of organic materials is purely electronic and, therefore, inherently faster.

In the context of emerging materials for optical applications, organic molecular materials whose optical properties can be switched by an external stimulus certainly deserve attention. For a long time, optical materials used to be passive, inorganic materials. The application was determined by the bulk linear optical properties, such as the refractive index. New optical materials emerged along two axes: On the one hand, there was the development of organic molecular materials, for which the optical properties are very much dependent on molecular parameters such as polarizability (rather than bulk refractive index) and molecular size and shape. On the other hand, inorganic nonlinear optical materials emerged as the first active optical materials for frequency conversion or electro-optic modulation. More recently, organic molecular materials have been used for active nonlinear optical components. The advantage of organic materials is that they can be optimized at the molecular engineering level for a specific application. Different engineering guidelines lead to different organic materials optimized for photorefractivity, holographic memory, or electro-optic modulation. Also within a chosen application, the chromophore can still be optimized for the specific wavelength used. Another advantage of organic materials is that they combine chemical functionality with their optical properties.

Not all organic materials display second-order NLO properties. First of all, at the molecular level, they need to be non-centrosymmetric. Organic synthesis can furnish a wealth of molecules that all have an inherently fast electronic response. However, not all of them are good candidates for NLO applications. The field of organics for nonlinear optics has been hampered by the lack of a widely applicable, simple and fast screening procedure for NLO applications. The technique that used to be used to determine how good an organic molecule was for nonlinear optics, was the Electric-Field-Induced Second-Harmonic Generation (EFISHG) technique. Since a second-order effect can only be observed from a non-centrosymmetric bulk arrangement, an external electric dc field was applied over a solution of neutral candidate molecules with a dipole. Only for neutral molecules could a dc field be established over the solution, and only through the interaction of the dipole with this dc field could the necessary non-centrosymmetry be established. From the partially oriented ensemble of molecules could a detectable second harmonic of the fundamental laserbeam be produced. Small wonder then, that the first paradigm of organic nonlinear optics was a

neutral molecule with a dipole, *i.e.*, *para*-nitroaniline. This small molecule has become the "*fruitfly*" of organic nonlinear optics. It is the most widely studied molecule in the field, it has taken up the responsibility as a primary reference to compare actual values and it is also amenable to theoretical calculations.

A number of structure-property relations have emerged from the EFISHG measurements on neutral, dipolar molecules. Extending the number of polarizable electrons through a longer conjugation path increases the polarizability, be it linear are nonlinear. To induce the non-centrosymmetry, an electron-donating (electron-rich) group and an electron-withdrawing (electron-poor) group can be covalently linked to this conjugation path. In this way, the first "*workhorse*" of organic nonlinear optics was engineered: 4-dimethylamino-4'-nitrostilbene that was used for a prototype of an all organic electro-optic modulator.

However, non-centrosymmetry does not automatically imply a dipolar molecule, or, more generally, vectorial properties. Also molecules without a dipole moment can exhibit second-order nonlinear optical properties. Tetrahedral molecules, such as CCl_4, and trigonal molecules, such as BCl_3, also lack centrosymmetry. However, they cannot be oriented in an electric field, due to the absence of a dipole moment. Therefore, they can simply not be measured by EFISHG. Also ionic species cannot be measured, since these migrate, rather than rotate, under the influence of an applied field.

2. NANOSECOND HYPER-RAYLEIGH SCATTERING

This technique is based on light scattering. Linear light scattering is caused by refractive index variations. However, for linear light scattering to be observed, fluctuations in refractive index need to be invoked. These fluctuations in refractive index are the consequence of density fluctuations or translational fluctuations by the molecules. These fluctuations change the number density, but not the symmetry. The intensity of this Rayleigh scattering is linearly dependent on the number density and the impinging laser intensity, and quadratically on the linear polarizability.[1] Second-order nonlinear light scattering can be observed from fluctuations in symmetry, caused by rotational fluctuations. It is only on average in time and space, that a solution is centrosymmetric. Locally in time and space, deviations from centrosymmetry occur and give rise to a second-order nonlinear optical response.[2] Hence, scattering by a fundamental laser beam can be detected at the second-harmonic wavelength. The intensity of this hyper-Rayleigh scattering is also linearly proportional to the number density, but quadratically dependent on the second-order nonlinear optical polarizability, or first hyperpolarizability, and also quadratically dependent on the fundamental intensity.[3]

2.1 Experimental details of nanosecond HRS

The generic experiment in hyper-Rayleigh scattering[4] consists of measuring the intensity of the second harmonic $I(2\omega)$ that is scattered by a fundamental laser beam impinging on a solution of nonlinear optical chromophores in a suitable solvent. This intensity should be quadratically dependent on the fundamental intensity $I(\omega)$.

$$I(2\omega) = QC\, I\left(\omega^2\right) \qquad \text{(Eq. 1)}$$

This is exemplified in Fig. 1 for *para*-nitroaniline in nitromethane.

$$QC = \frac{I_{2\omega}}{I_{\omega}^2} = G\left(N_{solvent}\beta_{solvent}^2 + N_{solute}\beta_{solute}^2\right) \qquad \text{(Eq. 2)}$$

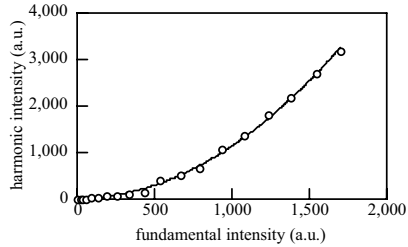

Figure 1. Typical quadratic dependence of HRS signal on IR intensity.

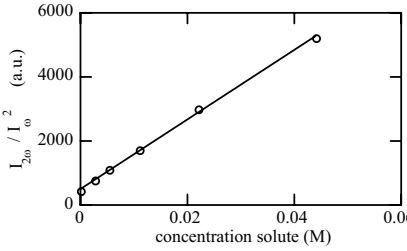

Figure 2. Typical linear dependence of QC on concentration.

G is a proportionality factor that includes both theoretical factors, such as the wavelength, the angular and distance dependence, and experimental factors, such as the photon detection efficiency and the photomultiplier gain.

When a non-centrosymmetric solvent is used, there is still hyper-Rayleigh scattering at zero solute concentration. The intercept is then determined by the number density of the pure solvent and the hyperpolarizability of the solvent. This provides a means of internal calibration, without the need for local field correction factors at optical frequencies. No dc field correction factors are necessary, since in HRS, unlike in EFISHG, no dc field is applied. By comparing intercept and slope, a hyperpolarizability value can be deduced for the solute from the one for the solvent. This is referred to as the internal reference method. Alternatively, or when the solvent is centrosymmetric, slopes can be compared directly. One slope is then for a reference molecule with an accurately known hyperpolarizability; the other slope is for the unknown, with the hyperpolarizability to be determined. This is referred to as the external reference method. If the same solvent is used, then no field correction factor is necessary. When another solvent needs to be used, the different refractive index calls for a local field correction factor at optical frequencies. The usual Lorentz correction factors can be used.

Since the efficiency for second-order scattering is fairly low, high peak power from a pulsed laser is necessary to observe any hyper-Rayleigh scattering. The generic laser type for hyper-Rayleigh scattering is still the nanosecond Neodymium^{3+}:YAG laser, with its mJoule energy in a 10 nanosecond pulse. This amounts to 1 MWatt peak power. The wavelength is then fixed at 1064 nm, resulting in a second-harmonic wavelength of 532 nm. For the earlier quest in nonlinear optics, *i.e.*, frequency doubling infrared diode lasers to the blue, this wavelength was not a limitation. The frequency-doubling material had to be transparent in the blue anyway. With the advent of direct lasing in the blue from GaN semiconductor lasers, this research shifted to electro-optic modulation at the near-infrared communications wavelengths. Therefore, transparency in the visible is not an issue anymore. To cope with this development, shifting the fundamental to longer wavelengths can be achieved through Raman shifting, or, more recently, with the aid of an optical parametric oscillator. Complete dispersion curves of the first hyperpolarizability are now accessible.

2.2 Paradigm shifts from nanosecond HRS

Although *para*-nitroaniline, the "*fruitfly*" of second-order nonlinear optics, has served as the benchmark for validating the HRS technique,[3] this nanosecond version of hyper-Rayleigh scattering has been instrumental in shifting the paradigm in organics for nonlinear optics from the neutral dipolar motif to the octopolar noncentrosymmetry.[5,6] The importance of correlations between nonlinear optical chromophores, as delivered by nature for bacteriorhodopsin in the purple membrane[7] was realized and optimized in artificial polymers.[8] It is instructive to notice how the protein bacteriorhodopsin cannot be measured by EFISHG either, since for a protein,

the amino acid residues carry charges. The protein would migrate in the field, rather than rotate. Even at its iso-electric point, where it would not migrate, since at that point, it carries no net charge; it would rotate through the interaction of the charges, rather than through that of the embedded dipole.

3. FEMTOSECOND HYPER-RAYLEIGH SCATTERING

With the advent of femtosecond pulse lasers, high peak power has become available from quasi-continuous-wave lasers. The generic laser type here is the Titanium^{3+}:sapphire laser, that is capable of generating 1 Watt of average power from an 80 MHz pulse train of 100 femtosecond pulses. The resulting peak power then amounts to 125 kWatt peak power. While this is still an order of magnitude lower than for the nanosecond laser, and for second-order nonlinear processes, this results in two orders of magnitude less signal, HRS experiments are possible. Advantage is taken from the much higher repetition rate, enhancing substantially the signal-to-noise ratio. The wavelength of the Titanium^{3+}:sapphire laser itself is 800 nm, but with the use of a femtosecond parametric oscillator, this wavelength can be shifted to 1300 or 1500 nm.

The experimental set-up for femtosecond hyper-Rayleigh scattering is in essence identical to the one for the nanosecond experiments.[9] Only the gated integrators for the nanosecond measurements are replaced by a chopper and a phase-sensitive detector in the high-frequency femtosecond experiment.

3.1 Advantages of femtosecond HRS

The use of femtosecond pulses in nonlinear optics has one obvious advantage: high peak power, necessary to observe the nonlinear effect, can be obtained from low total power in the pulse. This made samples with a low damage threshold amenable for HRS measurements. One example of such sample is amorphous polymer films. These films do not have the optical quality of single crystals. They are more susceptible to optical damage. With the femtosecond pulses, we have been able to perform HRS measurements on solid thin films, to study the orientational correlation between nonlinear optical chromophores in the film.[10-13]

A second advantage of the use of femtosecond is the much higher temporal resolution. Inasmuch as only scattering is measured, no temporal resolution was needed. However, with the design of new molecules along the guidelines offered by the wealth of experimental results obtained from nanosecond HRS, *e.g.*, longer conjugation paths between electron donor and acceptor, multi-photon fluorescence (MPF) was recognized as a second source of incoherent photons that could be detected in an HRS experiment. This second source enlarges the signal, resulting in an overestimation of the

retrieved hyperpolarizability value.[14] In wavelength space, no spectral discrimination can be made in general between HRS and MPF. At the second-harmonic wavelength, the signal can be comprised of both the narrow HRS and the broadband MPF. Measuring and subtracting the actual background is a time-consuming approach.[15] The most general way to discriminate between HRS and MPF should be based on the inherent difference in temporal properties between the immediate (nonlinear) scattering and the time-delayed (multi-photon) fluorescence.

This discrimination can be implemented directly in the time domain, with the use of very narrow and early time gates around the fundamental pulse.[16] Although the entire scattering is indeed collected in this time gate, and a large part of the total fluorescence intensity lies outside the early time gate, the exponentially decaying fluorescence contribution is still the largest in the early time gate.

3.2 Fluorescence suppression with femtosecond HRS

We have implemented the discrimination in the frequency domain. As is known in multifrequency phase fluorometry,[17] the time-delayed fluorescence acquires a phase shift φ and a reduction in amplitude M_F upon increasing the modulation frequency $\omega = 2\pi f$ of the sinusoidally modulated excitation. For a simple single exponential decay, this phase shift φ and demodulation M are given by:

$$\tan \varphi = \omega \tau \qquad \text{(Eq. 3)}$$

$$M = \frac{M_F}{M_{F,\omega=o}} = \frac{1}{\sqrt{1+\omega^2 \tau^2}} \qquad \text{(Eq. 4)}$$

In the time domain, the fluorescence acquires a phase shift and a demodulation, while the scattering does not suffer from a delay. In the frequency domain the phase shift always starts at 0° for low frequencies and tends to 90° in the limit for high frequencies, while the demodulation starts at 1 and tends to 0. However, for the immediate scattering, no phase shift and no demodulation is observed. This is exactly what is used in our approach: at very high modulation frequencies, the fluorescence is completely "demodulated" and does not contribute to the measurement signal, that is solely comprised of the not-demodulated scattering. Any HRS measurement at high modulation frequencies will reveal an inherent, fluorescence-free, hyperpolarizability value.

At first sight, it may seem difficult to get high-frequency modulated fundamental light, especially when still thinking about 10 Hz nanosecond lasers, as used in nanosecond HRS experiments. However, the repetitive pulse laser, as used in femtosecond HRS, naturally provides high frequencies: The harmonic content in the frequency domain of the very short pulse in the time domain extends to well in the GHz range.

The measurement now consists of determining, as a function of modulation frequency, the amplitude and phase of the signal at the second-

harmonic wavelength. For low frequencies, there might still be a multiphoton contribution, but for higher frequencies, this contribution will disappear. The measurement at a single frequency is performed analogous to heterodyne radio receiving. Since the photomultiplier is seeing all the frequencies at the same time (very much as a radio antenna is picking up all radio frequencies at the same time), we have to select a single measurement frequency by cross-correlation (tuning, or heterodyning). The output of the photomultiplier is the RF (radio frequency) input of the mixer, while the LO (local oscillator) input of the mixer is tuned to the harmonic at which we want to do the measurement. This is analogous to tuning the radio receiver to the frequency of the radio station. We apply a small offset in frequency, so that the cross-correlation product provides us with a low-frequency difference product. This product is then used to measure the amplitude and phase of the signal at the selected frequency very accurately with a low-frequency phase-sensitive detector.[18] Simultaneous fitting of the amplitude and phase as a function of modulation frequency allows the retrieval of the fluorescence lifetime, the fluorescence contribution and the fluorescence-free hyperpolarizability with good accuracy and precision.[19-21]

3.3 Design strategies for fluorescent ionic chromophores

A large number of fluorescent ionic species have been measured by this femtosecond hyper-Rayleigh scattering. Ionic crystals have the advantage of a higher number density than can be achieved by dispersed neutral chromophores in a polymer matrix. When the ionic crystal habit itself happens to be non-centrosymmetric, the problem of thermal and temporal relaxation of the non-centrosymmetry induced by poling the dipoles is also solved. In a polymer matrix, the required non-centrosymmetry has to be induced by orienting the dipolar guest in the polymeric host. This results in a thermodynamically non-stable situation that tends to relax to the isotropic, centrosymmetric, hence ineffective state. Ionic crystals from 4'-N,N-dimethylamino-4'-N'-methyl-4-stilbazolium tosylate have been reported with electro-optic coefficients up to 47 pm/V at 1.5 μm[22] and second-order nonlinear coefficients of 840 pm/V at 1.3 μm.[23] In-line intensity modulation in a thin-film waveguide of the crystal was observed up to 18 GHz and believed to extend beyond 100 GHz.[24] It is clear that incorporating an ionic dye in a non-centrosymmetric crystal is a very efficient way of assembling individual chromophores in a bulk structure. The individual chromophore itself, however, is not yet optimized: the conjugating bridge is short, the electron donating group is the classical dimethylamino group, and especially the potential of improving on the accepting part had not been explored. Recent synthetic efforts have improved the second-order nonlinear optical properties of stilbazolium dyes along two ways: elongation of the conjugating pathway, leaving the donor- and acceptor group unchanged;[25] and variation of the *N*-substitution pattern on the pyridinium nitrogen.[26]

Experimental studies of the effect of the *N*-substitution pattern on the pyridinium nitrogen in stilbazolium chromophores had shown previously the possibility of enhancing the first hyperpolarizability by *N*-arylation. The

values for the first hyperpolarizability of ruthenium(II) complexes with pyridinium ligands are larger for *N*-aryl pyridinium than for *N*-methyl pyridinium.[27] The ruthenium(II) centers are the electron donating moieties and the larger first hyperpolarizability values are the consequence of the larger electron-withdrawing capability of the *N*-aryl *versus* the *N*-alkyl group. The same design strategy was shown to hold for purely organic stilbazolium dyes.[27] The alkyl (methyl) group was substituted by phenyl; 2,4-dinitrophenyl; and 2-pyrimidyl. The corresponding compounds are labeled **_1**; **_2**; **_3**; and **_4**, *respectively*. A substantial red shift in the absorption spectrum was observed, in conjunction with an increase in the first hyperpolarizability. Also the subtle influence of the steric effect in the *N*-2,4-dinitrophenyl-pyridinium could be observed, resulting in a hyperpolarizability that is identical with the one for the *N*-phenylpyridinium.

Elongation of the conjugation pathway is since long one of the primary design rules for improving the nonlinear optical properties of organic molecules. It has experimentally been verified and is at the basis of the so-called transparency-nonlinearity trade-off, since the elongation of the conjugation reduces the energy level spacing between ground and excited states. This phenomenon is easily rationalized with the particle-in-the-box concept. The enhancement due to the longer conjugation pathway is not to be confounded with resonance enhancement. It is true that resonance enhancement is more likely with more extended molecules, since the measurement wavelength is normally in the infrared, and the wavelength of maximal absorption shifts closer to this wavelength in longer molecules. However, resonance enhancement can be accounted for. The resulting static hyperpolarizability, β_o, is still larger for the longer molecules.

For the first systematic study of the length effect of the hemicyanine dyes, higher homologues of the parent 4-{2-[4-(dimethylamino)phenyl]-ethenyl}-N-octadecylpyridiniumbromide, or 4-*N,N*-dimethylamino-4'-N'-octadecylstilbazolium had been synthetized. In these longer homologues, the ethenyl linkage had been replaced by a butadienylene, a hexatrienylene, an octatetraenylene, and finally a decapentaenylene link. The corresponding compounds are labeled **1_**; **2_**; **3_**; **4_**; and **5_**. From this first study, it has been concluded that elongation is indeed a viable strategy to enhance the first hyperpolarizability.[25] Up to the hexatrienylene linkage, good agreement between the experimental results from hyper-Rayleigh scattering and the theoretical results from MOPAC/INDO-CI/SOS calculations had been obtained. For the longer homologues, a discrepancy between experiment and theory was ascribed due to the inadequate fully optimized (*all*-trans) configuration for these longer molecules with a more probable *single*-cis configuration.

Based on these results for the ethenylene, butadienelyne and hexatrienylene linkage, we have varied the substitution pattern in combination with the butadienylene linkage. The additional compounds that were available are identified as **21**; **22**; **23** and **24**. The experimental values for the first hyperpolarizabilities have all been determined by femtosecond hyper-Rayleigh scattering with high-frequency demodulation of the two-photon fluorescence, both at 800 nm and at 1300 nm. All the stilbazolium

chromophores have been shown to exhibit this additional source of incoherent photons that could lead to an overestimation of the first hyperpolarizability value. Classical hyper-Rayleigh scattering with nanosecond pulses and time gating would not be capable of distinguishing between the immediate scattering and the time-delayed fluorescence, since a typical fluorescence lifetime is of the order of only a few nanoseconds.

3.4 Experimental results versus limiting theory

We have now critically analyzed the resulting first hyperpolarizabilities against a recent limiting theory for static hyperpolarizabilities, specifically derived for the diagonal hyperpolarizability tensor elements in the off-resonance regime.[28,29] The sum-rule-restricted (*SR*) three-level model results in a two-level-limit (*2L*) for the hyperpolarizabilities, depending solely on the reduced number N of electrons (with charge e and mass m) and the transition energy E_{10} between ground and first excited state. This reduced number of electrons, *i.e.,* only 2 electrons per double or triple bond in the conjugated π-electron system, has been shown earlier to reproduce correct linear absorption spectra and to provide the largest susceptibilities near the theoretical maximum limit. The limit for the first hyperpolarizability, β, is, for dressed (*) hyperpolarizabilities (*i.e*., the hyperpolarizability value as measured in a solvent with given refractive index n), given by Eq. 5:

$$\beta_{2L}^{*SR} \leq \sqrt[4]{3}\left(\frac{n^2+2}{3}\right)^3\left(\frac{e}{\sqrt{m}}\right)^3\frac{N^{3/2}}{E_{10}^{7/2}} \qquad \text{(Eq. 5)}$$

This theory was found to be in agreement with a large set of experimental dressed hyperpolarizability data. For the sake of our confrontation, this dressed hyperpolarizability in the off-resonance regime, β_{2L}^{*SR}, is identical to the static hyperpolarizability value measured in solution, β_0.[30] The same theory was recently shown to be very useful in pointing to possible systematic errors in the experiment.[30] The nature of a limiting theory provides a maximum value for the experimental result. A larger experimental value means an overestimate. One possible cause of overestimation of first hyperpolarizability values is multiphoton fluorescence. An experimental result larger than the theoretical limit is a strong indication of the presence of this systematic error.

In Fig. 3, we have plotted the so-called electron-number related (ENR) hyperpolarizability values, $\beta_0/N^{3/2}$ (symbols) to be compared with the limiting theory (line). We want to evaluate the resulting trend in the obtained averages in the light of the trend in the limiting curve. It is seen that the same trend is observed for both strategies: methyl < phenyl < 2,4-dinitrophenyl < 2-pyrimidyl for the two linkages (**_1** < **_2** < **_3** < **_4**); and ethenylene < butadienylene (**1_** < **2_**) for all four *N*-substitutions. This shows the independence of both strategies. It is thus clear that the largest value for $\beta_0/N^{3/2}$ is only obtained experimentally by combining the longest (butadienylene) linkage with the best (2-pyrimidine) *N*-aryl substitution (in **24**).

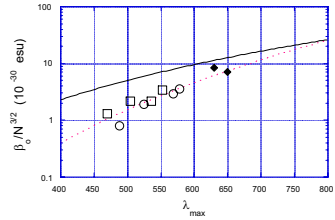

Figure 3. Electron-number related (ENR) static hyperpolarizability values, $\beta_0/N^{3/2}$ (symbols) as a function of wavelength of maximal absorption, λ_{max}, to be compared with the limiting theory (solid line).

In Fig. 3, the values for the electron-number-related static hyperpolarizability $\beta_0/N^{3/2}$ obtained for these ionic chromophores (open symbols) have been compared with the same values for the best dipolar, neutral chromophores reported so far (diamonds).[31,32] These chromophores, with a reduced number of electrons N equal to 20, have dynamic first hyperpolarizabilities approaching 3000 x 10^{-30} esu at a fundamental wavelength of 1.064 μm, in combination with a charge transfer (CT) absorption band around 650 nm. It is clear that at this point, the neutral NLOphores surpass the available ionic stilbazolium chromophores for second-order NLO applications, however, only at the molecular level. The chromophore number density that can be achieved in ionic crystals is larger than the optimal chromophore density in guest-host systems.

4. BACTERIORHODOPSIN AS NONLINEAR PHOTONIC CRYSTAL

Engineered materials with a periodicity in their linear optical properties are known as photonic bandgap materials, often also called photonic crystals.[33,34] The periodicity in optical properties results in a range of forbidden energies for a photon: Photons with the wavelength in the corresponding photonic bandgap cannot propagate through the material. The analogy with the band structure for electrons in a periodic potential is instructive. The effect has interesting applications in linear photonics, such as bending of light,[35] guiding of light in air,[36] photon localization for reduced-threshold lasing and, eventually, lasing-without threshold.[37]

Recently, a second-order nonlinear photonic crystal has been realized.[38] In this nonlinear optical bandgap material, there is a periodicity in the nonlinear optical properties of the engineered material. With this definition, a periodically poled second-order nonlinear optical material could be called a nonlinear photonic crystal. However, its linear optical properties do not show a periodicity, except for the (small and useless for birefringent phase-matching) poling-induced birefringence. Here, the material is the same in the complete structure. It is only periodically made into a non-centrosymmetric structure for second-order nonlinear and phase-matching

purposes. Therefore, the phase-matching condition is still determined by the refractive index of the nonlinear material. The nonlinear photonic crystal, however, has nonlinear optical material localized on the surface of optically linear spheres, constituting the photonic crystal. This periodicity has a high contrast ratio: the optical nonlinearity is either zero, where there is no nonlinear material (in the spheres), or high, in the nonlinear moiety (malachite green molecules, coated on the spheres). There is no nonlinear material in between crystal planes. Hence, phase matching is from plane to plane. The separation between the planes can be tuned by concentrating the suspension of spheres. The necessary and sufficient condition for a nonlinear photonic bandgap material is, hence, the decoupling of the optical nonlinearity of the harmonic generating material from the phase matching mechanism, determined by the linear optical properties of the linear material in between.

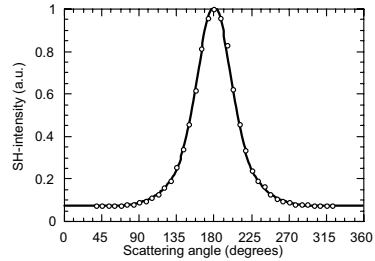

Figure 4. Open circles, angular dependence of the second-order scattered light intensity (hyper-Rayleigh scattering from 1064 to 532 nm) for a suspension of purple membrane patches of bacteriorhodopsin before any solubilization has taken place. Solid curve: best fit to the data by combining the nonlinear hyperpolarizability of retinal with the linear refractive index of the *apo*-protein.

Time-dependent[39] and angular-resolved[40] nonlinear light scattering experiments have been performed on aqueous suspensions of purple membrane of *Halobacterium salinarium* during solubilization. The angular dependence (See Fig. 4) can be explained by combining the optical nonlinearity of the small retinal moiety with the linear refractive index of the large protein matrix of bacteriorhodopsin. We obtain excellent agreement between experiment (open circles) en fitting (solid line) when taking as coherence length for the scattering in the forward (180°) direction 200 nm, and by using a value of 1.5 for the refractive index of the *apo*-protein.[41] The 200 nm is in excellent agreement with the purple membrane patch area of 39,000 nm^2,[42] as determined from Atomic Force Microscopy. The value of 1.5 for the refractive index is clearly a value for the apo-protein without the retinal: the refractive index for retinal is between 1.8 and 2.1 at the Sodium D line.[43]

Therefore, (nonlinear) photonic crystal properties can be attributed to purple membrane patches of bacteriorhodopsin. This is an important finding, since this natural material exhibits photonic bandgap properties without careful and costly engineering, but through self-assembly. In

addition, the methodology of analyzing the angular dependence of second-order nonlinearly scattered light proves to be a fast screening technique for nonlinear photonic bandgap properties of engineered materials in solution.

5. CONCLUSIONS AND PERSPECTIVES

We have exemplified current strategies for imparting second-order nonlinear optical properties to organic molecules, and for creating photonic crystals with specifically tailored defect modes. We have done so from an instrumentalist's point of view, by describing our experimental measurement capabilities for the determination of the linear and nonlinear optical properties of these newly designed molecules and engineered structures. At the molecular level, we have been able to identify design guidelines for enhancing the molecular second-order nonlinear response. These guidelines have been shown to be independently applicable, and, when combined, to lead to a theoretically predicted upper limit. We have shown that the natural protein bacteriorhodopsin can be described as a nonlinear photonic crystal.

ACKNOWLEDGEMENTS

This research was supported by research grants from the FWO-V (G. 0216. 02 and G.0201.02), the University of Leuven (GOA/2000/03) and from the Belgian government (IUAP V/3).

REFERENCES

1. K. Clays, A. Persoons, J. Chem. Phys., 113, 9706-9713 (2000)
2. K. Clays, A. Persoons, L. De Maeyer (1994) In: Evans M, Kielich S (eds) Modern Nonlinear Optics, Part 3 (Advances in Chemical Physics), vol 85. John Wiley & Sons, Inc., New York p 455-498
3. K. Clays, A. Persoons, Phys. Rev. Lett., 66, 2980-2983 (1991)
4. K. Clays, A. Persoons, Rev. Sci. Instrum., 63, 3285-3289 (1992)
5. T. Verbiest, K. Clays, A. Persoons, F. Meyers, J.-L. Brédas, Opt. Lett., 18, 525-527 (1993)
6. T. Verbiest, K. Clays, C. Samyn, J. Wolff, D. Reinhoudt, A. Persoons, J. Am. Chem. Soc., 116, 9320-9323 (1994)
7. K. Clays, E. Hendrickx, M. Triest, T. Verbiest, A. Persoons, C. Dehu, J.-L. Brédas, Science, 262, 1419-1422 (1993)
8. M. Kauranen, T. Verbiest, C. Boutton, M. N. Teerenstra, K. Clays, A. J. Schouten, R. J. M. Nolte, A. Persoons, Science, 270, 966-969 (1995)

9. K. Clays, A. Persoons, Rev. Sci. Instrum., 65, 2190-2194 (1994)
10. K. Clays, M. Wu, A. Persoons, J. Nonlin. Opt. Phys. Mat., 5, 59-71 (1996)
11. G. Olbrechts, E. J. H. Put, D. V. Steenwinckel, K. Clays, A. Persoons, C. Samyn, N. Matsuda, J. Opt. Soc. Am. B, 15, 369-378 (1998)
12. G. Olbrechts, E. J. H. Put, K. Clays, A. Persoons, N. Matsuda, Chem. Phys. Lett., 253, 135-140 (1996)
13. N. Matsuda, G. Olbrechts, E. J. H. Put, K. Clays, A. Persoons, Appl. Phys. Lett., 69, 4145-4147 (1996)
14. M. C. Flipse, R. de Jonge, R. H. Woudenberg, A. W. Marsman, C. A. van Walree, L. W. Jenneskens, Chem. Phys. Lett., 245, 297-303 (1995)
15. N. W. Song, T.-I. Kang, S. C. Jeoung, S.-J. Jeon, B. R. Cho, D. Kim, Chem. Phys. Lett., 261, 307-312 (1996)
16. O. F. J. Noordman, N. F. v. Hulst, Chem. Phys. Lett., 253, 145-150 (1996)
17. K. Clays, J. Jannes, Y. Engelborghs, A. Persoons, J. Phys.E: Sci. Instrum., 22, 297-305 (1989)
18. G. Olbrechts, R. Strobbe, K. Clays, A. Persoons, Rev. Sci. Instrum., 69, 2233-2241 (1998)
19. G. Olbrechts, K. Clays, A. Persoons, J. Opt. Soc. Am. B, 17, 1867-1873 (2000)
20. K. Wostyn, G. Olbrechts, K. Clays, A. Persoons, A. Watanabe, K. Nogi, X.-M. Duan, S. Okada, H. Oikawa, H. Nakanishi, H. Vogel, D. Beljonne, J.-L. Brédas, Nonlinear Opt., 25, 353-358 (2000)
21. K. Wostyn, K. Binnemans, K. Clays, A. Persoons, J. Phys. Chem. B, 105, 5169-5173 (2001)
22. F. Pan, G. Knopfle, C. Bosshard, S. Follonier, R. Spreiter, M. S. Wong, P. Gunther, Appl. Phys. Lett., 69, 13-15 (1996)
23. C. Bosshard, G. Knopfle, P. Pretre, S. Follonier, C. Serbutoviez, P. Gunter, Opt. Eng., 34, 1951-1960 (1995)
24. F. Pan, K. McCallion, M. Chiappetta, Appl. Phys. Lett., 74, 492-494 (1999)
25. K. Clays, K. Wostyn, G. Olbrechts, A. Persoons, A. Watanabe, K. Nogi, X.-M. Duan, S. Okada, H. Oikawa, H. Nakanishi, D. Beljonne, H. Vogel, J.-L. Brédas, J. Opt. Soc. Am. B, 17, 256-265 (2000)
26. B. J. Coe, J. A. Harris, I. Asselberghs, K. Clays, G. Olbrechts, A. Persoons, J. T. Hupp, R. C. Johnson, S. J. Coles, M. B. Hursthouse, K. Nakatani, Adv. Func. Mat., 12, 110-116 (2001)
27. B. J. Coe, J. A. Harris, K. Clays, A. Persoons, K. Wostyn, B. S. Brunschwig, Chem. Comm., 2001, 1548-1549 (2001)
28. M. G. Kuzyk, Phys. Rev. Lett., 85, 1218-1221 (2000)
29. M. G. Kuzyk, Opt. Lett., 25, 1183-1185 (2000)
30. K. Clays, Opt. Lett., 26, 1699-1701 (2001)
31. L. R. Dalton, W. H. Steier, B. H. Robinson, C. Zhang, A. Ren, S. Garner, A. Chen, T. Londergan, L. Irwin, B. Carlson, L. Fifield, G. Phelan, C. Kincaid, J. Amend, A. Jen, J. Mater. Chem., 9, 1905-1920 (1999)
32. G. H. Robinson, L. R. Dalton, A. W. Harper, A. Ren, F. Wang, C. Zhang, G. Todorova, M. Lee, R. Aniszfeld, S. Garner, A. Chen, W. H. Steier, S.

Houbrechts, A. Persoons, I. Ledoux, J. Zyss, A. K. Y. Jen, Chem. Phys., 245, 35-50 (1999)
33. J. D. Joannopoulos, P. R. Villeneuve, S. Fan, Nature, 386, 143-149 (1997)
34. J. S. Foresi, P. R. Villeneuve, J. Ferrera, E. R. Thoen, G. Steinmeyer, S. Fan, J. D. Joannopoulos, L. C. Kimerling, H. I. Smith, E. I. Ippen, Nature, 390, 143-145 (1997)
35. S. E. Barkou, J. Broeng, A. Bjarklev, Opt. Lett., 24, 46-48 (1999)
36. J. C. Knight, J. Broeng, T. A. Birks, P. S. J. Russell, Science, 282, 1476-1478 (1998)
37. O. Painter, R. K. Lee, A. Scherer, A. Yariv, J. D. O'Brien, P. D. Dapkus, I. Kim, Science, 284, 1819-1821 (1999)
38. J. Martorell, R. Vilaseca, R. Corbalán, Appl. Phys. Lett., 70, 702-704 (1997)
39. E. Hendrickx, T. Verbiest, K. Clays, A. Persoons, Proc. Soc. Photo-Opt. Instrum. Eng., 1853, 233-238 (1993)
40. K. Clays, S. V. Elshocht, A. Persoons, Opt. & Phot. News, 11, 31 (2000)
41. K. Clays, S. V. Elshocht, M. Chi, E. Lepoudre, A. Persoons, J. Opt. Soc. Am. B, 18, 1474-1482 (2001)
42. E. Hendrickx, A. Vinckier, K. Clays, A. Persoons, J. Phys. Chem., 100, 19672-19680 (1996)
43. A. B. Myers, R. B. Birge, J. Am. Chem. Soc., 103, 1881-1885 (1981)

DEVELOPMENT OF TOMOGRAPHY USING FEMTOSECOND INFRARED LASER : IMAGING OF BIOLOGICAL TISSUES

Gediminas JONUSAUSKAS, Emmanuel ABRAHAM, Edouard BORDENAVE, Jean OBERLE
Centre de Physique Moléculaire Optique et Hertzienne
Bordeaux 1 University, 351 Cours de la Libération, 33405 Talence, France
g.jonusauskas@cpmoh.u-bordeaux1.fr

Abstract Our recent developments of high speed imaging of biological tissues using optical radiation are presented in this paper. Especially, coherence optical gating (optical coherence tomography) and temporal optical gating (using femtosecond laser source) are able to provide video rate imaging of thick highly scattering biological samples with a transversal and depth resolution in the micrometer range.

Keywords: coherence gating, temporal gating, femtosecond laser, real-time imaging, biological imaging.

1. Introduction

Optical imaging of biological tissues is a real challenge due to the predominance of light scattering as incident photons propagate into the tissues. To minimize this problem, near-infrared wavelengths have to be used to reduce the scattering process and increase the penetration depth. Nevertheless, optical imaging of biological tissues by simple transillumination, as performed by X-ray radiology, is really inadequate because photons will experience multiscattering during the propagation through tick tissues. After a propagation of a few millimeters, the amount of photons corresponding to the incident direction will be negligible. Moreover, the photons will progressively lose their spatial coherence reducing drastically image contrast. The alternative to transillumination imaging consists of backscattering imaging. In this configuration, light is detected after round trip propagation into the sample limiting the maximum penetration depth to a few millimeters depending on the optical properties of the scattering tissues. To reduce the effect of backscattered light, a large number of techniques have been developed by selectively gating the fraction of the illuminating light which is unscattered by the tissues. These so-called "ballistic" pho-

E. C. Faulques et al. (eds.), Spectroscopy of Emerging Materials, 395–406.

tons are simply retroreflected from the internal sub-structures of the sample. For instance, in confocal microscopy, a spatial gate is performed by use of a pinhole aperture. However, the technique is limited to the first few hundreds micrometers of depth in highly scattering tissues such as the human skin. For deeper imaging in highly scattering materials, other techniques have to be developed to improve the "spatial gating" operated by confocal microscopy. One alternative is to perform "coherence gating", taking advantage of the short coherence length of a broadband light source. This technique, called "Optical Coherence Tomography" (OCT) is an effective interferometric technique, which can produce high resolution cross-sectional images of biological structures [1, 2]. The method is based on the measurement of the interferometric cross-correlation of the light backscattered from the sample with the light retro-reflected from a reference mirror, as with a conventional Michelson interferometer. Another alternative is to perform "time gating" or "temporal gating" to discriminate between the early-arriving backreflected (ballistic) photons and the time-delayed backscattered photons [3]. This method, generally based on nonlinear optical processes, requires a femtosecond laser source to image the microstructure of the tissues with a micrometer depth resolution. Whatever the selected imaging device, a fundamental feature concerns the final image acquisition speed. For *in vivo* imaging, video rate image acquisition (~ 25 Hz) is necessary to avoid any degradation of the image resolution due to the unintentional movements of the living sample. Considering a typical image size composed by 640×480 pixels, it means that the pixel acquisition rate has to be around 8 Mpixels per second. Consequently, specific apparatus have to be developed to reach this extremely high image acquisition speed. In this paper, some recent developments of video rate coherence and temporal optical gating will be presented, focusing on the performances of the devices concerning the high speed pixel acquisition rate.

2. COHERENCE OPTICAL GATING

With OCT, a high power optical source is required to provide adequate illumination of the sample in a short amount of time. Also, a high speed scanning delay line is necessary in the reference arm of the interferometer in order to produce a high speed depth image acquisition. Finally, computation has to be optimized to acquire, process and display the images in real time (~ 25 frames per second).

2.1 Scanning techniques

Standard OCT techniques require a heterodyne detection equipment to detect the small variations of the interference fringe intensity of the light source that has been focused and backscattered from the sample. Consequently, owing to the strong focalization of the light source onto the sample, this technique allows

high resolution transversal imaging. Recently, a lateral and depth resolution of the order of the micrometer has been obtained by using a superluminescent Ti:sapphire crystal as a light source [4]. However, besides the depth Z-scan (Z being the optical axis), standard OCT requires two lateral X- and Y-scans over the sample surface to reconstruct the sample volume. The fastest scanning OCT devices are able to get an approximately 2 Mpixels/s acquisition rate which corresponds to 6.5 images per second with a standard image size of 640×480 pixels. The sensitivity (signal-to-noise ratio) can reach 100 dB owing to the optical heterodyne detection limited by shot noise [5].

2.2 Wide field OCT

One alternative to standard scanning OCT is to perform so-called "wide-field OCT" or "parallel OCT", which does not require any lateral (X- or Y-) scans over the sample surface. The idea, derived from the principle of coherence radar [6] and white light interferometry, is to image an entire surface of the sample, with a collimated beam, instead of a single point as in the standard scanning configuration. By using a two-dimensional detector and recording the interferometric image directly, the lateral scanning of the light source (or sample) can be avoided. Obviously, the key parameter to perform wide-field OCT is the sensor used to detect the interference fringe pattern characterizing the OCT signal. Salathé *et al.* have proposed to use a silicon detector with a 2D array of pixels that performs heterodyne detection at each pixel in parallel [7, 8]. They demonstrated a fast 3D OCT imaging with a nearly 5 Mpixels/s acquisition speed (58×58×58 voxels imaged at 25 Hz) but with a limited sensitivity of 76 dB. However, comparing the performances with traditional 2D OCT imaging, the acquisition speed drops to 84100 pixels/s (58×58 pixels at 25 frames per second), which is far below the possibilities of standard scanning OCT. Another alternative for wide-field OCT consists to use a CCD camera as a detection device even if in that case the sensitivity of the system is strongly limited by the DC light level inherent in the signal that reaches the detector. This approach has been first used by Boccara *et al.* [9]. The authors applied a lock-in detection technique to extract the magnitudes of the modulated signals from each pixel of the CCD sensor. A high acquisition rate of 3.3 Mpixels/s (256×256 pixels at 50 Hz) has recently been obtained but with a limited sensitivity [10]. To reach an acceptable sensitivity (80 dB), a 1 s exposure time has been employed corresponding to 65500 pixels/s in that case. Nevertheless, by use of a broadband white-light thermal lamp, the authors obtained an excellent axial resolution of about 1 μm inside biological tissues. Finally, in our group, we proposed another wide-field OCT configuration (Figure 1) which uses a femtosecond Cr^{4+}:forsterite oscillator, generating pulses of 30 fs at 1220 nm, and an infrared CCD camera without any heterodyne detection [11]. A tradi-

tional phase-shifting interferometric operation is performed by recording four images, corresponding to optical phase shifts of 0, $\pi/2$, π and $3\pi/2$ between the reference and the probe lights. The phase shifts are induced by the displacement of the reference mirror installed on a piezoelectric translation stage (PZT). The final reconstructed image is obtained by using the expression :

$$I = 2\frac{\sqrt{\left[I(0) - I(\pi)\right]^2 + \left[I(\pi/2) - I(3\pi/2)\right]^2}}{I(0) + I(\pi/2) + I(\pi) + I(3\pi/2)} \tag{1}$$

where $I(0)$, $I(\pi/2)$, $I(\pi)$, and $I(3\pi/2)$ are the intensities of the interferometric images corresponding to the four PZT positions. This image corresponds to the XY transversal image (so-called "*en face* image") of the sample at a depth Z from the surface depending on the length difference between the reference and the probe arms. The sensitivity of the detection is approximately 80 dB (with an accumulation of 5 images), mainly limited by the electronic noise of the camera and the 12 bits image acquisition (72 dB dynamic range). Concerning the acquisition rate, an "*en face* image" (320×240 pixels) is obtained at approximately 4 Hz, corresponding to an acquisition rate of only 307000 pixels/s, which is slower than the standard scanning OCT. Since the principal limiting factor is the number of pixels of the InGaAs camera, the use of a higher resolution camera would strongly increase the acquisition speed of the instrument. For example, with a 1024×1024 pixels camera, an acquisition speed of 4.2 Mpixels/s could be reached. To perform the whole 3D reconstruction of the sample, the sample itself is installed on a computer controlled translation stage for Z scanning. After simple computation, we are able to visualize all the *en face* images in order to build a stack of XY transversal images. From this stack, owing to the 320×240 pixel number of the *en face* images, we can get 320 XZ and 240 YZ longitudinal slices of the object.

Such a longitudinal slice is represented in Figure 2, representing a mouse ear. The lateral resolution is about 35 μm (limited by the numerical aperture of imaging lens and the pixel size of our camera) and the depth resolution is 5 μm limited by the laser pulse duration. The central black band corresponds to the cartilage (C) of the ear. A double high intensity band, corresponding to the dense conjunctive capsule (cc) surrounds this region. Symmetrically to this region, two high intensity bands are recognizable, corresponding to the superficial epidermis (E). In the top right hand corner of the image, a portion of the stratum corneum is obviously seen to be in a desquamative process. Last, spots of high intensity and oblong areas of low intensity can be observed in the dermis (D). The first may be attributed to scattering structures usually found in the dermis, such as blood vessels or extra cellular matrix. With a stack of transversal slices, using a volume rendering software, we are also able to reconstruct the entire volume of the mouse ear. Moreover, this 3D image allows

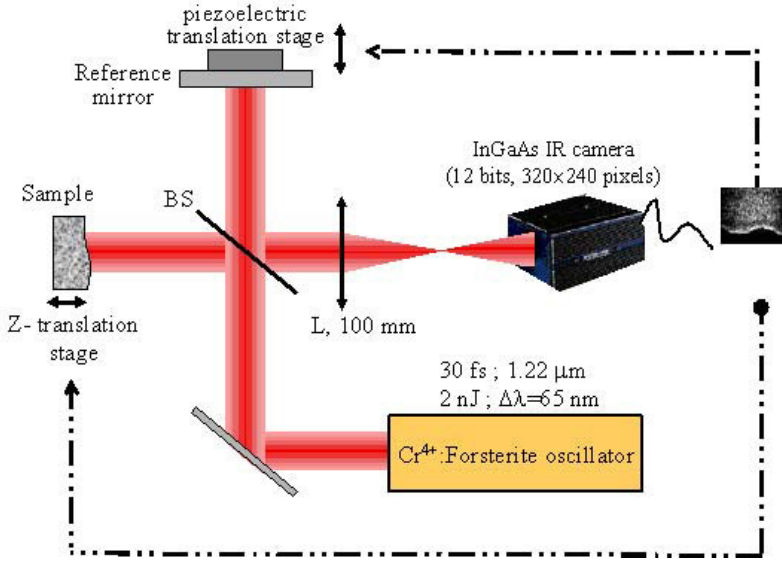

Figure 1. The set-up of wide field OCT experiment.

to clearly detail the surface of the mouse ear (many hair), which illustrates the high longitudinal resolution of the imaging system and its potential application for 3D imaging.

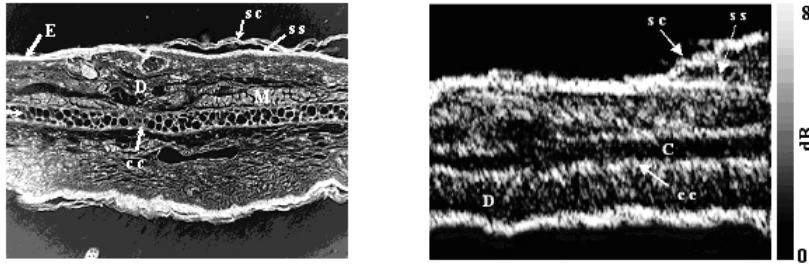

Figure 2. Images of a mouse ear : (left) HE histology ; (right) Full-field OCT image of nearly the same area as the HE histology. The image size is 700 μm $\times$ 930 μm and 750 μm $\times$ 1000 μm for (left) and (right) respectively. See text for other definitions.

3. TEMPORAL OPTICAL GATING

One alternative to real-time coherence gating (OCT) consists of temporal optical gating of the light backreflected by the sample, as explained in the introduction [3]. The system developed in our group employs a femtosecond sum-frequency generation in a non-linear crystal between a strong pump pulse and the backscattered probe pulse. In that case, the nonlinear interaction between the pump pulse at optical frequency ω and the probe pulse at the same frequency generates a sum-frequency signal at frequency 2ω which corresponds to the cross-correlation between the pump and the probe pulses. Using the sum-frequency generation in the nonlinear crystal, the imaging system can provide in a single laser shot procedure a transversal [16] or longitudinal [12, 13] image of the sample (acting as an "optical echograph" in the former case) depending on the configurations of beams.

3.1 Transversal imaging

As shown in Figure 3, the experimental setup consists of a amplified femtosecond Cr:forsterite laser system associated with an imaging correlator. The time- gating imaging system consists of a traditional nonlinear correlator. Briefly, the incident beam is divided by a polarizing beam splitter (PBS) into two perpendicularly polarized beams: a reference beam, sent to an optical delay line, and a probe beam. The polarization of the probe beam, which is reflected from the object, and that of the reference beam are both rotated by 90° by a double passage through quarter-wave plates, so that the beams merge again at the PBS and are directed onto a nonlinear potassium titanyl phosphate crystal (KTP, 1 mm thickness), where type II sum-frequency generation occurs. Therefore, the intensity of the second harmonic signal at 610 nm corresponds to the cross-correlation function between the perpendicularly polarized reference and reflected probe pulses. This means that the reference pulse gates the light which is backscattered from the object with a spatial window of about 20 μm related to the laser pulse duration. With this technique, it is thus possible to separate the ballistic light from the scattered light and perform time-gating imaging. The imaging configuration consists of a first lens (L1, 50 mm) which images the object in the nonlinear crystal plane (4F configuration, magnification 1:1) and a second lens (L2, 65 mm) transfers the intermediate image onto a standard 640×480 pixel CCD camera after filtering the remaining IR light. The camera is connected to a computer for image acquisition. The object area illuminated by the incident collimated probe beam is related to the 3 mm beam diameter at the output of the laser source. Therefore, our setup consists of macroscopic imaging as compared to the usual microscopic imaging used in standard OCT configuration. With this technique it is possible to obtain a complete 2D image in real-time which corresponds to the plane (or depth) of a single sliced object,

along with the exact location of this slice. The image acquisition rate is 7.7 Mpixels/s, which is faster than the previously described OCT devices. Moreover, the optical setup makes it possible to image at laser shot repetition rate. In our case, a 1 kHz acquisition rate could be achieved if the CCD camera is well adapted. This would correspond to an acquisition rate of more than 300 Mpixels/s, giving the opportunity to average 40 images in keeping an acquisition of 25 frames per second. To test the imaging characteristics of our method, we immersed a U.S. Air Force test pattern into 1% diluted Intralipid solution. The maximum transverse resolution of the imaging system is $\sim 20\ \mu$m and the chart has been imaged up to an attenuation of 15 mean free paths ($I/I_0 \approx 10^{6.5}$ or 130 dB) in the solution.

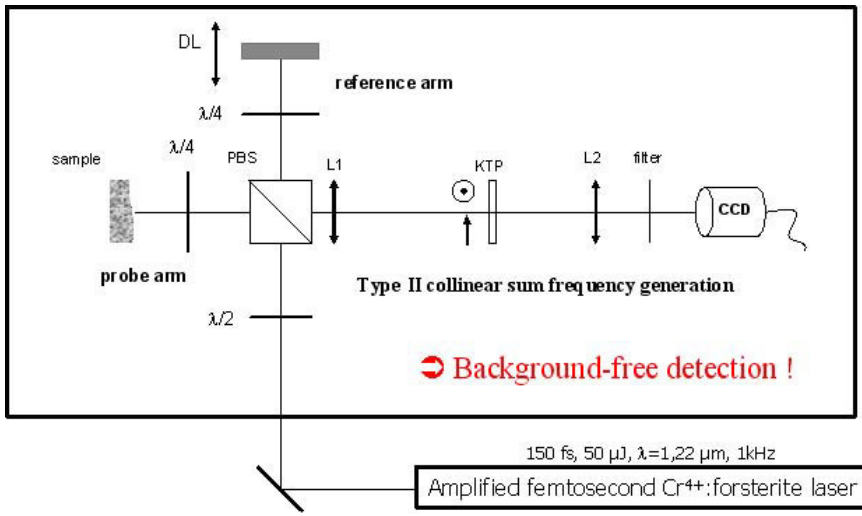

Figure 3. The set-up of transversal imaging using sum frequency generation.

3.2 Longitudinal imaging : "Optical echograph"

The system is based on the ability of a classical single-shot autocorrelator, widely used to measure the duration of picosecond and femtosecond laser pulses, to operate a time-to-space conversion [14]. After being reflected by a biological sample, a probe pulse supports a temporal stretching due to the different internal reflections occurring at different depths. In the nonlinear crystal, if the backscattered probe pulse interacts with the pump pulse in a non-collinear configuration, the temporal stretching can be converted into a spatial stretch-

ing. Figure 4 illustrates the non-collinear interaction in the nonlinear crystal between the pump pulse and two probe pulses delayed by the delay time $\Delta\tau$, symbolizing two reflections of the incident probe pulse from the sample at two different depths. As a result, two sum-frequency signals are generated in the direction corresponding to the phase matching conditions. These two signals are translated in space by a quantity Δz given by:

$$\Delta z = \frac{2c}{n_0(\lambda)\sin(\Phi/2)}\Delta\tau \tag{2}$$

where $n_0(\lambda)$ is for the refractive index of the nonlinear crystal at the wavelength λ, c is for the speed of the light in vacuum and Φ is for the angle between the two incident pulses on the crystal. This formula establishes the time-to-space conversion operated by the method. The direction of the spatial shift (z corresponds to the first coordinate (Z-axis) of the longitudinal image obtained by a CCD camera collecting the sum-frequency light emerging from the crystal. This coordinate simply represents the depth of the sample. Along this coordinate, the sample surface and the internal sub-structures can be visualized.

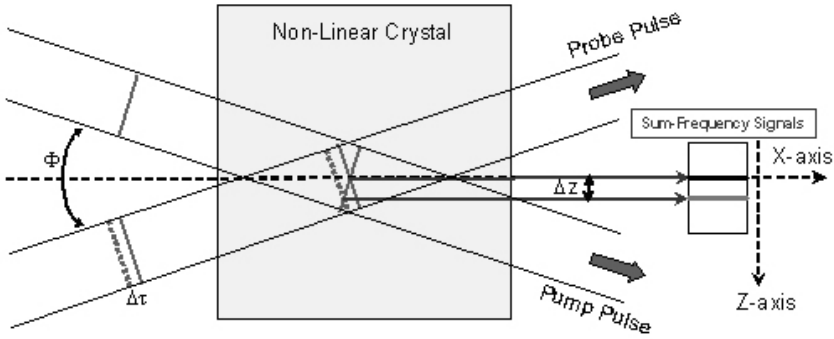

Figure 4. Principle of the optical echograph. Non-collinear interaction between the pump and probe pulses (frequency ω) into a non-linear crystal for sum-frequency generation at frequency 2ω.

The acquisition of the second coordinate of the longitudinal image is performed by illuminating the sample by use of a cylindrical lens (CL1, f = 80 mm) as is shown in the Figure 5. The light source is an amplified Ti:sapphire laser emitting pulses as short as 30 fs with a central wavelength at 800 nm and a pulse repetition rate of 1 kHz. It means that a light line is formed at the sample surface. The direction of this line represents the second coordinate (X- axis) of the 2D longitudinal image acquired by the CCD camera. To get this image, the illuminated area of the sample is imaged by the spherical

lens (L1, f = 100 mm) and cylindrical lens (CL2, f = 120 mm) onto a 1 mm BBO crystal. The pump pulse passes through an optical delay line (DL) and is combined with the backscattered probe pulse in the crystal where the previously described non- collinear sum-frequency generation is operated between the backscattered probe pulse and a pump pulse. Finally, a second spherical lens (L2, f = 100 mm) is used to collect the sum-frequency light at 400 nm and to image the crystal plane onto a standard CCD camera (640×480 pixels, 25 frames/s). Consequently, the image acquisition rate is 7.7 Mpixels/s, which is faster than the previously described OCT devices. Moreover, the optical setup makes it possible to image at laser shot repetition rate. In our case, a 1 kHz acquisition rate could be achieved if the CCD camera is well adapted. This would correspond to an acquisition rate of more than 300 Mpixels/s, giving the opportunity to average 40 images in keeping an acquisition of 25 frames per second.

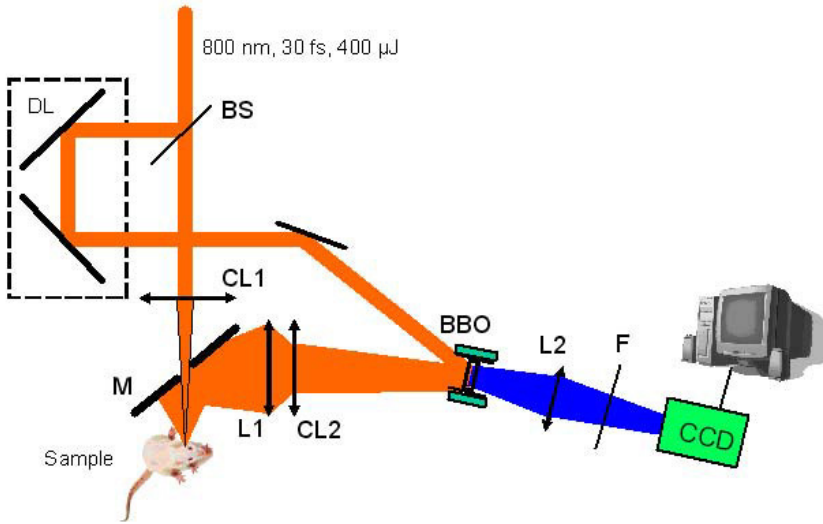

Figure 5. The set-up of longitudinal imaging using sum frequency generation.

First, we imaged a mouse ear to test the depth resolution (the sample is 330 μm thin) (Figure 6). The mouse ear is imaged a few hours after the biopsy and is put directly on the focalization line of the cylindrical lens CL1. By moving the ear, we can see the corresponding longitudinal slice for each position (and at video rate). One of these images is represented in the right of Figure 6. To allow a comparison, left picture in Figure 6 shows a hematoxylin-eosin stained histology (HE) obtain by photonic microscopy of the same species of mouse. Several constitutive tissues can be determined as well as the thickness

of the different layers. For example, the black band in the middle of the sample corresponds to the cartilage (C) and it has a thickness of about 50 μm. A double band with a strong signal surrounding this region is the conjunctive capsule (cc). Two high intensity bands, corresponding to the superficial epidermis (E) can be observed. Unfortunately, the longitudinal resolution does not allow to separate the different layers constituting the epidermis (stratum corneum (sc), stratum spinosum (ss)). However, the stratum spinosum of the mouse ear epidermis is very thin, since it consists of only one or two cellular layers. The optical echograph has been tested for imaging *in vivo* biological tissues. In dermatology, for example, it is of primary importance to develop non-invasive methods to study the different layers of human skin from the stratum corneum up to the underlying dermis. Also, detection of tumors such as malignant melanoma, have justified many efforts.

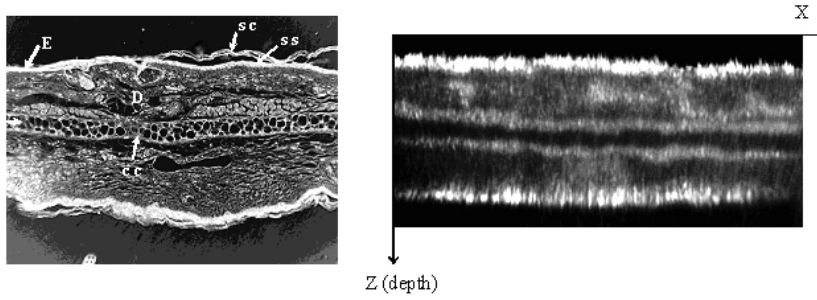

Figure 6. Imaging of a mouse ear : left) HE histology of a mouse ear, the image size is (0.93×0.7) mm^2 ; right) Longitudinal image of a mouse ear. Image size (1.2×0.5) mm^2. E: epidermis, sc: stratum corneum, D: dermis, cc: conjunctive capsule, C: cartilage.

A photograph obtained by photonic microscopy of hematoxylin-eosin stained histology (HE) reveals the different constitutive tissues of an *ex vivo* human skin (Figure 7(a)). The epidermis (E), with the stratum corneum (sc) at the interface air-sample, and the dermis (D) are clearly distinguished. With the longitudinal imaging system, we have imaged the skin of a volunteer in the region of the forearm (Figure 7(b)). For this experiment, the forearm of the volunteer is just put on the focalization line of the cylindrical lens. The probe beam is incident from the top of the figure. The lateral resolution, limited by the numerical aperture of the imaging lens is $\sim$ 30 μm and the depth resolution is $\sim$ 5 μm into the tissues, limited by the laser pulse duration. At the surface of the skin, the stratum corneum (sc) is clearly visible, represented by the high intensity band. Then, the rest of the epidermis (E) is observed, represented by the darker band. Finally appears a brighter area corresponding to the underlying dermis (D). Especially, the epidermal-dermal junction is clearly identified.

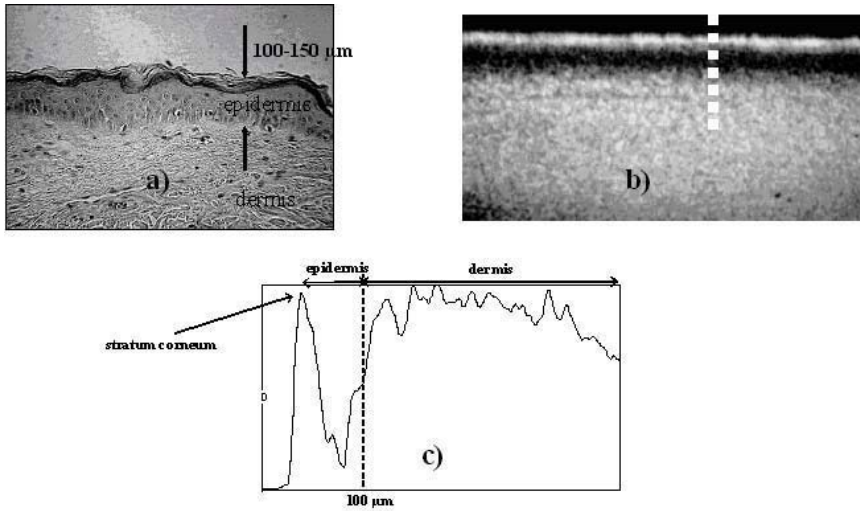

Figure 7. (a) HE histology of human skin. Image size: (0.53×0.4) mm^2; (b) Longitudinal image of an *in vivo* human skin in the region of the forearm. Image size: (1.5×0.6) mm^2; (c) Linear depth profile of the longitudinal image along the line on (b). E: epidermis, sc: stratum corneum, D: dermis.

An intensity profile along the line indicated in Figure 7(b) makes it possible to precisely measure the thickness of the epidermis at this position. The evolution of the image intensity along that line is plotted in Figure 7(c). The thickness of the epidermis is $\sim$ 100 μm at this position and internal structures can be observed inside the dermis at a depth of 40 μm below the interface. Then the intensity slowly changes in the dermis up to 400 μm in depth. Moreover, the signal intensity in the epidermis is lower than in the dermis, indicating that the probe light can propagate more easily in the epidermis than in the dermis. This shows that the scattering coefficient μ_s of the epidermis is smaller than that of the dermis, in agreement with previous studies concerning the optical properties of the human skin [15]. As the longitudinal imaging system makes it possible video rate imaging, the skin of the volunteer can be observed in real-time. Consequently, even if the volunteer moves his arm during the imaging session, the images appears still clear and well contrasted owing to the single laser shot acquisition of the images. On a practical point of view, this constitutes an important characteristic of the imaging system, since the patient does not need to be completely immobile during the imaging diagnosis.

4. CONCLUSION

In this paper, we have described some of the recent advances in real-time imaging of biological tissues, including coherence optical gating (Optical Coherence Tomography) and temporal optical gating. The devices are able to image at video rate highly scattering thick biological samples, in a backscattering configuration, and to produce longitudinal or transversal images with a micrometer resolution. The main improvement could consist of increasing the sensitivity of the detection to achieve imaging of tissues to several millimeters in depth.

References

[1] D. Huang, E.A. Swanson, C.P. Lin, J.S. Schuman, W.G. Stinson, W. Chang, M.R. Hee, T. Flotte, K. Gregory, C.A. Puliafito, and J.G. Fujimoto: Science **254** (1991) 1178.

[2] J.M. Schmitt: IEEE Journal of Selected Topics in Quantum Electronics **5** (1999) 1205.

[3] C. Yan and J.C. Diels: Appl. Opt. **31** (1992) 6869.

[4] A.M. Kowalevicz, T. Ko, I. Hartl, J.G. Fujimoto, M. Pollnau and R. Salathé: Opt. Express **10** (2002) 349.

[5] A.M. Rollins, M.D. Kulkarni, S. Yazdanfar, R. Ung-arunyawee and J.A. Izatt: Opt. Express **3** (1998) 220.

[6] T. Dresel, G. Häusler and H. Venzke: Appl. Opt. **31** (1992) 919.

[7] S. Bourquin, P. Seitz and R.P. Salathé, Opt. Lett. **26** (2001) 512.

[8] M. Laubscher, M. Ducros, B. Karamata, T. Lasser and R. Salathé: Opt. Express **10** (2002) 429.

[9] E. Beaurepaire, A.C Boccara, M. Lebec, L. Blanchot and H. Saint-Jalmes: Opt. Lett. **23** (1998) 244.

[10] L. Vabre, A. Dubois and A.C. Boccara: Opt. Lett. **27** (2002) 530.

[11] E. Bordenave, E. Abraham, G. Jonusauskas, N. Tsurumachi, J. Oberlé, C. Rullière, P.E. Minot, M. Lassègues and J.E. Surlève Bazeille: Appl. Opt. **41** (2002) 2059.

[12] E. Bordenave, E. Abraham, G. Jonusauskas, J. Oberle and C. Rulliere: Opt. Express **2** (2002) 35.

[13] E. Bordenave, E. Abraham, G. Jonusauskas, J. Oberlé and C. Rullière: Opt. Commun. **208** (2002) 275.

[14] F. Salin, P. Georges, R. Roger and A. Brun: Appl. Opt. **26** (1987) 4528.

[15] C.R. Simpson, M. Kohl, M. Essenpreis and M. Cope: Phys. Med. Biol. **43** (1998) 2465.

[16] E. Abraham, E. Bordenave, N. Tsurumachi, G. Jonusauskas, J. Oberlé, C. Rullière and A. Mito: Optics Letters **25** (2000) 929.

AUTHOR INDEX

LIST OF CONTRIBUTORS

Alexandr G. ANDERS, Faculty of Physics, Karazin Kharkov National University, 4 Svobody Sq., Kharkov 61077, Ukraine, e-mail: aanders@ilt.kharkov.ua

Valerie BRIOIS, LURE, Centre Universitaire Paris-Sud, BP34, 91898 Orsay Cedex, France, e-mail: briois@lure.u-psud.fr

Thomas CALLIGARO, Centre de Recherche et de Restauration des Musées de France, CNRS UMR-171, Palais du Louvre, 75041 Paris cedex 01, France, e-mail: thomas.calligaro@culture.gouv.fr

Koen CLAYS, Department of Chemistry, University of Leuven, University of Leuven, Celestijnenlaan 200D, B-3001 Leuven, Belgium, e-mail: koen.clays@fys.kuleuven.ac.be

Eric C. FAULQUES, Laboratoire de Physique Cristalline, Institut des Matériaux Jean Rouxel, 2 rue de la Houssinière, BP 32229, 44322 Nantes Cedex 03, France, e-mail: eric.faulques@cnrs-imn.fr

Vladimir P. GNEZDILOV, Verkin Institute for Low Temperature Physics and Engineering, Lenin Avenue 47, Kharkov, 61103 Ukraine, e-mail: gnezdilov@ilt.kharkov.ua

Victor G. IVANOV, Sofia University, Faculty of Physics, 5 J. Bourchier Blvd., BG 1164 Sofia, Bulgaria, e-mail: vgi@phys.uni-sofia.bg

Gediminas JONUSAUSKAS, Centre de Physique Moléculaire Optique et Hertzienne, Bordeaux 1 University, 351 Cours de la Libération, 33405 Talence, France, e-mail: g.jonusauskas@cpmoh.u-bordeaux1.fr

Gennadii V. KAMARCHUK, Verkin Institute for Low Temperature Physics and Engineering, Lenin Avenue 47, Kharkov, 61103 Ukraine, e-mail: kamarchuk@ilt.kharkov.ua

Victor A. KARACHEVTSEV, Verkin Institute for Low Temperature Physics and Engineering, Lenin Avenue 47, Kharkov, 61103 Ukraine, e-mail: karachevtsev@ilt.kharkov.ua

Yaroslav Z. KHIMYAK, Molecular Materials Centre, Department of Chemistry, The University of Liverpool, Liverpool L69 7ZD, United Kingdom, e-mail: khimyak@liverpool.ac.uk

Andrei V. KRAVCHENKO, Faculty of Chemistry, V. Karazin Kharkov National University, 4 Svobody Sq., Kharkov 61077, Ukraine

Vladimir S. KURNOSOV, Verkin Institute for Low Temperature Physics and Engineering, Lenin Avenue 47, Kharkov, 61103 Ukraine, e-mail: kurnosov@ilt.kharkov.ua

Karina V. LAMONOVA, 72 R. Luxemburg St., Galkin Donetsk PhysTech Institute, 83114 Donetsk, Ukraine, e-mail: lamonova@kinetic.ac.donetsk.ua

Serge LEFRANT, Institut des Matériaux Jean Rouxel, 2 rue de la Houssinière, BP 32229, 44322 Nantes Cedex 03, France, e-mail: Serge.Lefrant@cnrs-imn.fr

Peter LEMMENS, Max Planck Institute for Solid State Research, Heisenbergstr. 1, D-70569 Stuttgart, Germany, email: p.lemmens@fkf.mpg.de

David J. LOCKWOOD, Institute for Microstructural Sciences, National Research Council, Ottawa, ON, Canada, e-mail: David.Lockwood@nrc.ca

Rimma N. LYUBOVSKAYA, Institute of Problems of Chemical Physics RAS, Chernogolovka, M.D., 142432, Russia, e-mail: lyurn@icp.ac.ru

Rustem B. LYUBOVSKII, Institute of Problems of Chemical Physics RAS, Chernogolovka, M.D., 142432, Russia, e-mail: rustem@icp.ac.ru

Miroslav MENŠIK, Institute of Macromolecular Chemistry, Academy of Sciences of the Czech Republic, Heyrovsky Sq. 2, 162 06 Prague 6, Czech Republic, e-mail: mensik@imc.cas.cz

Philippe MOREAU, Institut des Matériaux Jean Rouxel, UMR6502 CNRS - Université de Nantes, Laboratoire de Chemie des Solides, 2 rue de la Houssinière, BP 32229, 44322 Nantes Cedex 03, France, e-mail: Philippe.Moreau@cnrs-imn.fr

Ron NAAMAN, Department of Chemical Physics, Weizmann Institute of Science, Rehovot 76100, Israel, e-mail: ron.naaman@weizmann.ac.il

Alexandr N. OGURTSOV, Verkin Institute for Low Temperature Physics and Engineering, Lenin Avenue 47, Kharkov, 61103 Ukraine, e-mail: ogurtsov@ilt.kharkov.ua

Yurii G. PASHKEVICH, 72 R. Luxemburg St., Galkin Donetsk PhysTech Institute, Donetsk, 83114 Ukraine, e-mail: pashkevi@kinetic.ac.donetsk.ua

Dale L. PERRY, Lawrence Berkeley National Laboratory, University of California, Berkeley, CA 94720, USA, e-mail: dlperry@lbl.gov

Alexei V. PESCHANSKII, Verkin Institute for Low Temperature Physics and Engineering, Lenin Avenue 47, Kharkov, 61103 Ukraine, e-mail: peschansky@ilt.kharkov.ua

Marina N. POPOVA, Institute of Spectroscopy, Russian Academy of Sciences, 142190 Troitsk Moscow region, Russia, e-mail: popova@isan.troitsk.ru

Alexandr P. POSPELOV, National Technical University "Kharkov Polytechnical Institute", Kharkov, Ukraine, e-mail: pospelow@kpi.kharkov.ua

Eugene Ya. SHERMAN, Institute for Theoretical Physics, RWTH-Aachen, 52056 Aachen, Germany, and Institute for Theoretical Physics, Karl-Franzens-University of Graz, A-8010, Graz, Austria

Alexandre A. SHVARTSBURG, USDoE Pacific Northwest National Laboratory, MS K8-98, Richland, WA 99352, USA, e-mail: alexandre.shvartsburg@pnl.gov

Bojan ŠOPTRAJANOV, Institute of Chemistry, Faculty of Science, “Sts Cyril and Methodius” University, Arhimedova 5, POB 162, MK-1000 Skopje, Macedonia, e-mail: bojan@manu.edu.mk

Igor K. YANSON, Verkin Institute for Low Temperature Physics, National Academy of Sciences of Ukraine, Lenin Avenue 47, Kharkov, 61103, Ukraine, e-mail: yanson@ilt.kharkov.ua

Andrei V. YEREMENKO, Institute for Low Temperature Physics, Kharkov, 61103 Ukraine, e-mail: andrerem@ilt.kharkov.ua

Petr V. ZINOVIEV, Verkin Institute for Low Temperature Physics and Engineering, Lenin Avenue 47, Kharkov, 61103 Ukraine

Sergey A. ZVYAGIN, National High Magnetic Field Laboratory, 1800 E. Paul Dirac Dr., Tallahassee, FL 32310, USA, e-mail: zvyagin@magnet.fsu.edu